Multi-Dimensional Point Magnetic Field Detection as the Basis for Integrated Current Sensing in Power Electronics

by

Muhammad H Alvi

A dissertation submitted in partial fulfillment of

the requirements for the degree of

Doctor of Philosophy

(Mechanical Engineering)

at the

UNIVERSITY OF WISCONSIN – MADISON

2020

Date of the final oral examination: 04/10/2020

The dissertation is approved by the following members of the Committee:

Jahns, Thomas M., Professor, Mechanical Engineering and Electrical & Computer Engineering

Sarlioglu, Bulent Associate Professor, Engineering Professional Development

Nellis, Gregory F., Professor, Mechanical Engineering

Venkataramanan, Giri, Professor, Electrical & Computer Engineering

Adamczyk, Peter G., Assistant Professor, Mechanical Engineering

Abstract

Increased power density and efficiency in power electronic systems require more compact and low-power current sensing. During recent years, strides have been made in utilizing 1-D Magnetoresistive (MR) Point Field Detector (PFD) array-based current sensing which is economical, compact, galvanically-isolated, and low in power consumption. However, PFD-based multiphase current sensing requires custom-designed conductors and precisely positioned PFDs which are vulnerable to disturbances caused by other nearby field sources.

The objective of this research is to develop methodologies to integrate multi-dimensional PFD-based current sensing into high-density Si and SiC power modules, three-phase busbars, and cables. Detecting the 2-D and 3-D spatial magnetic fields reduces the need for PFD arrays by providing the degrees of freedom via the field components in orthogonal dimensions. However, this multi-dimensional magnetic field in power-dense environments with multiple currents is highly cross-coupled and experiences frequency-dependent variations due to skin and proximity effects.

A multi-dimensional field decoupling methodology is developed to extract current information from cross-coupled magnetic field vectors in three-phase systems. This method, developed analytically, is demonstrated via simulation as well as experimentally to decouple and sense three-phase currents with <5% RMS error in power module leadframes, cables, and busbars using a single millimeter-scale 3-D MR PFD. Physics-based and neural network-based techniques have also been developed to reject and decouple disturbance fields from external sources.

Methodologies have also been developed to shape and analyze the multi-dimensional magnetic fields and to position PFDs for high-bandwidth current sensing. Conductor designs and

the use of the spatial vector fields is shown to enhance the current sensing bandwidth. Experimental tests of busbar current sensing using this approach have resulted in measured increases of the 5% bandwidth from under 500Hz to over 65kHz.

The research also focuses on integrating the 2-D and 3-D MR PFDs for multiphase current sensing into Si and SiC power modules. Field shaping inside power modules has been evaluated for integrated current sensing, and power module design guidelines have been established to enhance the multi-dimensional field shaping to achieve higher measurement bandwidths. These design guidelines address the interconnects, terminals, and baseplate and have been shown to have a negligible impact on the electrical or thermal parasitic characteristics of the power modules. Experimental evaluation of the SiC power module leadframe design has demonstrated 5% bandwidths of over 100kHz.

Acknowledgements

Gratitude is noble, and I would like to show my gratitude to my Creator and His beloved for the kindness that leads to so much good in the world.

I dedicate this dissertation to Professor Robert D. Lorenz for being there for me since my freshman year of college, for advising and mentoring me. He gave me hope and guidance when things looked grim. His selflessness and dedication inspired me to complete this dissertation. I will always be thankful to you Sir!

I thank Professor Tom Jahns who very graciously advised me and guided me to the completion of this dissertation. His commitment, dedication and hard work never ceases to amaze me. I also thank Prof Giri Venkataramanan who genuinely cares for the students and is always available to help. I also want to extend my utmost gratitude to my committee Prof. Sarlioglu, Prof. Nellis, and Prof. Adamczyk for serving as kind and knowledgeable faculty and teachers.

I am blessed to be a part of the WEMPEC family. I thank Jim Sember for his important role in tough times and making this journey pleasant for me. I also thank Kyle Hanson and Kathy Young for their effort in making WEMPEC labs a well-oiled machine.

Special thanks to my fellow WEMPEC students who are my treasured friends. I especially acknowledge Minhao Sheng, Tyler Brauhn, and Bryan Dow for their help with the research. Thank you to all members of WEMPEC between 2012 and 2020. I would especially like to thank Aditya Ghule, Daniel Erato, Eugene Rush, Hang Dai, Hao Zeng, Hasan Hakim, Huthaifa Flieh, Le Chang, Marc Petit, Patrick Dills, Peter Killeen, Tim Polom, Tim Slininger, Yuying Shi, and Zheng Gao. I truly believe that without you I would not be where I am.

Working with the MR PFDs would have been impossible without the support of Sensitec. I would like to thank the very supportive engineers and physicists of Sensitec who helped me learn the details of MR and provided me with PFDs. I would also thank Fuji Electric and Ansys for their support of my research with both equipment and software.

My family has been very supportive of my educational endeavors. I would like to thank them for raising me to love science. I would like to mention my parents, brothers, aunts, uncles, cousins and my wife. All of them provided me the support I needed after long hours in basement.

It has been an awesome journey that I will cherish and treasure.

Table of Contents

Abstract ..... *i*
Acknowledgements ..... *iii*
Table of Contents ..... *v*
List of Figures ..... *xii*
List of Tables ..... *xxiii*
Nomenclature ..... *xxiv*
Introduction *1*
Motivation 1
Research Objective 3
Research Opportunities 3
Research Contributions 7
Chapter Summaries 8
Chapter 1 Review of the State-of-the-Art 13
1.1 Need for Current Sensing 13
1.2 Current Regulator 15
1.3 Current Sensing Requirements 17
1.4 Current Sensing for AC drives: 24
1.4.1 Resistance-based current sensing 24
1.4.2 Pilot current sensing 30
1.4.3 Faraday's Induction-based current sensing 31
1.4.4 Field-based current sensing 35
1.4.5 Magnetic field vector 36
1.4.6 Hall effect current sensors 37
1.4.7 Fluxgate 42
1.5 MR PFDs 44
1.5.1 Anisotropic Magnetoresistance 44
1.5.2 Giant Magnetoresistance 49
1.5.3 Tunnel Magnetoresistance 52
1.5.4 Development of multi-dimensional MR PFDs 53
1.5.5 Evaluation and Selection of MR PFDs 54
1.5.6 1-D GMR evaluation for current sensing 56
1.5.7 2-D TMR evaluation for current sensing 61
1.6 Decoupling 1-D Magnetic Fields 65

1.6.1 Orthogonal decoupling 65
1.6.2 1-D weighted field cross-coupling decoupling 66
1.6.3 1-D Disturbance field decoupling 69
1.7 Artificial Neural Networks 71
1.8 1-D PFD Array Around the Conductor 72
1.9 Gradiometer 73
1.9.1 Open loop gradiometer 74
1.9.2 Closed loop gradiometer 75
1.10 1-D Busbar Gradiometers 76
1.11 2-D Gradiometer 77
1.12 AMR-based Commercial Current Sensors 80
1.13 Skin and Proximity Effects 81
1.14 Magnetic Field Shaping Metrics 83
1.14.1 1-D Flat Bandwidth 83
1.14.2 2-D Flux Density 84
1.14.3 2-D 5% Flat Bandwidth 85
1.14.4 Optimization Function 86
1.15 1-D Magnetic Field Shaping Conductors 87
1.16 Power Module Integration/Packaging 90
1.16.1 Bondwires 94
1.16.2 Planar interconnects 94
1.16.3 Pressure interconnects 101
1.16.4 Direct bond copper and baseplate 102
1.16.5 Terminals 103
1.17 2-in-1 SiC Power Module Integrated Current Sensing 105
1.18 Three-Phase Closed Loop Inverter Operation with Integrated GMR PFDs 106
1.18.1 Half-bridge silicon power modules 106
1.18.2 Three-phase full-bridge silicon power modules 108
Research Opportunities Identified 109
Chapter 2 Multi-Dimensional Magnetic Field Shaping and Analysis 113
2.1 Principles of Multi-Dimensional Point Field Detection 113
2.1.1 2-D point field detection 114
2.1.2 3-D point field detection 115
2.2 Rotated 2-D Magnetic Field Shaping Metrics 115

2.2.1 Rotated 2-D flux density and 2-D 5% FBW....116
2.2.2 Hybrid 1-D flux density....119
2.2.3 Hybrid 1-D 5% FBW....120
2.3 3-D Magnetic Field Shaping Metric....121
2.3.1 3-D 5% FBW....121
2.4 FBW with Single Current Injection....123
2.5 FBW With Three-Phase Current Injection....126
2.6 Finite Element Analysis for FBW....126
2.7 Summarizing Remarks....130
Chapter 3 Multi-Dimensional Magnetic Field Decoupling Methodology....131
3.1 2-D PFD-based Current Sensing with Cross-Coupling Field Decoupling....131
3.1.1 Analytical 2-D field decoupling and sensing of two currents....132
3.2 3-D PFD-based Current Sensing with Cross-Coupling Field Decoupling....134
3.2.1 Condition to avoid singularity in 3-D field decoupling....134
3.2.2 Analytical 3-D decoupling and sensing of three non-parallel currents....137
3.2.3 FEA-based 3-D decoupling for three parallel conductors with a bend....140
3.3 Calibration of Decoupling Matrices....144
3.3.1 Signal injection calibration....144
3.3.2 Direct calibration....146
3.3.3 Hybrid calibration....148
3.4 Characteristics of Coupling Matrix....150
3.4.1 Relative Positions of PFD and Currents....150
3.4.2 Inversion, Conditioning and Scaling of Coupling....150
3.5 Summarizing Remarks....154
Chapter 4 Three-Phase Current Sensing in Busbars and Cables using Multi-Dimensional Field Decoupling....155
4.1 2-D and 3-D GMR PFD....155
4.1.1 Fabricated 2-D and 3-D GMR PFD....155
4.1.2 MR PFD excitation and signal conditioning....157
4.1.3 Evaluation of GMR PFD....159
4.2 Three-Phase Current Sensing in Straight Cables Using two 2-D PFDs....162
4.2.1 Experimental three-phase straight cable current sensing....166
4.3 Balanced Three-Phase Current Sensing in Straight Cables Using a 2-D PFD....170

4.3.1 Experimental two-phase straight cable current sensing 171
4.4 Three-Phase Current Sensing in Bent Cables Using a 3-D PFD 173
4.4.1 Experimental three-phase bent cable current sensing....176
4.5 Range of Three-phase Cable Current Sensing 178
4.6 Three-phase Current Sensing in Bent Busbars Using a 3-D PFD 180
4.6.1 Experimental three-phase bent busbar current sensing 181
4.7 Summarizing Remarks.... 185
Chapter 5 Disturbance Magnetic Field Decoupling 186
5.1 Disturbance Magnetic Fields Decoupling and Rejection 186
5.2 Characteristics of Disturbance Magnetic Fields 187
5.2.1 Analysis of magnitude of flux density....187
5.2.2 Analysis of flux density in particular direction 189
5.3 Full Modelling of 3-D Disturbance Decoupling.... 192
5.4 3-D Disturbance Decoupling with Zero Spatial Gradient 193
5.4.1 Decoupling of disturbances without time gradient (DC)....196
5.4.2 Decoupling of disturbances with time gradient (AC)....197
5.5 Decoupling Disturbances with Spatial Gradient.... 199
5.5.1 Conditioning of the decoupling 202
5.6 Experimental Results of Disturbance Decoupling.... 203
5.7 Disturbance Rejection Using Magnetic Materials 209
5.8 Experimental Results of Disturbance Rejection 212
5.9 Summarizing Remarks.... 215
Chapter 6 Neural Networks for Magnetic Field Decoupling....216
6.1 Introduction to Neural Networks 216
6.2 Neural Network-based 2-D Magnetic Field Decoupling.... 218
6.2.1 Analytical/Simulation Results 218
6.2.2 Experimental Results....222
6.3 Neural Network-based Disturbance Decoupling 224
6.3.1 Analytical/Simulation Results 224
6.3.2 Limits of neural network-based decoupling and comparison with physics-based decoupling 227
6.4 Summarizing Remarks.... 230

Chapter 7 Power Module Electromagnetic Analysis for 2-D PFD-based Current Sensing.....231

7.1 Three-Phase Full Bridge IGBT Power Module 231

7.2 Magnetic Field Analysis of the Power Module 232

7.3 Experimental 2-D PFD-based Power Module Integrated Current Sensing 236

7.3.1 Frequency response analysis of phase A magnetic field 236
7.3.2 Closed loop current control of three-phase currents 238

7.4 Power Module Electromagnetic Analysis to Increase the FBW 242

7.4.1 Skin and proximity effects in power module components 242

7.5 Techniques to Reduce Proximity Effect in Power Modules 245

7.5.1 Material of the baseplate 245
7.5.2 Comb laminations on the baseplate 246
7.5.3 Multiphysics evaluation of baseplate comb lamination 248

7.6 Experimental Evaluation of Baseplate Proximity Effects 250

7.6.1 100 A three-phase full-bridge Si power module 250
7.6.2 Frequency response analysis with cut baseplate 251

7.7 Terminal and Interconnect Design for 2-D PFD-based Current Sensing 254

7.7.1 Evaluation of 2-D field shaping terminal interconnect 254
7.7.2 Multiphysics evaluation of power module compared to the commercial module 257

7.8 Summarizing Remarks 260

Chapter 8 Full Bridge Power Module Design for 3-D Magnetic Field Shaping 261

8.1 Methodology for 3-D Magnetic Field Shaping in Power Modules 261

8.2 Terminal and Interconnect Design for 3-D PFD-based Current Sensing 263

8.2.1 Design Analysis in FEA 263

8.3 Experimental Evaluation of 3-D leadframes 272

8.3.1 Single-phase frequency response 272
8.3.2 Three-phase frequency response 275
8.3.3 Experimental three-phase current decoupling 278
8.3.4 Multiphysics evaluation of power module compared to the commercial module 281

8.4 Further Optimization of Leadframe Integrated Power Module 286

8.5 Summarizing Remarks 288

Chapter 9 SiC Power Module Design for High Bandwidth Integrated Current Sensing.....289

9.1 Half-bridge SiC MOSFET Power Module 289

9.2 DBC Stack-up 291

9.3 Magnetic Field Analysis of the Power Module 293

9.3.1 Experimental frequency response analysis 294

9.4 Comparison of Bondwire with Ribbon Interconnects for Field Shaping 297

9.5 Ribbon Interconnect and Terminal Design 300

9.5.1 Design Analysis in FEA 300
9.5.2 Experimental frequency response analysis 302

9.6 Leadframe Interconnect and Terminal Design 304

9.6.1 Design Analysis in FEA 304
9.6.2 Experimental frequency and time response analysis 307
9.6.3 Multi-dimensional bandwidth extension 310
9.6.4 Tolerance of positioning PFD.....313
9.6.5 Multiphysics evaluation of power module compared to the commercial module 316

9.7 Summarizing Remarks..... 320

Chapter 10 Bandwidth Extension using the Multi-Dimensionality of the Magnetic Field 321

10.1 Simulated Bandwidth Extension with Vector Magnetic Fields..... 321

10.2 Experimental Bandwidth Extension with Vector Magnetic Fields 326

10.3 Mathematics of Bandwidth Extension with X and Y Fields 329

10.4 Summarizing Remarks..... 331

Chapter 11 Conclusions, Contributions and Future Work.....332

11.1 Research Conclusions 332

11.1.1 Multi-Dimensional Magnetic Field Shaping and Analysis 332
11.1.2 Multi-Dimensional Magnetic Field Decoupling Methodology 332
11.1.3 Three-Phase Current Sensing in Busbars and Cables using Multi-Dimensional Field Decoupling 334
11.1.4 Disturbance Magnetic Field Decoupling 335
11.1.5 Neural Networks for Magnetic Field Decoupling 335
11.1.6 Power Module Electromagnetic Analysis for 2-D PFD-based Current Sensing.....336
11.1.7 Power Module Design for 3-D Magnetic Field Shaping 337

11.1.8 SiC Power Module Integrated High-Bandwidth Current Sensing.....338
11.1.9 Bandwidth Extension using the Multi-Dimensionality of the Field.....339
11.2 Research Contributions.....340
11.3 Recommended Future Work.....343
***References*.....346**

List of Figures

Fig. 1.1-1: Block Diagram of Indirect Field Oriented Control (IFOC)[11] 14
Fig. 1.1-2: Block Diagram of Direct Field Oriented Control (DFOC)[12] 15
Fig. 1.2-1: Current Regulators 17
Fig. 1.3-1: Schematic of 3-Phase inverter with AC machine 19
Fig. 1.3-2: Illustration of bandwidth metric in decibel and absolute units 20
Fig. 1.3-3: Definition of step response metrics [15] 21
Fig. 1.3-4: Open power module with components labelled [17] 23
Fig. 1.4-1: Model of shunt resistor with parasitic reactance [21] 26
Fig. 1.4-2: Commercial shunts designed for low inductance and high temperature stability from Isabellenhuette and Powertek [22][23][2] 27
Fig. 1.4-3: Power Modules with integrated current measuring shunts [26][27] 28
Fig. 1.4-4: Buck Converter with current sensing using the resistance of the MOSFET [3] 29
Fig. 1.4-5: Equivalent circuit of SenseFET [30] 30
Fig. 1.4-6: Schematic of current transformer [31] 31
Fig. 1.4-7: Commercial current transformer and closed loop current transformer with DC sensing [34], [35] 33
Fig. 1.4-8: Schematic of Rogowski Coil [3] 33
Fig. 1.4-9: Commercial Rogowski coil [38] 34
Fig. 1.4-10: Ansys Maxwell Field Solving method based upon physics [39] 35
Fig. 1.4-11: Hall effect illustration [1] 38
Fig. 1.4-12: Commercial Hall effect sensor with a core 39
Fig. 1.4-13: Experimental FRFs of commonly used commercial current sensors with respect to actual currents normalized to 100Hz value 40
Fig. 1.4-14: Schematic of closed loop Hall effect sensor [3] 41
Fig. 1.4-15: IC and schematic of open loop Hall effect sensor with gradiometer topology [44] 42
Fig. 1.4-16: IC and system schematic of closed loop fluxgate current sensor [47] 43
Fig. 1.5-1: Model of AMR strip [46] 44
Fig. 1.5-2: Characteristic curves for AMR with and without barber poles [48] 45
Fig. 1.5-3: AMR strip with Barber poles [48] 46
Fig. 1.5-4: AMR characteristic curve flipping [6] 47
Fig. 1.5-5: Characteristic curve dependence on barber poles and AMR bridge [6] 47
Fig. 1.5-6: Commercial AMR sensors from Honeywell [50] 48
Fig. 1.5-7: Typical output characteristic curve of commercial AMR [51] 48
Fig. 1.5-8: Multilayer GMR structure with layer magnetization determining the relative resistance [6] 50

Fig. 1.5-9: Spin Vale GMR structure with layer magnetizations determining the relative resistance [6] 51
Fig. 1.5-10: Wheatstone bridge of GMR elements [6] 51
Fig. 1.5-11: Layer structure of TMR element [46] 52
Fig. 1.5-12: Schematic of Sensitec GMR GF705 [28] 57
Fig. 1.5-13: Characteristic curve of Sensitec GMR GF705 [66] 57
Fig. 1.5-14: Current supply and signal condition circuit for GF705 [20] 58
Fig. 1.5-15: Voltage output of GMR GF705 as a function of temperature [7] 59
Fig. 1.5-16: Voltage output of shielded GMR GF705 as a function of temperature [7] 59
Fig. 1.5-17: GMR-based current measurement offset with and without temperature decoupling/compensation [7] 60
Fig. 1.5-18: Illustration of hysteresis in GF705 [66] 60
Fig. 1.5-19: Important parameters of GF705 as a function of swept range [64] 61
Fig. 1.5-20: 2-D TMR PCB [64] 62
Fig. 1.5-21: Schematic of TF952 [64] 62
Fig. 1.5-22: Characteristic curve of TF952 with best fit line and linearity error [64] 63
Fig. 1.5-23: FRF of the current input and TMR voltage output [64] 64
Fig. 1.5-24: Minor Loops (hysteresis) of TMR PFD [68] 64
Fig. 1.5-25: Dynamic hysteresis as a function of current [68] 64
Fig. 1.6-1: Three conductor and three PFD system [71] 66
Fig. 1.6-2: PFD output of the three conductor and three PFD system [28] 67
Fig. 1.6-3: Decoupled currents from three conductor and three PFD system [28] 68
Fig. 1.6-4: Weighted field decoupling in three-phase cables [72] 68
Fig. 1.6-5: Equations to model and decouple the disturbance [69][20] 70
Fig. 1.6-6: Error in decoupled current as a function of condition number of coupling matrix [20] 71
Fig. 1.7-1: A typical sigma neuron [73] 71
Fig. 1.9-1: Schematic of Magnetoresistance gradiometer 74
Fig. 1.10-1: Straight busbar MR gradiometer [64] 76
Fig. 1.10-2: AMR gradiometer voltage output with respect to current [64] 77
Fig. 1.11-1: Busbar to shape field gradients in 2-D with S cutout 78
Fig. 1.11-2: FRF of relationship between the current input and fabricated 2-D GMR output 79
Fig. 1.11-3: 2-D GMR gradiometer voltage outputs (X left, Y right) with respect to current [68] 79
Fig. 1.12-1: Illustration of Sensitec's commercial sensor with closed loop gradiometer and U shape primary conductor for creating field gradient [80] 80
Fig. 1.12-2: Commercial Sensitec AMR-based current sensors with magnets [6] 81

Fig. 1.13-1: Magnetic field distribution around rectangular conductor at 2 different frequencies [82] 82
Fig. 1.14-1: Definition of 5% flat bandwidth at 2 points [84] 83
Fig. 1.14-2: Flow chart of MATLAB script to calculate the flat bandwidth [28] 83
Fig. 1.14-3: Magnetic field distribution around rectangular conductor and FBW [82] 84
Fig. 1.14-4: X, Y components and 2-D flux around a rectangular cross section (4 x 1.5 mm) copper conductor with 1A DC current [64] 85
Fig. 1.14-5: X, Y and 2-D 5% FBWs for a rectangular cross section (4 x 1.5 mm) copper conductor with 1A current [64] 86
Fig. 1.14-6: Schematic of 2-D PFD positioning methodology [64] 86
Fig. 1.15-1: 5% flat bandwidth around bondwire with fixed copper sheet at the bottom and top copper sheet at variable distance [82] 88
Fig. 1.15-2: Model of regions of 5% flat bandwidth around bondwires [85] 89
Fig. 1.15-3: Leadframe for power module and magnetic field around it [67] 89
Fig. 1.15-4: Folded trace for high bandwidth and strength [87] 90
Fig. 1.16-1: Typical power module electrical topologies [88][89] 91
Fig. 1.16-2: Open power module with components labelled [17] 92
Fig. 1.16-3: Traditional power module with components labelled [90] 93
Fig. 1.16-4: Module topology with interconnects for connections 93
Fig. 1.16-5: Aluminum (left) and copper (right) bondwires 94
Fig. 1.16-6 Illustration of planar interconnects and of double sided cooling [99][100] 95
Fig. 1.16-7: Leadframes power modules for integrated sensing [7][8] 96
Fig. 1.16-8: Leadframes in latest power modules [102][103] 96
Fig. 1.16-9: Proposed copper clip technology [104] 97
Fig. 1.16-10: Semikron SKiN [107][108] 98
Fig. 1.16-11: Ribbon interconnect testing criterion [90] 99
Fig. 1.16-12: Ribbon interconnect testing and failure mechanisms [90] 99
Fig. 1.16-13: Planar packing based upon Siemens SiPLIT [109] 100
Fig. 1.16-14: 3-D planar interconnects [110] 100
Fig. 1.16-15: Transient liquid phase double sided DBC [99] 101
Fig. 1.16-16: Fuji Copper pin interconnect style [111] 101
Fig. 1.16-17: Pressure interconnect style [112] 102
Fig. 1.16-18: Infineon Press fit terminals 103
Fig. 1.16-19: Semikron spring terminals 104
Fig. 1.17-1: FRF of positive DC bus current in SiC module [115] 105
Fig. 1.18-1: Bandwidth of GMR PFD-based sensing [7] 106
Fig. 1.18-2: Overlay of three-phase currents and reference Hall sensors [7] 107
Fig. 1.18-3: Power Module with leadframes and GMR PFD locations [67] 108

Fig. 1.18-4: (a) Overlay of three-phase currents and reference Hall sensors and (b) errors [67] 108
Fig. 2.1-1: Illustration of magnetic field vector sum and X and Y components 114
Fig. 2.2-1: Rotation of XY coordinate system 117
Fig. 2.2-2: Rotated X, Y components and 2-D flux density around a rectangular cross section (4 x 1.5 mm) copper conductor with 1A quasi-DC current 117
Fig. 2.2-3: 45 deg rotated X, Y and 2-D 5% FBWs for a rectangular cross section (4 x 1.5 mm) copper conductor 118
Fig. 2.2-4: Hybrid 1-D magnetic flux density along direction V around a rectangular cross section (4 x 1.5 mm) copper conductor with 1A quasi-DC current 119
Fig. 2.2-5: Hybrid 1-D FBW around a rectangular cross section (4 x 1.5 mm) copper conductor 120
Fig. 2.3-1: Bent busbar to produce 3-D magnetic fields 122
Fig. 2.3-2: X, Y and Z 1-D FBW and 3-D FBW around a bent rectangular cross section (4 x 1.5 mm) copper conductor 122
Fig. 2.4-1: 5% FBW using real component and magnitude of phasor field around a three-phase cable for single-phase current injection 124
Fig. 2.4-2: 5% FBW in X-direction and symmetric direction around a three-phase cable for single-phase current injection 125
Fig. 2.6-1: Example FRFs of PFD output with respect to actual current normalized to 100 Hz value to show the 5% FBW error in response to minor FRF differences. 129
Fig. 3.1-1: Dual conductor single 2-D PFD sensing system 132
Fig. 3.1-2: X and Y output voltage of the 2-D PFD in the dual conductor system 133
Fig. 3.1-3: Analytically decoupled currents with a single 2-D PFD in the dual conductor system in simulation 133
Fig. 3.2-1: Three straight parallel conductors for 3-D decoupling 134
Fig. 3.2-2: Three straight parallel conductors for 3-D decoupling with rotated PFD 136
Fig. 3.2-3: Three straight non-parallel conductors for 3-D decoupling 137
Fig. 3.2-4: X, Y and Z output voltage of the 3-D PFD due the three straight non-parallel conductors 139
Fig. 3.2-5: Analytically decoupled currents with a single 3-D PFD in the non-parallel three-conductor system in simulation 139
Fig. 3.2-6: X, Y and Z output voltage of the 3-D PFD due the three straight non-parallel conductors carrying unbalanced currents 140
Fig. 3.2-7: Analytically decoupled currents with a single 3-D PFD in the non-parallel three-conductor system in simulation with unbalanced currents 140
Fig. 3.2-8: Three bent parallel conductors for 3-D decoupling with a 3-D PFD 141
Fig. 3.2-9: X, Y and Z output voltage of the 3-D PFD in the three bent parallel conductor system 143

Fig. 3.2-10: FEA-based decoupling of three-phase currents with a single 3-D PFD in the three bent parallel conductor system 143
Fig. 3.2-11: FEA-based decoupling of three-phase unbalanced currents with a single 3-D PFD in the three bent parallel conductor system 144
Fig. 3.4-1: Three bent parallel conductors for 3-D decoupling with 3-D PFDs close to the bend..... 152
Fig. 3.4-2: X, Y and Z output voltage of the 3-D PFD 2 from Fig. 3.4-1..... 152
Fig. 3.4-3: X, Y and Z output voltage of the 3-D PFD 3 from Fig. 3.4-1..... 153
Fig. 4.1-1: Fabricated 2-D GMR PFD PCB..... 156
Fig. 4.1-2: Fabricated 3-D GMR PFD PCB (pictures taken at different angle) 156
Fig. 4.1-3: Schematic of signal conditioning of X-GMR PFD output..... 158
Fig. 4.1-4: Signal conditioning and source excitation PCB..... 158
Fig. 4.1-5: GF705 characteristic curve with best fit line and linearity error 159
Fig. 4.1-6: Experimental FRF of GMR PFD output with respect to actual current normalized to 100 Hz value..... 160
Fig. 4.1-7: Step response of GMR PFD-based current sensing 161
Fig. 4.1-8: Triangle response of GMR PFD-based current sensing..... 162
Fig. 4.2-1: Three-phase cable with So16 IC containing 2-D PFDs 163
Fig. 4.2-2: Magnitudes of magnetic flux density around the cable at 0.1Hz 1A three-phase current injection..... 164
Fig. 4.2-3: 2-D 5% FBWs for three-phase cable with single-phase B current injection (left) and with three-phase current (right) 165
Fig. 4.2-4: X and Y output voltages of the 2-D PFDs due to the three-phase currents in the cable..... 168
Fig. 4.2-5: Experimental decoupling and sensing of three-phase currents with two 2-D PFD in a straight three-phase cable..... 169
Fig. 4.3-1: 2-D flux density for dual conductor system with 1A quasi-DC current in wire 1 170
Fig. 4.3-2: 2-D 5% FBW for dual conductor system with current injection in wire 1 170
Fig. 4.3-3: X and Y output voltages of the 2-D PFD due to the two phase currents 171
Fig. 4.3-4: Experimental decoupling and sensing of three-phase currents with a single 2-D PFD in two phase cable 173
Fig. 4.4-1: Copper core of bent three-phase cable with PFD on the field analysis plane..... 174
Fig. 4.4-2: Magnitude of the magnetic flux density on the analysis plane around the cable at 0.1Hz 1 A three-phase current injection 174
Fig. 4.4-3: Individual direction and 3-D 5% FBW for a bent three-phase cable with three-phase current injection..... 175
Fig. 4.4-4: Experimental setup of current sensing in three-phase cable 176
Fig. 4.4-5: X, Y and Z output voltages of the 3-D PFD due to the bent three-phase cable..... 177

Fig. 4.4-6: Experimental decoupling and sensing of three-phase currents with a single 3-D PFD in bent three-phase cable 178
Fig. 4.6-1: Stacked bent busbar to produce 3-D fields 180
Fig. 4.6-2: Magnitude of flux density and 3-D 5% FBW for stacked busbars with 1A three-phase current injection 181
Fig. 4.6-3: Experimental setup of current sensing in three-phase busbar 182
Fig. 4.6-4: X, Y and Z output voltages of the 3-D PFs due to the bent three-phase busbars 183
Fig. 4.6-5: Experimental decoupling and sensing of three-phase currents with a single 3-D PFD in bent three-phase busbar 184
Fig. 5.2-1: Magnitude of magnetic flux density around a straight circular cross-section of a wire carrying 1A quasi-DC current 188
Fig. 5.2-2: Magnetic flux density and its spatial gradient around a straight circular cross-section of a wire carrying 1A and 2A currents 189
Fig. 5.2-3: Y-direction magnetic flux density as function of X position around a straight circular cross-section wire carrying 1A currents 190
Fig. 5.2-4: Y-direction magnetic flux density as function of Y position around a straight circular cross-section wire carrying 1A currents 190
Fig. 5.2-5: X- and Y-direction magnetic flux density around a straight circular cross-section wire carrying 1A currents 191
Fig. 5.4-1: Bent three-phase conductors with two 3-D PFDs for current sensing with 3-D disturbance decoupling 194
Fig. 5.4-2: X, Y and Z output voltages of the two 3-D PFDs in the three bent parallel conductor system with superimposed disturbance having zero spatial gradient 196
Fig. 5.4-3: FEA-based decoupling of three-phase currents with two 3-D PFDs in the three bent parallel conductor system with superimposed disturbance 197
Fig. 5.4-4: FEA-based decoupling of disturbance magnetic field with two 3-D PFDs in the three bent parallel conductor system 197
Fig. 5.4-5: X, Y and Z output voltage of the two 3-D PFDs in the three bent parallel conductor system with superimposed AC disturbance having zero spatial gradient 198
Fig. 5.4-6: FEA-based decoupling of three-phase currents with two 3-D PFDs in the three bent parallel conductor system with superimposed AC disturbance 198
Fig. 5.4-7: FEA-based decoupling of AC disturbance magnetic field with two 3-D PFDs in the three bent parallel conductor system 198
Fig. 5.5-1: Three-phase conductors with five 2-D PFDs for current sensing in which phase C is considered a disturbance 199
Fig. 5.5-2: Decoupling two currents with no modelling of the disturbance 200
Fig. 5.5-3: Decoupling disturbances with multi-order model approximations 201
Fig. 5.5-4: Condition number of decoupling matrices used with a variable number of PFDs 203

Fig. 5.6-1: Experimental decoupling and sensing of two-phase current with a single 2-D PFD in straight parallel wires 204
Fig. 5.6-2: Experimental current sensing error as function of RMS current sensed with 2-D PFD 1 205
Fig. 5.6-3: Experimental current sensing error as function of RMS current sensed with 2-D PFD 2 205
Fig. 5.6-4: Experimental decoupling and sensing of two-phase current with and without implementation of disturbance decoupling 207
Fig. 5.6-5: Experimental current sensing error as function of RMS current sensed with 2-D PFDs 208
Fig. 5.6-6: Experimental current sensing error as function of RMS current sensed with 2-D PFDs with fine-tuned model of disturbance 209
Fig. 5.7-1: Illustration and magnetic circuit of shielding the PFD from magnetic disturbance using magnetic core material 210
Fig. 5.7-2: Schematic of magnetic circuit for calculating magnetic flux from the current being sensed 211
Fig. 5.7-3: Magnetic flux density around a wire carrying 1 A quasi-DC with and without disturbance and shielding 212
Fig. 5.8-1: Test set up of PFD-based current sensing with disturbance rejection using a core 213
Fig. 5.8-2: Experimental PFD-based current sensing with disturbance rejection using magnetic core material 213
Fig. 5.8-3: FFT of PFD-based current sensing with and without disturbance rejection using magnetic core material 214
Fig. 6.1-1: Illustration of a neural network 217
Fig. 6.1-2: Neural network training tool on Matlab 218
Fig. 6.2-1: Feedforward neural network on Matlab for 2-D field decoupling 219
Fig. 6.2-2: Neural network-based 2-D field decoupling on a simulated data set 220
Fig. 6.2-3: Neural network-based 2-D field decoupling on unbalanced simulated data set 221
Fig. 6.2-4: Neural network-based decoupling on simulated data set with superimposed disturbance 221
Fig. 6.2-5: Neural network-based 2-D field decoupling on experimental data 222
Fig. 6.2-6: Neural network-based 2-D field decoupling on unbalanced experimental data set 223
Fig. 6.3-1: Illustration of currents and PFDs used in the neural network-based decoupling 225
Fig. 6.3-2: Neural network on Matlab for disturbance decoupling 225
Fig. 6.3-3: Neural network-based disturbance decoupling on simulated data 226
Fig. 6.3-4: Neural network-based disturbance decoupling on simulated data 227
Fig. 6.3-5: Neural network-based disturbance decoupling on simulated data 229
Fig. 7.1-1: Three-phase full-bridge power module for integrated current sensing 232

Fig. 7.2-1: X, Y, and Z flux density on analysis plane for 6A quasi-DC phase C injection..... 233
Fig. 7.2-2: 5% FBW on the analysis plane for phase C current..... 234
Fig. 7.2-3: 2-D flux density and 2-D 5% FBW on analysis plane for phase C injection..... 235
Fig. 7.3-1: Test setup for measuring the frequency response function of the magnetic field (PFD outputs) with respect to actual currents..... 236
Fig. 7.3-2: Electric schematic of power amplifier and power module setup for current injection to measure the FRFs of the PFD outputs..... 237
Fig. 7.3-3: Experimental FRFs of PFD outputs (close to phase A terminal) with respect to actual current normalized to 100 Hz value. 238
Fig. 7.3-4: Dynamometer, test inverter and load inverter tower with controller and protection circuitry..... 239
Fig. 7.3-5: Closed loop control using experimentally decoupled currents with three 2-D PFDs integrated in three-phase power module used as test machine inverter. (ω^*= 17.7 rad/s)..... 241
Fig. 7.3-6: Closed loop control using experimentally decoupled currents with three 2-D PFDs integrated in three-phase power module used as test machine inverter (ω^*= 35.3 rad/s)..... 242
Fig. 7.4-1: Typical power module structure [90]..... 243
Fig. 7.4-2: 5% 2-D FBW on the analysis plane for phase C (right most terminal) with eddy effect elimination..... 244
Fig. 7.4-3: Eddy Currents in baseplate at 0 deg wrt to 6 A cosine phase C current at 1kHz..... 244
Fig. 7.5-1: 5% 2-D FBW on the analysis plane for phase C with AlSiC baseplate..... 246
Fig. 7.5-2: Comb like laminated baseplate in the three-phase full-bridge power module..... 247
Fig. 7.5-3: 5% 2-D FBW on the analysis plane for phase C with comb laminated baseplate 248
Fig. 7.5-4: Thermal FEA of regular and comb laminated (simplified) power module with max temperature programmed to be the thermal resistance from IGBT chip to bottom of the baseplate..... 249
Fig. 7.6-1: Three-phase full-bridge Si power module for evaluation of the impact of baseplate on field shaping..... 251
Fig. 7.6-2: Three-phase full-bridge power module with its baseplate milled off..... 252
Fig. 7.6-3: Three-phase full-bridge power module with GMR PFD inside it..... 252
Fig. 7.6-4: Experimental FRFs of GMR PFD output with respect to actual current in the phase terminal of power module with regular baseplate and cutout baseplate normalized to 100 Hz values..... 253
Fig. 7.7-1: Phase B and C leadframes in three-phase full-bridge power module for 2-D PFD-based current sensing..... 255
Fig. 7.7-2: 2-D flux density and 2-D 5% FBW of phase B and C leadframe in the power module..... 256
Fig. 7.7-3: Parasitic electric properties of half-bridge power module..... 258

Fig. 8.2-1: Phase A, B, and C leadframes in three-phase full-bridge power module for 3-D PFD-based current sensing 264
Fig. 8.2-2: Flux density around the leadframes on the analysis plane in Fig. 8.2-1 for 0.1 Hz 3A three-phase currents 265
Fig. 8.2-3: 5% FBW around the leadframes on the analysis plane in Fig. 8.2-1 for balanced three-phase current injection 266
Fig. 8.2-4: 5 deg phase FBW around the leadframes on the analysis plane in Fig. 8.2-1 for three-phase currents injection 267
Fig. 8.2-5: 1-D 5% FBW around the leadframes on the analysis plane in Fig. 8.2-1 for single-phase current injection 268
Fig. 8.2-6: 3-D 5% FBW around the leadframes on the analysis plane in Fig. 8.2-1 for single-phase currents injection 269
Fig. 8.2-7: 5% FBW around the leadframes on the analysis plane in Fig. 8.2-1 for balanced three-phase current injection 270
Fig. 8.2-8: 5% FBW around the leadframes on the analysis plane in Fig. 8.2-1 for balanced three-phase current injection 271
Fig. 8.3-1: Fabricated 3-D leadframes with the 3-D PFD placed in the middle 272
Fig. 8.3-2: Experimental FRFs of GMR PFD with respect to actual test currents in the leadframes normalized to 100 Hz values 273
Fig. 8.3-3: Experimental FRFs of GMR PFD with respect to actual test currents in the leadframes above the laminated baseplate normalized to 100 Hz values 274
Fig. 8.3-4: Experimental FRFs of 3-D GMR PFD for three-phase currents in the leadframes above a 15mm laminated baseplate with respect to actual test currents normalized to 100 Hz values 276
Fig. 8.3-5: Experimental FRFs of 3-D GMR PFD for three-phase currents in the leadframes above a 10mm laminated baseplate with respect to actual test currents normalized to 100 Hz values 277
Fig. 8.3-6: Experimental FRFs of 3-D GMR PFD for three-phase currents in the leadframes without a baseplate with respect to actual test currents normalized to 100 Hz values 277
Fig. 8.3-7: X, Y and Z output voltages of the 3-D PFD placed in the 3-D leadframes 278
Fig. 8.3-8: Experimental decoupling and sensing of three-phase currents with a single 3-D PFD in 3-D leadframes 279
Fig. 8.3-9: Experimental decoupling and sensing of three-phase currents with a single 3-D PFD in 3-D leadframes at fault condition 280
Fig. 8.3-10: Thermal FEA of regular and laminated (simplified) power module with max temperature programmed to be the thermal resistance from IGBT chip to bottom of the baseplate 282
Fig. 8.3-11: Ratio of FRFs of thermal impedance of power modules with and without comb laminations 283
Fig. 8.3-12: Parasitic electric properties of half-bridge power module 284

Fig. 8.4-1: 5% FBW around the leadframes on the analysis plane for balanced three-phase current injection with 10mm and 15 mm long lamination cuts 287
Fig. 9.1-1: Half-bridge SiC power module for integrated current sensing 289
Fig. 9.1-2: Rohm half-bridge power module current path and field analysis plane 290
Fig. 9.2-1: X-direction DC flux density, field phase lag at 100Hz and 1-D 5% FBW for stack-up 292
Fig. 9.3-1: X-direction flux density and 1-D 5% FBW around the phase terminal with 5 A current injection 293
Fig. 9.3-2: Electric schematic of power amplifier and power module setup for current injection to measure the FRFs of the PFD outputs 295
Fig. 9.3-3: Experimental FRFs of GMR PFD output with respect to reference current in SiC power module normalized to 100 Hz values 296
Fig. 9.3-4: Experimental FRFs of GMR PFD output with respect to reference current in SiC power module normalized to 100 Hz values at high FBW point. 297
Fig. 9.4-1: Three investigated versions of ribbon interconnect designs 298
Fig. 9.4-2: X-direction DC flux density and 1-D 5% FBW of power modules with various ribbon interconnect sizes 299
Fig. 9.5-1: Ribbon interconnect and its terminal in the power module 301
Fig. 9.5-2: Flux density for 5A, quasi-DC current in each terminal and 5% FBW for new ribbon interconnect terminal (left) and original bondwire terminal (right) 302
Fig. 9.5-3: Fabricated ribbon interconnect and its terminal 303
Fig. 9.5-4: Experimental FRFs of GMR PFD output for tested ribbon interconnect terminal with respect to actual test current normalized to 100 Hz values 304
Fig. 9.6-1: Leadframe interconnect and its terminal 305
Fig. 9.6-2: Flux density for 5A, quasi-DC current in each terminal and 5% FBW for leadframe interconnect terminal (left) and bondwire terminal (right) 306
Fig. 9.6-3: Fabricated leadframe interconnect and its terminal 307
Fig. 9.6-4: Experimental FRFs of GMR PFD for leadframe interconnect terminal with respect to actual test current normalized to 100 Hz values 308
Fig. 9.6-5: Experimental FRFs of GMR PFD for leadframe interconnected terminal with respect to actual test current calibrated every half a decade of frequency. 309
Fig. 9.6-6: Measured sinusoidal current in the leadframe interconnect terminal using GMR PFD 310
Fig. 9.6-7: Flux density for 5A, quasi-DC current in each terminal and 5% FBW for leadframe interconnect terminal (left) and bondwire terminal (right) at 38 deg from the X-direction 311
Fig. 9.6-8: Experimental FRFs of GMR PFD at 38 deg for leadframe interconnect terminal with respect to actual test current normalized to 200 Hz values 312

Fig. 9.6-9: Experimental X, Y and hybrid direction FRFs of GMR PFD leadframe interconnect terminal with respect to actual test current normalized to 200 Hz values 313
Fig. 9.6-10: Leadframe interconnect and its terminal with PFD path 314
Fig. 9.6-11: Experimental FRFs of GMR PFD for leadframe interconnect terminal with respect to actual test current (raw and normalized to 100 Hz values) at 10 points..... 315
Fig. 9.6-12: Experimental FRFs of GMR PFD for commercial power module with respect to actual test current normalized to 100 Hz values..... 316
Fig. 9.6-13: Typical thermal FEA of the Power module with baseplate step 317
Fig. 9.6-14: Parasitic electric properties of half-bridge power module 318
Fig. 10.1-1: Rectangular cross-section busbar with orthogonal analysis plane and XYZ coordinate axes 322
Fig. 10.1-2: X-direction flux density and hybrid 1-D flux density with 1A quasi-DC current around the busbar..... 323
Fig. 10.1-3: X-direction and hybrid 1-D 5% FBW around busbar 324
Fig. 10.1-4: Simulated FRFs of PFD outputs with respect to actual current normalized to 10 Hz value at the point shown in Fig. 10.1-3 325
Fig. 10.2-1: View of 2-D GMR PFD positioned in close proximity to rectangular busbar (3.1mm x 25.3mm). Not shown: Signal conditioning PCB, power amplifier, and Venable frequency response analyzer. 326
Fig. 10.2-2: Experimental FRFs of PFD output with respect to actual current normalized to 10 Hz value at the point shown in Fig. 10.1-3 327
Fig. 10.2-3: Experimental FRFs of PFD outputs with respect to actual at to the point shown in Fig. 10.1-3..... 328
Fig. 10.3-1: Sine and cosine in the first quadrant 329
Fig. 10.3-2: Experimental FRFs of PFD outputs with respect to actual current normalized to 10 Hz at the point shown in Fig. 10.1-3 330

List of Tables

Table 1.4.1 Appropriate field detectors for frequency ranges [40][41] 36
Table 1.4.2 Appropriate field detectors for sensitivity 36
Table 7.7.1 Self and mutual inductances in nH 258
Table 7.7.2 Resistance in the power module in mΩ 259
Table 8.3.1 Self and mutual inductances in nH 284
Table 8.3.2 Resistance in the power module in mΩ 285
Table 9.6.1 Results of thermal FEA of regular and stepped baseplate power module 317
Table 9.6.2 Self and mutual inductances in nH 319
Table 9.6.3 Resistance in the power module in mΩ 319

Nomenclature

Symbol	Description
B	Magnetic flux density
C	Coupling coefficients
D	Decoupling coefficients
I	Current
L	Inductance
VB	PFD output voltage (due to Magnetic flux density)
C	Coupling matrix
D	Decoupling matrix
R	Rotation matrix
θ	Angle (spatial)
$\mathcal{R}$	Reluctance
ϕ	Magnetic flux
( )’	Quantity rotated in space
$( )_a$	Quantity related to phase A current (or current 1)
$( )_b$	Quantity related to phase B current (or current 2)
$( )_c$	Quantity related to phase C current (or current 3)
$( )_h$	Quantity in Hybrid direction
$( )_x$	Quantity in X direction
$( )_y$	Quantity in Y direction
$( )_z$	Quantity in Z direction

Abbreviations	Description
1-D	One-Dimensional
2-D	Two-Dimensional
3-D	Three-Dimensional
AC	Alternating Current
AMR	Anisotropic Magnetoresistive/Magnetoresistance
dB	Decibel
DBC	Direct Bond Copper
DC	Direct Current
FBW	Flat Bandwidth
FEA	Finite Element Analysis
FFT	Fast Fourier Transform
FRA	Frequency Response Analyzer
FRF	Frequency Response Function
GaN	Gallium Nitride
GMR	Giant Magnetoresistive/Magnetoresistance
IGBT	Insulated Gate Bipolar Transistor
MR	Magnetoresistive/Magnetoresistance
PCB	Printed Circuit Board
PFD	Point Field Detector
PWM	Pulse Width Modulation
Si	Silicon
SiC	Silicon Carbide
SNR	Signal-to-Noise Ratio
TMR	Tunnel Magnetoresistive/Magnetoresistance
WBG	Wide bandgap

Introduction

Motivation

Current sensing is a key component of electric drives and power electronics converters for control and protection. In state-of-the-art industrial and traction drives, there are three major types of current sensing: resistance-based, Faraday induction-based, and magnetic field detection-based. The resistive methods are simple but have major drawbacks including thermal dependence, parasitic inductance, power loss, common-mode voltage, and the lack of galvanic isolation [1]. The latest shunts integrated into inverters have been designed to be thermally stable and have minimal inductance [2]. Faraday induction-based current sensing includes transformers with bulky and expensive cores. Rogowski coils which are air-core transformers make the sensors coreless but are also limited to AC systems [3].

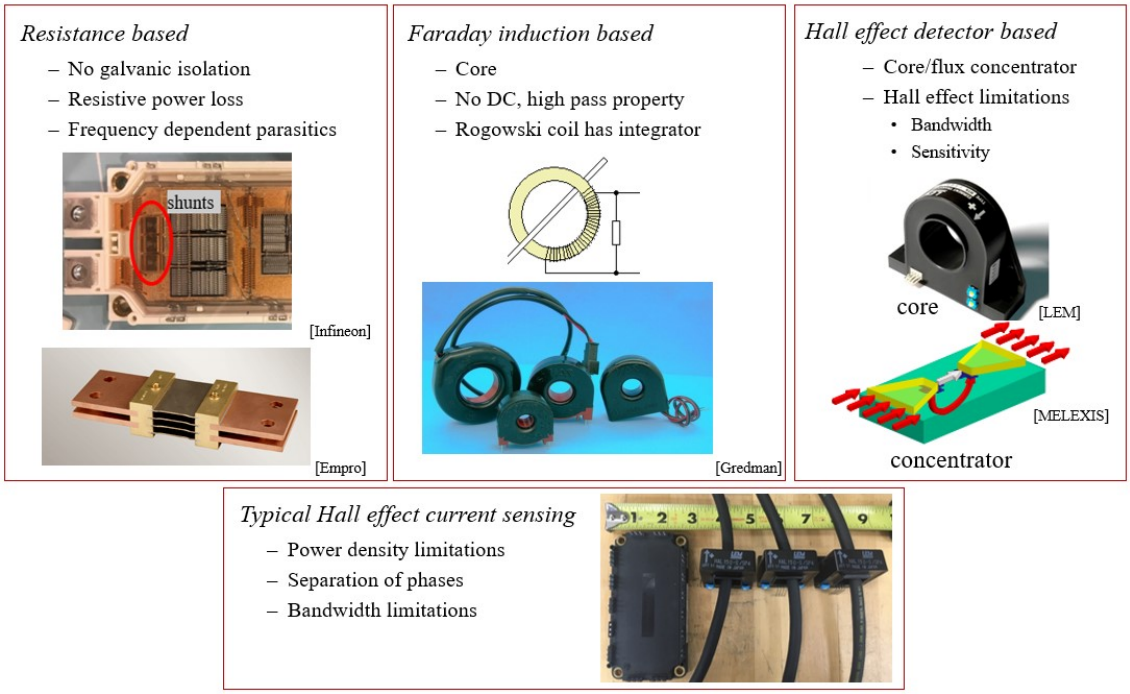

State-of-the-art current sensing technologies

Magnetic field detection methods based on Maxwell-Ampere's Law are widely adopted using Hall effect detectors. Hall effect-based current sensors are very reliable, but due to their low sensitivity, they generally require bulky cores that are an impediment to achieving high power density in power electronics [4]. All core-based current sensors require at least one turn of each individual phase conductor to distinguish its current value, leading to the need to separate the three-phase conductors in order to make individual phase current sensing possible.

Magnetoresistance (MR) Point Field Detectors (PFDs) are inexpensive submillimeter detectors that exhibit a change in resistance in the presence of magnetic fields. Their high sensitivity and bandwidth make them an appealing candidate for coreless current sensing. 1-D Anisotropic Magnetoresistive (AMR) PFDs are used in commercial sensors but require a special conductor structure for rejecting disturbances [5][6]. 1-D Giant Magnetoresistive (GMR) PFDs have been integrated into half-bridge as well as full-bridge Si and SiC power modules with cross-coupled field decoupling [7][8][9]. The integration of these PFD sensors into the modules yields a higher power density and reduction in cost, but it requires module customization and arrays of physically-spaced sensors to achieve high bandwidths and effective decoupling of cross-coupled fields. The strategic placement of PFDs causes manufacturing and placement complexity.

Multi-dimensional MR PFDs can be used to detect a magnetic field as a 3-D spatial vector or as a 2-D planar vector, unlike 1-D PFDs that only detect fields along a single axis of sensitivity. Sensing the 2-D and 3-D spatial fields reduces the need for PFD arrays by providing the degrees of freedom corresponding to the magnetic field components in different dimensions (i.e., orthogonal directions). The goal of this work is to develop the methodologies and design guidelines that are necessary to enable high-bandwidth current sensing in high density power electronic systems using multi-dimensional PFDs.

Research Objective

The major objective of this research is to develop integrated current sensing methodologies for power electronics using multi-dimensional Magnetoresistive (MR) Point Field Detectors (PFDs). To increase the power density of electromechanical systems, it is imperative to achieve high-bandwidth, compact, low-power, and galvanically-isolated current sensing. Integrated current sensing using magnetic field detectors provides this opportunity. In this work, methodologies are developed for 2-D and 3-D MR PFD-based integrated current sensing in power electronic busbars, cables, and power modules. Furthermore, design guidelines are developed for power electronic modules to enable the integration of PFD-based current sensing.

Research Opportunities

- **Methodology to shape, analyze and utilize magnetic fields in multi-dimensions**

State-of-the-art point field detector-based current sensing is based on magnetic field detection along a single axis. With the development of 2-D MR PFDs and the emerging development of 3-D MR PFDs, there is a significant research opportunity to characterize and shape magnetic fields in power electronic modules, busbars, and cables in multi-dimensions. New metrics are required for defining the suitability of a point in space for multi-dimensional MR PFD placement. These metrics are also needed to design and optimize conductors for high-bandwidth multi-dimensional field shaping while reducing the impact of skin and proximity effects.

Furthermore, the magnetic field is a spatial vector that can be detected along any single direction in space. There is a research opportunity to study fields as a spatial vector and identify directional axes least affected by frequency-dependent skin and proximity effects in order to increase access to high flat-bandwidth regions in power electronics.

- **Methodology to decouple cross-coupled fields in multi-dimensions at a point in space**

There is a major research opportunity to expand the 1-D magnetic field decoupling technique demonstrated in the literature to multi-dimensions. Information can be lost if the magnetic field is sensed as a single dimensional quantity. Hence, there is a need to develop physics-based methods to extract information about multiple currents from the cross-coupled 3-D magnetic field at a point.

1-D PFDs rely on spatial distances between them to detect unique information in the magnetic fields from multiple currents, thereby providing the basis for decoupling. Multi-dimensional PFDs may be able detect the unique information in the orthogonal field dimensions as an alternative to spatial distances. Physics- and mathematics-based investigation needs to find singularity constraints of multi-dimensional field decoupling. The identification of conditions where orthogonal components of the magnetic field provide unique information about multiple currents are desired to form a non-singular sensing system. A non-singular multi-dimensional current sensing system can be used to reduce the number of PFDs and the sensing footprint required to achieve high performance in interphase and disturbance decoupling, particularly inside high power density modules.

There is also an opportunity to investigate the use of machine learning algorithms like neural networks to implement cross-coupled field decoupling. Neural networks have gained popularity for many linear and non-linear mapping problems. Field decoupling can be classified as a linear input to output mapping problem for which neural networks can be used. Neural networks can eliminate the calibration steps in decoupling and provide immunity from predictable errors.

- **Methodologies for rejecting/decoupling external magnetic disturbances**

There is a research opportunity to develop methods to reduce the impact of uncalibrated magnetic disturbances on PFD-based current sensing. The field decoupling methodology

decouples fields from currents whose positions are fixed and field outputs are calibrated. However, in real systems, there is a possibility of disturbance fields being superimposed on the fields generated by the currents being sensed, leading to the current measurement errors. Methodologies are needed to either model and decouple these disturbances or to reject them altogether.

- **Technique for three-phase current sensing using a single sensor in conventional conductors without phase separation**

There is an opportunity to develop a technique to sense three-phase currents by integrating a single multi-dimensional MR PFD into three-phase cables and busbars. Typically, for a galvanically-isolated current sensing system, wires carrying individual phase currents are wrapped around their respective cores or passed through their respective field-shaping structures, both of which can compromise the desired power density performance metrics in power electronics. A multi-dimensional PFD-based current sensing technique for three-phase cables and busbars accounting for the bandwidth, range, and cross-coupling decoupling of magnetic fields needs to be developed. Without requiring phase conductor separation or specialized cores, this technique holds potential to increase the power density.

- **Design methodology for power module integration of multi-dimensional MR PFD-based current sensing**

There is a major opportunity to develop a three-phase power module with high bandwidth, multi-dimensional field shaping to implement PFD-based current sensing. In the literature, integration of PFDs has been demonstrated in power modules that have special 1-D leadframes. 2-D and 3-D PFDs can reduce the number of PFDs required to implement multiphase current sensing but require specialized power module interconnects to shape fields in multi-dimensions. Design recommendations are needed for Si and SiC three-phase full-bridge power modules with

high-bandwidth integrated current sensing functionality and without degrading the module performance in terms of inductance and thermal characteristics. The outcome of these design recommendations can improve the density of the power electronics system.

As a preliminary step to power module design, there is a need for a holistic electromagnetic analysis of commercial power modules. Field analysis of typical conductive structures including terminals, interconnects, direct-bond copper (DBC) substrates, and baseplates in commercial power modules need to be conducted to identify their impact on high-bandwidth and high-fidelity field shaping to suppress skin and proximity effects.

- **Design methodology for SiC power modules for very high bandwidth integrated current sensing**

There is a research opportunity to develop SiC power modules with integrated current sensing with bandwidths suitable for wide-bandgap (WBG) switching frequencies that are rapidly increasing. Field analysis of leadframes, ribbons, and bondwires needs to be conducted to design interconnects with low frequency dependence. As interest in applications of planar interconnects increase, design guidelines are needed for planar interconnects from the perspective of magnetic field shaping. These design guidelines need to encompass the conductive structures in the vicinity of the interconnects due to the electromagnetic field interactions in power-dense environments.

Research Contributions

This research has developed economical, efficient, galvanically-isolated, and high-bandwidth integrated current sensing methodologies for power electronics using multi-dimensional Magnetoresistive (MR) Point Field Detectors (PFDs). These methodologies are designed to detect the 2-D and 3-D spatial magnetic fields to reduce the need for PFD arrays and cores and to enable higher power densities in power electronic systems.

The following list presents the major research contributions of this dissertation. Details of each of these contributions are presented in the last chapter.

- Developed methodologies to shape and analyze multi-dimensional spatial magnetic fields for high-bandwidth current sensing.
- Developed a physics-based methodology to decouple the magnetic fields at a point in a multi-dimensional space.
- Developed a technique to sense three-phase currents in cables and busbars with a single PFD.
- Developed techniques to minimize the sensing error due to external magnetic field disturbances.
- Developed neural network-based methods for multi-dimensional field decoupling.
- Developed a design methodology for full-bridge power modules to enable integrated current sensing using multi-dimensional PFDs.
- Developed a design methodology for SiC power modules using planar interconnects for high-bandwidth integrated current sensing.

Chapter Summaries

- Chapter 1 explains the motivation for the research by establishing the need for current sensing in power electronics and by discussing state-of-the-art current sensing solutions in detail. The physics and development status of MR PFDs is explained and a literature review is provided for current sensing solutions using MR PFDs. Prior research on 1-D field shaping and decoupling methods needed for 1-D MR PFD integration in power electronics is outlined. Furthermore, conventional and newly-proposed power module packaging and integration methods are discussed. The outcome of this chapter is a summary of research opportunities presented at the end of the chapter.

- Chapter 2 conceptualizes the detection of magnetic field as a multi-dimensional vector quantity and explains the metrics used for the multi-dimensional magnetic field analysis. Methods are developed for the evaluation of magnetic fields in rotated coordinates and along various directions in a 2-D plane to achieve a high bandwidth and signal-to-noise ratio in sensing. 3-D magnetic field analysis metric to enable 3-D field detection is defined. The chapter also includes a discussion about the electromagnetic FEA for analyzing fields in the single-phase and the three-phase systems. The main purpose of this chapter is to develop a multi-dimensional magnetic field shaping and evaluation methodology to enable high bandwidth sensing using a PFD.

- Chapter 3 develops methodologies to decouple and sense multiple currents using cross-coupled multi-dimensional fields at a point. First, a physics-based method for analytical decoupling of the 2-D cross-coupled fields from two independent currents is summarized. This is followed by analytical decoupling of 3-D cross-coupled magnetic fields from three independent

currents. The physical and mathematical basis of singularity constraints are explained for 3-D decoupling of fields. The chapter also includes a detailed discussion of experimental calibration of decoupling matrices when analytical and FEA methods are not convenient. The main purpose of this chapter is to develop methodologies to sense multiple currents from a linearly cross-coupled multi-dimensional field at a point detected by a multi-dimensional PFD.

- Chapter 4 demonstrates multi-dimensional field decoupling for sensing three phase currents in convectional parallel conductors. A detailed steady-state and transient evaluation of a GMR PFD used for current sensing is presented. A multi-dimensional GMR PFD is positioned in regions of adequate FBW and then the 2-D or 3-D field decoupling methodology is used to decouple the cross-coupled vector field into three phase currents. Results are shown for the three-phase current sensing in straight cables with 2-D PFDs and in bent cables and busbars with a 3-D PFD. The main purpose of this chapter is to experimentally evaluate the multi-dimensional field decoupling methods in real systems.

- Chapter 5 develops methodologies to decouple disturbance magnetic fields from unknown sources that are not included in the coupling matrix calibration. Magnetic fields around currents are evaluated in detail and spatial models are presented for decoupling these fields. A zero-order model is shown to decouple the disturbance fields with zero spatial gradients. The chapter discusses the tradeoffs of higher-order disturbance decoupling and demonstrates adequate accuracy with zero-order decoupling. In addition to active decoupling, a passive disturbance rejection method with magnetic material is also proposed in this chapter. The main purpose of this chapter is to develop methodologies to reduce the impact of disturbances on PFD-based current sensing.

- Chapter 6 develops neural networks as an alternative to physics-based field decoupling. Neural networks are developed and trained in Matlab using built-in functions. The networks are designed to take cross-coupled X- and Y-direction fields detected by the PFD as inputs and compute the currents producing the fields. Neural networks are also evaluated for disturbance field decoupling in cases when there is a third current which is a source of disturbance that is not used in the training. This chapter also investigates the physics-based model inherent in the operation of the neural networks as well as the limits of the network functionality. The main purpose of this chapter is to explore the use of neural networks for extracting currents from cross-coupled fields from multiple sources.

- Chapter 7 investigates multi-dimensional field shaping of a three-phase full-bridge IGBT power module and identifies the components that need to be redesigned for high-bandwidth PFD-based current sensing. Evaluation of 2-D PFD-based current sensing in a commercial power module is used as basis for recommending design changes to the terminals, DBC-to-terminal interconnects, and the baseplate for field shaping. A power module design for 2-D PFD-based integrated current sensing is proposed at the end of this chapter. The main purpose of this chapter is to demonstrate the viability of integrated sensing and propose the design changes required for current sensing using multi-dimensional field decoupling inside the highly cross-coupled, power-dense, and fast-switching power modules.

- Chapter 8 develops the design methodology for three-phase full-bridge power modules to enable high bandwidth current sensing using a single 3-D PFD. DBC-to-terminal leadframes are designed to shape the three-phase current paths for producing a 3-D cross-coupled field containing information about all three currents. The frequency-dependent field behavior of the

leadframes is evaluated outside and then inside the power module using single-phase and three-phase current injection. Guidelines to enhance the bandwidth of current sensing by reducing proximity effects and taking advantage of the geometric size of the 3-D PFD are also discussed. A single 3-D PFD is used to decouple and sense three-phase currents in the power module leadframes using the multi-dimensional field decoupling method. The main purpose of this chapter is to develop the design methodology for a full-bridge power module which has a 3-D PFD integrated inside it for three-phase current sensing.

- Chapter 9 studies the field shaping of bondwires and various types of ribbon and leadframe interconnects for a half-bridge SiC power module. A ribbon and leadframe interconnect along with the terminal structure and stepped baseplate are designed to enable high-bandwidth integrated current sensing with planar packaging of the power module. Furthermore, two methods are proposed to extend the field sensing bandwidth in leadframes interconnects, which are also shown to be immune to the positioning tolerance of the PFD. The main purpose of this chapter is to develop high-bandwidth integrated current sensing methodologies suitable for SiC power modules.

- Chapter 10 presents a methodology to extend the bandwidth of current sensing by using the multi-dimensionality of magnetic fields. The field analysis metrics from Chapter 2 are used to analyze the magnetic field in directions with higher bandwidth around a rectangular busbar. The detailed physical as well as mathematical basis for multi-dimensional magnetic field detection is presented to extend the current sensing bandwidth. The main purpose of this chapter is to develop a methodology to extend current sensing bandwidth using magnetic field as a physical vector quantity.

- Chapter 11 presents the major conclusions and contributions for this work. It also includes recommendations for future research.

Chapter 1 Review of the State-of-the-Art

This chapter explains the motivation for this research by establishing the need for current sensing in power electronics and by discussing state-of-the-art current sensing solutions in detail. The physics and development status of MR PFDs is explained and a literature review is provided for current sensing solutions using MR PFDs. Prior research on 1-D field shaping and decoupling methods needed for 1-D MR PFD integration in power electronics is outlined. Furthermore, conventional and newly-proposed power module packaging and integration methods are discussed. The outcome of this chapter is a summary of research opportunities presented at the end of this chapter.

1.1 Need for Current Sensing

Current sensing is one of the most important building blocks of electromechanical systems which actively regulate current. Current sensors are used in a wide spectrum of power electronic applications. From high power utility applications to very low power DC-DC converters, current sensing has a wide spectrum of applications.

This work focuses on current sensing in AC drives in which current regulators are an integral part of motion control. Motion control is achieved via an outer velocity control loop in combination with an inner, lower energy, torque control loop. This torque control loop is sometimes referred to as the torque modulator and is tuned to a bandwidth of several times the velocity control bandwidth. This leads to a much faster torque modulator which can essentially be treated as a gain of unity under appropriate operating conditions.

Torque modulator can be achieved via two main classes of control, namely Direct Torque Control (DTC) and Field Oriented Control (FOC) [10]. FOC which has been extensively studied

and used by industry has many variants. These variants heavily rely on robust current regulation. Fig. 1.1-1 shows the general schematic of Indirect Field Oriented Control (IFOC) in induction machine. IFOC is a popular control strategy mainly due to the simplicity of its control algorithm. It does not use flux observers, due to which rotor flux is essentially open loop [11]. Due to the need for fast and accurate torque control, current regulator forms a central part of torque and rotor flux control. In Deadbeat-Direct Torque and Flux Control as well as deadbeat current regulator, current sensors are used to provide input to current observer.

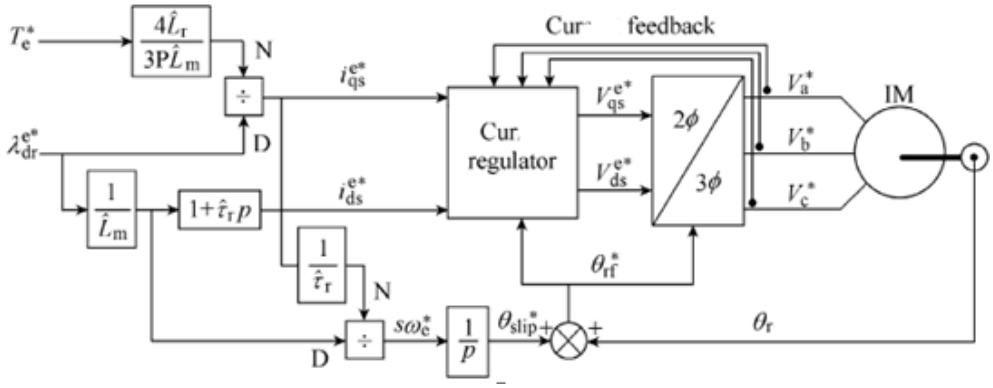

Fig. 1.1-1: Block Diagram of Indirect Field Oriented Control (IFOC)[11]

Another type of torque modulator uses the Direct Field Oriented Control (DFOC). Although this control allows for closed loop control of torque and rotor flux, it is more complex and costly to implement due to the need for a flux sensor or observer. Fig. 1.1-2 shows the schematic of a DFOC implementation. It must be noted that DFOC also relies on a current regulator.

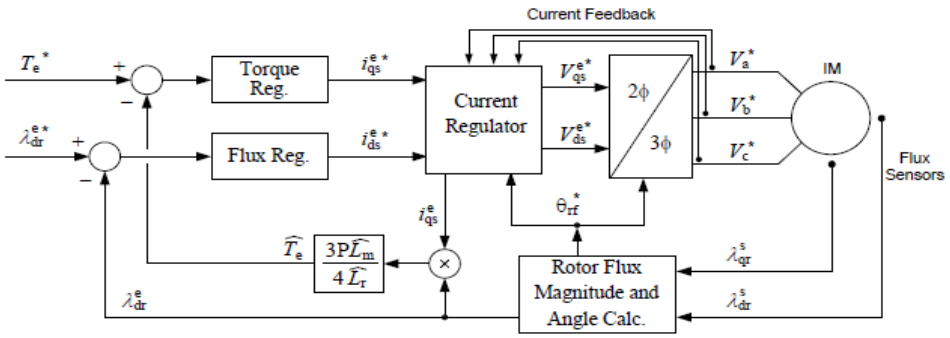

Fig. 1.1-2: Block Diagram of Direct Field Oriented Control (DFOC)[12]

1.2 Current Regulator

One of the most rudimentary forms of current regulators is the hysteresis or bang-bang current regulator. Hysteresis current regulators aim to keep the current error inside predefined error bands, thereby usually providing sufficient command tracking performance for certain application [10]. However, they have uncontrolled switching and nonlinearities which can be highly undesired. The PI current regulator (PICR) is usually used in synchronous frame to regulate the d- and q-axis current [10]. They are considered simple to implement and can in most cases achieve satisfactory results. Overtime PI has evolved to Cross-Coupling Decoupling PI Current Regulators which is parameter sensitive but yields superior performance over a range of excitation frequencies [13]. A further improvement on Cross-Coupling Decoupling PICR is the Complex Vector Current Regulator (CVCR) which is essentially a complex PICR with much less parameter sensitivity [14]. In purely discrete control theory, there are options of Deadbeat Current Regulator (DBCR) which converges in one-time step, provided feasible command trajectory, and Finite Settling Step Current Regulator (FSSC) which converges in a finite number of steps which are calculated using optimization control algorithm.

Each of the current regulators has tradeoffs between various aspects of performance, complexity and the need for accurate parameter estimation. However, all these current regulators need a current feedback for closing the loop. A few commonly used current regulators are shown in Fig. 1.2-1 to highlight the importance of current feedback. Current sensors are the ubiquitous and simplest form of current feedback.

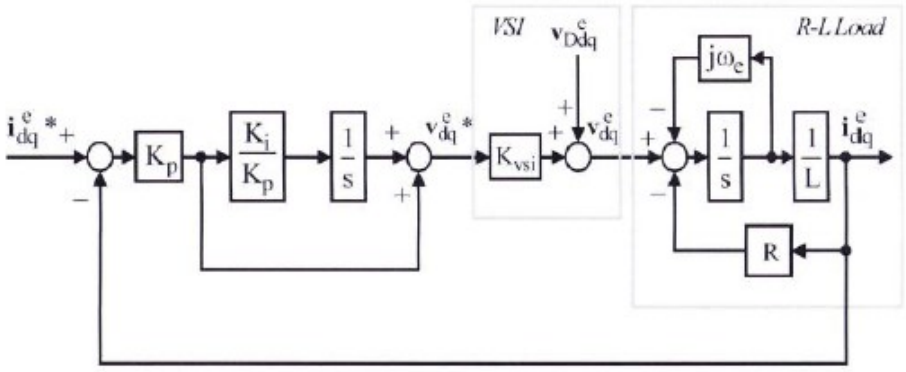

Block Diagram of PI Current Regulator for SMPMSM simplified to RL load [10]

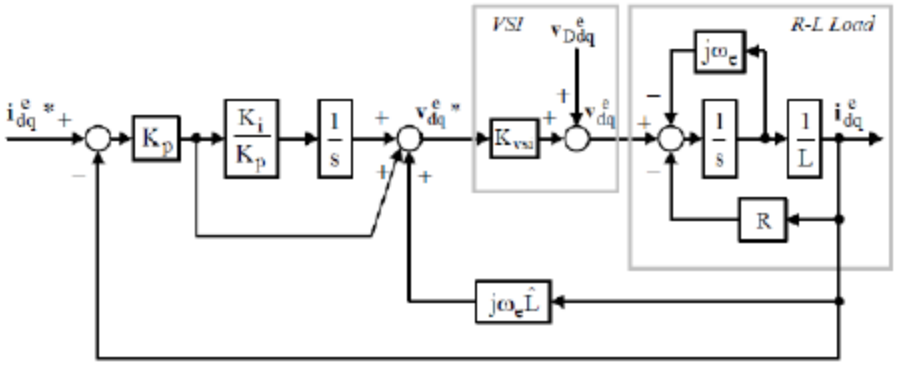

Block Diagram of Cross-Coupling Decoupling PI Current Regulator for SMPMSM simplified to RL load [13]

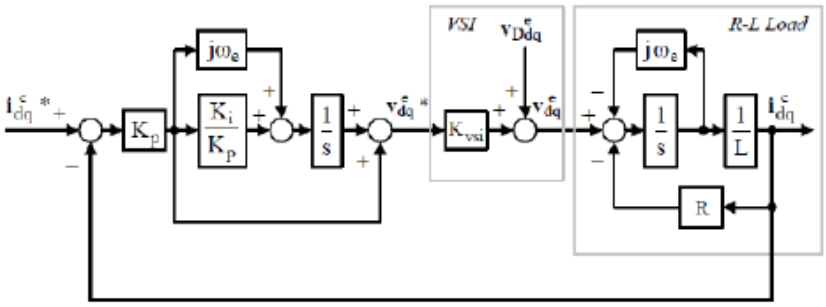

Block Diagram of Complex Vector Current Regulator for SMPMSM simplified to RL load [14]

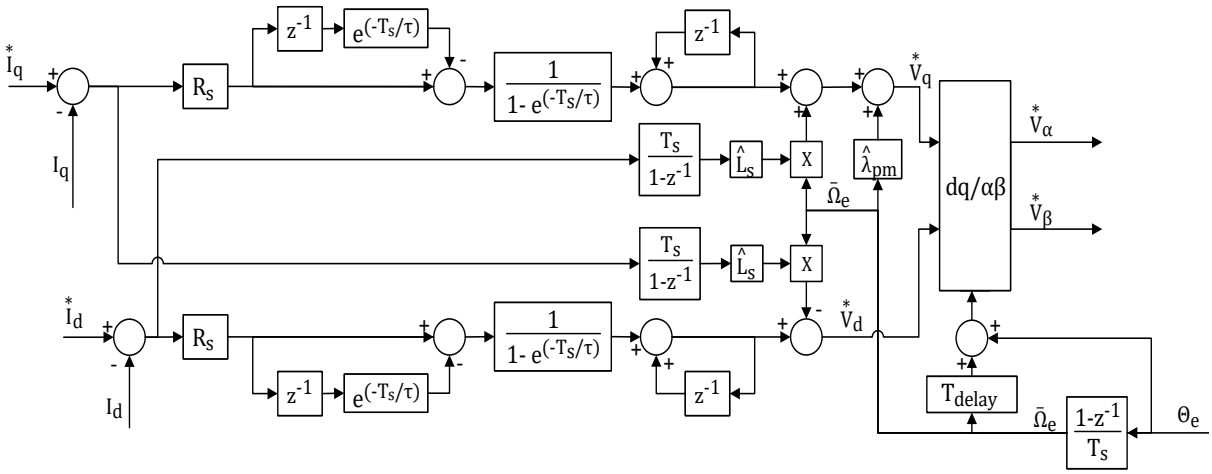

Block Diagram of Deadbeat Current Regulator for SMPMSM simplified to RL load

Fig. 1.2-1: Current Regulators

1.3 Current Sensing Requirements

Integration

The concept of integrated current sensing is very appealing. Integration makes systems simpler, smaller, and in the long run cheaper. It reduces the mechanical, electrical as well as firmware design effort. It also leads to sensing current very close to where it is transformed without the need of extra equipment. There has been significant integration effort in small power level

modules, but immense advantages can be achieved by also including the higher power levels where integration is not a focus yet. Integrating current sensing leads to the need of much more compact current sensing systems which are critical for future power density standards.

Module Design and Manufacture

Power module manufacturers are making efforts to increase the sensing functionality of the modules, but there are some inherent physics and engineering-based challenges. The most important challenge for sensing integration in power modules originates from the push for increased power density and multiphysics sensing in modules. Due to this, modules are getting smaller, space on DBC is expensive and pin count cannot be increased. The other challenge in integration emerges for financial side of production. Currently, power modules have a defined production process with high inertia. Sensing integration steps should not complicate or increase the price of production.

With the increased development of integrated current sensing, there are untapped opportunities in sensing of different currents including bond wire current, direct bonded copper (DCB) current, free-wheeling diode current, DC bus current, as well as the phase currents. All these contain valuable information and can be useful for R&D purposes but after a cost benefit analysis with present level of technology, the basic need is for phase currents. If the application device is an AC motor with neutral point, this requirement can be further reduced in some cases to two-phase sensing. Fig. 1.3-1 shows three-phase inverter and three-phase motor with neutral point.

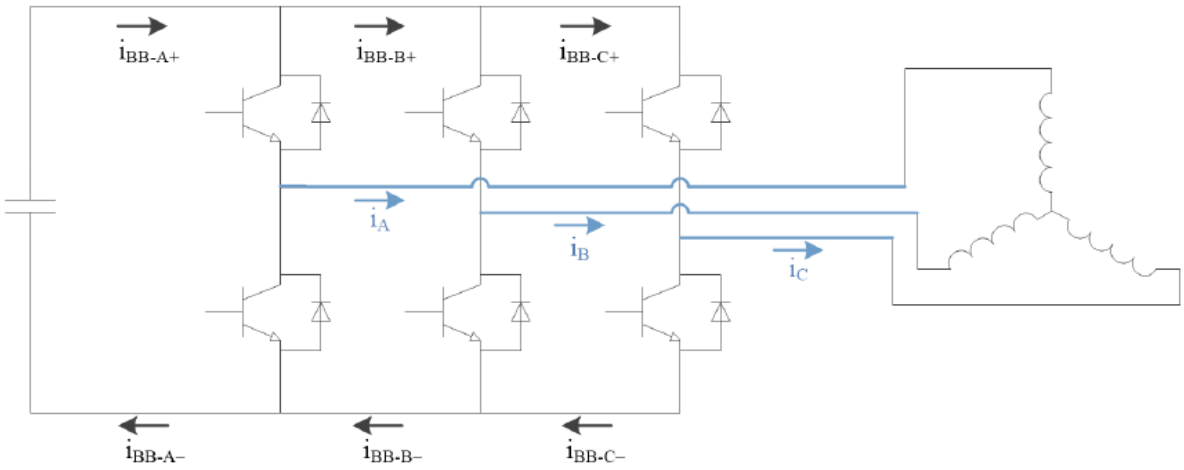

Fig. 1.3-1: Schematic of 3-Phase inverter with AC machine

Bandwidth

The bandwidth of the current sensor is one of the most important requirements. Bandwidth can have many far-reaching consequences due to which in most cases bandwidth is over specified. Generally, in commercial drives only fundamental frequency is of importance for current control. In the current market, the highest fundamental synchronous frequency is generally under 1.5kHz. This upper limit of synchronous frequency is expected to stay constant even as higher switching frequencies with Silicon Carbide and Gallium Nitride reduce switching losses. In the very long term, over some decades perhaps, the highest fundamental frequencies might increase as corresponding motors are designed.

The bandwidth required for 1.5kHz current sensing is upwards of 20kHz. The reason for using a 20kHz or higher bandwidth sensor is simply buried in the definition of -3dB bandwidth system. Fig. 1.3-2 shows the bode plot of 15.9 kHz first order system. The decibel and absolute gain plots describe that -3dB refers to 70% of DC value, whereas drive engineers are looking for 1% flat bandwidth specification. A sensor with bandwidth defined in 1% flat bandwidth of 1.5kHz is

sufficient for today's drive market. Another driver for bandwidth requirement is phase delay which should not exceed a few degrees.

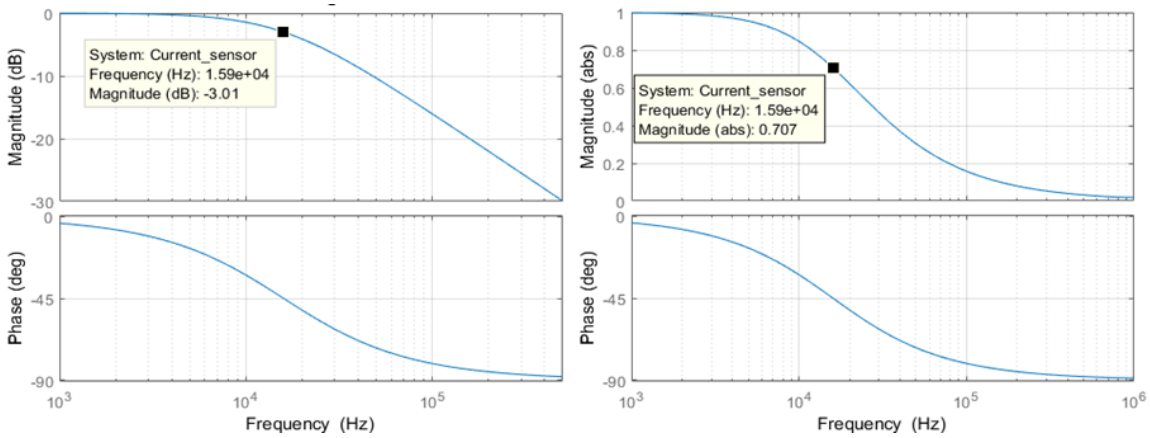

Fig. 1.3-2: Illustration of bandwidth metric in decibel and absolute units

Response Time

The response time is a key requirement of the sensor especially in over current detection. In most drive applications, to prevent permanent damage, the system needs to shut down within 5µs of over current occurrence. This leads to a tight requirement for over current detection of 1µs. Fig. 1.3-3 illustrates the time characteristics of the step current measurement. The most important one usually is the response time. For perfectly modeled dynamic systems, the pole, bandwidth and time constant are strictly physically and mathematically related quantities. However, due to complex nature of sensors, these quantities still have similar relationship to first or second order systems.

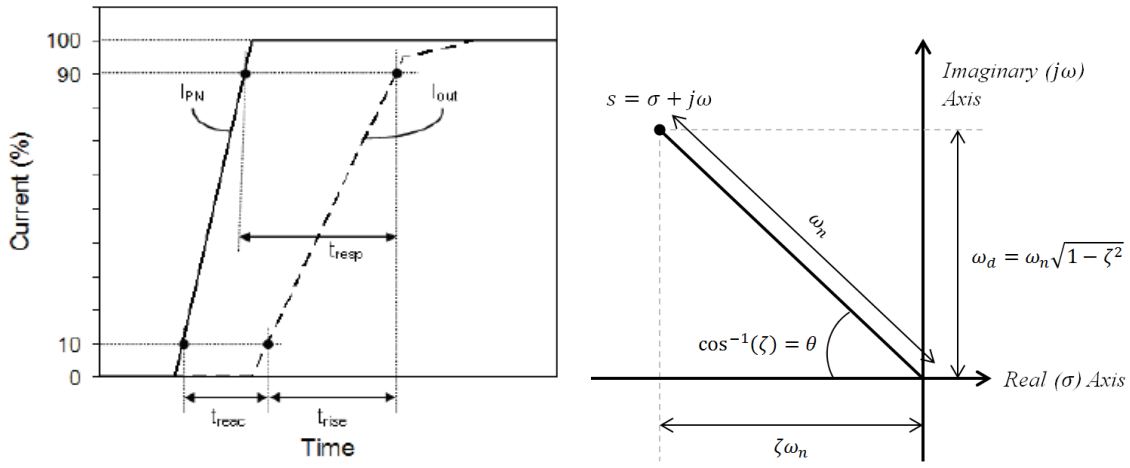

Fig. 1.3-3: Definition of step response metrics [15]

Range

The range for current sensing is entirely application dependent, which reduces the engineering challenge of designing the sensors. This also leads to a natural market division for current sensors based upon there nominal values. Current sensors are expected to be accurate up to 3 time the nominal value. They should, however, be able to detect the current up to 5 times the nominal value with lesser accuracy.

Digital Output

The current sensor can be either digital or analog. However, due to more compatibility and, improved noise immunity, a digital output sensor is the preferred choice of the future.

Price

For better quality and integrated current sensors, customers are willing to pay slightly higher than the cost of separate modular current sensors like LEM. The baseline price for current sensing is set by the state-of-the-art integrated sensor which is shunt. Although the shunt itself is only a few cents, the system cost increases by up to $4 due to sigma delta and Sinc filters. A reasonably competitive price for integratable sensor would be $4 per phase. Price, however, is relative and

drive manufacturers might be willing to pay for enhanced functionality, robustness or simpler design integration effort.

Accuracy

For most applications, a combined accuracy of 2% is required. This combined accuracy includes linearity, gain, temperature drift and offset drift errors. Furthermore, the frequency dependency of sensor well under its bandwidth also induces error. However, the total sensing error is seldom qualified and if each source of error is at its worst the combined error can be higher. Additionally, to avoid significant quantization error due to digitization, a resolution of 16 bits is required. The accuracy must be guaranteed in normal operating range of -20 to 125℃. It must be noted that the normal operating temperature range mentioned here is based upon the ambient temperature in the power module. Depending upon the location of the current sensor in the power module and the module itself, the temperature requirement might increase.

Despite, the strict requirements set for the combined accuracy of the current sensing, it is well documented that electric drives remain stable with significant error [16]. In control course and lab, it is common to assume around 5% error in the current sensors. In applications with strict requirements, look up tables as well as engineering techniques like delayed sampling and frame rotations are used for current sensing correction.

Temperature Sensing

Most power modules have a thermistor to detect the temperature. This thermistor occupies space, needs an output pin and adds to the total system cost. Current sensors with temperature sensing capability would be an added advantage. With long term engineering effort, there is an expectation that current sensors can provide better temperature sensor than the thermistor. Over-temperature and temperature fatigue are some of the most important causes of power module

failure and a robust current sensor with temperature capabilities can help solve that problem. Fig. 1.3-4 shows the typical structure in Danfoss power modules.

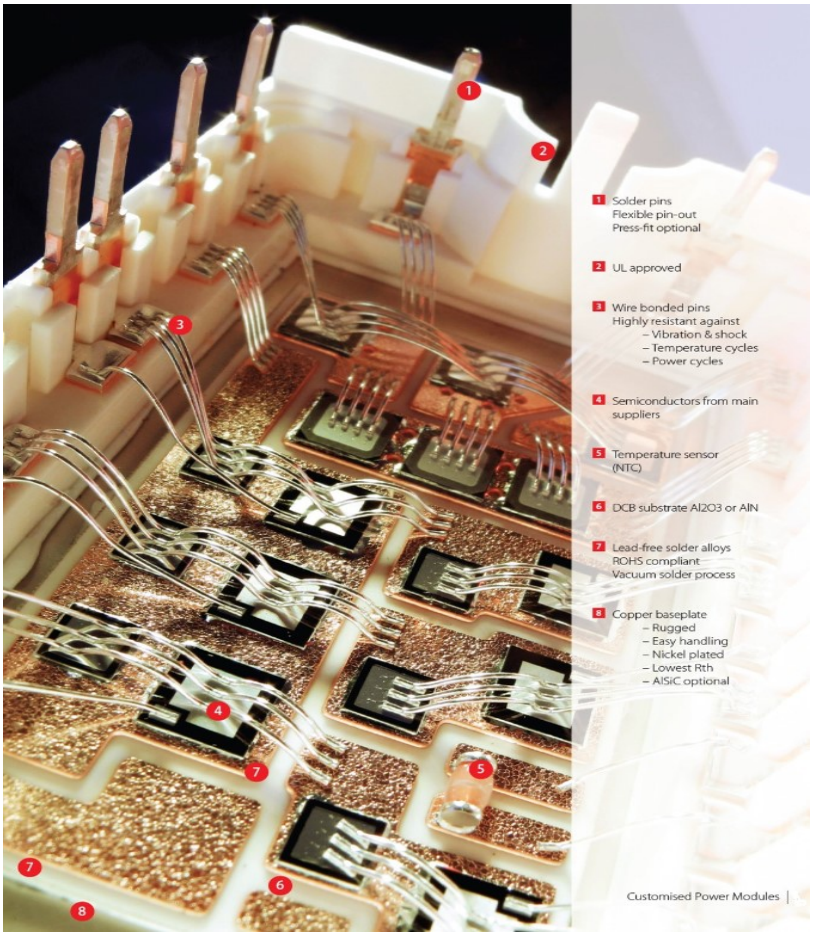

Fig. 1.3-4: Open power module with components labelled [17]

EMI Protection

Integrated current sensing must be able to withstand high dV/dt rates. With increasing switching rates in wide bandgap devices, very typical dV/dt experienced by the sensor would be 10kV/µs corresponding to 1 kV with a switching time of 0.1µs. These voltages changes can cause ripple in current measurement output which need to be damped to accuracy requirements before the sampling can occur. The time delay between switching event and current sampling depends on

the switching frequency. The higher the frequency of the PWM carrier or switching frequency, the more the need for settling due to faster sampling. This requirement is around 1 μs currently and is expected to tighten. Increased switching frequencies, although greatly beneficial for the operation of the drive by smoothening the current, make current sensing more challenging. They increase ripples and reduce the time required to dampen the ripple.

1.4 Current Sensing for AC drives:

Current sensing for AC drive applications can be divided into three types: resistance-based, Faraday's induction-based, and magnetic field-based. These are described below with discussion on their integrability.

1.4.1 Resistance-based current sensing

Resistance-based current sensing involves passing the current through a known resistance and measuring the voltage across the resistor. This information can be used to compute the current using the Ohm's Law in (1.4-1).

$$V = I R \tag{1.4-1}$$

This form of current sensing is very simple, cheap and well established. However, with operating condition changes, resistance-based current sensing develops far reaching drawbacks.

Galvanic Isolation

A current sensing resistor is an inherent part of the power circuit [18]. Any malfunction in the resistor directly impacts the performance of the power circuit. By being a part of the circuit, the resistor takes important and expensive space in the power circuit. This is a major issue in the power module integrated current sensing resistor, where DBC space is extremely precious due to manufacturing costs and power density.

Power Loss

Current passing through a resistor causes power dissipation in the resistor, although current sensing resistors are usually designed in the few milliohm range. With higher currents the power dissipation can accumulate quickly [1] and is calculated using (1.4-2). Small shunts, due to low voltage also need differential amplifiers which add to the cost [1][19]. Due to this resistive current sensing is generally implemented on systems that experience currents under 400A.

$$P_{loss} = I^2 R \tag{1.4-2}$$

Temperature

Resistivity of most materials is a function of the temperature due to which (1.4-3) shows that resistance is a function of temperature too. The temperature dependence of resistance is especially relevant in combination with power loss. The heat generated in the material of the resistor can cause temperature changes and hence the resistance changes. Oil baths and DSP-based temperature compensation are solution to temperature dependency of shunts [20]. In most cases, however, this adds cost, complexity, and adds a temperature sensor. Oil baths are not a practical solution in AC drives due to material handling concerns as well as non-integratablility. The other more realistic method of temperature independence is using material whose resistivity is virtually independent of temperature or thermal design to maintain temperature.

$$R(T) = \rho(T) \frac{L}{A} \tag{1.4-3}$$

Equivalent Series Inductance and Capacitance:

The more complete relationship between current and voltage in a resistor should account for the impedance in the resistor instead of the resistance alone.

$$V = I Z_{total} \quad (1.4\text{-}4)$$

(1.4-4) implies that parasitic inductance and capacitance of the resistor will also impact the relationship between measured voltage and computed current [18]. This is a major drawback of resistors since capacitive and inductive reactance is a function of frequency as shown in Fig. 1.4-1. Due to skin and proximity effects the resistance itself can also be a function of frequency [21]. This frequency dependency leads to limited current sensing bandwidth, typically under 1 MHz, with shunts [18]

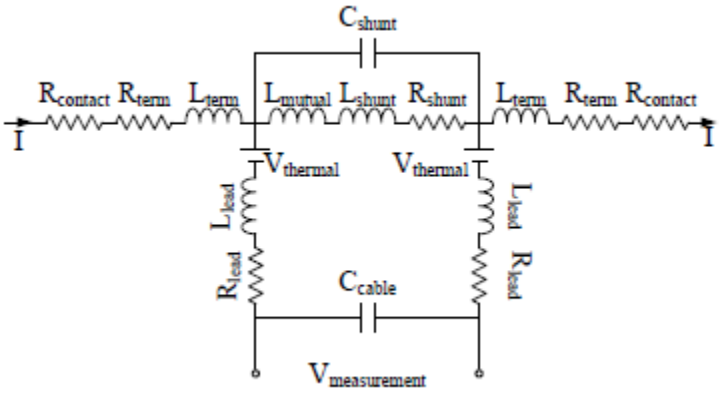

Fig. 1.4-1: Model of shunt resistor with parasitic reactance [21]

Shunt

Shunts are resistors specifically designed for current sensing and have features to overcome the drawbacks of current sensing. Coaxial shunts null the flux of the current thereby reducing the frequency impacts [18]. These coaxial shunts however, increase in size with current amplitude and are not suitable for integration [1]. Parallel plate shunts are also very frequency and temperature insensitive however, are impractical due to the large size. Common shunt designs are shown in Fig. 1.4-2.

Fig. 1.4-2: Commercial shunts designed for low inductance and high temperature stability from Isabellenhuette and Powertek [22][23][2]

Siemen's has large inverter drives with Semikron power modules which have Isabellenhuette shunts integrated [2]. These shunts can dissipate from 30-100W of power. Next generation of Rockwell and ABB drives are also designed with integrated shunts. United Technologies demonstrated gate drive integrated shunts for Cree SiC 6-in-1 power module [24]. Although the power loss is significant in many cases with shunts, these shunts are designed for these ratings. These shunts have enough surface area and temperature ratings such that they can keep stable temperature for operation.

Integrated shunts in power modules have also been designed with minimal temperature and frequency dependency. Shunts with optimized temperature and frequency behavior have been integrated in commercial Infineon, Danfoss and Semikron power modules [18][19][25]. Some shunts in power modules are shown in Fig. 1.4-3. These shunts have been reported to have acceptable performance in the operating region typically under 600A and need design changes based upon the nominal value of current being measured. However, concerns remain about: measuring shunt voltage since it is on DC link potential, losses in short circuit situation, space on DBC and parasitic inductance [19].

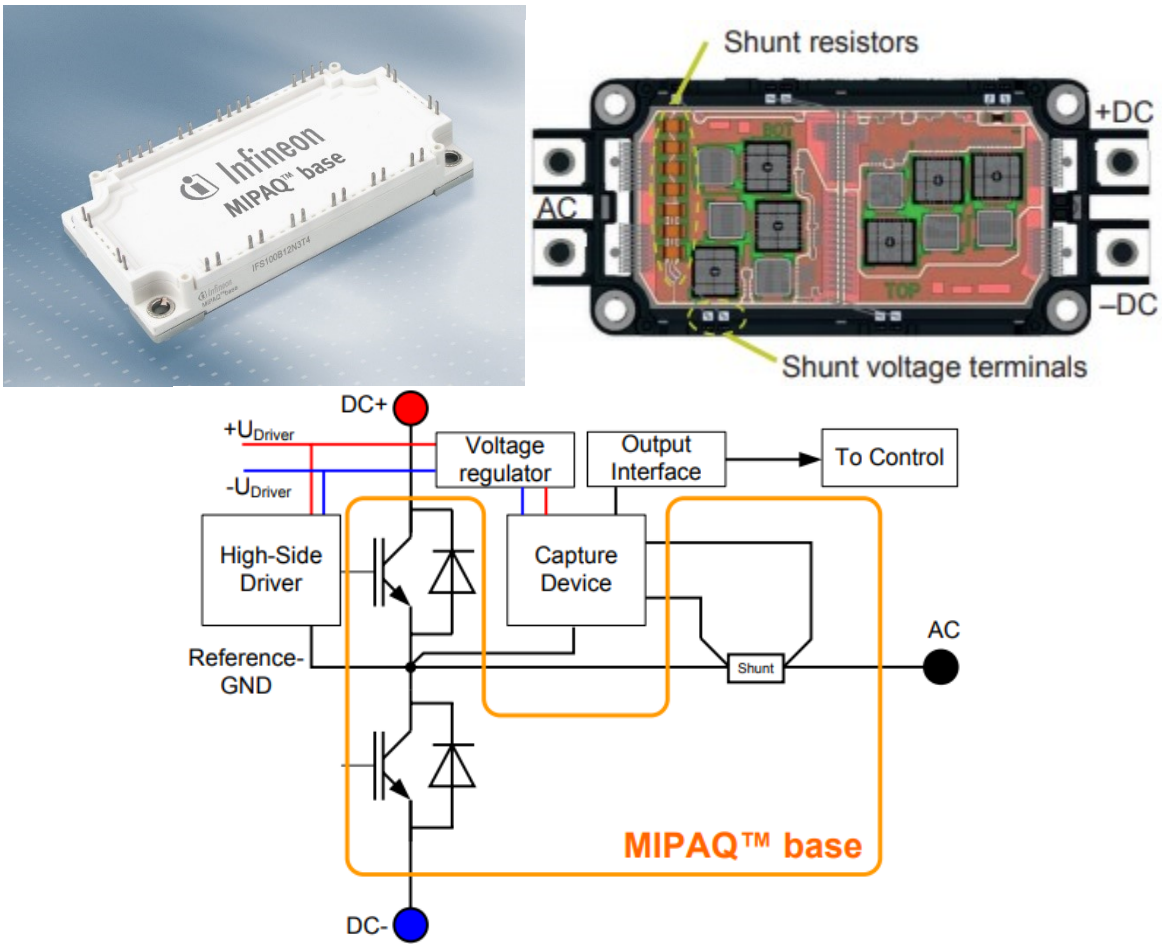

Fig. 1.4-3: Power Modules with integrated current measuring shunts [26][27]

Shunts also require a voltage measurement system. Recent advances in sigma delta technology can provide isolation as well appropriate resolution. However, sigma delta voltage measurement is a complicated system to implement and requires extra computational power. The combined measurement error from the shunt and Sigma delta measurement system adds up [27]. Voltage measurement connections including traces or leads also need to be well designed since they are essentially part of the shunt until the voltage signal is read. Techniques like four wire sensing can be used to decouple the effects of connection leads [1].

PCB Traces and Inductor Resistance

Resistances of PCB traces also lead to using them or other conductors in the power circuit as shunts [3]. Especial designs need to be implemented to avoid the typical issues of resistor-based current sensing. In case of a reliable design, there is no added size consideration, however, design to assure accuracy is very hard to achieve.

[3] demonstrates the internal resistance of inductors can be salvaged to measure current. This method requires extra inductor or capacitors, careful tuning as well as elaborate signal conditioning.

Conduction Resistance of Transistor

In the effort to reduce the size and complexity of current sensing, research has shown that parameters from the transistor itself can be used to compute the current. When the gate current is supplied, and transistor is conducting, the current causes a voltage drop. This voltage drop due to the internal resistance of the transistor in combination with internal resistance data can be used to calculate the current though the transistor when it is conducting [3]. The main limitations of this method are temperature dependence, measurement during conduction via transistor only and not the diode and dependence on gate signal. Fig. 1.4-4 shows the implementation of a buck converter with a MOSFET that is capable of on resistance-based current sensing.

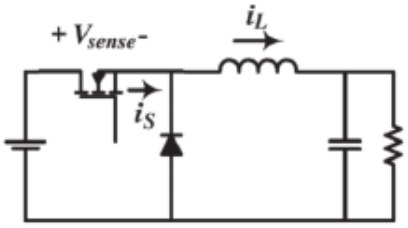

Fig. 1.4-4: Buck Converter with current sensing using the resistance of the MOSFET [3]

1.4.2 Pilot current sensing

The die of the MOSFET consists of parallel individual MOSFET cells. Pilot current sensing works by replacing, around 1/500 of these MOSFET cells with SenseFET [28]. If an assumption is made that each cell conducts equal amount of current, the SenseFET can transmit a current into the sensing system which is proportional to the power circuit current [3]. This method provides die integrated current sensing but occupies expensive area on the die, can be temperature dependent, and still requires sensing of the SenseFET current usually with a resistive device or a more complex virtual earth method. An equivalent circuit of SenseFET in shown in Fig. 1.4-5. Principles similar to SenseFET have been used by Powerex Inc in IGBT modules where a portion of collector current is passed through an auxiliary sense emitter [29]. This current can be measured via methods like mirroring.

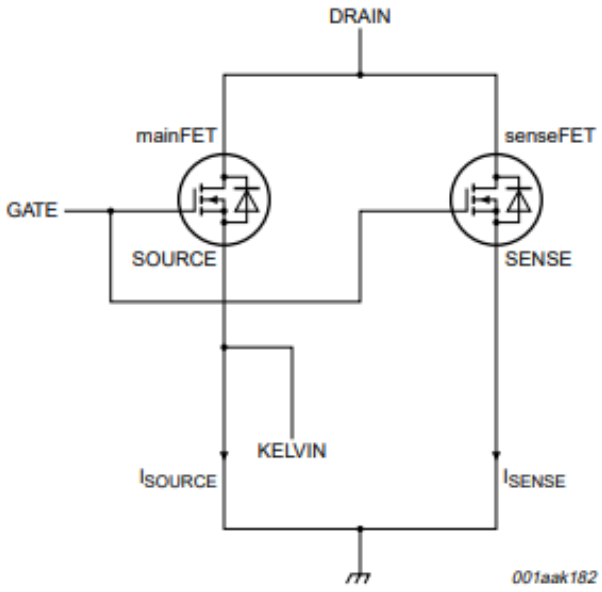

Fig. 1.4-5: Equivalent circuit of SenseFET [30]

1.4.3 Faraday's Induction-based current sensing

Transformers

The basic schematic of the current transformer (CT) is shown in Fig. 1.4-6. Current transformers can be modeled using the Faraday-Maxwell equation (1.4-5). The current through the primary winding (single turn) causes a varying magnetic flux in the core. Due to the current being alternating the flux has a rate of change. This rate of change of flux induces a voltage and current in the closed loop of secondary winding which has a burden resistor. Compared to a regular voltage transformer, there is usually single primary turn and, the voltage input is minimal hence the power transfer is very little. The voltage across the burden resistor is a measure of the current in the primary conductor. Value of burden resistor impacts the losses, it also along with number of secondary turns impacts the output voltage range [1].

$$V = -N\frac{d\phi}{dt} \tag{1.4-5}$$

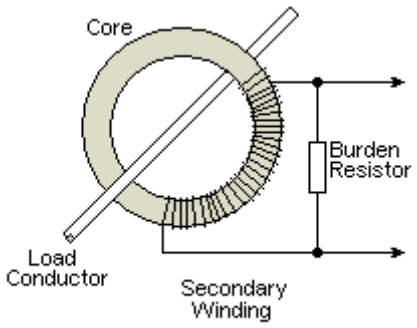

Fig. 1.4-6: Schematic of current transformer [31]

In general, the secondary winding carries much less but scalar multiple of the primary conductor. CTs are specifically designed devices and are operated with defined parameters due to possibilities of high output voltages.

CTs provide galvanic isolation and can be used over a larger frequency range as well as current magnitude range, although with design changes to avoid core saturation [18]. Core saturation is a practical issue which can cause nonlinearities and inaccurate measurement [32]. To prevent the saturation, the cores become larger with higher currents as well as lower frequencies. Core may also experience hysteresis losses and is bulky and expensive. There are also losses in the burden resistor and may also be prone to issues described in the resistance-based current sensing.

Current transformers have a high pass property. This means that although bandwidth can be tuned to very low frequency, the DC component of the current will be filtered out and can also cause core saturation.

Current output in DC-DC converter has been measured using CTs in two of the switching devices [33]. This is possible due to switching devices experiencing current changes every switching cycle. However sensing DC components using CTs requires extra passive devices and complex circuitry rendering them unusable for integration.

Hybrid Current transformers have been designed to measure DC components using a closed loop core. The magnetic field sensors in the core monitor flux and provide a feedback to the secondary winding to produce current to null the flux. This closed loop principle although not strictly a transformer can yield DC sensing but with bandwidth well below 1MHz [32]. Commercial CT and DC-CT are shown in Fig. 1.4-7.

Current transformers provide galvanic isolation, but the presence of core renders them impractical for integration.

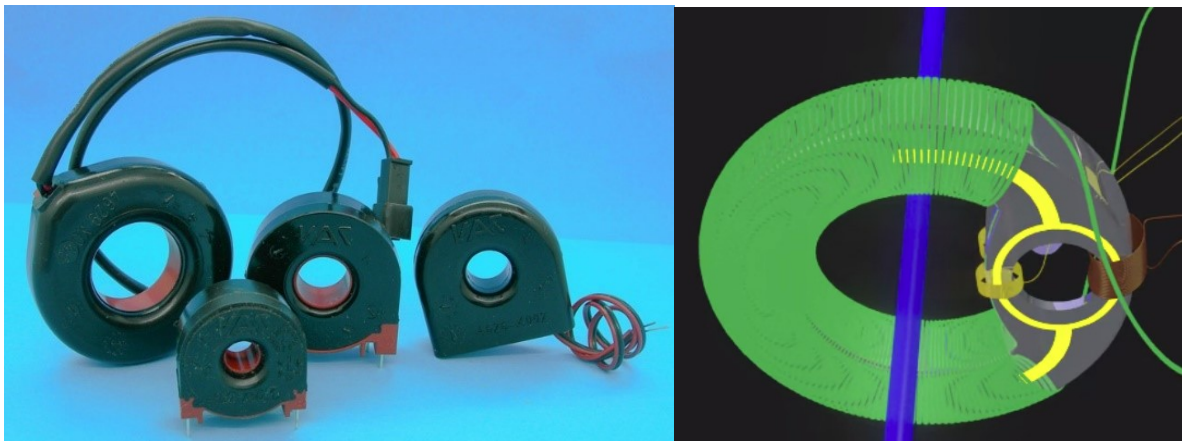

Fig. 1.4-7: Commercial current transformer and closed loop current transformer with DC sensing [34], [35]

Rogowski Coil

The Rogowski coil has the same fundamental basis as the current transformer but has some clear distinctions in design and operation. As Fig. 1.4-8 shows, the primary conductor passes through a secondary coil which experiences a voltage output due to the alternating current producing time changing magnetic flux. (1.4-6) shows the models of Rogowski coil.

$$V = -N\frac{d\phi}{dt} = -NA\frac{dB}{dt} = K\frac{di}{dt} \qquad (1.4\text{-}6)$$

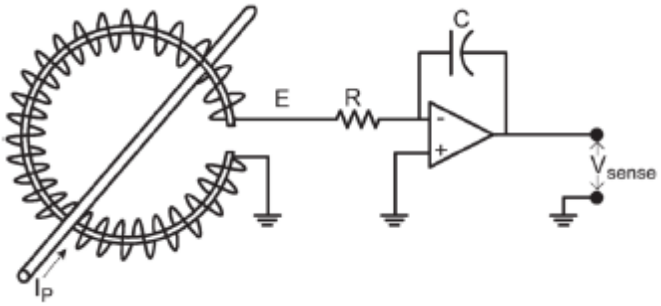

Fig. 1.4-8: Schematic of Rogowski Coil [3]

Compared to a current transformer, the core is simple air, or some other structure for support and not for flux concentration and never saturates. It must be noted that by Maxwell-Faraday

equation, the voltage induced in the secondary coil has a phase shift compared to the primary current. This phase shift is cancelled by an integrator.

Rogowski coil as shown in Fig. 1.4-9, due to lack of a core, do not experience the issues a regular current transformer experience. They do however, only work with AC systems since Faraday induction is the basic operating principle [1]. They also might experience error due to off centering of primary conductor in secondary winding [1][3]. Due to lack of core Rogowski coil require decoupling, shielding, appropriate positioning and layout [32].

Rogowski coils are capable of being used in power module integrated current sensing using planar structure [18][36]. [37] presents a terminal/gate driver integrated Rogowski coil. The Rogowski coil is integrated in a PCB in close contact with SiC power module terminal. The current sensing works with high currents within 1% while measuring switch currents.

Rogowski coils have complicated and expensive manufacturing due to more turns in secondary coil to compensate for lack of core. The coils also have a comparable size to bondwires, essentially becoming a short circuit and power density issue. They also have propensity to experience delays due to integrator circuitry.

Fig. 1.4-9: Commercial Rogowski coil [38]

1.4.4 Field-based current sensing

Magnetic field-based current sensing uses the magnetic field created by a current to measure current. (1.4-7) shows the Maxwell-Ampere's law (without the Maxwell addition) which models the relationship between the magnetic field and the current producing the magnetic field in magnetostatics. It must be noted that solving magnetic field around an AC current is a tedious task especially if field is needed as a 3-D vector quantity. Electromagnetic finite element analysis (FEA) software is generally used to compute 3-D fields. Fig. 1.4-10 is the snapshot of the FEA software Ansys Maxwell 3D's field computation methodology.

$$\int B\, dl = \mu I$$

$$B = \frac{\mu I}{2\pi r} \tag{1.4-7}$$

Maxwell's Equations

The eddy current field simulator solves for time harmonic electromagnetic fields governed by Maxwell's equations:

$$\nabla \times \boldsymbol{H} = \boldsymbol{J} + \frac{\partial \boldsymbol{D}}{\partial t}$$

$$\nabla \times \boldsymbol{E} = -\frac{\partial \boldsymbol{B}}{\partial t}$$

$$\nabla \bullet \boldsymbol{D} = \rho$$

$$\nabla \bullet \boldsymbol{B} = 0$$

where:

- $\boldsymbol{E}$ is the electric field.
- $\boldsymbol{D}$ is the electric displacement, $\varepsilon \boldsymbol{E}$.
- $\boldsymbol{B}$ is the magnetic flux density.
- $\boldsymbol{H}$ is the magnetic field intensity, B/μ.
- $\boldsymbol{J}$ is the conduction current density, $\sigma \boldsymbol{E}$.
- ρ is the charge density.

The eddy current solver assumes that all time-varying electromagnetic quantities in the problem have the form:

$$\boldsymbol{F}(t) = F_m \cos(\omega t + \theta)$$

Fig. 1.4-10: Ansys Maxwell Field Solving method based upon physics [39]

The choice of magnetic field detector depends upon many factors described later in this section. One of the main factors is the range of field. Magnetic field-based current sensing has different topologies based upon the field detector used. Table 1.4.1 shows the typical field and frequency range of different field detectors. Table 1.4.2 shows the sensitivity of the common field detectors.

Table 1.4.1 Appropriate field detectors for frequency ranges [40][41]

Sensor type:	min. B	max. B	Frequency range
Induction coils	100 fT	unlimited	0.1 mHz – 1 MHz
Hall sensors	10 nT	20 T	0 – 100 MHz
Magnetoresistive Sensors	100 pT	100 mT	0 – 100 MHz
Fluxgates	10 pT	1 mT	0 – 100 MHz
SQUIDs	5 fT	1000 nT	0 – 100 kHz

field range TMR>GMR>AMR

Table 1.4.2 Appropriate field detectors for sensitivity

PFD	Typical Sensitivity
Hall	05mV/mT
Fluxgate	10mV/mT
AMR	10 mV/mT
GMR	40 mV/mT
TMR	50 mV/mT

The following detectors are the most commonly used field detectors used for current sensing. These detectors can work in open as well as closed loop topologies. Closed loop field detection is explained under Hall effect.

1.4.5 Magnetic field vector

Magnetic field is a 3-D spatial vector quantity. As described above, Electromagnetic finite element analysis (FEA) software is generally used to compute 3-D fields. In many cases like for a

long straight wire, the fields can be planar, meaning in an appropriately defined cartesian coordinate system, one the dimension will have zero field.

Most of the field detectors have a defined axis of sensitivity. Due to this the field detected for current sensing is only in 1-D. The single dimension selected is mainly geometric and for accessibility reasons too. Orienting the detector in particular direction or dimension has not been studied in the literature.

1.4.6 Hall effect current sensors

Hall effect magnetic field detectors work on the principle first discovered by Edwin Hall [1]. The principle stems from Lorentz force law which quantifies the force on charges moving in a perpendicular magnetic field. Hall detector work on the same principle as shown in Fig. 1.4-11 and (1.4-8). A small current passing though the detector will pass in a straight path in the absence of magnetic field. However, if a perpendicular magnetic field is present, the current which is essentially moving charges experiences a force, causing a change in current trajectory. A concentration of charges on one end of the detector causes a voltage across the detector. This voltage is proportional to the magnetic field and hence the current producing the magnetic field. Hall effect is well studied, and the limitations of its physics are well documented. Hall detectors are inexpensive, compact, simple and their design is well understood.

$$F = Q E + (Qv \times B) \qquad (1.4\text{-}8)$$

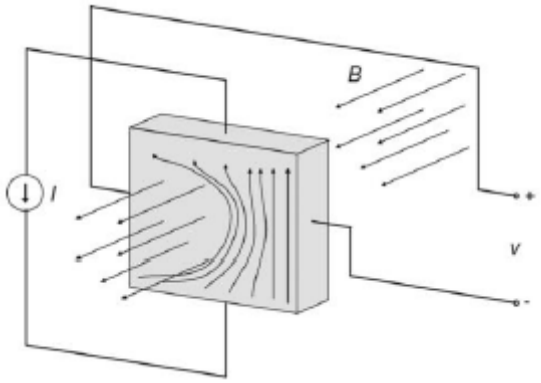

Fig. 1.4-11: Hall effect illustration [1]

Hall detectors are sensitive to temperature in addition to the magnetic field [18][32]. This temperature dependence needs temperature decoupling or compensation adding to the complexity of the system. Hall detectors also have inherent manufacturing offsets which requires careful consideration [1]. Another major drawback of the Hall detectors is their low sensitivity to magnetic field [3]. To reduce the impact of low sensitivity, Hall effect detectors are used with a core or flux concentrator. Both act to collect the magnetic flux and direct it to the Hall detector for a more sensitive output. Presence of a core make the current sensor bulky and prone to core issues described with current transformers like core hysteresis losses, eddy current losses, cost, manufacturability and most importantly nonlinearities due to core saturation [3]. Having a core to shape the field on to the detector also puts a physical limitation on the bandwidth of current sensing. Fig. 1.4-12 shows the core of a commercial Hall effect sensor. The need for core also stems from the need to reject disturbance magnetic fields. If flux from the current being sensed is well preserved and directed to the Hall detector, the need for decoupling the disturbance fields is reduced. New Hall PFDs can have higher sensitivity, range of ±50 mT but bandwidth of only few tens of kHz [42].

In Fig. 1.4-12 it can also be seen that the individual phase currents need to be separated and passed through the core or sometimes wrapped around the core. This setup is necessary to ensure that hall detector on experiences the field from a single current.

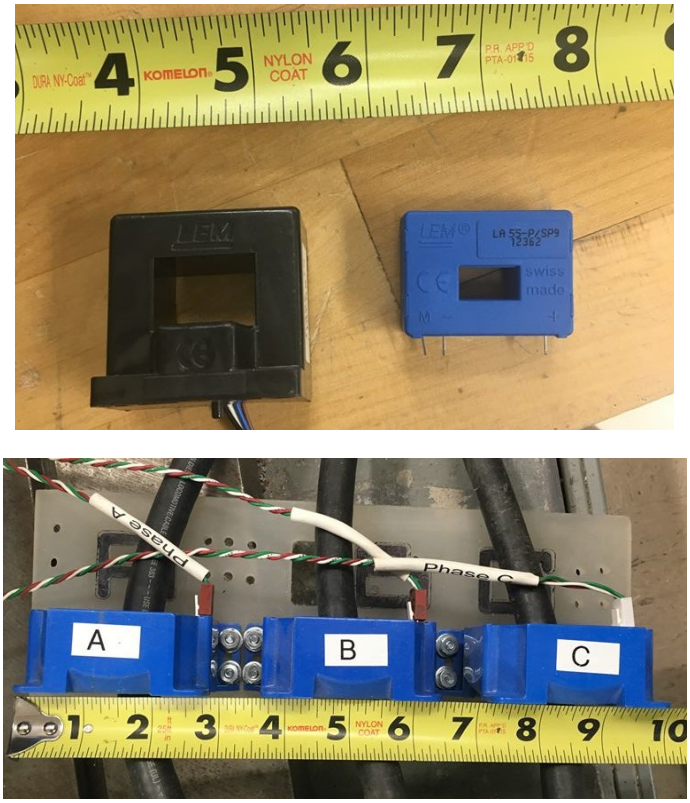

Fig. 1.4-12: Commercial Hall effect sensor with a core

The FRFs in the Fig. 1.4-13 shows the frequency dependency of two commercial Lem current sensors and a Honeywell current sensor. Lem LA 55p is a closed loop sensor with -1dB bandwidth of 200 kHz sensor, whereas the Lem HAL 50 is an open loop sensor with -3dB bandwidth of 50kHz sensor. The Honeywell CSCA series sensor is also open loop and has a -3dB bandwidth of 50kHz as well. It can be noted that despite the bandwidths being advertised as much higher and accuracy as 1 or 2%, the frequency dependent error is present even at low frequencies. The gain error reaches 5% at a fraction of rated bandwidth.

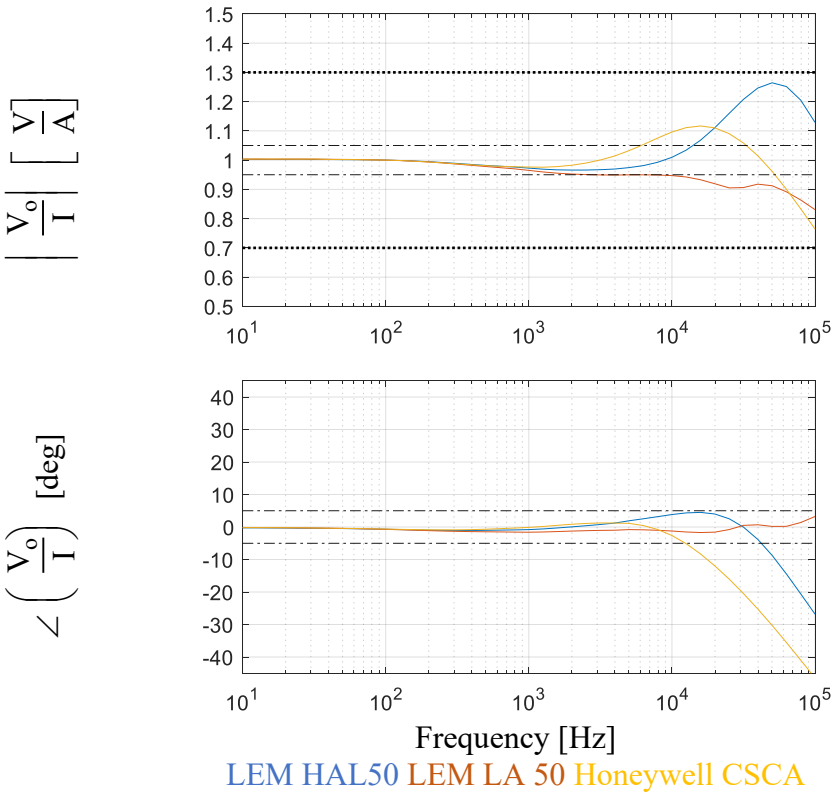

Fig. 1.4-13: Experimental FRFs of commonly used commercial current sensors with respect to actual currents normalized to 100Hz value

Closed Loop Field Detection

Issues with Hall and other field detectors are limited linear range of the core, temperature and sensitivity drifts. An engineering solution to this is to use field detector in closed loop [3]. This requires extra power and circuitry; however, this circuitry improves the performance. The closed loop current detection system works by nulling the voltage output of the detector. Analog controllers are used to produce a current in a compensating conductor close to the detector. The control system maintains a current in this compensating conductor such that the net magnetic field from the current being sensed and the compensating conductor is nulled at the detector location. Hall, Fluxgate, AMR, GMR, TMR can all be used in closed loop sensing for more accurate and reliable performance.

Fig. 1.4-14 shows the principle of close loop Hall sensor which keeps the Hall effect operating close to the zero point where linearity is best, hysteresis is very minimally experienced, linearity and accuracy is high, and thermal drifts are lower. However, these advantages of closed loop Hall sensors come at the cost of increased power dissipation, lower bandwidth and limited range of compensating current producing circuitry [3].

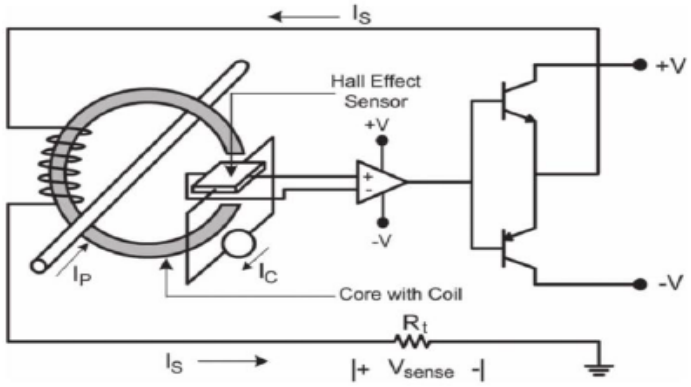

Fig. 1.4-14: Schematic of closed loop Hall effect sensor [3]

Coreless Hall Current Sensors

There are open loop Hall detectors-based current sensing products which don't use cores to avoid disturbance fields from coupling into the Hall detector. Instead they use Hall detectors in spatial positions around specifically shaped current path such that disturbance fields are not rejected but decoupled [43][44]. One such commercial sensor is shown in Fig. 1.4-15.

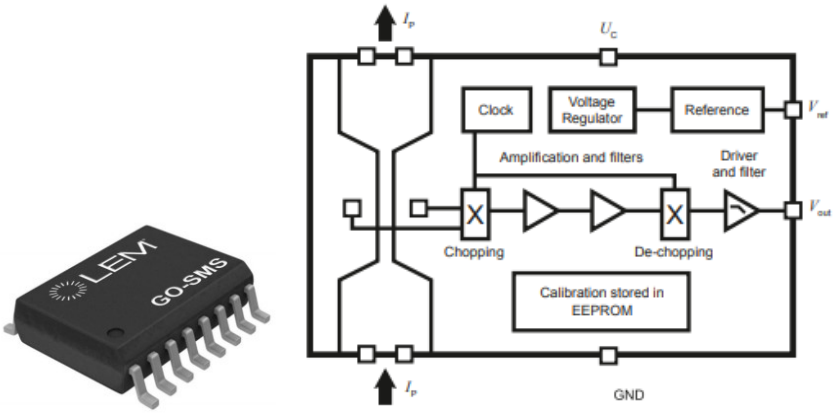

Fig. 1.4-15: IC and schematic of open loop Hall effect sensor with gradiometer topology [44]

Such products detect the field gradient using the two Hall detectors placed at locations where field gradient exists. Field gradient also has a linear relationship with current. The effectiveness of this decoupling method will be described in the field decoupling section later in this chapter.

Hall effect current sensors are becoming compact, galvanically isolated, and integratable. They have increasing bandwidths typically reaching 100kHz starting from DC [18]. As field detectors they can be used with disturbance decoupling methods inside power modules. The biggest challenge to integrating Hall detectors is their offset, thermal drift, limited bandwidth and sensitivity.

1.4.7 Fluxgate

Fluxgate magnetic field detectors utilize the core saturation which causes nonlinearity between B and H. Flux gate detectors have many different topologies and operating principle and have been studied since 1930 [1]. A simple fluxgate works with achieving field density saturation on positive and negative sides. Presence of external magnetic field causes an unbalance in the saturation which is detected in a sense winding. They are mainly used for low magnetic field and precision applications in laboratories.

Recently TI has developed closed loop fluxgate which is small in size, has 3MHz bandwidth but is designed for very low currents and requires a core for proper functionality as shown in Fig. 1.4-16. [45] describes another IC integrated fluxgate current sensor. The major issue with this current sensor is low sensitivity with a typical range of 1nT to 1μT and limited bandwidth [46]. Sensitivity and bandwidth can be improved by increasing excitation frequency and number of turns in sense winding [1]. Flux gate sensors require complex circuity for measurement readout since FFT and harmonic filtering is needed in most cases. Flux gates can work in open or closed loop and have good temperature stability [1]. In general, fluxgate detectors are non-integratable in power electronics due to size, cost, complexity and a need for core.

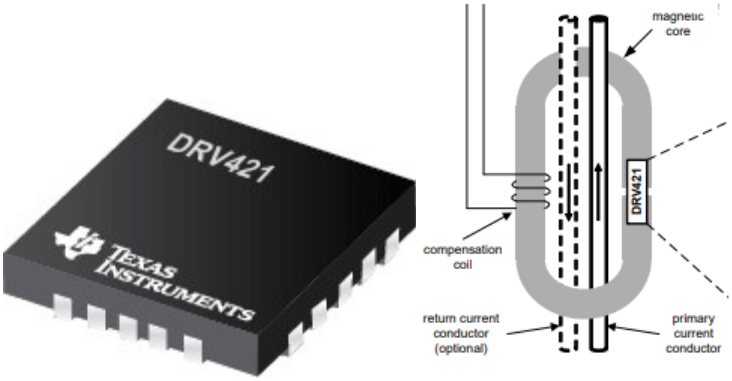

Fig. 1.4-16: IC and system schematic of closed loop fluxgate current sensor [47]

Very similar to fluxgate sensors are saturated inductors which work with inductors being saturated easily. The presence of an external magnetic field causes a change in the saturation property and is used to detect the magnetic field [3]. Saturable inductors require core, have larger power dissipation and complex design for higher bandwidths [3].

1.5 MR PFDs

1.5.1 Anisotropic Magnetoresistance

An Anisotropic Magnetoresistor (AMR) is a resistor that changes resistance based upon the magnetic field subjected to it. The AMR effect was first recorded by William Thompson Kalvin in 1850s [46]. However, it was in the 1970s when the first AMR sensors were developed after the thin film technology matured. Thin films have an explicit relationship between the external magnetic field and their differential resistance [48]. AMR is easily noticeable in thin films of ferromagnetic material. The material generally used is Perm alloy (Ni-Fe) laid on top of Si and SiO wafer. A maximum change in resistance is about 3-5% after which saturation occurs [41].

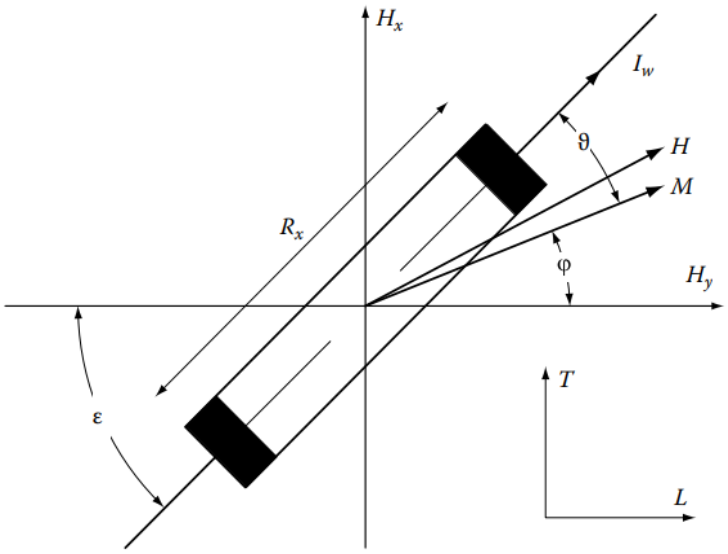

Fig. 1.5-1: Model of AMR strip [46]

The detailed of AMR physics have been studied for decades. The physics of AMR delves into the spintronics and quantum physics. However, it is possible to have a sufficient understanding of AMR effect with just magnetism and energy. Fig. 1.5-1 shows the basic AMR strip at angle ε from the H_y axis known as the anisotropy axis or the easy axis. For simplicity, the angle ε =0 in

this explanation. The anisotropic or easy axis is the direction in which the strip has an inherent anisotropic magnetic field H_k defined during manufacturing. The net angle of magnetization (ϕ) of the strip with respect to the easy axis is simply given by (1.5-1) [48].

$$\text{Sin}\phi = \frac{H_x}{H_k + H_y} \tag{1.5-1}$$

(1.5-1) is a result of summing magnetic field vectors. This can also be derived from the magnetostatic energy equation. The relative change of resistance of the strip in the easy axis is a function of the angle between the magnetization direction and the current passing through the strip. It is modeled by (1.5-2) and (1.5-3) [48] where Θ is the angle between the current and anisotropic axis and equal to ϕ, since $\varepsilon = 0$.

$$\frac{\Delta R}{R} = -\frac{\Delta\rho}{\rho}\sin^2\theta \tag{1.5-2}$$

$$\frac{\Delta R}{R} = -\frac{\Delta\rho}{\rho}\left(\frac{H_x}{H_k + H_y}\right)^2 \tag{1.5-3}$$

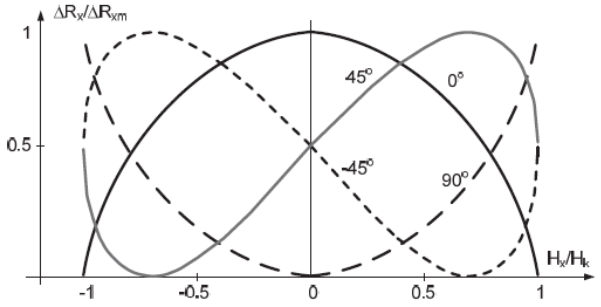

Fig. 1.5-2: Characteristic curves for AMR with and without barber poles [48]

The relationship between relative resistance and field perpendicular to the anisotropic axis is plotted in Fig. 1.5-2. The 0 deg curve is unipolar and parabolic due to the squared relationship. This means the AMR detector cannot distinguish the direction of magnetic field and has very limited linear region. A physics and engineering method of improving the linearity of the AMR

strip is to provide a strong bias field in H_x or H_y direction. Another method is to put thin layers of aluminum or another strong conductor in the strip as shown in the Fig. 1.5-3. These layers of conductor in the AMR strip are called as barber poles owing to their aesthetic design. The barber poles cause a net shift in the direction of current which is essentially the same as strong bias field. Barber poles at 45 deg can make the AMR characteristic curve more linear and bipolar as shown in Fig. 1.5-3 [41]. The strong bias field and barber pole effect is to change the angle between the magnetization of the AMR strip and current such that external magnetic fields will cause this angle to change and maintain a bipolar relation with respect to relative resistance along the anisotropic axis within limits of operation.

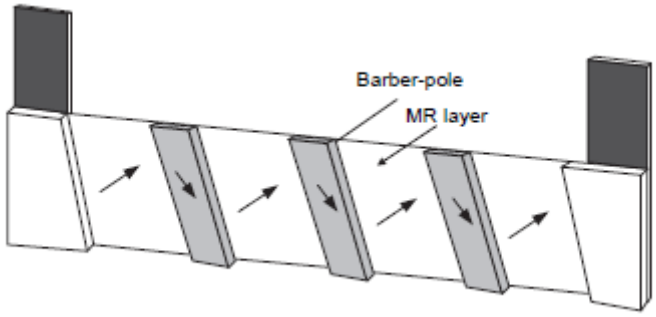

Fig. 1.5-3: AMR strip with Barber poles [48]

The AMR output is dependent upon the angle between current and magnetization. This means that a magnetic field which causes an impact on the magnetization direction of the AMR element will be detected. This also leads to unstable situations where very large external fields can cause a permanent reversal of the easy axis thereby causing a substantial change in magnetization axis. To prevent this from happening large biasing field in a technique called flipping is used [49]. Flipping produces a large alternating field parallel and anti-parallel to easy axis using coils close to AMR elements, however it increases the complexity and power requirement as well as may reduce the bandwidth. Fig. 1.5-4 shows the effect of flipping on characteristic curve.

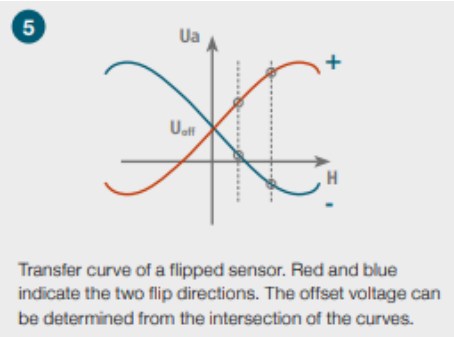

Fig. 1.5-4: AMR characteristic curve flipping [6]

AMR characteristic curve, its sensitivity, linear range and total range is dependent upon its exact structure and bias fields. In general, sensitivity is much higher than Hall effect detector [46]. The relative resistance change output of AMR element is read in the form of voltage using the Wheatstone bridge topology. This helps decouple the temperature impact on AMR and as well as increase the sensitivity of the output. Fig. 1.5-5 shows the Wheatstone bridge layout of the AMR detector which is formed on submillimeter die. Most AMR detectors have bandwidth of few MHz and range in few mT.

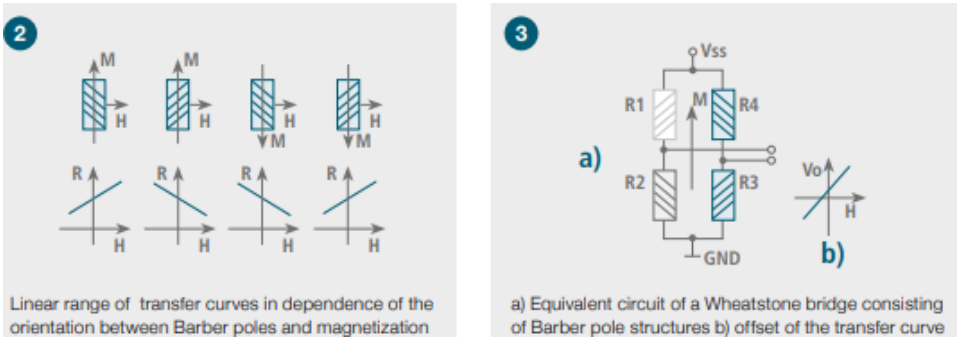

Fig. 1.5-5: Characteristic curve dependence on barber poles and AMR bridge [6]

The AMR elements in the Wheatstone bridge are such that elements in each branch have sensitivities in antiparallel direction and diagonal elements have same sensitivity. This leads to minimal offset and quadruples the sensitivity of single element AMR. Additionally, the Wheatstone topology decouples the temperature effects.

AMR sensors went through a fast development phase when they were used as magnetic reading heads [46]. Although now they have been replaced by GMR in reading heads, they continue to be important in commercial current sensors, magnetic switches and position sensors because they are the most mature of MR technology.

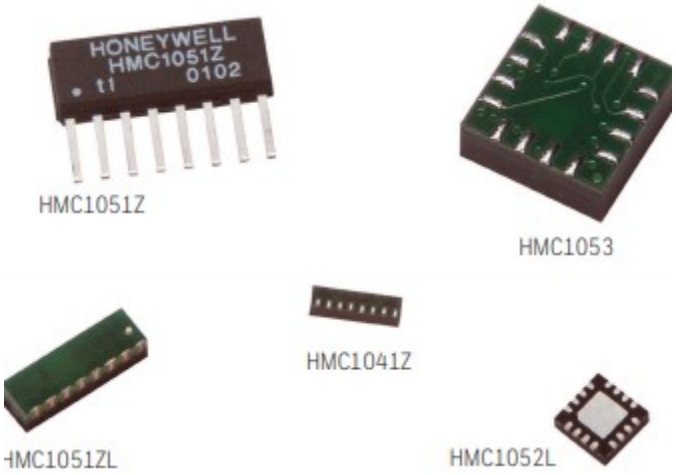

Fig. 1.5-6: Commercial AMR sensors from Honeywell [50]

Honeywell HMC series shown in Fig. 1.5-6 has 1, 2, and 3 axis AMR detectors respectively. They have been designed for various applications including current sensing. They have a decent sensitivity and hysteresis, however, they have a linear range of under 0.6mT which makes them suitable for low current applications only [50].

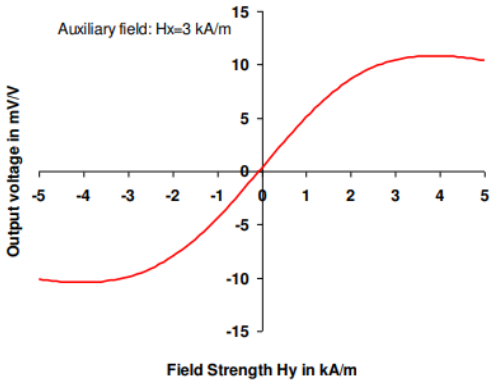

Fig. 1.5-7: Typical output characteristic curve of commercial AMR [51]

Fig. 1.5-7 shows the characteristic curve of TE KMY, KMZ series AMR detectors. Unlike most detectors they have full bridge with only one branch sensitive to the magnetic fields whereas the second branch provides the reference. The linear field range is around ± 2mT which can be utilized for current sensing applications [51]. The characteristic curve is very sensitive to bias magnetic fields, making it sensitive to disturbances and positional errors.

Sensitec's AFF700 has an AMR Wheatstone bridge along with a flipping coil for higher accuracy. It has moderate sensitivity, however, the range is under ±1 mT rendering is unsuitable for higher current sensing [6].

1.5.2 Giant Magnetoresistance

The Giant Magnetoresistance effect like AMR effect causes a change in resistance of GMR element in the presence of magnetic field. GMR effect was discovered in 1988 by Peter Grunberg and Albert Fert and resulted in a Noble prize for them in 2007 [46]. GMR, unlike AMR, is only noticed in thin layer structure of a few nanometers and not present in bulk material. It has up to 10-30 times higher sensitivity than AMR hence the name Giant. GMR effect is a result of electron spin in thin layers and their interaction with each other and is explained using electron magnetic moment and spin in the branch of physics called spintronics and quantum physics.

GMR sensors are mass produced for hard disk read heads. They are also used in angular and linear position detection applications. They also work as good magnetic switches. GMRs due to their compact size, sensitivity and linearity are good candidates for PFDs which can be integrated.

GMR can be divided based upon the layer structure which can impart different properties. Two common types are Multilayer and Spin Valve. Some GMR topologies are very suitable for integrated current and temperature sensing owing to their compact size, good linearity and high sensitivity.

1.5.2.1 Multilayer GMR

Multilayer GMR consists of many layers of magnetic material (Fe, Cr, Co and Perm Alloy usually) stacked up sometimes with a conducting spacer to cause coupling between layers. The exact material and structure of the layer is a design parameter to control the sensitivity and range of the multilayer GMR. The magnetization direction alternates between the stacked layers as shown in Fig. 1.5-8. Application of external magnetic field causes a change in the magnetization of the layers and leads to relative resistance change as shown in Fig. 1.5-8 [52].

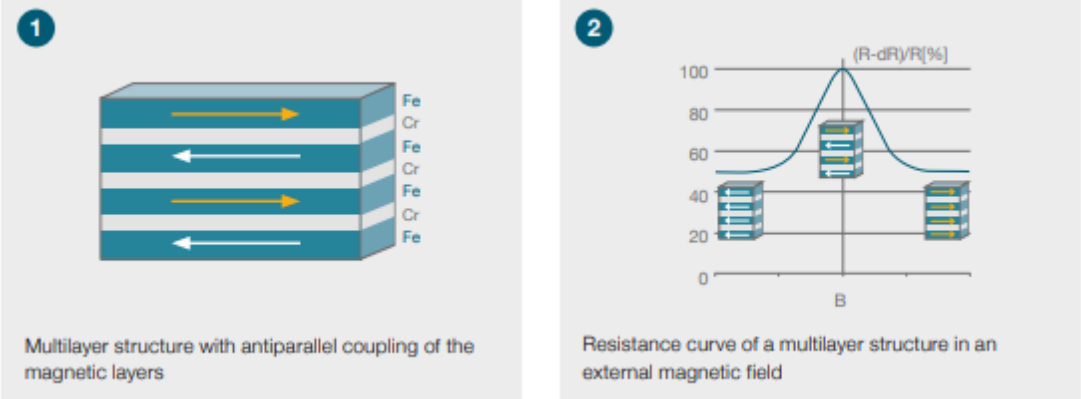

Fig. 1.5-8: Multilayer GMR structure with layer magnetization determining the relative resistance [6]

The Multilayer GMR effect is unipolar [48] however much more sensitive than Hall and AMR. The bandwidth of the GMR is similar to AMR at few MHz and range of GMR is few mT but generally larger than AMR. The GMR output only depends on the magnitude of the field parallel to layers and is independent of the direction of field. It must be noted that multilayer GMR effect is more stable to perpendicular fields, and has larger range compared to Spin Valve. [53] shows the AC current sensing using a unipolar GMR leads to only positive half cycle data.

1.5.2.2 Spin valve GMR

Spin Valve GMR is a further development of the multilayer GMR effect with higher sensitivity, less noise and bipolarity. Spin Valve also consists of thin layers but with much less

coupling due to the extra spacer [48]. Generally, there is a pinned layer with has substantial magnetization. The second layer is the free layer with much less coercivity. An external magnetic field changes the direction of magnetization of the free layer and the angle of magnetization between the pinned and free layer determines the resistance of the GMR spin valve element. Fig. 1.5-9 shows an example of the layered structure. Spin valve GMR, although much more sensitive than multilayer GMR, offers much less linear range.

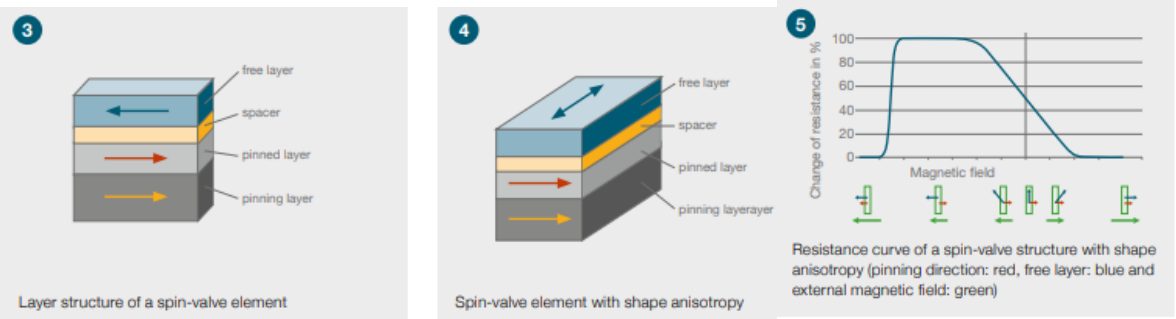

Fig. 1.5-9: Spin Vale GMR structure with layer magnetizations determining the relative resistance [6]

In general, just like AMR sensors, to increase the sensitivity and decouple temperature effects, GMR spin valve and multilayer are both manufactured in Wheatstone bridge topology. Also, just like the AMR, the Wheatstone bridge can be voltage or current supplied. The differential output of the bridge is dependent upon the magnetic field.

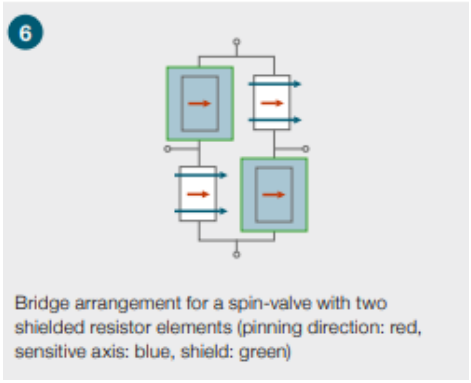

Fig. 1.5-10: Wheatstone bridge of GMR elements [6]

Fig. 1.5-10 shows the topology where one set of diagonal elements of the Wheatstone bridge have identical sensitivity, whereas the other diagonal is shielded from magnetic field. The output of the bridge is double the output of single element.

1.5.3 Tunnel Magnetoresistance

TMR effect much like AMR and GMR effect leads to a change in resistance in the presence of a magnetic field. Tunnel magnetoresistance, also known as Magnetic tunnel junction and spin dependent tunneling GMR among other names was first observed in 1970, however, the development of stable TMR elements has only recently started [46]. The complications in development of TMR elements originates from the fact that one of the layers is 0.2 nm thick. This layer is an insulator layer and controls the resistance, and sensitivity which can be as high as 50-500%. (1.5-4) shows the Julliere's model with P being the spin polarization [48][46].

$$\frac{\Delta R}{R} = \frac{2P_1P_2}{1+P_1P_2} \qquad (1.5\text{-}4)$$

Although the layer stack-up looks similar to spin valve GMR with two ferromagnetic materials separated by the thin insulator such as Magnesium or Aluminum Oxide as shown in Fig. 1.5-11, the difference comes from the fact that path of the current in TMR is perpendicular to the layers. The current travels through the layers.

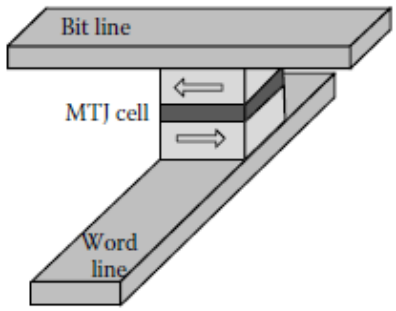

Fig. 1.5-11: Layer structure of TMR element [46]

Theoretical models for TMR sensors were developed before successfully manufacturing them. They were expected to have high sensitivity and bandwidth compared to AMR and GMR, which was later experimentally verified in literature. They generally have a higher impedance compared to GMR and AMR due to the thin insulating layer. TMR sensors suffer from inherent noise and hysteresis and have been found to be ESD sensitive [46]. If these problems are overcome and a stable oxide layer is formed, TMR sensors could overtake GMR and AMR sensors owing to their higher sensitivity, inherent bipolarity and similar die size.

NVE, MDT, Crocus and TDK (SAE magnetics) have commercial TMR-based sensors most of which are angle sensors with Sine and Cos signal from two Wheatstone bridges with orthogonal sensitivity [54][55][56]. Most of these sensors have been commercially released in 2017-18. Theoretically these TMR PFDs can be used to measure alternating magnetic fields, however, none of the manufacturers have experimental characteristic curves provided in the datasheets. It is evident that they are rated for high fields and have high hysteresis.

TMR improves upon the range and sensitivity of the AMR and GMR. It is also bipolar, and the die is similar in size making it a suitable candidate for integration in power electronics.

.

1.5.4 Development of multi-dimensional MR PFDs

In the past few year, multidimensional MR PFDs have gained interest. These PFD have the ability to sense fields along two or three orthogonal axes at the same time and independently. The main motivation of these 2-D and 3-D PFDs have been position detection applications. One sub application of position detection is encoder application. A few 2-D TMR PFDs have been released in the market in the past couple years with two orthogonal axes of sensitivity [54][57][58]. The

main proposed application has been position-detection in rotatory machines as well as linear machines.

3-D MR PFDs are much rarer and primarily exist in research settings. In [59][60][61], 3-D GMR have been proposed for magnetometer application such as a compass for geomagnetic fields. These are low frequency devices that use planar sensor for sensing X and fields and a flux guide to direct the Z field onto the planar sensors. At this stage these sensors require complicated modulation and calibration schemes to capture an accurate low amplitude and frequency field signal. [62] has described the development of a 3-D TMR-based field sensor by NVE. The sensor was also proposed for low frequency applications shows the commercial interest in these sensors but has not been found in the market. Another 3-D TMR is proposed in [63] for catheter tracking in biomedical applications. Both the 3D TMR sensors have three TMRs positioned orthogonally.

1.5.5 Evaluation and Selection of MR PFDs

PFD selection for a particular current sensing application is a crucial step. The PFD properties determine its functionality in integrated current sensing. Each of the property on the detector level translates to the sensor property after signal conditioning [64]. It is essential that PFDs exhibit the properties that will appropriately translate to the required properties in the final current sensing system. The properties that are tested in [64] are explained below.

Sensitivity is one of the most important properties of the PFD. A lack of sensitivity leads to a compromised SNR and lower resolution of the signal processing. A higher sensitivity on the other hand makes the SNR better, signal resolution increases, signal conditioning is simpler and small fields can be easily measured. A rule of thumb in the MR industry is that higher sensitivity leads to lower field range, so a compromise must be made.

Bipolarity is sensitivity in both positive and negative direction of magnetic field. A unipolar PFD produces a positive output voltage for both positive and negative magnetic fields. A bipolar sensor produces a positive voltage output for the field in the positive direction and a negative voltage output of the field in the negative direction. This is essential for measuring the alternating currents' magnetic fields which alternate in positive and negative directions.

Linear range is the range of the magnetic field in which the output voltage of the PFD changes linearly with the magnetic field. Within the linear range, the relationship between the magnetic field and output voltage has linearity error of less than 1%. The linear magnetic field measurement range leads to the range of the current that can be linearly measured (modeled by Ampere's law).

The MR PFDs are generally laid out in a Wheatstone bridge to double or quadruple their sensitivity and provide thermal stability. However, there are PFDs with half-bridge structures. The Wheatstone topology of the MR PFD is useful for increasing the sensitivity as well as decoupling the effect of the temperature. Ideally, all MR elements experience same temperature due to which, although their resistivity changes, the change is constant over all 4 of the resistors thereby not affecting the output.

The PFDs for integration need to be compact. Most MR dies are under $1mm^2$. Compact size, low material and manufacturing cost and simple structure are some of the reasons, MR PFD is an important integratable option.

Hysteresis in MR PFD refers to the gap that forms in the characteristic curve due to the remanence and coercivity. Hysteresis occurs due to the different trajectories of the characteristic curve as magnetic field increases and as it decreases, thus causing significant linearity errors. PFD hysteresis needs to be characterized to make sure that linearity of the PFD is maintained.

AMR, GMR and TMR are all theoretically expected to have bandwidth in high MHz range [41]. In practice, however, the bandwidth is in low MHz [6][46].

Eight different PFDs were evaluated in [64]. PFDs have a range of MR effect (AMR, GMR, TMR), sensitivity, linearity, hysteresis and offsets. GMR GF759 and TMR TA901nv have irregular hysteresis and characteristic curves that lead to insufficient linearity for any current sensing application. TMR CT219 is a high sensitivity and high linearity TMR PFD but suffers from inherent noise issues hence become a good option for sensing application which either have lower accuracy requirement or can use higher order expensive filtering. AMR AF720 is a robust AMR with bipolarity, noise, sensitivity and range that could be appropriate for most current sensing applications but the need for bias field complicates its use. AMR AFQ720, which is AF720 with on-chip hard bias is a natural improvement but due to the presence of permanent magnet of chip, temperature effects need additional decoupling. Also, external bias field superimposed on the hard bias change the characteristic curve of this PFD. AMR AFQ720 is a good option for disturbance field-free environment which mostly operates at similar temperature, else complicated decoupling techniques are needed. GMR GF709 is a bipolar, high sensitivity and low range spin valve GMR, which could be used for low current measurements, like gate currents. The main complication in its use comes from hysteresis. GMR GF705 is a unipolar multiplayer GMR but provides high sensitivity and linear range. TMR TF952, has initial development problems with hysteresis and ESD protection. Apart from these TF952 is the most versatile PFD having 2-D property, bipolarity, high sensitivity as well as high range.

1.5.6 1-D GMR evaluation for current sensing

Sensitec's GMR GF705 has been rigorously evaluated and used in current sensing [65][7][64]. GF705 is a unipolar multilayer GMR. GF705 is a Wheatstone bridge with elements in one diagonal

being GMR sensitive in the same direction and another diagonal being shielded GMR. Each element has a resistance of around 5 kΩ and supply voltage is 5V. The size of the chip is 1.46 x 0.96mm. Fig. 1.5-12 shows the schematic of the electrical layout of GF705.

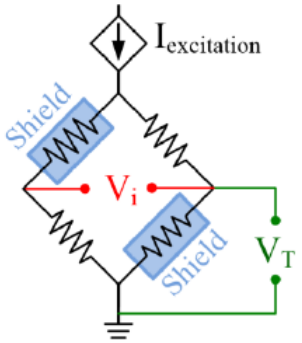

Fig. 1.5-12: Schematic of Sensitec GMR GF705 [28]

Fig. 1.5-13 shows the characteristic curve of GF705. The output voltage is positive regardless of the direction of magnetic field along the axis of sensitivity.

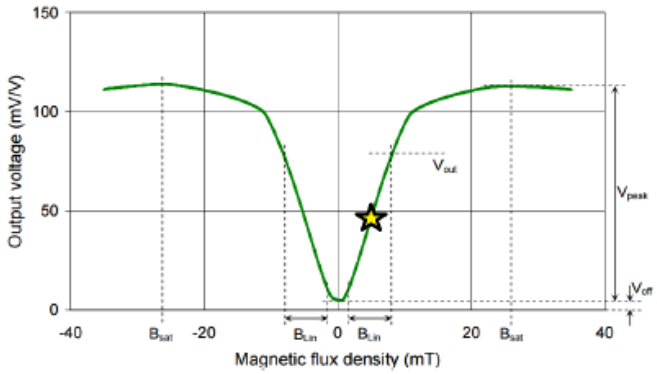

Fig. 1.5-13: Characteristic curve of Sensitec GMR GF705 [66]

The unipolar output of the GMR is converted to bipolar output by shifting the zero point of the field to the location marked with star in Fig. 1.5-13. This is a critical to be able to measure alternating magnetic field from AC currents. This shifting is done so by placing a small permanent magnet whose field falls right in between the linear region of the curve.

GF705 is used with a current source and output signal conditioning as shown in Fig. 1.5-14. The IC components used in the GF705 current excitation and signal conditioning warrant bandwidth of above several kHz. These can be fine-tuned to MHz level as well, but the size and vulnerability of the signal conditioning remains a concern for integration. More information on development of signal conditioning PCB is presented in [65][67].

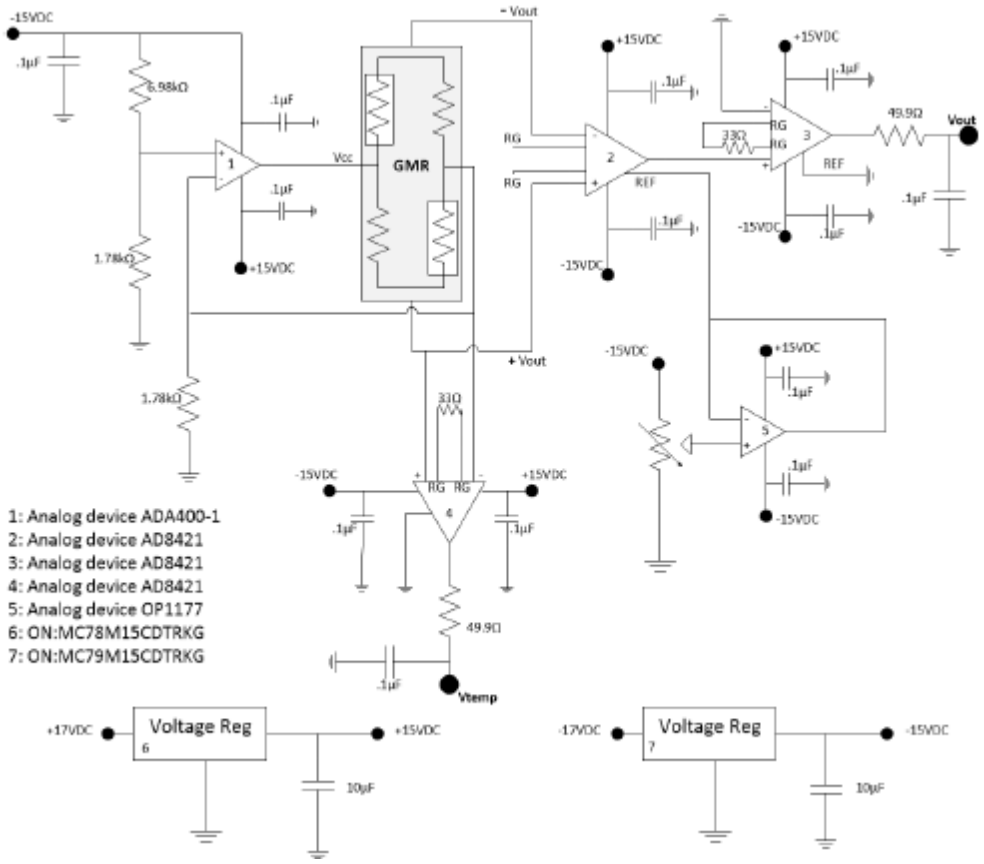

Fig. 1.5-14: Current supply and signal condition circuit for GF705 [20]

Fig. 1.5-15 shows the GF705 bridge output as a function of temperature. It can be noticed that temperature impact on GMR is only a few mV over a 60℃ temperature range.

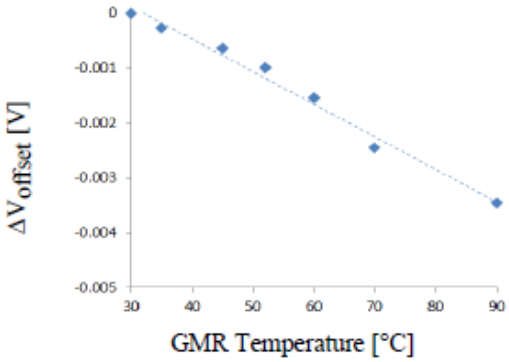

Fig. 1.5-15: Voltage output of GMR GF705 as a function of temperature [7]

The voltage across the shielded element of the GMR can be used to gain temperature information. Fig. 1.5-16 shows the relationship between this voltage and the temperature.

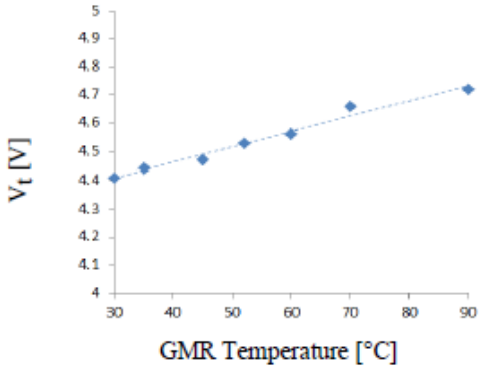

Fig. 1.5-16: Voltage output of shielded GMR GF705 as a function of temperature [7]

Although the GF705 is itself very resistant to temperature changes, it must be noted that the bias field permanent magnet has considerable temperature dependency. This dependency leads to a shift of bias point based upon temperature. The temperature information from the shielded resistor is useful decoupling the temperature effects from the GMR output. Fig. 1.5-17 shows the improvements attained by temperature decoupling. [7] describes a second method with the matrix-based decoupling of permanent magnet temperature effects by completely decoupling the bias field. This bias field decoupling is an extension of disturbance decoupling which is described later.

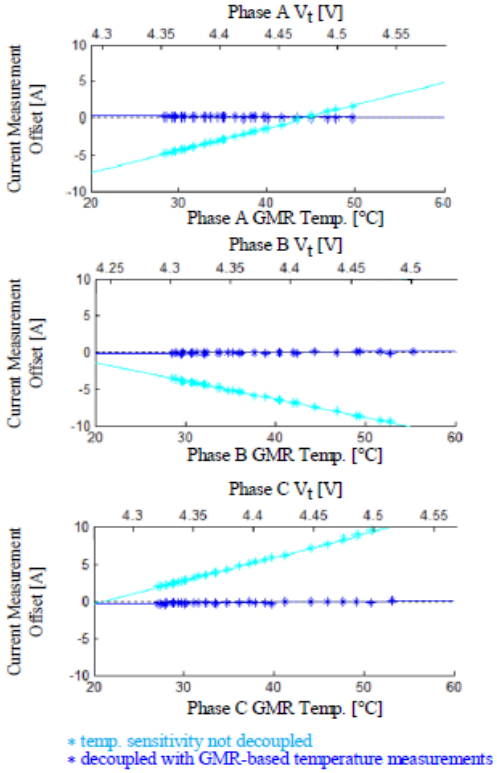

Fig. 1.5-17: GMR-based current measurement offset with and without temperature decoupling/compensation [7]

GF705 has hysteresis and limited linear range. Fig. 1.5-18 shows the illustration of hysteresis in GF705 which 0.054mT. The linear range with 2% linearity error is 1.8 to 8 mT [66].

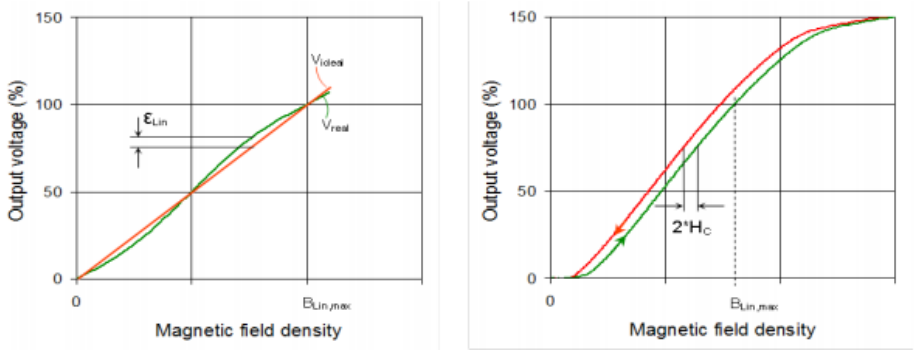

Fig. 1.5-18: Illustration of hysteresis in GF705 [66]

Fig. 1.5-19 from [64] summarizes the properties of GF705 as a function of magnetic field sweep range. None of the parameters shown are relevantly impacted by the upper limit of sweep.

Although sensitivity and linear range seems to have a correlation with range of sweep, studying data more closely shows that it is not the upper limit or range of sweep but increased number of data points leading to a better best fit line reduced linearity error. Another important reason for linearity trend is larger sweep leads to larger linear region being part of the sweep. It is safe to use the data points for upper limit of 12.5 mT to obtain hysteresis and sensitivity. Offset and hysteresis are not relevant since GF705 is used with a virtual zero point and will never experience hysteresis and offset around 0mT.

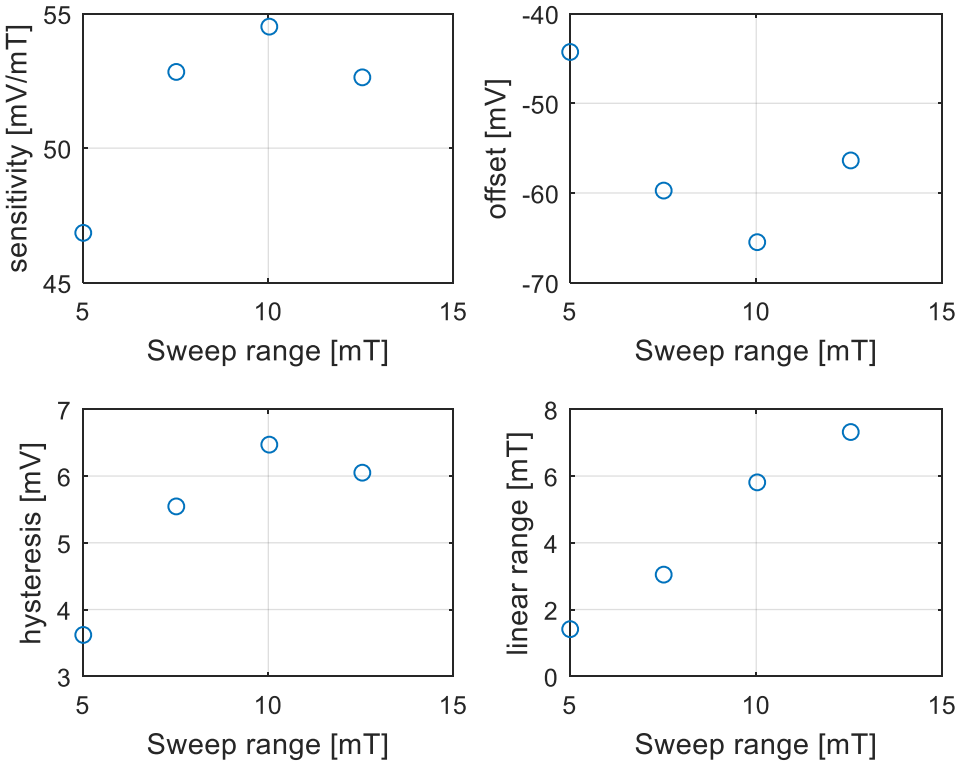

Fig. 1.5-19: Important parameters of GF705 as a function of swept range [64]

1.5.7 2-D TMR evaluation for current sensing

The 2-D TMR PFD (TF952) was still in its development phase in Sensitec when [64]was written. Due to this, only the bare die is available for this PFD. Fig. 1.5-20 shows the bondwired

PFD on its separate PCB. This PFD PCB was connected to signal conditioning and excitation board using standard six pin connector.

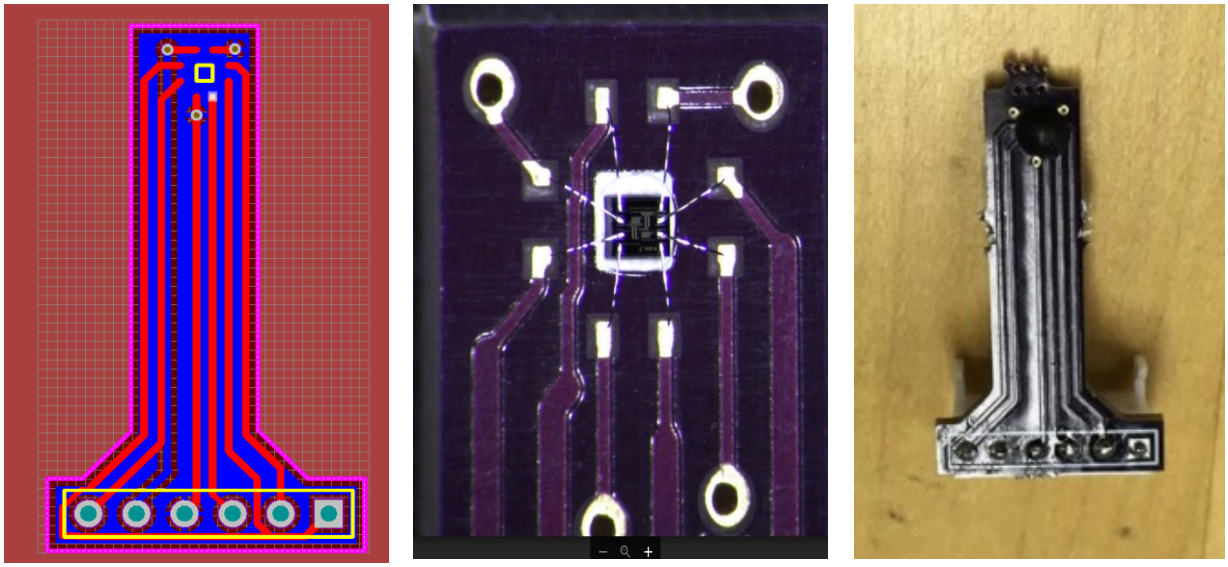

TMR PCB layout | Bondwired TMR die on PCB | TMR PCB with potting and connector

Fig. 1.5-20: 2-D TMR PCB [64]

The size of the chip is 0.85 x 0.7mm. Fig. 1.5-21 shows the schematic of the TF952.This generation of TF952 is ESD sensitive and breaks down with unshielded human touch.

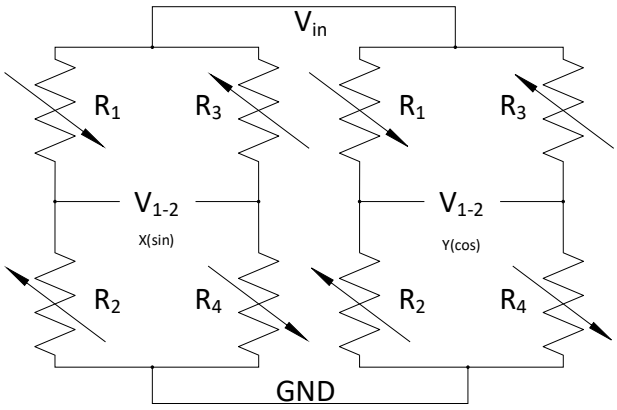

Fig. 1.5-21: Schematic of TF952 [64]

The main advantage of TMR over AMR or multilayer GMR is inherent bipolarity and no need of bias. Fig. 1.5-22 shows the characteristic curve of TF952 with linearity error over a sweep of ± 12.5 mT.

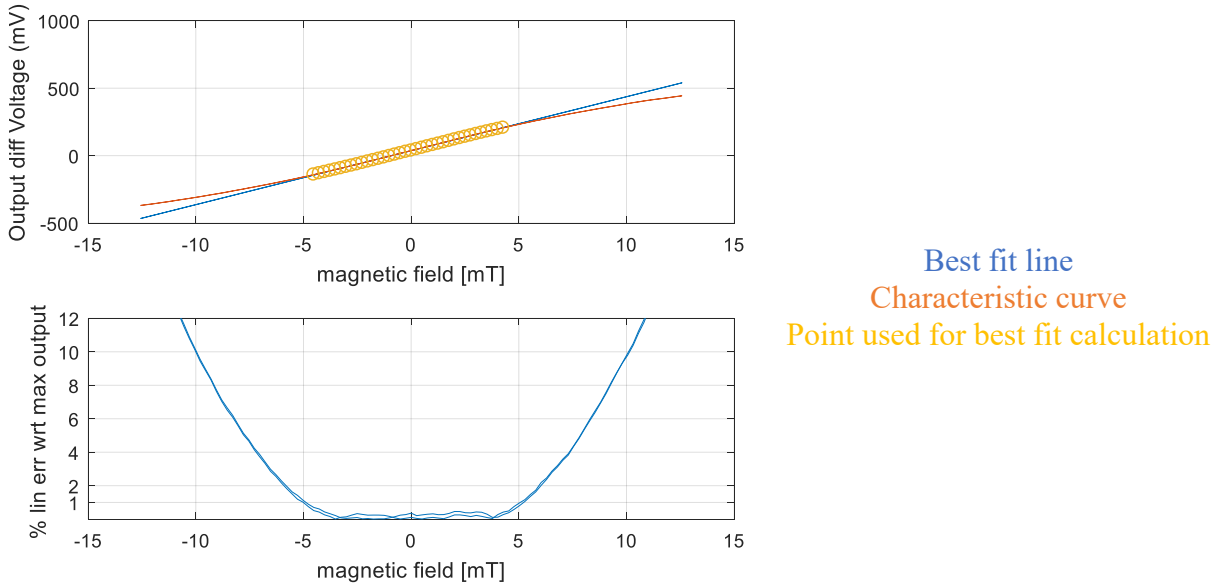

Fig. 1.5-22: Characteristic curve of TF952 with best fit line and linearity error [64]

The frequency response of TMR current sensing was evaluated in [68] by passing current through the wire with frequency of sine wave increased from 10 Hz to 10 kHz, The results of single sine frequency sweep FRF and Venable FRF are shown in Fig. 1.5-23.

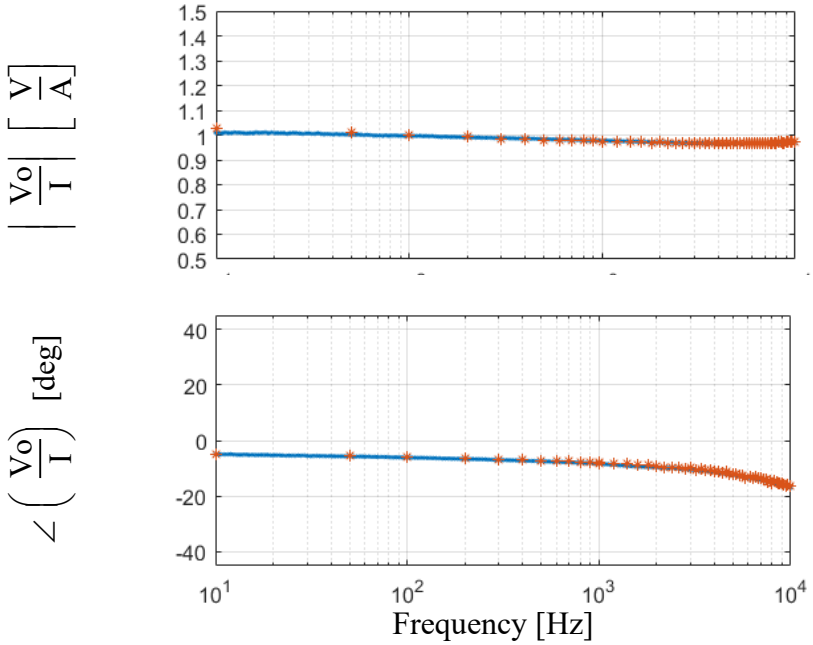

Fig. 1.5-23: FRF of the current input and TMR voltage output [64]

The magnitude remains within 3.5% for the 10kHz range. The most noticeable feature of frequency response in Fig. 1.5-23 is the phase. There is frequency dependency as well as an offset. Extensive testing was completed in [64] to explain and verify that the reason for the phase offset characteristic is hysteresis in the TMR.

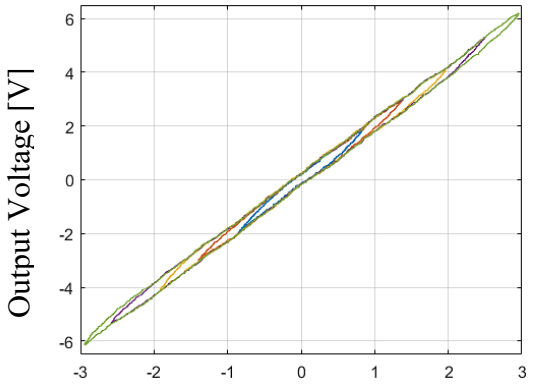

Input current at 100 Hz triangle wave at different amplitudes

Fig. 1.5-24: Minor Loops (hysteresis) of TMR PFD [68]

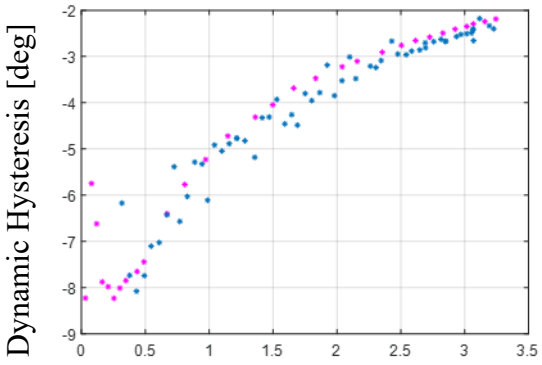

Fig. 1.5-25: Dynamic hysteresis as a function of current [68]

The hysteresis loops were be formed in [68] by plotting current reference on X axis and, TMR PFD conditioned output on Y axis. Different minor loops are plotted in Fig. 1.5-24 by increasing the amplitude of the triangular wave in the wire. Hysteresis was significant and remained virtually constant with the current range. The experimental dynamic hysteresis in degrees was calculated as the relative phase between the reference current and the TMR PFD output. Simulated dynamic hysteresis in degrees was calculated as relative phase between ideal TMR and TMR PFD with hysteresis for sensing current. The simulation used experimentally collected minor loops which are noisy. The overlay of experiment and simulation in Fig. 1.5-25 shows that dynamic hysteresis reduces as the amplitude of the sinusoid increases. Dynamic hysteresis is theoretically independent of the frequency of operation.

1.6 Decoupling 1-D Magnetic Fields

1.6.1 Orthogonal decoupling

Orthogonal decoupling is a simple method of decoupling or rejecting fields from sources other than the current being measured. Orthogonal decoupling as described in [69] uses the single axis property of the MR detector. Since MR detectors have a defined axis of sensitivity, they only measure magnetic fields in that direction. This inherently leads to the ability to reject fields that are orthogonal to the axis of sensitivity. Any magnetic field vector will be detected by the MR detector if there is a finite vector dot product of that vector with the axis of sensitivity as shown in (1.6-1).

$$V_{\text{out of PFD}} = \mathbf{S}\,\mathbf{B} \tag{1.6-1}$$

Where **S** is the PFD sensitivity vector and **B** is the magnetic field vector. This method of decoupling field is only useful in ideal circumstances when the field being produced has a defined

angle and fields from other sources are orthogonal to it. This method loses information about the external fields since they are outright rejected and not decoupled. If accurate information is needed about the magnetic field being measured, it is challenging due to dot product mathematics in which the angle and the magnitude of net magnetic field vector remain unknown.

1.6.2 1-D weighted field cross-coupling decoupling

The magnetic fields from various sources couple together and the MR detector only senses the net magnetic field at a point in space. This raises the need for decoupling the magnetic fields from one another. [69][70] proposes the weighted decoupling of cross-coupled fields from different conductors. In a typical three-phase system there are three conductors as shown in Fig. 1.6-1. If a MR PFD is placed close to each of the wire, the magnetic field sensed by each of the detectors has components of magnetic fields from other conductors. This phenomenon is shown in Fig. 1.6-2.

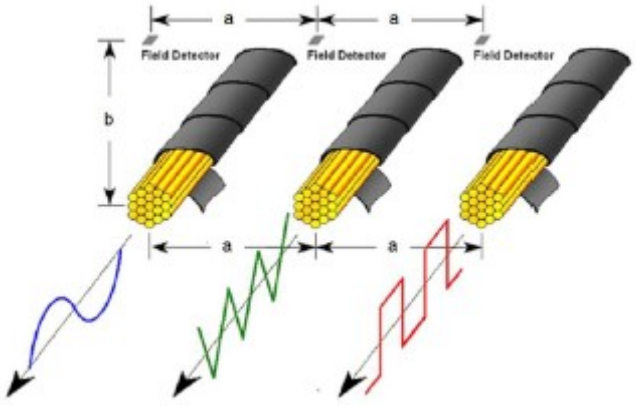

Fig. 1.6-1: Three conductor and three PFD system [71]

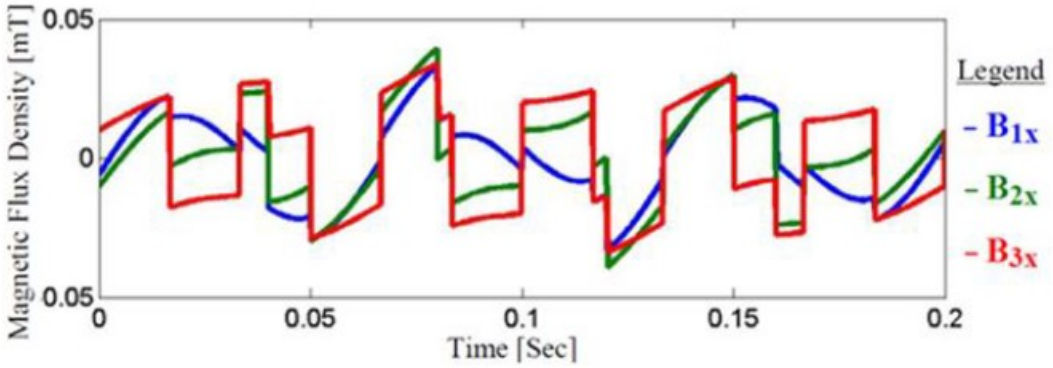

Fig. 1.6-2: PFD output of the three conductor and three PFD system [28]

The magnetic field signals observed in Fig. 1.6-2, can be modeled using the Ampere's law and are shown in (1.6-2). The inverse of the coupling matrix between currents and magnetic fields can be inversed as shown in (1.6-3) to decouple currents from coupled magnetic field data as shown in Fig. 1.6-3 [28]. These coupling and decoupling matrices can also be determined experimentally by passing one current at a time and recording its impact on each of the PFDs.

$$V = \frac{\mu}{2\pi}\begin{bmatrix} \frac{1}{a} & \frac{a}{a^2+b^2} & \frac{a}{a^2+4b^2} \\ \frac{a}{a^2+b^2} & \frac{1}{a} & \frac{a}{a^2+b^2} \\ \frac{a}{a^2+4b^2} & \frac{a}{a^2+b^2} & \frac{1}{a} \end{bmatrix}\begin{bmatrix} I_1 \\ I_2 \\ I_3 \end{bmatrix} = \begin{bmatrix} B_{1x} \\ B_{2x} \\ B_{3x} \end{bmatrix} \quad (1.6\text{-}2)$$

$$V = \begin{bmatrix} \hat{I}_1 \\ \hat{I}_2 \\ \hat{I}_3 \end{bmatrix} = \frac{2\pi}{\mu}\begin{bmatrix} \frac{1}{a} & \frac{a}{a^2+b^2} & \frac{a}{a^2+4b^2} \\ \frac{a}{a^2+b^2} & \frac{1}{a} & \frac{a}{a^2+b^2} \\ \frac{a}{a^2+4b^2} & \frac{a}{a^2+b^2} & \frac{1}{a} \end{bmatrix}^{-1}\begin{bmatrix} B_{1x} \\ B_{2x} \\ B_{3x} \end{bmatrix} \quad (1.6\text{-}3)$$

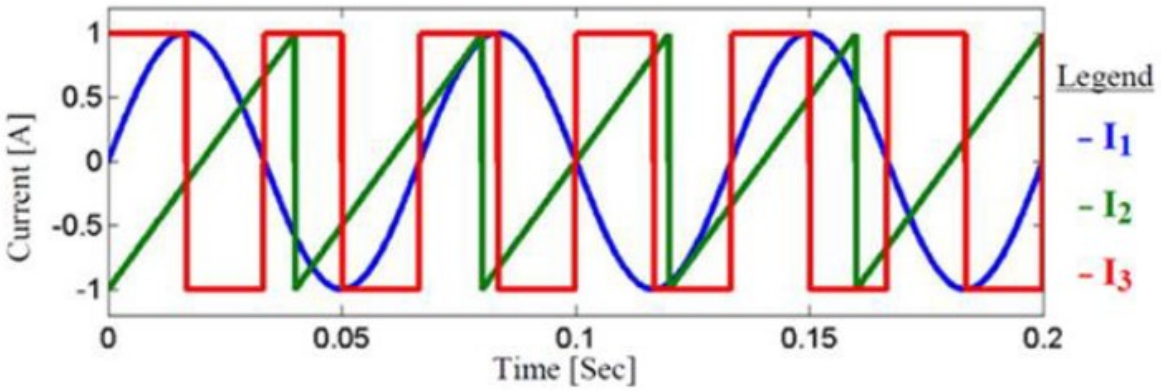

Fig. 1.6-3: Decoupled currents from three conductor and three PFD system [28]

The weighted field decoupling method is used in [72] to sense currents in a three-phase cable. The decoupling method proposed is essentially the same as the work in [69][71], however, it does involve more than one axis of detector sensitivity. The system is defined in cylindrical coordinates as shown in Fig. 1.6-4 and proposes using either the tangential or the radial axis of sensitivity of sensing the fields. The system which is only described analytically is in fact 1-D in terms of sensing, as field in only one of the axes at time is measured for decoupling. There is no analysis of AC currents and no experimental evidence shown.

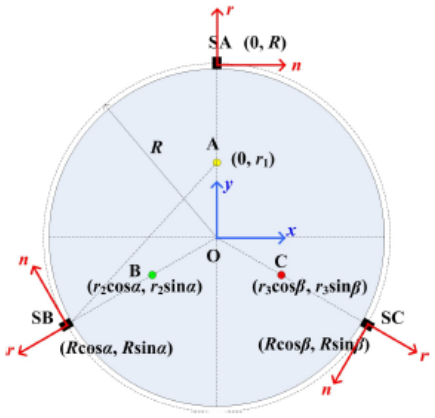

Fig. 1.6-4: Weighted field decoupling in three-phase cables [72]

1.6.3 1-D Disturbance field decoupling

The weighted field method of cross-coupling decoupling has been used in [65][7][67] to decouple the currents in a three-phase system. A 1-D MR PFD simply senses the magnetic field parallel to its axis of sensitivity, this can also lead to magnetic field measurement from disturbance sources like permanent magnets in the vicinity, electromagnetic motors among other sources of disturbances. [69] extended the weighted field decoupling method to decouple the disturbance fields as well. The details of this method are presented in [65] and implemented in [7]. Additional PFDs can be used to model the disturbance fields which can be decoupled. The process is illustrated in Fig. 1.6-5 and only accounts for disturbances in one direction.

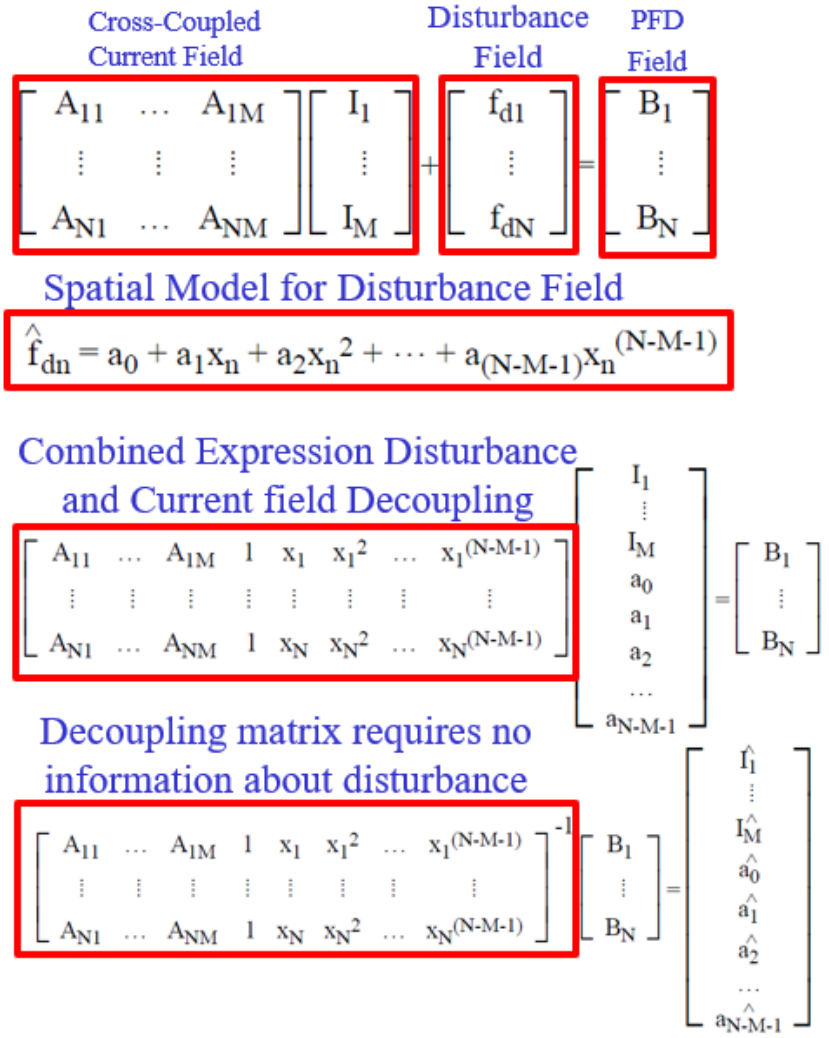

Fig. 1.6-5: Equations to model and decouple the disturbance [69][20]

In [20] the decoupling of disturbance fields is further developed and evaluated. The coupling and decoupling matrix should be square and invertible i.e. full rank. [20] also describes the concept of condition number which describes the sensitivity of the linear solution of to a change in input. A low condition number means the matrix would be less prone to transferring the error from input to output. Fig. 1.6-6 shows the error in decoupled current as a function of condition number of coupling matrix.

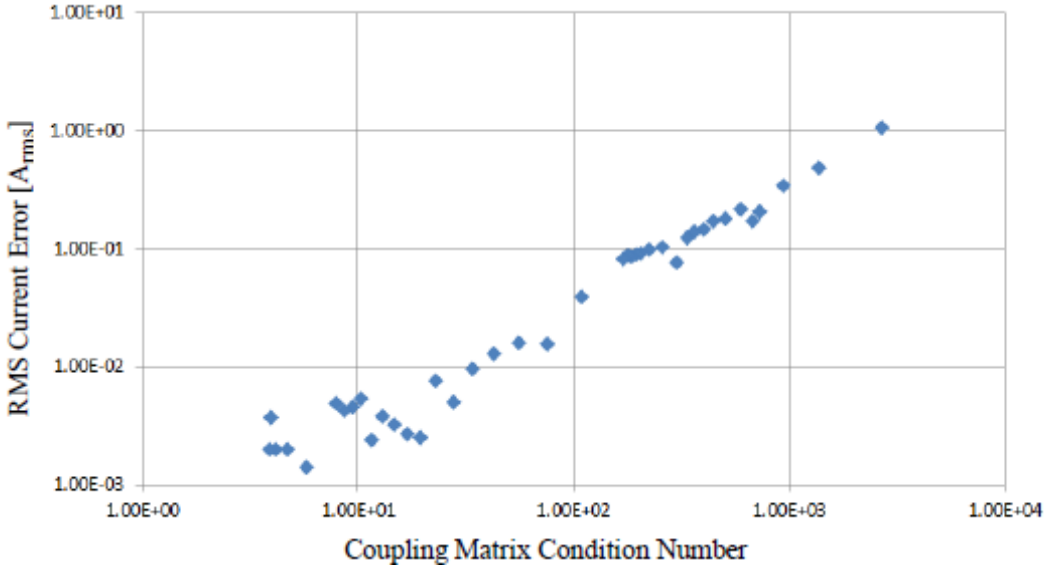

Fig. 1.6-6: Error in decoupled current as a function of condition number of coupling matrix [20]

1.7 Artificial Neural Networks

Artificial neural networks have been used for a variety of modelling applications even in non-linear and discontinuous [73]. A neuron, shown in Fig. 1.7-1, is the basic unit of the neural network. It consists of the sum of weighted inputs and a bias that are passed through a non-linear function referred to as the activation function. Common non-linear functions include the logistic function, tanh function, and rectified linear unit (ReLU).

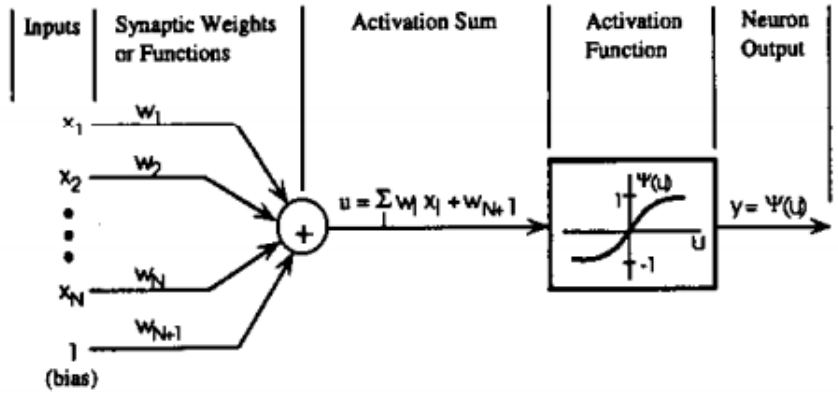

Fig. 1.7-1: A typical sigma neuron [73]

A group of neurons, each with their own set of weights and bias, form a neural network. Neural networks have three main types of layers. First is the input layer, which feeds into the into the hidden layers, in which the inputs are weighted and summed before passing through a non-linear function. There may be one or more hidden layers, where each successive layer is fed by the previous layer. The outputs of the final hidden layer are passed to the output layer. The number of hidden layers can be increased to go into the territory of deep learning. A three layer network with a single hidden layer is used based upon the Universal approximation theorem [74] which states that three layer network can approximate any function arbitrarily well with sufficient nodes in the hidden layer and appropriate weights.

A feedforward neural network (FNN) consists of many neurons in layer which are cross-coupled and cascaded [73]. The key characteristic FNN is unidirectional information flow which can be used to model linear and non-linear functions. If the system model includes an integrations, a recurrent neural network model it well by including an FNN with a feedback path.

Magnetic field cross-coupling in air from multiple currents can be modelled using a linear model without any integration. This means that FNN can be used to model and decouple the fields into the currents producing it. This a simple application of FNN without any non-linear modelling and is yet to be studied.

1.8 1-D PFD Array Around the Conductor

Field detectors can be arranged in circular arrays around conductors to measure AC and DC currents. The primary goal of arrays of PFDs is to sense a current and to reject the disturbances [75][76]. The PFD used in circular arrays include AMR, TMR, fluxgates as well as hall sensors. In [75], a mathematical algorithm is proposed which is able to sense the current inside the circular array of the PFDs. The algorithm is able to distinguish between the current inside and outside the

array thereby reducing the impact of disturbance fields from other currents. The algorithm, however, only works with DC currents since it cannot account for the frequency dependency of the currents.

[76] and [77] propose complex mathematical algorithms to be able to sense currents using PFD arrays. In [77], a harmonic analysis-based mathematical signal processing is proposed to sense three-phase currents in parallel conductors. The sensing is shown to work within common frequency band. The system, however, is very theoretical and uses finite element or a very tedious calibration process to capture the frequency dependency of the field.

[78] and [79] have investigated the errors which are commonly encounter in the PFD circular array-based current sensing. [79] has used commercial TMR sensors as the PFD and analyzed the issue of off center conductor in a circular array. [78] has evaluated the realistic issue of circular array-based current sensing in terms of range and rejection of disturbances and proposed disturbance compensation as a solution.

Despite the array of PFDs, this method of current sensing requires significant design and computation effort for accurate current sensing. The other major issue is the range of the PFD, which can become saturated with higher currents.

1.9 Gradiometer

Field detectors can be arranged in different topologies, locations and orientations inside the field detector die or cell. Fluxgate, Hall and MR detectors all have different electrical topologies and physical orientations and locations around the conductor to achieve features such as disturbance decoupling, increased sensitivity and higher range.

The gradiometer topology is different from simple PFD, in that they have larger dies with two field detection areas. These detection areas are typically around 1mm apart. The differential output

of the gradiometer detector is proportional to the field gradient between the two detection areas. Sensing the field gradient filters, the homogenous disturbances.

1.9.1 Open loop gradiometer

They are one of the most reliable and simplest forms of magnetic field-based current sensing with inherent disturbance field decoupling. Fig. 1.9-1 shows the schematic used to represent a MR gradiometer. The half-bridge branches of the gradiometer essential act as independent point field detectors with voltage output being proportional to the field at that point, albeit with opposite polarity. The differential voltage hence becomes proportional to the difference between the magnetic fields (B_1-B_2) at the two points. Although, the Fig. 1.9-1 shows the gradiometer schematic with generic MR detectors, they could be Hall, AMR, GMR or TMR.

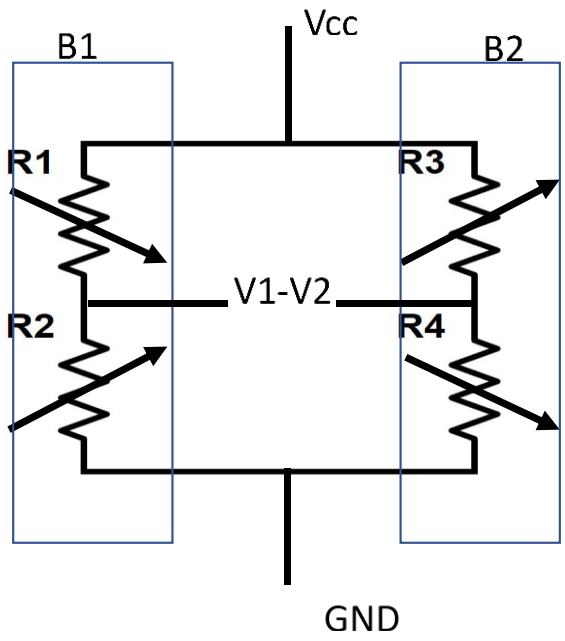

Fig. 1.9-1: Schematic of Magnetoresistance gradiometer

Due to the very small distance, typically a few millimeters, between 2 points of magnetic field measurement, any disturbance fields are assumed to be homogenous over the gradiometer, thereby

impacting both branches equally. The result is that any fields equal over both branches get cancelled out in the differential voltage which only registers differential fields.

Gradiometers function over a basic assumption that disturbance fields are homogenous over both the branches. A disturbance field with high spatial gradient can cause problems in functioning of the gradiometer. Gradiometers are open loop, hence are prone to any and every problem point field detectors are vulnerable to. Furthermore, gradiometer function with a field gradient, to use them for current sensing current must pass through primary conductor which produces a field gradient. Primary conductor design to produce appropriate magnitude and direction of field gradient requires significant engineering effort and money.

1.9.2 Closed loop gradiometer

Closed loop gradiometers in principle are an extension of open loop gradiometers described above. They use an external regulator, usually an ASIC, to produce a compensation current that nulls the voltage output of the gradiometer by producing a magnetic field equal and opposite to the external field. Since the spatial relationship of the compensation current and gradiometer output is constant, the value of current flowing through the compensation coil is proportional to the external magnetic field gradient. Closed loop gradiometers are considered very robust because they reduce the impacts of slight changes in sensitivity and temperatures while providing the usual benefits of the gradiometer.

The basic building block of closed loop gradiometers is the open loop gradiometer. Hence most problems mentioned earlier for the point field detector and gradiometer hold true. However, the extent to which they hold true are much reduced. For example, since ideally the closed loop gradiometer is operating about zero, the sensitivity changes, linearity limits and hysteresis might

never be encountered. Also, temperature dependency of gradiometer can be reduced by sensing temperature in the regulator and compensating for it.

Closed loop gradiometer performance also depends upon the functionality of the null regulator or the ASIC. Due to this the complication of the system increases. This also leads to cost and size increases. Another issue with closed loop gradiometer is the power loss in the compensation coil.

1.10 1-D Busbar Gradiometers

The gradiometer approach has been used to design a 1-D MR gradiometer [64] integrated on a straight busbar. The current sensing gradiometer consists of two AMR PFDs (AFQ720) integrated across a busbar shown in Fig. 1.10-1.

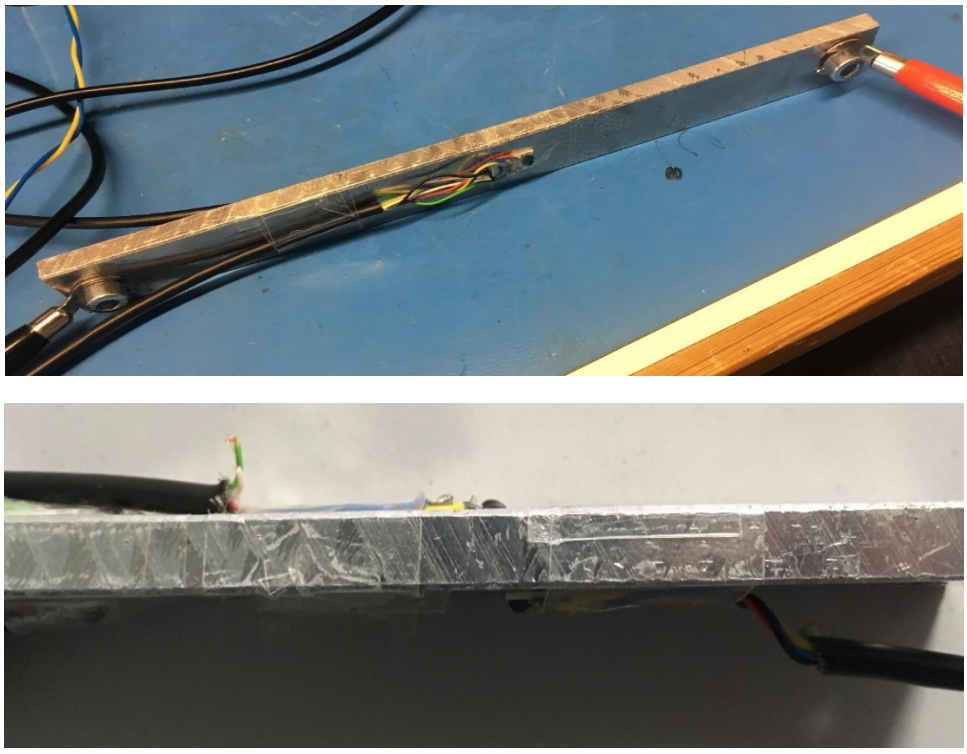

Fig. 1.10-1: Straight busbar MR gradiometer [64]

The axis of sensitivity of both PFDs is identical; as current flows, the output voltages of the PFDs move in opposite directions as they experience equal and opposite fields. Fig. 1.10-2 shows

the differential voltage between the two PFDs increases linearly as the current passing through the busbar increases.

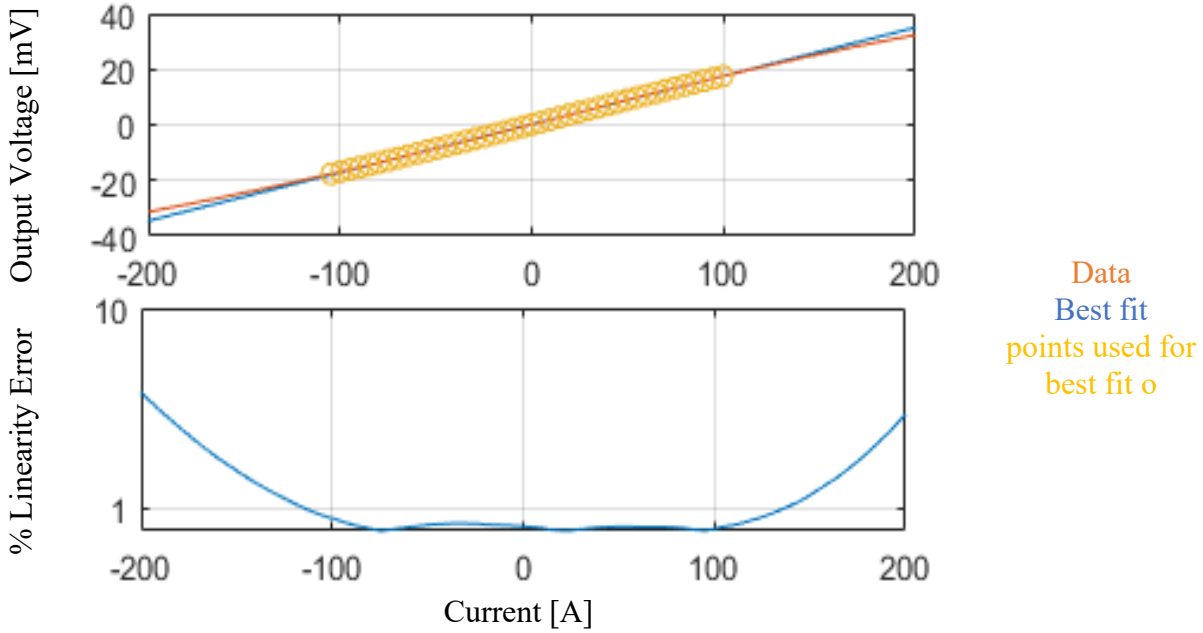

Fig. 1.10-2: AMR gradiometer voltage output with respect to current [64]

The disturbance to be rejected by the sensing must be homogenous over both the PFDs and is modeled by (1.10-1).

$$C_x \begin{bmatrix} 1 & 1 \\ -1 & 1 \end{bmatrix} \begin{bmatrix} I \\ D_{x/y} \end{bmatrix} = \begin{bmatrix} VB_{x1} \\ VB_{x2} \end{bmatrix} \qquad (1.10\text{-}1)$$

This gradiometer is a very promising option for PFD-based current sensing with inherent disturbance decoupling. If the disturbance is not uniform over the two points of field detection, the disturbance will not be decoupled or rejected. Senis AG busbar current sensing [43] also uses this 1-D gradiometer principle, albeit with hall effect detectors.

1.11 2-D Gradiometer

The 2-D PFD is used to create a 2-D gradiometer integrated in a busbar conductor [68]. This gradiometer essentially replicates the 1-D gradiometer in 2-dimensions to create redundancy. A

conductor is designed in [64] to create field gradients in 2-D which can be sensed by the 2-D PFD gradiometer. Fig. 1.11-1 shows the design of this conductor. As current flows along the length of the busbar, its path is shaped such that it has flow in both X and Y axis. This path allows magnetic field generation in both the X and Y axes. This 2-D gradiometer doubles the degrees-of-freedom and creates a redundancy without additional PFDs. The differential voltages in X and Y of the 2-D PFDs are both proportional to the field gradient and the current though the busbar. Measuring gradient filters disturbances which are homogenous over the gradiometer.

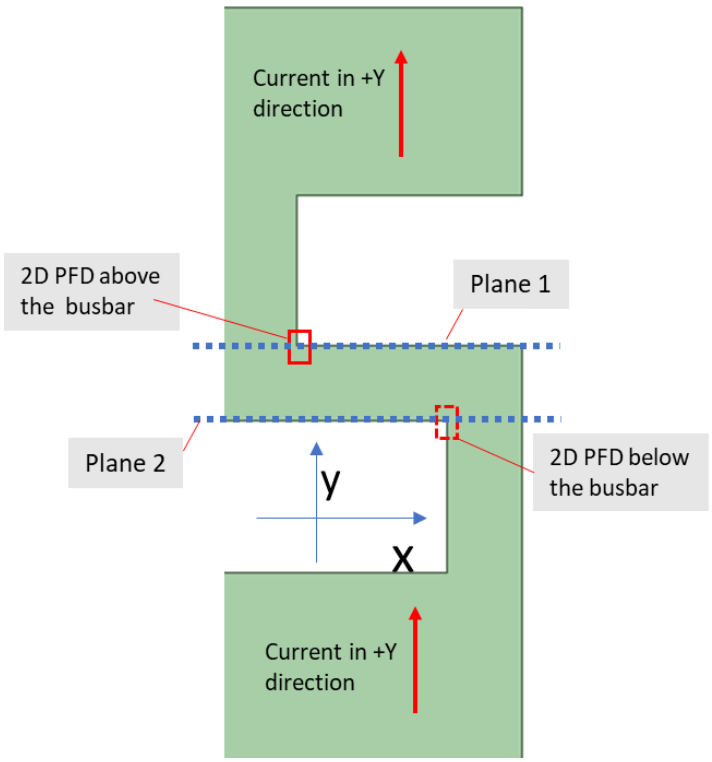

Fig. 1.11-1: Busbar to shape field gradients in 2-D with S cutout

The 2-D field gradient between the top and bottom of the conductor can achieve current sensing with inherent disturbance field decoupling as shown in (1.11-1). This model applies to both axes independently.

$$C_{x/y}\begin{bmatrix} 1 & 1 \\ -1 & 1 \end{bmatrix}\begin{bmatrix} I \\ D_{x/y} \end{bmatrix} = \begin{bmatrix} VB_{x1/y1} \\ VB_{x2/y2} \end{bmatrix} \quad (1.11\text{-}1)$$

Where I is the current being sensed, VB1 is the output voltage of the PFD 1, VB2 is the output voltage of the PFD 2, D represents the disturbance and C represents the coefficients for converting I to VB. X or Y refer to the axis being used.

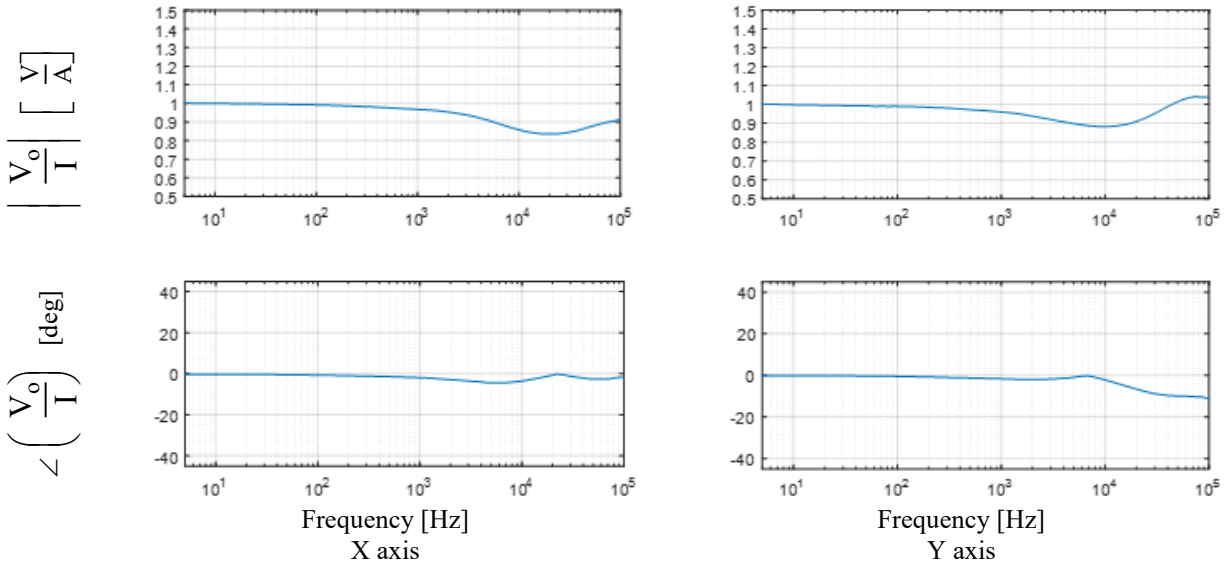

Fig. 1.11-2: FRF of relationship between the current input and fabricated 2-D GMR output

The FRF in Fig. 1.11-2 shows that the gradiometer can provide 5% FBW for well over 1kHz and 3dB performance of well over 100 kHz in both axes. Fig. 1.11-3 shows the voltage output with respect to the current in the busbar. 2-D gradiometer outputs have twice the sensitivity of the PFDs and the output is linear and is expected to stay linear with in the magnetic range of the PFDs.

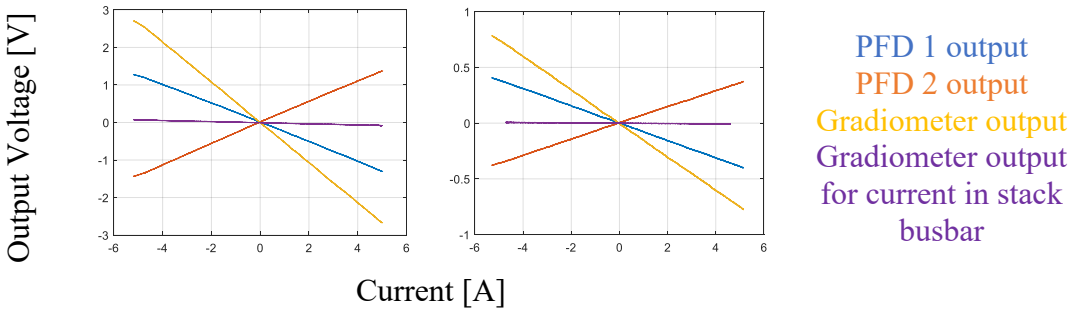

Fig. 1.11-3: 2-D GMR gradiometer voltage outputs (X left, Y right) with respect to current [68]

1.12 AMR-based Commercial Current Sensors

AMR-based closed loop gradiometer current sensing is used in Sensitec's four current sensor product lines for low to medium current ranges. AMR being the least prone to noise and hysteresis and most mature of the MR technology is a reliable magnetic field detector. However, it is not very sensitive, requires a bias magnetic field to create linear behavior and cannot naturally distinguish between the fields from currents and stray sources. To compensate for these problems in the AMR-based sensors, Sensitec has specially engineered current sensors. These sensors work with closed loop null regulation to increase the accuracy and sensitivity of sensing system. The U shape primary conductor is used to create a field gradient over very small distances as shown in Fig. 1.12-1. This gradient is detected and outputted as a differential voltage when detected by AMR chip structure laid out as a gradiometer. Since the field gradient is measured over distance of around 1 mm, the disturbance fields are automatically decoupled since they are homogenous over both points used for gradient. Fig. 1.12-2 shows the commercial AMR current sensors with the U shape primary conductor and permanent bias magnet.

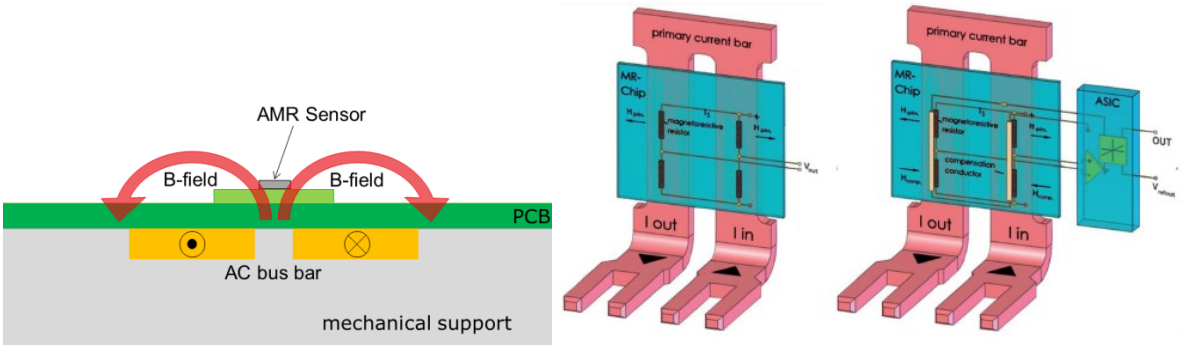

Fig. 1.12-1: Illustration of Sensitec's commercial sensor with closed loop gradiometer and U shape primary conductor for creating field gradient [80]

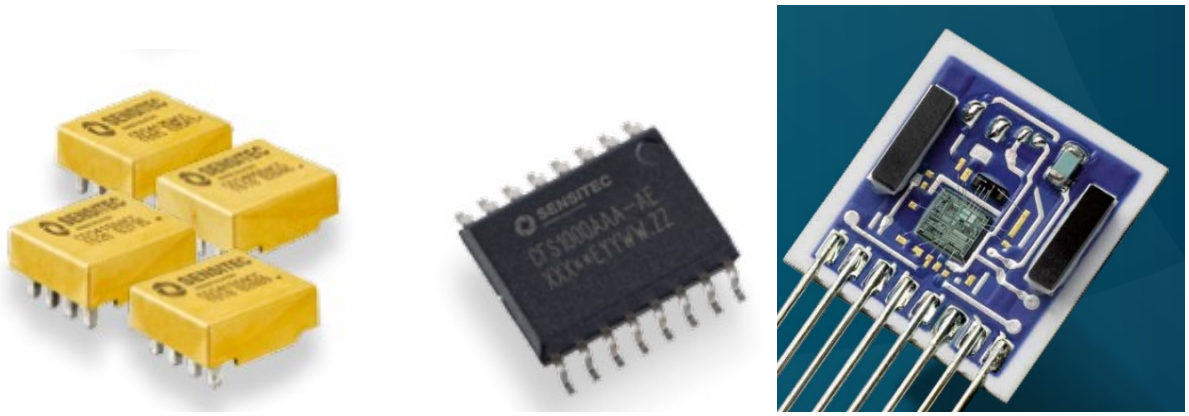

Fig. 1.12-2: Commercial Sensitec AMR-based current sensors with magnets [6]

1.13 Skin and Proximity Effects

Skin effect is a frequency dependent effect that causes a change in distribution of current density in the cross section of a conductor. Skin effect causes the current density to increase towards the outer edges of the conductor at higher frequencies [81][69][28]. Skin effect originates from the phenomena described in the Maxwell-Faraday equation and can also be attributed to the internal inductance. Skin effect for this work can be modelled using (1.13-1). The model shows that the depth of the current in the conductor will decrease with an increase in the frequency.

$$J = J_s\, e^{-(1+i)d/\,\delta}$$
$$\delta^2 = \frac{1}{f\,\pi\,\mu\,\sigma} \qquad (1.13\text{-}1)$$

The skin depth (δ) is the depth (d) in the conductor at which current density (J) is 1/e times surface current density (J_s). It depends on material properties: permeability (μ) and conductivity (σ) which is the inverse of resistivity (ρ). This explains that materials with higher permeability like magnetic materials and conductors experience skin effect at relatively lower frequencies.

The change in the current distribution causes a change in the magnetic field around the conductor as well. Hence, skin effect is responsible for frequency dependent magnetic field

changes around a conductor. In case of round conductor, magnetic field doesn't undergo frequency dependent changes, since current close to circumference of the circular cross section still can be modeled as being at the center point of the cross section due to symmetry. In the case of rectangular conductor, the skin effect causes the current density to increase close to the vertices of the cross section. The magnetic field follows the current. Fig. 1.13-1 from [82] shows the skin effect in a rectangular conductor in an arbitrary cross-sectional plane.

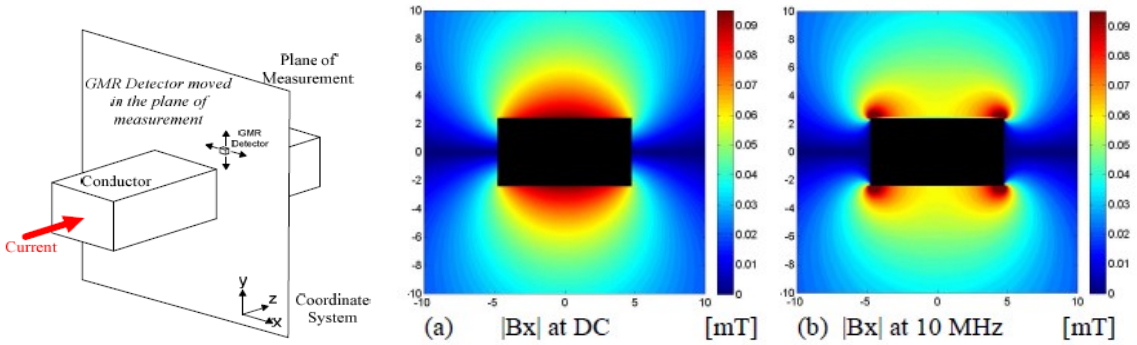

Fig. 1.13-1: Magnetic field distribution around rectangular conductor at 2 different frequencies [82]

The magnetic field is computed using Ansys Maxwell software which computes the magnetic fields using FEA, with details of computation presented in [69].

Proximity effect is a frequency dependent effect which causes a change in magnetic field around a conductor if another conducting material is present near the conductor. The proximity effect just like skin effect originates from the phenomena explained in the Maxwell equations, especially Faraday's induction. Proximity effect causes a change in outlook of the magnetic field at high frequency with conducting material in the vicinity.

Proximity and skin effects generally occur at similar frequencies. In most real practical cases there is always conducting material near the current carrying conductor. Due to this, frequency

dependent effects on the magnetic field around conductors are grouped under proximity and skin effects, both of which originate due to eddy current induction described in Maxwell equations.

FEA analysis and details of skin and proximity effects on magnetic field with single and multiple conductor systems typical to power modules and busbars is deeply studied in[20][28][69][65][82].

1.14 Magnetic Field Shaping Metrics

1.14.1 1-D Flat Bandwidth

5% Flat Bandwidth (FBW) at a point in space is the frequency at which the magnetic field originating from the current deviates by ± 5% from its value at DC. FBW is developed and defined in [83][84], which maps the frequency dependency of the magnetic field at a spatial point. Fig. 1.14-1 shows the magnetic field magnitude at two points above the conductor as a function of frequency. As shown in Fig. 1.14-1 FBW is the frequency marked with a vertical line where the normalized field strength crosses the ± 5% band defined from DC strength. Fig. 1.14-2 shows the flow chart to calculate the bandwidth.

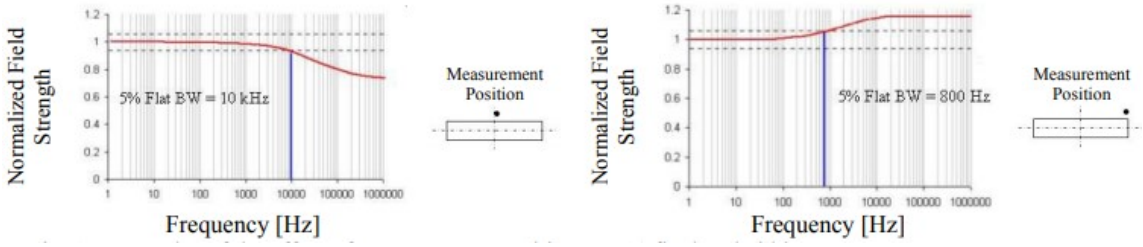

Fig. 1.14-1: Definition of 5% flat bandwidth at 2 points [84]

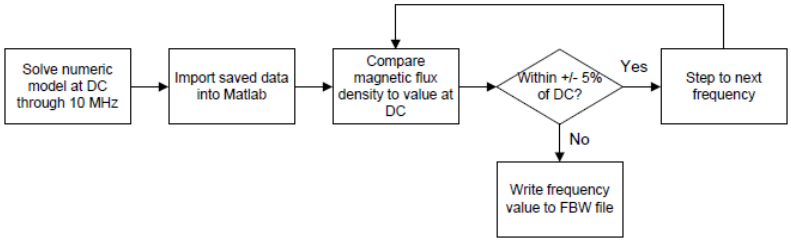

Fig. 1.14-2: Flow chart of MATLAB script to calculate the flat bandwidth [28]

The FBW error percentage is application dependent. The percentage can be tightened or loosened based upon the accuracy and precision requirement. The conventional 3dB translates to 30% band whereas 5% FBW translates to a much tighter band of 5%. Fig. 1.14-3 shows the magnetic field and FBW around a rectangular conductor.

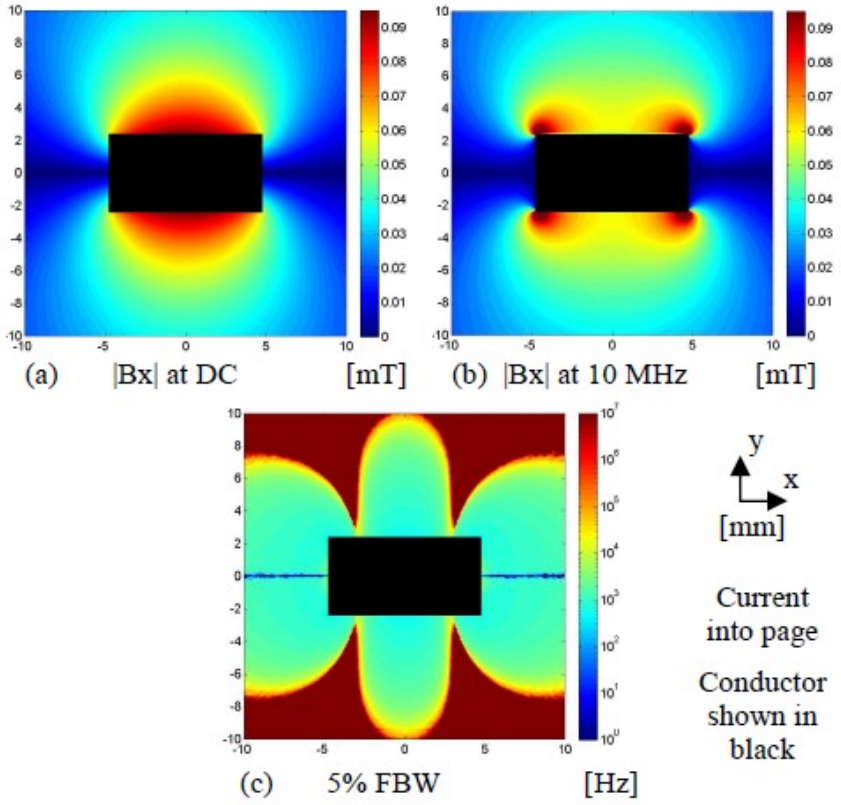

Fig. 1.14-3: Magnetic field distribution around rectangular conductor and FBW [82]

1.14.2 2-D Flux Density

The 2-D Flux density metric is the product of magnetic flux density in the X and Y axes [64]. This metric is a useful one since it can filter out regions where one or both of the axes have very low magnetic flux density. The 2-D flux density is measured in units of Tesla^2. 2-D flux density is computed using the X and Y magnetic field from the FEA software in post-processing. Fig. 1.14-4 shows the flux densities around a rectangular conductor to illustrate the 2-D flux density as

well as the frequency dependency of the magnetic fields. It must be noted that 2-D flux density is an auxiliary metric to X and Y field densities. Any point deemed inappropriate in 2-D flux density should not be used for 2-D PFD placement.

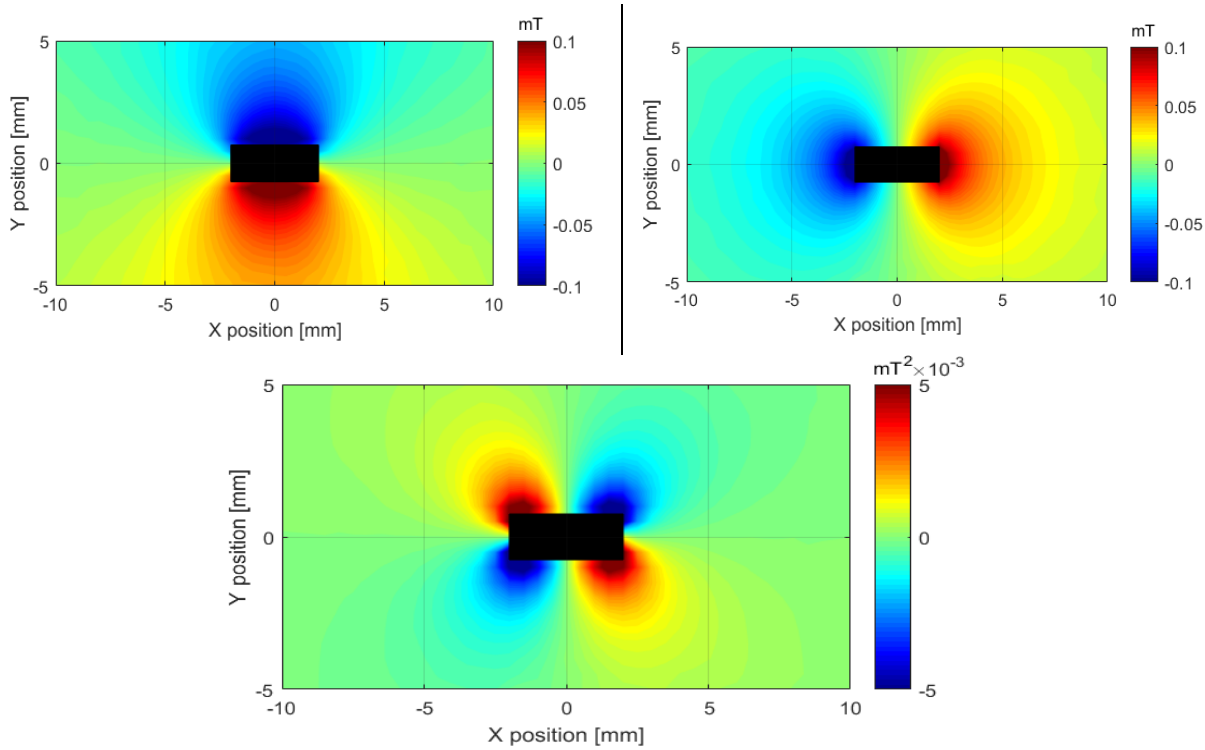

Fig. 1.14-4: X, Y components and 2-D flux around a rectangular cross section (4 x 1.5 mm) copper conductor with 1A DC current [64]

1.14.3 2-D 5% Flat Bandwidth

Flat bandwidth is essentially defined for magnetic field in one dimension, or for field in a single axis. The 2-D 5% FBW is computed using the lower of the X and Y 5% FBW at each point [64]. This metric combines the information from two separate bandwidths into a single bandwidth metric, due to which 2-D PFD can be placed with higher reliability.

Fig. 1.14-5 shows the 2-D 5% FBW around the same rectangular conductor along with the X and Y bandwidth. The 2-D FBW is derived from the individual X and Y bandwidth due to which the 2-D FBW can be used without the need for inspecting X and Y bandwidths.

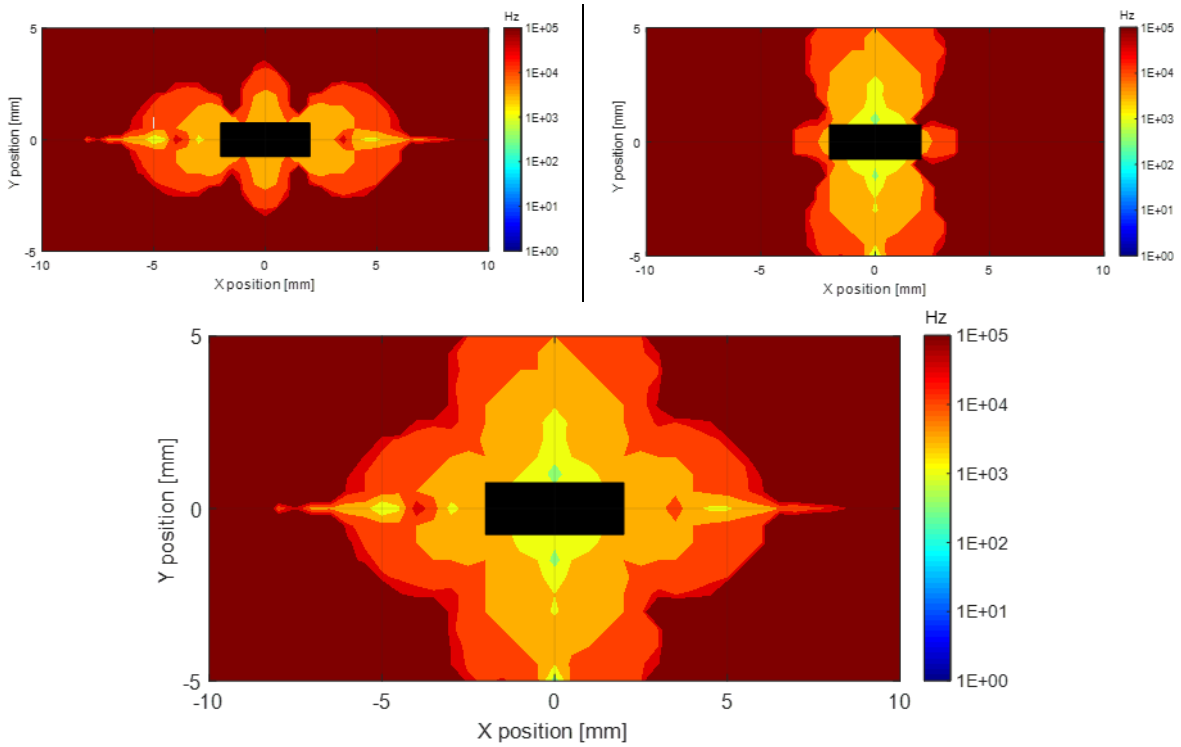

Fig. 1.14-5: X, Y and 2-D 5% FBWs for a rectangular cross section (4 x 1.5 mm) copper conductor with 1A current [64]

The 2-D PFD positioning methodology proposed in [64] uses 2-D FBW as a first metric to filter the regions which have less frequency dependency. These regions are further filtered using the 2-D flux density and then with X and Y flux densities. This is shown in Fig. 1.14-6.

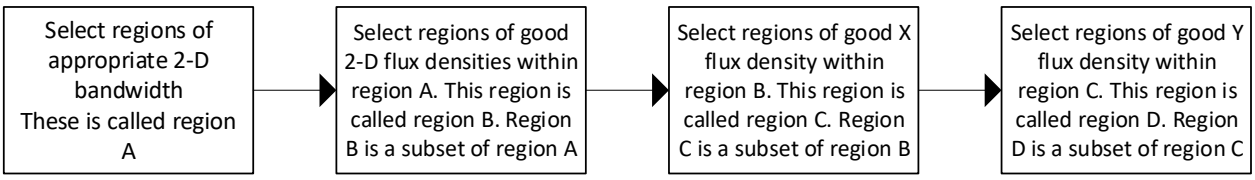

Fig. 1.14-6: Schematic of 2-D PFD positioning methodology [64]

1.14.4 Optimization Function

Flat bandwidth can be a misleading metric when not used in combination with flux density. A region far from a conductor will have zero magnetic field at DC and this will stay zero independent of the frequency.

Instead of using strength and bandwidth separately, [69] presented an optimization metric which combines the bandwidth and strength in a single metric with a value between 0 and 1.

(1.14-1) shows the optimization function [69]. The indices m and n signify the relative importance of strength and bandwidth. A_{norm} shown in

(1.14-1) is the maximum value of optimization function anywhere in the space and is used to normalize the optimization function.

$$\bar{O}(x,y) = \frac{1}{A_{norm}} \left| B(x,y) \right|^m FBW(x,y)^n \tag{1.14-1}$$

$$A_{norm} = \max\left(\left| B(x,y) \right|^m \right) \max\left(FBW(x,y)^n \right)$$

1.15 1-D Magnetic Field Shaping Conductors

To use the point field detection for current sensing, the PFD must be placed at a point in space with an appropriate output of optimization function. This means that both the FBW and flux density should be in a reasonable range. In power electronics there are typical structures including power modules bondwires, leadframes, terminals, connecting wires and busbars. These structures have been investigated in detail in [20][28][69][65][82]. These dissertations have detailed FEA and experimental verifications of flux density and bandwidth in typical conductors in AC drives and identified regions appropriate for PFD placement as well as modifications to improve the regions of high fidelity, strength and bandwidth. Skin and proximity effects play key roles in flat bandwidth regions in power electronics due to the high density of the conductors which are inductively coupled. [85] proposes methodologies to shape the regions of high bandwidth by taking advantage of proximity effect. Fig. 1.15-1 shows that in typical power module, bondwires have a copper sheet close to them. This copper sheet is under the insulating substrate and shapes

the bandwidth region between the bondwire and copper. Placing another copper sheet as shown in Fig. 1.15-1 can shape the bandwidth region up to MHz. This figure also models the frequency dependency of flat bandwidth region and relative geometry of conductors like bondwires.

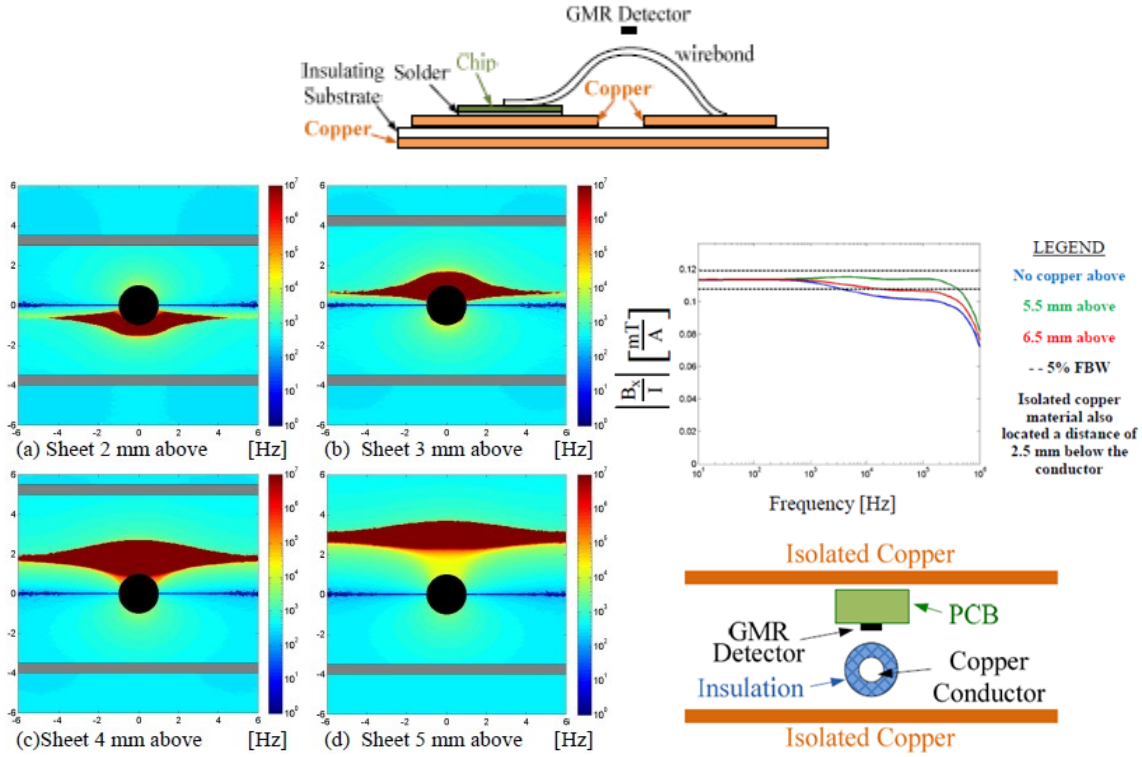

Fig. 1.15-1: 5% flat bandwidth around bondwire with fixed copper sheet at the bottom and top copper sheet at variable distance [82]

[85] models the region of high FBW with respect to the bondwire geometry. Fig. 1.15-2 shows that high bandwidth regions exist above the bondwires.

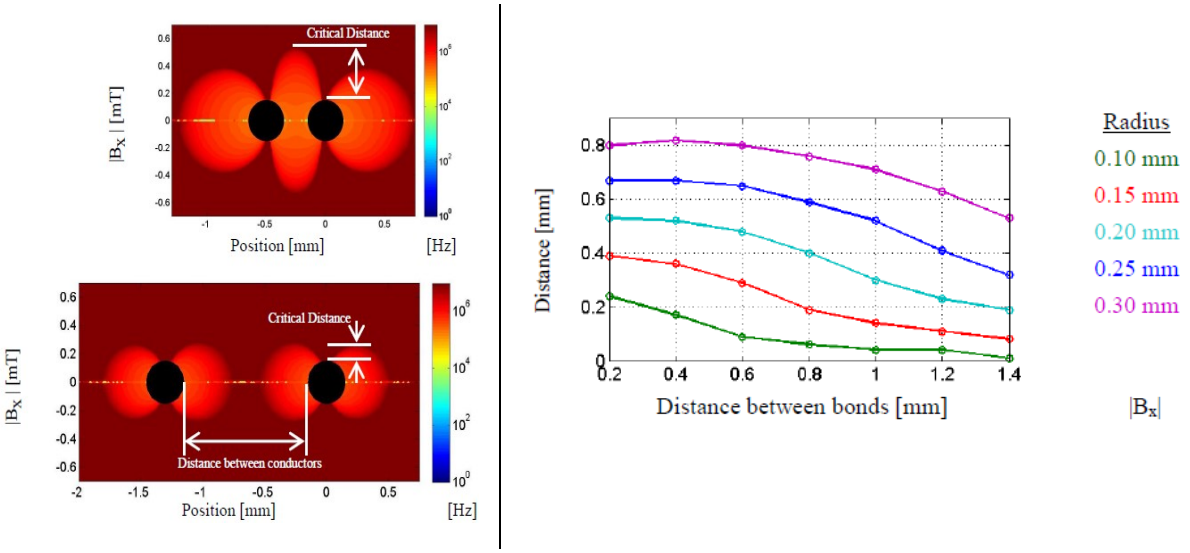

Fig. 1.15-2: Model of regions of 5% flat bandwidth around bondwires [85]

[69] and [86] have evaluated power module design specifically focusing on interconnects made out of flex foil to evaluate the performance of PFDs around such structures. [20] categorizes and analyzes the magnetic field strength and bandwidth around typical three-phase busbars in inverters. [67] has a methodology for designing leadframe for power modules. These leadframes have location of high strength and bandwidth for high fidelity magnetic field measurement. Fig. 1.15-3 shows the leadframe design and magnetic field outlook around it. This leadframe is scalable in all dimensions for appropriate power density.

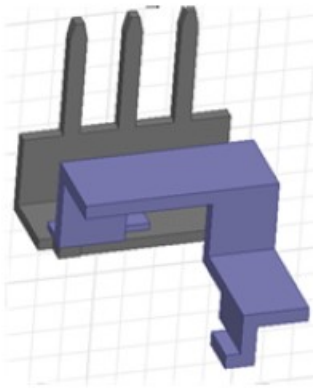

Fig. 1.15-3: Leadframe for power module and magnetic field around it [67]

[87][5] proposes field shaping using a folded trace structure to increase the flat bandwidth. The folded trace provides high strength, bandwidth and EMI protection to PFDs inside the loop of the trace. Fig. 1.15-4 shows the trace which was used to sense current with AMR PFD for closed loop GaN half-bridge converter.

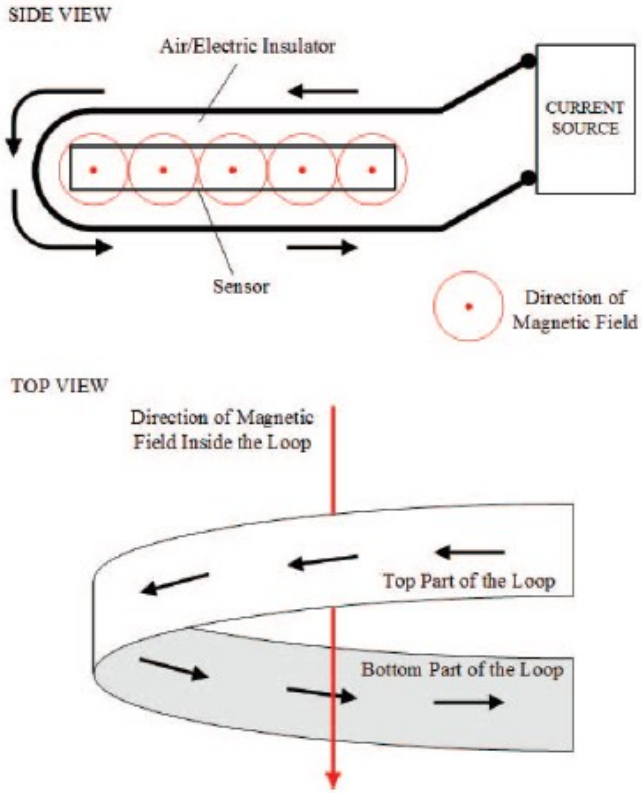

Fig. 1.15-4: Folded trace for high bandwidth and strength [87]

1.16 Power Module Integration/Packaging

A power module is a package of semiconductor devices with terminals connections at various nodes of the circuit topology implemented inside the module. There are multiple semiconductor topologies available in power modules. Two of the most common topologies are shown in Fig. 1.16-1. These are the 2-in-1 half-bridge topology and 6-in-1 three-phase inverter topology. Other

topologies are available as well, such as full-bridge rectifier and three-phase inverter with chopper, etc.

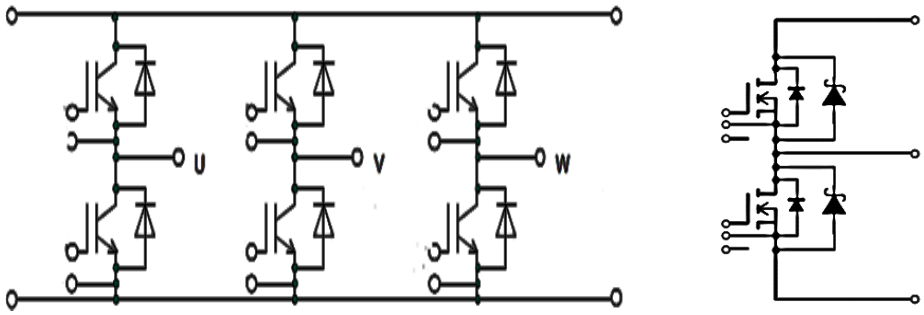

Fig. 1.16-1: Typical power module electrical topologies [88][89]

Power modules have various levels of functionality in terms of controls of the power module. Some power modules have integrated temperature [88] and current sensors [26]. Some branded as intelligent power modules [25] even have gave drivers incorporated in the module. Power modules are generally designed for higher power levels with voltages generally above 1200 V and current above 80 Amps. The module is designed to handle the head generated with conduction and switching at hundreds of kilowatts. At such high power levels Si IGBTs, Si diodes and SiC MOSFETS and diodes are typically used.

The structure of the power module is designed for electrical, thermal and mechanical purposes. Fig. 1.16-2 shows a typical power module and its internal components.

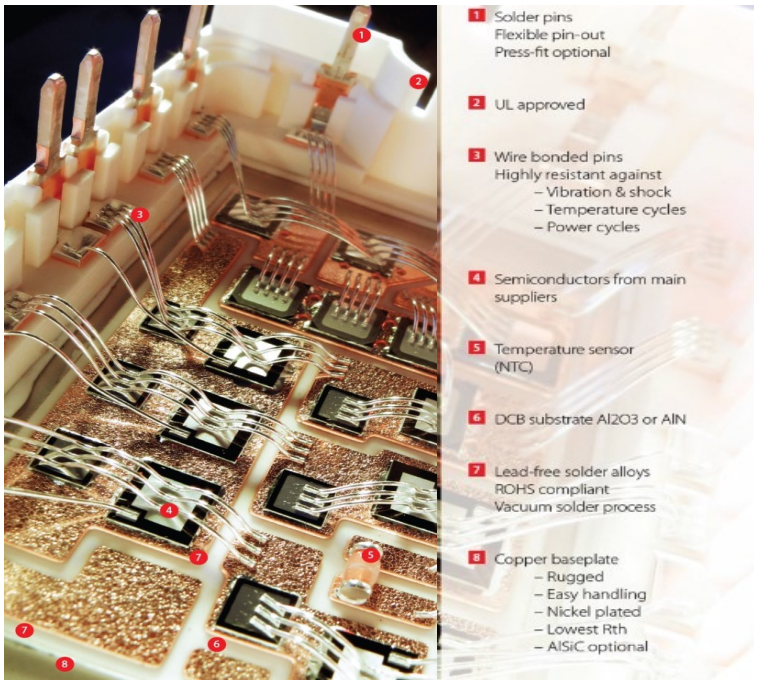

Fig. 1.16-2: Open power module with components labelled [17]

The electrical design of the power module involves conducting the current into the module from the DC terminals, through the semi-conductor devices and out through the phase terminal. As a fast switching and high current conducting circuit, there are very consequential considerations of path inductance and resistance involved in the electrical design.

The thermal design of the power module is aimed at keeping the junction temperature of the semiconductors below their operating limit. The power module due to switching and conduction losses can produce kilowatts of heat that must be dissipated. The mechanical design of the module is not only aimed at enclosure strength but also at thermal expansion and failures that can occur due to thermal fatigue. Fig. 1.16-3 shows the cross-sectional view of a traditional power module.

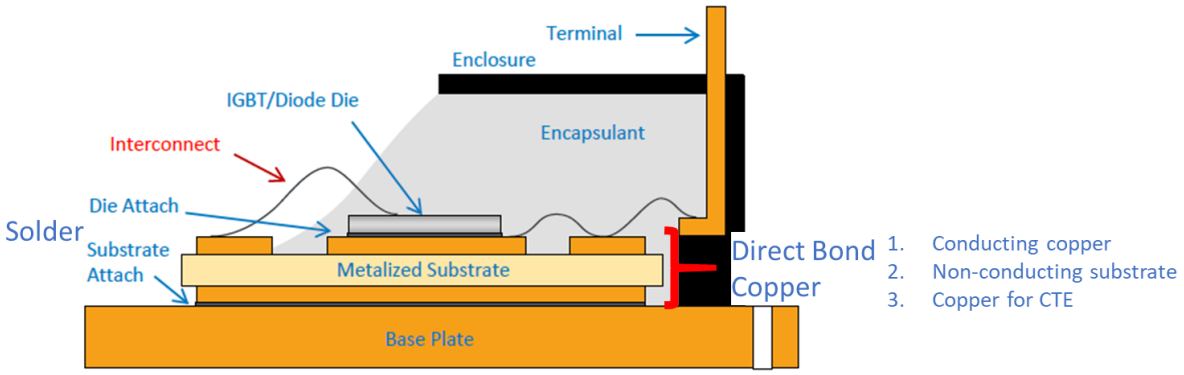

Fig. 1.16-3: Traditional power module with components labelled [90]

Interconnects are used to form electrical connection between components of the power module. Fig. 1.16-4 shows bondwire interconnects used for terminal to DBC connections as well as for multiple other connections.

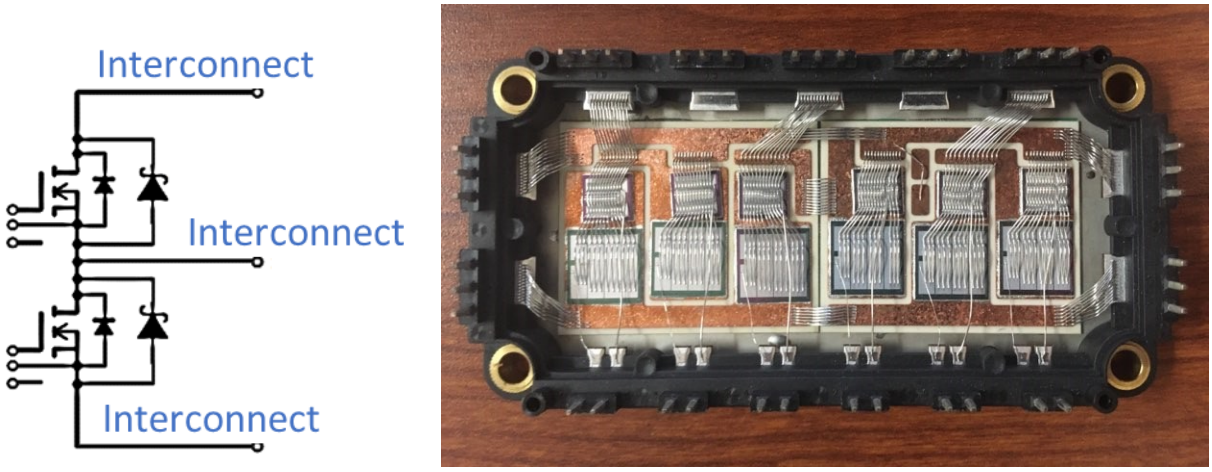

Fig. 1.16-4: Module topology with interconnects for connections

Interconnects requires electromechanical design consideration. Interconnects are prone to lift off which can occur due to shear stress originating from CTE mismatch between interconnect material and the connection point such as the semiconductor die. Another important property for interconnects is inductance. Due to high switching speed, the inductance of the interconnects is minimized to avoid voltage overshoots.

1.16.1 Bondwires

Aluminum bondwires with dimeter between 0.1 and 0.5mm are the most common form of interconnects. They are cheap and easy to manufacture using ultrasonic bonding. However, they can experience thermal fatigue induced shear stress which causes lift off and sometimes heel failure making it one of the most typical cause of failure [91][92][93]. Bondwires by definition form a loop which can be an inductance concern [94]. Copper bondwires with die top side metalized with copper is has been used to improve the CTE mismatch issue [95]. However, copper is a harder material, has corrosion concerns and requires a more intensive manufacturing process [96]. Fig. 1.16-5 shows the Copper bondwires with Copper layer on top of semiconductor.

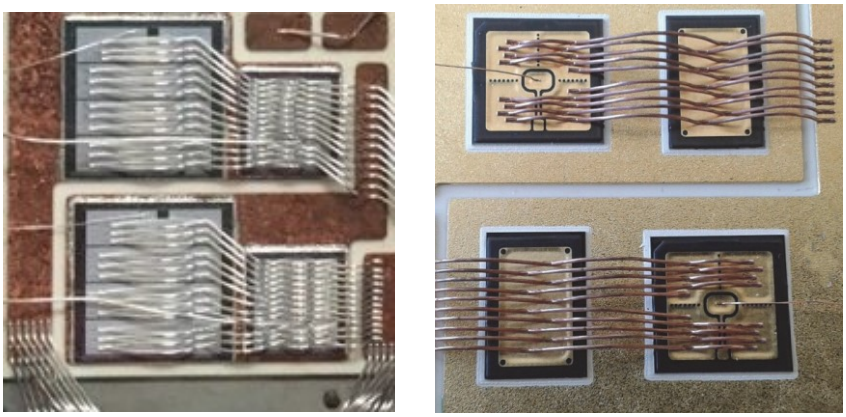

Fig. 1.16-5: Aluminum (left) and copper (right) bondwires

1.16.2 Planar interconnects

Planar interconnects refer to interconnects that have close to flat top allowing for compact packing and in most cases double sided cooling. This is illustrated in Fig. 1.16-6. Double sided cooling allows lower thermal resistance from semiconductor junction to the ambient. Being able to dissipate the loss of the semiconductor allows more diligent operation. It has been reported that Tesla model 3 [97] and Chevrolet Volt [98] both have planar interconnects in their traction inverters.

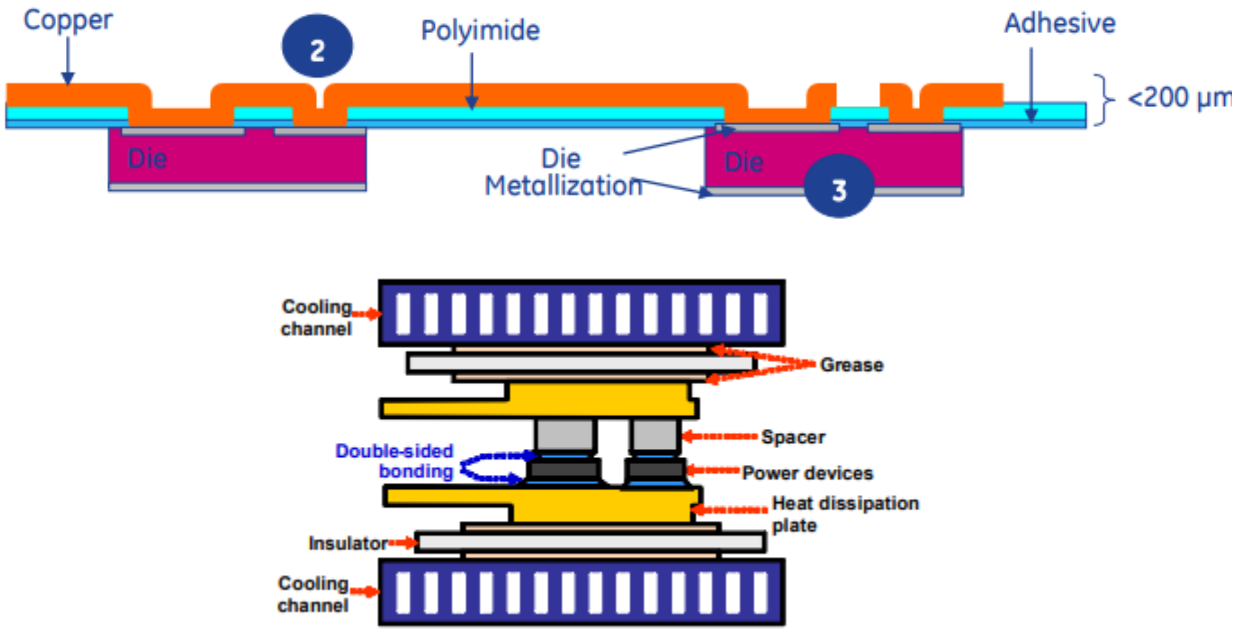

Fig. 1.16-6 Illustration of planar interconnects and of double sided cooling [99][100]

1.16.2.1 Leadframes

A very well utilized alternative to bondwires is copper leadframes. Fig. 1.16-7 shows the leadframes used inside Fuji power modules [8] and [7]. These leadframes which shape field in 1-D, are very similar to leadframes used in mass produced power modules. Copper leadframes provide higher reliability from CTE mismatch-based failures if they are connected to DBC or copper coated die. Leadframes also act to dissipate heat due to their high conductivity and larger cross-sectional area. Leadframes despite being an older type of interconnect, remain very widely used and are in one of the futuristic high density modules from Fuji [101]. Another major advantage of leadframe is that they are the same material as DBC (both being cooper). This allows more reliable bonding technology to be used, like ultrasonic welding with higher contact area.

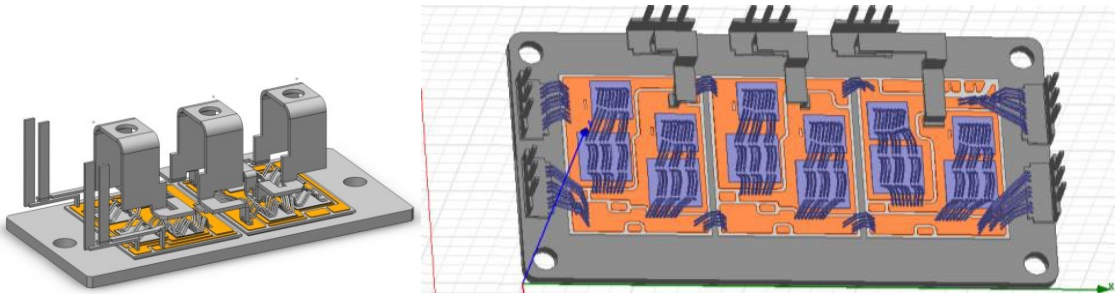

Fig. 1.16-7: Leadframes power modules for integrated sensing [7][8]

The leadframes due to their superior electromechanical performance are replacing bondwires as the DBC to terminal interconnect. Fig. 1.16-8 shows the leadframes in power modules that are just being commercialized. One of the major reasons that leadframes are being commercial used now is easy availability of ultrasonic welding.

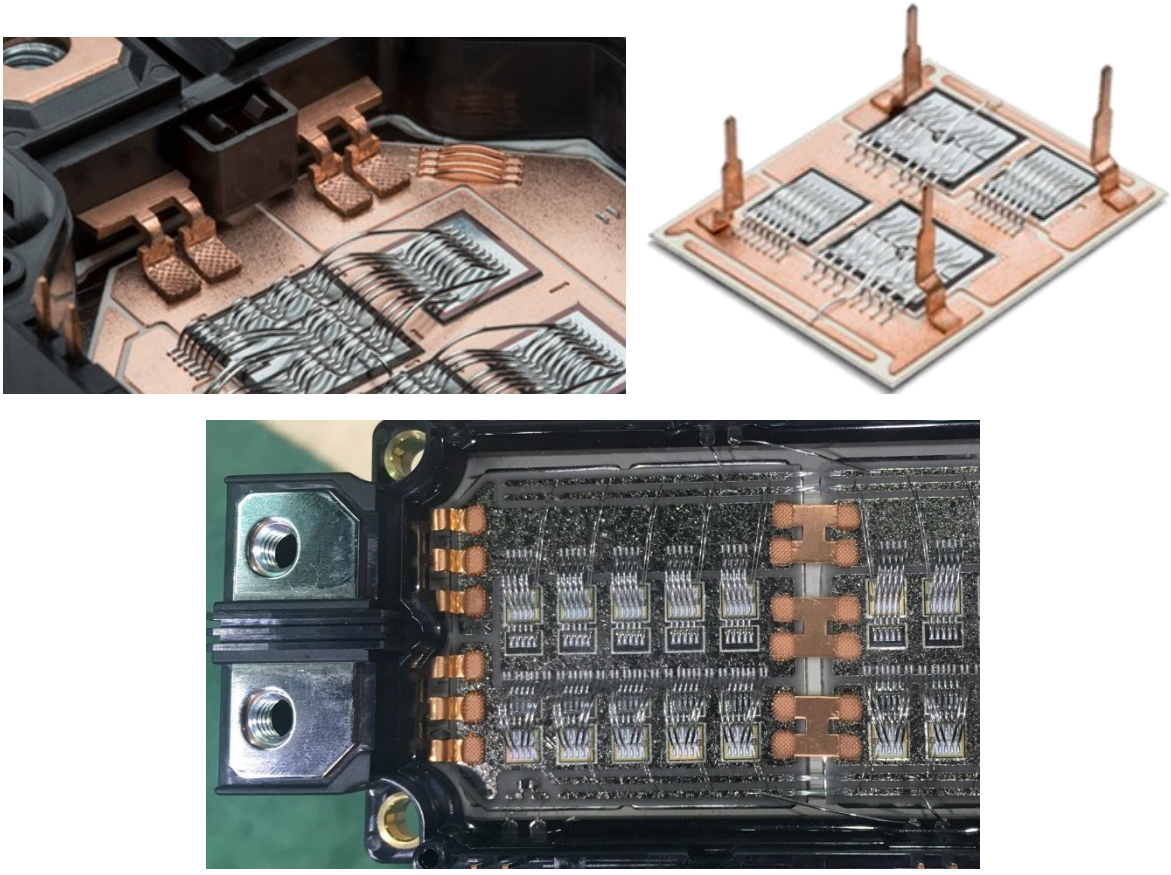

Fig. 1.16-8: Leadframes in latest power modules [102][103]

A derivative of the leadframe is the copper clip and leadframe technology. Fig. 1.16-9 shows the automotive power module proposed with this technology which uses a copper clip similar to those in discrete devices [104]. Shunts can be incorporated into the clip to measure current.

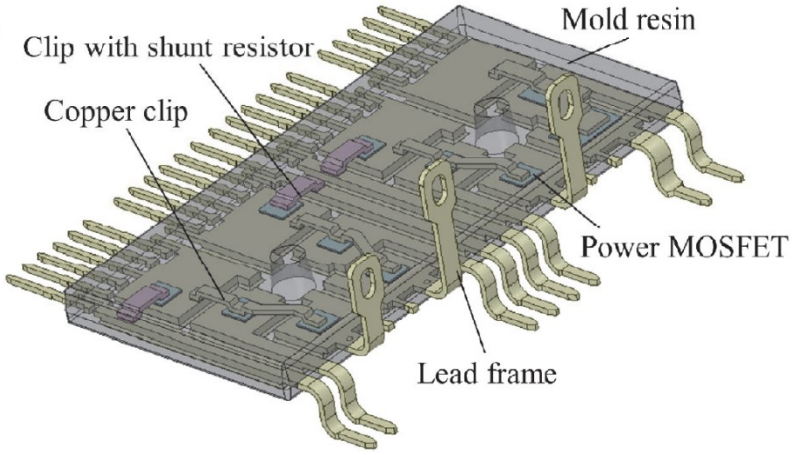

Fig. 1.16-9: Proposed copper clip technology [104]

1.16.2.2 Flexfoil

One of the most anticipated interconnect technologies is the flexible foil (also known as flexfoil) or the ribbon interconnect. There are many derivatives of the foil technology however, the gist of the technology are thin, wide and flexible interconnects. Semikron Skin technology is one of the leading flexible foil interconnect design and is shown in Fig. 1.16-10. It can be seen in the prototype that the interconnect consists of a think flexible PCB. The joins of the flex foil with DBC or the top side of the die is done using silver diffusion sintering. Sintering is also used to attach the die to the DBC. Sintering the flexfoil increases the contact area between the die and the interconnect leading to better thermal conduction. The flexfoil PCB has two layers leading to very low inductance as well. Compared to a power module with bondwires, the flexfoil shows drastic improvements in thermal and electrical characteristics. However, there is no notable drawbacks mentioned in Semikron research papers [105] [106] [107] [108] on this topic, which makes the

analysis very much an advertisement. Some of the issues that remain unanswered are reliability of sinter joints, CTE mismatch of flexfloil, sinter joint and the die as well as manufacturing cost and flexfoil lay out limitations.

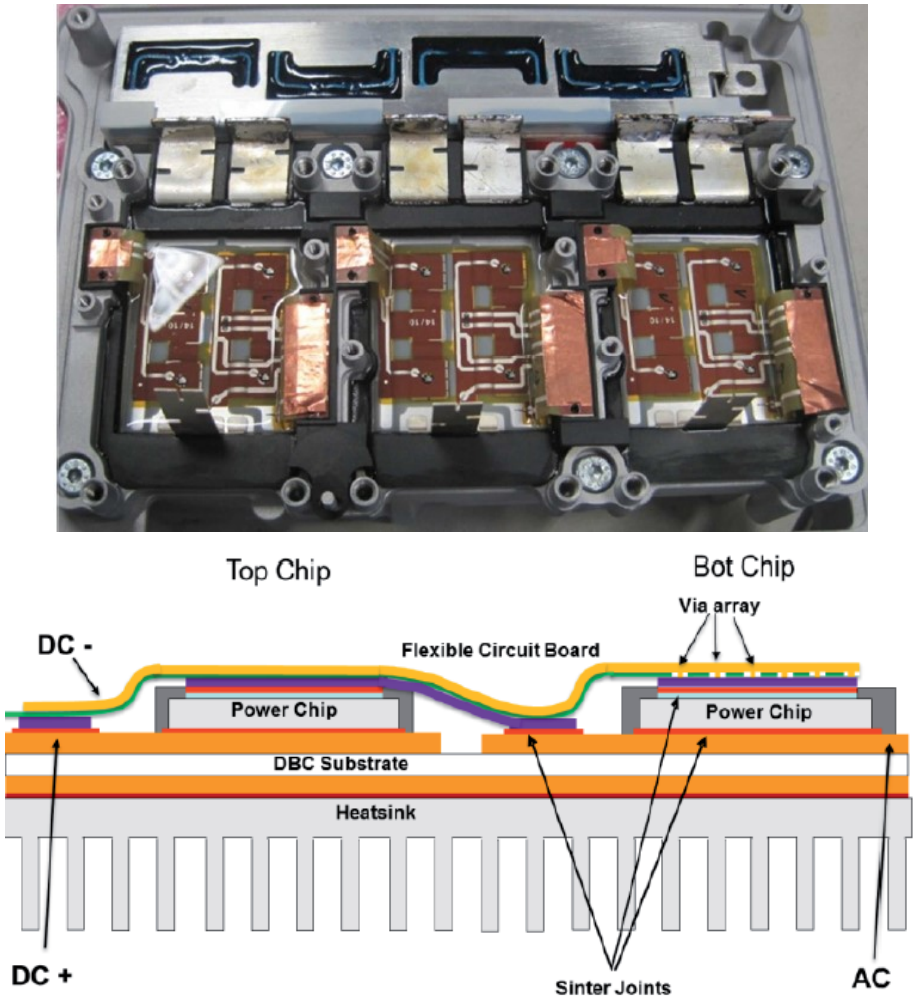

Fig. 1.16-10: Semikron SKiN [107][108]

There has been significant work on ribbon or flexible interconnect technology. In a reliability testing project, the criterion showed in Fig. 1.16-11 were tested [90]. There was comprehensive testing of different types of ribbon compared to a bondwire control case. The tests include regular pull, temperature elevation, cycling, vibration, corrosion and power cycling.

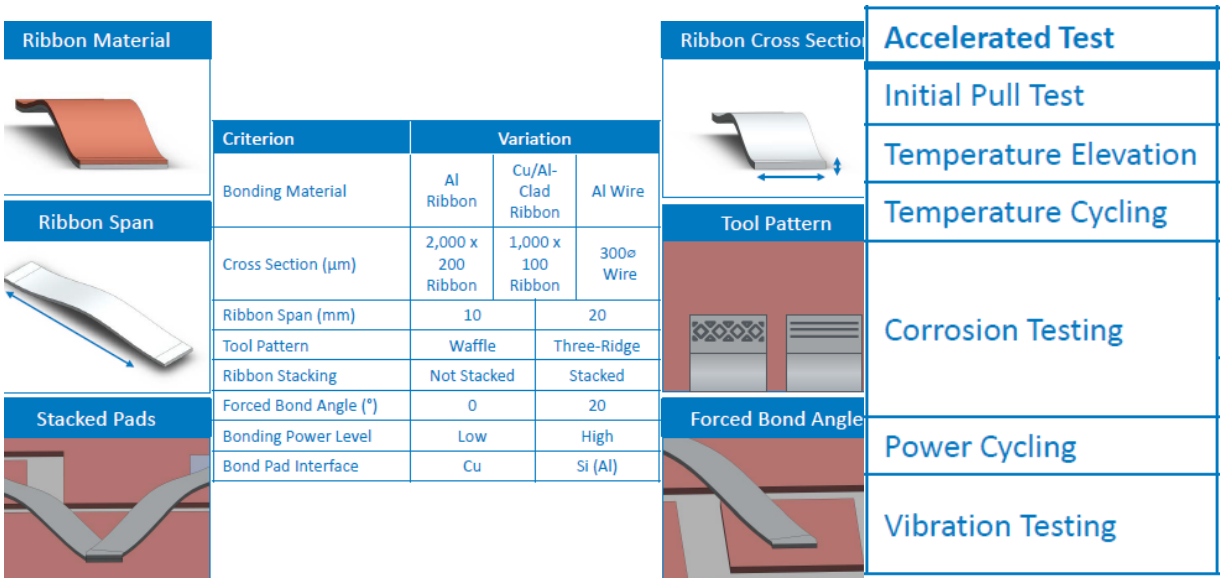

Fig. 1.16-11: Ribbon interconnect testing criterion [90]

Fig. 1.16-12 shows the ribbon interconnect failure mechanisms which are also true for bondwire failure. Ribbon interconnect failure models have been developed, and it was found that their higher cross-sectional area handled pull better naturally, but bondwires had a better pull test performance. It was also found that bondwires were prone to liftoff, and ribbon interconnects are more prone to heel failures.

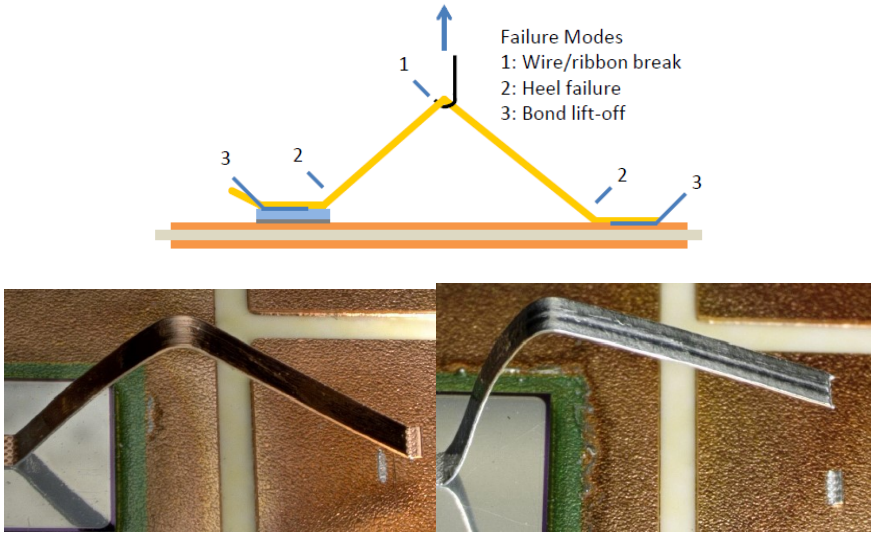

Fig. 1.16-12: Ribbon interconnect testing and failure mechanisms [90]

Very similar to the flexfoil technology is the metalized layer technology shown in Fig. 1.16-13 developed by Siemens. The interconnect is made out of hard layer of copper shaped to form a connections [109].

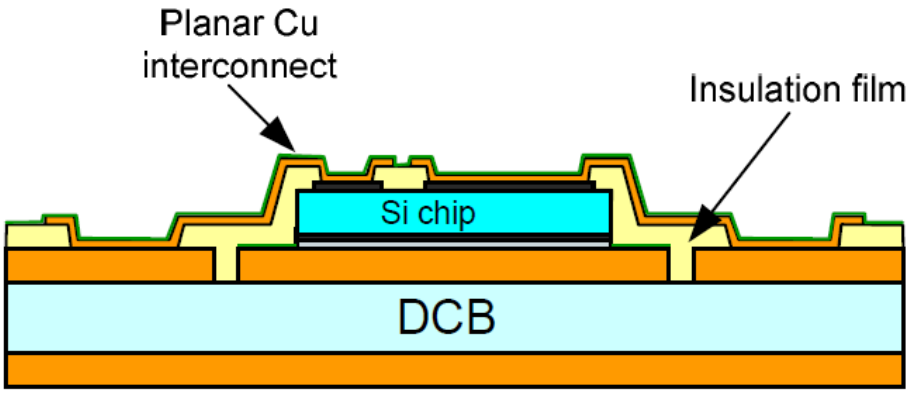

Fig. 1.16-13: Planar packing based upon Siemens SiPLIT [109]

The 3-D planar interconnect is also a derivative of the ribbon interconnects and is shown in Fig. 1.16-14. The key motive for this technology, much like many other flexfoil and ribbon technologies is double sided cooling.

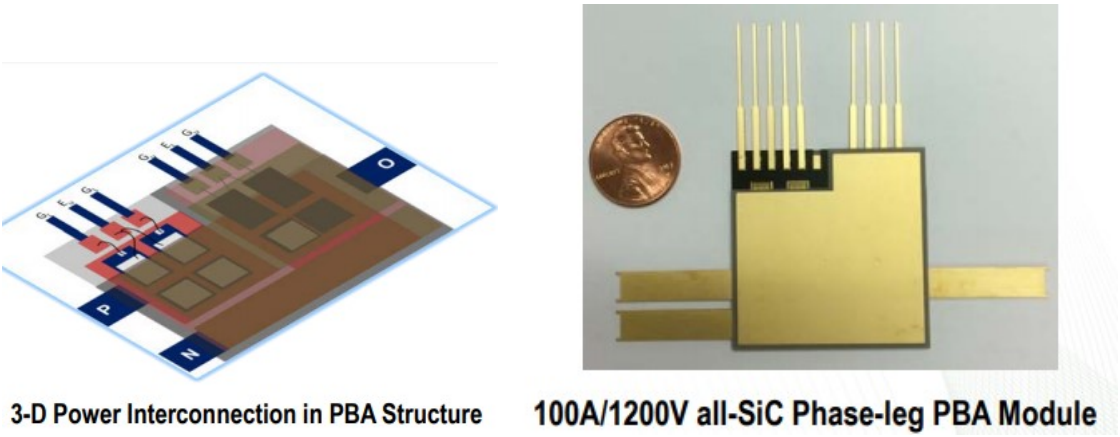

Fig. 1.16-14: 3-D planar interconnects [110]

Another planar interconnect solution is proposed in [99]. The solution essentially uses DBC on both sides of the chips and is shown in Fig. 1.16-15. The key development is high temperature transient liquid phase bonding to prevent the much less reliable solder joints.

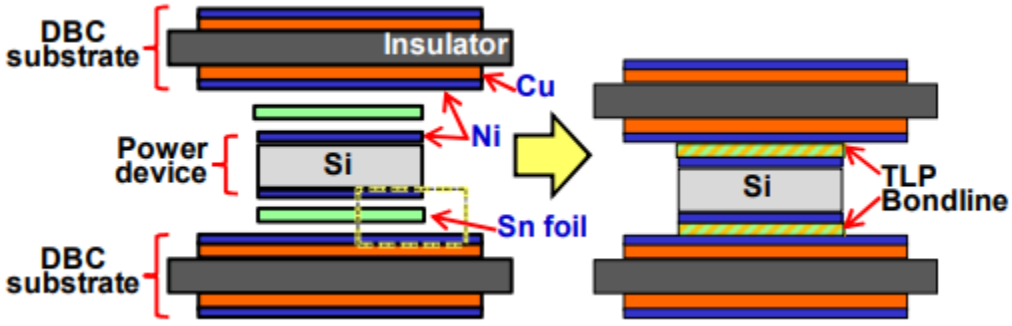

Fig. 1.16-15: Transient liquid phase double sided DBC [99]

Another type of planar interconnect is the Fuji's Copper pin interconnect shown in Fig. 1.16-16. This simplifies the interconnects into a simple PCB which can be connected to the semiconductor die using Copper pins. The pins do allow double sided cooling and reduce thermal resistance by not patterning the DBC which is needed for bondwiring. The rigid epoxy used to fill the case reduces the mechanical strain as well.

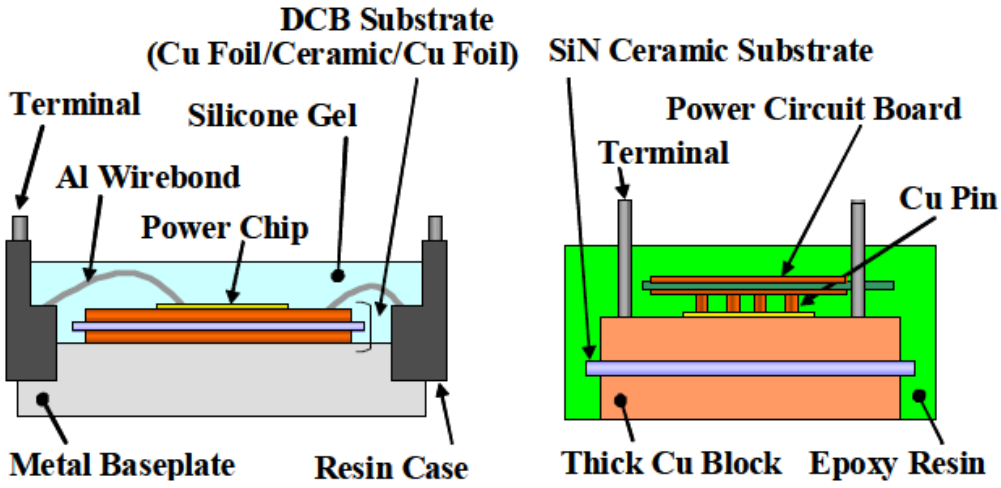

Fig. 1.16-16: Fuji Copper pin interconnect style [111]

1.16.3 Pressure interconnects

Pressure interconnects use spring force to establish an electrical connection. Since there is no solid connection at the interface, there is no issue of CTE mismatch. Pressure interconnects have been used in commercial modules and are considered reliable. They have been used in Semikron

as well as Infineon SiC modules. Fig. 1.16-17 shows the pressure interconnect illustrations. It can be noticed that pressure interconnects don't allow for double sided cooling and have mechanical contacts which are prone to corrosion and other vibrational issues.

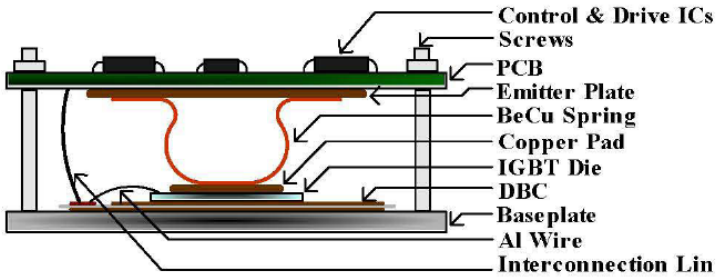

Fig. 1.16-17: Pressure interconnect style [112]

1.16.4 Direct bond copper and baseplate

The direct bond copper (DBC) shown in Fig. 1.16-3 generally consists of a non-conducting ceramic substrate sandwiched between two layers of copper. The top layer of copper houses the semiconductor chips on top if it and is used to form the power circuit of the module. The ceramic substrate in between, usually made out of Aluminum oxide or Aluminum nitrate, is the electrical insulator used to isolate the power circuit from the thermal components. The bottom layer of the copper is mainly present for stability and CTE mismatch between the top copper and the ceramic. The connection between the layers in DBC is done using the so called "direct bonding" which involves pressure and elevated temperatures slightly below the melting point [113].

The baseplate in most power modules is connected to the bottom of the DBC using a solder layer. The baseplate, to a slight degree helps with CTE mismatch. The main purpose of the baseplate is to provide a thermal capacitance and heatsinking. The baseplate is anywhere from 3mm to 8mm thick and serves to spread the heat out and into the cooling system. Most baseplates are made up of copper. Less often, the matrix materials like AlSiC have also been used [114].

Baseplates can also be entirely omitted from the power module and DBC can be put in thermal contact with an external heatsink. The presence of baseplates is advantageous since they can be highly controlled with convex or concave design to allow good thermal contact and bimetal effect [96].

1.16.5 Terminals

There are four main types of terminal structures to attach the power module with the inverter PCB etc. The first one is the solder pin connection. These are standard pins that can go through holes in the PCB and be soldered on. A close derivative of the pin connation is the press fit pin shown in Fig. 1.16-18 . This sort of pin has a spring type structure which when inserted in the PCB hole can applies a spring force against the hole and eventually form a stable mechanical and electrical connection.

Fig. 1.16-18: Infineon Press fit terminals

Another commonly used type of connection is the screw terminal. This terminal simply allows either a PCB or wire connection to the PCB with a reliable mechanical force. In Power modules with multiple connections, Semikron has used spring in addition to screws to get the inverter PCB in electrical contact with the DBC. Fig. 1.16-19 shows the two different types of spring terminals that require a screw to keep the springs loaded.

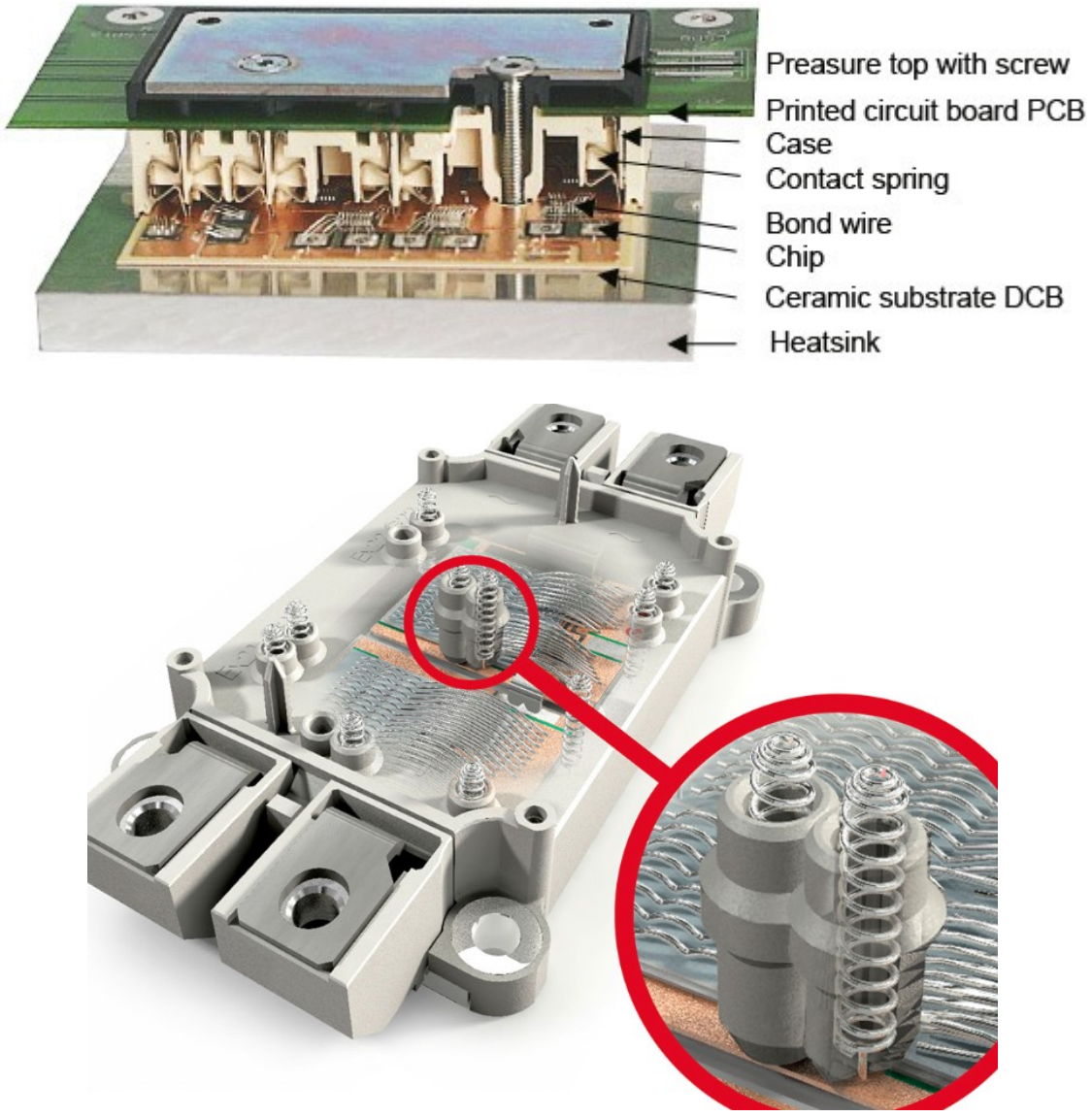

Fig. 1.16-19: Semikron spring terminals

1.17 2-in-1 SiC Power Module Integrated Current Sensing

The 1-D GMR PFD is integrated in the 2-in-1 Rohm SiC power module in the die region. In [115] and [9] a method is presented to extend the bandwidth of current sensing. One of the major issues with the Rohm module is reported to be the current sensing phase shift that occurs because of the protective Nickel plating on the baseplate. Additionally, there also the regular skin and proximity effects that degrade the field. The papers study the imaginary field from the induced eddy currents and defines the imaginary flat bandwidth metric to avoid the frequency dependent effects. However, in the cases where imaginary FBW is not available, the bandwidth extension method is used.

This FBW extension method uses the varied frequency content of field at different locations using PFD arrays. The fields from these different locations are combined to yield a flat frequency response. Extension of the bandwidth results in being able to sense high frequency content as shown in Fig. 1.17-1.

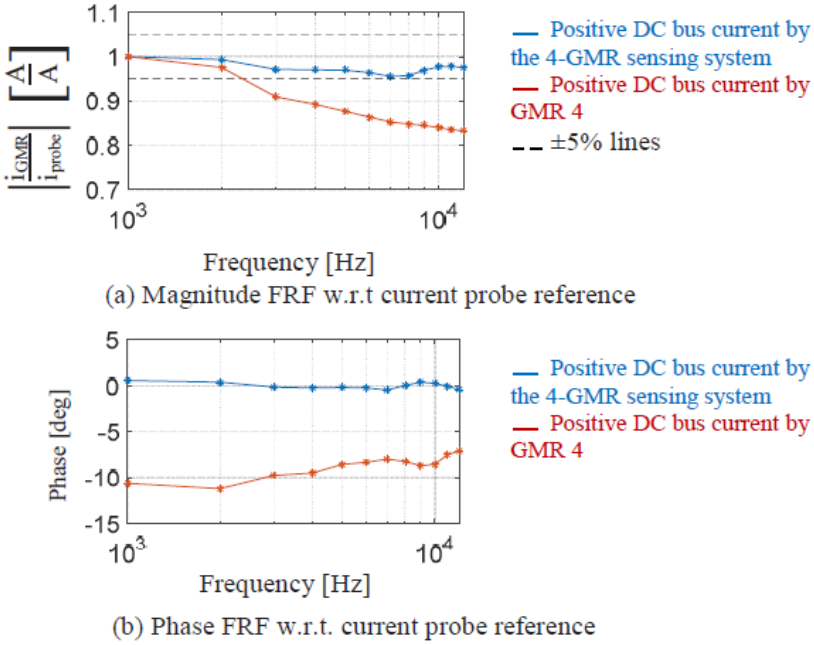

(a) Magnitude FRF w.r.t current probe reference

(b) Phase FRF w.r.t. current probe reference

Fig. 1.17-1: FRF of positive DC bus current in SiC module [115]

1.18 Three-Phase Closed Loop Inverter Operation with Integrated GMR PFDs

1.18.1 Half-bridge silicon power modules

[65][7] describes the implementation of GMR PFD-based integrated current sensing in customized Fuji 2-in-1 power modules. The leadframes of the power module are analyzed for locations of high bandwidth and GMR detectors are placed at those locations. Fig. 1.18-1 shows the bandwidth comparison of GMR PFDs and Hall sensor with respect to current probe.

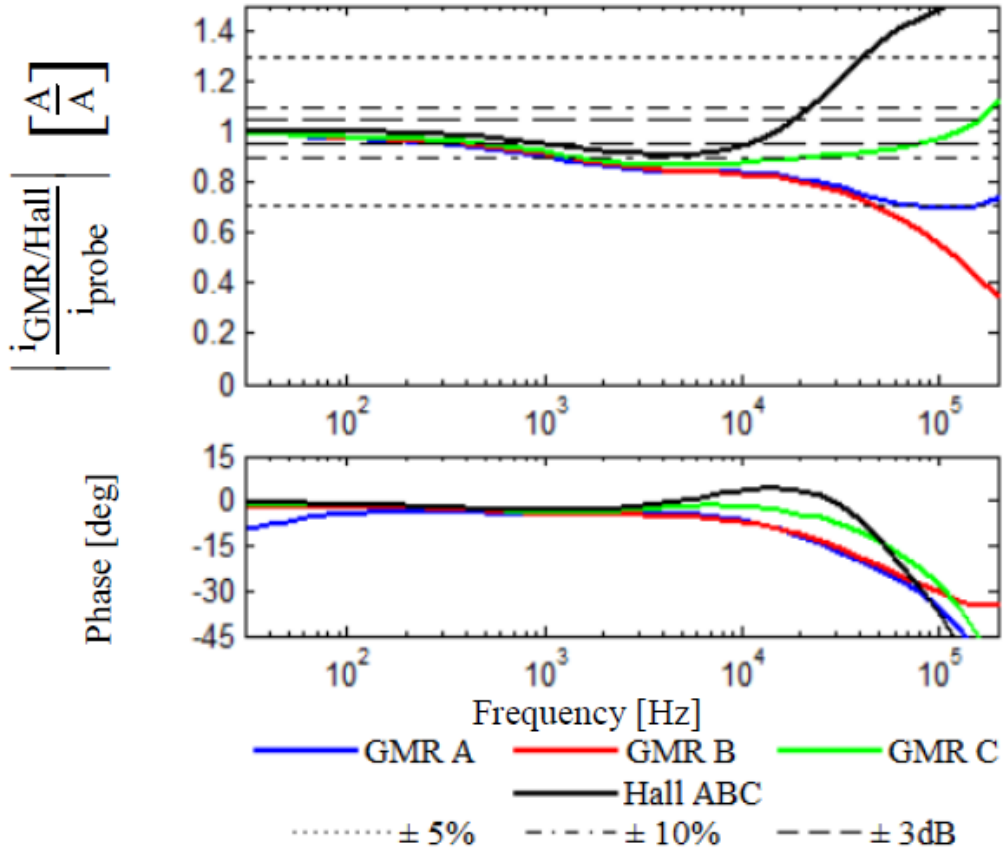

Fig. 1.18-1: Bandwidth of GMR PFD-based sensing [7]

The Fuji modules are used to make a three-phase inverter for FOC induction machine on a back-to-back dynamometer. The inverter has commercial Hall current sensors as well as GMR PFD-based current sensing implemented. The GMR current sensor is used to provide current

feedback in the current regulator of the test machine of the dynamometer which operates in speed control. The load machine is in torque control and provides constant torque loads, which leads to different amplitudes of current when the torque is varied.

There is decoupling implemented for three-phase cross-coupling in the inverter. There is also decoupling of bias fields which also decouples the temperature effects on the bias magnets. The noise from a permanent machine fan is also decoupled using a similar technique. Fig. 1.18-2 shows the results of cross-coupling decoupling as well as fan noise decoupling at different speeds and at different load torques.

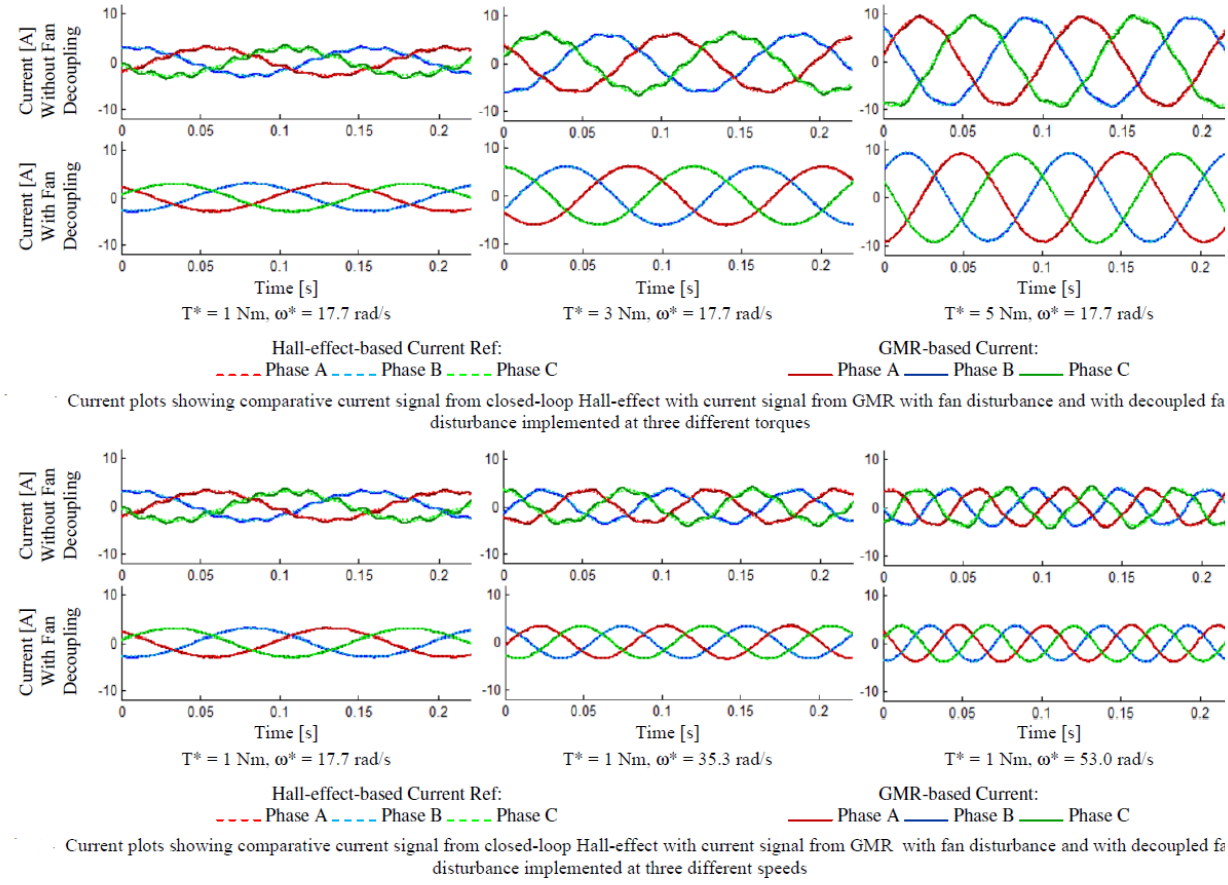

Fig. 1.18-2: Overlay of three-phase currents and reference Hall sensors [7]

1.18.2 Three-phase full-bridge silicon power modules

[67] incorporated especially designed leadframes in Fuji 6-in-1 power module to create high FBW and flux density regions. Fig. 1.18-3 shows the power module with the leadframes. The colored red, blue and green smiley faces show the GMR PFD locations in the power module.

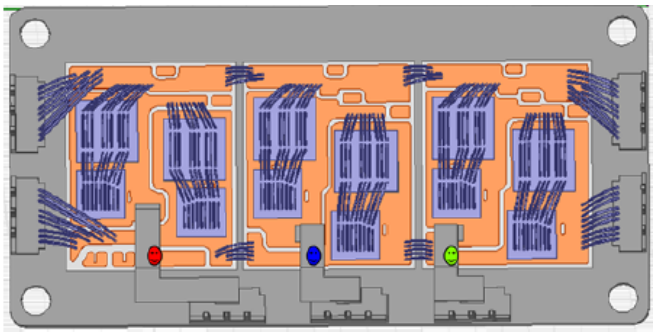

Fig. 1.18-3: Power Module with leadframes and GMR PFD locations [67]

This customized Fuji power module is used as a three-phase inverter, GMR PFD-based current sensing is implemented with fan decoupling and interphase decoupling. Fig. 1.18-4 shows the comparison between the Hall sensor and GMR PFD-based current sensing in the back-to-back induction machine dynamometer's test machine inverter.

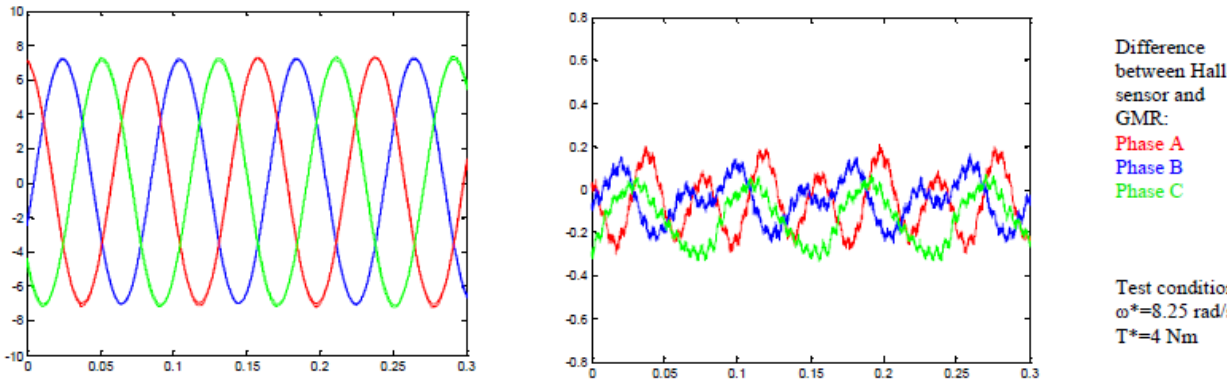

Fig. 1.18-4: (a) Overlay of three-phase currents and reference Hall sensors and (b) errors [67]

Research Opportunities Identified

1-D PFD-based integrated current sensing is compact, economical, galvanically isolated and consumes very low power. However, it requires separate conductors to shape the field from the currents and precisely positioned PFDs that are physically spaced to detect adequately unique cross-coupled magnetic field from the currents. Such PFD placement leads to system level complexities.

Based upon the state-of-the-art-review, the following research opportunities have been identified.

- **Methodology to shape, analyze and utilize magnetic fields in multi-dimensions**

In the state-of-the-art of point field detector-based current sensing, magnetic field analysis exists primarily in a single axis. With the development of the 2-D MR PFDs and the possibility of the development of 3-D MR PFDs, there is a significant research opportunity to characterize and shape magnetic fields in power electronic modules, busbars, and cables in multi-dimensions. New metrics are required for defining the suitability of a point in space for the multi-dimensional MR PFD placement. These metrics are also needed to design and optimize conductors for high bandwidth multi-dimensional field shaping while reducing the impact of skin and proximity effects.

Furthermore, the magnetic field being a spatial vector can also be detected along any single direction in space. There is a research opportunity to study fields as a spatial vector and identify directions least impacted by the frequency dependent skin and proximity effects to increase access to high flat bandwidth regions in power electronics.

- **Methodology to decouple cross-coupled fields in multi-dimensions at a point in space**

There is a major research opportunity to expand the 1-D magnetic field decoupling technique demonstrated in the literature to multi-dimension. Information can be lost if the magnetic field is sensed as a single dimensional quantity, hence there is a need to develop physics-based methods to extract information about multiple currents from the cross-coupled 3-D magnetic field at a point.

1-D PFDs rely on spatial distances among them to detect unique information in the magnetic fields from multiple currents for decoupling. Multi-dimension PFDs may be able detect the unique information in the field dimensions as a substitute to spatial distance. Physics and mathematics-based investigation needs to find singularity constraints of multi-dimensional field decoupling. The identification of conditions, where the orthogonal components of the magnetic field have unique information from currents, are desired to form a non-singular sensing system. A non-singular multi-dimensional current sensing system can be used to reduce the net number of PFDs and the sensing footprint required to achieve high performance in the interphase and disturbance decoupling especially inside high-power density modules.

There is also an opportunity to investigate the use of machine learning algorithms like neural networks for the cross-coupled field decoupling. Neural networks have gained popularity for many linear and non-linear mapping problems. Field decoupling can be classified as a linear input to output mapping problem for which neural networks can be used. Using neural networks can eliminate the calibration steps in decoupling and provide immunity from predictable errors.

- **Methodologies for rejecting/decoupling external magnetic disturbances**

There is a research opportunity to develop methods to reduce the impact of the uncalibrated magnetic disturbances on PFD-based current sensing. The field decoupling methodology decouples fields from currents whose position is fixed and field outputs are calibrated. However,

in real systems, there is a possibility of the disturbance field being superimposed on fields from the current being sensed leading to the current measurement errors. Methodologies are needed to either model and decouple these disturbances or to reject them all together.

- **Technique for three-phase current sensing using a single sensor in conventional conductors without phase separation**

There is an opportunity to develop a technique to sense the three-phase currents by integrating a single multi-dimensional MR PFD in the three-phase cables and busbars. Typically for a galvanically isolated current sensing system, individual phase currents are wrapped on their respective cores or passed through their respective field shaping structures, both of which can compromise the trend of power density improvements in power electronics. A multi-dimensional PFD-based current sensing technique for three-phase cables and busbars accounting for the bandwidth, range and cross-coupling decoupling of magnetic fields needs to be developed. Without having phase conductor separation and specialized cores, this technique can increase the power density.

- **Design methodology for power module integration of multi-dimensional MR PFD-based current sensing**

There is a major opportunity to develop a three-phase power module with high bandwidth, multi-dimensional field shaping to implement PFD-based current sensing. In the literature, integration of PFDs has been demonstrated in power modules that had special 1-D leadframes. 2-D and 3-D PFDs can reduce the number of PFDs required to implement multiphase current sensing but require specialized power module interconnects to shape fields in multi-dimensions. Design recommendations are needed for Si and SiC three-phase full-bridge power modules with high bandwidth integrated current sensing functionality and without the degradation of performance of

the modules with regard to inductance and thermal characteristics. The outcome of these design recommendations can improve the density of the power electronic system.

As a preliminary step to the power module design, there is a need for a holistic electromagnetic analysis of commercial power modules. Field analysis of typical conductive structures like terminals, interconnects, DBC and baseplate in commercial power modules need to be conducted to identify their impact on high bandwidth and fidelity field shaping via skin and proximity effects.

- **Design methodology for SiC power modules for very high bandwidth integrated current sensing**

There is a research opportunity to develop SiC power modules with integrated current sensing with bandwidths suitable for WBG switching frequencies which are increasing quickly. Field analysis of leadframes, ribbons and bondwires needs to be conducted to design interconnects with low frequency dependency. As interest in and applications of planar interconnects increase, design guidelines are needed for planar interconnects from the magnet field shaping perspective. The design guidelines need to encompass the conductive structures around the interconnects due to the electromagnetic field interactions in power dense environments.

.

Chapter 2 Multi-Dimensional Magnetic Field Shaping and Analysis

This chapter conceptualizes the detection of magnetic field as a multi-dimensional vector quantity and explains the metrics used for the multi-dimensional magnetic field analysis. Methods are developed for the evaluation of magnetic fields in rotated coordinates and along various directions in a 2-D plane to achieve a high bandwidth and signal-to-noise ratio in sensing. 3-D magnetic field analysis metric to enable 3-D field detection is defined. The chapter also includes a discussion about the electromagnetic FEA for analyzing fields in the single-phase and the three-phase systems.

The main purpose of this chapter is to develop a multi-dimensional magnetic field shaping and evaluation methodology to enable high bandwidth sensing using a PFD in later chapters.

Elements of this chapter are also documented in [116] and [117].

2.1 Principles of Multi-Dimensional Point Field Detection

A magnetic field is a 3-dimensional physical vector quantity. All super-imposed magnetic fields, from their respective origins, are added up at a point in space to form a net magnetic field vector. A PFD detects the net magnetic field vector. The PFD restricts detection to components of fields in the direction of its axis of sensitivity, that is, the PFD only detects the magnetic field component parallel to its sensitivity vector. Typical PFDs are 1-D, which means that they only have one axis of sensitivity and any magnetic field which is not parallel to this axis is inherently rejected. A 1-D PFD can detect the entire magnetic field if it is oriented to have its sensitivity

direction along the direction of the vector field. In cross-coupled dynamic systems, this is impossible to achieve as magnetic fields can change in magnitude and direction.

2.1.1 2-D point field detection

In the case of a 2-D PFD, there are two independent outputs with orthogonal axes of sensitivity referred to as X (sometimes as Sine) and Y (sometimes as Cosine). Fig. 2.1-1 shows the conceptualization of super-imposed magnetic field vectors and the breakdown of the net magnetic field into X- and Y-directions.

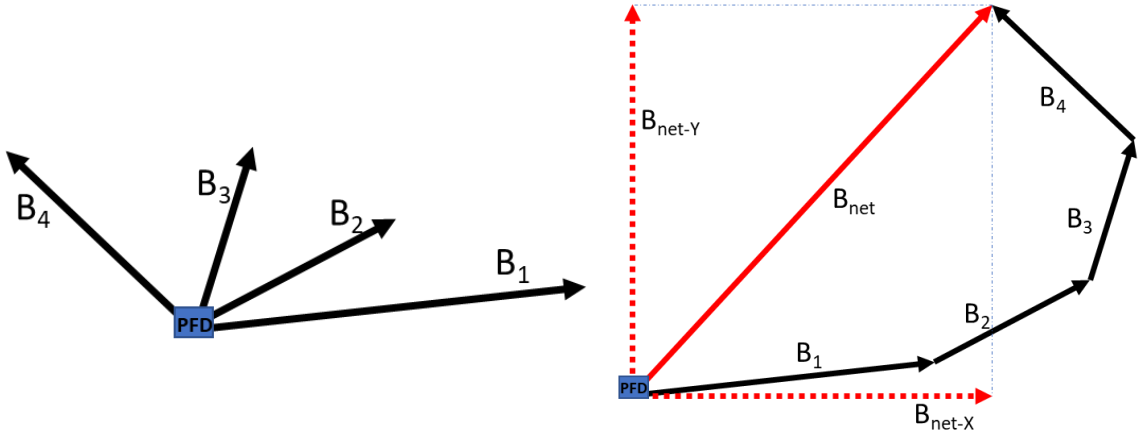

Fig. 2.1-1: Illustration of magnetic field vector sum and X and Y components

It must be noted that a magnetic field is always a vector. The 2-D PFD breaks down the net magnetic planar field vector into its orthogonal components referred to as X and Y. X and Y are defined by the orientation of the PFD, whereas any field in the Z axis, or the third orthogonal direction is rejected. There are systems in which the magnetic field is naturally two dimensional and does not develop a component in the third dimension. A simple example of such a system is a straight current carrying conductor.

Any field can be detected as a planar field in 2-D, i.e. along the X and Y axis of the PFD, if the PFD is positioned appropriately. An appropriate 2-D PFD location is where the magnetic field vector has a component in the PFD's X- and Y-directions. For the sake of convention and

uniformity, the PFD's X and Y axes are aligned with conventional cartesian X and Y axes in this chapter, if not stated otherwise.

2-D magnetic field shaping is referred to as the design of the conductors such that currents through them produce fields with high fidelity, high bandwidth and high strength in the orthogonal axes of a 2-D PFD.

2.1.2 3-D point field detection

A 3-D PFD is superior to a 2-D PFD because it detects the complete 3-D magnetic field vector. The net magnetic field vector is detected using X, Y and Z components. Therefore, using a 3-D PFD makes it possible to detect the entire magnetic field at a point in space. An appropriate location for the 3-D PFD is where the 3-D magnetic field is strong enough to be detected. Even if a magnetic field vector can be fully described in 1-D or 2-D due to non-existent or very small orthogonal components, a 3-D PFD is still useful since it detects the complete magnetic field vector information.

3-D magnetic field shaping refers to designing conductors which produce 3-D magnetic fields with non-zero component in all three directions. Multi-dimensional field shaping involves multiple currents which have cross-coupled fields in each of the dimensions. It is also possible, that each current produces a field in only one of the dimensions.

The simulation tool for magnetic field shaping in this research is electromagnetic finite element analysis (FEA). FEA of magnetic fields is done using Ansys Maxwell with the eddy current solution type on Ansys electromagnetic desktop (details to follow).

2.2 Rotated 2-D Magnetic Field Shaping Metrics

The 2-D magnetic flux density metric, discussed in detail in chapter 1, is the product of magnetic flux densities in the X and Y axes. This metric is a useful one since it can filter out

regions where one or both of the axes have a very low magnetic flux density. The 2-D flux density is measured in units of Tesla[2].

The flat bandwidth (FBW), also discussed in detail in chapter 1, at a point in space is the frequency at which the magnetic field originating from the current deviates by ± 5% from its value at a reference frequency [83]. A quasi-DC frequency of under 0.1 Hz is used as the reference frequency in FEA simulation, whereas 10 or 100Hz can be used in experiments. Flat bandwidth is defined for magnetic field in one dimension and two dimensions. The 2-D 5% FBW is computed using the lower of the X and Y 5% FBW at each point [68]. The main reason for frequency dependent change of magnetic field is skin and proximity effect.

2.2.1 Rotated 2-D flux density and 2-D 5% FBW

Generally, cartesian coordinate system (X, Y) is used to define the points in space and the magnetic field components, B_x and B_y at each point. In some cases, the standard X and Y axes might not lead to the ideal magnetic field and its bandwidth. One method to evaluate the flux densities and FBW for other non-standard X and Y axes is to rotate the coordinate plane with respect to the Z axis. It must be noted that rotating the coordinate axis is a new perspective of the same magnetic field. Rotation about Z axis can be done using (2.2-1) and is demonstrated in Fig. 2.2-1.

$$\mathbf{R}_z(\theta) = \begin{bmatrix} \cos\theta & \sin\theta & 0 \\ -\sin\theta & \cos\theta & 0 \\ 0 & 0 & 1 \end{bmatrix} \tag{2.2-1}$$

$$\begin{bmatrix} B_{x'} \\ B_{y'} \\ B_{z'} \end{bmatrix} = \begin{bmatrix} \cos\theta & \sin\theta & 0 \\ -\sin\theta & \cos\theta & 0 \\ 0 & 0 & 1 \end{bmatrix} \begin{bmatrix} B_x \\ B_y \\ B_z \end{bmatrix}$$

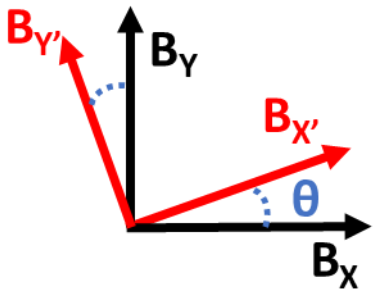

Fig. 2.2-1: Rotation of XY coordinate system

Fig. 2.2-2 shows the flux densities around a rectangular conductor along the X' and Y' axes which are rotated 45 deg counter-clockwise from their standard orientation. The rotated 2-D flux density for the system is also shown. Changing the axis along which the magnetic field is analyzed changes the magnetic field outlook, demonstrating the importance of direction in field detection.

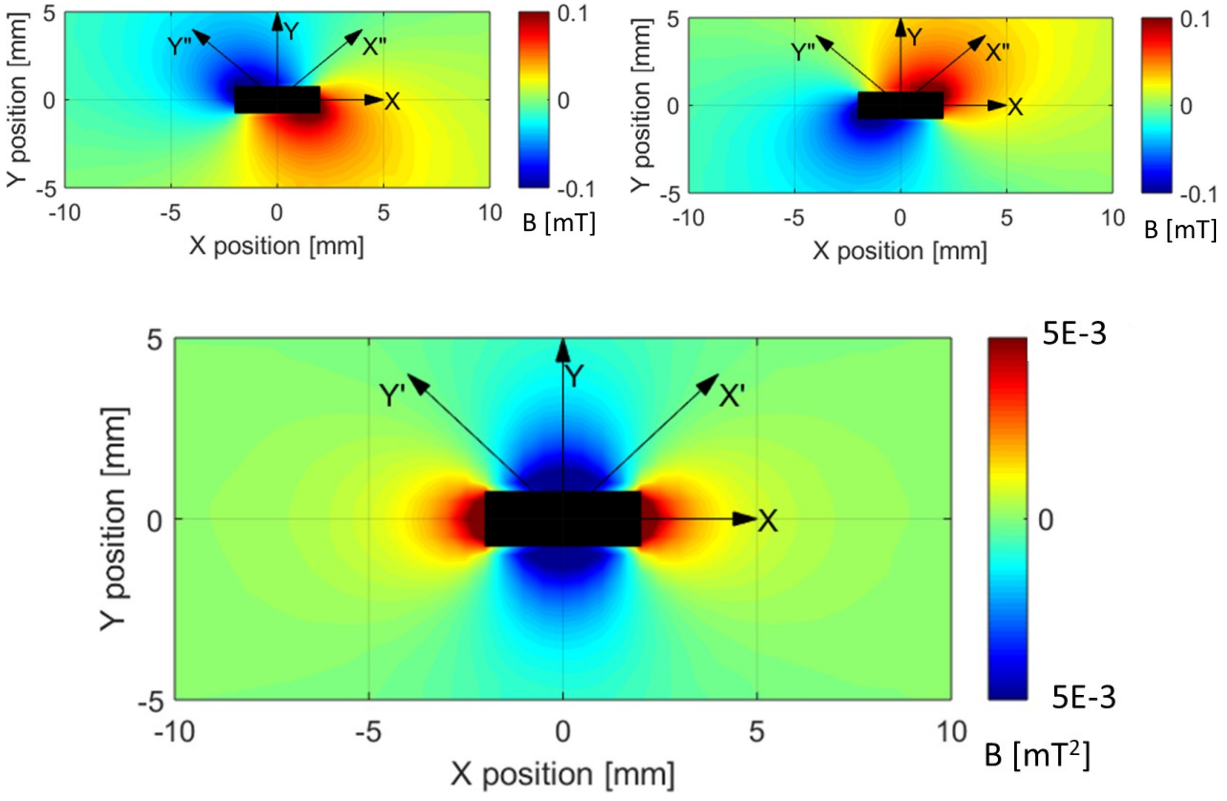

Fig. 2.2-2: Rotated X, Y components and 2-D flux density around a rectangular cross section (4 x 1.5 mm) copper conductor with 1A quasi-DC current

Since the magnetic field is the same and only the reference coordinates have changed, the 2-D PFD can still be oriented with respect to the standard cartesian coordinates and its output can be mathematically transformed to provide the field along the rotated coordinate frame.

Fig. 2.2-3 shows the 2-D FBW for rotated X and Y axes. Such a rotation can lead to high FBW access to regions previously unusable. For example, in Fig. 2.2-3, the dark regions of high bandwidth are much closer to the busbar than with the conventional X and Y axis shown in Fig. 1.14-5. This rotational property can be exploited in practical applications for reasons of manufacturing and placement of PFD.

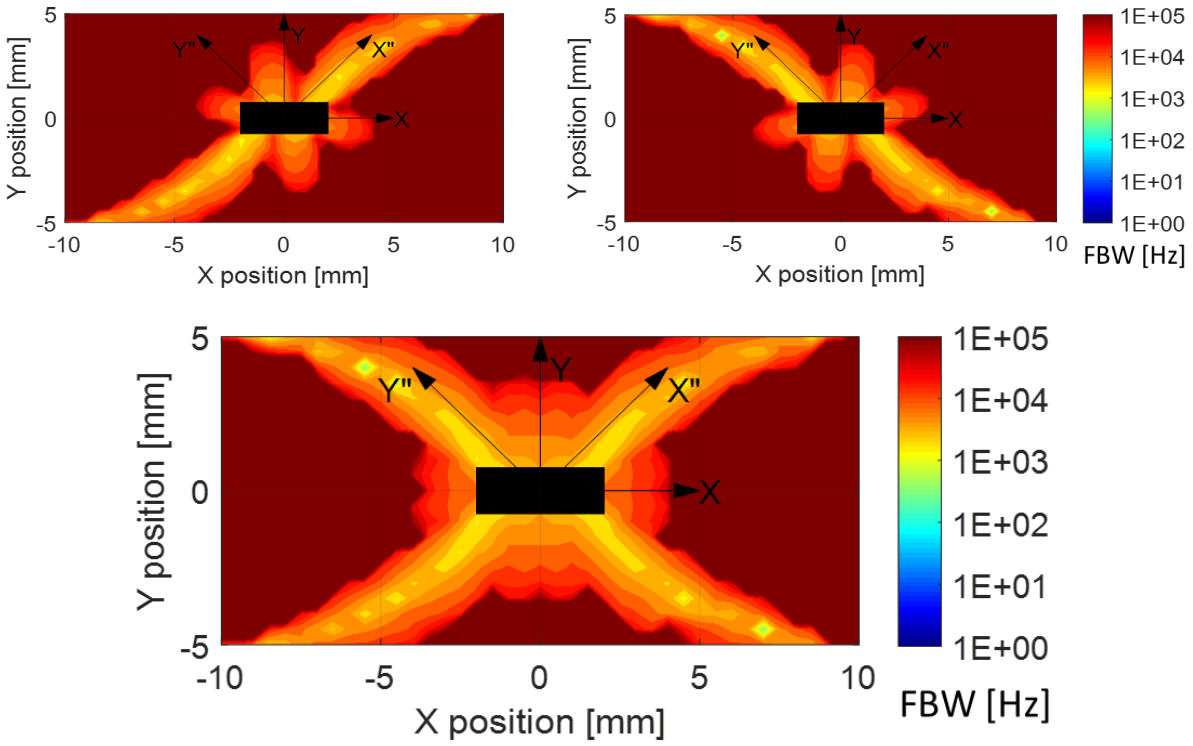

Fig. 2.2-3: 45 deg rotated X, Y and 2-D 5% FBWs for a rectangular cross section (4 x 1.5 mm) copper conductor

2.2.2 Hybrid 1-D flux density

One very important result of rotating the X and Y axes about the Z axis, is the ability to evaluate the magnetic field vectors along any direction within the XY 2-D plane. This opens the possibility of finding field directions with higher bandwidth, better signal-to-noise ratio (SNR), easier manufacturing, or less exposure to disturbance magnetic fields.

The X and Y magnetic field can be used to find a direction with better field characteristics. In real applications, a 1-D MR PFD can be used to detect the field with its sensitivity axis aligned with the identified direction. The other option is to use a 2-D MR PFD to detect the X and Y field and compute the field along the hybrid (identified) direction using trigonometry or rotation matrices. This mathematical manipulation of two dimensions to evaluate vector field along any direction in a 2-D plane leads to hybrid 1-D flux density. Shown in Fig. 2.2-4 is hybrid 1-D flux density along a direction 30 degrees from the X axis.

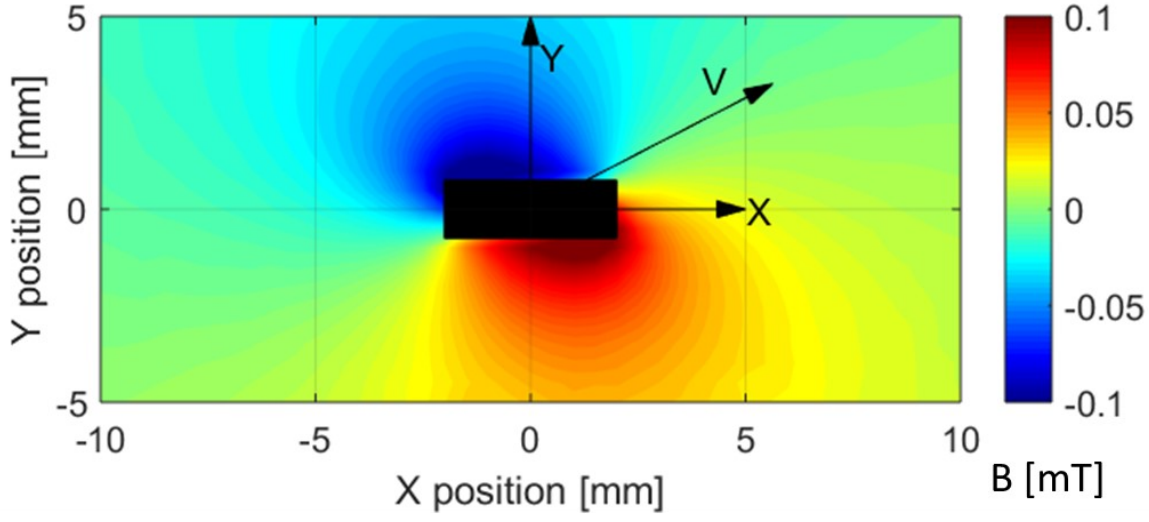

Fig. 2.2-4: Hybrid 1-D magnetic flux density along direction V around a rectangular cross section (4 x 1.5 mm) copper conductor with 1A quasi-DC current

2.2.3 Hybrid 1-D 5% FBW

The FBW for the hybrid 1-D field is the frequency at which the value of the field in the hybrid (identified) direction changes by more than 5% from its value at the reference frequency (which is quasi-DC in FEA simulation). Fig. 2.2-5 shows the hybrid 1-D FBW for the direction 30 degrees from the X axis. Compared to 1-D FBW for X-direction magnetic field shown in Fig. 1.14-5, the FBW for hybrid direction is completely different and provides access to points closer to the busbar. For any conductor system an intensive analysis of all directions in 2-D can lead to identification of directions with higher FBW at a given point.

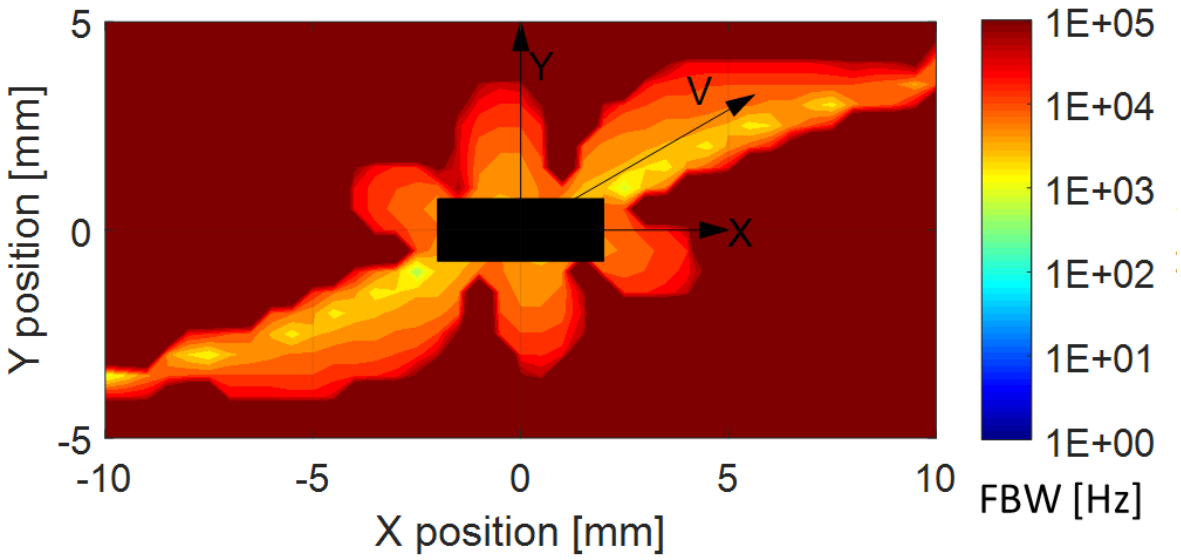

Fig. 2.2-5: Hybrid 1-D FBW around a rectangular cross section (4 x 1.5 mm) copper conductor

2.3 3-D Magnetic Field Shaping Metric

Straight current carrying conductors only produce 2-D magnetic fields in planes perpendicular to the conductor. However, in real applications, the majority of conductors have bends and turns leading to the creation of 3-D magnetic field.

In this work, 3-D flux density analysis is done on individual field components instead of a product 3-D flux density metric. The reason for this is the misleading nature of a three flux density product. The product weighs the three directions equally, and in the case where one direction of the flux density is unreasonably weak or strong, it might lead to the wrong conclusion. If the 3-D PFD is positioned in a region with one of the flux densities too strong, it might saturate and if it is positioned at a region with one of the flux densities too weak, the SNR will suffer.

2.3.1 3-D 5% FBW

3-D FBW is defined as the lowest of the X, Y and Z 5% 1-D FBW. This metric combines the information from three separate bandwidths into a single bandwidth metric, due to which 3-D PFD can be placed with higher reliability. A script compares the X, Y and Z 5% FBW at each point and picks the lower one for 3-D FBW.

Although a single busbar can be used to demonstrate 2-D and 3-D field shaping metrics, the main purpose of using 2-D and 3-D metrics is multi-conductor, multi-current systems. These systems will be discussed in later sections and chapters.

To use the 3-D FBW, it should be noted that a preliminary condition is the existence of 3-D magnetic fields. To demonstrate the 3-D FBW, a bent busbar, shown in Fig. 2.3-1, which produces 3-D field is used. Such busbars are common in EV inverters [20].

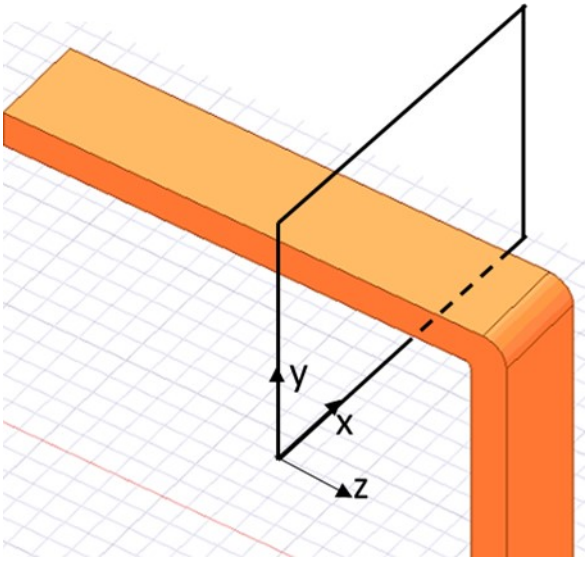

Fig. 2.3-1: Bent busbar to produce 3-D magnetic fields

Fig. 2.3-2 shows the X, Y, and Z 1-D FBW as well as the 3-D FBW around the bent busbar. In the regions of high FBW, the 3-D PFD can detect X, Y, and Z flux density from the busbar without being impacted by the skin effects.

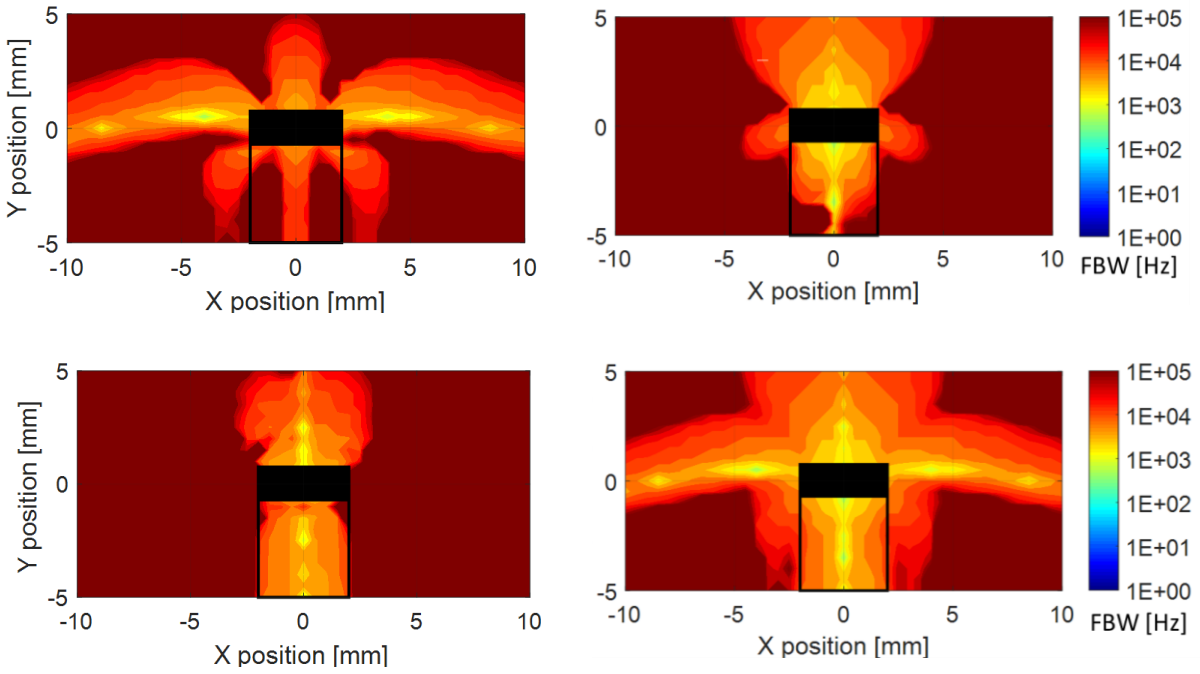

Fig. 2.3-2: X, Y and Z 1-D FBW and 3-D FBW around a bent rectangular cross section (4 x 1.5 mm) copper conductor

2.4 FBW with Single Current Injection

In the single-phase systems used in this chapter, the magnetic flux density at any given point is in-phase with the current at low frequencies. At higher frequencies, the magnetic field starts to develop a lag or lead phase angle due to the skin and proximity effects. In the state-of-the-art, the FBW is defined and computed using the real component of the phasor magnetic field. This means that the imaginary component is not part of the FBW calculations. Using only the real component of the magnetic field for the bandwidth analysis is preferred because the imaginary component is relatively small at frequencies of interest and negligible at low frequencies. Furthermore, the frequency dependent behavior of the real component is nearly identical to the behavior of the magnitude of the phasor field.

In some cases, magnetic flux density phasor can develop a phase shift at higher frequencies due to the small imaginary component which remains undetected if FBW is computed using phasor magnitude. However, it is detected in FBW using the real component because the real and imaginary components of the fields are coupled according to physics. Thus, the FBW metric can also account for phase shifts in the field.

Fig. 2.4-1 shows the FBWs calculated using the real component as well as the magnitude of the flux density phasor. It can be noticed that both yield very similar results. Similar comparison was done for various conductors used in this research and no significant difference was found. Due to this and to keep the analysis consistent with state-of-the-art, the real component of the flux density phasor is used in this work for calculating the FBW when a single current is injected.

Using *magntiude* of the phasor field

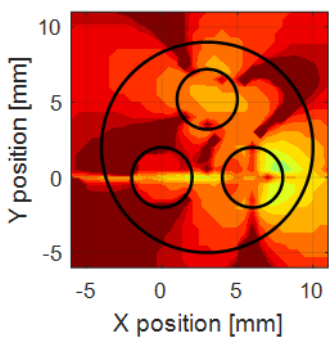

X-direction FBW

Using *real component* of the phasor field

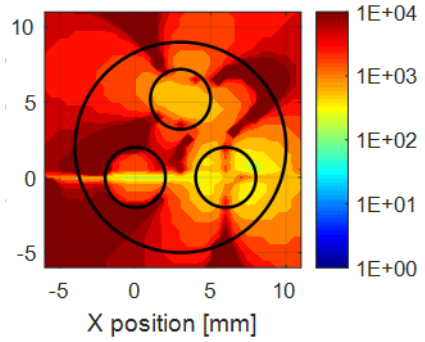

X-direction FBW

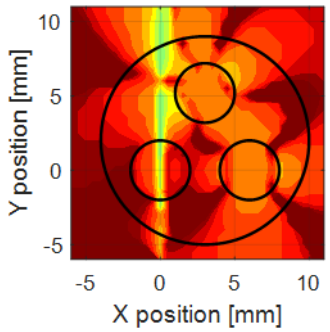

Y-direction FBW

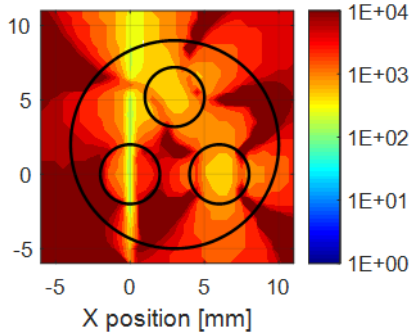

Y-direction FBW

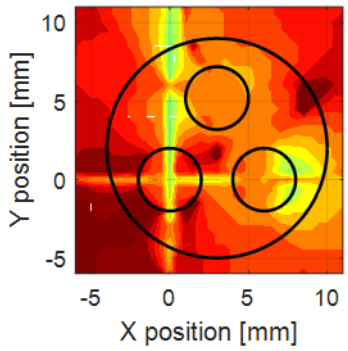

2-D FBW

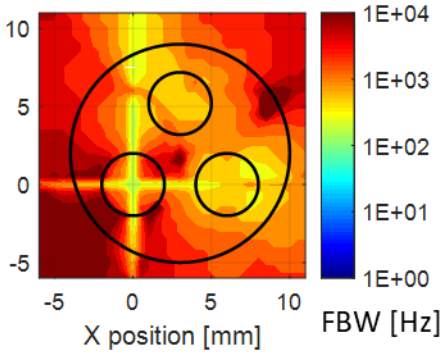

2-D FBW

Fig. 2.4-1: 5% FBW using real component and magnitude of phasor field around a three-phase cable for single-phase current injection

The three-phase cable has a rotational symmetry of 120 deg. However, the magnetic fields analyzed are in X and Y direction due to which the symmetry becomes convoluted. To understand the symmetry Fig. 2.4-2 can be observed. The X-direction FBW for Phase A, B and C injection

have different shapes. However, if the field is computed and analyzed at ±120 deg from the X axis, the rotational symmetry becomes clear.

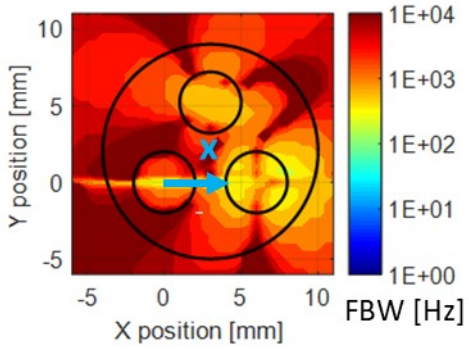

X-direction FBW for phase A injection

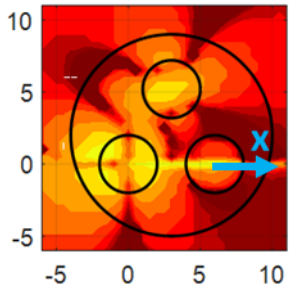

X- FBW for phase B injection

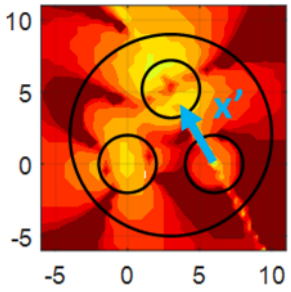

X'- FBW for phase B injection

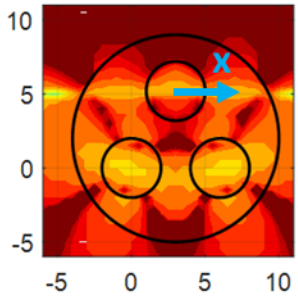

X- FBW for phase C injection

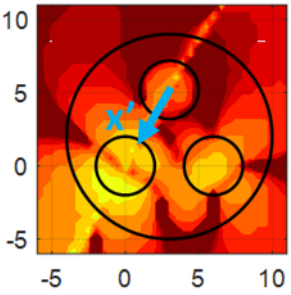

X'- FBW for phase C injection

Fig. 2.4-2: 5% FBW in X-direction and symmetric direction around a three-phase cable for single-phase current injection

2.5 FBW With Three-Phase Current Injection

1-D, 2-D and 3-D FBW can be computed using the cross-coupled field from multiple currents. This is especially relevant in three-phase systems in which the magnetic field can be a cross-coupled multi-dimensional quantity. Using the three-phase cross-coupled fields for computing the FBW in systems in which the phase conductors are close to each other is important to model the fields and their frequency dependency due to skin and proximity effects. There are regions in which the phase magnetic fields cancel each other or add to each other at different instants during the AC current cycle. Thus, the net sinusoidal magnetic flux density has an amplitude and phase which is a result of the cross-coupling between the phase current fields.

In three phase systems, the magnetic field at any given point can have phase angle anywhere between -180 and +180 depending upon the cross-coupling from phases A, B and C. Due to this, the ratio of real and imaginary component of the magnetic flux density phasor is an important variable. Unlike single-phase systems, the imaginary component is as important as the real component, even at low frequencies. Hence, in this work, magnitude of the flux density phasor is used work for calculating the FBW when three-phase currents are injected.

2.6 Finite Element Analysis for FBW

Electromagnetic Finite Element Analysis (FEA), which solves the four Maxwell equations using numerical methods, is used in this work to calculate the magnetic fields. The electromagnetic FEA software used in this research is Ansys Maxwell 3D and in some cases Q3D. Both programs are used on the Ansys Electromagnetics desktop which combines many of Ansys electromagnetic software packages in the same interface. Since most of the analysis in this work is done using an alternating current, the AC solution also known as eddy current solution type is implemented.

The typical process of FEA to calculate the FBW starts with the 3-D CAD model of the conductor and components around it. However, lower currents are more compatible with the finite region with Neuman boundary condition. Materials are specified in the 3-D CAD which is very important for the solution since it requires the material property to implement the Maxwell equations. The materials are idealized and don't account for any impurities and in many cases might be slightly different than the actual objects. The excitations are defined as the input and output current on the faces of the 3-D CAD model. The excitation by definition is Cosine function with phase and amplitude as input properties. Since the systems under analysis in this work are non-magnetic and linear, the amplitude of AC current excitation can be set to anything.

The next setup in setting up the FEA is the meshing and analysis setup. Both these steps are crucial for accuracy. FEA methods are prone to errors since they are not closed form analytical solutions. Maxwell 3D is also prone to error if the input settings are not appropriate. Mesh size limitations can be defined to improve the settings at the cost of computational speed. Maxwell 3D has the so called adaptive meshing in which the software meshes and refines meshes until it converges to defined limits at the adaptive frequency (set to 10 MHz). The setup has input for maximum number of mesh refinements (set to 100) and percent error (set to 1%) allowed. In this work, manual mesh settings are also added to ensure a fine mesh for critical parts of the geometry to assure accuracy.

Maxwell 3D is a near field solver and requires a region in which it solves. Anything beyond the region is not solved. The default as well as the recommended boundary condition on the region is Neuman which means the perpendicular magnetic flux density on the region is set to zero whereas parallel can be non-zero. Due to this, a larger region is good for accuracy, but it does increase the computational time. In this work, a reasonably sized regions are used which can help

capture the frequency dependent characteristics of the magnetic fields. If a conductor touches the region boundary in Maxwell 3-D and a full current path to the end of region is available, leakage current can follow which can cause unwanted excitations. This can be avoided by interrupting leakage currents paths in the FEA using a thin insulator.

The key component of analysis is the frequency sweep of the current. Maxwell 3D allows the setup to include solution at various user defined frequencies. This capability is used in most analysis to solve the systems from quasi-DC to 10 MHz. A complete electromagnetic solution is implemented at each frequency providing insight into the frequency dependent proximity and skin effect. The frequencies are discrete and swept on log intervals.

Due to the high usage of Maxwell in this work, most of the setup and data output from Maxwell 3D is done using Visual Basic scripts. The X, Y, and Z magnetic fields at each of the solved frequency for a 3-D mesh of selected points is outputted as text files. This 3-D mesh of output points is discrete and generally spaced at 0.5mm. Matlab is used to read these files and compute the flat bandwidth at each of the points. It should be noted that since the frequencies are discrete and there are 10 steps per decade, there is an inherent error associated with the FBW. The frequency at which the error has already crossed 5% is reported by Matlab as the flat bandwidth at a particular point.

Electromagnetic FEA is one of the tools whose accuracy is as good as the model, material and solution settings. Advice and recommendations on the FEA setting solutions from Ansys engineers and state-of-the-art helped to increase the fidelity of the FEA results. It is common to have some discrepancy between FEA and experiments, primarily due to these reasons. In this work, FEA is used as a preliminary design and analysis tool with a balance of computation time versus accuracy. The main purpose of FEA in this work is to show the validity of methods developed, and to verify

the conclusions and FBW spatial trends from FEA in experiments within reasonable margins of uncertainty.

Sometimes, the experimental and FEA FBW have a very significant difference. It is because FBW is a non-linear metric and despite an under 5% magnetic field error between FEA and experiments, that FBW could change by many orders of magnitude. This situation can be notice in the magnetic field frequency response function (FRF) in Fig. 2.6-1. FRF 1 and FRF 2 have less than 5% error for majority of the frequency range, however, the 5% FBW of FRF 1 is 800 Hz and 5% FBW of FRF 2 is over 20kHz.This shows that sometimes a low error between simulated and experimental FRFs can lead to a very high error in FBW.

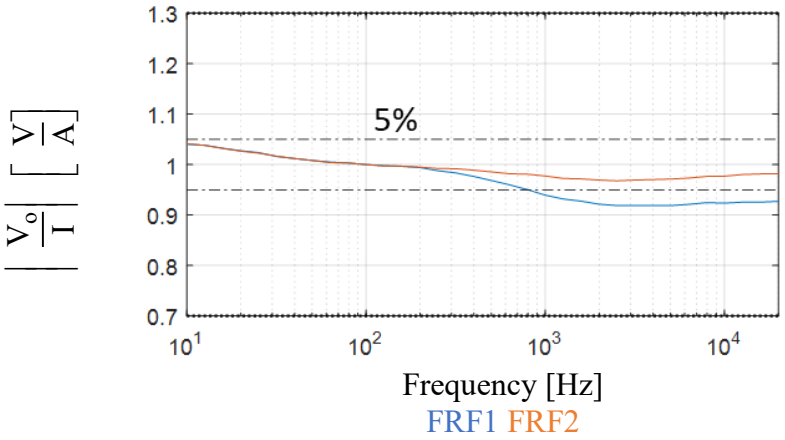

Fig. 2.6-1: Example FRFs of PFD output with respect to actual current normalized to 100 Hz value to show the 5% FBW error in response to minor FRF differences.

2.7 Summarizing Remarks

A concise summary of the chapter is available at its beginning. The conclusions and contributions for this chapter are available in the last chapter.

This chapter explains that a magnetic field is a 3-D spatial vector quantity. Sensing the field with a 3-D PFD captures all the information about it, whereas sensing it with 1-D or 2-D PFD inherently filters the information in the field. The rotational orientation of a 1-D or 2-D PFD i.e. the direction for sensing fields is an important degree of freedom. If utilized properly, the rotational orientation of the PFD can lead to higher sensing bandwidth and SNR.

In this chapter, analytical and FEA tools are developed to analyze the magnetic fields in various directions and to utilize the direction of multi-dimensional magnetic field for sensing properties. The rotated 2-D magnetic flux density and FBW metric can be used to determine the SNR and bandwidth for sensing the fields along any two orthogonal directions on a given plane. The use of rotation matrices reduces the computational effort as a single set of FEA results can model the magnetic fields and capture their frequency dependency in any direction in a 3-D space.

The 3-D FBW metric is also defined in this chapter. This combines information from three 1-D FBWs, can be used to evaluate magnetic fields in all three dimensions and to position a 3-D PFD for high-bandwidth sensing. The multi-dimensional FBW metrics are useful for shaping current paths and designing conductors for PFD based current sensing in the multi-current systems.

This chapter also contains a detailed discussion of the FEA based methods to compute the frequency dependent fields and FBW. The intricacies of single current and three-phase current injections in the FEA and FBW computation are described as well.

Chapter 3 Multi-Dimensional Magnetic Field Decoupling Methodology

This chapter develops methodologies to decouple and sense multiple currents using the cross-coupled multi-dimensional fields at a point. First, the physics-based method for analytical decoupling of the 2-D cross-coupled fields from two independent currents is summarized. This is followed by the analytical decoupling of 3-D cross-coupled magnetic fields from three independent currents. The physical and mathematical basis of singularity constraints are explained for 3-D decoupling of fields. The chapter also includes a detailed discussion of experimental calibration of decoupling matrices when the analytical and FEA methods are not convenient.

The main purpose of this chapter is to develop methodologies to sense multiple currents from the linearly cross-coupled multi-dimensional field at a point detected by a PFD.

Elements of this chapter are also documented in [64], [116] and [118].

3.1 2-D PFD-based Current Sensing with Cross-Coupling Field Decoupling

This subsection summarizes the work done in [64].

Magnetic fields from nearby currents always cross-couple linearly in air, and the combined total field contains information about all of the currents contributing to the field. As explained in chapter 1, the methods have been developed in literature to detect the cross-coupled field using 1-D PFDs at physically separate locations and to decouple it.

The 2-D PFD-based current sensing is superior to 1-D PFD-based current sensing due to the reduction in the number of PFDs for multicurrent or multiphase current sensing. As described in

chapter 1, to decouple and sense 2N currents, the minimum number of 1-D PFDs required is also 2N. However, the same 2N currents can be sense with only N 2-D PFDs.

The 2-D PFD has the magnetic field sensing capability equivalent to two orthogonal PFDs. This provides the degrees of freedom for one single 2-D PFD to sense and decouple two currents. Compared to 1-D PFD current sensing, using 2-D reduces the number of PFDs by half.

3.1.1 Analytical 2-D field decoupling and sensing of two currents

A dual conductor, single 2-D PFD system is setup as shown in Fig. 3.1-1. There are two thin long wires and one 2-D PFD.

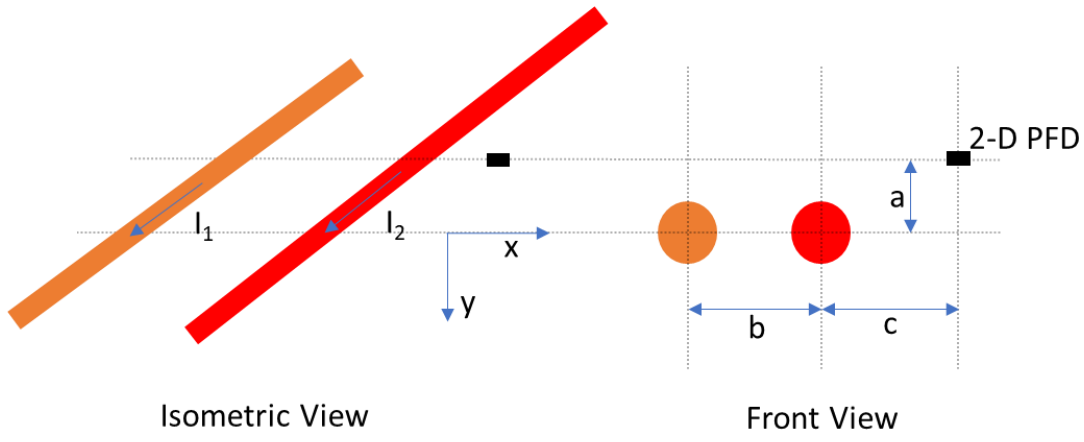

Fig. 3.1-1: Dual conductor single 2-D PFD sensing system

Using the geometry and dimensions defined, X and Y magnetic field contribution from each of the two currents can be calculated at the PFD location. This relationship is shown in (3.1-1). G is the PFD PCB gain, S is the PFD sensitivity, VB_x is the X output and VB_y is the Y output of 2-D PFD.

$$\frac{G\,S\,\mu}{2\pi}\begin{bmatrix} \frac{a}{r_1^2} & \frac{a}{r_2^2} \\ \frac{b+c}{r_1^2} & \frac{c}{r_2^2} \end{bmatrix}\begin{bmatrix} I_1 \\ I_2 \end{bmatrix} = \begin{bmatrix} VB_x \\ VB_y \end{bmatrix} \tag{3.1-1}$$

The coupling matrix can be inverted to compute the decoupling matrix as shown in (3.1-2).

$$\frac{G\,S\,\mu}{2\pi}\begin{bmatrix} I_1 \\ I_2 \end{bmatrix} = \begin{bmatrix} \frac{a}{r_1^2} & \frac{a}{r_2^2} \\ \frac{b+c}{r_1^2} & \frac{c}{r_2^2} \end{bmatrix}^{-1} \begin{bmatrix} VB_x \\ VB_y \end{bmatrix} \tag{3.1-2}$$

where $r_1^2 = a^2 + (b+c)^2$ and $r_2^2 = a^2 + c^2$

This purely analytical calculation of the coupling and decoupling matrices is used to sense phase A and B currents of amplitude 10 A and 500 Hz with a single 2-D PFD in a Matlab simulation. Fig. 3.1-2 shows the simulated 2-D PFD outputs and Fig. 3.1-3 shows an overlay of reference decoupled currents. The PFD outputs demonstrate the cross-coupling in the field by being phase shifted from the reference currents. The X and Y outputs have different levels of cross-coupling from the two currents, which is imperative for decoupling.

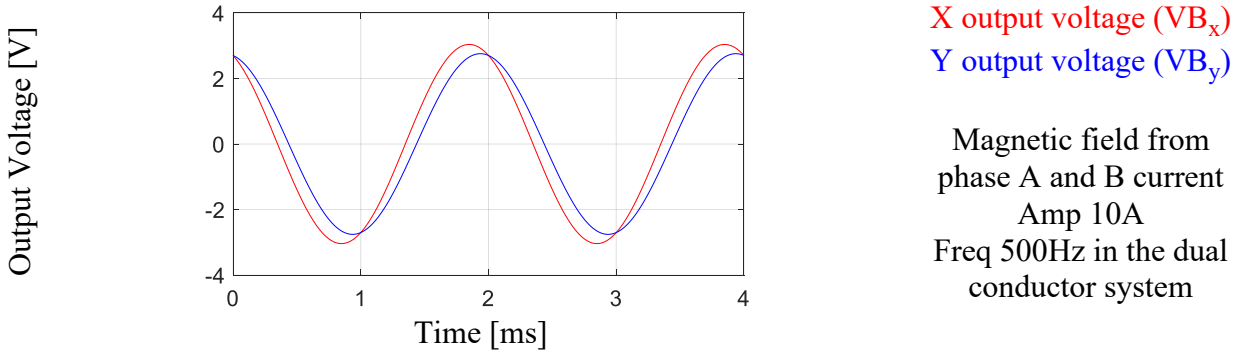

Fig. 3.1-2: X and Y output voltage of the 2-D PFD in the dual conductor system

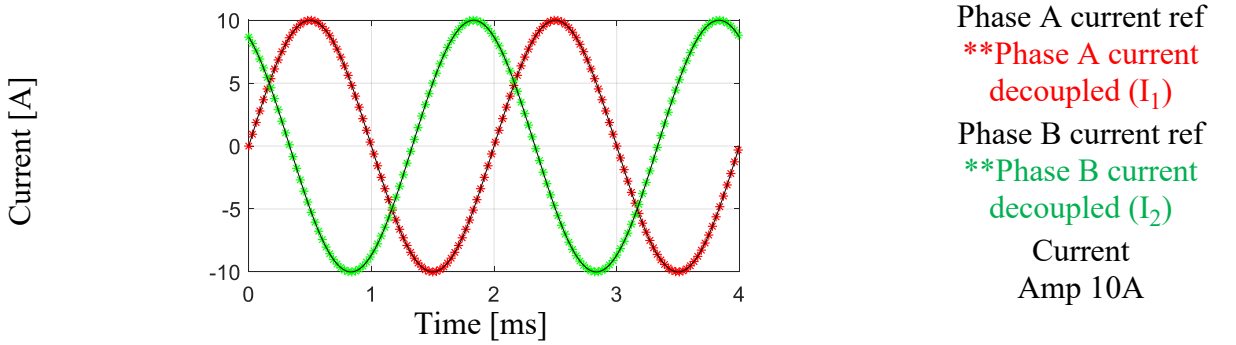

Fig. 3.1-3: Analytically decoupled currents with a single 2-D PFD in the dual conductor system in simulation

3.2 3-D PFD-based Current Sensing with Cross-Coupling Field Decoupling

The 3-D PFD has the magnetic field sensing capability equal to three orthogonal 1-D PFDs. Due to this, one single 3-D PFD can be used to sense and decouple three currents. Compared to 1-D PFD current sensing, using 3-D reduces the number of PFDs to a third.

3.2.1 Condition to avoid singularity in 3-D field decoupling

3-D magnetic field decoupling can be very advantageous as will be discussed later in this chapter, but it requires extra caution because it is prone to singularity if the orthogonal axes of PFD have the same information. In other words, it is possible for orthogonal axes of the 3-D PFD to either have no information at all or the same information as the other two axes.

Three Straight Parallel Conductors

One of the simplest cases of 3-D field decoupling seems to be sensing three-phase currents in three parallel conductors typically used in AC drives as shown in Fig. 3.2-1 .

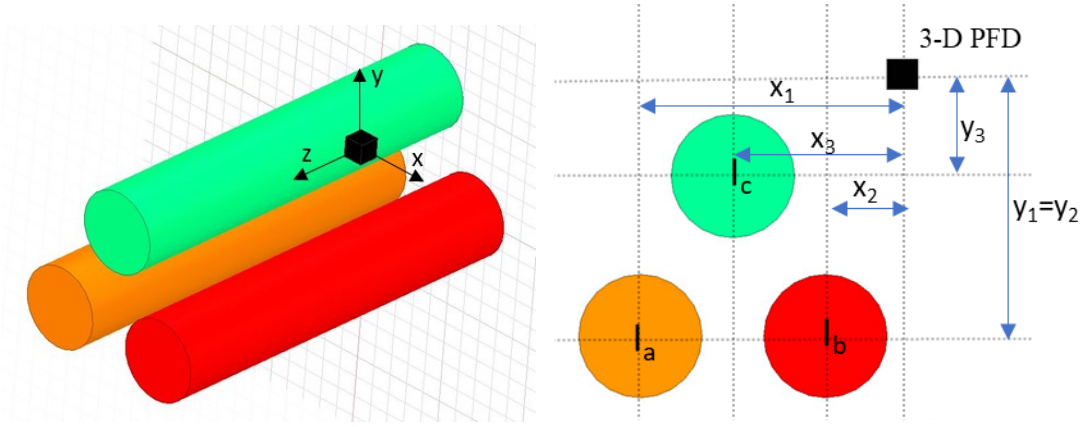

Fig. 3.2-1: Three straight parallel conductors for 3-D decoupling

There are three dimensions in the 3-D PFD and each of them will have cross-coupled fields from the three-phases. The primary instinct is to use 3-D decoupling much like the 2-D by analyzing the system in 2-D.

Using the geometry and dimensions defined, the X, Y, and Z magnetic field contributions from each of the three currents can be calculated at the 3-D PFD location. This relationship is shown in (3.2-1)

$$\frac{G\,S\,\mu}{2\pi}\begin{bmatrix} \frac{y_1}{r_1^2} & \frac{y_2}{r_2^2} & \frac{y_3}{r_3^2} \\ -\frac{x_1}{r_1^2} & -\frac{x_2}{r_2^2} & -\frac{x_3}{r_3^2} \\ 0 & 0 & 0 \end{bmatrix}\begin{bmatrix} I_a \\ I_b \\ I_c \end{bmatrix} = \begin{bmatrix} VB_x \\ VB_y \\ VB_z \end{bmatrix} \tag{3.2-1}$$

where $r_1^2 = x_1^2 + y_1^2$, $r_2^2 = x_2^2 + y_2^2$ and $r_3^2 = x_3^2 + y_3^2$

where G is the PFD PCB gain, S is the PFD sensitivity and $VB_{x,\,y,\,z}$ are the 3-D PFD outputs.

The coupling matrix in (3.2-1) signifies the issue of singularity in 3-D decoupling. The third row of the matrix is entirely zero leading to a condition number of infinity, determinant of zero and a singular matrix. There exists no inverse for singular matrices, due to which, this cross-coupling cannot be decoupled. The physics-based explanation of the singularity comes from the 2-D planar field shape of the straight conductors. The planar field means that Z axis of the PFD detects no fields, hence the system is attempting to decouple three currents using two inputs which is impossible.

The first perceived solution to making use of the 3-D PFD is to rotate it about its Y axis. This way, the original field in X-direction is detected by the PFDs X and Z outputs, thereby evoking the service of all three dimensions in the 3-D PFD as shown in Fig. 3.2-2.

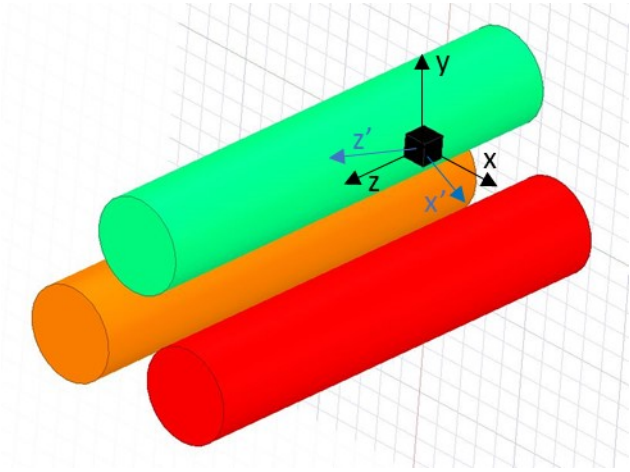

Fig. 3.2-2: Three straight parallel conductors for 3-D decoupling with rotated PFD

A very simple analytical method to calculate the new coupling matrix is to use the rotation matrix as shown in (3.2-2).

$$\mathbf{R}_{y=}(\theta) = \begin{bmatrix} \cos\theta & 0 & \sin\theta \\ 0 & 1 & 0 \\ -\sin\theta & 0 & \cos\theta \end{bmatrix} \text{ for reference frame rotation in clockwise } \theta \tag{3.2-2}$$

$$\frac{G\,S\,\mu}{2\pi}\mathbf{R}_y \begin{bmatrix} \frac{y_1}{r_1^2} & \frac{y_2}{r_2^2} & \frac{y_3}{r_3^2} \\ -\frac{x_1}{r_1^2} & -\frac{x_2}{r_2^2} & -\frac{x_3}{r_3^2} \\ 0 & 0 & 0 \end{bmatrix} \begin{bmatrix} I_a \\ I_b \\ I_c \end{bmatrix} = \begin{bmatrix} VB_x \\ VB_y \\ VB_z \end{bmatrix}$$

where $r_1^2 = x_1^2 + y_1^2$, $r_2^2 = x_2^2 + y_2^2$ and $r_3^2 = x_3^2 + y_3^2$

The new coupling matrix is still singular. In general, multiplying a singular matrix by a non-singular matrix always yields a singular matrix. This leads to the understanding that no matter how the 3-D PFD is positioned and oriented, if the field from the three conductors is planar, the system cannot be used to sense and decouple the three currents. However, even if one of the three conductors produce non-planar field, the magnetic field become 3-D and the system becomes non-singular.

3.2.2 Analytical 3-D decoupling and sensing of three non-parallel currents

3-D decoupling for straight parallel, conductors results in singularity. However, even if one of the three conductors are not parallel or straight, the magnetic field at the PFD location becomes 3-D instead of being 2-D. To develop a 3-D decoupling system, a simple three conductor system is shown in Fig. 3.2-3 where one of the three conductors is rotated about the X axes of the PFD by 90 degree.

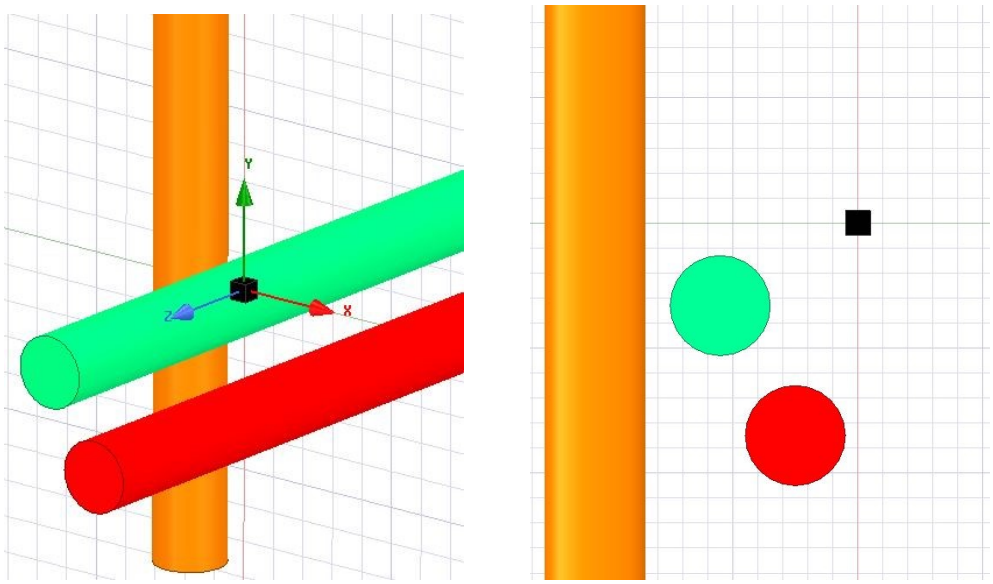

Fig. 3.2-3: Three straight non-parallel conductors for 3-D decoupling

The coupling matrix of this three conductor system with one of the conductors rotated can also be computed using rotations matrices. The rotation matrix is for rotating the vector instead of the reference frame. In a physical sense, the rotation of the wire about the X axis swaps the Y and Z fields from the wire at the 3-D PFD location. All the rest of the coupling terms stay the same. Hence, the column vector for coupling terms from the rotated current is calculated in (3.2-3).

$$\mathbf{R}_{x=}(\theta) = \begin{bmatrix} 1 & 0 & 0 \\ 0 & \cos\theta & -\sin\theta \\ 0 & \sin\theta & \cos\theta \end{bmatrix} \tag{3.2-3}$$

$$\mathbf{R}_x \begin{bmatrix} \frac{y_1}{r_1^2} & \frac{y_2}{r_2^2} & \frac{y_3}{r_3^2} \\ \frac{x_1}{r_1^2} & \frac{x_2}{r_2^2} & \frac{x_3}{r_3^2} \\ 0 & 0 & 0 \end{bmatrix} = \begin{bmatrix} \frac{y_1}{r_1^2} & \cdots & \cdots \\ 0 & \cdots & \cdots \\ \frac{x_1}{r_1^2} & \cdots & \cdots \end{bmatrix}$$

The coupling terms from the other two currents stay the same. (3.2-4) shows the coupling matrix for the three-conductor system with one of the conductors rotated about X axis. The system is not singular, and decoupling is possible.

$$\frac{G\,S\,\mu}{2\pi} \begin{bmatrix} \frac{y_1}{r_1^2} & \frac{y_2}{r_2^2} & \frac{y_3}{r_3^2} \\ 0 & \frac{x_2}{r_2^2} & \frac{x_3}{r_3^2} \\ \frac{x_1}{r_1^2} & 0 & 0 \end{bmatrix} \begin{bmatrix} I_a \\ I_b \\ I_c \end{bmatrix} = \begin{bmatrix} VB_x \\ VB_y \\ VB_z \end{bmatrix} \tag{3.2-4}$$

$$\frac{G\,S\,\mu}{2\pi} \begin{bmatrix} I_a \\ I_b \\ I_c \end{bmatrix} = \begin{bmatrix} \frac{y_1}{r_1^2} & \frac{y_2}{r_2^2} & \frac{y_3}{r_3^2} \\ 0 & \frac{x_2}{r_2^2} & \frac{x_3}{r_3^2} \\ \frac{x_1}{r_1^2} & 0 & 0 \end{bmatrix}^{-1} \begin{bmatrix} VB_x \\ VB_y \\ VB_z \end{bmatrix}$$

Fig. 3.2-4 shows the results of cross-coupled PFD outputs that require decoupling in a Matlab simulation. The decoupled three-phase currents are shown in Fig. 3.2-5. The decoupling matrix from (3.2-4) is used to decouple the fields and sense these three currents.

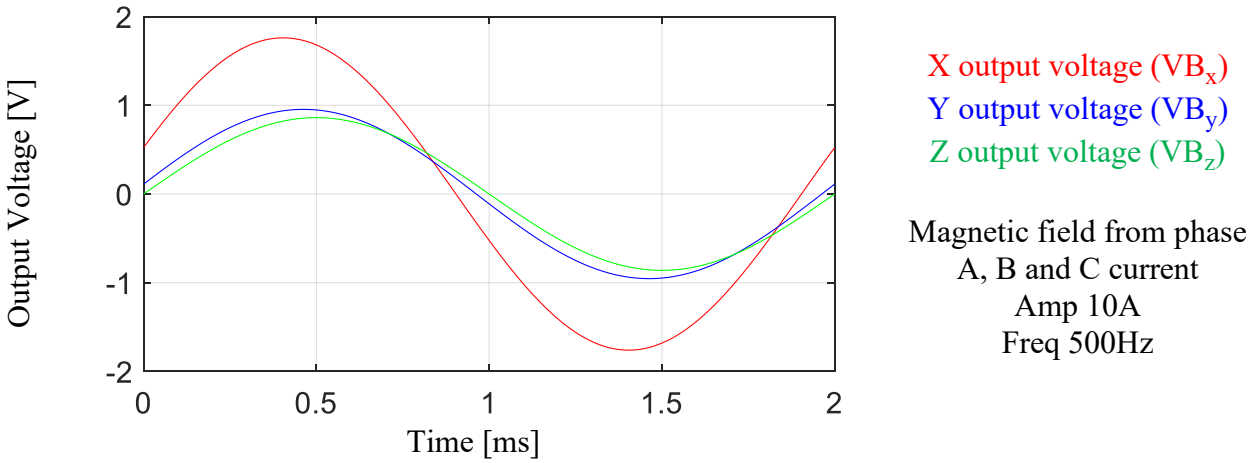

Fig. 3.2-4: X, Y and Z output voltage of the 3-D PFD due the three straight non-parallel conductors

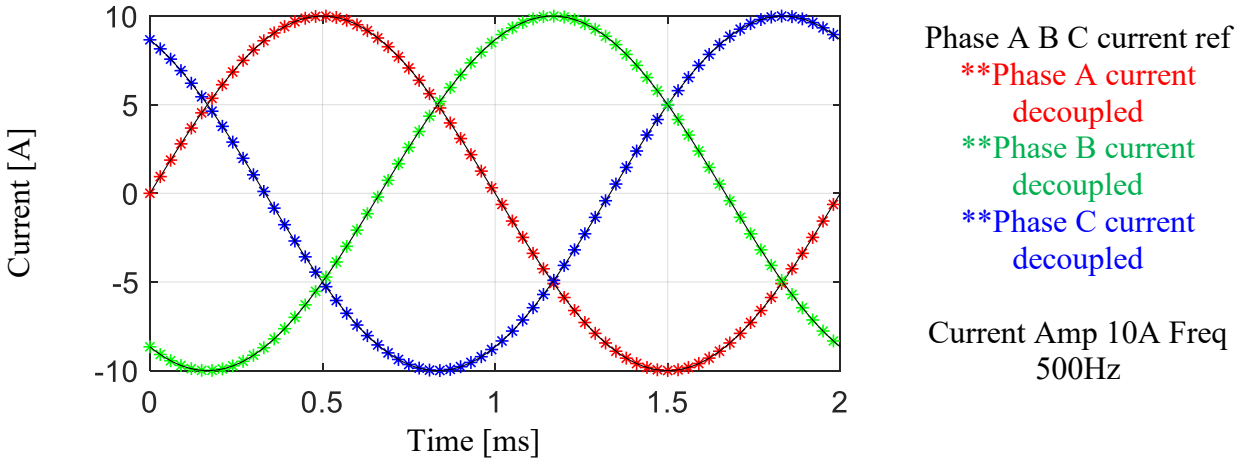

Fig. 3.2-5: Analytically decoupled currents with a single 3-D PFD in the non-parallel three-conductor system in simulation

To demonstrate the functionality of the decoupling for independent currents, Fig. 3.2-6 and Fig. 3.2-7 show the decoupling of three currents each of which has different amplitude and frequency characteristics. These results show that 3-D decoupling technique does not require a balanced three-phase system assumption. It physically separates the magnetic fields from each of the currents based upon the Maxwell-Amperes law.

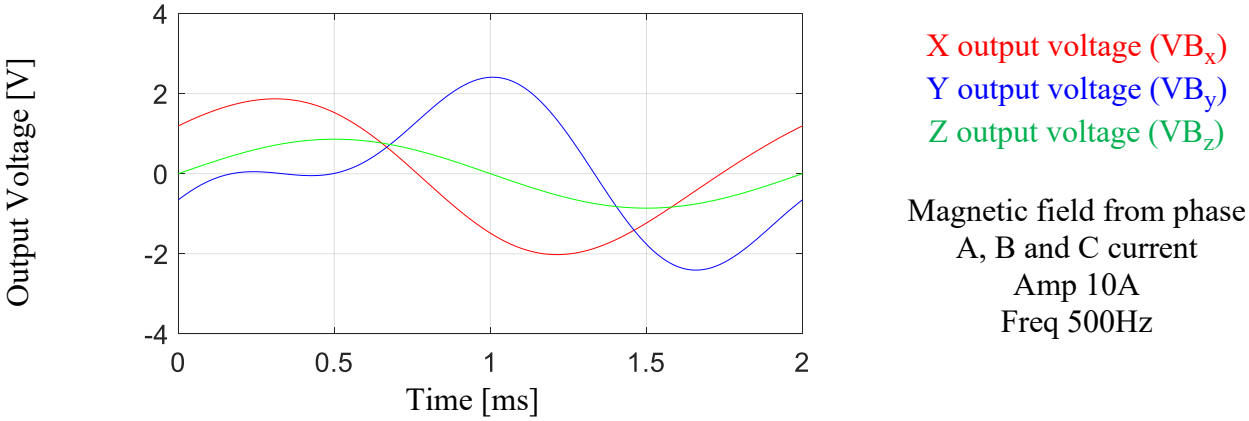

Fig. 3.2-6: X, Y and Z output voltage of the 3-D PFD due the three straight non-parallel conductors carrying unbalanced currents

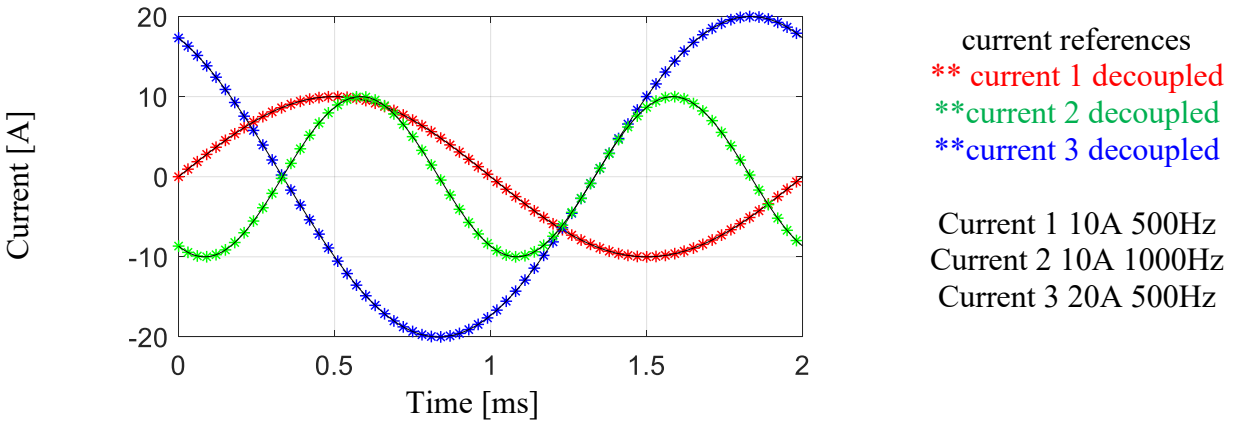

Fig. 3.2-7: Analytically decoupled currents with a single 3-D PFD in the non-parallel three-conductor system in simulation with unbalanced currents

3.2.3 FEA-based 3-D decoupling for three parallel conductors with a bend

The non-parallel system shown in sec. 3.2.2, for 3-D decoupling is mainly used to develop an analytical 3-D field decoupling approach. In real applications, most conductors are parallel. However, as explained in sec. 3.2.1, three straight parallel currents cannot be decoupled due to singularity caused by 2-D field. In practical applications three-phase parallel conductors will have some bends or turns, due to which, the field produced is naturally a 3-D vector quantity. One very simple case is shown in Fig. 3.2-8 to demonstrate the idea of 3-D decoupling in parallel bent conductors.

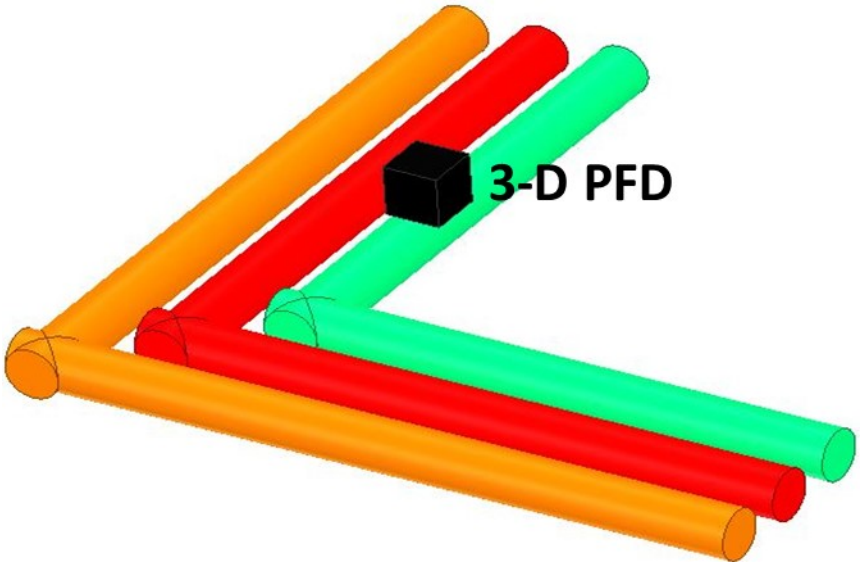

Fig. 3.2-8: Three bent parallel conductors for 3-D decoupling with a 3-D PFD

(3.2-5) can be used to model the current and magnetic field relationship. However, in this situation, the Maxwell-ampere's law-based analytical solution for coupling matrix, unlike the one in (3.1-1), is very complicated and unnecessarily tedious.

$$\begin{bmatrix} C_{xa} & C_{xb} & C_{xc} \\ C_{ya} & C_{yb} & C_{yc} \\ C_{za} & C_{zb} & C_{zc} \end{bmatrix} \begin{bmatrix} I_a \\ I_b \\ I_c \end{bmatrix} = \begin{bmatrix} VB_x \\ VB_y \\ VB_z \end{bmatrix} \tag{3.2-5}$$

In complicated scenarios a close substitute to using an analytical approach to find the coupling matrix is to use the FEA which also uses the Maxwell equation. In the model in Ansys Maxwell FEA software, unit AC current is passed through each of the conductors, one at a time. The value of the X, Y and Z components of the magnetic flux density is recoded at the 3-D PFD location at the peak instance of the current. The process is repeated for each current to form a coupling matrix as shown in (3.2-6).

$$\begin{bmatrix} C_{xa} & C_{xb} & C_{xc} \\ C_{ya} & C_{yb} & C_{yc} \\ C_{za} & C_{zb} & C_{zc} \end{bmatrix} = \begin{bmatrix} B_{xa} & B_{xb} & B_{xc} \\ B_{ya} & B_{yb} & B_{yc} \\ B_{za} & B_{zb} & B_{zc} \end{bmatrix} \quad (3.2\text{-}6)$$

Where B_{xa} refers to the X component of the magnetic field when phase A current is passed and is at its peak value. (3.2-6) shows that the coupling terms are exactly equal to the field computed through FEA for each of the currents and field directions. This relationship should be scaled in case of non-unity amplitude current. The decoupling matrix is the inverse of the coupling matrix.

To check the validity of the coupling and decoupling matrices computed using FEA, the following test case is used. In the FEA all three currents (at their respective amplitude and phase) are passed at the same time and the net magnetic flux density at the PFD location is sampled 36 times as X, Y and Z component over one period. Fig. 3.2-9 shows the voltages which the 3-D PFD will output in response to the magnetic fields. Fig. 3.2-10 shows the results of decoupling. It is worth noting that the output of the FEA using frequency domain solver is based upon phase instants rather than time, hence the X axis is shown as phase in radian. This can easily be converted to a time series as well.

The decoupling error is less than 1%. This is primarily because the FEA is solved in a finite region with a fine mesh. This leads a close to analytical solution without any noise. However, the system can be further improved with even larger region and finer mesh. An important point to note is the low phase difference (around 3deg with inversion) between the Y and Z output. This is primarily because of ill-conditioned decoupling matrix and will be explained and remedied over the next sections.

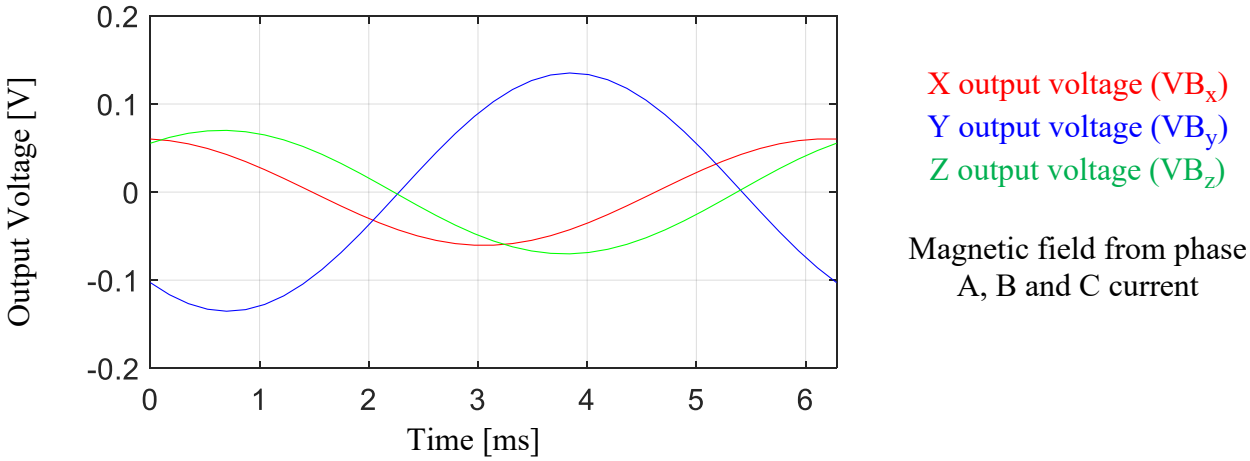

Fig. 3.2-9: X, Y and Z output voltage of the 3-D PFD in the three bent parallel conductor system

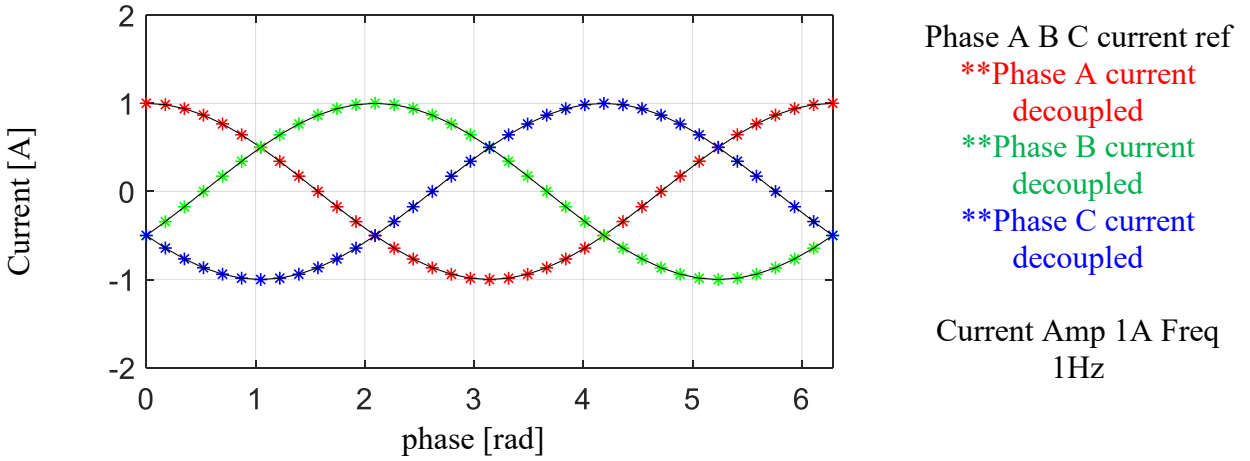

Fig. 3.2-10: FEA-based decoupling of three-phase currents with a single 3-D PFD in the three bent parallel conductor system

Furthermore, Fig. 3.2-11 demonstrates the decoupling in an unbalanced system. The same decoupling matrix as above is used with this system. The decoupling can extract the three currents even when they are unbalanced showing that the method works independently of current characteristics.

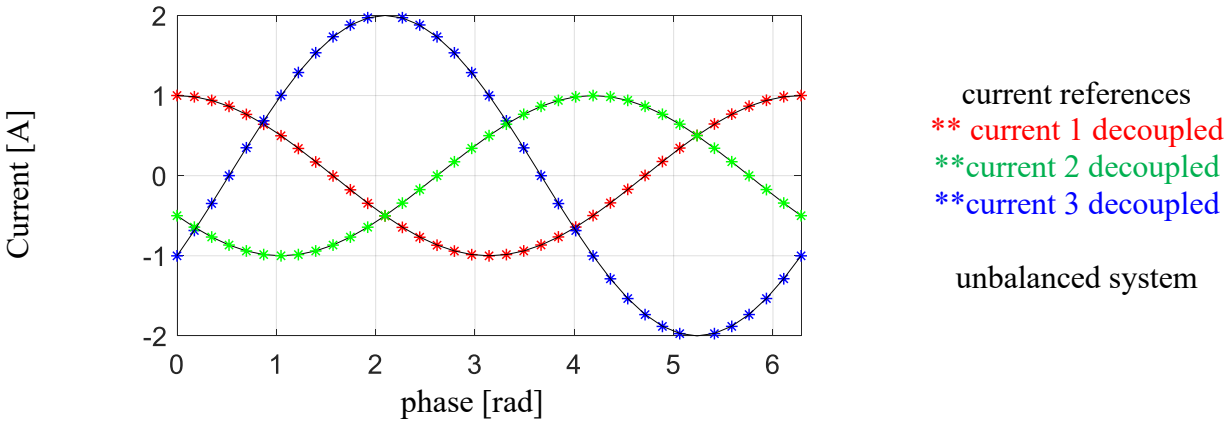

Fig. 3.2-11: FEA-based decoupling of three-phase unbalanced currents with a single 3-D PFD in the three bent parallel conductor system

3.3 Calibration of Decoupling Matrices

The calibration of decoupling matrix in this chapter has been done analytically using Maxwell-Amperes law and then using an FEA method which uses a numerical version of Maxwell-Ampere's law. Both of these methods of finding the decoupling matrices are very theoretical and cannot be used directly to find matrices in real current sensing systems. More practical and experimental methods are needed to find the decoupling matrices.

3.3.1 Signal injection calibration

The first experimental method to find the decoupling matrix for current sensing involves signal injection [69]. (3.3-1) shows the method for two currents and a 2-D PFD system. The coupling matrix is 2x2. The terms of this coupling matrix can be found by passing one current at a time and recording the X and Y outputs of the 2D PFD. Since the other current is zero, the coupling terms in the column are the PFD output scaled by the current.

$$\begin{bmatrix} C_{xa} & C_{xb} \\ C_{ya} & C_{yb} \end{bmatrix} \begin{bmatrix} I_a \\ I_b \end{bmatrix} = \begin{bmatrix} VB_x \\ VB_y \end{bmatrix} \tag{3.3-1}$$

$$\begin{bmatrix} C_{xa} & - \\ C_{ya} & - \end{bmatrix}\begin{bmatrix} I_a \\ 0 \end{bmatrix} = \begin{bmatrix} VB_x \\ VB_y \end{bmatrix} \qquad C_{xa} = VB_x/I_a \mid C_{ya} = VB_y/I_a$$

$$\begin{bmatrix} - & C_{xa} \\ - & C_{yb} \end{bmatrix}\begin{bmatrix} 0 \\ I_b \end{bmatrix} = \begin{bmatrix} VB_x \\ VB_y \end{bmatrix} \qquad C_{xb} = VB_x/I_b \mid C_{yb} = VB_y/I_b$$

This method can be extended to a three current, 3-D PFD system shown in (3.3-2).

$$\begin{bmatrix} C_{xa} & C_{xb} & C_{xc} \\ C_{ya} & C_{yb} & C_{yc} \\ C_{za} & C_{zb} & C_{zc} \end{bmatrix}\begin{bmatrix} I_a \\ I_b \\ I_c \end{bmatrix} = \begin{bmatrix} VB_x \\ VB_y \\ VB_z \end{bmatrix} \qquad (3.3\text{-}2)$$

$$\begin{bmatrix} C_{xa} & - & - \\ C_{ya} & - & - \\ C_{za} & - & - \end{bmatrix}\begin{bmatrix} I_a \\ 0 \\ 0 \end{bmatrix} = \begin{bmatrix} VB_x \\ VB_y \\ VB_z \end{bmatrix} \qquad C_{xa} = VB_x/I_a \mid C_{ya} = VB_y/I_a \quad C_{za} = VB_z/I_a$$

$$\begin{bmatrix} - & C_{xb} & - \\ - & C_{yb} & - \\ - & C_{zb} & - \end{bmatrix}\begin{bmatrix} 0 \\ I_b \\ 0 \end{bmatrix} = \begin{bmatrix} VB_x \\ VB_y \\ VB_z \end{bmatrix} \qquad C_{xb} = VB_x/I_b \mid C_{yb} = VB_y/I_b \quad C_{zb} = VB_z/I_b$$

$$\begin{bmatrix} - & - & C_{xc} \\ - & - & C_{yc} \\ - & - & C_{zc} \end{bmatrix}\begin{bmatrix} - \\ - \\ I_c \end{bmatrix} = \begin{bmatrix} VB_x \\ VB_y \\ VB_z \end{bmatrix} \qquad C_{xc} = VB_x/I_c \mid C_{yc} = VB_y/I_c \quad C_{zc} = VB_z/I_c$$

$$\begin{bmatrix} C_{xa} & C_{xb} & C_{xc} \\ C_{ya} & C_{yb} & C_{yc} \\ C_{za} & C_{zb} & C_{zc} \end{bmatrix}^{-1} = \begin{bmatrix} D_{xa} & D_{xb} & D_{xc} \\ D_{ya} & D_{yb} & D_{yc} \\ D_{za} & D_{zb} & D_{zc} \end{bmatrix}$$

If an AC current injection is used with a high sampling frequency, fast Fourier transform of the reference current and PFD outputs can be used to find the terms. The other method would be to simply divide the PFD output signals with the reference current signal and use the median of the ratio. The median reduces the impact of noise without being skewed by outliers.

The calibration process needs to reduce the impact of noise and other anomalies. To improve the calibration accuracy, the C terms in the coupling matrix can be refined by repeating the calibration using currents at a few different frequencies and amplitude. Statistical mean or median of the coupling terms can be used to find the exact terms.

The decoupling matrix is the inverse of the coupling matrix.

3.3.2 Direct calibration

The second practical method of finding the decoupling matrix involves passing known currents together instead of one at a time [119]. The method is shown for two current 2-D PFD system in (3.3-3). Each of the currents can be computed using a unique combination of the two PFD outputs. The coefficients of the combination are the decoupling terms. The decoupling terms can be found by recording the PFD outputs and current values at particular time instants. With two instants, a system of four linear equations and four unknowns is formed. The system can be solved to find the decoupling matrix.

$$\begin{bmatrix} D_{x1} & D_{y1} \\ D_{x2} & D_{y2} \end{bmatrix}\begin{bmatrix} VB_x(t_1) \\ VB_y(t_1) \end{bmatrix}=\begin{bmatrix} I_1(t_1) \\ I_2(t_1) \end{bmatrix} \qquad (3.3\text{-}3)$$

$$\begin{bmatrix} D_{x1} & D_{y1} \\ D_{x2} & D_{y2} \end{bmatrix}\begin{bmatrix} VB_x(t_2) \\ VB_y(t_2) \end{bmatrix}=\begin{bmatrix} I_1(t_2) \\ I_2(t_2) \end{bmatrix}$$

In real applications, the frequency of the reference currents should be the nominal frequency of the system and the amplitude should be high enough for an acceptable SNR. The PFD outputs and even the current reference might still have noise on them. In order to eliminate the impact of noise during calibration, the calibration process should be repeated multiple times by using two different time instants every time. Repeating the calibration is a very simple process and only involves a loop in a solver like Matlab. With a sampling frequency of 1MHz and data for 100 ms,

there are 100k sampling instants, hence system can be solved thousands of times in a loop and the statistical median can be used to tune the decoupling matrix.

For a three-current 3-D PFD system, the direct decoupling matrix calibration method is represented in (3.3-4). By capturing data at three time instants, a nine equations, nine unknowns system is formed. This system can be solved to form the decoupling matrix.

$$\begin{bmatrix} I_a(t_1) \\ I_b(t_1) \\ I_c(t_1) \end{bmatrix} = \begin{bmatrix} D_{xa} & D_{ya} & D_{za} \\ D_{xb} & D_{yb} & D_{zb} \\ D_{xc} & D_{yc} & D_{zc} \end{bmatrix} \begin{bmatrix} VB_x(t_1) \\ VB_y(t_1) \\ VB_z(t_1) \end{bmatrix} \quad \text{where } t_1 \text{ is replaced with } t_2 \text{ and } t_3 \text{ to obtain the system of 9 linear equations} \qquad (3.3\text{-}4)$$

Unlike the 2x2 decoupling matrix, 3x3 decoupling matrix calibration is prone to finding solutions which do not represent the Maxwell-Amperes law. In a three current, 3-D PFD system, there are three PFD signals which are combined to form the currents. In a test case with commonly used three-phase sinusoidal currents and hence sinusoidal PFD outputs, mathematically, there are multiple ways of synthesizing the current sinusoidal signals from the three PFD output signals. However, based upon Maxwell-Amperes law only one decoupling matrix is valid.

For sinusoidal signals if the three sampling instants are selected randomly, there is a chance that the system of equation might lead to the non-physics-based decoupling matrix. This is especially true if a balanced three-phase system is used for calibration. The solutions of the decoupling matrices will decouple the PFD signals into balanced three-phase currents. The decoupling matrix solutions can hold true for different frequencies and amplitude of the currents too, albeit only for a balanced system. If there is a fundamental change in the system such as an imbalance of one of the currents, the decoupling matrix is likely to fail. It is empirically found, that if the system is solved using many different three time instants datasets, the median of terms tries to converge to the Maxwell-Ampere's law-based decoupling matrix solution which is also

same as the signal injection method. The physics-based decoupling solution is statistically more likely to have fewer extreme values and high occurrences.

Another way to look at this issue in calibration is shown in (3.3-5). The decoupling terms can directly be solved in equivalent form. If the PFD outputs matrix (VB) is singular, the system does not solve correctly. The condition number is used to discard datasets with singular VB and I matrices. The condition number of the matrix is a measure of its singularity. It measures how much of a change will be caused in the inverse in response to a slight change in the matrix.

$$D \qquad VB \qquad = \qquad I \qquad (3.3\text{-}5)$$

$$\begin{bmatrix} D_{xa} & D_{ya} & D_{za} \\ D_{xb} & D_{yb} & D_{zb} \\ D_{xc} & D_{yc} & D_{zc} \end{bmatrix} \begin{bmatrix} VB_X(t_1) & VB_X(t_2) & VB_X(t_3) \\ VB_Y(t_1) & VB_Y(t_2) & VB_Y(t_3) \\ VB_Z(t_1) & VB_Z(t_2) & VB_Z(t_3) \end{bmatrix} = \begin{bmatrix} I_a(t_1) & I_a(t_2) & I_a(t_3) \\ I_b(t_1) & I_b(t_2) & I_b(t_2) \\ I_c(t_1) & I_c(t_2) & I_c(t_3) \end{bmatrix}$$

It must, however, be remembered that the physical system or the decoupling matrix is not singular. It is the calibration data matrix that can be singular. Although efforts can be made to tune the decoupling matrix as precisely as possible, the decoupling matrix is still far from perfect.

It is not recommended to use the direct calibration of decoupling matrix for systems with three or more currents due to the risk of non-Maxwell-Amperes law-based decoupling matrix solutions which will work only with balanced system. The direct decoupling requires the least calibration effort and can be used as a preliminary proof of viability of decoupling.

3.3.3 Hybrid calibration

The hybrid calibration technique combines the signal injection and direct calibration to achieve a fine-tuned decoupling matrix. The technique involves the signal injection-based calibration as a first step. This leads to a preliminary coupling matrix which is inverted to get a decoupling matrix. The second step is to use the direct decoupling to fine tune the decoupling

matrix found via signal injection. A term is selected from each of the rows of the decoupling matrix from step one and used in step two to constrain the solution and ensure that it converges to Maxwell-Amperes law-based decoupling matrix as shown in (3.3-6) and (3.3-7).

$$\begin{bmatrix} C_{xa\text{-}si} & C_{xb\text{-}si} & C_{xc\text{-}si} \\ C_{ya\text{-}si} & C_{yb\text{-}si} & C_{yc\text{-}si} \\ C_{za\text{-}si} & C_{zb\text{-}si} & C_{zc\text{-}si} \end{bmatrix}^{-1} = \begin{bmatrix} D_{xa\text{-}si} & D_{ya\text{-}si} & D_{za\text{-}si} \\ D_{xb\text{-}si} & D_{yb\text{-}si} & D_{zb\text{-}si} \\ D_{xc\text{-}si} & D_{yc\text{-}si} & D_{zc\text{-}si} \end{bmatrix} \quad \text{Decoupling matrix from signal injection} \quad (3.3\text{-}6)$$

$$\begin{bmatrix} I_a(t_1) \\ I_b(t_1) \\ I_c(t_1) \end{bmatrix} = \begin{bmatrix} D_{xa\text{-}si} & D_{ya} & D_{za} \\ D_{xb\text{-}si} & D_{yb} & D_{zb} \\ D_{xc\text{-}si} & D_{yc} & D_{zc} \end{bmatrix} \begin{bmatrix} VB_x(t_1) \\ VB_y(t_1) \\ VB_z(t_1) \end{bmatrix}$$

$$\begin{bmatrix} I_a(t_2) \\ I_b(t_2) \\ I_c(t_2) \end{bmatrix} = \begin{bmatrix} D_{xa\text{-}si} & D_{ya} & D_{za} \\ D_{xb\text{-}si} & D_{yb} & D_{zb} \\ D_{xc\text{-}si} & D_{yc} & D_{zc} \end{bmatrix} \begin{bmatrix} VB_x(t_2) \\ VB_y(t_2) \\ VB_z(t_2) \end{bmatrix} \quad \text{Decoupling terms solved again} \quad (3.3\text{-}7)$$

In the direct calibration step, only two terms are solved for in each row. This ensures that there is only one set of solution for the decoupling terms which is also the Maxwell-Amperes law-based solution. If data is collected with a high sampling rate or for longer time period, the six elements in the decoupling matrix can be solved over and over to reduce the impact of noise. This technique also helps to nullify the very small phase lags that might be present in the PFD signals when a single current is injected in step one. Overall, the hybrid technique gives the best decoupling matrix.

3.4 Characteristics of Coupling Matrix

3.4.1 Relative Positions of PFD and Currents

It must also be noted that the decoupling matrix is calibrated while assuming that the relative position of the currents and PFDs will stay constant. Changes in the relative position can also cause significant errors in the decoupling matrix, hence the relative position of current and PFDs must be kept constant for sensing setup.

3.4.2 Inversion, Conditioning and Scaling of Coupling

Coupling and decoupling matrices should also be tested using an inversion test. The physics of the Maxwell-Ampere's law and decoupling dictates that coupling matrix needs to be invertible for decoupling magnetic fields. In [20], there is a detailed discussion of the invertibility of the matrix and positioning within the FBW regions for 1-D PFDs.

A more practical criteria for evaluating the viability of decoupling is its condition number. The condition number is a metric that quantifies the error prone nature of the matrix inversion. A coupling or decoupling matrix with a low condition number is good for inversion and current decoupling. If the condition number is high, the system is prone to calibration error, noise and is referred to as ill-conditioned.

The linear algebra basis of condition number is the singular value decomposition (SVD). The generalized SVD of the coupling matrix is shown in (3.4-1).

$$\mathbf{C}\,[\mathrm{NxM}] = \mathbf{U}\,[\mathrm{NxN}]\,\mathbf{\Sigma}[\mathrm{NxM}]\,\mathbf{V}^{\mathbf{T}}[\mathrm{MxM}] \tag{3.4-1}$$

The coupling matrix, **C**, can be broken down into **U** and **V** matrices which are the basis of the space spanned by columns and row of C respectively. The **Σ** matrix contains the singular values of the **C** matrix. The singular values are square root of the eigen values of the square matrix $\mathbf{C}^{\mathbf{T}}\mathbf{C}$. The singular values are non-negative numbers that form the diagonal of Σ in a descending order.

The condition number is the ratio of the largest singular value to smallest singular value as shown in (3.4-2).

$$\text{Condition number} = \frac{\sigma_1}{\sigma_p} \tag{3.4-2}$$

If the matrix is singular, the σ_p, the smallest singular value is zero, which leads to a condition number of infinity. This also means that the inverse of **C** does not exist, and **C** is not full rank. The SVD-based method of writing the inverse of **C** which is the decoupling matrix is shown in (3.4-3).

$$\text{Decoupling matrix} = \mathbf{C}^{-1} = \sum_{i=1 \text{ to } p} \left(\frac{1}{\sigma_i} v_i u_i^T\right) \tag{3.4-3}$$

The key point to note is that the decoupling matrix is dependent upon the inverse of singular values. The closer the singular value is to zero, the larger and more unstable the decoupling terms become. This also means that any noise or other errors in the PFD outputs will be exaggerated into large errors when they go through the decoupling.

The condition number is a very important characteristic of the coupling matrix and needs to be as close to unity as possible. Physically, a condition number close to unity represents unique information in PFD outputs, whereas a high condition number means that the information in the PFD outputs is repeated.

To elaborate the concept of condition in a decoupling, the bent three conductor system from sec. 3.2.3 is analyzed. The Fig. 3.4-1 shows three PFD locations labelled 1, 2 and 3. The figure also shows a semi-transparent symmetry plane which lies at 45 deg between the 90 deg wire bend. The system is solved in FEA and the coupling matrix is calibrated for each of the PFD locations.

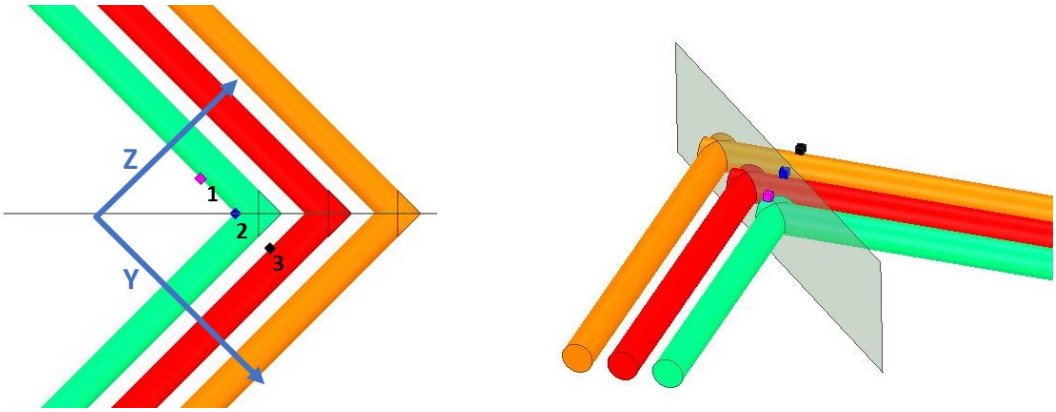

Fig. 3.4-1: Three bent parallel conductors for 3-D decoupling with 3-D PFDs close to the bend

As shown, in sec. 3.2.3, the magnetic field in this system is inherently 3-D and can be decoupled. However, the quality of decoupling is dependent upon the conditioning of the system. From the perspective of the 2-D PFD, which lies on the symmetry plane, the Y and Z magnetic fields from the conductors are symmetrically and equal. The PFD cannot distinguish between them. This leads to bad conditioning (condition number > 3100) in decoupling entirely due to the positioning of the 3-D PFD. Any PFD which lies along this plane of symmetry will have this issue. Fig. 3.4-2 shows the PFD 2 output in response to a three-phase current. It can be seen that the Y and Z outputs of the PFD are equal, albeit with direction inversion. This shows that the Y and Z PFD outputs have identical information.

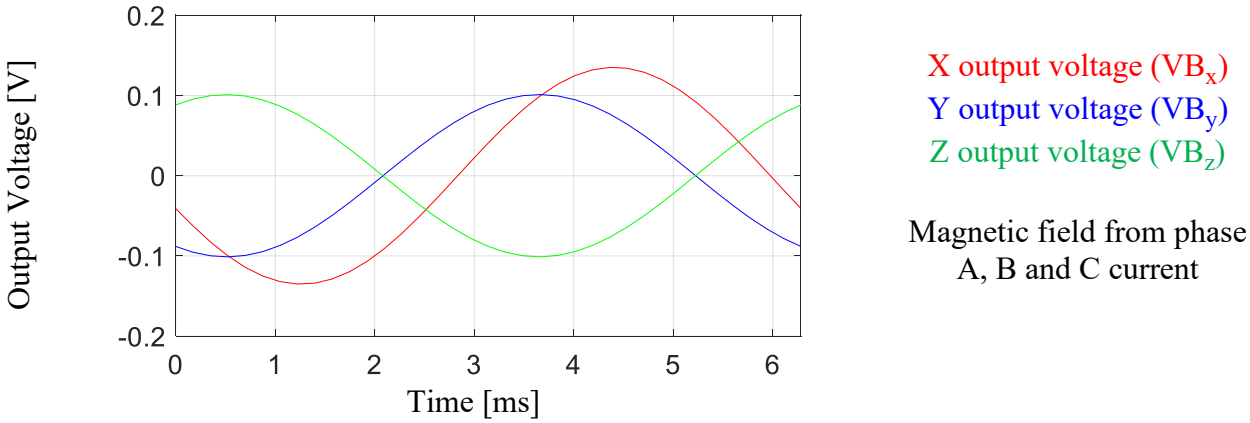

Fig. 3.4-2: X, Y and Z output voltage of the 3-D PFD 2 from Fig. 3.4-1.

PFD 1 and PFD 3 on the other hand are away from the symmetry plane and therefore have better conditioning. The PFD 3 has a position which is away from the symmetry plane. It can also be noticed in Fig. 3.4-1 that PFD 3 will detect a uniquely cross-coupled field in all three directions. This leads to a decent condition number of 27. Fig. 3.4-3 shows that X, Y and Z outputs of the 3-D PFD 3 each have a different amplitude and phase which represents unique information in each of them.

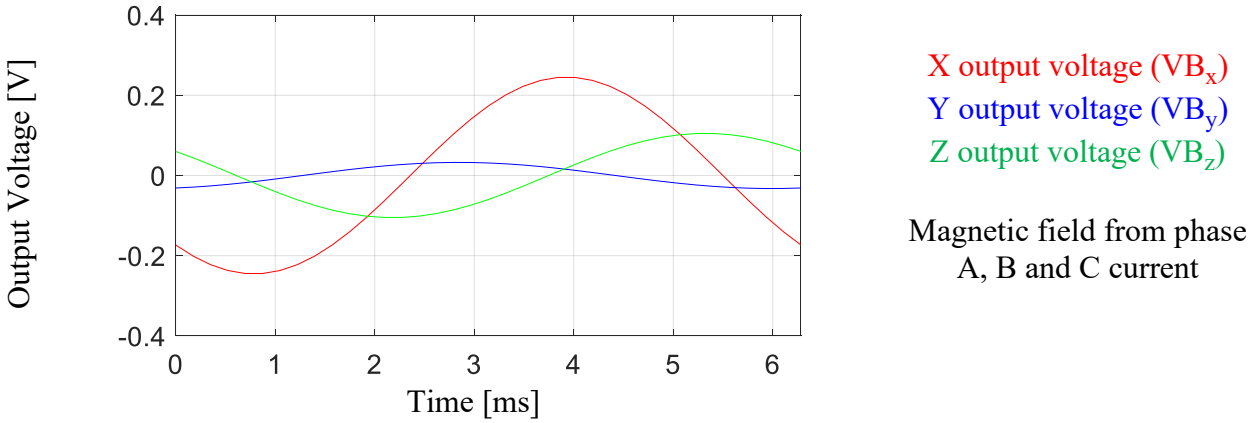

Fig. 3.4-3: X, Y and Z output voltage of the 3-D PFD 3 from Fig. 3.4-1.

PFD 1 on the other hand has a condition number of 169, which is much better than PFD 2's condition number of above 3100. This condition number is not ideal, however, can be used based upon other constrains in the system.

Another important characteristic of the decoupling matrix is the scaling. If the terms in the decoupling matrix are very large, in addition to scaling the actual PFD outputs they will also scale the noise and any other errors superimposed upon the PFD outputs. The smaller decoupling terms ensure that noise and other errors found in the PFD outputs are not amplified via decoupling.

3.5 Summarizing Remarks

A concise summary of the chapter is available at its beginning. The conclusions and contributions for this chapter are available in the last chapter.

This chapter develops the methodology to decouple the magnetic fields from nearby currents which cross-couple linearly in a 3-D space. Independent currents are decoupled from the multi-dimensional cross-coupled fields using Ampere's Law model and the geometric relationship of the currents and the PFD. It is shown via analytical and FEA simulation that sensing the 2-D and 3-D spatial magnetic fields reduces the number of PFDs required for sensing currents by utilizing the degrees of freedom associated with the magnetic field in different dimensions.

This chapter also studies the vulnerability of 3-D field decoupling to having a singularity if the vector field is planar. The singular cases of decoupling have a field in one dimension, which is a linear combination of fields in the other orthogonal dimensions. Arranging the currents appropriately can generate 3-D fields with unique information in each dimension which can be decoupled using the 3-D decoupling methodology developed in this chapter.

The practical considerations of multi-dimensional field decoupling are discussed in detail in this chapter. Two calibration techniques for coupling matrices used in literature are evaluated and a hybrid approach of the two is proposed. Furthermore, the condition numbers of the coupling matrix associated with the PFD locations is described as measure of propagation of uncertainty in field decoupling sensing.

Chapter 4 Three-Phase Current Sensing in Busbars and Cables using Multi-Dimensional Field Decoupling

This chapter demonstrates the multi-dimensional field decoupling by sensing three-phase currents in the convectional conductors. A detailed steady state and transient evaluation of GMR PFD used for the current sensing is presented. The multi-dimensional GMR PFD is positioned in regions of adequate FBW and then the 2-D or 3-D field decoupling methodology is used to decouple the cross-coupled vector field into the three-phase currents. Results are shown for the three-phase current sensing in straight cables with 2-D PFDs and in bent cables and busbars with a 3-D PFD.

The main purpose of this chapter is to experimentally evaluate the multi-dimensional field decoupling methods in real systems.

Elements of this chapter are also documented in [116].

4.1 2-D and 3-D GMR PFD

4.1.1 Fabricated 2-D and 3-D GMR PFD

As described in chapter 1, monolithic multi-dimensional PFDs are still under research and are not developed enough for current sensing. For this work, a 2-D PFD is fabricated with two 1-D GMR PFDs (GF705, same as the one in literature chapter 1) positioned orthogonal to each other. The fabricated 2-D PFD consists of two PFDs with one sensitive to magnetic field in the X-direction and the other sensitive to magnetic field in the Y-direction. These two GMR PFDs are placed on opposite sides of the printed circuit boards (PCB) with a perfect overlap. The thickness of the PCB is 1.6 mm in the Z axis. Fig. 4.1-1 shows the fabricated 2-D PFD.

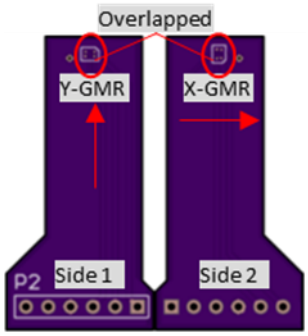

Fabricated 2-D GMR PFD PCB layout

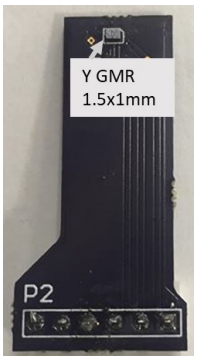

Soldered GMR flip chip the PCB

Fig. 4.1-1: Fabricated 2-D GMR PFD PCB

To extend the 2-D PFD to a 3-D PFD, a Z-direction GMR PFD on a separate PCB is positioned within 5mm of the 2-D GMR using plastic fixtures. This version 1 fabricated 3-D GMR PFD is used in experiments in this chapter. Later on, two connected PCBs were engineered to the have X, Y and, Z GMR PFD within a couple millimeters of each other. The fabricated 3-D GMR PFD is shown Fig. 4.1-2. This version 2 fabricated 3-D GMR PFD is used in experiments in later chapters.

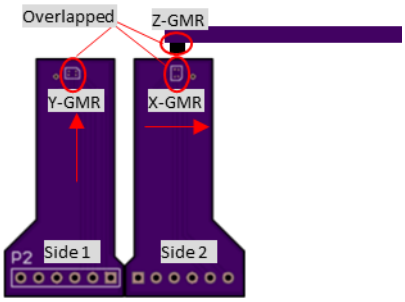

fabricated 3-D GMR PCB layout in Altium version 1

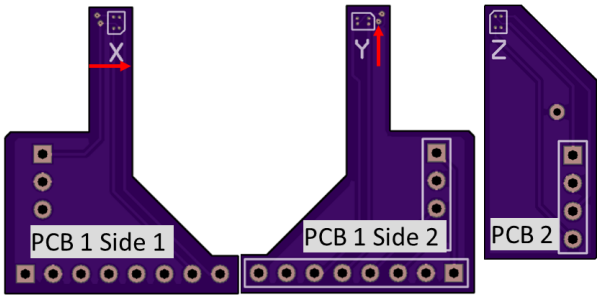

Fabricated 3-D GMR on connected PCBs in Altium version 2

Fig. 4.1-2: Fabricated 3-D GMR PFD PCB (pictures taken at different angle)

This fabricated 2-D and 3-D setup is for research purposes only, since 2-D MR PFDs available in the commercial market lack the properties for accurate current sensing. Furthermore, there is no appropriate commercially available 3-D MR PFD. A review of 2-D and 3-D MR PFDs is presented in chapter 1. However, with modern fabrication techniques, it is entirely possible to fabricate the 2-D and 3-D MR PFDs. One purpose of this work is to motivate the production of high accuracy 2-D and 3-D MR PFDs. The findings of previous work have motivated the development of MR PFDs for current sensing applications, so the trend is expected to continue.

4.1.2 MR PFD excitation and signal conditioning

The PFD should be placed at an easily accessible location on the PCB. The PFD must be positioned such that it can be close to the conductor in power electronics without any physical hindrance. To allow greater flexibility with PFD positioning, the PFD is on one PCB and the signal conditioning and excitation are on a second PCB. The two PCBs can be connected via generic pin connectors. This is for research purposes only and eventually, for commercial purposes, the PFD excitation and conditioning can all be in a single IC.

Each individual GMR in the 3-D GMR PFD has its own outputs leading to the need for signal conditioning for each independently. The voltage inputs, as well as, the ground connections of the Wheatstone bridges of the PFD are connected on the same bus.

The simplified excitation and signal conditioning schematic is shown in Fig. 4.1-3 and the PCBs are shown in Fig. 4.1-4. The PFD on the PCB is excited using a 5V supply (LT1121IST) in version 2 and using a potential divider in version 1. The X, Y and Z outputs of the PFD are passed through an instrumentational amplifier (AD8421ARZ), tuned to a gain of close to 100V/V. The instrumentation amplifier is powered using positive (MC78M15ACDTRKG) and negative voltage regulators (MC79M15CDTG). There are various decoupling capacitors to filter the power

voltages. The gain and low pass filter of the output can be tuned based upon the application. Space on the PCB is saved by using the vertical BNC (51K101-400A5) connector as well as using a voltage supply instead of a current supply. The PCB also has an 8-pin header connector for board-to-board connection with the 3-D PFD PCB. It must also be noted that this PCB design is based on the designs presented in [65].

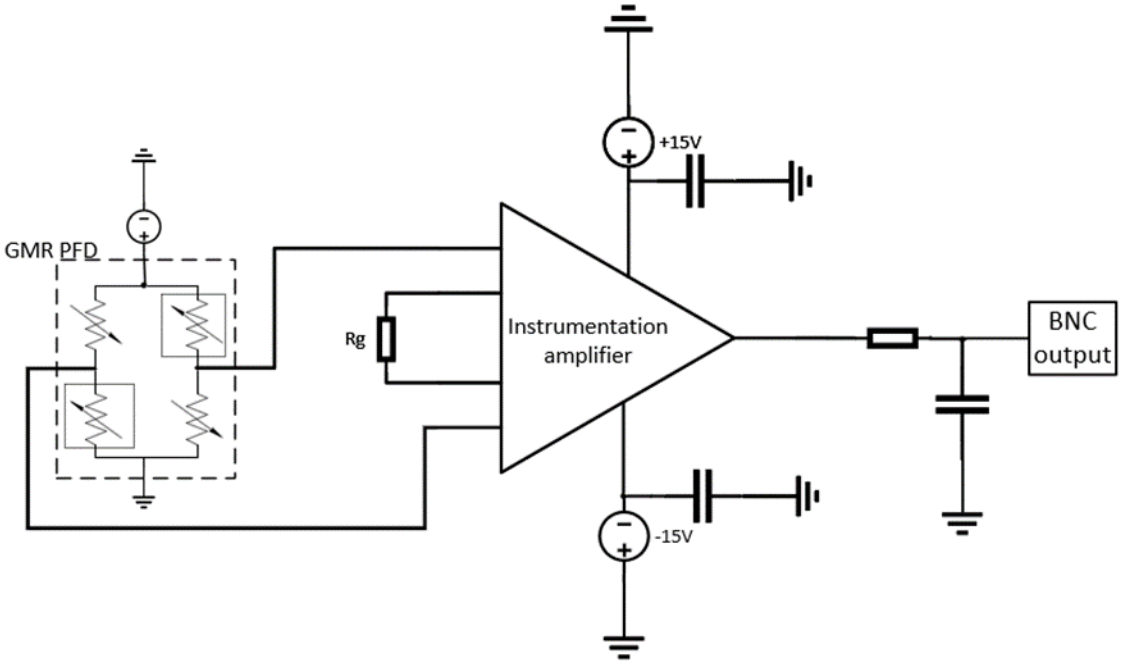

Fig. 4.1-3: Schematic of signal conditioning of X-GMR PFD output

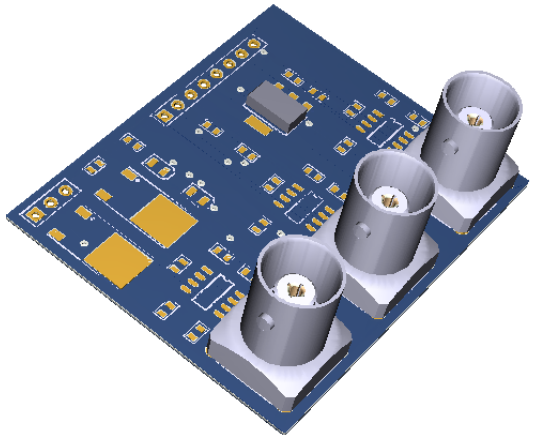

Fig. 4.1-4: Signal conditioning and source excitation PCB

4.1.3 Evaluation of GMR PFD

The following evaluation will focus on 1-dimension of the GMR PFD assuming that second and third dimension have similar performance.

Fig. 4.1-5 shows the characteristic curve of the GMR PFD. A specialized test set up explained in [64] is used. The curve is symmetric about the zero flux density making the GMR unipolar. As described in the chapter 1, the bias field can be used to move the zero point to the middle of the linear region to make the GMR PFD bipolar.

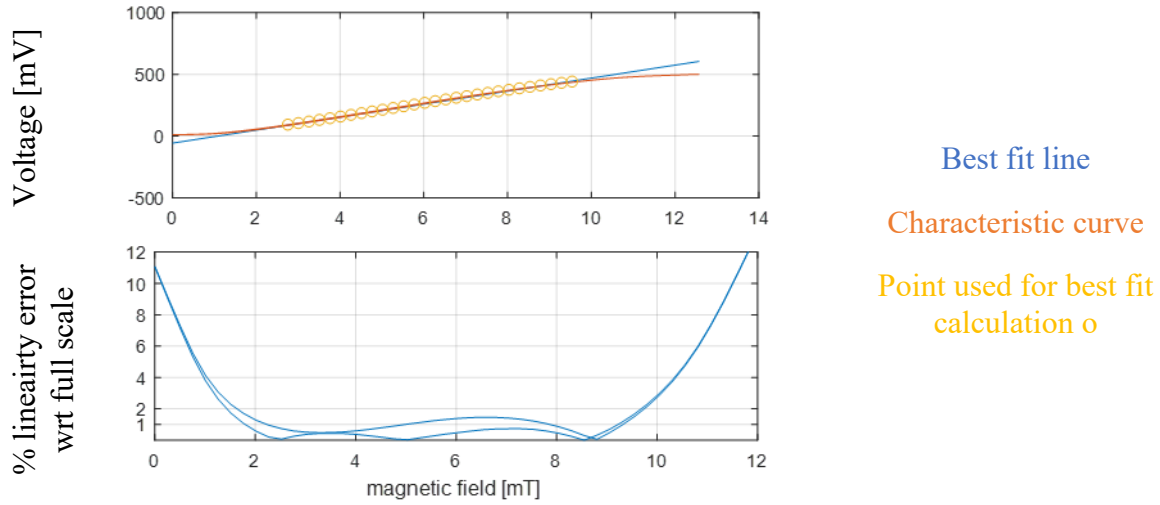

Fig. 4.1-5: GF705 characteristic curve with best fit line and linearity error

The GMR PFD has very low hysteresis which is hard to see in the output voltage vs field characteristic curve but it does become visible in the linearity error plot as a gap due to different upward and downward trajectory. The linearity error reduces if the range of the magnetic field sensed is a smaller subset of the total range. The linearity and hysteresis errors are close to 1.5% for the full scale range between 2 and 8.0 mT i.e. ±3 mT about 5.0mT virtual zero point. In this work, the range of field for current sensing is ± 0.1mT due to which it is safe to assume that non-linearity errors are lower than 1.5 % but they do exist in PFD as well as the rest of the sensing circuit much like any other system. The virtual zero point is attained using a bias field from a

permanent magnet kept in the vicinity of the PFD. Due to the smaller range of field required for current sensing, the bias point can be much lower than 5mT.

The baseline frequency response function of the GMR PFD-based current sensing is evaluated by passing an AC current through a straight circular cross-section wire with its frequency increased from 10 Hz to 100 kHz. The results of GMR PFD output and actual current are analyzed using a Venable frequency response analyzer. Fig. 4.1-6 shows the FRF whose magnitude stays within ±3% until 100kHz.

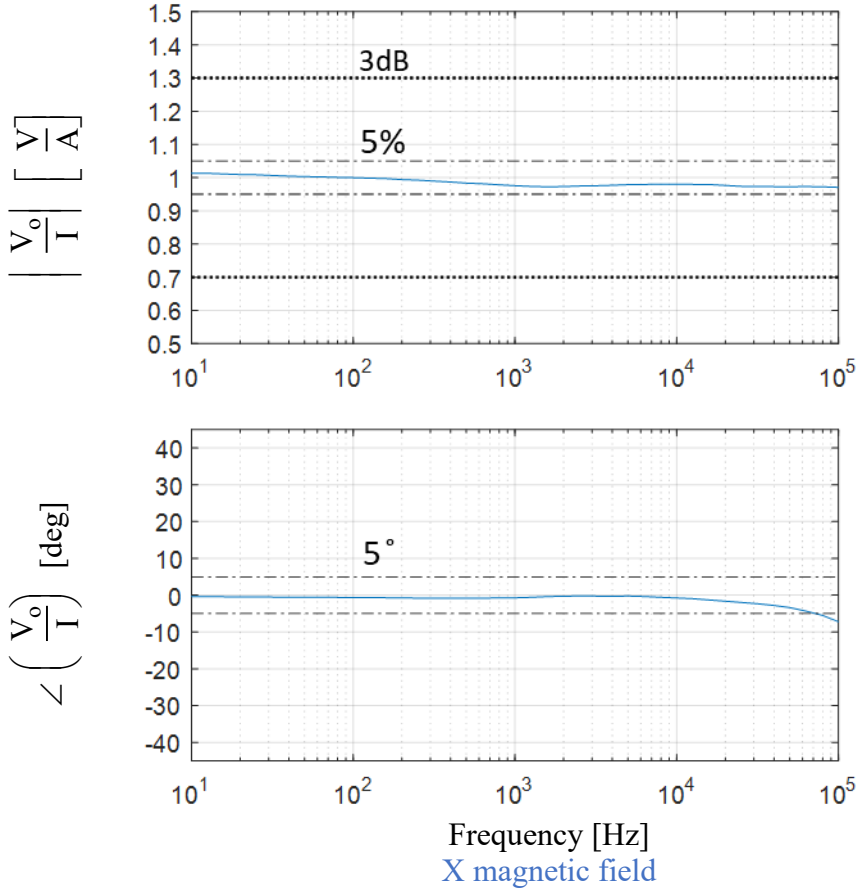

Fig. 4.1-6: Experimental FRF of GMR PFD output with respect to actual current normalized to 100 Hz value

There are 5% and 3dB threshold lines drawn on the FRF gain plot. The ±5% gain error refers to 1.05 and 0.95 times the normalized gain. The 3dB on the non-logarithmic Y axis is not

symmetric because +3dB refers 1.4 times and -3dB refers to 0.7 times the normalized gained. In this work, +3dB is also referred to as 1.3 times the normalized gain to have symmetry and follow the convention set in literature [7], [115]. The GMR PFD FRF typically has less than 1% non-linear errors due to hysteresis and characteristic curve non-linearity. The error would disappear due to normalization if the amplitude of the current, i.e. the field sensed by the GMR PFD was constant for all frequencies. However, the AC current source used falls sharply after 20kHz, and is reduces to half the current amplitude by 100kHz. Due to a steady current output for frequencies between 10 Hz and 20kHz, non-linearity error in the FRF below 20kHz are expected to be less than 0.5%. This is true for experimental FRFs throughout this work.

The step response of the GMR PFD is shown in Fig. 4.1-7. The power amplifier used to produce the square current also a has limited bandwidth due to which its current has a rise time of 5μs. However, it is clear that GMR PFD and reference Lecroy probe have a very close match showing that GMR PFD has a fast reaction time.

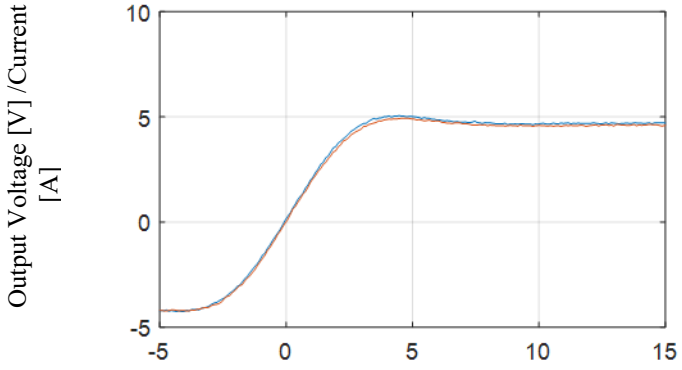

Current Freq =100Hz square wave from HP signal generator/Power amplifier
Lecroy Oscilloscope data collection at 10M samples/s
Current Reference GMR output

Fig. 4.1-7: Step response of GMR PFD-based current sensing

Fig. 4.1-8 shows the triangle current response of GMR mimicked using a 5kHz wave. Again, the GMR PFD and reference probe have a very similar response.

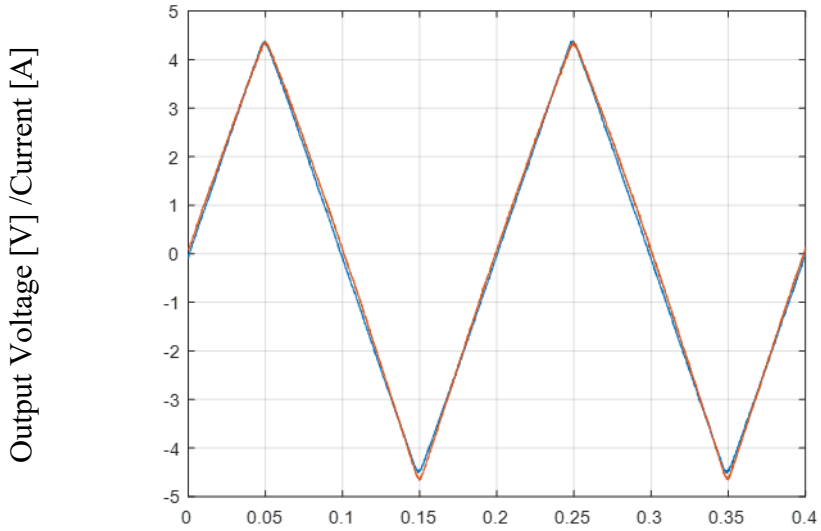

Current Freq =5 kHz duty ratio = 50% triangular wave from /Power amplifier
Lecroy Oscilloscope data collection at 10M samples/s
Current Reference GMR output

Fig. 4.1-8: Triangle response of GMR PFD-based current sensing

4.2 Three-Phase Current Sensing in Straight Cables Using two 2-D PFDs

Three-phase cable is a standard conducting structure used in the three-phase AC drives. Sensing the three-phase current in such cables is of immense importance and can be done using an array of 2-D PFD inside an IC. As described in chapter 3, a straight cable produces 2-D fields and using 3-D decoupling results in singularity. Hence, a 2-D MR PFD array is used to sense and decouple the phase currents.

The analysis of sensing three-phase currents in straight cables begins with modelling a scaled version of the cable in FEA and finding flux densities and 2-D FBW regions. Fig. 4.2-1 shows the

three core cable model and the SO16 IC which can contain two 2-D PFDs and signal conditioning. The placement of the IC should follow the field analysis results.

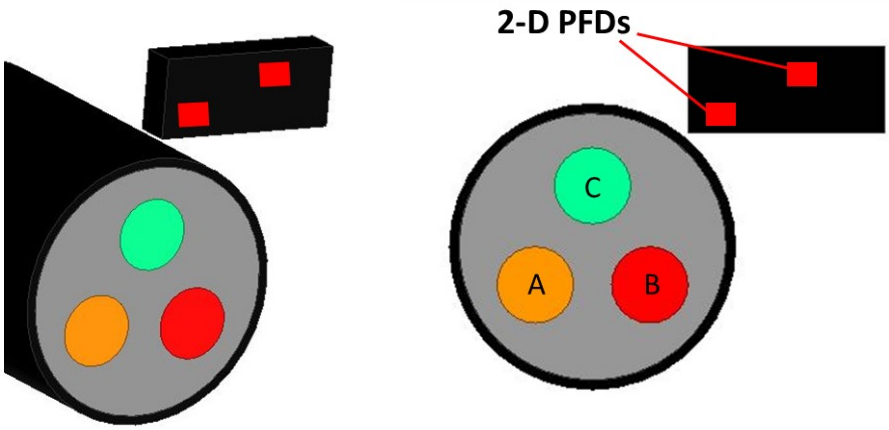

Fig. 4.2-1: Three-phase cable with So16 IC containing 2-D PFDs

It is important to locate the 2-D PFD in regions of high SNR and 2-D FBW. The flux densities are shown in Fig. 4.2-2. The three-phase cable cannot be wrapped around the core of a hall current sensor or current transformer because the sum of the balanced three-phase currents is zero, causing the resulting field in the core to likewise be zero. However, there is a net magnetic field around the cable because the three-phase cable imposes a physical distance between the conductors and the point where the magnetic field is being measured. This net magnetic field is generally very small, but it can be detected using a MR PFD because of its high sensitivity. If the current is larger, the cables become larger too and the PFD mounted on the outside of the insulation is naturally pushed further away from the conductors. As a result, for currents even in the range of hundreds of Amperes, the sensed magnetic field is expected to stay within a few milliTesla which is the under the limit of the linear range of many MR PFDs as described in [64].

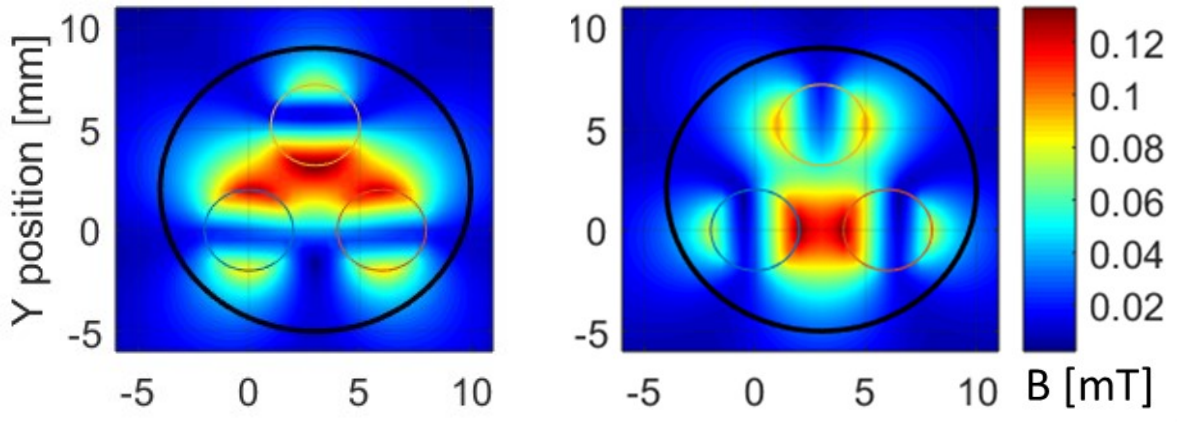

Magnitude of X magnetic flux density Magnitude of Y magnetic flux density

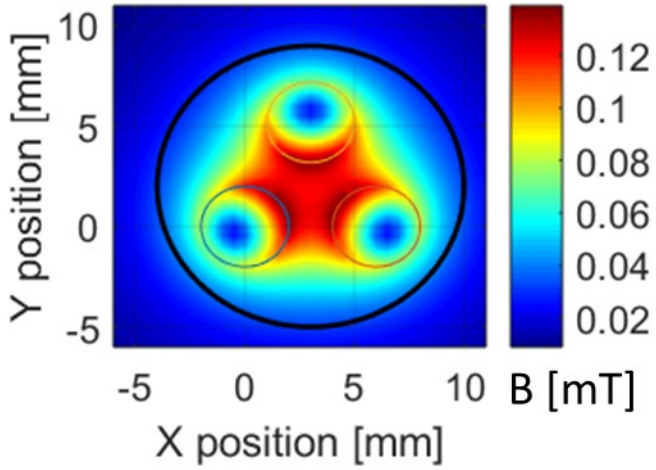

Magnitude of magnetic flux density

Fig. 4.2-2: Magnitudes of magnetic flux density around the cable at 0.1Hz 1A three-phase current injection

The FBW is shown in Fig. 4.2-3 to identify regions appropriate for the 2-D PFD placement. The 2-D metric for only phase B as well as all three-phases in a balanced system is shown. The method to compute the three-phase FEA is explained in detail in chapter 2. There are regions available around 1.5 kHz on the top right of the cable where PFDs are placed.

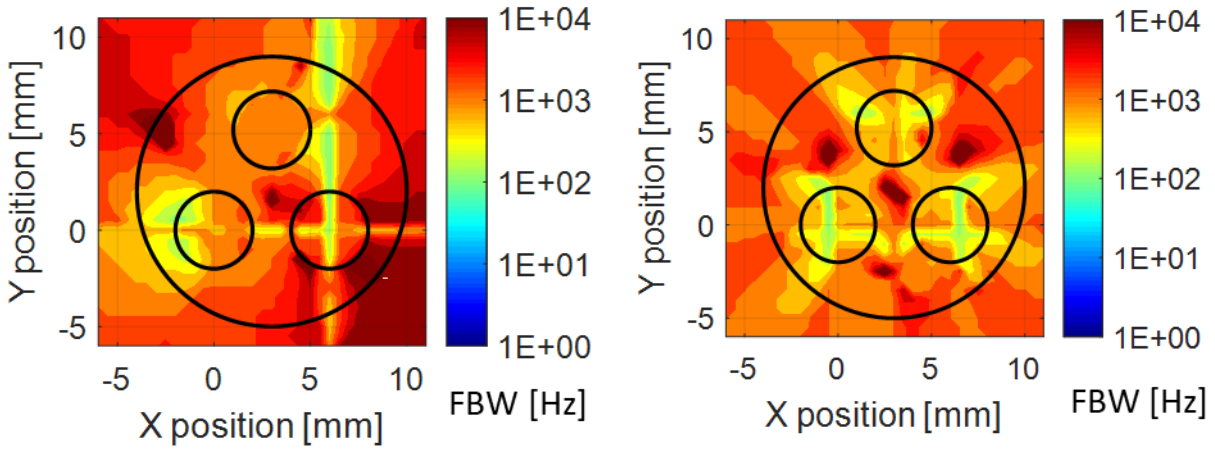

Fig. 4.2-3: 2-D 5% FBWs for three-phase cable with single-phase B current injection (left) and with three-phase current (right)

The Phase B FBW is only shown here as a representative for other phases as well. The cuboidal region of FEA solution might introduce errors close to edges. The idea, however, remains that individual phase has immense areas of sufficient FBW. The single-phase FBW should be used as the first metric to find locations appropriate for PFD placement. These locations should be further fine-tuned using the three-phase FBW.

It is important to understand that a single current and three-phase current cases will have different field outlook. At any given point of time, for a balanced three-phase system currents add to zero. This leads to the field being cancelled out or added together at each point, thereby changing the FBW for single-phase FEA to three-phase FEA. This is explained in greater detail in in detail in chapter 2. The 2-D PFD should be placed in a region where each of the individual phases as well as the three-phase FEA have high FBW. Since the individual phase FBW is high in most accessible regions, it is safe to use just the three-phase FBW.

Once the bandwidth is confirmed, it is safe to use the 2-D PFD for frequencies up to the bandwidth. The 2-D decoupling at three locations can be model using (4.2-1).

$$\begin{bmatrix} C_{xa1} & C_{xb1} & C_{xc1} & 1 \\ C_{ya1} & C_{yb1} & C_{yc1} & 0 \\ C_{xa2} & C_{xb2} & C_{xc2} & 1 \\ C_{ya2} & C_{yb2} & C_{yc2} & 0 \end{bmatrix} \begin{bmatrix} I_A \\ I_B \\ I_C \\ D_x \end{bmatrix} = \begin{bmatrix} VB_{x1} \\ VB_{y1} \\ VB_{x2} \\ VB_{y2} \end{bmatrix} \quad (4.2\text{-}1)$$

Where $C_{\mathbf{xa1}}$ refers to the coupling term for X-direction field, phase A current and PFD number 1, D_x refers to disturbance in X-direction and VB_{x1} refers to the X-direction output of PFD number 1. It should be noted that due to the availability of four outputs, it is possible to detect three currents and a disturbance. In the model above the X disturbance is used, a similar model could be used for a Y disturbance. The other option which is more practical is to add another detector so that both X and Y disturbances can be decoupled. Disturbance decoupling is discussed in detail in later chapters.

4.2.1 Experimental three-phase straight cable current sensing

In order to test the three-phase current sensing in a straight cable, 14-3 gauge cable is used. This is the wire used in many power cords with three individual wires generally for live, neutral and ground. In this test, these wires were used for phases A, B and C. The three-phase currents are provided by a three-phase power supply with floating ground. The AC power supply has a variable voltage and frequency. The wye-connected resistors are used as a load for the power supply. The straight cable is used to connect the load with the supply. The data for the reference currents and GMR PFDs is recorded using an eight channel Lecroy oscilloscope which also has three-phase current probes. The sampling is AC coupled and is at 500kHz.

The mathematical model for decoupling is shown in (4.2-2) when no disturbance is applied. Only one of the dimensions of the second 2-D PFD is used.

$$\begin{bmatrix} C_{xa1} & C_{xb1} & C_{xc1} \\ C_{ya1} & C_{yb1} & C_{yc1} \\ C_{ya2} & C_{yb2} & C_{yc2} \end{bmatrix} \begin{bmatrix} I_a \\ I_b \\ I_c \end{bmatrix} = \begin{bmatrix} VB_{x1} \\ VB_{y1} \\ VB_{y2} \end{bmatrix} \tag{4.2-2}$$

The decoupling matrix is calibrated using the direct calibration method, despite its flaws, to show the viability of the decoupling method at this stage and prevent the tedious process of injecting the three signals separately. (4.2-3) illustrates the decoupling model. The 200 Hz, 9A pk data is used for calibration and the decoupling matrix is kept constant for all other conditions.

$$\begin{bmatrix} I_a \\ I_b \\ I_c \end{bmatrix} = \begin{bmatrix} D_{xa1} & D_{ya1} & D_{ya2} \\ D_{xb1} & D_{yb1} & D_{yb2} \\ D_{xc1} & D_{yc1} & D_{yc2} \end{bmatrix} \begin{bmatrix} VB_{x1} \\ VB_{y1} \\ VB_{y2} \end{bmatrix} \tag{4.2-3}$$

Fig. 4.2-4 shows the cross-coupled results of the PFD output and the reference currents producing it to display the level of cross-coupling. It is clear that the Y outputs have very similar information leading due to a lack of spatial distance between the currents as well as the two PFDs. The current and PFD signals are recorded with AC coupling on oscilloscope and filtered with a 75 kHz, digital low pass filter.

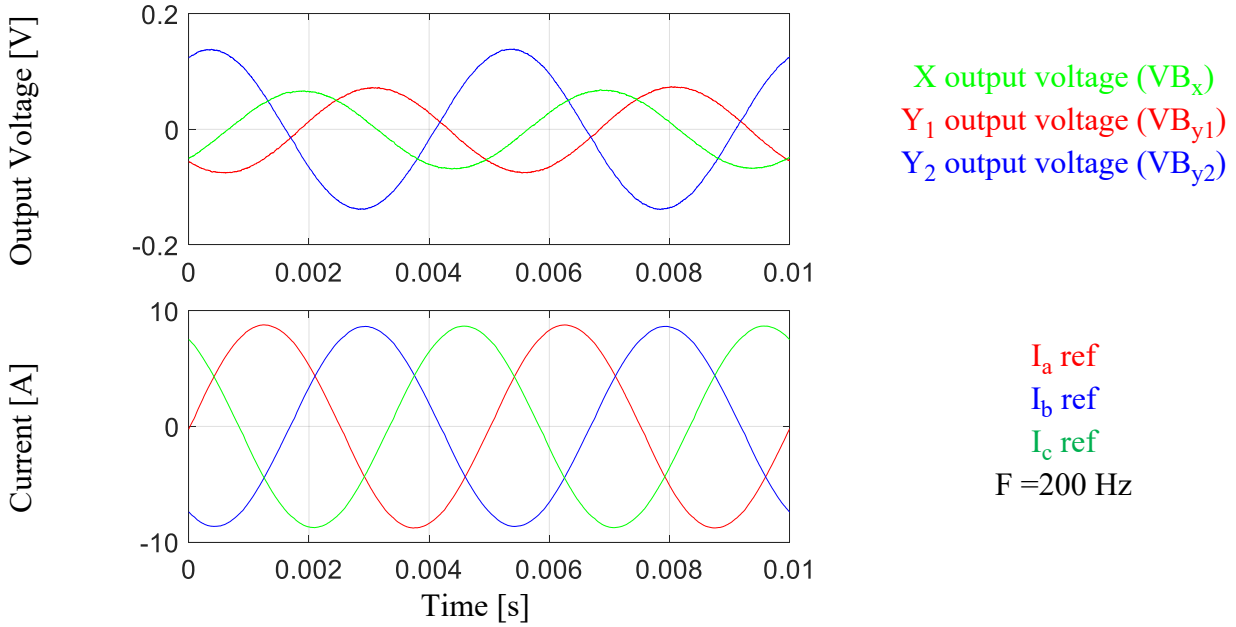

Fig. 4.2-4: X and Y output voltages of the 2-D PFDs due to the three-phase currents in the cable

The results of current sensing at three different frequencies and two different amplitudes are shown in Fig. 4.2-5. The maximum percentage rms error is 2.8% and the maximum instantaneous error in all of the results is at 6.0%. It must be noted that only low current sensing is conducted which compromises the SNR. Another reason for the decoupling error is the close proximity of the two PFD which leads to similar spatial information in the field signals and inaccuracy in the decoupling matrix.

This test is done with 2-D decoupling and direct calibration to show what is possible. In applications that require higher precision, the hybrid method of decoupling is recommended in chapter 3. This method requires more effort in fine-tuning the terms but is more reliable.

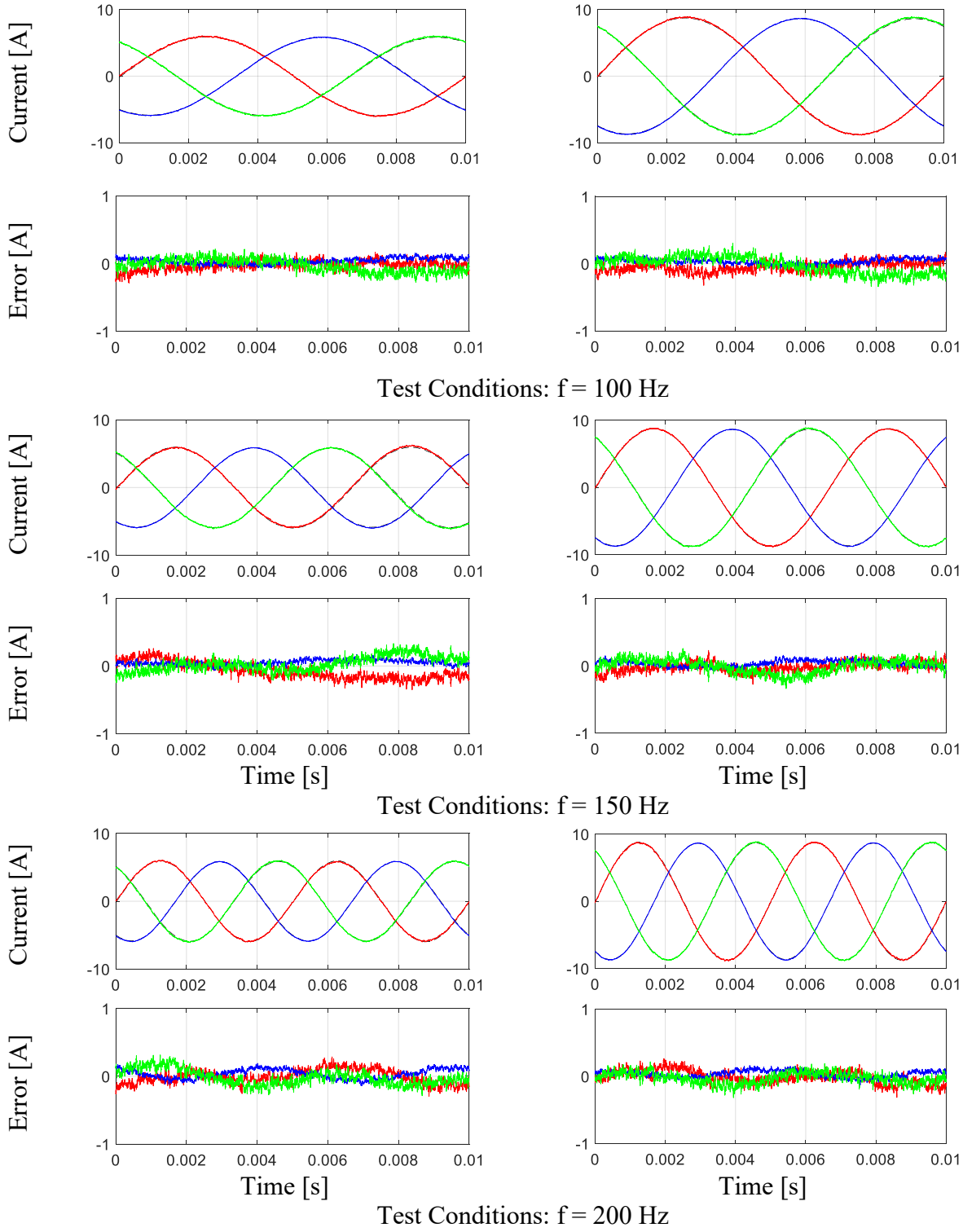

Fig. 4.2-5: Experimental decoupling and sensing of three-phase currents with two 2-D PFD in a straight three-phase cable

4.3 Balanced Three-Phase Current Sensing in Straight Cables Using a 2-D PFD

In many three-phase current sensing applications, only two of the phase currents are measured and the third current is computed using the balanced system assumption. In such a case, a single 2-D PFD is enough to sense two phase and compute the third phase. It should be noted however, that the third phase connection is assumed to be far away from the two phases to avoid cross-coupling from it.

The 2-D Flux density and 5% 2-D FBW of parallel wires is shown in Fig. 4.3-1 and Fig. 4.3-2. For simplicity and available symmetry, the current is passed only in Phase A to show the areas of high FBW. The 2-D PFD should position in the region of high FBW.

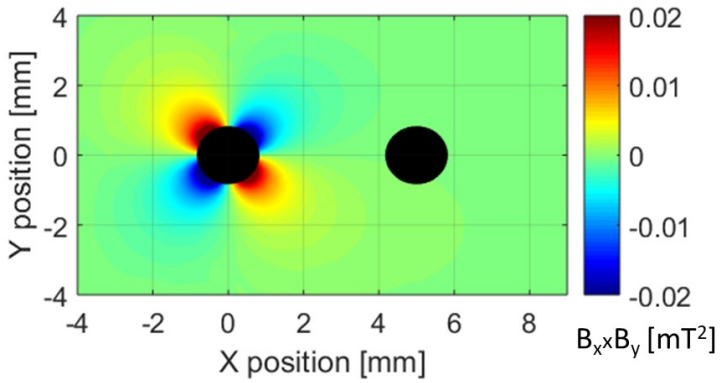

Fig. 4.3-1: 2-D flux density for dual conductor system with 1A quasi-DC current in wire 1

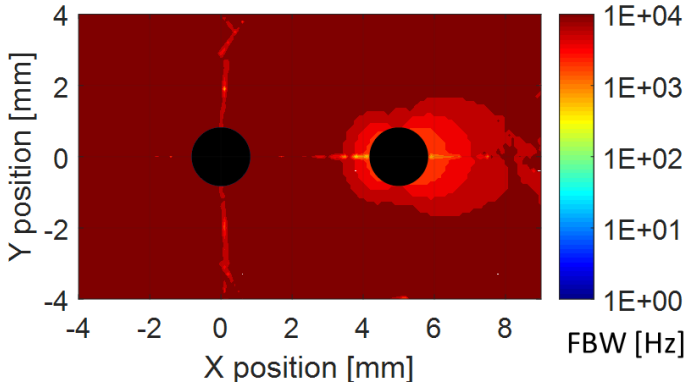

Fig. 4.3-2: 2-D 5% FBW for dual conductor system with current injection in wire 1

4.3.1 Experimental two-phase straight cable current sensing

A 2-D GMR PFD is used to experimentally decouple the two currents. The three-phase power supply with a wye-connected load is used to generate the three-phase currents. The phase C wire is kept at more than hundred times the distance between phase A and phase B to avoid the influence of phase C on current sensing. The rest of the set up remains the same as sec. 4.2.1.

The decoupling matrix is obtained using the direct decoupling matrix calibration which involved solving a system of four algebraic equations for four decoupling terms as shown in (4.3-1). Direct decoupling calibration is very reliable for two current systems.

$$\begin{bmatrix} D_{x1} & D_{y1} \\ D_{x2} & D_{y2} \end{bmatrix}\begin{bmatrix} VB_x(t_1) \\ VB_y(t_1) \end{bmatrix}=\begin{bmatrix} I_1(t_1) \\ I_2(t_1) \end{bmatrix} \& \begin{bmatrix} D_{x1} & D_{y1} \\ D_{x2} & D_{y2} \end{bmatrix}\begin{bmatrix} VB_x(t_2) \\ VB_y(t_2) \end{bmatrix}=\begin{bmatrix} I_1(t_2) \\ I_2(t_2) \end{bmatrix} \qquad (4.3\text{-}1)$$

In this experiment, 150 Hz phase currents are passed for calibration. The PFD output voltages and the reference currents are shown in Fig. 4.3-3 to demonstrate the extent of cross-coupling. The current and PFD signals are recorded with AC coupling on the oscilloscope and filtered with a 75 kHz, digital low pass filter.

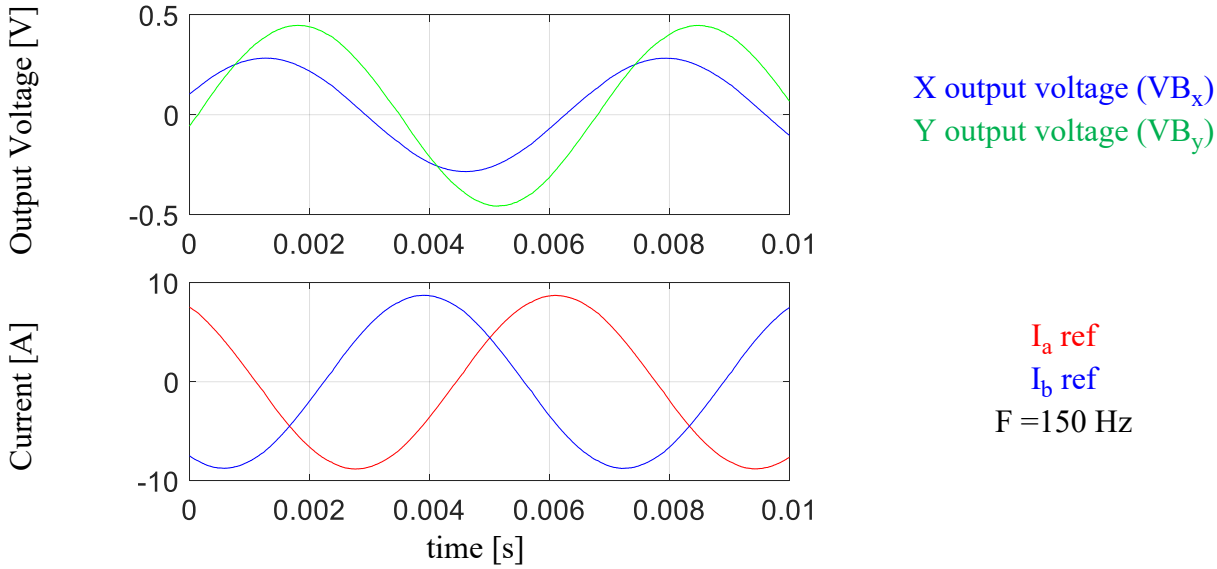

Fig. 4.3-3: X and Y output voltages of the 2-D PFD due to the two phase currents

The results of current sensing at three different frequencies and two different amplitudes are shown in Fig. 4.3-4. The third phase is computed using the balanced system. The maximum current sensing percentage rms error with respect to Lecroy probe is 2.8% and maximum instantaneous error is measured at 5.5%. The decoupling matrix is kept constant throughout the testing. The repeating nature of error shows that there is room for better calibration of decoupling matrix. Additionally, the error can be improved by having a higher SNR, and a more robust experimental setup with positioning stiffness. In chapter 5, the experiment is repeated to get a much lower error.

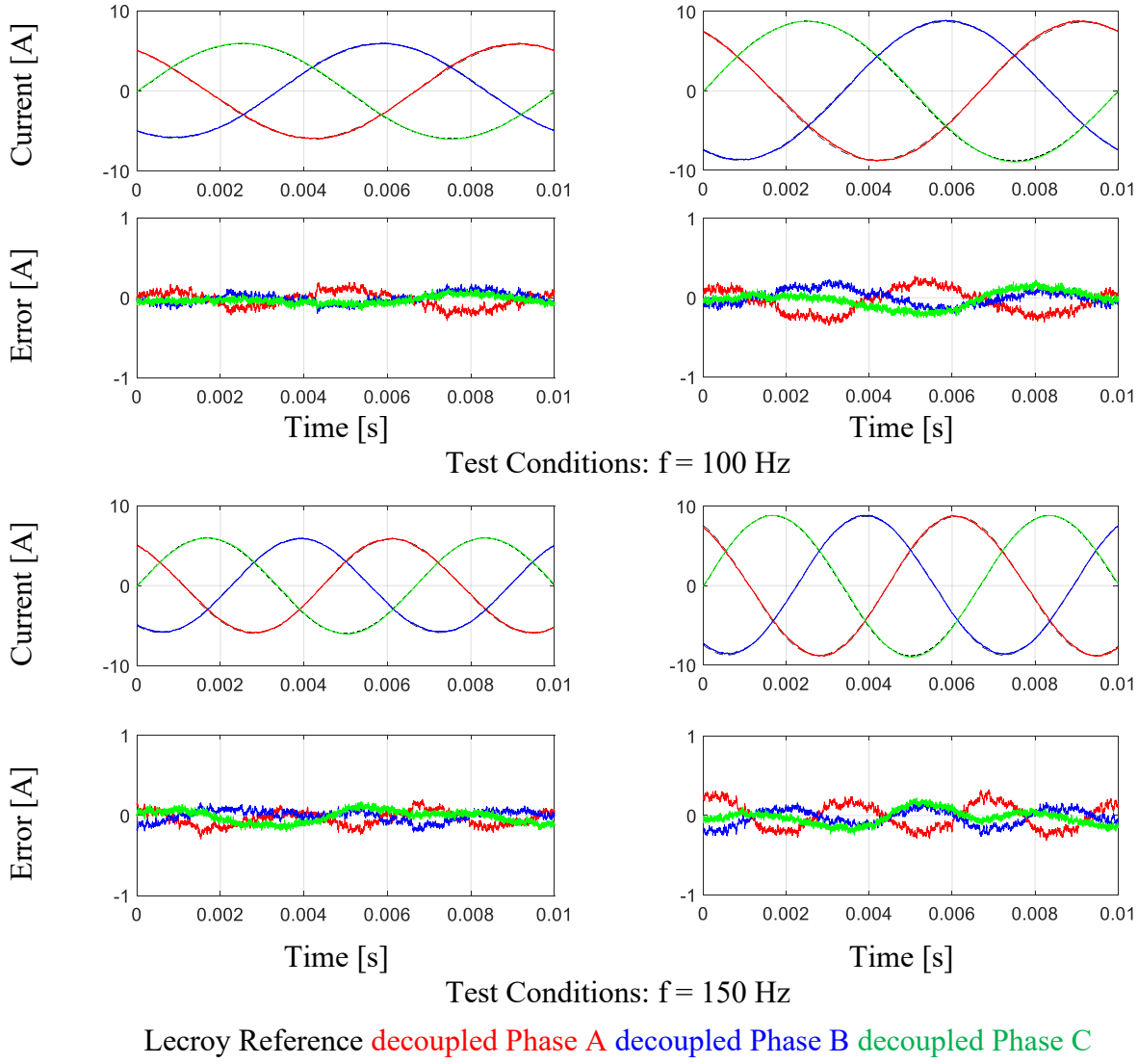

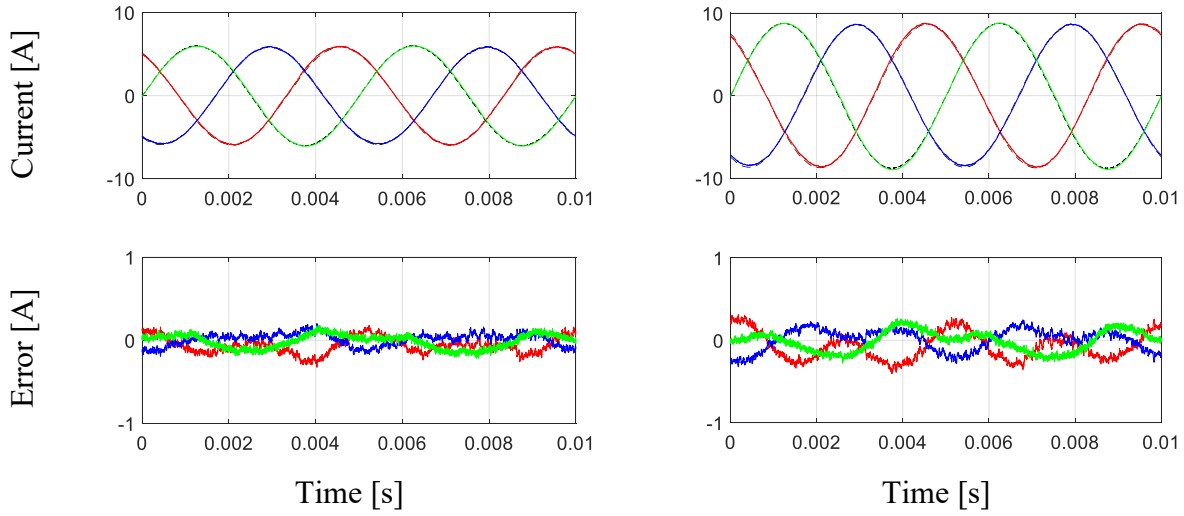

Test Conditions: f = 200 Hz

Lecroy Reference decoupled Phase A decoupled Phase B decoupled Phase C

Fig. 4.3-4: Experimental decoupling and sensing of three-phase currents with a single 2-D PFD in two phase cable

4.4 Three-Phase Current Sensing in Bent Cables Using a 3-D PFD

The three-phase cable is a standard conducting structure used in the three-phase AC drives. Very often, this cable will have a turn or a bent. Such a bent creates a 3-D magnetic field which provides the opportunity to sense three-phase currents using a single 3-D PFD by implementing 3-D decoupling. This decoupling measures all three currents independently.

The radius of curvature of the three-phase cable bends depends upon its thickness and the product architecture. As shown in Fig. 4.4-1, a generic three-phase cable is used in the FEA. The diameter of each core is 4mm, close to a 6-3 cable. The bend is done at a sharp 90 degree. This is unrealistic in real applications however, it is a worst case scenario as the sharp edges increase the skin and proximity effects and cause flat bandwidth degradation.

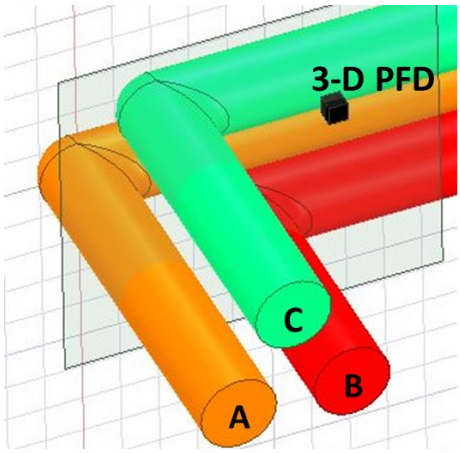

Fig. 4.4-1: Copper core of bent three-phase cable with PFD on the field analysis plane

Fig. 4.4-2 shows the magnitude of the flux density around the three-phase cable on the plane shown in Fig. 4.4-1. The three-phase cable wrapped around a core have zero flux because the sum of the balanced three-phase currents is zero, causing the resulting field in the core to likewise be zero. However, there is a net magnetic field around the cable because the three-phase cable imposes a physical distance between the conductors and the point where the magnetic field is being measured. The bend also helps with the asymmetry. This net magnetic field is generally very small, but it can be detected using a coreless MR PFD because of its high sensitivity

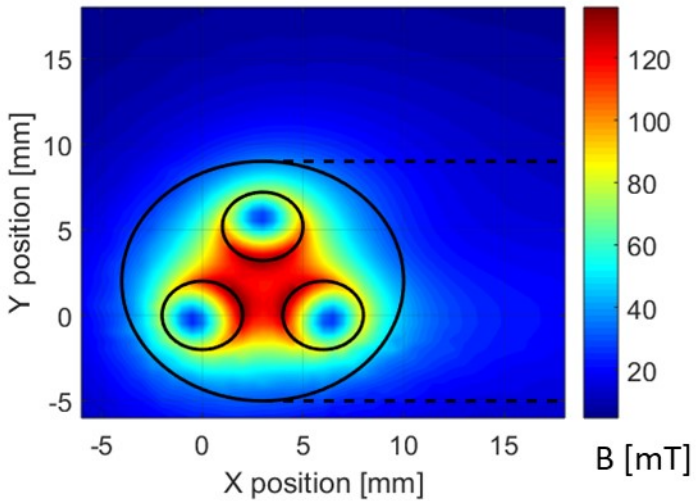

Fig. 4.4-2: Magnitude of the magnetic flux density on the analysis plane around the cable at 0.1Hz 1 A three-phase current injection

The regions of high 3-D FBW are identified in Fig. 4.4-3 by passing three-phase currents through the cable. The figure shows the X-FBW, Y-FBW, Z-FBW as well as the 3-D FBW consisting of the minimum of the three. There are some regions of high 5% FBW represented by darker color close to the top dotted line. This 3-D bandwidth can be used to sense the fundamental currents up to 1.5 kHz.

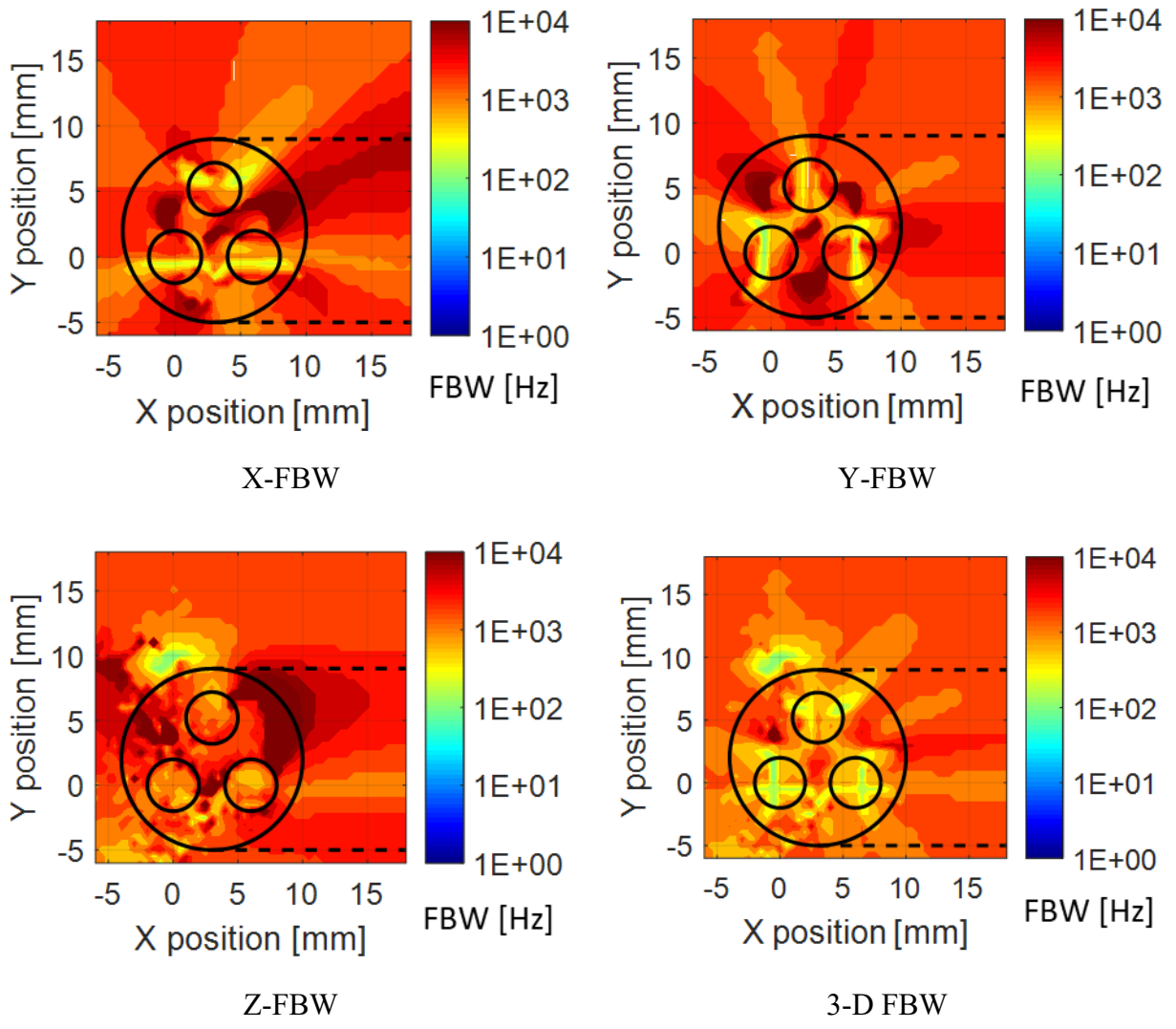

Fig. 4.4-3: Individual direction and 3-D 5% FBW for a bent three-phase cable with three-phase current injection

4.4.1 Experimental three-phase bent cable current sensing

The experimental setup for the conducting wires is the same as sec. 4.2.1 with a 14-3 gauge power cord used as a three-phase cable. The wire is bent and fixed to a plastic fixture as shown in Fig. 4.4-4.

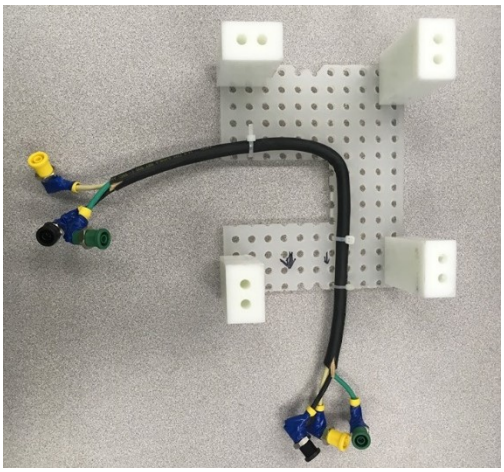

Fig. 4.4-4: Experimental setup of current sensing in three-phase cable

The current sensing of the single 3-D PFD system is tested by supplying the currents to the load from the three-phase power supply at different frequencies and magnitudes. The 3-D GMR PFD is positioned close to the bent in a region of high FBW.

The first step in sensing the three-phase currents using a single 3-D PFD is to calibrate the decoupling matrix. In this experiment, the hybrid calibration method is used. As shown in (4.4-1) 3-D decoupling, the number of terms in the matrix increases due to which the process is more complex than in 2-D.

$$\begin{bmatrix} I_a \\ I_b \\ I_c \end{bmatrix} = \begin{bmatrix} D_{xa} & D_{ya} & D_{za} \\ D_{xb} & D_{yb} & D_{zb} \\ D_{xc} & D_{yc} & D_{zc} \end{bmatrix} \begin{bmatrix} VB_x \\ VB_y \\ VB_z \end{bmatrix} \tag{4.4-1}$$

The outputs of the PFD captured with AC coupling of oscilloscope to filter the DC bias of GMR PFD are filtered using a 75 kHz, digital low pass filter. Fig. 4.4-5 shows the results of X, Y

and Z outputs of the 3-D PFD to represent the high cross-coupling of phase fields and need for current sensing. The data shown is at 150 Hz current and used for calibrating the decoupling matrix.

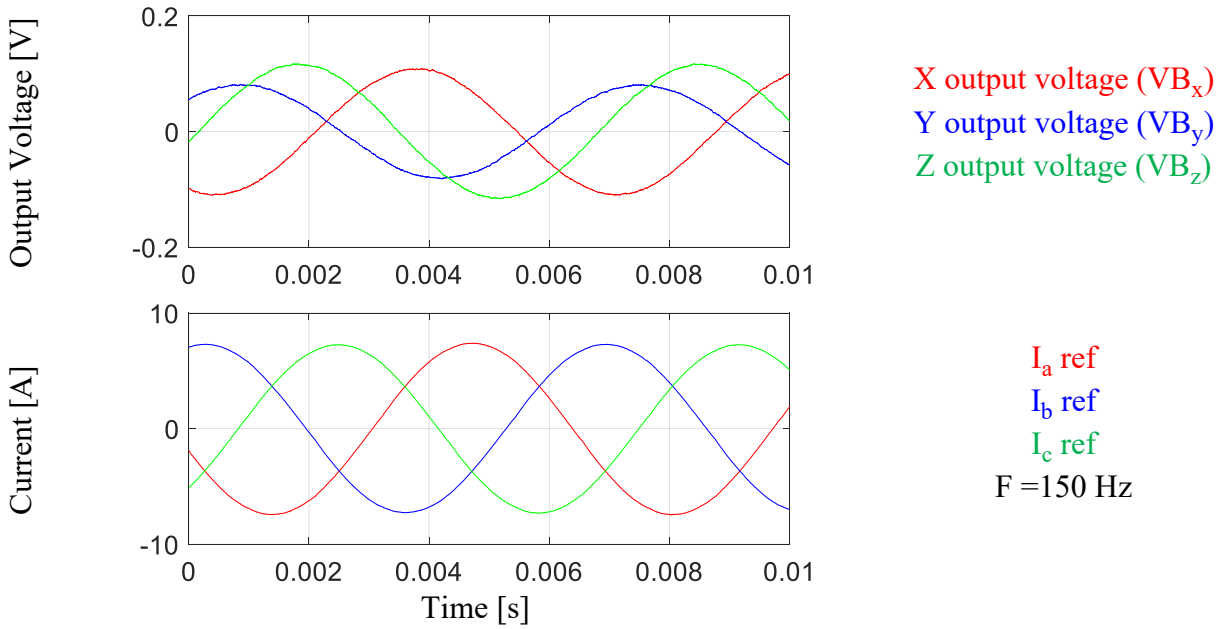

Fig. 4.4-5: X, Y and Z output voltages of the 3-D PFD due to the bent three-phase cable

The results of current sensing at two different frequencies and two different amplitudes are shown in Fig. 4.4-6. For all the tests results shown, the maximum error rms error is 3.4% and the maximum instantaneous error is 6.3%. One of the main reasons for the error is an imprecise calibration of the decoupling matrix and its condition number. The error can be improved by moving the PFD to a region with all three outputs detecting unique field information (better conditioning) with a better SNR. Another source of error is the non-ideality of the GMR PFD which has inherent hysteresis and linearity error associated with it.

It should also be noted that only low currents are being sensed which exaggerates the error. This technique will work much more accurately in high current sensing.

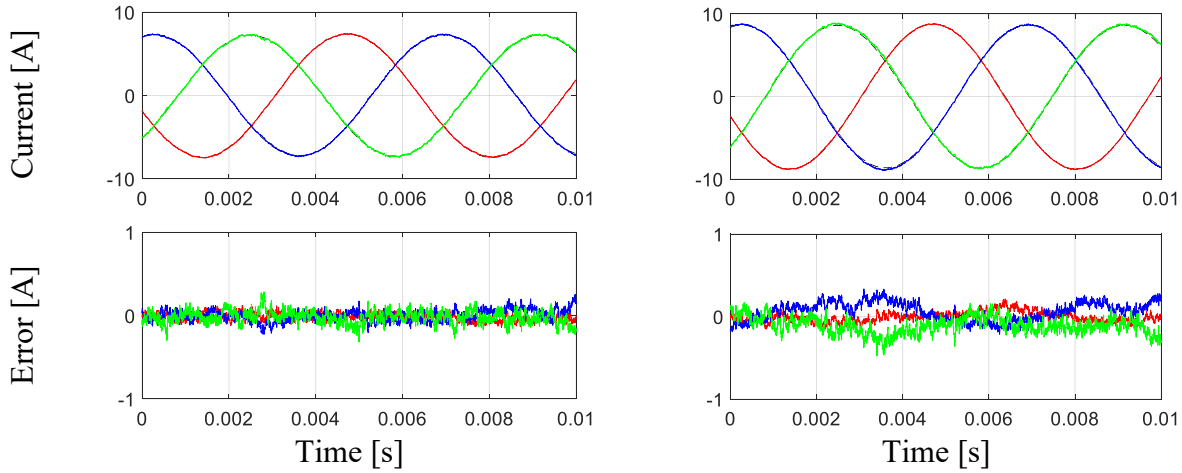

Test Conditions: f = 150 Hz

Lecroy Reference decoupled Phase A decoupled Phase B decoupled Phase C

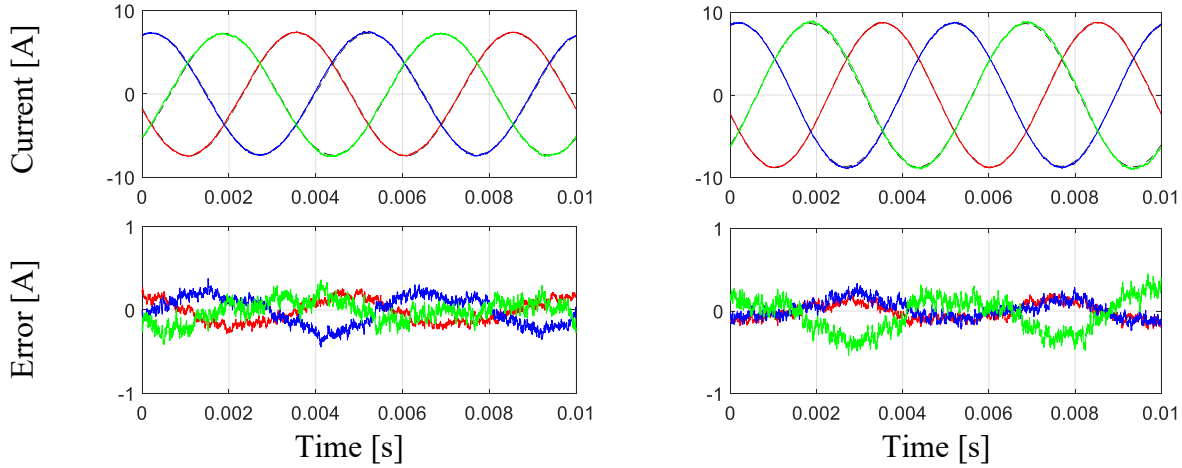

Test Conditions: f = 200 Hz

Lecroy Reference decoupled Phase A decoupled Phase B decoupled Phase C

Fig. 4.4-6: Experimental decoupling and sensing of three-phase currents with a single 3-D PFD in bent three-phase cable

4.5 Range of Three-phase Cable Current Sensing

All PFDs have a finite range and an even smaller linear range as discussed in detail in chapter 1. It is important that the PFD operates within the linear range for current being sensed. One of the biggest versatilities of an MR PFD-based current sensing is that there is theoretically no upper

limit to current sensing. This is achieved by moving the PFD closer for low nominal currents and further away from higher nominal currents. For the three-phase cable current sensing, the similar technique of positioning the 3-D PFD close or far based upon the nominal current rating of the system is possible.

The three-phase cable current sensing is not possible with the core-based current sensors without separating the phases due to the cross-coupling of the fields. The three-phase cable cannot be wrapped into a hall current sensor or current transformer core because the superimposed fields of the three phases are ideally zero in the core. The balanced three-phase currents sum to zero which means that if the phase currents were perfectly superimposed there would be no net magnetic field around.

In three-phase cables, there is a finite distance between the phase currents, due to which there is a net field around the cable. This field is very small due to small distances between the currents. If the current is larger, the cables become larger too and the PFD being on the outside of the insulation is naturally pushed further apart. Due to this for currents even in hundreds of amperes the field is expected to stay within ±5mT. A specialized PFD with sensitivity and range [64] can be employed for cable current sensing.

4.6 Three-phase Current Sensing in Bent Busbars Using a 3-D PFD

One of the very common conducting structures in the inverters is busbars. Very often, they are stacked to conduct three-phase currents as shown in Fig. 4.6-1.

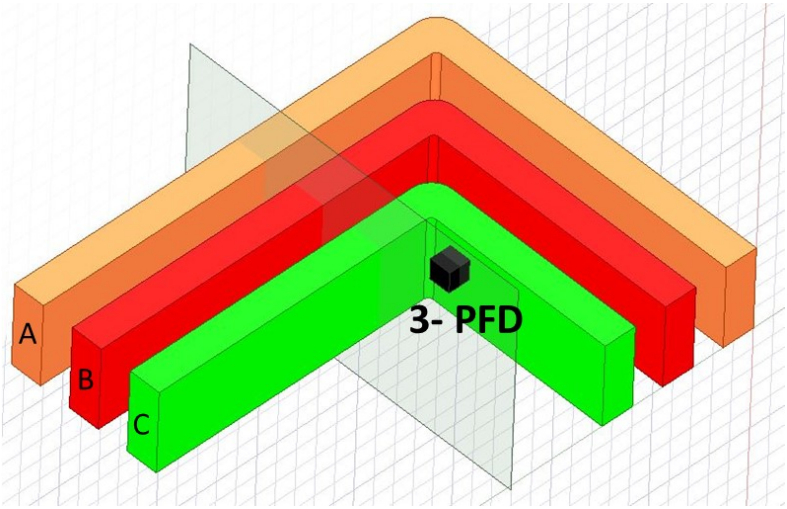

Fig. 4.6-1: Stacked bent busbar to produce 3-D fields

Due to the bend in the busbars and the 3-D field shaping, the 3-D field decoupling is possible, and a single PFD can be used to sense all three currents. The 3-D FBW needs to be analyzed to position the 3-D PFD in the appropriate location. Fig. 4.6-2 shows the magnitude of the flux density and the 3-D bandwidth. There are regions with FBW well above 10 kHz making the positioning of 3-D PFD more reliant on the flux density.

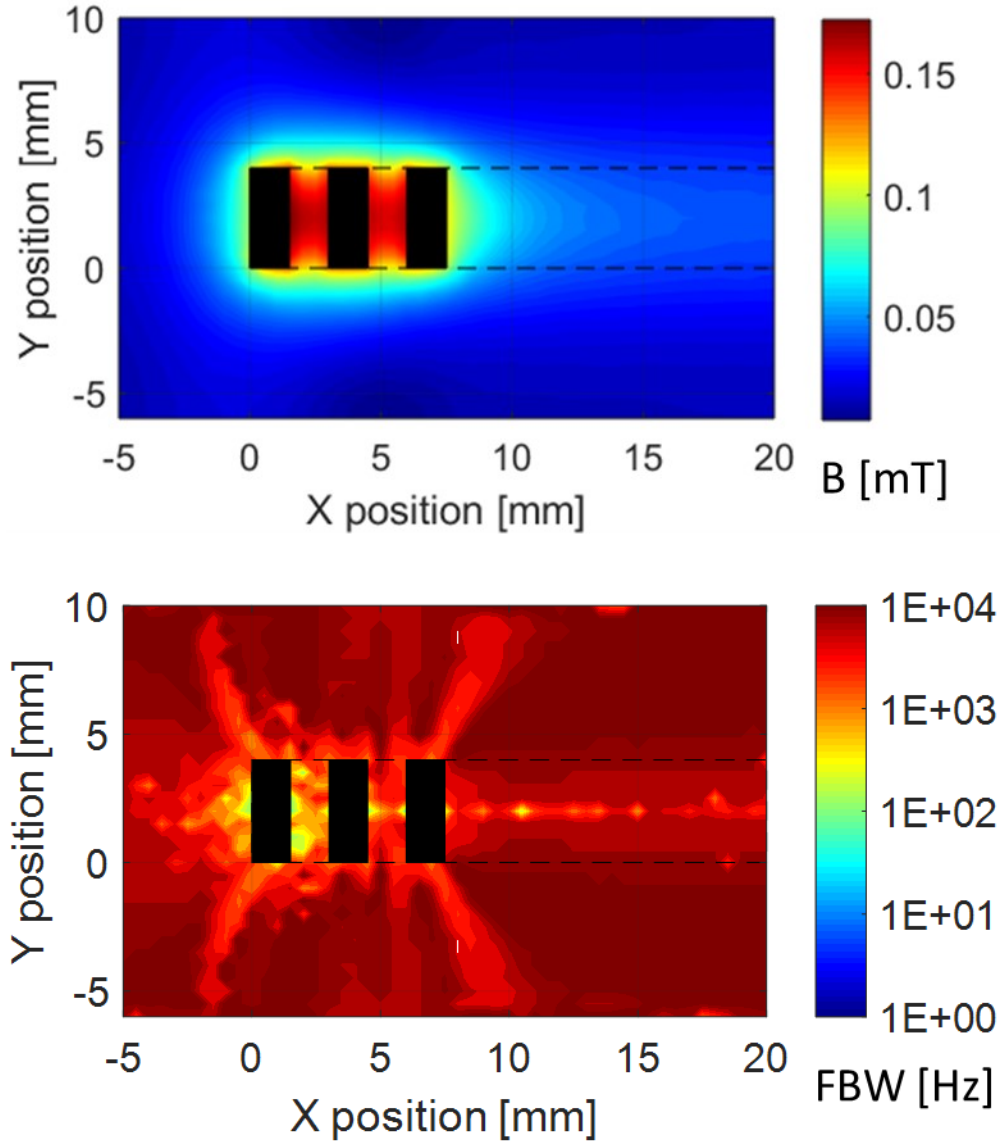

Fig. 4.6-2: Magnitude of flux density and 3-D 5% FBW for stacked busbars with 1A three-phase current injection

4.6.1 Experimental three-phase bent busbar current sensing

The experimental set up used to sense current in the bent three-phase busbar is the same as the bent three-phase cable setup as described in sec. 4.2.1. The only difference is that instead of the cable, the connection between the power supply and load is done partially using the bent busbar shown in Fig. 4.6-3. The decoupling model is also identical to the bent three-phase cable in sec.

4.4.1. In the experiments, the busbars used are much wider and thinner as compared to FEA, due to this, the FBW changes and PFD is not necessarily in a high FBW region. The thin and wide busbars were used due to their malleability and manufacturability. Furthermore, the experimental objective is to demonstrate the decoupling and not the bandwidth.

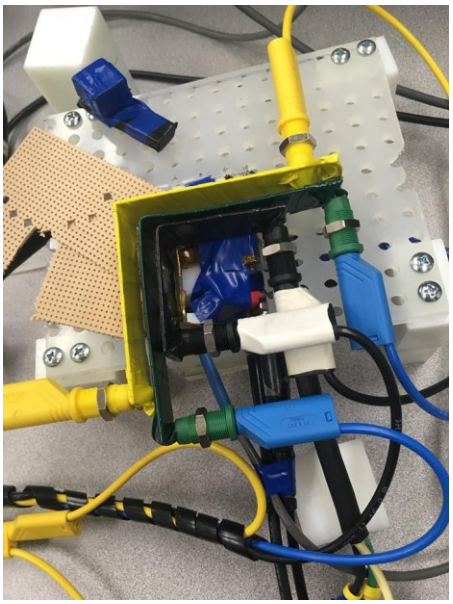

Fig. 4.6-3: Experimental setup of current sensing in three-phase busbar

Fig. 4.6-4 shows the results of X, Y and Z outputs of the 3-D PFD to represent the cross-coupling of phase fields and the need for decoupling. The data shown is at 150 Hz current and used for calibrating the decoupling matrix using the direct method. The reference current and PFD outputs are filtered with a 75 kHz digital low pass filter.

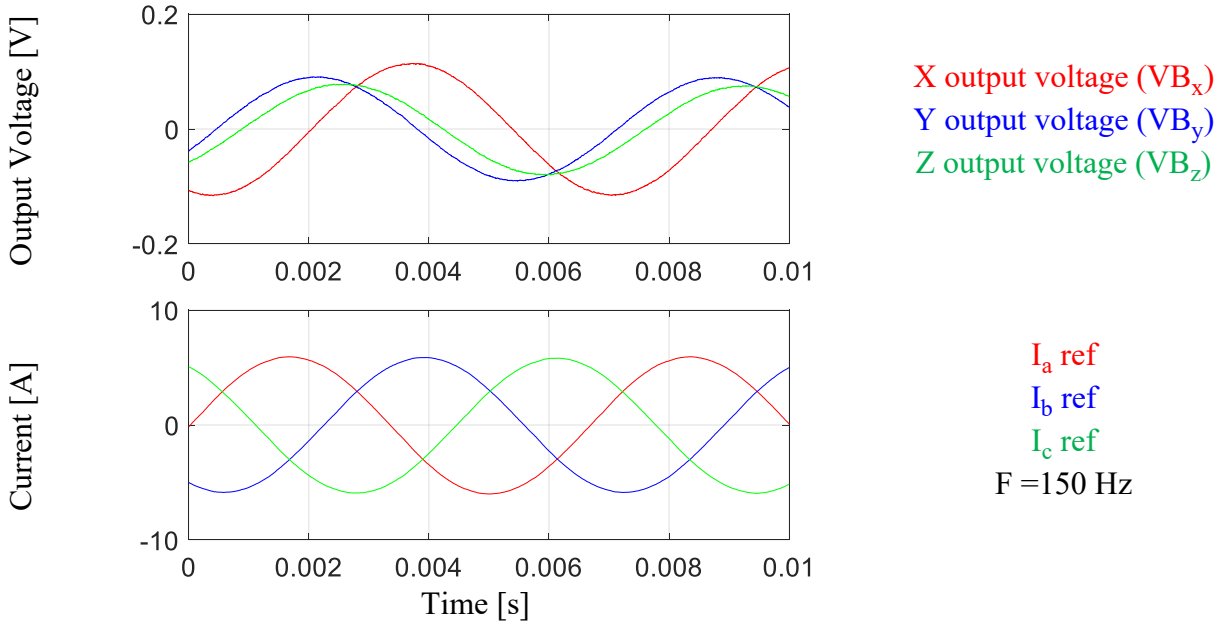

Fig. 4.6-4: X, Y and Z output voltages of the 3-D PFs due to the bent three-phase busbars

The results of current sensing at three different frequencies and two different amplitudes are shown in Fig. 4.6-5. For all the tests results shown, the maximum rms error is 2.9% and the maximum instantaneous error is recorded at 4.8%. It must be noted that only low current sensing is conducted which compromises the SNR and leads to a relatively high error percentage. Another reason for error is the skin and proximity effects of the thin and wide experimental busbars. It should be noted that the constant decoupling matrix is used throughout the frequency despite the fact that the 3-D PFD is not particularly positioned in high bandwidth region. Some of the error can also be attributed to the non-ideality of the GMR PFD, which has inherent hysteresis and linearity error associated with it.

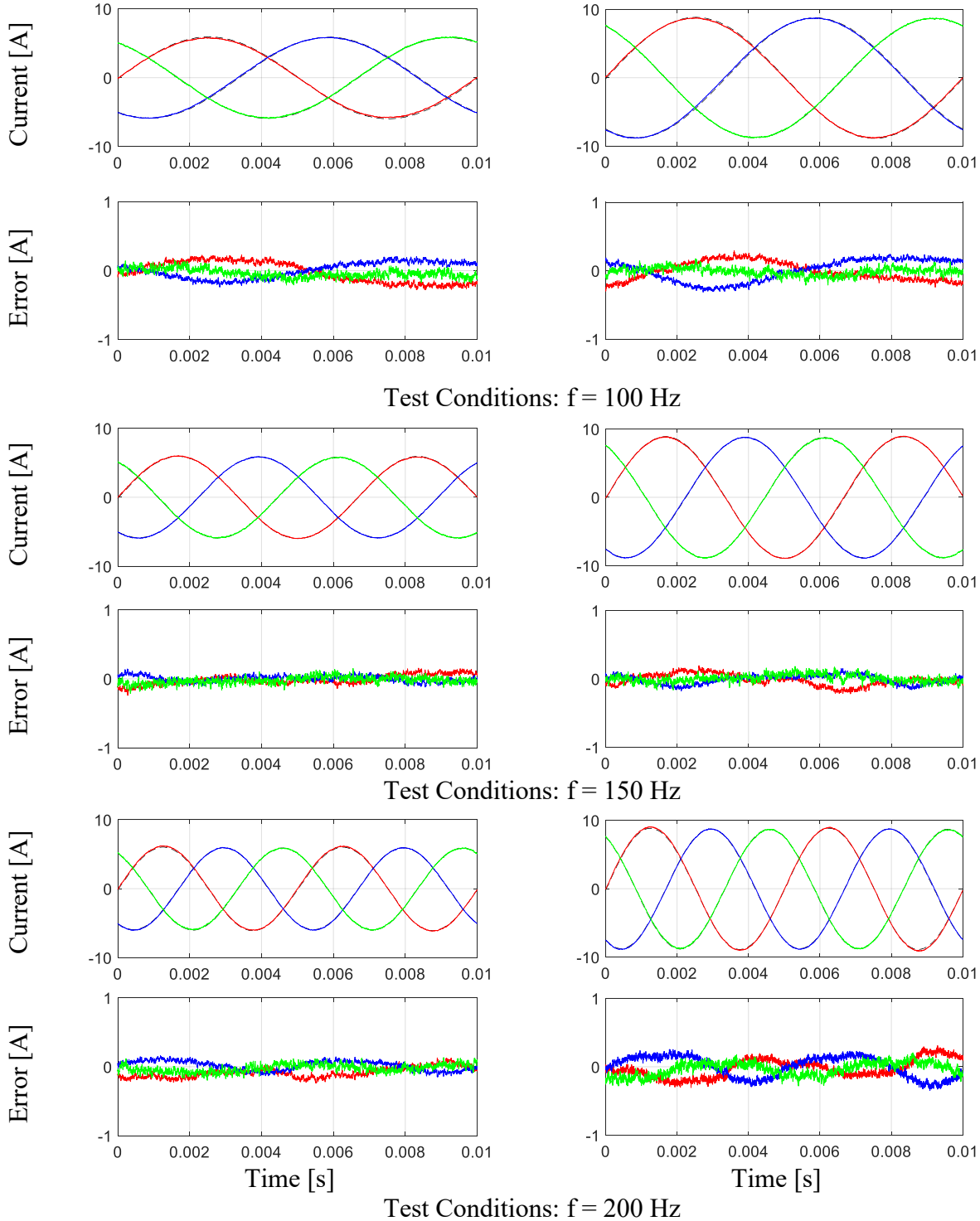

Fig. 4.6-5: Experimental decoupling and sensing of three-phase currents with a single 3-D PFD in bent three-phase busbar

4.7 Summarizing Remarks

A concise summary of the chapter is available at its beginning. The conclusions and contributions for this chapter are available in the last chapter.

In this chapter, the multi-dimensional field decoupling methodology is demonstrated experimentally by sensing three-phase currents in cables and busbars. Due to the lack of availability of monolithic 3-D GMR PFD, three 1-D GMR PFDs are strategically positioned on a PCB to emulate a 3-D GMR PFD and the properties of the GMR PFD for current sensing are evaluated.

The multi-dimensional field decoupling methodology is used for three-phase currents sensing in a straight cable with 2-D PFDs and in a bent cable with a single 3-D PFD in this chapter. Time domain plots of X-, Y- and Z-direction fields detected by the PFD are shown to have high cross-coupling. The cross-coupled fields are decoupled using a constant coupling matrix which is calibrated using the methods in previous chapter. The results of current sensing at various operating conditions of amplitude and frequency are included in the chapter. The bandwidth, range as well as sources of errors in current sensing are also discussed. The results show that the field decoupling methodology is well-suited for three-phase AC drives.

Chapter 5 Disturbance Magnetic Field Decoupling

This chapter develops methodologies to decouple multi-dimensional disturbance magnetic fields from unknown sources that have not been used in the coupling matrix calibration. Magnet fields around currents are evaluated in detail and spatial models are presented for decoupling these fields. The zero-order model is shown to decouple the disturbance fields with zero spatial gradients. The chapter discusses the tradeoffs of higher order 2-D disturbance decoupling and demonstrates an adequate accuracy with zero order decoupling. In addition to active decoupling, a passive disturbance rejection method with magnetic material is also proposed in this chapter.

The main purpose of this chapter is to develop methodologies to reduce the impact of disturbances on the PFD-based current sensing.

Elements of this chapter have not been documented in technical papers yet.

5.1 Disturbance Magnetic Fields Decoupling and Rejection

In this work, cross-coupled magnetic fields from multiple sources have been decoupled. The decoupling requires calibration of coupling and decoupling matrices based upon Maxwell-Ampere's law as described in earlier chapters. A disturbance magnetic field in this work is defined as one originating from a source that has not been calibrated or accounted for in the coupling matrix. It is assumed that no information is available about the source of this magnetic field due to which it cannot be decoupled via the techniques in previous chapters. The issue of disturbance magnetic fields cross-coupled into magnetic fields from calibrated sources is known to cause current sensing errors. There are two options to reduce the impact of these disturbance fields.

First is to create an approximate model of the magnetic field and decouple it. This technique provides information about the disturbance as well. Disturbance decoupling for 1-D magnetic fields is explained in chapter 1. In this chapter, methods to decouple the magnetic field in 2-D and 3-D space will be developed.

The second method to reduce the impact of a disturbance magnetic field is to reject it all together. This leads to the output signal of the PFD to have a minimized impact of disturbance. The disturbance rejection can be done using orthogonal or differential field detection as explained in chapter 1. In this chapter a passive method to reject the field will be shown.

5.2 Characteristics of Disturbance Magnetic Fields

5.2.1 Analysis of magnitude of flux density

The most common source of disturbance magnetic fields are currents in power electronics or electric machines. The first choice is to calibrate the system for these currents. This is only possible if the sources of disturbance magnetic field have a fixed position with respect to the PFDs and have been shown to work for 1-D fields in the literature in chapter 1. In certain rare cases, the source of disturbance magnetic field might have position variance due to which the calibration of the cross-coupling matrix is not possible.

In such a case, it is useful to understand the characteristics of magnetic fields around currents. One of the most important property of magnetic fields around the current is its first order decay in space away from the current. (5.2-1) reiterates the Ampere law which models the magnetic flux density around the current. This simplified version, when there is no displacement current, is a good way to understand the magnetic fields. Fig. 5.2-1 shows the decay in the flux density in the close vicinity of the current. It also shows the magnetic field strength as a function of position.

$$\mu_o I_{enclosed} = \oint B.dl$$
$$B = \frac{\mu_o I_e}{2\pi r}$$
$$\frac{B_1}{B_2} = \frac{r_2}{r_1} \qquad (5.2\text{-}1)$$

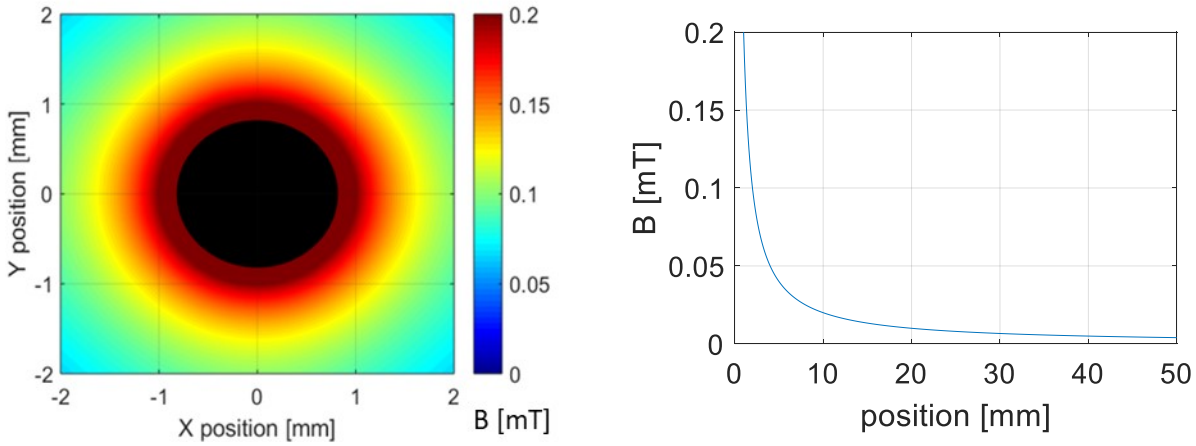

Fig. 5.2-1: Magnitude of magnetic flux density around a straight circular cross-section of a wire carrying 1A quasi-DC current

One of the most important property for formulating the spatial model of the magnetic field is its spatial gradient. (5.2-2) shows the model of the gradient of the magnetic field with respect to the radial position. The spatial gradient is inversely proportional to the square of the radial distance. There is a steep negative gradient in the magnetic field in the beginning. As the distance increases the gradient gets closer to zero. Fig. 5.2-2 shows the spatial gradient of the magnetic flux density in the vicinity of ideal 1A and 2A currents.

$$\frac{\sigma B}{\sigma r} = \frac{-\mu_o I_e}{2\pi r^2} \qquad (5.2\text{-}2)$$

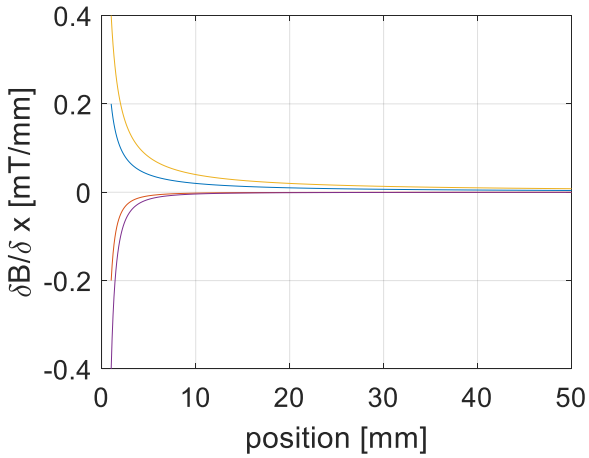

For 1 Amp Magnetic flux density Spatial gradient of magnetic flux density
For 2 Amp Magnetic flux density Spatial gradient of magnetic flux density

Fig. 5.2-2: Magnetic flux density and its spatial gradient around a straight circular cross-section of a wire carrying 1A and 2A currents

The spatial gradient of current approaches zero as the distance from the current increases. The spatial gradient is the partial derivative with respect to distance and is also dependent upon the amplitude of the current. The amplitude of the current linearly scales the spatial gradient of magnetic field. Due to this, at higher currents, it takes a relatively longer distance for the gradient to approach zero. However, it is safe to assume that no matter how large the current, the magnetic field's spatial gradient will converge to zero due its inverse proportionality with square of the distance. In other words, the magnetic field can be assumed to be spatially homogenous at an appropriate distance away from the current.

5.2.2 Analysis of flux density in particular direction

The above analysis of magnitude of flux density can be made more thorough by studying the behavior of magnetic flux density in a single direction as will be detected by a 1-D PFD. The behavior of the magnetic field in Y-direction is analyzed. Fig. 5.2-3 shows the magnetic flux density in Y-direction as a function of X distance at a few Y positions. The blue curve is at y=0 and is identical to plot shown in Fig. 5.2-1. This is because, at y=0, the Y-direction magnetic field

is the same as total magnetic field. It is noticed that due to the angular term involved in the calculation of Y-direction fields, the trends in it vary with the Y position. However, after a certain distance, the angular term approaches unity due to which the difference between fields at different Y positions becomes insignificant.

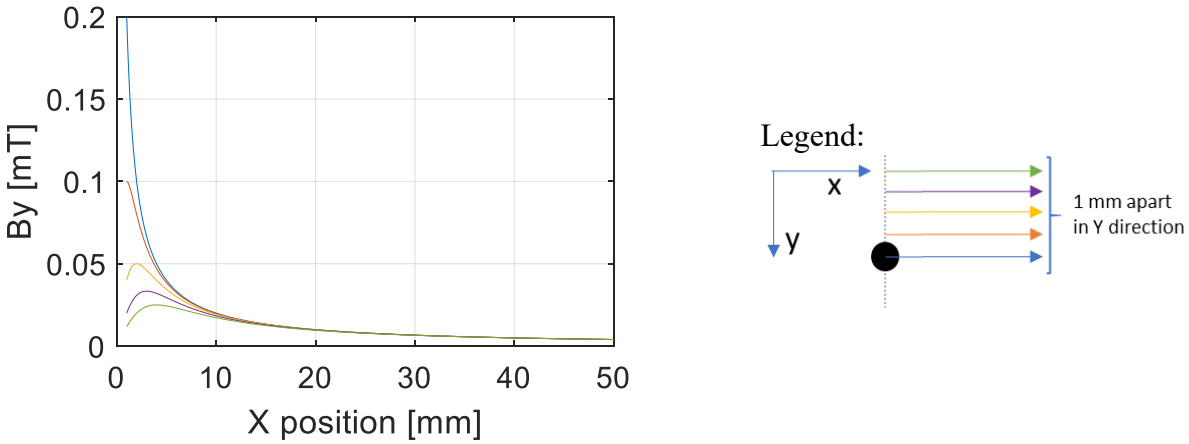

Fig. 5.2-3: Y-direction magnetic flux density as function of X position around a straight circular cross-section wire carrying 1A currents

Fig. 5.2-4 shows the Y-direction field as a function of Y position at a few X positions, starting at x=1mm. This offset in X-direction allows the field to be plotted from y=0. The trend remains the same with steep a decline in the beginning and a low gradient after some distance.

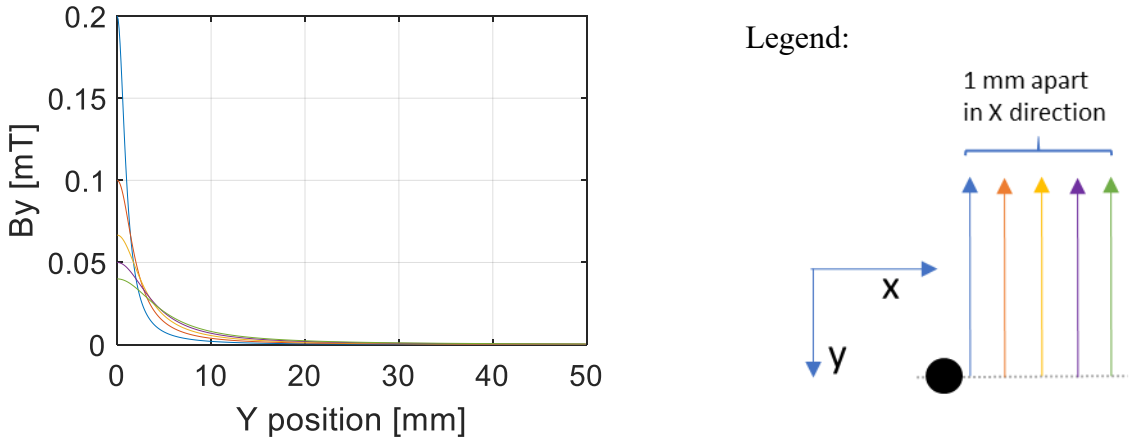

Fig. 5.2-4: Y-direction magnetic flux density as function of Y position around a straight circular cross-section wire carrying 1A currents

Since the X- and Y-direction magnetic field at a point is a function of X and Y positions, surface plots are generated for magnetic fields from current at location (-1mm,-1mm). These surfaces, shown in Fig. 5.2-5, in addition to showing the magnitude of X and Y flux densities also display the spatial gradient of fields.. Since most disturbance magnetic fields have sources far away from PFDs, the findings about the magnitude of flux density still apply. The spatial gradient of fields show convergence to zero.

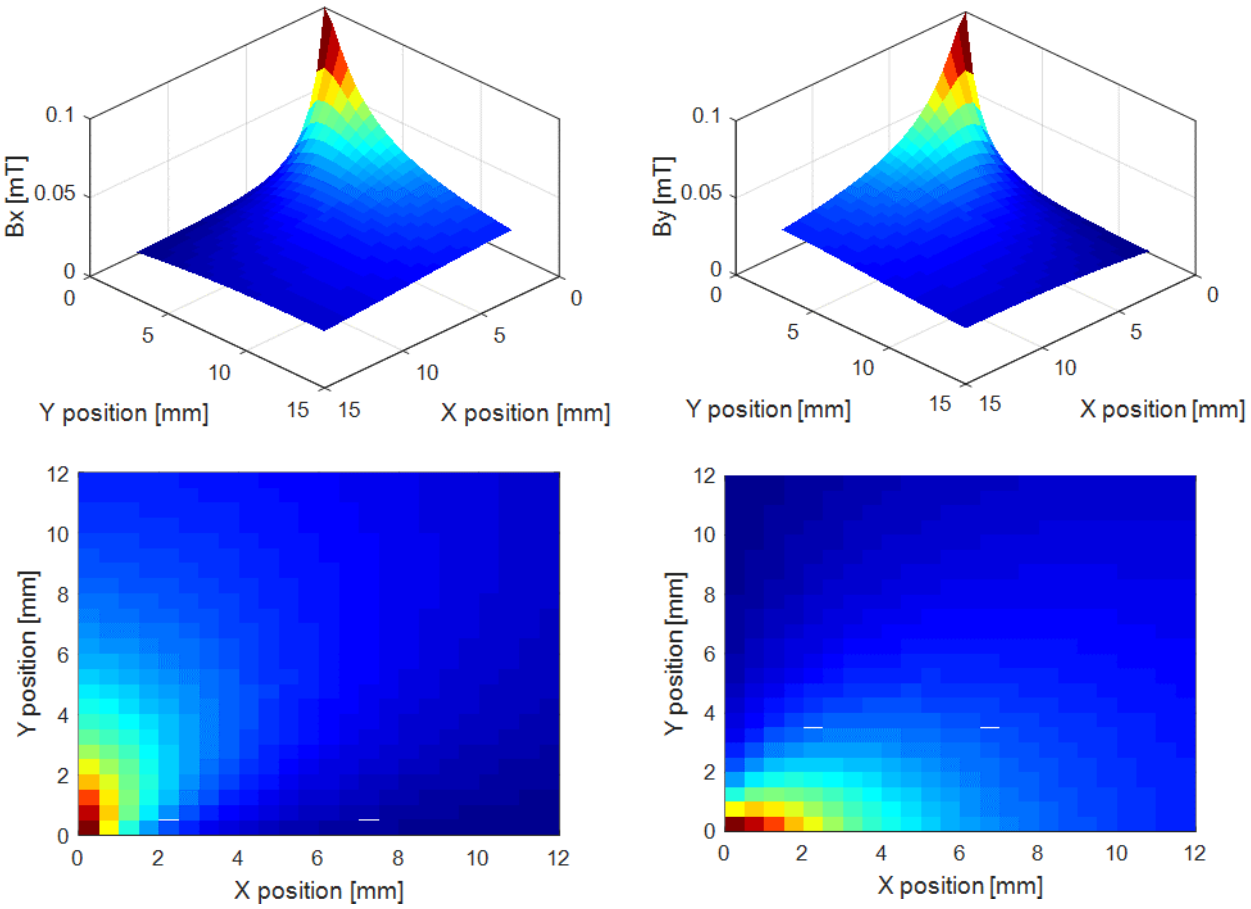

Fig. 5.2-5: X- and Y-direction magnetic flux density around a straight circular cross-section wire carrying 1A currents

5.3 Full Modelling of 3-D Disturbance Decoupling

The physical model of cross-coupled magnetic fields from currents and disturbance can be expressed using (5.3-1). The equation is generalized for *M* number of currents and *N* 3-D PFDs and is based upon 1-D magnetic field analysis in [69].

$$\begin{bmatrix} C_{x11} & \cdots & C_{xM1} \\ C_{y11} & \cdots & C_{yM1} \\ C_{z11} & \cdots & C_{zM1} \\ \vdots & \vdots & \vdots \\ C_{x1N} & \cdots & C_{xMN} \\ C_{y1N} & \cdots & C_{yMN} \\ C_{z1N} & \cdots & C_{ZMN} \end{bmatrix} \begin{bmatrix} I_1 \\ \vdots \\ I_M \end{bmatrix} + \begin{bmatrix} Dist_{x1} \\ Dist_{y1} \\ Dist_{z1} \\ \vdots \\ \vdots \\ \vdots \\ Dist_{xN} \\ Dist_{yN} \\ Dist_{zN} \end{bmatrix} = \begin{bmatrix} VB_{x1} \\ VB_{y1} \\ VB_{z1} \\ \vdots \\ \vdots \\ \vdots \\ VB_{xN} \\ VB_{yN} \\ VB_{zN} \end{bmatrix} \tag{5.3-1}$$

The magnetic disturbances in X-, Y-, or Z-directions can be modelled as spatial quantities with n-th order polynomials. Theoretically, the disturbance model is a function of x, y and z positions of the PFDs. However, to simplify the system, one of the dominant directions can be used to describe the spatial model of the disturbance. This is shown in (5.3-2) and is valid if the spatial gradients in other directions are very low.

$$\begin{aligned} Dist_x &= \sum_{i=0}^{n} a_{x\text{-}i}\, x^i + \sum_{i=0}^{n} b_{x\text{-}i}\, y^i + \sum_{i=0}^{n} c_{x\text{-}i}\, z^i \approx \sum_{i=0}^{n} a_{x\text{-}i}\, x^i \\ Dist_y &= \sum_{i=0}^{n} a_{y\text{-}i}\, x^i + \sum_{i=0}^{n} b_{y\text{-}i}\, y^i + \sum_{i=0}^{n} c_{y\text{-}i}\, z^i \approx \sum_{i=0}^{n} b_{y\text{-}i}\, y^i \\ Dist_z &= \sum_{i=0}^{n} a_{z\text{-}i}\, x^i + \sum_{i=0}^{n} b_{z\text{-}i}\, y^i + \sum_{i=0}^{n} c_{z\text{-}i}\, z^i \approx \sum_{i=0}^{n} c_{z\text{-}i}\, z^i \end{aligned} \tag{5.3-2}$$

Combining (5.3-1) and (5.3-2) leads to

(5.3-3), which shows that the net magnetic field vector detected by 3-D PFDs can be described using a cross-coupling matrix which links the magnetic fields from currents and disturbances. The

cross-coupling matrix includes the Maxwell-Ampere's law terms from current coupling and spatial position terms for modelling the disturbance.

$$\begin{bmatrix} C_{x11} & \cdots & C_{xM1} & 1 & x_1 & \cdots & x_1^n & 0 & 0 & \cdots & 0 & 0 & 0 & \cdots & 0 \\ C_{y11} & \cdots & C_{yM1} & 0 & 0 & \cdots & 0 & 1 & y_1 & \cdots & y_1^n & 0 & 0 & \cdots & 0 \\ C_{z11} & \cdots & C_{zM1} & 0 & 0 & \cdots & 0 & 0 & 0 & \cdots & 0 & 1 & z_1 & \cdots & z_1^n \\ \vdots & \vdots & \vdots & \vdots & \vdots & \vdots & \vdots & \vdots & \vdots & \vdots & \vdots & \vdots & \vdots & \vdots & \vdots \\ C_{x1N} & \cdots & C_{xMN} & 1 & x_N & \cdots & x_N^n & 0 & 0 & \cdots & 0 & 0 & 0 & \cdots & 0 \\ C_{y1N} & \cdots & C_{yMN} & 0 & 0 & \cdots & 0 & 1 & y_N & \cdots & y_N^n & 0 & 0 & \cdots & 0 \\ C_{z1N} & \cdots & C_{zMN} & 0 & 0 & \cdots & 0 & 0 & 0 & \cdots & 0 & 1 & z_N & \cdots & z_N^n \end{bmatrix} \begin{bmatrix} I_1 \\ \vdots \\ I_M \\ a_{x0} \\ a_{x1} \\ \vdots \\ a_{xn} \\ b_{y0} \\ b_{y1} \\ \vdots \\ b_{yn} \\ c_{z0} \\ c_{z1} \\ \vdots \\ c_{zn} \end{bmatrix} \begin{bmatrix} VB_{x1} \\ VB_{y1} \\ VB_{z1} \\ \vdots \\ \vdots \\ \vdots \\ VB_{xN} \\ VB_{yN} \\ VB_{zN} \end{bmatrix} \quad (5.3\text{-}3)$$

5.4 3-D Disturbance Decoupling with Zero Spatial Gradient

Based upon the analysis in sec. 5.2, if the source of the disturbance magnetic field is far away and the PFDs detecting it are close to each other, assuming a zero spatial gradient of the disturbance field is a good approximation. In other words, the disturbance field detected by the PFDs is close to being identical or homogenous.

The cross-coupling decoupling methodology can be extended to homogenous disturbance decoupling. Since all three dimensions are being used, for accurate current sensing the disturbance fields in all three dimensions should be decoupled. The simplest method of decoupling disturbance involves increasing the number of 3-D PFDs close to the currents being measured. If the three-phase currents and X, Y and Z disturbances are being measured, six degrees of freedom are needed to decouple them. Having two 3-D PFDs provides enough information to be able to decouple these six quantities. The locations of the PFD should have different spatial magnetic field content from

the currents being measured to avoid singularity. Singularity occurs if same magnetic field information is detected in both 3-D PFDs. The caveat is that the magnetic field detected by 3-D PFDs from currents being measured should be as different as possible whereas the disturbance magnetic field detected by both PFDs should be the same.

Fig. 5.4-1 shows the bent 3-D conductor system that is used in chapter 3. Instead of using a single 3-D PFD for three-phase current sensing, this time two 3-D PFDs are used since the three disturbances also need to be decoupled and sensed.

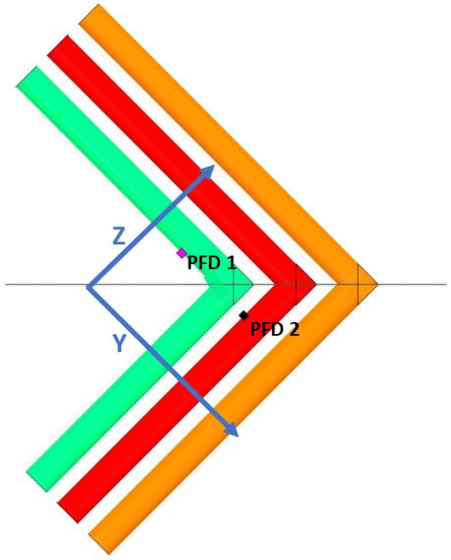

Fig. 5.4-1: Bent three-phase conductors with two 3-D PFDs for current sensing with 3-D disturbance decoupling

(5.4-1) shows the model that approximates the disturbance as spatially homogeneous over the two 3-D PFDs. This equation is a zero order disturbance model version of and is based upon the work on 1-D fields in [69] explained in detail in chapter 1. The three-phase currents are calibrated whereas no information is known about the source of disturbance.

$$\begin{bmatrix} C_{xa1} & C_{xb1} & C_{xc1} & 1 & 0 & 0 \\ C_{ya1} & C_{yb1} & C_{yc1} & 0 & 1 & 0 \\ C_{za1} & C_{zb1} & C_{zc1} & 0 & 0 & 1 \\ C_{xa2} & C_{xb2} & C_{xc2} & 1 & 0 & 0 \\ C_{ya2} & C_{yb2} & C_{yc2} & 0 & 1 & 0 \\ C_{za2} & C_{zb2} & C_{zc2} & 0 & 0 & 1 \end{bmatrix} \begin{bmatrix} I_a \\ I_b \\ I_c \\ D_x \\ D_y \\ D_Z \end{bmatrix} = \begin{bmatrix} VB_{x1} \\ VB_{y1} \\ VB_{z1} \\ VB_{x2} \\ VB_{y2} \\ VB_{z2} \end{bmatrix} \quad (5.4\text{-}1)$$

$C_{\mathbf{xa1}}$ refers to the coupling term for X-direction field, phase A current and PFD number 1, D_x refers to the unknown spatially homogenous disturbance in X-direction and VB_{x1} refers to the X-direction output of PFD number 1. The diagonal unity terms in the last three columns represent the coupling terms of spatially homogenous disturbances in X-, Y- and Z-directions. The coupling matrix can be inverted to form the decoupling matrix as shown in (5.4-2)

$$\begin{bmatrix} I_a \\ I_b \\ I_c \\ D_x \\ D_y \\ D_Z \end{bmatrix} = \begin{bmatrix} D_{xa1} & D_{ya1} & D_{za1} & D_{xa2} & D_{ya2} & D_{za2} \\ D_{xb1} & D_{yb1} & D_{zc1} & D_{xb2} & D_{yb2} & D_{zc2} \\ D_{xc1} & D_{yc1} & D_{zc1} & D_{xc2} & D_{yc2} & D_{zc2} \\ D_{xx1} & D_{yx1} & D_{zx1} & D_{xx2} & D_{yx2} & D_{zx2} \\ D_{xy1} & D_{yy1} & D_{zy1} & D_{xy2} & D_{yy2} & D_{zy2} \\ D_{xz1} & D_{yz1} & D_{zz1} & D_{xz2} & D_{yz2} & D_{zz2} \end{bmatrix} \begin{bmatrix} VB_{x1} \\ VB_{y1} \\ VB_{z1} \\ VB_{x2} \\ VB_{y2} \\ VB_{z2} \end{bmatrix} \quad (5.4\text{-}2)$$

Where

$D_{xa1} = -D_{xa2}$, $D_{ya1} = -D_{ya2}$, $D_{za1} = -D_{za2}$

$D_{xb1} = -D_{xb2}$, $D_{yb1} = -D_{yb2}$, $D_{zb1} = -D_{zb2}$

$D_{xc1} = -D_{xc2}$, $D_{yc1} = -D_{yc2}$, $D_{zc1} = -D_{zc2}$

The diagonalized unity terms in the coupling matrix, lead to an interesting mathematical behavior in the decoupling matrix. For the first three rows, column one is equal and opposite to column four, columns two is equal and opposite to column five and column 3 is equal and opposite

to column six. These equal and opposite terms effectively lead to the differential signals of PFDs' outputs, thereby filtering out the homogeneous disturbance incident on both PFDs.

5.4.1 Decoupling of disturbances without time gradient (DC)

The first three columns of the coupling matrix are found using the FEA method described in chapter 3. To check the validity of the coupling and decoupling matrices computed using FEA, a test case is run after calibration. In the FEA, three-phase currents (at their respective amplitudes and phases) are passed at the same time. The net magnetic flux densities at the PFD location 1 and 2 are recorded as their X, Y, and Z components multiple times during a current cycle. A magnetic field disturbance is numerically superimposed in the X-, Y- and Z-directions on the PFD outputs. Fig. 5.4-2 shows the PFD output signals which are decoupled into currents and disturbance signals in Fig. 5.4-3 and Fig. 5.4-4. It is worth noting that the output of the FEA is based upon phase instants rather than time, hence the X axis is shown as phase in radians. This can easily be converted to time series as well.

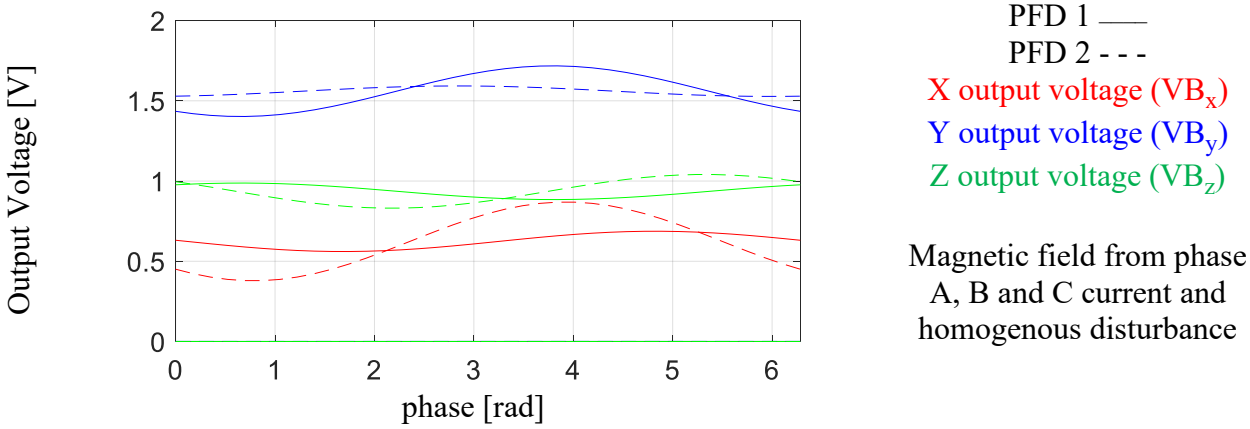

Fig. 5.4-2: X, Y and Z output voltages of the two 3-D PFDs in the three bent parallel conductor system with superimposed disturbance having zero spatial gradient

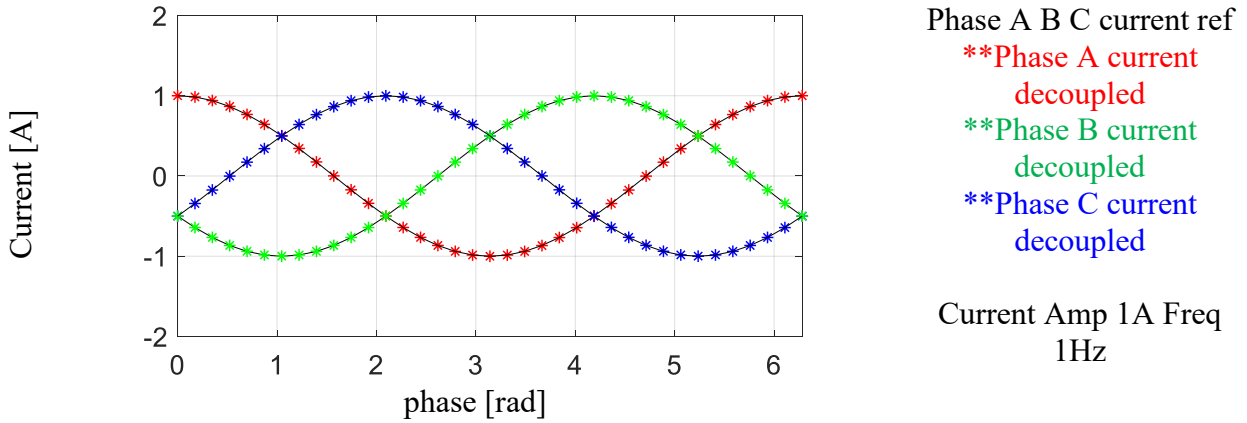

Fig. 5.4-3: FEA-based decoupling of three-phase currents with two 3-D PFDs in the three bent parallel conductor system with superimposed disturbance

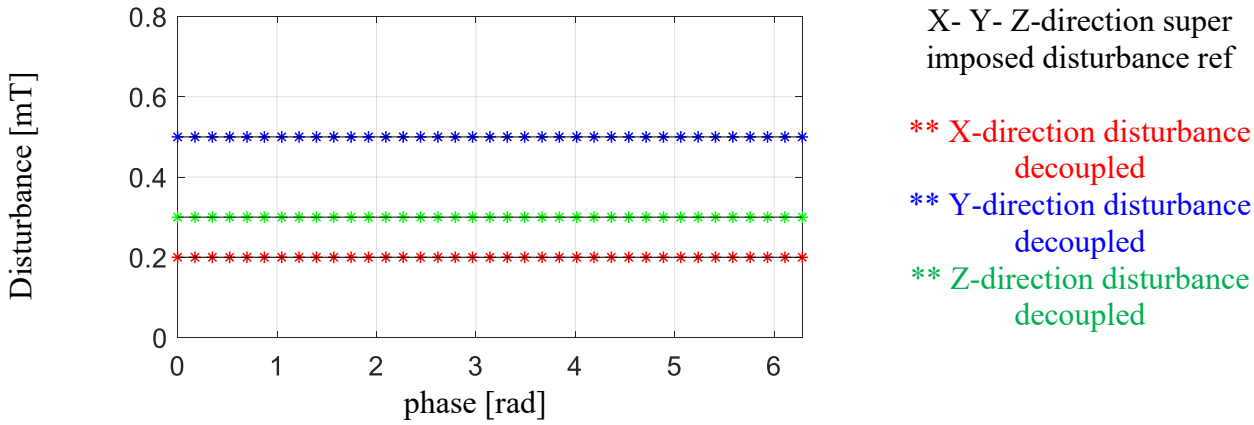

Fig. 5.4-4: FEA-based decoupling of disturbance magnetic field with two 3-D PFDs in the three bent parallel conductor system

The results show that with only two 3-D PFDs, it is possible to sense three currents while decoupling all spatially homogenous disturbances.

5.4.2 Decoupling of disturbances with time gradient (AC)

Disturbances with a time gradient can also be decoupled using the same method. The only constraint in the method is the spatial gradient. Fig. 5.4-5 shows the PFD output signals with cross-coupled AC disturbance and three-phase magnetic fields. The decoupled currents and AC disturbance signals are shown in Fig. 5.4-6 and Fig. 5.4-7. The decoupling is perfect within margins of computational accuracy of FEA.

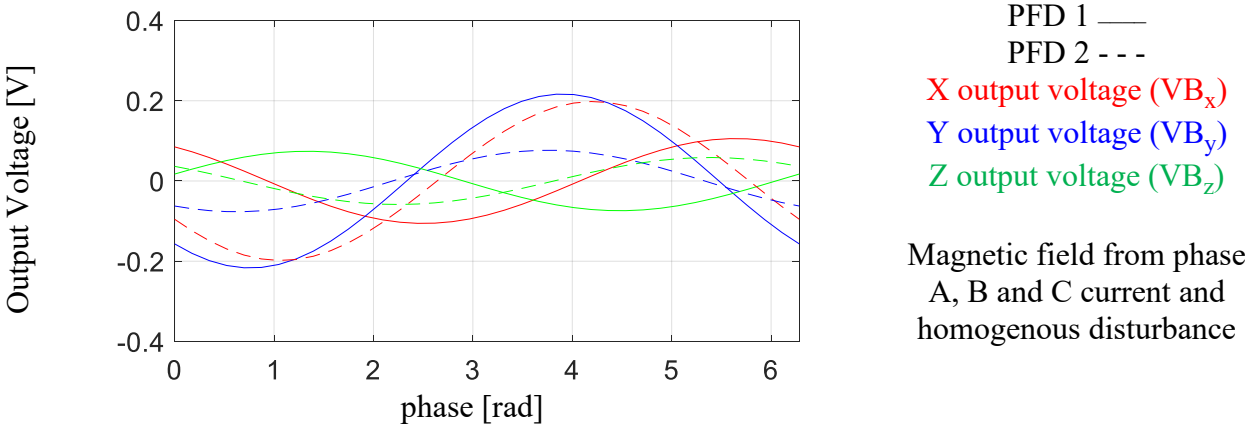

Fig. 5.4-5: X, Y and Z output voltage of the two 3-D PFDs in the three bent parallel conductor system with superimposed AC disturbance having zero spatial gradient

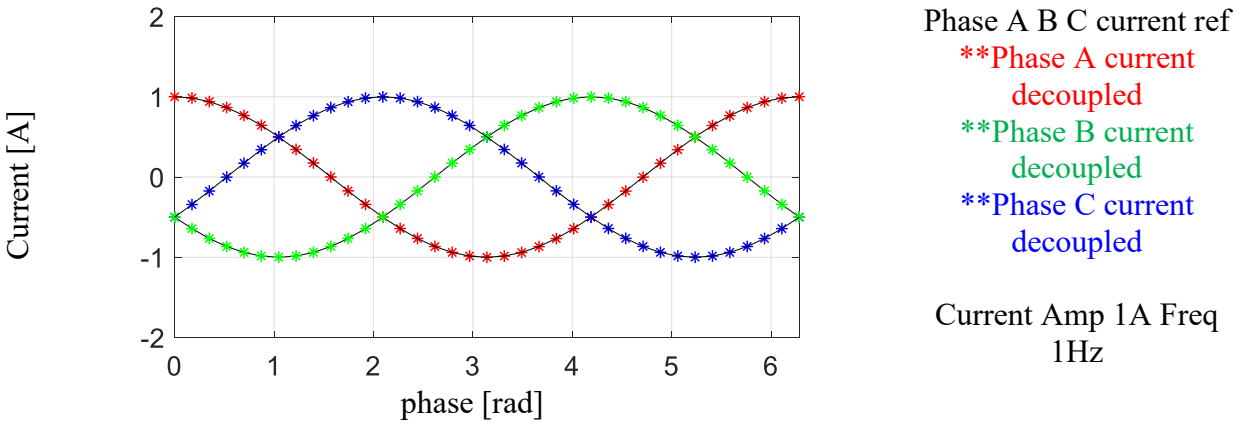

Fig. 5.4-6: FEA-based decoupling of three-phase currents with two 3-D PFDs in the three bent parallel conductor system with superimposed AC disturbance

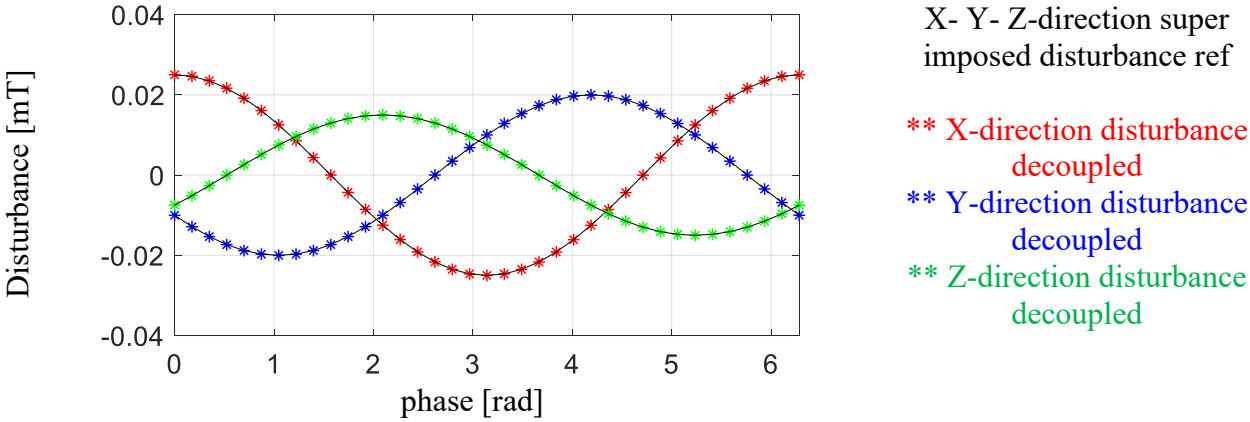

Fig. 5.4-7: FEA-based decoupling of AC disturbance magnetic field with two 3-D PFDs in the three bent parallel conductor system

5.5 Decoupling Disturbances with Spatial Gradient

The spatial gradient of the disturbance magnetic fields is very small. However, for accurate current sensing, it needs to be a part of the disturbance model because approximating the disturbance as a spatially homogenous quantity can lead to small errors. To remove these errors, a higher order spatial modelling approach for disturbances can be used. (5.5-1) provides the model of the disturbance. The model approximates the disturbance as an n-th order polynomial in x, y, z which are the positions of the PFD.

$$\text{Disturbance in X-direction} = \sum_{i=0}^{n} a_i \, x^i + \sum_{i=0}^{n} b_i \, y^i \sum_{i=0}^{n} c_i \, z^i \approx \sum_{i=0}^{n} a_{x\text{-}i} \, x^i \qquad (5.5\text{-}1)$$

To keep the system relatively simple, only two dimensional systems are studied using FEA for higher order modelling of the disturbances. The findings can easily be extended to 3-D. Fig. 5.5-1 shows the three-phase conductors with two of the phases being sensed using the calibration-based decoupling. The phase C which is located relatively farther away is the uncalibrated source of disturbance. This disturbance will have a spatial and time gradient. The figure also shows the locations of five arbitrarily placed PFDs some of which will be used in disturbance decoupling.

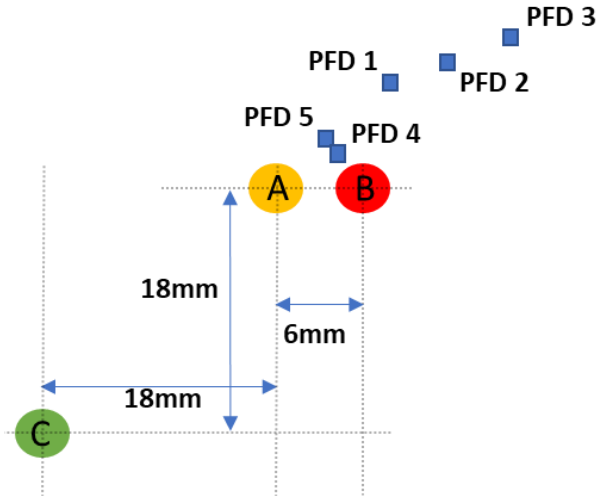

Fig. 5.5-1: Three-phase conductors with five 2-D PFDs for current sensing in which phase C is considered a disturbance

Two currents require a single 2-D PFD for current sensing as modelled in (5.5-2) and explained in earlier chapters. However, due to the cross-coupled disturbance magnetic field from phase C current, using a single 2-D PFD results in significant error in current sensing in Fig. 5.5-2.

With one 2-D PFD
Disturbance in X = $D_x = 0$
Disturbance in Y = $D_y = 0$

$$\begin{bmatrix} C_{xa1} & C_{xb1} \\ C_{ya1} & C_{yb1} \end{bmatrix}\begin{bmatrix} I_a \\ I_b \end{bmatrix} + \begin{bmatrix} Dist_x \\ Dist_y \end{bmatrix} = \begin{bmatrix} VB_{x1} \\ VB_{y1} \end{bmatrix}$$

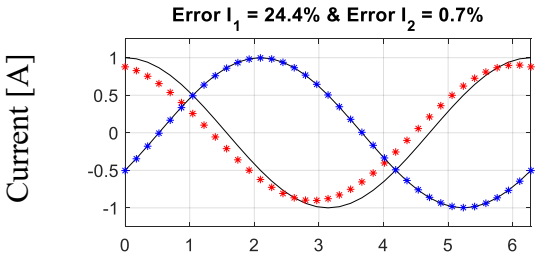

Fig. 5.5-2: Decoupling two currents with no modelling of the disturbance

Despite the lack of modelling and decoupling of disturbance, one of the currents has a very low error. This is a mathematical coincidence described in the set of equations (5.5-2). Although efforts could be made to achieve such a situation by design, the nature of disturbance is by definition impossible to control.

$$\begin{bmatrix} D_{xa1} & D_{ya1} \\ D_{xb1} & D_{yb1} \end{bmatrix}\begin{bmatrix} VB_{x1} - D_x \\ VB_{y1} - D_y \end{bmatrix} = \begin{bmatrix} I_a \\ I_b \end{bmatrix} \qquad (5.5\text{-}2)$$

Even if D_x and D_y are unknown and non-zero, no error occurs in I_a if $D_{xa1} D_x = - D_{ya1} D_y$ and no error occurs in I_b if $D_{xb1} D_x = - D_{yb1} D_y$

The outputs of the additional PFDs shown in Fig. 5.5-1 can be used to model the disturbance and decouple it. The order of the disturbance model is determined by the number of PFDs used. Zero order model which considers the disturbance as spatially homogenous requires one additional PFD. A first order model which models the disturbance as a linear quantity requires two additional PFDs and so on. Fig. 5.5-3 shows the zero, first and second order modelling and decoupling of the

disturbance from the currents. In this FEA simulation, as expected, having a higher order model of disturbance improves the efficacy of the disturbance decoupling.

With two PFDs (PFD1 and PFD3)
Disturbance in X = Dx
Disturbance in Y = Dy

$$\begin{bmatrix} C_{xa1} & C_{xb1} & 1 & 0 \\ C_{ya1} & C_{yb1} & 0 & 1 \\ C_{xa3} & C_{xb3} & 1 & 0 \\ C_{ya3} & C_{yb3} & 0 & 1 \end{bmatrix} \begin{bmatrix} I_a \\ I_b \\ D_x \\ D_y \end{bmatrix} = \begin{bmatrix} VB_{x1} \\ VB_{y1} \\ VB_{x3} \\ VB_{y3} \end{bmatrix}$$

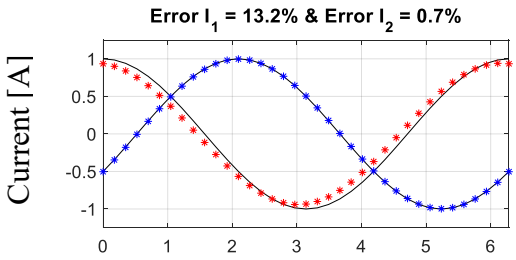

With three PFDs (PFD1, PFD3 and PFD5)
Disturbance in X = $D_x + D_{x\text{-grad}}\, x$
Disturbance in Y = $D_y + D_{y\text{-grad}}\, y$

$$\begin{bmatrix} C_{xa1} & C_{xb1} & 1 & x_1 & 0 & 0 \\ C_{ya1} & C_{yb1} & 0 & 0 & 1 & y_1 \\ C_{xa3} & C_{xb3} & 1 & x_3 & 0 & 0 \\ C_{ya3} & C_{yb3} & 0 & 0 & 1 & y_3 \\ C_{xa5} & C_{xb5} & 1 & x_5 & 0 & 0 \\ C_{ya5} & C_{yb5} & 0 & 0 & 1 & y_5 \end{bmatrix} \begin{bmatrix} I_a \\ I_b \\ D_x \\ D_{x\text{-grad}} \\ D_y \\ D_{y\text{-grad}} \end{bmatrix} = \begin{bmatrix} VB_{x1} \\ VB_{y1} \\ VB_{x3} \\ VB_{y3} \\ VB_{x5} \\ VB_{y5} \end{bmatrix}$$

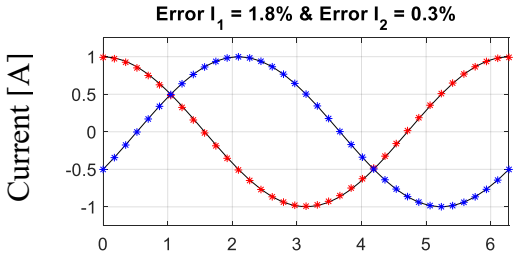

With four PFDs (PFD1, PFD3, PFD4 and PFD5)
Disturbance in X = $D_x + D_{x\text{-grad}}\, x + D_{x\text{-grad2}}\, x^2$
Disturbance in Y = $D_y + D_{y\text{-grad}}\, y + D_{y\text{-grad2}}\, y^2$

$$\begin{bmatrix} C_{xa1} & C_{xb1} & 1 & x_1 & x_1^2 & 0 & 0 & 0 \\ C_{ya1} & C_{yb1} & 0 & 0 & 0 & 1 & y_1 & y_1^2 \\ C_{xa3} & C_{xb3} & 1 & x_3 & x_3^2 & 0 & 0 & 0 \\ C_{ya3} & C_{yb3} & 0 & 0 & 0 & 1 & y_3 & y_3^2 \\ C_{xa4} & C_{xb4} & 1 & x_4 & x_4^2 & 0 & 0 & 0 \\ C_{ya4} & C_{yb4} & 0 & 0 & 0 & 1 & y_4 & y_4^2 \\ C_{xa5} & C_{xb5} & 1 & x_5 & x_5^2 & 0 & 0 & 0 \\ C_{ya5} & C_{yb5} & 0 & 0 & 0 & 1 & y_5 & y_5^2 \end{bmatrix} \begin{bmatrix} I_a \\ I_b \\ D_x \\ D_{x\text{-grad}} \\ D_{x\text{-grad2}} \\ D_y \\ D_{y\text{-grad}} \\ D_{xy\text{-grad2}} \end{bmatrix} = \begin{bmatrix} VB_{x1} \\ VB_{y1} \\ VB_{x3} \\ VB_{y3} \\ VB_{x4} \\ VB_{y4} \\ VB_{x5} \\ VB_{y5} \end{bmatrix}$$

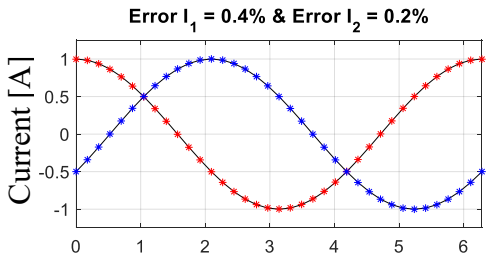

Fig. 5.5-3: Decoupling disturbances with multi-order model approximations

5.5.1 Conditioning of the decoupling

A higher order of disturbance modeling is generally expected to improve the decoupling performance. However, this general trend is also dependent on the condition number of the decoupling matrix and practical implementation. As explained in chapter 3, a high condition number makes the system prone to decoupling errors. Due to this, as the condition number of the decoupling matrix increases, so does the error induced from even small errors in the PFD outputs.

N 2-D PFDs use a square decoupling matrix of size *2N* x *2N*. As the size of this matrix increases, probabilistically the condition number also increases. This is physically explained by the fact that all PFDs are in the same vicinity and detect similar magnetic field information. If an additional PFD is added to the small region, it is like to have very similar information to the others. Fig. 5.5-4 shows the condition number of the decoupling matrices used in Fig. 5.5-3 with a variable number of 2-D PFDs. The higher the number of PFDs, the higher is the condition number. If ideal analytical PFD outputs are used, higher condition number has no relevance and higher order disturbance decoupling will be superior. However, the non-idealities of the PFD outputs even due to small residual errors in FEA simulation start to push the current sensing error higher. This is explained in detail in chapter 3.

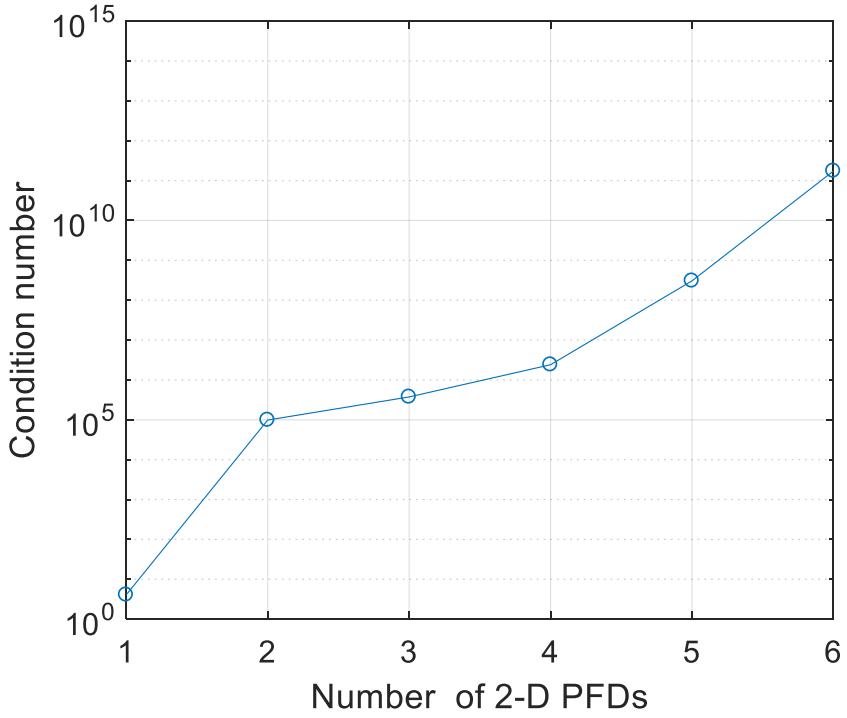

Fig. 5.5-4: Condition number of decoupling matrices used with a variable number of PFDs

5.6 Experimental Results of Disturbance Decoupling

An experiment is setup to evaluate the performance of disturbance decoupling. The experiment involves passing two-phase currents through two parallel wires which are 1 cm apart. The phase currents are generated using an AC power supply. Two 2-D PFDs are positioned close to these wires 3.5 mm apart to sense the current in them. A third wire with a current from a power amplifier is placed close to 8 cm away. The current in this wire is the source of disturbance magnetic field.

The experimental testing is started from the basics and gradually the level of complexity is increased. In the first test, a single 2-D PFD is used to sense the two phase currents. The disturbance current is zero and the second 2-D PFD is unused. Fig. 5.6-1 shows the PFD outputs,

the decoupled current and current sensing error for an arbitrarily selected current frequency and amplitude.

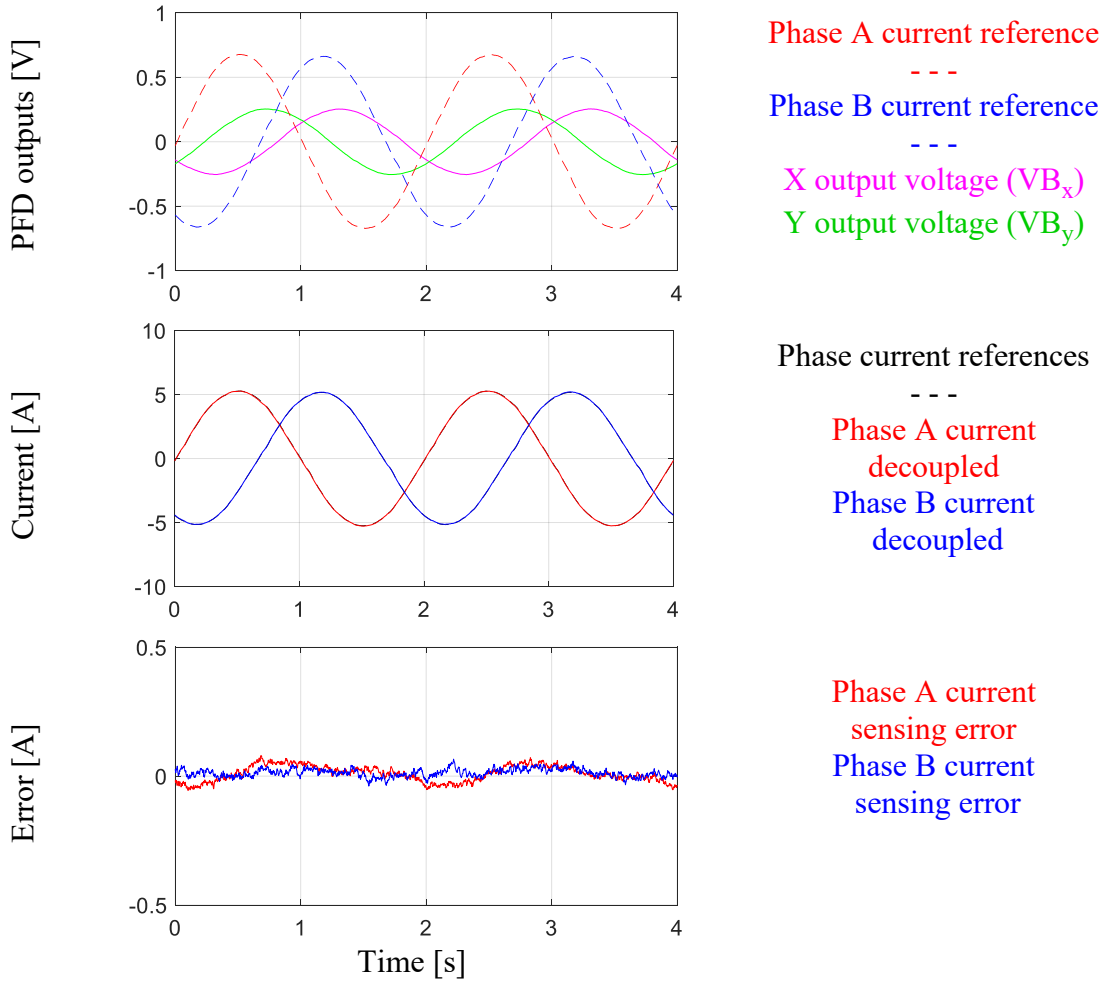

Test Conditions: f = 500 Hz

Fig. 5.6-1: Experimental decoupling and sensing of two-phase current with a single 2-D PFD in straight parallel wires

The same test is repeated at many different amplitudes of AC current. Fig. 5.6-2 shows the percentage RMS error as a function of RMS current. The current sensing error is very low due to careful calibration and sturdy setup. A higher current tends to have lower percentage error. This is because the impact of ambient disturbances and noise is minimized and SNR is improved.

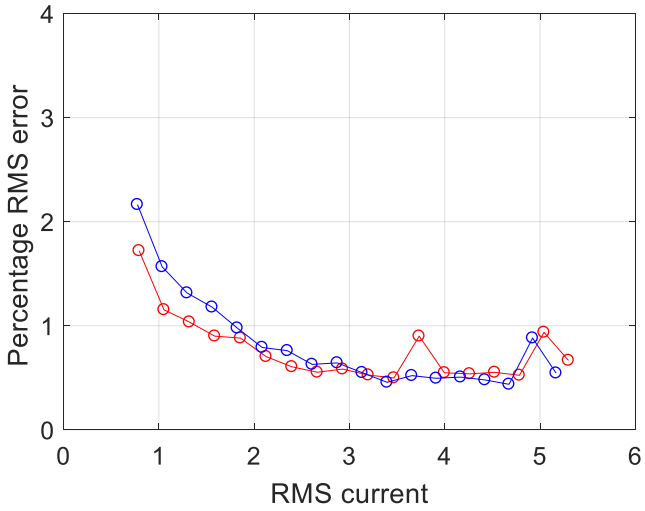

Phase A current sensing error Phase B current sensing error

Fig. 5.6-2: Experimental current sensing error as function of RMS current sensed with 2-D PFD 1

In these results, only one of the 2-D PFDs is used. The second 2-D PFD can also be used for sensing the two currents independently when the disturbance current is zero. Fig. 5.6-3 shows the current sensing error when the second 2-D PFD is used. The second PFD has a slightly higher error due to a higher condition number. However, the error is still very low.

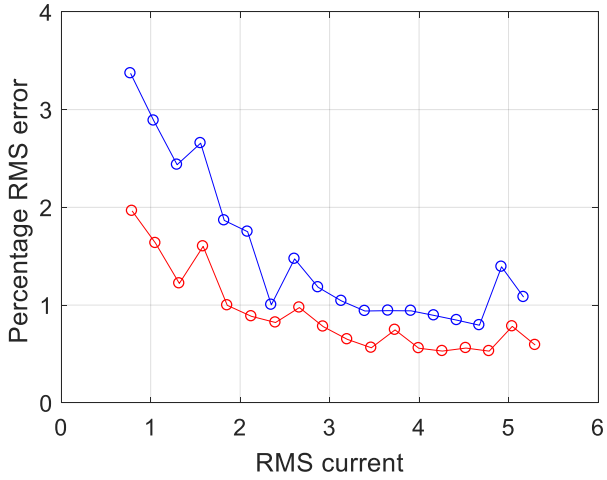

Phase A current sensing error Phase B current sensing error

Fig. 5.6-3: Experimental current sensing error as function of RMS current sensed with 2-D PFD 2

The mathematical model for sensing two currents with a single 2-D PFD is reiterated in (5.6-1). The experimental calibration is done using the direct calibration method.

$$\begin{bmatrix} C_{xa1} & C_{xb1} \\ C_{ya1} & C_{yb1} \end{bmatrix}\begin{bmatrix} I_a \\ I_b \end{bmatrix} = \begin{bmatrix} VB_{x1} \\ VB_{y1} \end{bmatrix} \tag{5.6-1}$$

$$\begin{bmatrix} C_{xa2} & C_{xb2} \\ C_{ya2} & C_{yb1} \end{bmatrix}\begin{bmatrix} I_a \\ I_b \end{bmatrix} = \begin{bmatrix} VB_{x2} \\ VB_{y2} \end{bmatrix}$$

The mathematical model of decoupling the disturbance which is modelled as a spatially homogeneous quantity is shown in (5.6-2). The first two columns of the coupling matrix are taken from (5.6-1). The inverse of the coupling matrix, i.e. the decoupling matrix has terms that lead to a differential signal of PFD outputs as described in sec. 5.4.

$$\begin{bmatrix} C_{xa1} & C_{xb1} & 1 & 0 \\ C_{ya1} & C_{yb1} & 0 & 1 \\ C_{xa2} & C_{xb2} & 1 & 0 \\ C_{ya2} & C_{yb2} & 0 & 1 \end{bmatrix}\begin{bmatrix} I_a \\ I_b \\ D_x \\ D_y \end{bmatrix} = \begin{bmatrix} VB_{x1} \\ VB_{y1} \\ VB_{x2} \\ VB_{y2} \end{bmatrix} \tag{5.6-2}$$

A test is conducted with phase A and B currents at 500 Hz with variable amplitudes, whereas the disturbance current is fixed at 1 A peak and 1kHz. The two 2-D PFDs detect a cross-coupled magnetic field from three sources. The PFD output signals are shown in Fig. 5.6-4. The extent of the 1kHz disturbance cross-coupled into 500Hz is clear in the distorted sinusoidal PFD outputs. The PFD signals are passed through the decoupling matrices to compute the current signals which are also plotted in Fig. 5.6-4. The decoupled current error plot shows that the disturbance decoupling using two PFD is significantly more successful in reducing the impact of disturbance in current sensing.

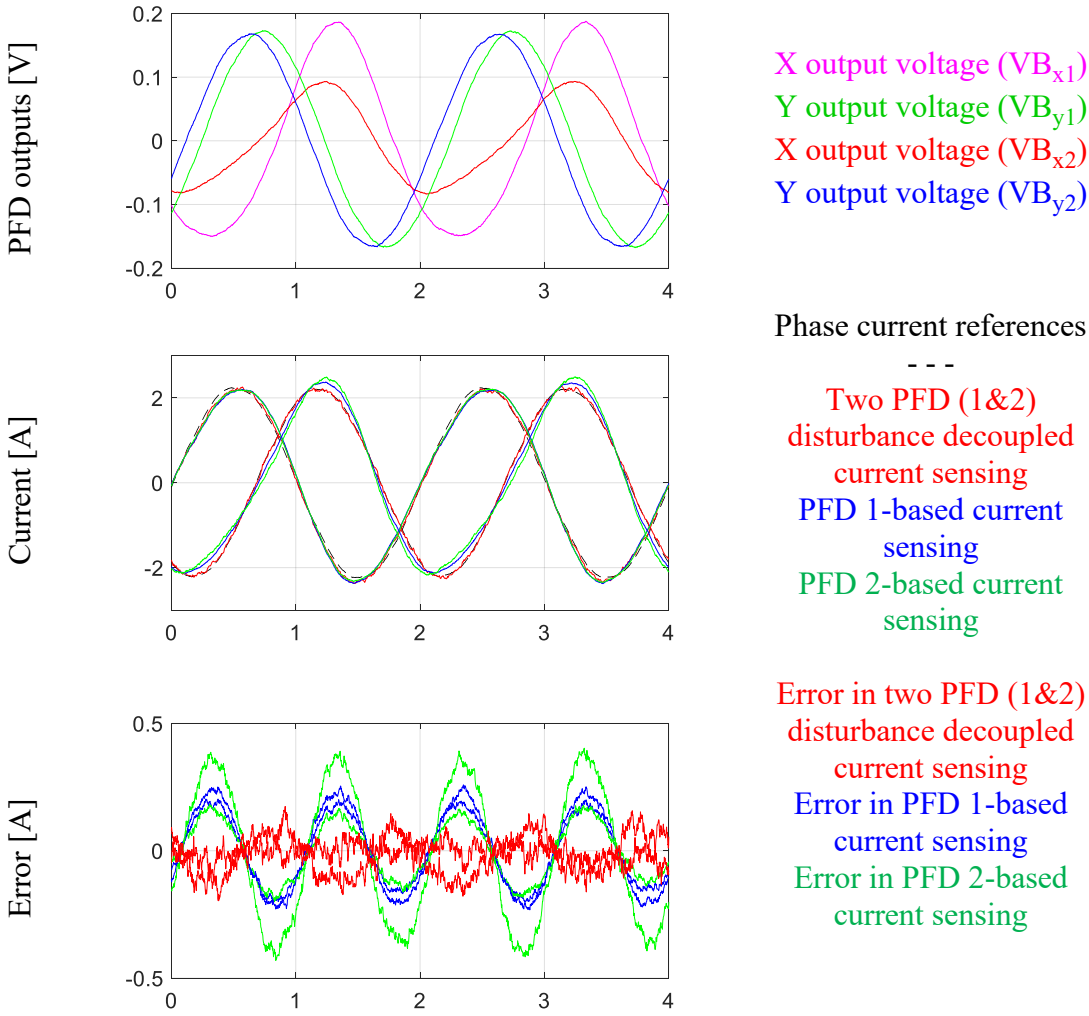

Test Conditions: f = 500 Hz

Fig. 5.6-4: Experimental decoupling and sensing of two-phase current with and without implementation of disturbance decoupling

The impact of disturbance magnetic field on current sensing is dependent upon its relative amplitude with respect to the magnetic field from the currents. Fig. 5.6-5 shows the percentage rms error in the decoupled current sensing as function of magnitude of the AC current. A higher amplitude of the magnetic field from the current being sensed naturally subdues the impact of disturbance magnetic field, thereby reducing the error. The most noticeable thing, in the plots in Fig. 5.6-5, is the utility of disturbance decoupling at lower currents when the disturbance magnetic

field might be relatively higher. However, at higher amplitudes of the sensed currents, the higher condition number of the disturbance decoupling and relatively lower magnetic disturbance reduce the advantage of disturbance decoupling.

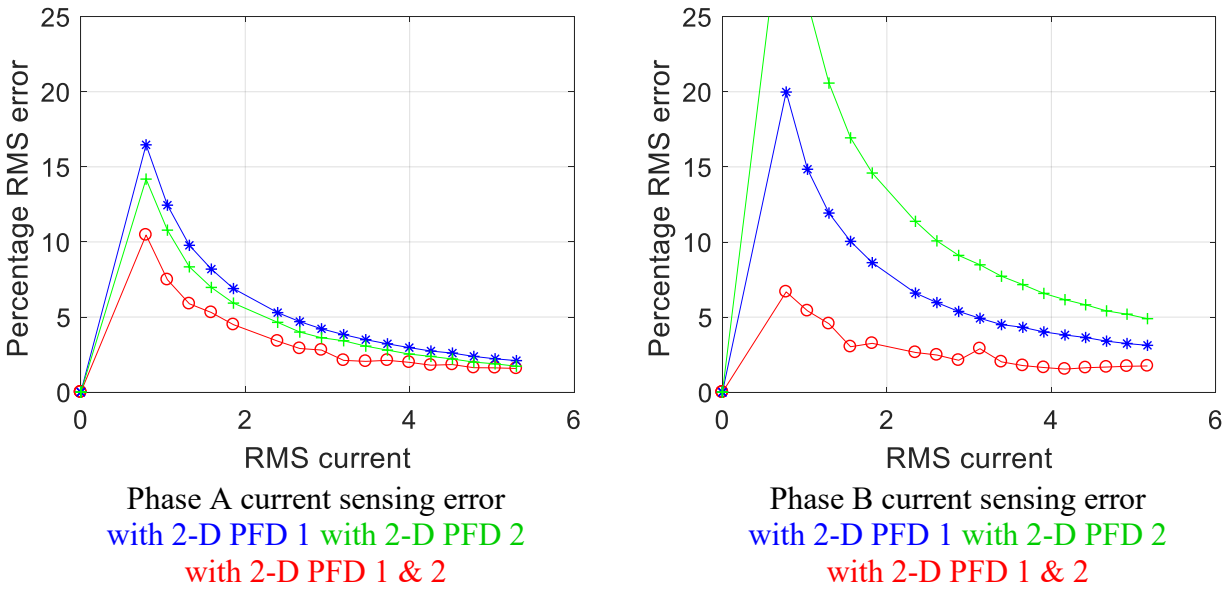

Fig. 5.6-5: Experimental current sensing error as function of RMS current sensed with 2-D PFDs

The key to disturbance decoupling lies in how well the disturbance is modelled over the locations of the PFDs. Based upon the analysis in sec. 5.2, the disturbance magnetic field is approximated as a spatially invariant quantity over the two PFDs in the above experiments. However, it is possible to do slightly better. If the exact ratio of disturbance incident upon the two PFDs is known, the disturbance can be fully decoupled in simulation. In practical, if there is any information about the direction from which the disturbance is originating and the relative position of the PFDs, the model of the disturbance over the two PFDs can be intuitively tweaked. For example, in the experiments above, it is known that the X-direction disturbance is originating from a source such that its incidence will be stronger on PFD 1 than PFD 2. Based upon this, the term to model the disturbance over PFD 2 reduced by 20% compared to the term for PFD 1. This

improves the model of the disturbance as seen by the two PFDs and reduces the current sensing RMS error as shown in Fig. 5.6-6.

$$\begin{bmatrix} Cxa1 & Cxb1 & 1 & 0 \\ Cya1 & Cyb1 & 0 & 1 \\ Cxa2 & Cxb2 & 0.80 & 0 \\ Cya2 & Cyb2 & 0 & 1 \end{bmatrix} \begin{bmatrix} Ia \\ Ib \\ Dx \\ Dy \end{bmatrix} = \begin{bmatrix} VBx1 \\ VBy1 \\ VBx2 \\ VBy2 \end{bmatrix} \tag{5.6-3}$$

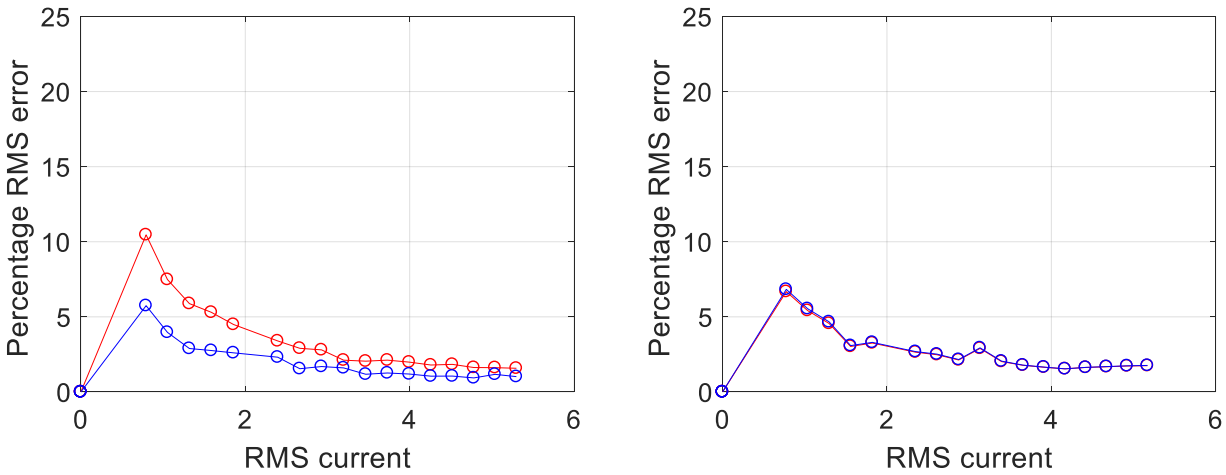

Fig. 5.6-6: Experimental current sensing error as function of RMS current sensed with 2-D PFDs with fine-tuned model of disturbance

5.7 Disturbance Rejection Using Magnetic Materials

The analysis in this section is idealized and does not account for frequency dependent effects and saturation. It is intended to show the possibility of the method and can be used as starting point for an engineering effort to minimize the impact of external disturbances using passive materials.

Magnetic materials can be used to divert the disturbance magnetic field from the PFDs. Typical magnetic shielding works by providing a lower reluctance path to the disturbance magnetic field. Fig. 5.7-1 shows an example of shielding a PFD from magnetic field from a disturbance

current using a core material. The magnetic field from the disturbance current is diverted through the path of lower reluctance that the core provides. The PFD on the inside of the core experiences virtually zero disturbance. The magnetic circuit model can be used to analytically study this shunting of disturbance fields.

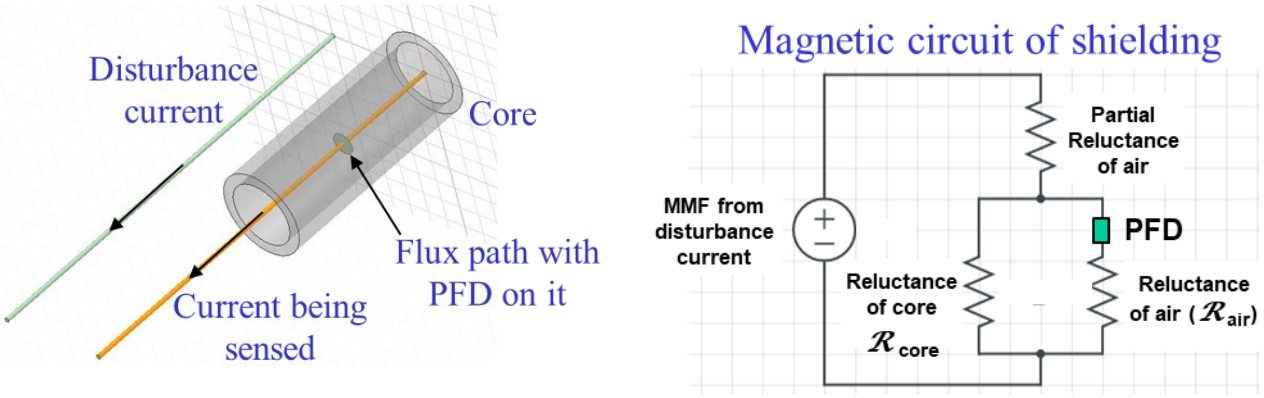

Fig. 5.7-1: Illustration and magnetic circuit of shielding the PFD from magnetic disturbance using magnetic core material

The magnetic circuit in Fig. 5.7-1 leads to (5.7-1) which show that magnetic flux from disturbance current is close to zero at the PFD due to core.

$$\text{MMF} = \mathcal{R}_{\text{total}}\,\Phi_{\text{total-dist}} \tag{5.7-1}$$

$$\Phi_{\text{total-dist}} = \Phi_{\text{air -dist}} + \Phi_{\text{core-dist}}$$

$$\Phi_{\text{air-dist}} = \Phi_{\text{total-dist}}\,\frac{\mathcal{R}_{\text{core}}}{\mathcal{R}_{\text{core}} + \mathcal{R}_{\text{air}}}$$

$$\text{Since } \mathcal{R}_{\text{core}} << \mathcal{R}_{\text{air}} \Rightarrow \frac{\mathcal{R}_{\text{core}}}{\mathcal{R}_{\text{core}} + \mathcal{R}_{\text{air}}} \Rightarrow \Phi_{\text{air-dist}} \Rightarrow 0$$

The magnetic flux from the current being sensed in the region surrounded by the core remains unchanged in ideal modelling using the circuit in Fig. 5.7-2. Due to this, the PFD is expected to sense the same field for a given current without core when the disturbance is zero.

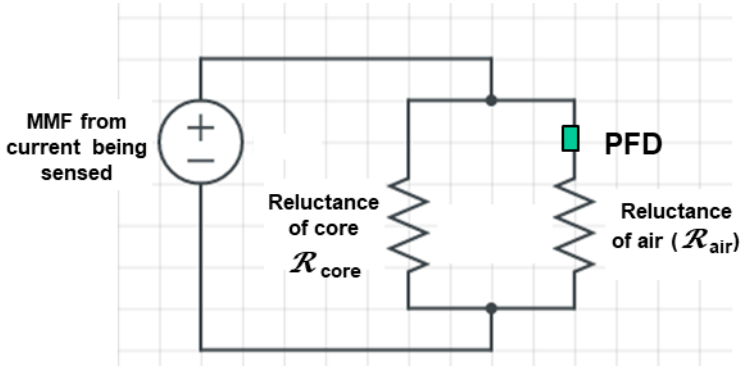

Fig. 5.7-2: Schematic of magnetic circuit for calculating magnetic flux from the current being sensed

The analysis is confirmed using an ideal FEA simulation at low frequencies. Fig. 5.7-3 shows four cases of magnetic flux density around the current being sensed and disturbance current. It is found that the presence and absence of core has no significant impact on the magnetic field in the region in the interior of the core close to the current. The core does determine if the external magnetic field from the disturbance current reaches its interior or not. The core provides a low reluctance path to the disturbance field which originates from its exterior, thereby preventing it from entering the region in the interior of the core. The FEA is run at quasi DC due to which the core is idealized and does not have eddy currents which will become important in real applications. As stated in the beginning of the section, engineering efforts will be required on a case by case basis to provide this sort of passive shielding. For example, saturation can be avoided by shielding all three-phases and eddy currents can be avoided by using a thin lamination core.

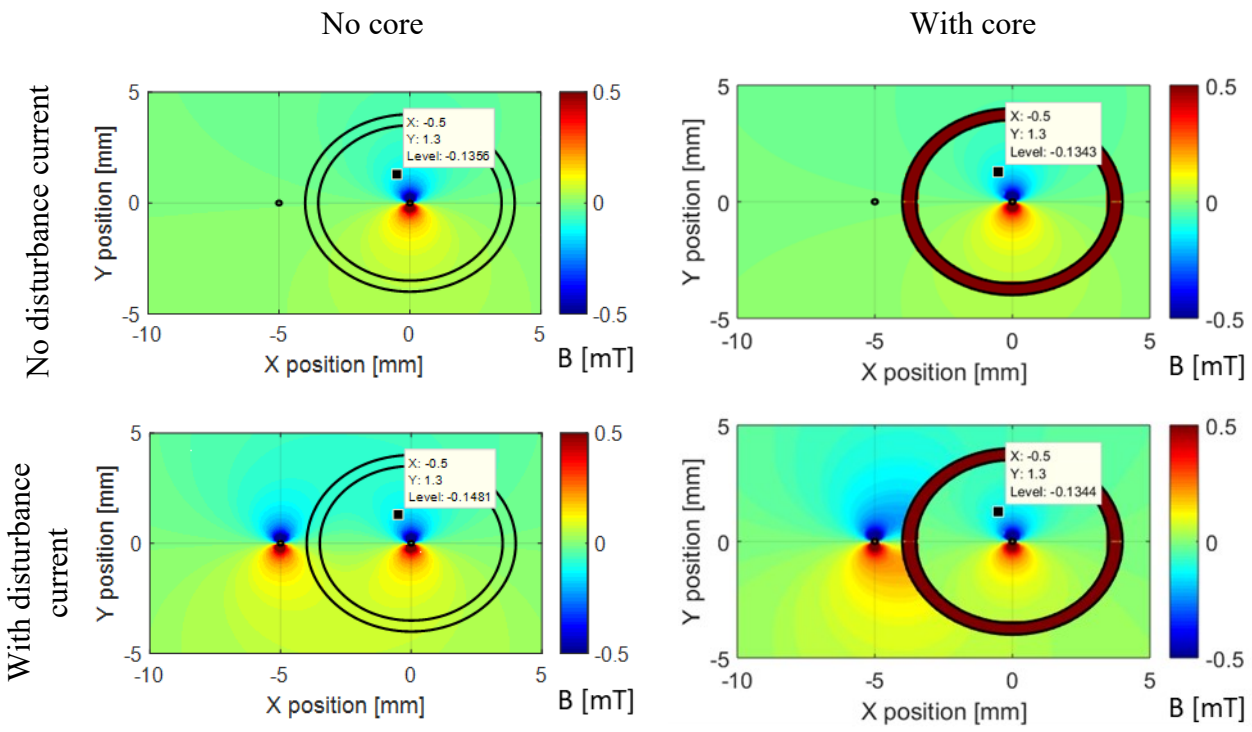

Fig. 5.7-3: Magnetic flux density around a wire carrying 1 A quasi-DC with and without disturbance and shielding

5.8 Experimental Results of Disturbance Rejection

The method of using a core to reject the disturbance magnetic field is tested experimentally. A 1-D GMR PFD is positioned on top of a busbar carrying 100Hz current. A second busbar with 500 Hz current is put a few centimeters above and parallel to the first busbar. Fig. 5.8-1 shows the test setup. The setup does not show the second core which is placed back-to-back to increase the length of the core. The core is a typical solid choke used in lab for high frequency noise filtering. It has a high permeability and is arbitrarily selected to demonstrate the disturbance rejection method.

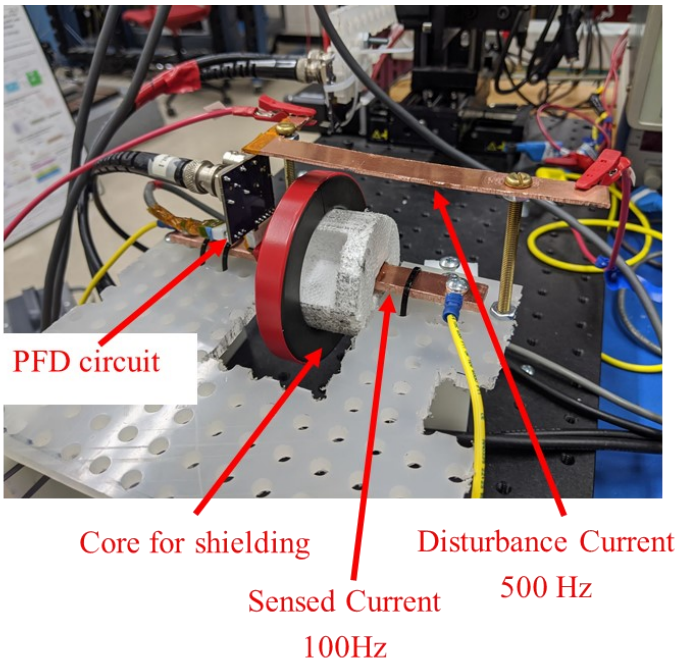

Fig. 5.8-1: Test set up of PFD-based current sensing with disturbance rejection using a core

Fig. 5.8-2 shows the results of sensing current in the busbar with the GMR PFD with and without the choke shielding. Clearly, the magnetic material in the choke rejects the disturbance from reaching the PFD making the PFD-based current sensing much more accurate.

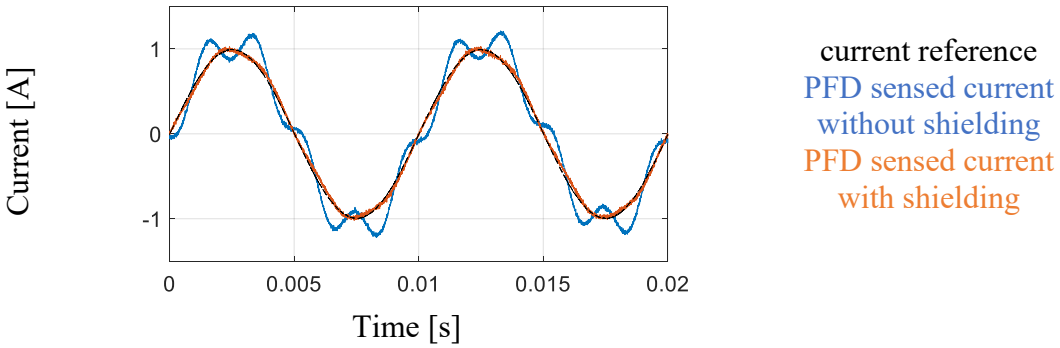

Test Conditions: f = 100 Hz with 500Hz disturbance

Fig. 5.8-2: Experimental PFD-based current sensing with disturbance rejection using magnetic core material

Since the disturbance signal is at 500 Hz and current signal is at 100Hz, the FFT of the PFD output can be used to analyze the disturbance rejection. Fig. 5.8-3 shows the FFT of the PFD output

with and without the shielding implemented. The presence of the shield reduces the signal content at 500 Hz to a very low level which improves the SNR from 5.2 to 33.9. Due to the non-ideality of the test setup, the signal content at 100 Hz is also reduced by 10% due to shielding. This is because choke radius is not large enough enabling the choke to interact with the magnetic field from sensed current. Ideally, the magnetic material should be positioned far enough that it does not interact with the field from the sensed current at the PFD location.

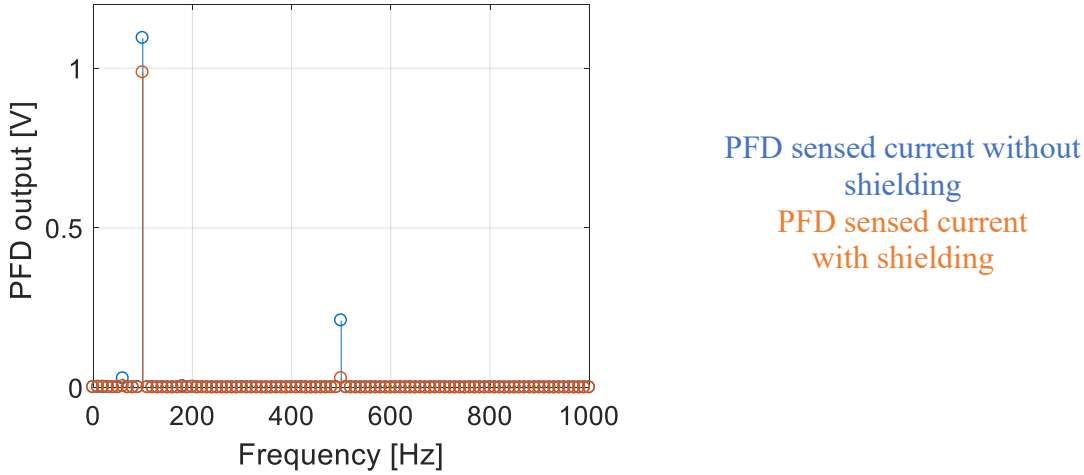

Fig. 5.8-3: FFT of PFD-based current sensing with and without disturbance rejection using magnetic core material

5.9 Summarizing Remarks

A concise summary of the chapter is available at its beginning. The conclusions and contributions for this chapter are available in the last chapter.

This chapter develops the methods to reduce the impact of disturbance magnetic field on multi-dimensional PFD based current sensing. As a first step to decoupling or rejection, the magnetic field disturbances around a current are analyzed analytically and their spatial properties are evaluated to model them. The spatial gradient of the magnetic flux density around a current is inversely proportional to the square of the distance from the current. Due to this, the magnetic field disturbance from an unknown source can be modelled as a function of X, Y, and Z positions of the PFDs used in the sensing system. Furthermore, it is shown via FEA simulation that if the AC or DC disturbance source is far enough, the magnetic disturbance can be approximated with zero spatial gradient and modelled as a constant and decoupled with one additional PFD.

This chapter uses FEA to prove that multi-dimensional magnetic disturbances with spatial gradients can be decoupled to an adequate level by increasing the order of their model with an N^{th} order disturbance model requiring $N+1$ additional PFDs. However, a higher number of PFDs leads to an increase in the condition number of the coupling matrix which exaggerates the uncertainties in the sensing. A zero order disturbance model with only one additional multi-dimensional PFD is shown experimentally to provide an adequate decoupling of disturbance in a real system.

Additionally, in this chapter, a method is developed via magnetic circuit modelling and FEA to use passive magnetic materials to provide a low reluctance path to the disturbance fields and prevent them from reaching the PFDs.

Chapter 6 Neural Networks for Magnetic Field Decoupling

This chapter develops neural networks as an alternative to physics-based field decoupling. Neural networks are developed and trained in Matlab using the built-in functions. The networks are designed to take cross-coupled X- and Y-direction fields detected by the PFD as inputs and compute the currents producing the fields. Neural networks are also evaluated for disturbance field decoupling in cases when there is a third current which is a source of disturbance and not used in the training. This chapter also investigates the physics-based model inherent in the operation of the neural networks as well as the limits of the network functionality.

The main purpose of this chapter is to explore the use of neural networks for extracting currents from cross-coupled fields from multiple sources.

Elements of this chapter have not been documented in technical papers yet.

6.1 Introduction to Neural Networks

Neural networks can be used for a variety of data fitting, pattern recognition, and classification applications. One of the most common uses of neural networks, that falls under the data fitting applications, is the mapping of input data points to target points. This is exactly what the decoupling matrices carry out in the cross-coupled field decoupling. Due to this, neural networks are used as a replacement for physics-based decoupling in this chapter.

A neuron is the basic unit of the neural network. It consists of the sum of weighted inputs that are passed through a non-linear function. Common non-linear functions include the logistic function, tanh function, and rectified linear unit (ReLU). A group of neurons, each with their own set of weights and bias, form a layer. Neural networks have three main types of layers, as shown

in Fig. 6.1-1. First is the input layer, which in this research is the PFD outputs. The input layer feeds into the hidden layers, in which the inputs are weighted and summed before passing through a non-linear function. There may be one or more hidden layers, where each successive layer is fed by the previous layer. The outputs of the final hidden layer are passed to the output layer. The number of hidden layers can be increased to go into the territory of deep learning. For this research, a three layer network with a single hidden layer is used based upon the Universal approximation theorem [74] which states that three layer network can approximate any function arbitrarily well with sufficient nodes in the hidden layer and appropriate weights.

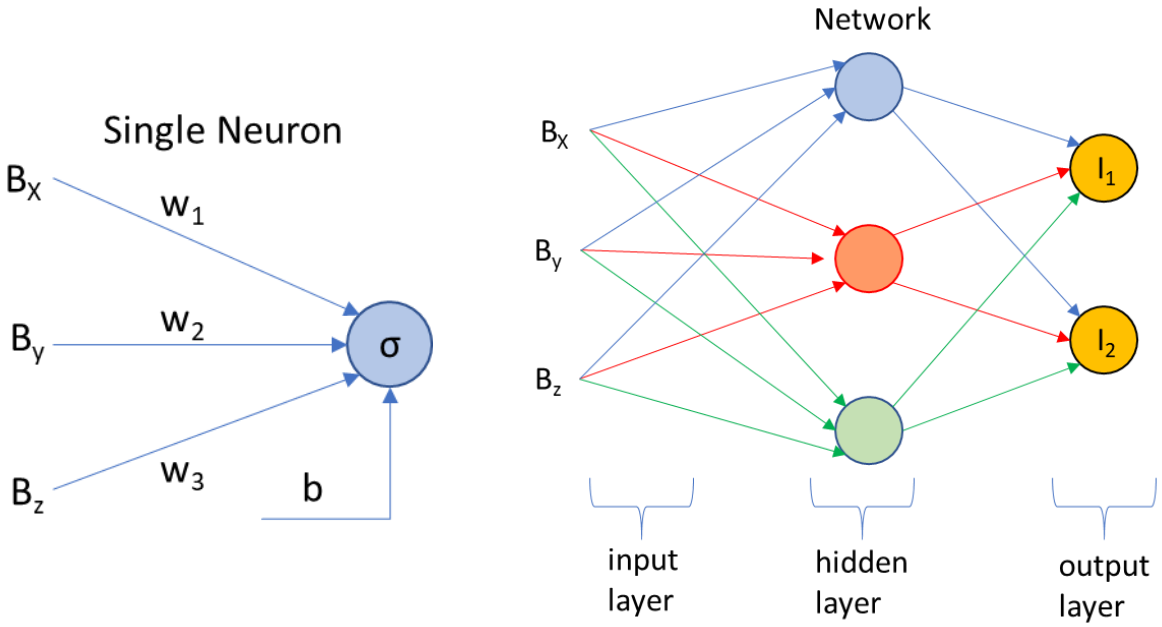

Fig. 6.1-1: Illustration of a neural network

Matlab is used to develop and train neural networks. It has built-in functions and documentation available for developing neural networks. Fig. 6.1-2 shows the neural network training tool on Matlab. The main selection parameter to setup the neural network is the number of neurons or the hidden nodes. The feedforward neural network, in which data flows from input to output only, is trained using the Levenberg-Marquardt (LM) optimization algorithm which is

highly recommended on the Matlab platform. The number of epochs, gradient and performance criteria are also selected to train the network to an appropriate level. The variable μ is a control parameter in the LM algorithm and is set to its default value of 1e10.

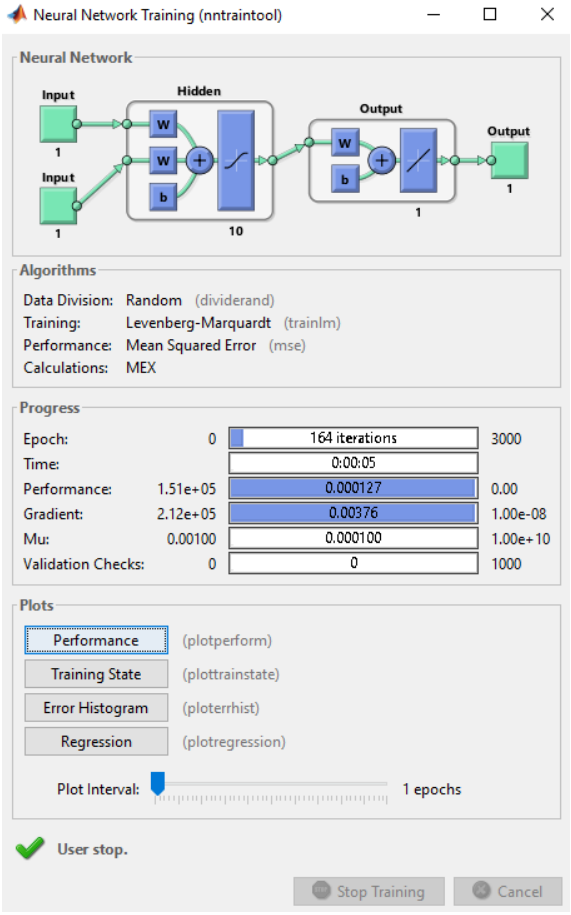

Fig. 6.1-2: Neural network training tool on Matlab

6.2 Neural Network-based 2-D Magnetic Field Decoupling

6.2.1 Analytical/Simulation Results

A simulation is set up to check the viability of neural network to decouple the cross-coupled multi-dimensional magnetic field into the currents producing it. In the 2-D simulation, two straight and parallel currents are placed at (0,0mm) and (5,0mm). A 2-D PFD is positioned at (6,3mm). Using the analytical Maxwell-Amperes law, the magnetic field is computed at the PFD location

for the many different combinations of the two currents. The known current and magnetic field information is used to train neural network. Two neural networks are trained, one for each current. Although, it is entirely possible to have one neural network output both currents, in this section networks were trained with a single output. Fig. 6.2-1 shows the pictorial representation of the network with X and Y-direction field input and current output. The training time for neural network depends on the number of neurons and training data set. In this case, 10 neurons are used with a small training data set of 25500 points. The network trains to a reasonable accuracy in less than five minutes.

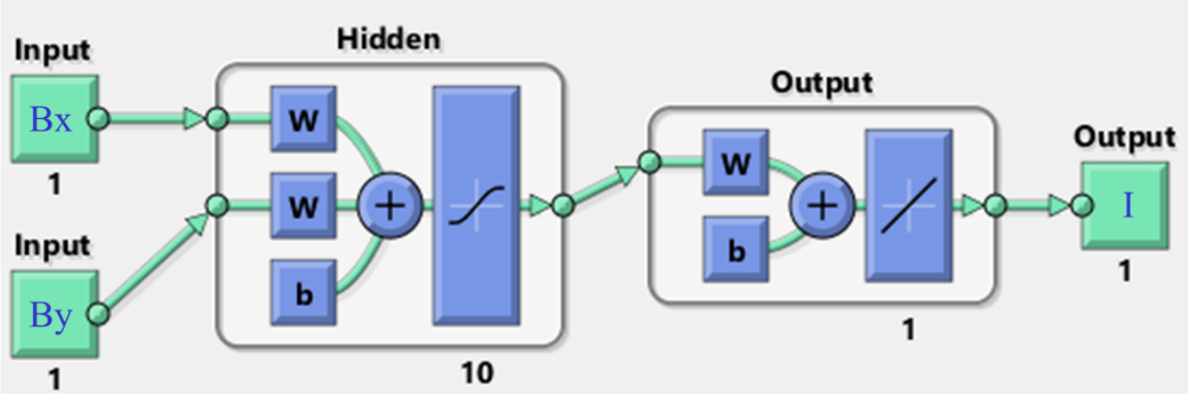

Fig. 6.2-1: Feedforward neural network on Matlab for 2-D field decoupling

The trained neural network is used to decouple the cross-coupled fields from the two currents. Fig. 6.2-2 shows the test case with 8 A phase A and B currents. The X and Y magnetic field (or the PFD output voltage) is inputted into the neural networks which output the currents. The error signal with a maximum value of under 0.01 A shows that neural networks has a very good performance.

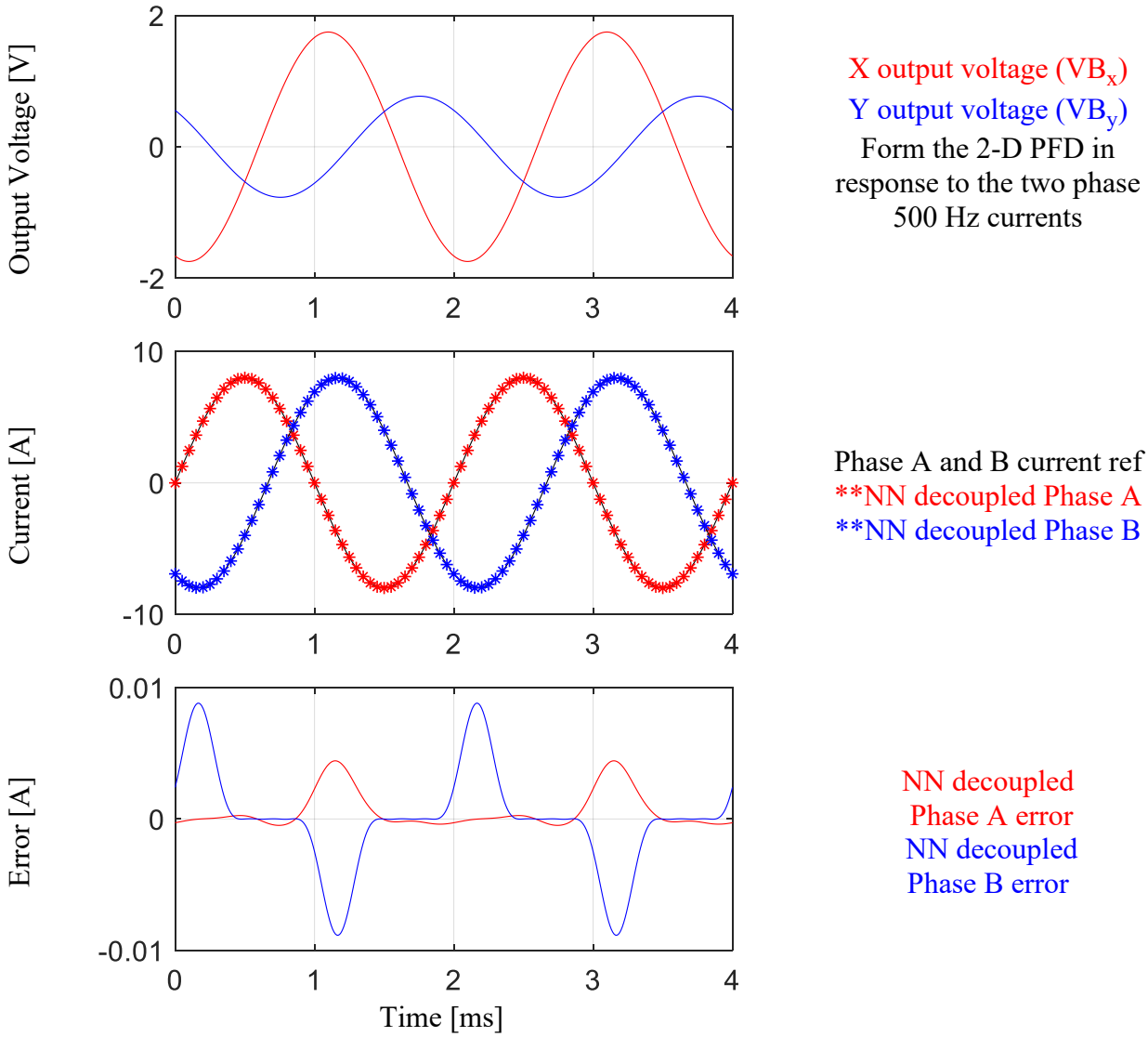

Fig. 6.2-2: Neural network-based 2-D field decoupling on a simulated data set

The neural network does not require the currents to have same amplitude or frequency to work. Fig. 6.2-3 shows the currents decoupled with neural network overlaid on the reference current. One current is 0 Amp DC whereas the other one is 8 A but with twice the frequency used in training.

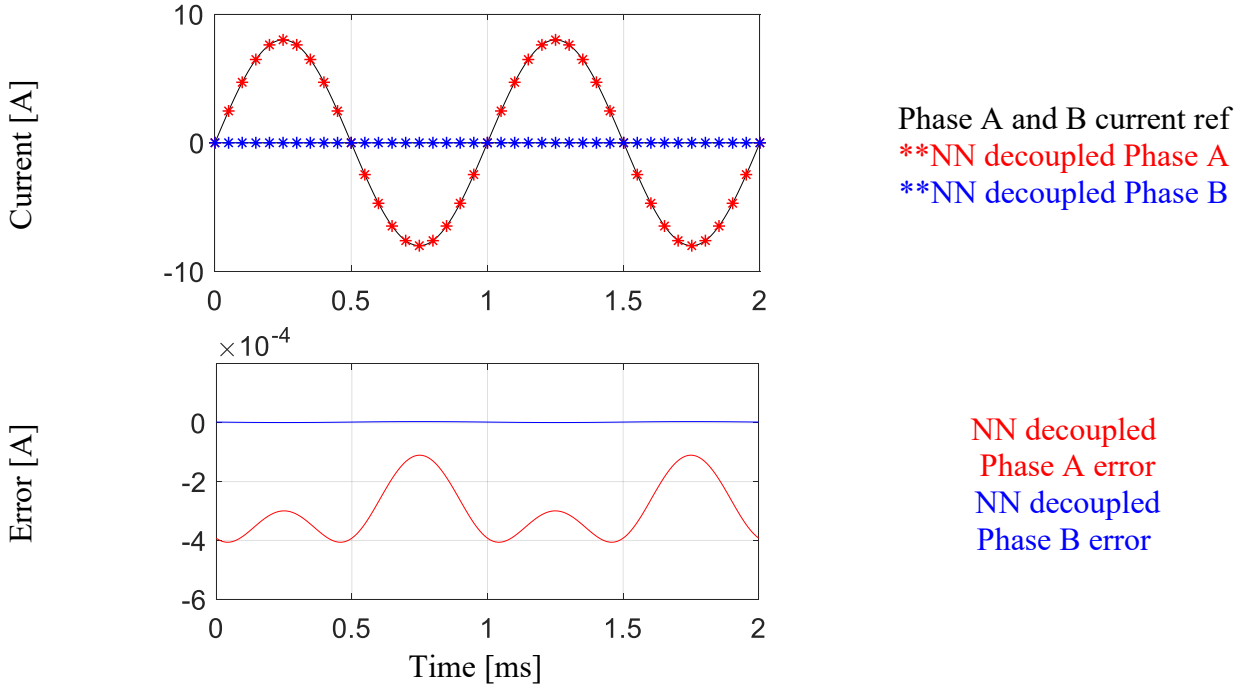

Fig. 6.2-3: Neural network-based 2-D field decoupling on unbalanced simulated data set

Furthermore, it is important to verify that the neural network is actually mimicking the physics-based decoupling. One way to check this is to compare physics-based and neural network-based decoupled currents for non-ideal situations. Fig. 6.2-4 shows the decoupled currents when there is a random disturbance added to the system. The physics-based and neural network-based decoupling have the same response. This shows that due to the initial training, the neural network tuned its weights and biases to replicate physics.

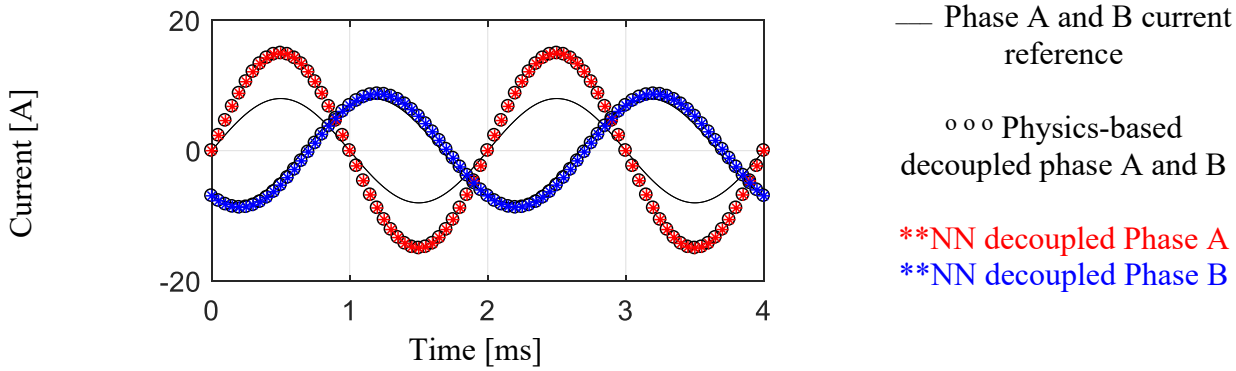

Fig. 6.2-4: Neural network-based decoupling on simulated data set with superimposed disturbance

6.2.2 Experimental Results

The test set up in sec. 5.6 in chapter 5 is used to experimentally evaluate the performance of a neural network-based 2-D field decoupling. The setup has two currents and two 2-D PFDs. There is no disturbance in the system due to which only one of the 2-D PFD is needed to sense both currents. The 2-D PFD is positioned 4mm above and 2mm to the right of first current. The second current is about 1 cm right of the first current. The three-phase AC power supply is used to supply the two currents.

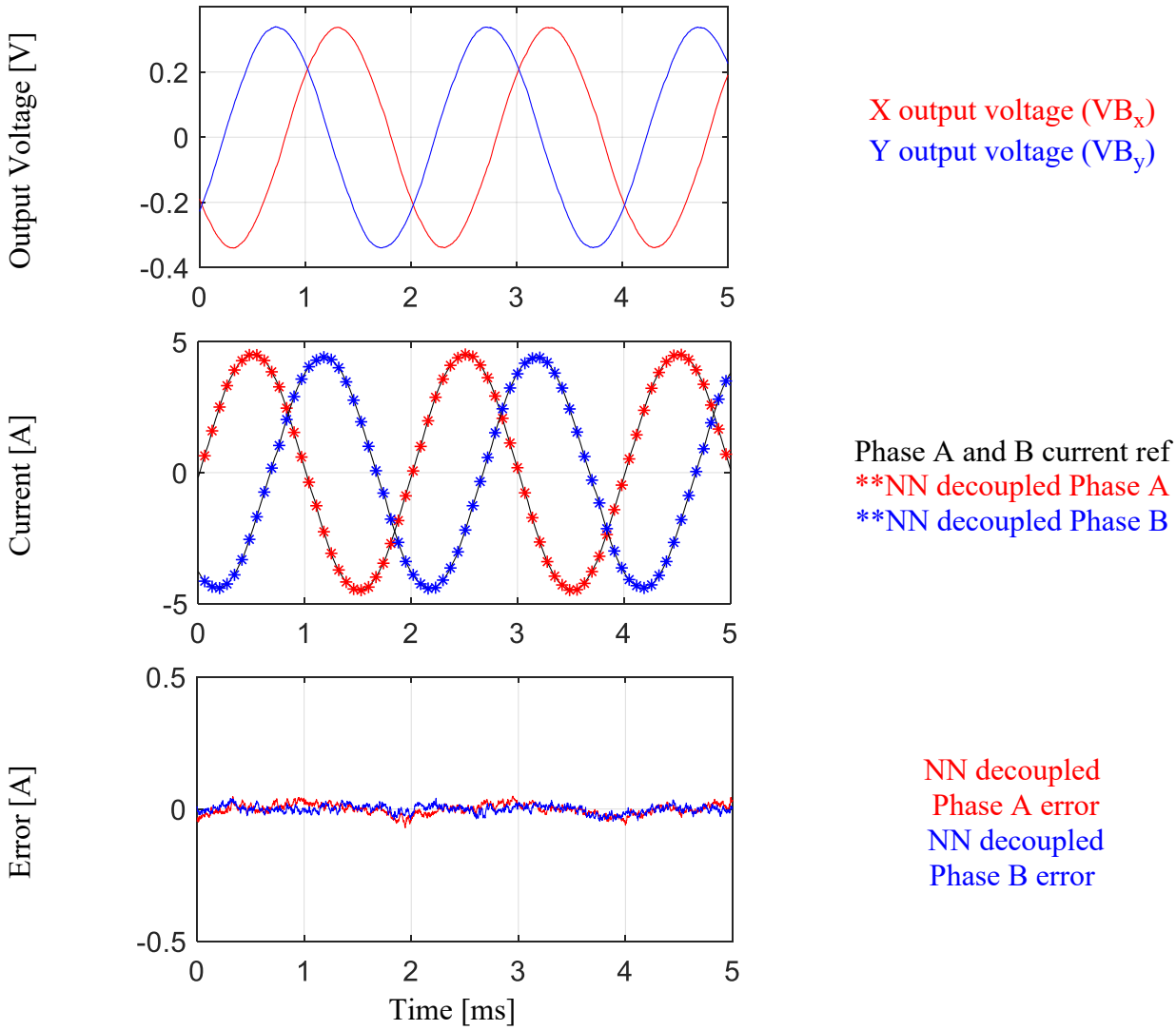

Fig. 6.2-5: Neural network-based 2-D field decoupling on experimental data

The neural network is trained by collecting the X and Y PFD outputs and current measurements at fifteen different amplitudes. The frequency of the currents is kept constant in the training data which is used in Matlab to train the neural network using the same settings as the simulation described in sec. 6.2.1. The performance of the neural network is tested by inputting it with X and Y PFD outputs for a set of currents not used in the training. Fig. 6.2-5 shows that the neural network is able to decouple PFD outputs into the currents producing it with an RMS percentage error of under 0.65% which is comparable to using physics-based decoupling in for the same setup.

To check the neural network performance on experimental data more thoroughly, another data set in which one of the currents is zero is shown in Fig. 6.2-6. The RMS error is slightly higher than the steady state case but is still under 1%

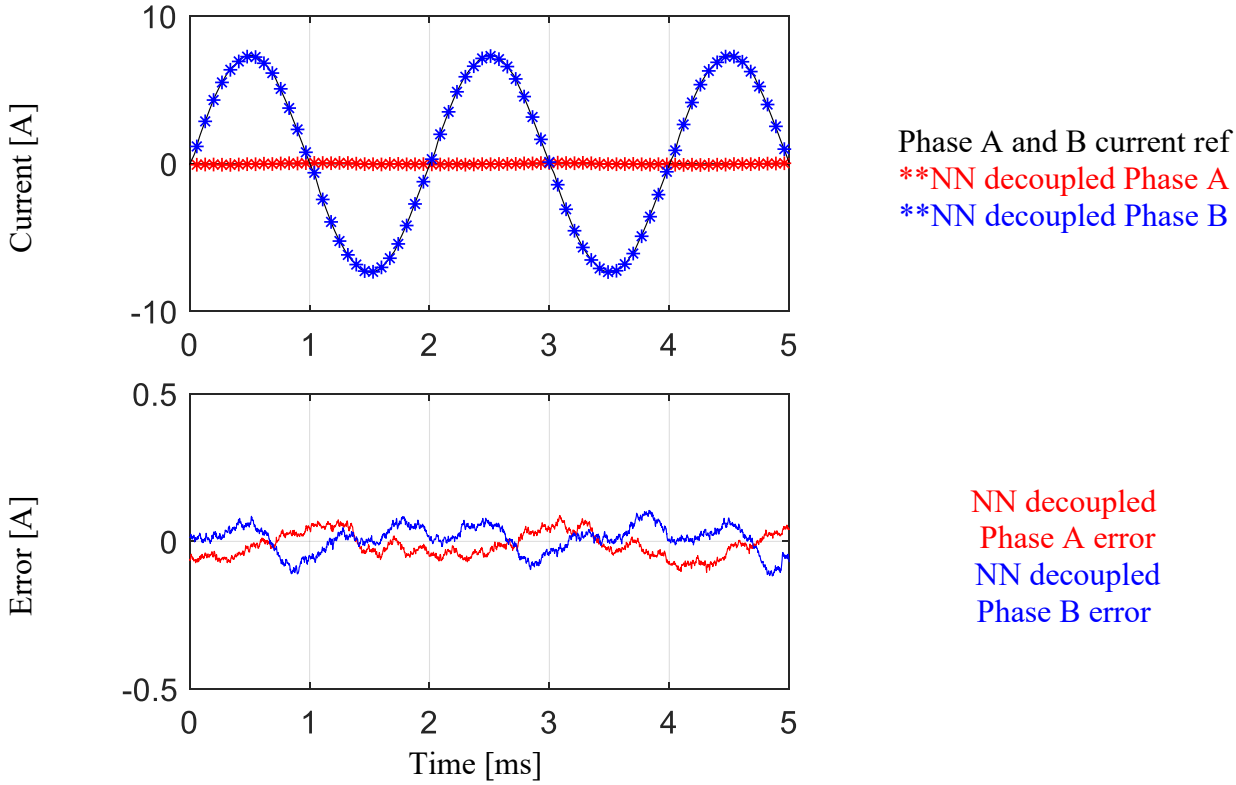

Fig. 6.2-6: Neural network-based 2-D field decoupling on unbalanced experimental data set

In this chapter, the neural network-based decoupling is done offline. It is computationally intensive due to the higher number of computations for current calculations. However, with the processor improvements it can become more relevant and usable in the next few years.

6.3 Neural Network-based Disturbance Decoupling

In the last section, the neural networks were used to decouple the 2-D cross-coupled magnetic fields into the two currents producing it. The training of neural network requires the knowledge of the actual current references, however, once the training is complete, the PFD outputs can be decoupled reliably by the network.

The method of using neural networks to decouple the cross-coupled magnetic fields can be extended to decouple the disturbance magnetic fields. The primary defining factor for disturbance decoupling is that the disturbance magnetic field originates from a source about which nothing is known. Due to this, there is no reference value available for disturbance, the way there is for the currents being measured. However, neural networks can be trained to decouple the disturbance and output only the currents for which it is trained using the actual current information.

Physics-based decoupling requires involved calibration of matrices using the knowledge of field source (which are electrical currents in this application). Unlike the physics-based decoupling, neural networks have no issue with decoupling cross-coupled fields to output only the currents for which they are trained using references. In other words, neural network-based decoupling matrix can be non-square because it does not require matrix inverse unlike physics-based techniques in chapter 3.

6.3.1 Analytical/Simulation Results

In an analytical simulation, there are three straight and parallel currents and two 2-D PFDs at the positions shown in Fig. 6.3-1. Currents A and B are to be sensed, whereas the third current is

the source of disturbance and no information about it is used in training the neural network. This disturbance has a non-zero spatial and time gradient. The reason for using two PFDs instead of one is to provide enough degrees of freedom to the decoupling system which is effectively trying to measure four quantities, two currents and X and Y disturbances. The measured disturbance is not outputted since there is no training for it.

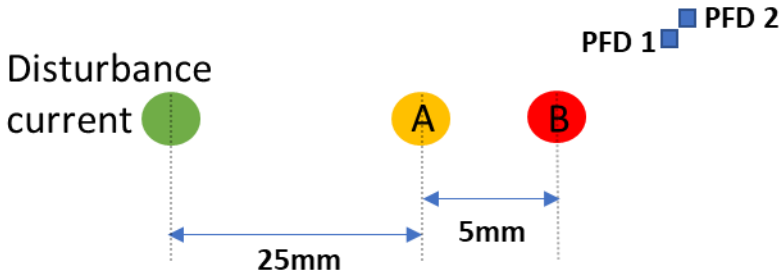

Fig. 6.3-1: Illustration of currents and PFDs used in the neural network-based decoupling

The matlab-based pictorial representation of the neural network is shown in Fig. 6.3-2. The network takes the X and Y field at the two PFD locations as input to 100 neurons or nodes in the hidden layer. This network is set up to output both currents. The training of the network involves inputting fields generated by hundreds of different combinations of currents A and B as well as constant amplitude AC disturbance current. These fields are mapped to the known values of currents A and B.

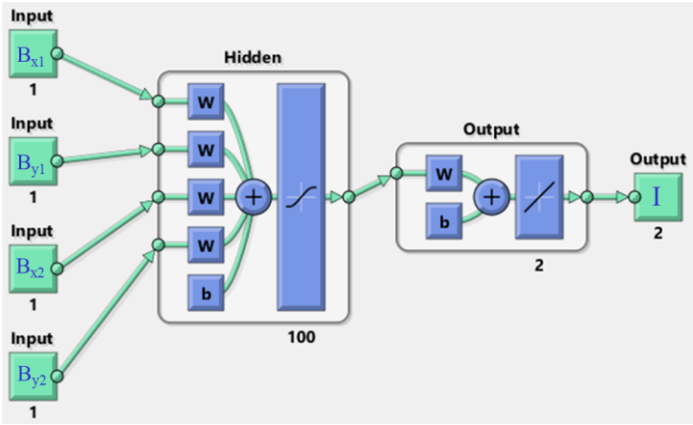

Fig. 6.3-2: Neural network on Matlab for disturbance decoupling

Fig. 6.3-3 shows the neural network-based decoupling of the two currents when 50 A 500 Hz AC disturbance current is also flowing. The neural network-based decoupling leads to a maximum error of under 1%. With more training, this error can be further reduced. On the other hand, the tradition physics-based techniques of decoupling have a much higher error. Using a single 2-D PFD to sense two currents in the presence of a much stronger disturbance current leads to a maximum error of 174%, whereas the two 2-D PFD-based zero order disturbance decoupling which approximates the disturbance as a spatially homogenous quantity has a maximum error of 25%. It must be noted that in this example the disturbance current is more than six times stronger than the currents being sensed due to which physics-based decoupling has such a high error. This is only done to show the robustness of neural network for disturbance decoupling.

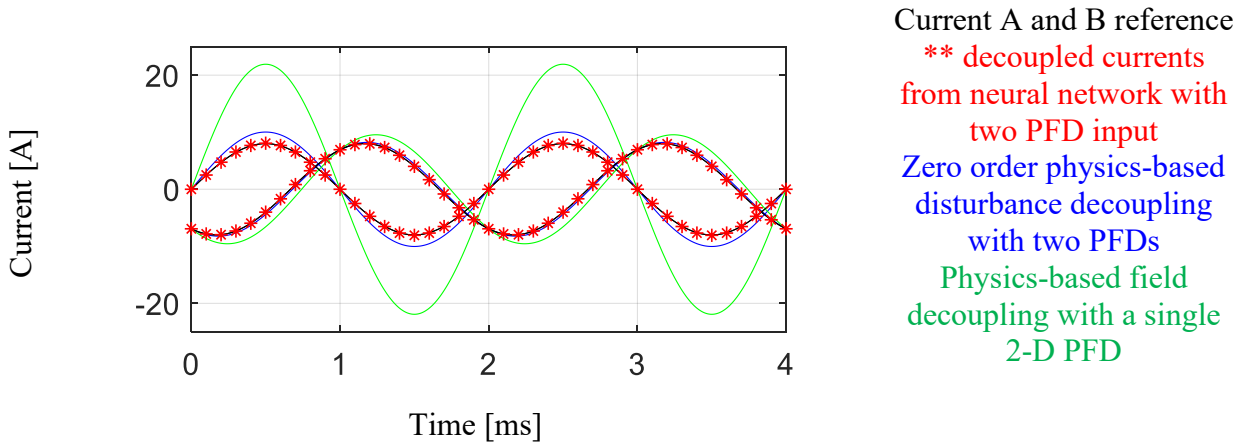

Fig. 6.3-3: Neural network-based disturbance decoupling on simulated data

The neural network is successful in decoupling the disturbance irrespective of its amplitude and frequency. Fig. 6.3-4 shows the decoupling performance of the three approaches with 10 A 1kHz disturbance current. The neural network-based decoupling has a maximum error below 0.2%. In this example the two PFD-based disturbance decoupling also performs well since the amplitude of the disturbance is much lower.

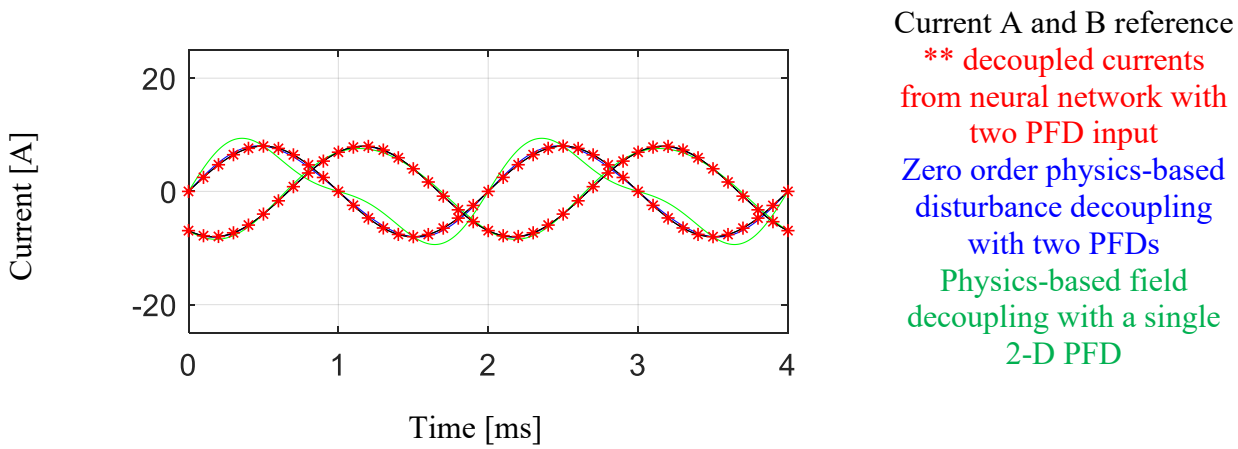

Fig. 6.3-4: Neural network-based disturbance decoupling on simulated data

6.3.2 Limits of neural network-based decoupling and comparison with physics-based decoupling

It is important to understand the functionality and the reason behind the consistent performance of the neural network in terms of disturbance decoupling and the limits of its functionality. This process also gives insight into how the neural network is functioning. At the simplest level, the functioning of the neural network with two 2-D PFD inputs and two current outputs can be modelled using (6.3-1).

$$\begin{bmatrix} D_{xa1} & D_{ya1} & D_{xa2} & D_{ya2} \\ D_{xb1} & D_{yb1} & D_{xb2} & D_{yb2} \end{bmatrix} \begin{bmatrix} VB_{x1} \\ VB_{y1} \\ VB_{x2} \\ VB_{y2} \end{bmatrix} = \begin{bmatrix} I_a \\ I_b \end{bmatrix} \tag{6.3-1}$$

The model is different from the physics-based methodology in chapter 3 and 4 because of the non-square nature of decoupling matrix. Physics-based decoupling until now has always had a square coupling and decoupling matrix for calibration and invertibility as shown in (6.3-2) as an example.

$$\begin{bmatrix} C_{xa1} & C_{xb1} & C_{xc1} & C_{xd1} \\ C_{ya1} & C_{yb1} & C_{yc1} & C_{yd1} \\ C_{xa2} & C_{xb2} & C_{xc2} & C_{xd2} \\ C_{ya2} & C_{yb2} & C_{yc2} & C_{yd2} \end{bmatrix} \begin{bmatrix} I_a \\ I_b \\ I_c \\ I_d \end{bmatrix} = \begin{bmatrix} VB_{x1} \\ VB_{y1} \\ VB_{x2} \\ VB_{y2} \end{bmatrix} \tag{6.3-2}$$

$$\begin{bmatrix} D_{xa1} & D_{ya1} & D_{xa2} & D_{ya2} \\ D_{xb1} & D_{yb1} & D_{xb2} & D_{yb2} \\ D_{xc1} & D_{yc1} & D_{xc2} & D_{yc2} \\ D_{xd1} & D_{yd1} & D_{xd2} & D_{yd2} \end{bmatrix} \begin{bmatrix} VB_{x1} \\ VB_{y1} \\ VB_{x2} \\ VB_{y2} \end{bmatrix} = \begin{bmatrix} I_a \\ I_b \\ I_c \\ I_d \end{bmatrix} \rightarrow$$

$$\begin{bmatrix} D_{xa1} & D_{ya1} & D_{xa2} & D_{ya2} \\ D_{xb1} & D_{yb1} & D_{xb2} & D_{yb2} \end{bmatrix} \begin{bmatrix} VB_{x1} \\ VB_{y1} \\ VB_{x2} \\ VB_{y2} \end{bmatrix} = \begin{bmatrix} I_a \\ I_b \end{bmatrix}$$

Although after inversion of the 4x4 square coupling matrices and omitting the last two rows, the decoupling matrix does give the same equation as the physics-based decoupling, this omission of rows is not typically done due to the unused degrees of freedom on the input as well as due to inversion and calibration issues. The calibration issues are discussed in detail in chapter 3.

On the other hand, a neural network does not require an exact match of input and output degrees of freedom or a square matrix. The training of neural network is equivalent to the calibration process in physics-based decoupling. However, the training algorithm uses large data sets with multiple operating points to optimize the network weights, that in the end follow the physics without the typical problems of calibration.

The training of neural network for disturbance decoupling identifies the existence of superimposed magnetic field from a disturbance current and calibrates its weights to account for it. The disturbance current is decoupled irrespective of its amplitude and frequency. However, the caveat comes in when the disturbance current has moved. The terms in the first two rows of the

decoupling model of the neural network, although only used to compute the two currents, are dependent on the location of disturbance current. This becomes clearer if the mathematical system is followed from the coupling matrix in (6.3-2).

Fig. 6.3-5 shows the decoupling of currents in the setup from sec. 6.3.1 with disturbance current of 50 A 500 Hz but this time the disturbance current is moved by 10 mm in both X- and Y-direction from its original position used in training. The neural network-based decoupling, which inadvertently relies on the identification of disturbance current, has a much higher error. In fact, the physics-based zero order disturbance decoupling has the lowest error from the three approaches.

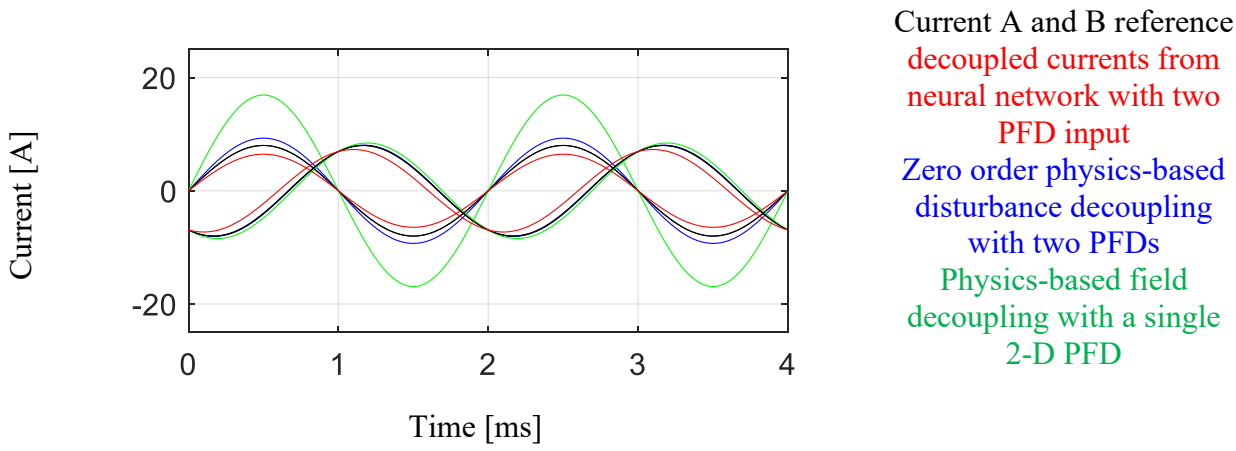

Fig. 6.3-5: Neural network-based disturbance decoupling on simulated data

Neural networks perform well to decouple disturbances from sources that are relatively stationary, however, as the source of disturbance moves, the weights in neural network become inaccurate and decoupling error develops. There is reason to believe that if the relative motion of the disturbance source is repeatable, with appropriate training, neural networks can still be used.

The experimental testing of neural networks for disturbance decoupling is not shown due to the scope of this work. The train of neural network requires hundreds of thousands of data points at hundreds of operating conditions. Since neural networks are not the primary focus of this work,

the tedious process of training is not completed. However, the tests done with small data sets did show the trend that neural networks with appropriate training can decouple disturbances in experiments.

6.4 Summarizing Remarks

A concise summary of the chapter is available at its beginning. The conclusions and contributions for this chapter are available in the last chapter.

In this chapter, feedforward neural networks, which have been used in the literature for various linear and non-linear modelling applications are trained to model and map the multi-dimensional cross-coupled field input to current output. After adequate training, the neural network-based field decoupling gives identical results as physics-based decoupling.

The chapter shows that the neural networks can also be used to decouple the magnetic disturbance from unknown sources because there is no matrix inverse calculation. Further investigation shows that the neural network-based disturbance decoupling identifies the disturbance current without any reference from it in the training data. In order for the neural network to decouple the disturbance successfully, the disturbance current needs to be at a fixed position.

Chapter 7 Power Module Electromagnetic Analysis for 2-D PFD-based Current Sensing

This chapter investigates the multi-dimensional field shaping of a three-phase full-bridge IGBT power module and identifies the components that need to be redesigned for high bandwidth PFD-based current sensing. Evaluation of 2-D PFD-based current sensing in a commercial power module is used as basis for recommending design changes to the terminals, DBC-to-terminal interconnects and the baseplate for field shaping. A power module design for 2-D PFD-based integrated current sensing is proposed at the end of this chapter.

The main purpose of this chapter is to demonstrate the viability of integrated sensing and propose the design changes required for current sensing using multi-dimensional field decoupling inside the highly cross-coupled, energy dense and fast switching power modules.

Elements of this chapter are also documented in [64], [116] and [118].

7.1 Three-Phase Full Bridge IGBT Power Module

Most three-phase full-bridge IGBT power modules have a similar design as described in chapter 1. A commercial Fuji power module [88] with a typical design is used in this chapter, hence the analysis and conclusions can be applied to most commercial power modules.

The power module used for field analysis and integrated current sensing has Si power switches and comes under the brand name of 6th Generation V series M633 package. Analysis of this module can be applied to many current and future Si and SiC power modules. The module is rated for 150A 1200V and can be used as a three-phase inverter. The baseplate is 122x62mm and

the height of the package is 21mm. This power module has solder pin terminals and its interconnects are bondwires. Fig. 7.1-1 shows the power module.

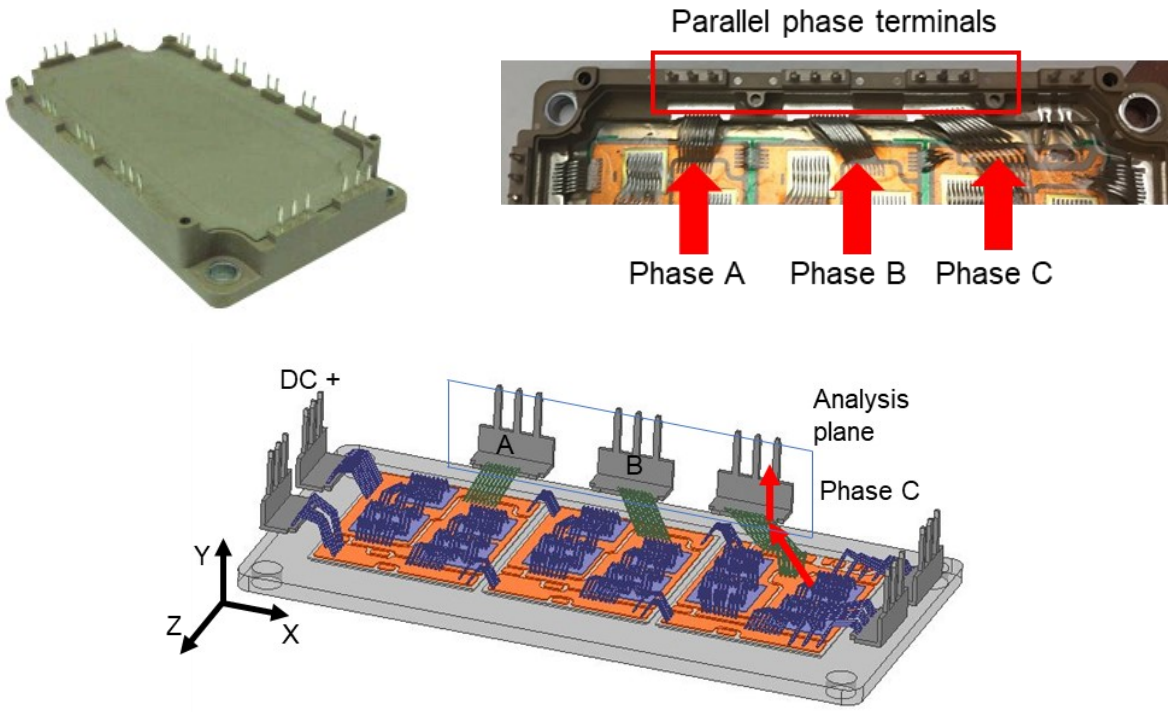

Fig. 7.1-1: Three-phase full-bridge power module for integrated current sensing

The magnetic field shaping of the power module is analyzed using electromagnetic FEA. The most accessible locations in the power module with high flux density and bandwidth are closest to the output phase terminals. Phase terminals are also appropriate locations for field detection for current sensing since no matter the switching state, the path of the phase current in the module will always be through the terminal. Fig. 7.1-1 shows the phase currents flow into the terminal via DBC-to-terminal bondwires. Due to the path of the phase currents, there is a 3-D magnetic field in the region close to the terminal. Magnetic fields in all three dimensions need to be analyzed.

7.2 Magnetic Field Analysis of the Power Module

The flux densities in X-, Y- and Z-directions and 1-D FBWs are shown in Fig. 7.2-1 and Fig. 7.2-2 on the analysis plane shown in Fig. 7.1-1. Since all the phase terminals are very similar, the

analysis in this section is limited to phase C current injection only. Unlike the work in [X], there are no other current paths. The cross sections of all the terminals are shown as a geometric reference. The X and Z field have relatively better regions of FBW as well as a higher flux density. The power module has limited regions of high FBW due to skin and proximity effects in the DBC, terminals and baseplate. Most of the high FBW region is above 12 mm Y position where the lid of the module casing lies. Y positions up to 20 mm are shown here since that is where the pin terminals end.

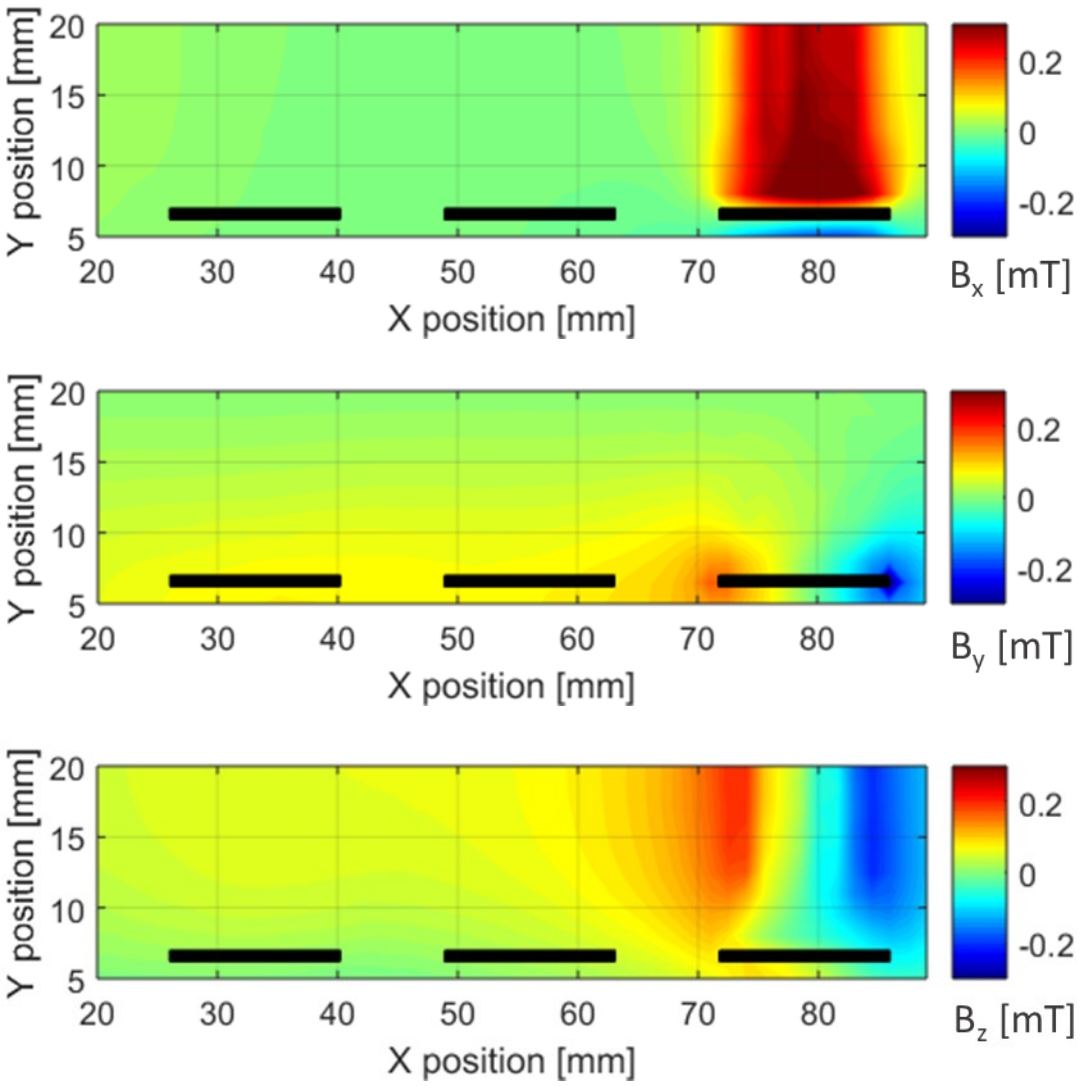

Fig. 7.2-1: X, Y, and Z flux density on analysis plane for 6A quasi-DC phase C injection

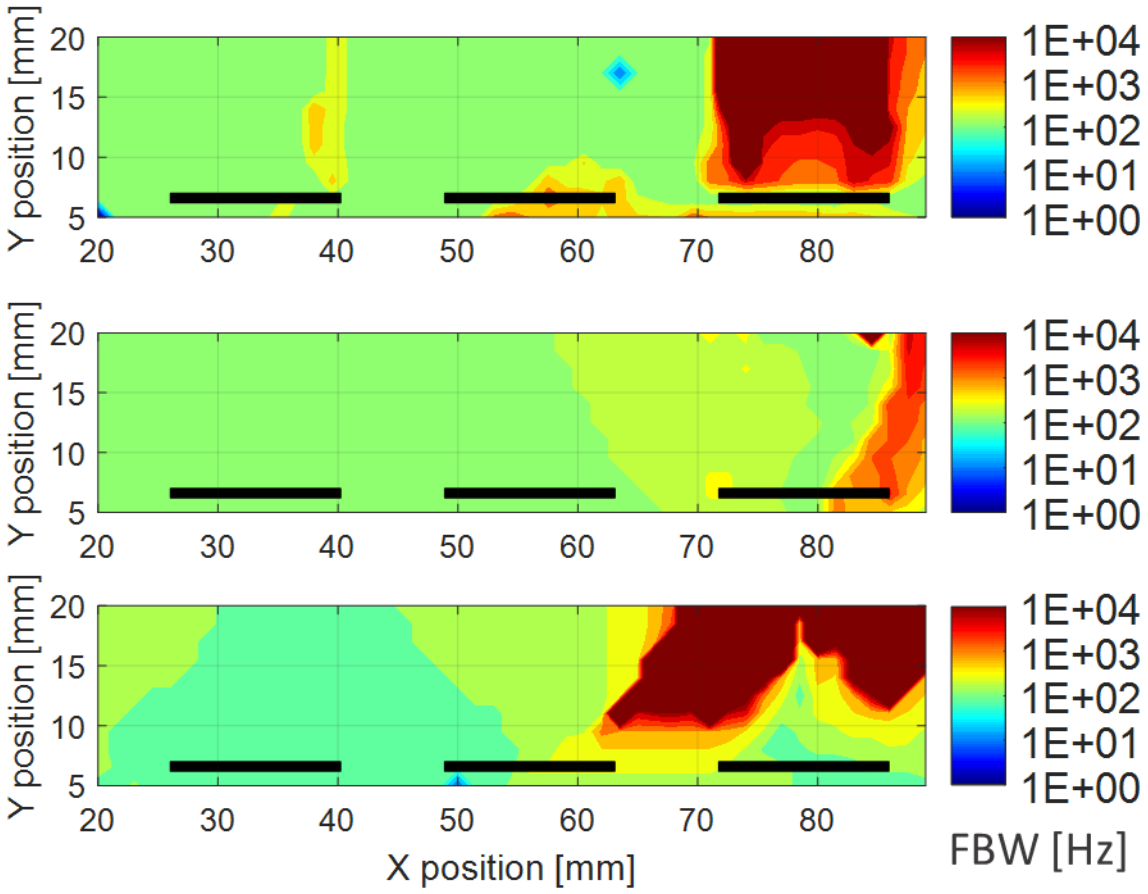

Fig. 7.2-2: 5% FBW on the analysis plane for phase C current

The important observation from FEA is the limited cross-coupling of the field between the phases. The field is concentrated close to the terminal which carries the current. The field from phase C is only slightly spread to phase B region. If a 2-D PFD has to measure two independent currents, its position must have 2-D FBW and 2-D flux density from both currents. This means that if both phase B and C were to be measured with a single 2-D PFD in the power module using a cross-coupling decoupling technique, there should be a location where 2-D flux density and 2-D FBW of both terminals coincide.

The 2-D FBW as well as 2-D flux density of phase C terminals on the analysis plane is shown in Fig. 7.2-3. This plane provides accessibility for the 2-D PFD placement as well as exhibits

adequate 2-D flux density. However, the bandwidth of the phase C field is only limited to the region above its terminal. This means that a 2-D PFD positioned in the region between phase B and phase C terminals where there is cross-coupling will only be able to sense the currents with very low bandwidth.

This shows the limitation of commercial power modules field shaping. 2-D PFD-based current sensing is still possible due to the cross-coupling between neighboring phases but FBW is poor, hence 2-D PFD is placed in the region of cross-coupling despite the low bandwidth. 3-D PFD-based current sensing is not suitable for commercial power module due to the lack of a region with three-phase cross-coupling.

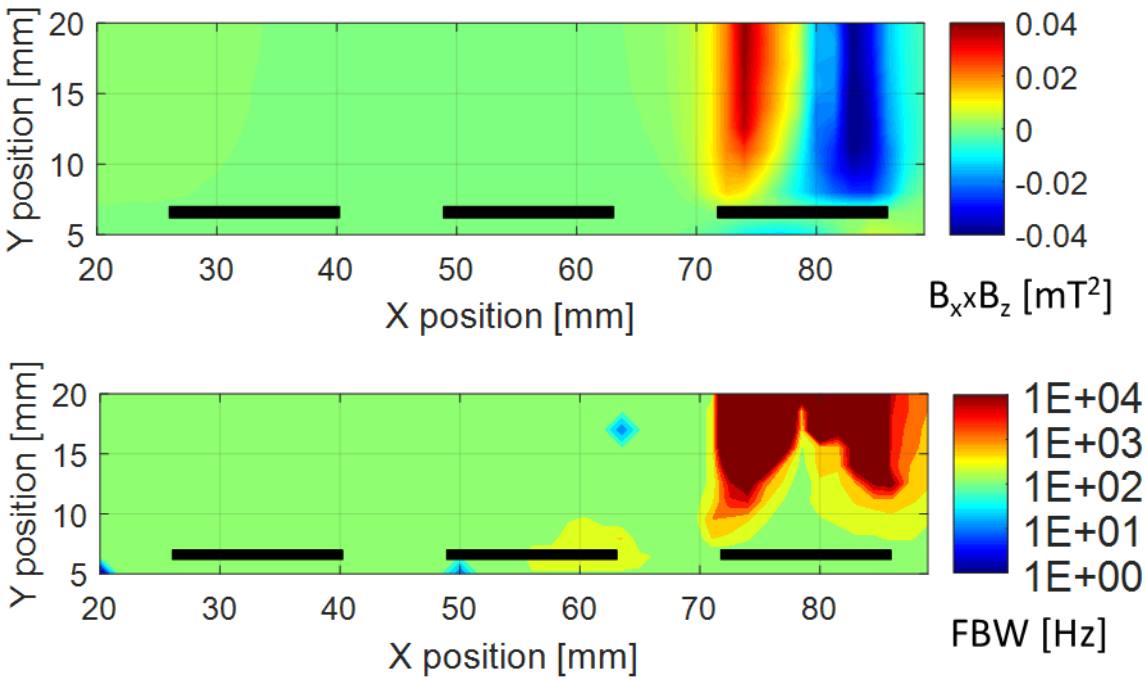

Fig. 7.2-3: 2-D flux density and 2-D 5% FBW on analysis plane for phase C injection

It must be noted that a 2-D PFD still has the capability of essentially two 1-D PFDs. This capability can be utilized in other ways if the field is not shaped for one application. For example, a 2-D PFD positioned in the regions of high 2-D flux density and 2-D bandwidth for each of the

terminal can be used to create a redundancy in phase current sensing. These 2-D PFDs can also be used to implement disturbance decoupling, power module reliability and other diagnostics.

7.3 Experimental 2-D PFD-based Power Module Integrated Current Sensing

7.3.1 Frequency response analysis of phase A magnetic field

The test setup to experimentally evaluate the bandwidth of the three-phase power module is shown in Fig. 7.3-1. The testing involves passing current through phase A of the module so that the magnetic fields are generated around the terminal and its interconnect. This current is passed through phase A of the module from positive and negative DC bus as shown in Fig. 7.3-2. The 5-dimensional precise positioning stage is used to position the 2-D GMR PFD in the power module. The 2-D GMR PFD signal is analyzed with respect to the actual current measured by a probe on the Venable frequency response analyzer (FRA). The FRA controls the power amplifier which produces the sinusoidal current at each frequency in the experiment. The FRA does a DFFT at the frequency its analyzing, hence the impact of noise or other disturbances is not recorded.

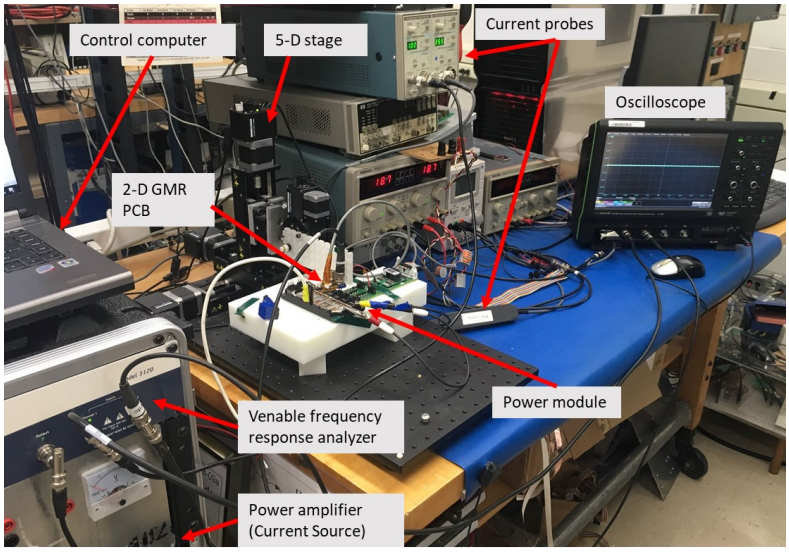

Fig. 7.3-1: Test setup for measuring the frequency response function of the magnetic field (PFD outputs) with respect to actual currents

The GMR PFD FRF typically has less than 1% non-linear errors due to hysteresis and characteristic curve non-linearity. The error would disappear due to normalization if the amplitude of the current, i.e. the field sensed by the GMR PFD was constant for all frequencies. However, the AC current source used falls sharply after 20kHz, and is reduces to half the current amplitude by 100kHz. Due to a steady current output for frequencies between 10 Hz and 20kHz, non-linearity error in the FRF below 20kHz are expected to be less than 0.5%.

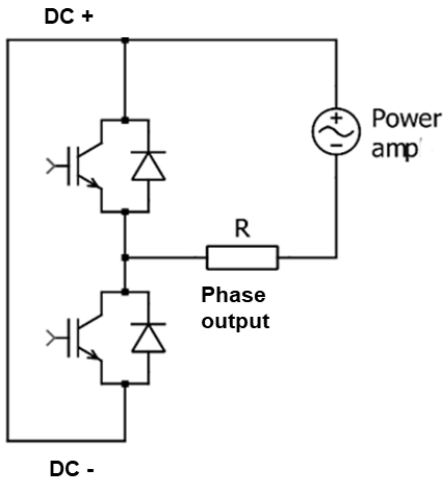

Fig. 7.3-2: Electric schematic of power amplifier and power module setup for current injection to measure the FRFs of the PFD outputs

The frequency response of phase A, X and Z direction magnetic field is recorded close to the terminal interconnect region and is shown in Fig. 7.3-3. This PFD is located taken inside the module at around Y= 10 mm and X =37mm above the terminal in Fig. 7.2-3. There are better points available in terms of bandwidth, but this point is representative of field inside the lid of the power module which is at 12mm. Due to its position, this point also allows limited cross coupling with phase B, albeit with a very low bandwidth.

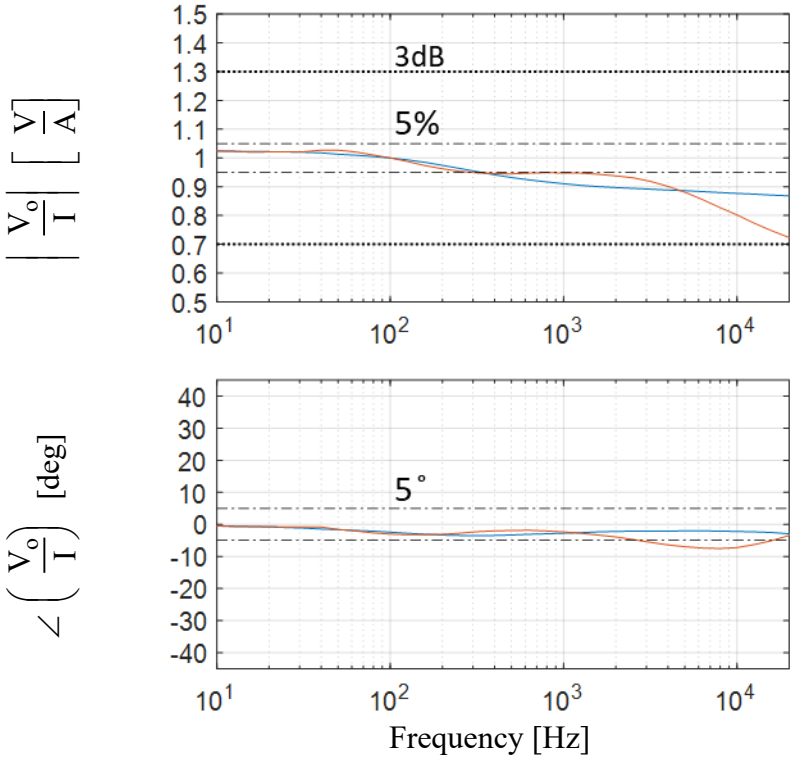

Fig. 7.3-3: Experimental FRFs of PFD outputs (close to phase A terminal) with respect to actual current normalized to 100 Hz value.

7.3.2 Closed loop current control of three-phase currents

This section summarizes the work in [64].

2-D PFDs are integrated in the power module for three-phase current sensing. The functionality of commercial power module integrated current sensing is tested on the inverter of the test machine on a back-to-back induction machine dynamometer. This is the same dynamometer setup used in [65][7]. Induction machine 1 is run in torque control mode and is used to provide load torque to induction machine 2 which runs in motion control. Both machines are run using IFOC and have inverters which share the same DC bus. The switching frequency is 10 kHz. Machine 1 inverter uses a Semikron 6-in-1 power module whereas the Fuji 6-in-1 power

module with integrated sensors is used in the machine 2 inverter. Concept gate drivers [120] are used in the machine 2 inverter. This test setup is shown in Fig. 7.3-4.

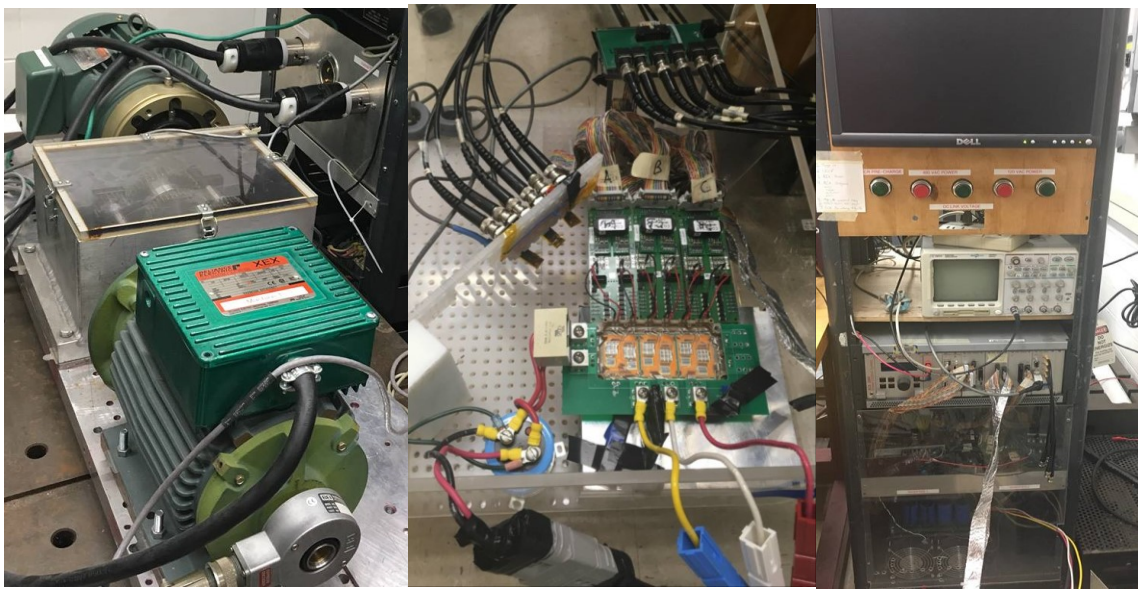

Fig. 7.3-4: Dynamometer, test inverter and load inverter tower with controller and protection circuitry

A variable transformer is used to step the 230 V AC by an appropriate factor which is then rectified. The system is designed to take an input up to 460 V AC, however, there is no need for such high voltage in this research work. Protection electronics are used to prevent the inrush current as well as over current.

The controller used is the AIX system XCS 2000. The motion control, current control, as well as observers are all implemented in C++. The AIX is bridged to Matlab for simpler control and data processing. AIX provides the gate signals to the gate drivers for inverter control. The AIX is also programmed to read the current sensor signals and record them synchronously with the PWM signals.

Lem HAL50-SP1 are the current sensors used on all three-phases of both motors. These current sensors are used to provide the current feedback for the current regulation and to provide the reference measurements when 2-D MR PFDs are used to measure the current.

The results of current sensing with one and two 2-D PFDs have a high error and are shown in [X]. A well-designed power module with field shaping will work with a single 2-D MR PFD in the case of a balanced system and two 2-D MR PFDs in the case of an unbalanced system. However, the commercial power module has a field shaping limitation, in that there are no positions for 2-D MR PFDs with appropriate cross-coupled 2-D flux density and 2-D FBW. Three 2-D PFDs were integrated in the power module. This leads to each of the 2-D PFD detecting a high 2-D flux density from one of the phases. This is only done to reduce the error and to further demonstrate the proposed methodology. (7.3-1) shows the sensing and decoupling model for three-phase currents which is implemented in the AIX controller for current regulation and remains constant for all test conditions.

$$\begin{bmatrix} D_{a1} & D_{a2} & D_{a3} & D_{a4} & D_{a5} & D_{a6} \\ D_{b1} & D_{b2} & D_{b3} & D_{b4} & D_{b5} & D_{b6} \\ D_{c1} & D_{c2} & D_{c3} & D_{c4} & D_{c5} & D_{c6} \end{bmatrix} \begin{bmatrix} VB_{x1} \\ VB_{y1} \\ VB_{x2} \\ VB_{y2} \\ VB_{x3} \\ VB_{y3} \end{bmatrix} = \begin{bmatrix} I_A \\ I_B \\ I_C \end{bmatrix} \tag{7.3-1}$$

It can be noticed that a non-square matrix is used since there are six PFD outputs and only three currents to be sensed. It is theoretically possible to detect six currents; however, since there are only three currents to be sensed, the potential remains unused and the last three rows of the decoupling matrix are omitted. The decoupling matrix is calibrated by a direct decoupling method but with samples at six instances. Since the system is only tested in a steady state three-phase condition, the direct calibration is used despite its major short comings described in chapter 3. A

more ideal approach to calibrate the system would be a hybrid approach which requires signal injection in the phases and then fine-tuning of the decoupling terms with direct approach using a 6x6 square matrix.

The test machine is commanded a speed of 17.7 rad/s whereas the load torque is maintained at 1 Nm and 3 Nm. The same test is then repeated at a speed of 35.3 rad/s. Fig. 7.3-5 and Fig. 7.3-6 show these four test cases with two amplitude and two frequencies, with current feedback coming from the PFDs in the inner motor control loop. The decoupling filtering and decoupling of the PFD outputs is implemented in the AIX controller. The measured instantaneous current error with respect to the reference LEM sensors is generally under 2%. Of all the cases shown, the worst case instantaneous error is 2.72% error and the worst case percentage error is 2.2%.

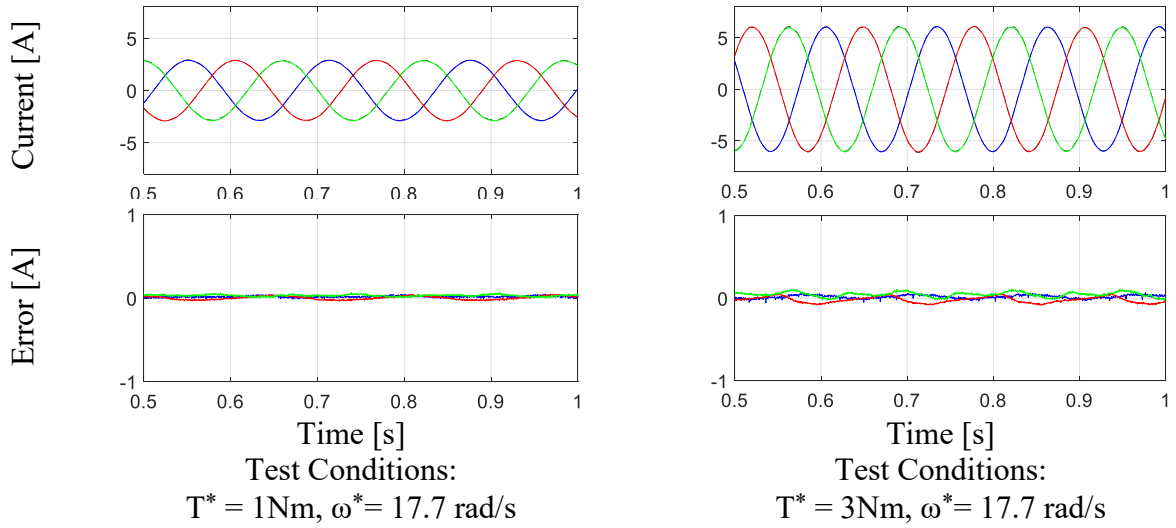

Fig. 7.3-5: Closed loop control using experimentally decoupled currents with three 2-D PFDs integrated in three-phase power module used as test machine inverter. (ω^*= 17.7 rad/s)

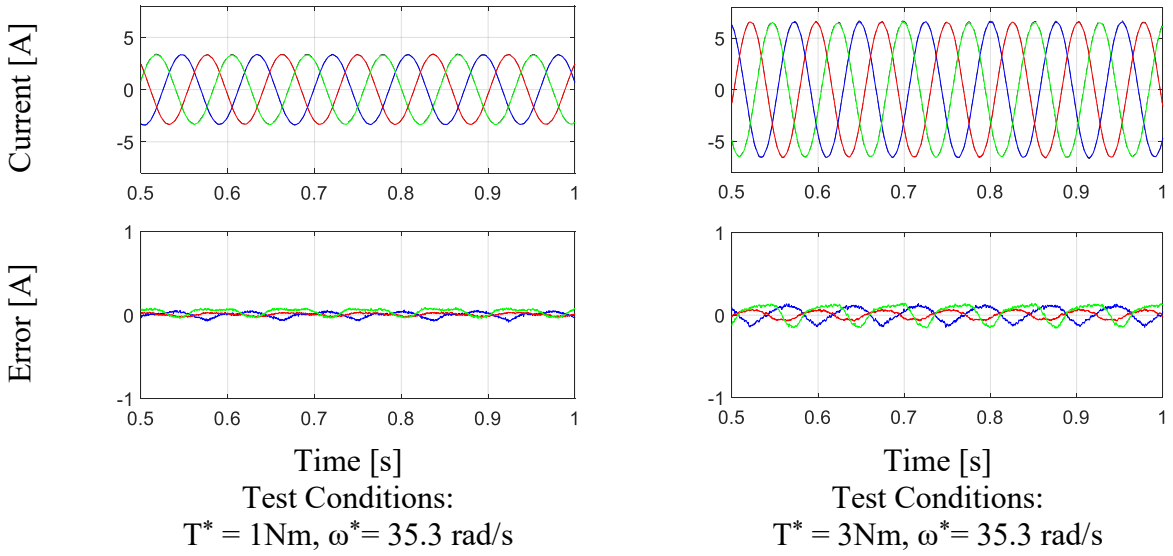

Fig. 7.3-6: Closed loop control using experimentally decoupled currents with three 2-D PFDs integrated in three-phase power module used as test machine inverter (ω^*= 35.3 rad/s)

7.4 Power Module Electromagnetic Analysis to Increase the FBW

To integrate high bandwidth multi-dimensional PFD-based current sensing in a power module, there needs to be an appropriate field shape. The three-phase full-bridge Fuji power module is analyzed extensively in FEA to identify the features in standard power modules that lead to FBW degradation.

7.4.1 Skin and proximity effects in power module components

A power module is a dense environment in terms of conducting and non-conducting layers. The typical stack-up of the module is made up of semiconductor, solder, copper, ceramic substrate, copper, solder and baseplate as shown in Fig. 7.4-1. The stack-up is a product of electrical, electromagnetic, mechanical and thermal constraints. Above the semiconductor die are interconnects which provide various connections including that to the terminal. A detailed discussion of the power module integration and packaging is presented in chapter 1.

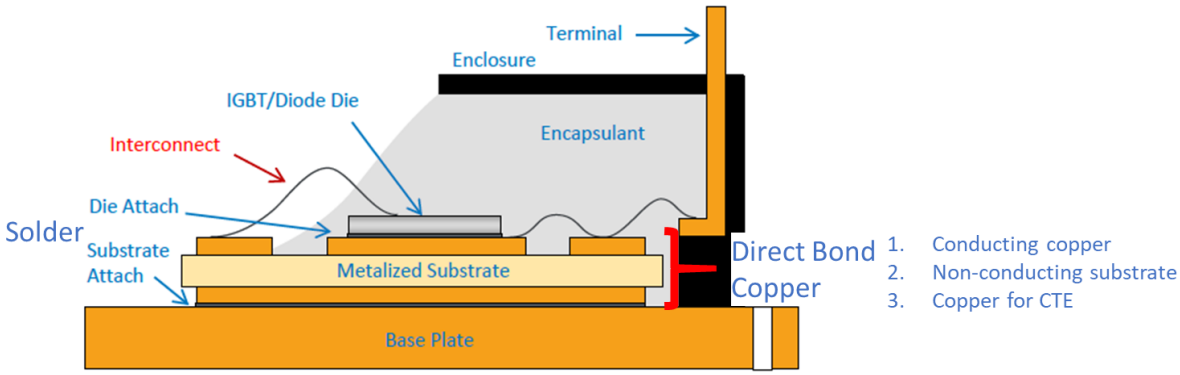

Fig. 7.4-1: Typical power module structure [90]

All the current conducting structures in the power module experience skin effect. Another important factor in power modules is the proximity effect between current conducting structures and the thermal or mechanical structures made out of electrically conductive materials but not conducting current. Typically, the commercial power modules are not made with an informed analysis of skin and proximity effect due to lack of a motive. The Fuji module is studied to improve its design for field shaping by reducing skin and proximity effects within the module.

The Ansys Maxwell electromagnetic FEA by default enables the eddy effect for all structures made out of a conducting material. The eddy effect refers to the skin and proximity effects, both of which are due to induced eddy currents. The eddy effect for any structure can also be disabled which removes the skin and proximity effects properties. This helps to identify the structures in the module which have the most skin and proximity effects leading to FBW degradation. The evaluation is done using the phase C current only due to the fact that each of the phases have very similar magnetic field.

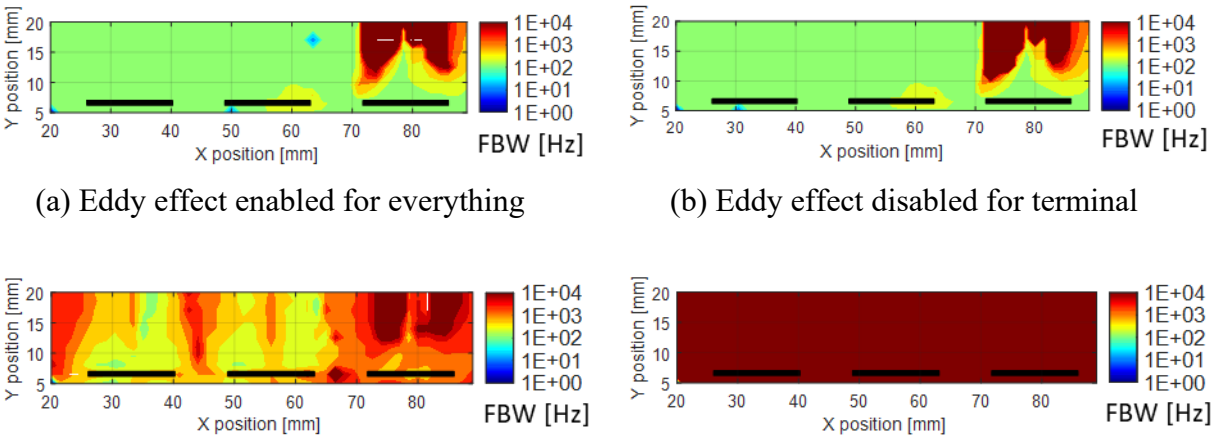

(a) Eddy effect enabled for everything

(b) Eddy effect disabled for terminal

(c) Eddy effect disabled for baseplate

(d) Eddy effect disabled for everything

Fig. 7.4-2: 5% 2-D FBW on the analysis plane for phase C (right most terminal) with eddy effect elimination

Fig. 7.4-2 shows the 2-D FBW for the power module under various conditions. In (a) the phase C 2-D FBW is shown for the commercial design as it exists. High FBW is limited close to terminal region. In (b) the eddy effect is disabled only for the terminal which does not a have significant impact on FBW. The reason for this is shown in (c) when the eddy effect in the baseplate is disabled. The baseplate is a thick sheet of copper that is designed to have a heat sinking property. Due to this, the proximity effect or Faraday's induced voltages cause large eddy currents which impact the FBW. In (d) the eddy effect is disabled for all structures in the module. The result is as expected that the FBW becomes perfect throughout the module since there are no frequency dependent effects.

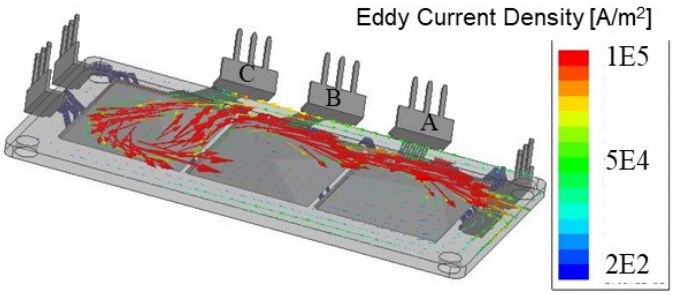

Fig. 7.4-3: Eddy Currents in baseplate at 0 deg wrt to 6 A cosine phase C current at 1kHz

Fig. 7.4-3 shows the baseplate eddy currents due to phase C current at 1kHz. The Faraday induced voltage is proportional to the rate of change of flux. This means that the induced voltage is 90 deg out of phase with phase current. The induced eddy currents, however, are dependent on the high frequency impedance of the baseplate as well as the higher order cross-coupled electromagnetic effects. The existence of eddy currents in the baseplate close to the terminal region is one of the most important factor in FBW degradation.

7.5 Techniques to Reduce Proximity Effect in Power Modules

7.5.1 Material of the baseplate

The baseplate, as explained before, is made out of copper which is not only very thermally conductive but also very electrically conductive. In the literature and commercial products, several alternative materials to copper have been used to build baseplates in less widespread applications [96][114]. One such material is Aluminum Silicon Carbide (AlSiC). This material has been proposed due to its superior thermo-mechanical performance but never due to its electromagnetic properties.

AlSiC is a metal matrix composite whose properties can be controlled by adding SiC. A commercially available AlSiC for power electronics application can have thermal conductivity of 180W/mK which is half as much as copper and electrical resistivity of 0.207μΩm which is an order of magnitude higher than copper. The higher electrical resistivity can substantially reduce the eddy currents in the baseplate.

Fig. 7.5-1 shows the 2-D FBW for phase C injection in the power module with all eddy currents enabled. The only difference is that the baseplate material is changed to AlSiC. The high

resistivity of the AlSiC reduces the proximity effect in the baseplate and increases the regions of high FBW. The same conclusion is predicted by the skin depth model.

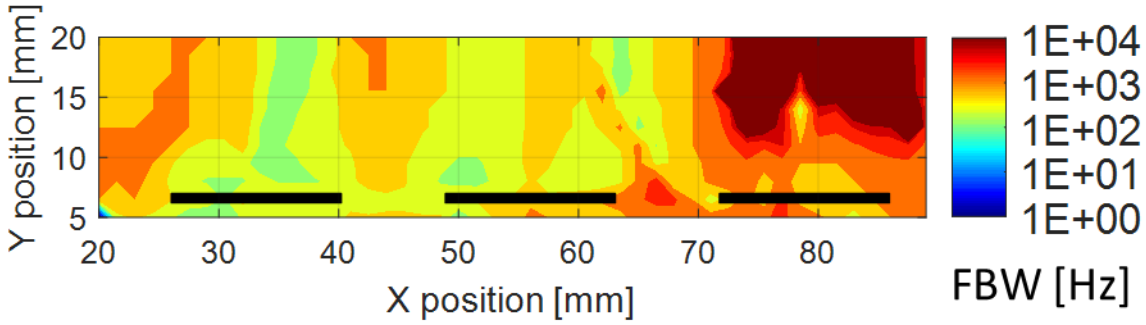

Fig. 7.5-1: 5% 2-D FBW on the analysis plane for phase C with AlSiC baseplate

7.5.2 Comb laminations on the baseplate

One tried and tested approach to reduce the eddy currents is to break their path using laminations. This approach is commonly used in magnetic transformers as well as electric machines. There are multiple ways of laminating the baseplate. Although a few of them were tried, only the one with the best multiphysics results is shown in Fig. 7.5-2. There are comb like cuts or laminations made in the typical baseplate. This simplifies the manufacturing process, and intuitively the thermal performance will be very close to that of a standard module due to a very little change in baseplate area.

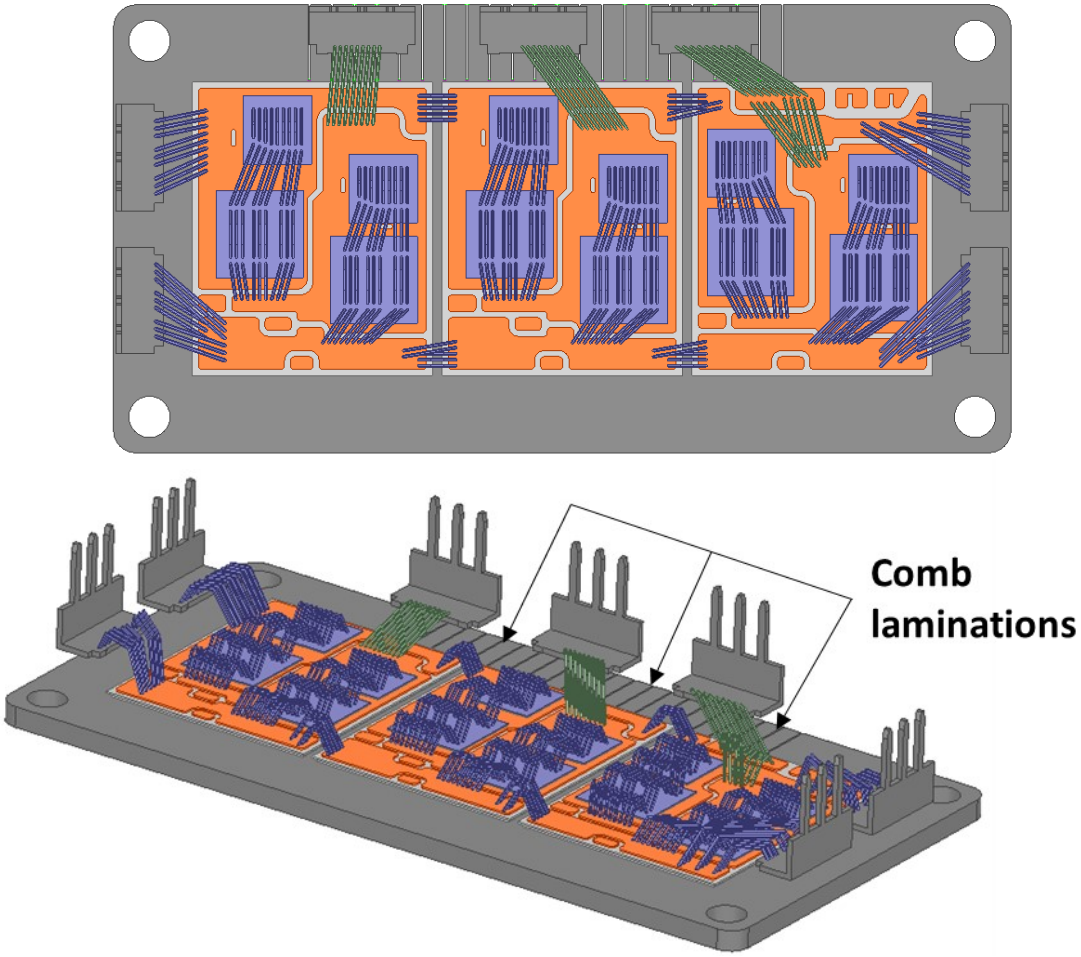

Fig. 7.5-2: Comb like laminated baseplate in the three-phase full-bridge power module

The 2-D FBW for phase C in Fig. 7.5-3 shows that the comb laminations are helpful for PFD positioning. They do not improve the FBW as much as completely eliminating the eddy effect, but they do improve the field shape for practical use. The laminations can be optimized to reduce the eddy currents as needed. For example, in Fig. 7.5-3, the FBW is significantly increased on the right side of the terminal but decreased on the left side of the terminal due to comb laminations. This is due to the new path of the eddy currents in the baseplate due to discontinuity from laminations.

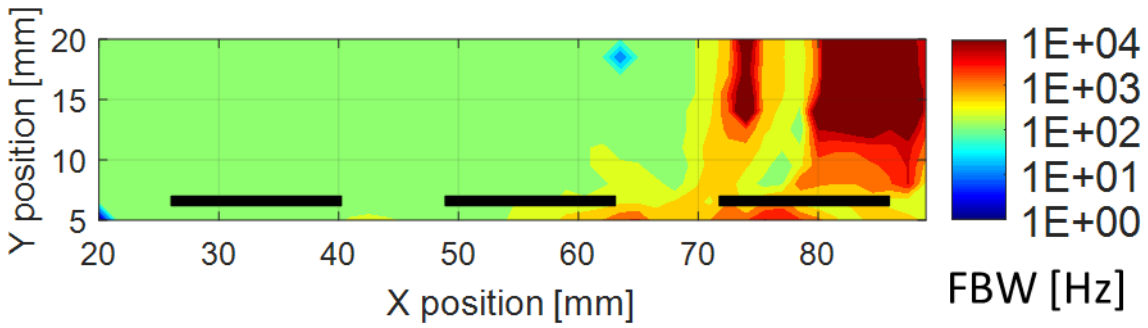

Fig. 7.5-3: 5% 2-D FBW on the analysis plane for phase C with comb laminated baseplate

7.5.3 Multiphysics evaluation of baseplate comb lamination

In a power module design, there are multiphysics concerns with design changes which include mechanical stress strain, thermal resistance, and inductance. Since the laminations are not touching the DBC and are only on the outer edges of the baseplate, the mechanical strength of the power module and bonding strength is not expected to be impacted. The permeabilities of copper and air or any filler material for the lamination is nearly identical. Due to this, there is no impact on the inductance of the laminations. The only real concern is thermal impedance of the baseplate since the area and mass of the baseplate are reduced.

The steady state thermal FEA is conducted on Ansys Mechanical on Workbench with heat passing from phase B IGBT chip to the bottom of the baseplate. Since the main interest is in thermal resistance through the baseplate, it is only a comparative analysis between the regular baseplate module and the comb laminated module. Assuming a linear system, the parameters in the FEA are set such that the peak temperature is equal to the thermal resistance from the IGBT chip to the ambient below the bottom of the baseplate. The convection coefficient is selected to set the convection resistance from the bottom of baseplate to ambient at 1 C/W. It must be noted that the FEA computed resistance for the regular power module has the same order of magnitude but a large error compared to the one reported on the datasheet. The discrepancy is primarily because of

contact resistance between different layers. This is, however, irrelevant to this investigation which is using the thermal FEA as a tool to compare the difference between the regular and comb laminated power modules only.

Fig. 7.5-4 shows the FEA results of the simplified power modules. The comb laminated module is found to have thermal resistance of 0.6198 C/W while the regular power module has a thermal resistance of 0.6102 C/W. This shows that the comb lamination increased the thermal resistance by only 1.57%.

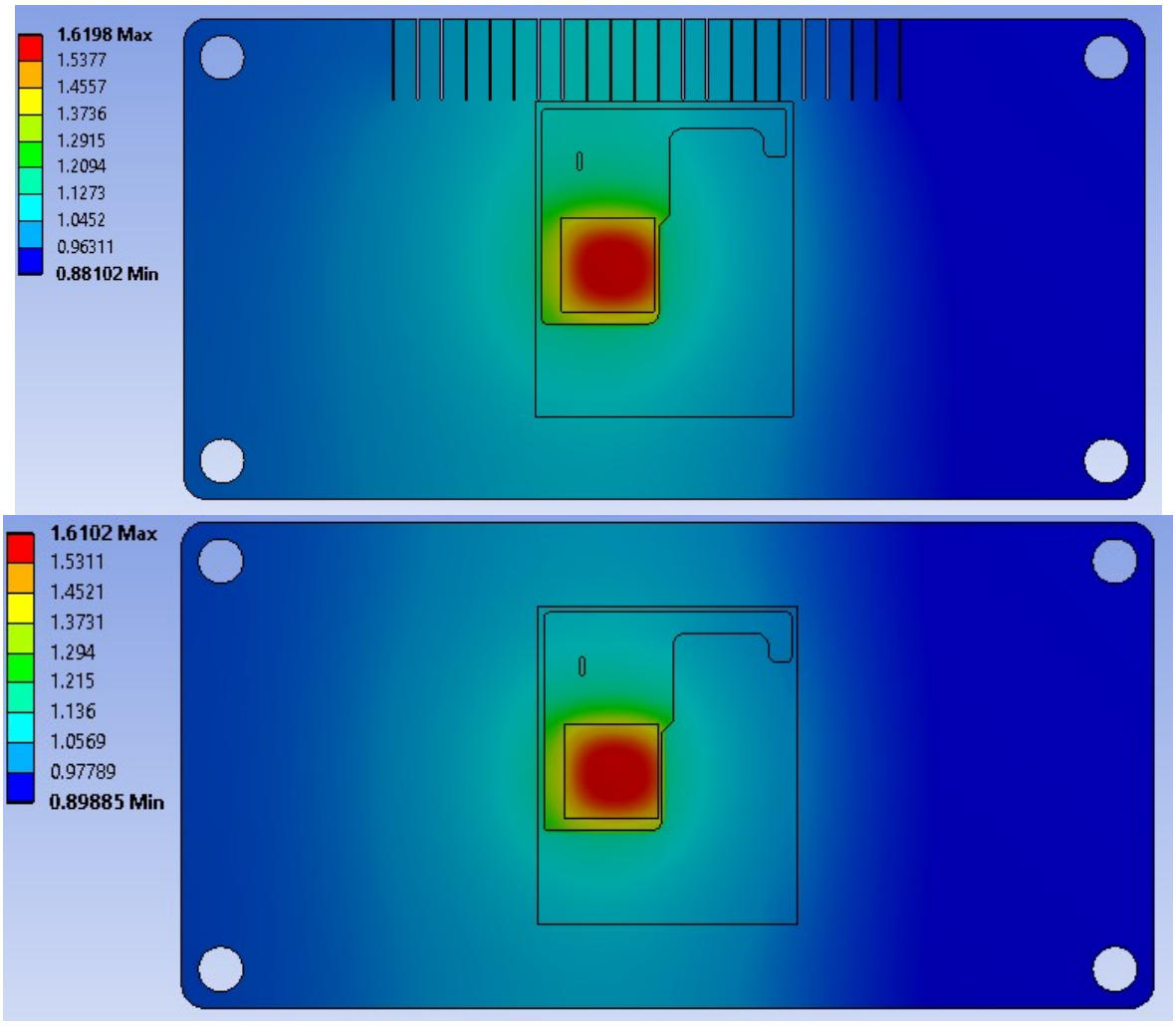

Fig. 7.5-4: Thermal FEA of regular and comb laminated (simplified) power module with max temperature programmed to be the thermal resistance from IGBT chip to bottom of the baseplate

Analytically, if the baseplate thermal resistance is computed using the plane wall formula shown in (7.5-1), the difference in the thermal resistance comes from the area alone. The lamination causes the area to be reduced and thermal resistance to be increased by 0.8%. The analytical value is off from the FEA value because the analytical formula is accurate for the entire wall conducting equally, whereas in the FEA the heat path is from a small chip to the much larger bottom surface of the baseplate.

$$R_{cond\text{-}wall} = \frac{L}{KA} \tag{7.5-1}$$

Where R is the thermal resistance, L is the length of the heat path, K is the conductivity of the material and A is the cross-sectional area of the heat path.

The thermal capacitance of the baseplate is modelled in (7.5-2). It is shown that the change in capacitance is the same as the change in the bottom surface area which decreases by 0.8%. Furthermore, the lumped capacitance time constant stays nearly the same between the regular and comb laminated baseplate.

$$C = m\,c \tag{7.5-2}$$

$$m = \rho V = k\,A$$

Where C is the thermal capacitance, m is the mass, c is the thermal heat capacity, ρ is the density, V is the volume, k is a constant and A is the baseplate area.

7.6 Experimental Evaluation of Baseplate Proximity Effects

7.6.1 100 A three-phase full-bridge Si power module

The impact of the baseplate on the FBW is experimentally evaluated in the three-phase full-bridge power module. Since the testing is destructive in nature, it is done using an older 100A power module with similar packaging style to the state-of-the-art modules and came under the

brand name of Fuji S series [121]. Since the major upgrades in power modules are on the chip level rather than packaging or integration, this power module is adequate for testing. The size of the baseplate of this module is identical to the next generation of power module which is used for simulation and experiments until now. Fig. 7.6-1 shows the power module with its solder pin terminals and bondwire interconnects. One of the packaging and integration differences between this module and the 150 A next generation power module is the presence of the extra unconnected phase terminals.

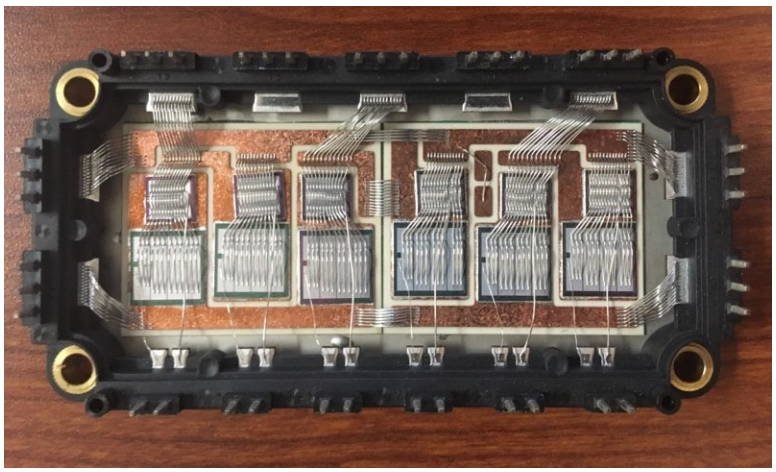

Fig. 7.6-1: Three-phase full-bridge Si power module for evaluation of the impact of baseplate on field shaping

7.6.2 Frequency response analysis with cut baseplate

To test the impact of the baseplate on the frequency response of the magnetic field experimentally, the baseplate of the power module is shaved off using a mill. Fig. 7.6-2 shows the baseplate of the machined power module. It is infeasible to machine the comb lamination on a baseplate that is already connected to the module so instead the baseplate is simply machined off. Under the phase B terminal, the baseplate is cut such that a 0.3 mm sheet is left. For the region on either side of phase B, the baseplate is cut such that the remaining baseplate has a thickness of 1.2 mm. This serves to reduce the eddy current paths much like the laminations.

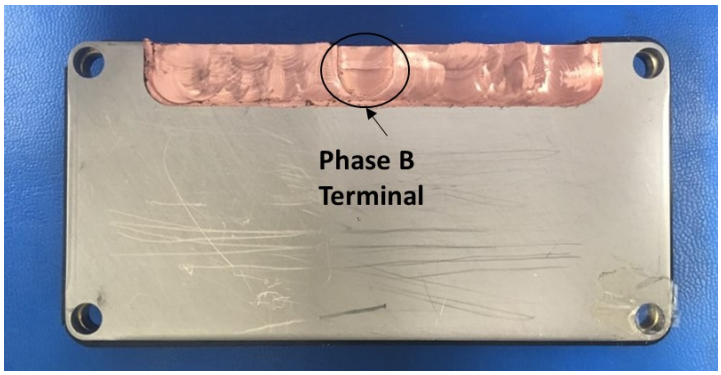

Fig. 7.6-2: Three-phase full-bridge power module with its baseplate milled off

The power module with the milled baseplate is compared against an identical power module but with a whole baseplate. The frequency response function (FRF) of the field at six locations close to the phase B terminal are experimentally measured. The experimental setup is identical to the one used in sec. 7.3.1. A 1-D GMR PFD (X axis only) is positioned close to the terminal and used to sense the fields generated due to the currents.

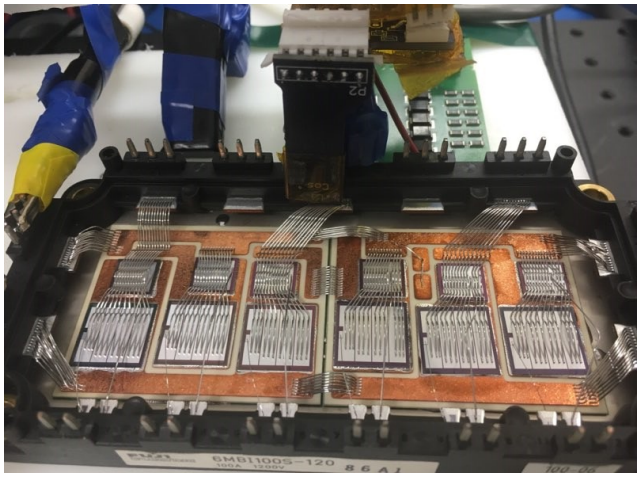

Fig. 7.6-3: Three-phase full-bridge power module with GMR PFD inside it

Fig. 7.6-3 shows the power module with the GMR PFD inside it to sense the fields. The 5-dimensional PFD positioning stage is used to move the GMR PFD precisely to 6 different spots in the vicinity of phase B terminal and its interconnect bondwire. Fig. 7.6-4 shows the overlaid FRF of the GMR PFD output with respect to the actual current. At all six locations the cut baseplate

outperforms the power module with the regular baseplate, in some cases even doubling the FBW. It should be noted that the six locations include three points across the length of the terminal and two locations away from the terminal. Each of the locations has its own FBW, however, it is very clear that with the milled baseplate, most locations have the field stay within 5% till close to 1 kHz. It is also worth noting that the points used for this testing do not represent the best location for current sensing and were arbitrarily selected to show the general improvement caused by the milling of the baseplate.

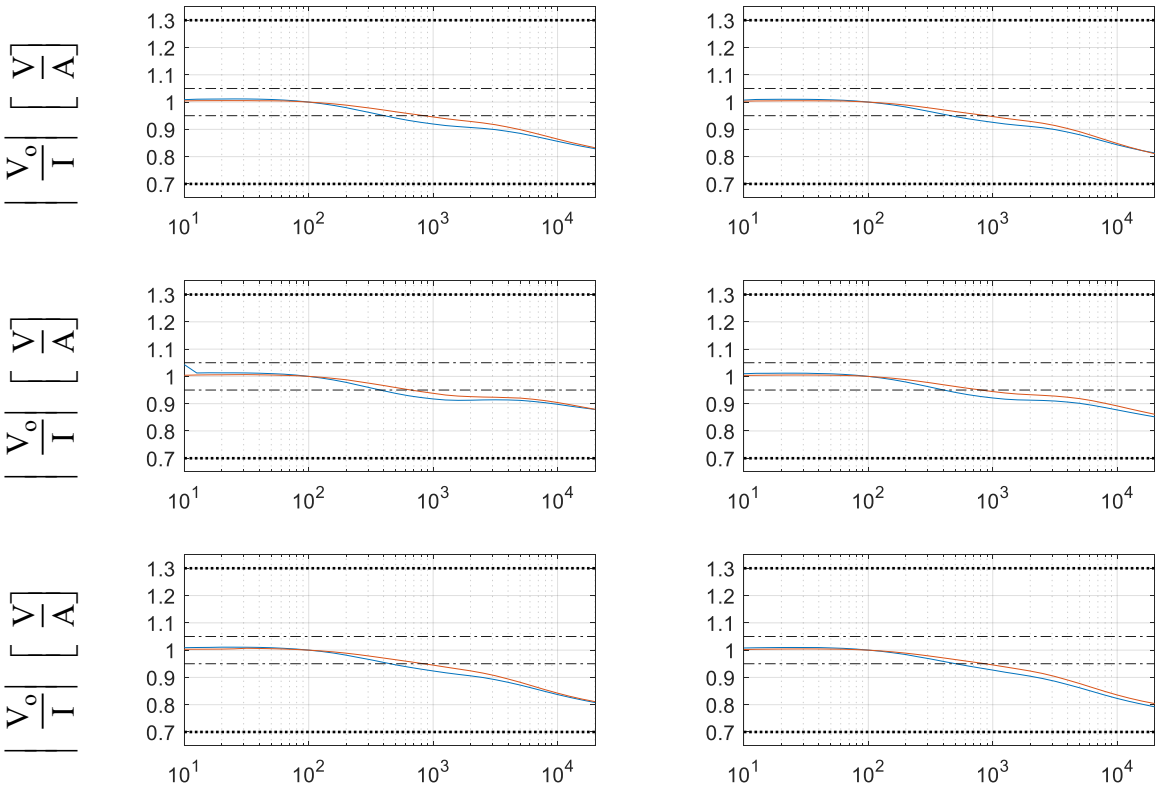

Fig. 7.6-4: Experimental FRFs of GMR PFD output with respect to actual current in the phase terminal of power module with regular baseplate and cutout baseplate normalized to 100 Hz values

7.7 Terminal and Interconnect Design for 2-D PFD-based Current Sensing

To implement 2-D PFD-based current sensing, there is a need for two phases to be cross-coupled. Cross-coupling is required at the location of the 2-D PFD to extract information of two currents using the field decoupling methodology. This is needed to reduce the number of PFDs to sense multiple currents using a single multi-dimensional PFD. The analysis in sec. 7.5 shows that despite the FBW improvement by reducing the proximity effect, the region of high FBW is limited to the region close to the respective phase terminal. Due to the fundamental path of the phase currents into and out of the terminal, there are no regions where cross-coupled fields from multiple phases have high FBW. Terminals and their interconnect can be designed to shape cross-coupled fields from multiple phases for high FBW.

7.7.1 Evaluation of 2-D field shaping terminal interconnect

For a full-bridge power module, the three-phase currents can be sensed with a single 2-D PFD if the system is assumed to be balanced. In the case of sensing all three-phases, a second PFD is required. The second PFD can be 1-D since the 2-D PFD will be able to sense two of the phases and the 1-D PFD can sense the third phase. The objective is to sense two phase currents using a single 2-D PFD by designing the terminals and their interconnects which lead to a high 2-D FBW for the cross-coupled field.

Multiple leadframe designs were simulated and manually optimized. Fig. 7.7-1 shows the terminal and leadframes designed for the power module for 2-D field shaping with adequate results. The two leadframes positioned close to each other orthogonally produce cross-coupled fields with high 2-D FBW which makes the use of a 2-D PFD to sense two phases possible. It is critical to note that at the location where the 2-D PFD is positioned, there will be X and Y components of the cross-coupled field from phases B and C. The resultant magnetic field vector can be broken into X and Y components, each of which should have an FBW appropriate for current sensing.

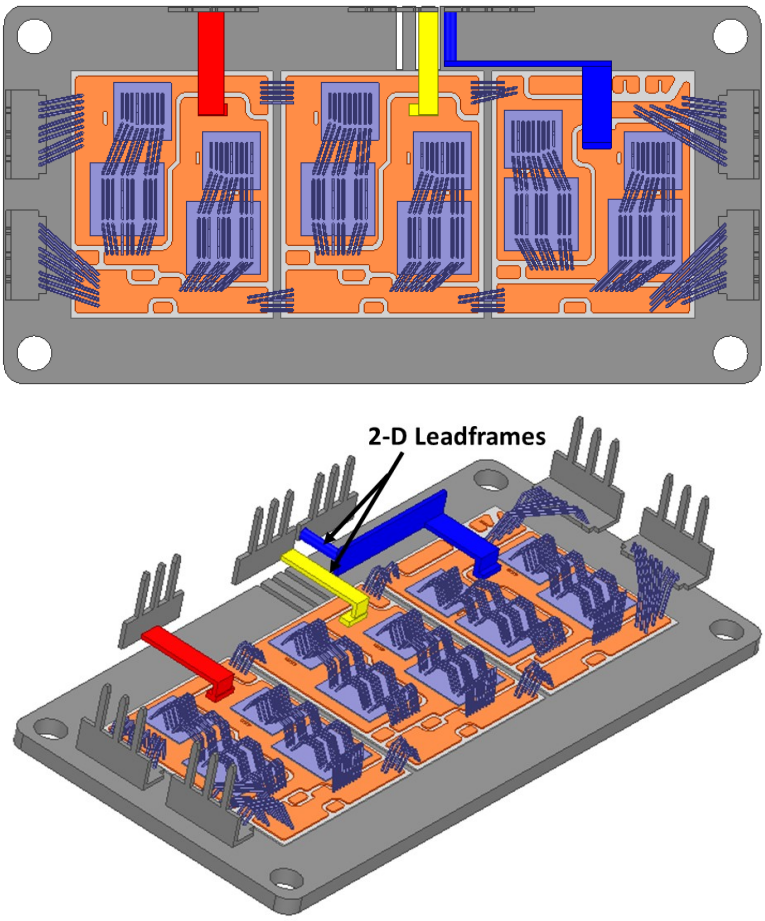

Fig. 7.7-1: Phase B and C leadframes in three-phase full-bridge power module for 2-D PFD-based current sensing

Fig. 7.7-2 shows the magnitude of 2-D flux density and 2-D FBW for the power module that is computed with all three-phases passing through the power module. As shown in Fig. 7.7-1, there are three comb like laminations in the base plate below the leadframes to avoid induced eddy currents in the baseplate from impacting the FBW. The orange region of 2-D FBW around the rectangular cross section leadframe design is mainly between 1 and 2 kHz which is enough for most modern day applications. However, if the fundamental frequency of the current is above that, such as in high pole number machines, the same design methodology can be used to further optimize the system by reducing skin and proximity effects.

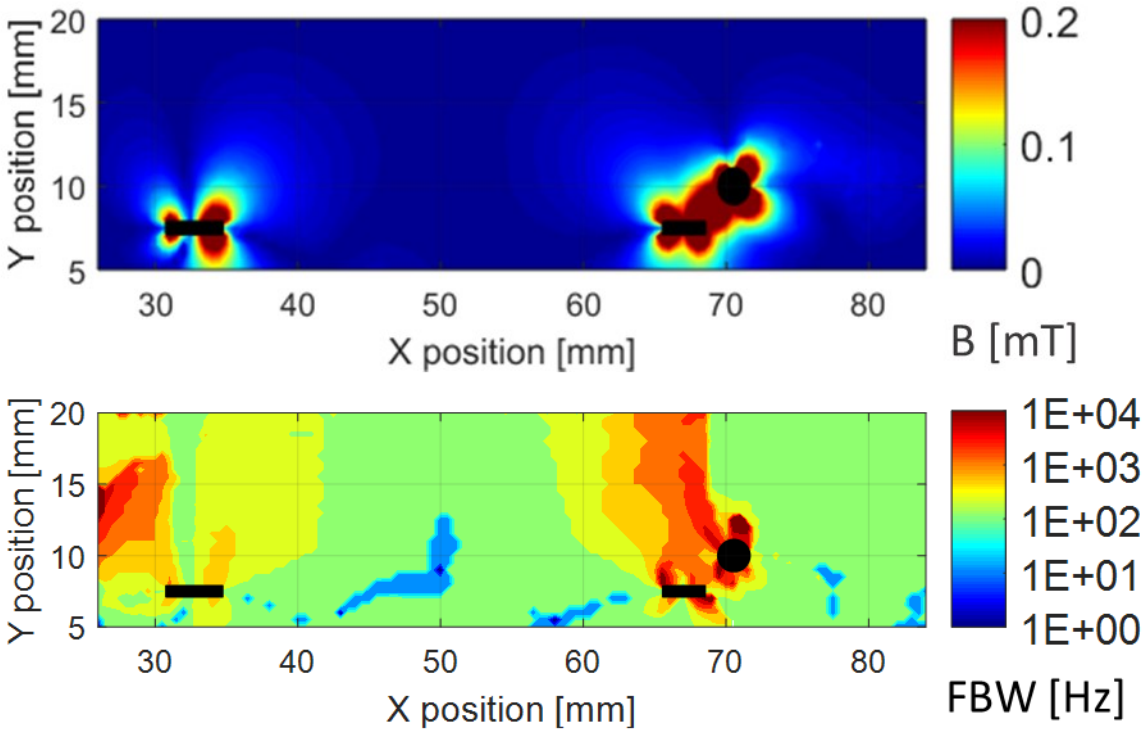

Fig. 7.7-2: 2-D flux density and 2-D 5% FBW of phase B and C leadframe in the power module

The phase A leadframe is not designed for 2-D field shaping and without the comb laminations below, it has a very low 2-D FBW. However, the point to be noted is that phase A needs to be

analyzed with 1-D FBW since it is far away from other phases. 1-D FBW for phase A has been optimized in previous work [8] and not a focus of this work.

Passing all three-phases together in highly cross-coupled cases is important since in multiphase systems, phase fields might work to cancel each other. FEA with all three-phases flowing together provides FBW with cross-coupling accounted for. It also accounts for realistic proximity effect between the phase current paths.

7.7.2 Multiphysics evaluation of power module compared to the commercial module

7.7.2.1 Thermal evaluation

The baseplate design of the 2-D field shaping power module is very similar to the one for 3-D field shaping power module. The analysis in chapter 0 sec. 8.3.4 applies to the three cut comb lamination directly. The FEA predicts a 0.15% increase in thermal resistance due to the three cuts.

7.7.2.2 Parasitic evaluation

The impact of the 2-D leadframes on the electrical performance of the power module is gauged using their parasitic analysis. The commutation loop, shown in Fig. 7.7-3, has inductance which is a very important parameter in power modules. A significant design effort is attributed to reduce this inductance in the commercial modules to allow fast switching and prevent the voltage transients that might be generated from the switching.

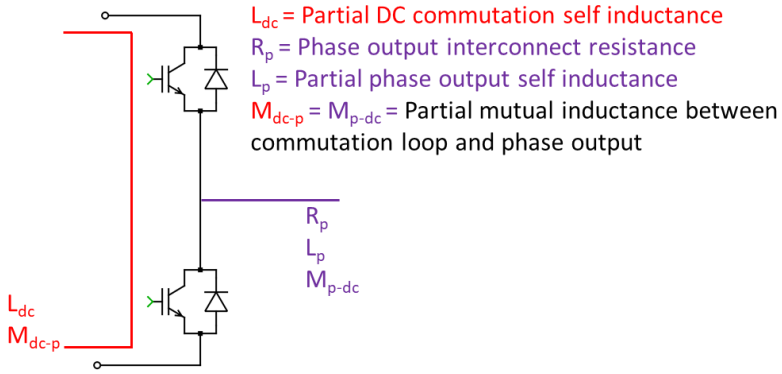

Fig. 7.7-3: Parasitic electric properties of half-bridge power module

The inductance analysis of the power module is conducted with respect to the standard bondwire power module to see if the field shaping leadframes have any impact on the self or mutual inductance of the DC commutation loop. Partial self and mutual inductances are computed in the FEA software, Q3D, on Ansys Electronics Desktop for the standard power module and the module with leadframes. The solution frequency is 200 MHz to allow skin effects to fully develop. The results of the inductances are shown in Table 7.7.1 at 10MHz for DC side and 1kHz for leadframes.

Table 7.7.1 Self and mutual inductances in nH

Standard power module				
	DC @10MHz	Phase A interconnect @1kHz	Phase B interconnect @1kHz	Phase C interconnect @1kHz
DC (3x parallel)	14.36			
Phase A bondwires	-0.47	6.89		
Phase B bondwires	-0.36		8.84	
Phase C bondwires	-0.33			13.35
2-D field shaping power module				
DC (3x parallel)	14.31			
Phase A leadframe	-0.52	9.61		
Phase B leadframe	-0.25		10.71	
Phase C leadframe	-0.32			22.22

It can be seen that the field shaping leadframes have a much higher self-inductance than the bondwires. Self-inductance is the property as shown in (7.7-1), that defines the flux per unit current. Field shaping naturally increases the flux per unit current, i.e. the self-inductance of the leadframe. Self-inductance for the leadframe is an innocuous property since the load of the power module will have hundreds of thousands of times more self-inductance making the phase interconnect completely negligible. The most important property in the module is the commutation inductance which is shown to decrease within the error margin of the FEA. The mutual inductance between the phase and DC commutation loop is negative which means that phase field cancels the DC field to improve the switching performance.

$$L_S = \frac{\phi}{I} \tag{7.7-1}$$

The resistance of the leadframe with respect to the bondwires being replaced is shown in Table 7.7.2 in milliOhms at 1kHz. All leadframes have a lower resistance than the bondwire interconnects, primarily due to the high cross-sectional area. Compared to switching losses around the order of kilowatts, the conduction loss in the interconnects is negligible.

Table 7.7.2 Resistance in the power module in mΩ

Standard power module	DC	1.42
	Phase A bondwires	0.29
	Phase B bondwires	0.39
	Phase C bondwires	0.62
2-D field shaping power module	DC	1.42
	Phase A leadframe	0.11
	Phase B leadframe	0.15
	Phase C leadframe	0.23

7.8 Summarizing Remarks

A concise summary of the chapter is available at its beginning. The conclusions and contributions for this chapter are available in the last chapter.

In this chapter, a typical three-phase full-bridge power module is analyzed for multidimensional magnetic field shaping. It is found that the commercial power modules do not use field shaping metrics for design, due to which there is no region with appropriate magnetic field shaping and FBW for multi-dimensional field sensing commercial power modules. Multi-dimensional PFD based current sensing is integrated in the commercial power module, despite its non-ideal field for viability and baseline testing. The time domain decoupling and frequency response of the current sensing provide insights into the design improvements needed as well as validate the possibility of integrated current sensing.

This chapter also includes a detailed FEA-based evaluation of power module structures including the baseplate, interconnects, DBC and terminals experiencing skin and proximity effects. It is identified that the fields from eddy currents in the baseplate due to proximity effects, cross-couple into the field sensed by the PFDs and lead to FBW degradation in the power module. Baseplates with comb-style laminations or baseplate made out of low conductivity AlSiC material can improve the FBW by reducing the eddy currents while having a minimal impact on the thermal characteristics of the power module.

Experimental verification of frequency-dependent effects of baseplate is completed in this chapter. In addition to design changes to baseplate, leadframe interconnect design is also proposed to shape the planar cross-coupled magnetic field from two phases to sense them with a single 2-D PFD.

Chapter 8 Full Bridge Power Module Design for 3-D Magnetic Field Shaping

This chapter develops the design methodology for three-phase full-bridge power modules to enable high bandwidth current sensing using a single 3-D PFD. DBC-to-terminal leadframes are designed to shape three-phase current paths for producing 3-D cross-coupled field with information about all three currents. The frequency dependent field behavior of the leadframes is evaluated outside and then inside the power module using single-phase and three-phase current injection. Guidelines to enhance the bandwidth of current sensing by reducing proximity effects and taking advantage of the geometric size of the PFD are also discussed. A single 3-D PFD is used to decouple and sense three-phase currents in the power module leadframes using the multi-dimensional field decoupling method.

The main purpose of this chapter is to develop the design methodology for a full-bridge power module which has a 3-D PFD integrated inside it for three-phase current sensing.

Elements of this chapter are under peer review for documentation in technical paper.

8.1 Methodology for 3-D Magnetic Field Shaping in Power Modules

Shaping the three-phase magnetic field to be cross-coupled and have components in three directions requires 3-D current paths which are arranged to produce uniquely cross-coupled field in each direction. In the power module, these paths are only available at the terminals and DBC-to-terminal interconnect.

The methodology to design three-phase power module's terminals and interconnects mainly involves magnetic field shaping by controlling current paths at a wide band of frequencies. The

first step is to design conductors with the geometric constraints from power module layout using an analytical understanding of Maxwell equations as well as skin and proximity effects. The preliminary design of the three-phase conductors then needs to be evaluated in electromagnetic FEA for magnetic field cross-coupling and bandwidth specifications. The FEA is able to account for material properties and frequency dependent effects to a high degree of accuracy if the input settings are well-tuned as described in chapter 2 . A frequency sweep is completed in FEA which can be computationally intensive so simplifying the geometry in early iterations improves productivity. The results of frequency swept FEA are post-processed to produce plots of appropriate field shaping metrics. In addition to the field shaping metrics, the current density is also analyzed in FEA which helps eliminate undesired frequency dependent eddy currents and current density changes. For various frequencies solved, the field and current density are analyzed in detail and design changes are made to counter the skin and proximity effects. The analysis leads to a manual optimization of the geometry and pathways of the currents in the conducting structures. The design of the leadframes, i.e., the conductive structures, is an iterative process, since frequencies dependent effects are far reaching and higher order and not just quid pro quo. The design changes are made until the field shaping metrics show the desired results.

The leadframes for 3-D field shaping can be designed to be fully inside the power module case without impacting the power module performance electrically or mechanically. It must be noted that leadframes, can be adapted for most three-phase full-bridge and single-phase half-bridge power modules. The leadframes and this methodology, in general, can also be used to shape conductors in inverters for compact, coreless and galvanically isolated 1-D, 2-D or 3-D PFD-based current sensing as well. This is particularly relevant when the inverter design does not have a conventional power module and instead the semi-conductor chips are integrated in the inverter.

The leadframe is a very reliable technology and it allows planar packaging, double sided cooling and reliable ultrasonic welding. Leadframes are used in many modern modules and are expected to be integrated in the future ones as well using the ultrasonic welding process as explained in chapter 1. The leadframes provide the opportunity to shape field in the X-, Y- and Z-directions which the bondwires alone lack.

8.2 Terminal and Interconnect Design for 3-D PFD-based Current Sensing

In this section, three-phase output terminals and DBC-to-terminal leadframe interconnects are designed to fit inside a commercial power module and to enable the 3-D PFD-based three-phase current sensing. The power module is the same from last chapter and due to it typical design, the design and conclusions from this chapter can be adapted for most full-bridge power module.

To use a single 3-D PFD to sense three-phase currents, fields from all three-phases need to be cross-coupled at the detector location. The cross-coupled vector field from the three-phases should also have a high FBW. As explained in chapter 7, there are very little 2-D cross-coupled fields and no 3-D cross-coupled fields in the typical commercial power modules.

8.2.1 Design Analysis in FEA

The three-phase currents can be sensed with a single 3-D PFD integrated into the power module without a balanced system assumption. In order to achieve this objective, the DBC-to-terminal bondwires in the power module are replaced with leadframes to generate the 3-D frequency-invariant magnetic fields with cross-coupling from all three phase currents. The leadframe interconnects are malleable and able to shape current paths which the bondwires cannot in such a way that each field direction has unique information from the three-phase currents leading to a well-conditioned system.

Fig. 8.2-1 shows the design of the 3-D leadframes, terminals and the baseplate which help shape the magnetic field in the X-, Y-, and Z-directions inside the same package dimensions of the power module. The phase A leadframe produces field in the Z direction, phase B leadframe produces field in the X-direction, and phase C leadframe produces field in the Y-direction due to the geometry and current path. It must be noted that although each of the leadframes is designed to produce the majority of its field in one of the directions, it also produces field components in the other two directions as well. The net magnetic field in the 3.5mm-wide region between the three leadframes has a highly cross-coupled field originating from all phase currents and with components in all three directions. The cross-coupling matrix of the field in between the leadframes due to the current paths has condition number close to unity.

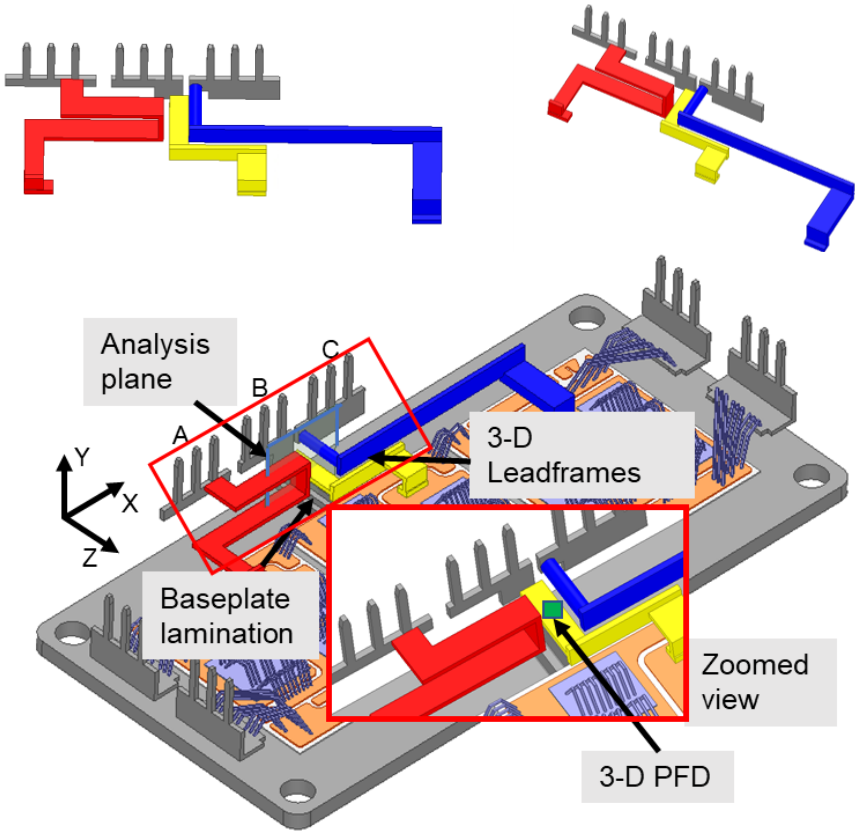

Fig. 8.2-1: Phase A, B, and C leadframes in three-phase full-bridge power module for 3-D PFD-based current sensing

8.2.1.1 Outside the Power Module

The leadframes and terminals are evaluated in an electromagnetic FEA outside the power module in the preliminary analysis. The phasor magnitude of X, Y and Z direction flux density as well as the net flux density for the three-phase quasi-DC current passing through the leadframes is shown in Fig. 8.2-2 on the analysis plane. Due to the current paths, the X flux density is stronger close to phase B leadframe, Y is stronger close to phase C leadframe and Z is stronger close to phase A leadframe. At majority of points between the leadframes, there is a 3-D magnetic field which contains information from all three-phase currents.

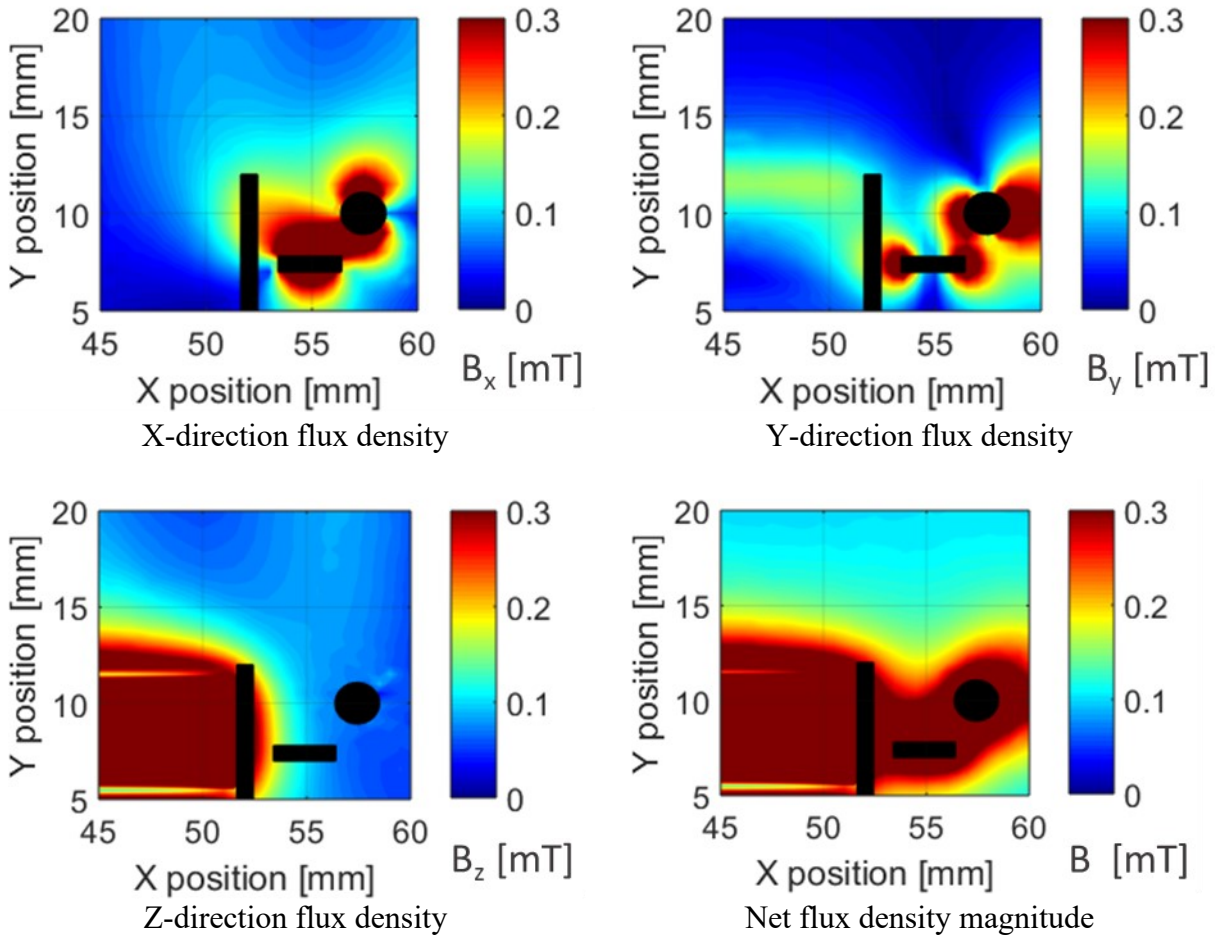

Fig. 8.2-2: Flux density around the leadframes on the analysis plane in Fig. 8.2-1 for 0.1 Hz 3A three-phase currents

The X, Y, and Z magnetic field components have frequency-dependent changes due to skin and proximity effects which cause a frequency-dependent redistribution of the current. For high-bandwidth current sensing, the 3-D PFD must be placed in a region of high 5% flat bandwidth (FBW) of the 3-D fields. Fig. 8.2-3 shows the 1-D FBW in X-, Y- and Z-directions as well as the 3-D FBW which combines the 3-D bandwidth information into one plot for the leadframes on the analysis plane. There is a region between the leadframes where the X, Y, and Z components of the cross-coupled magnetic field have a 5% FBW well above 1kHz. This region is achieved by minimizing the skin and proximity effects by reducing the excess copper in the conductors.

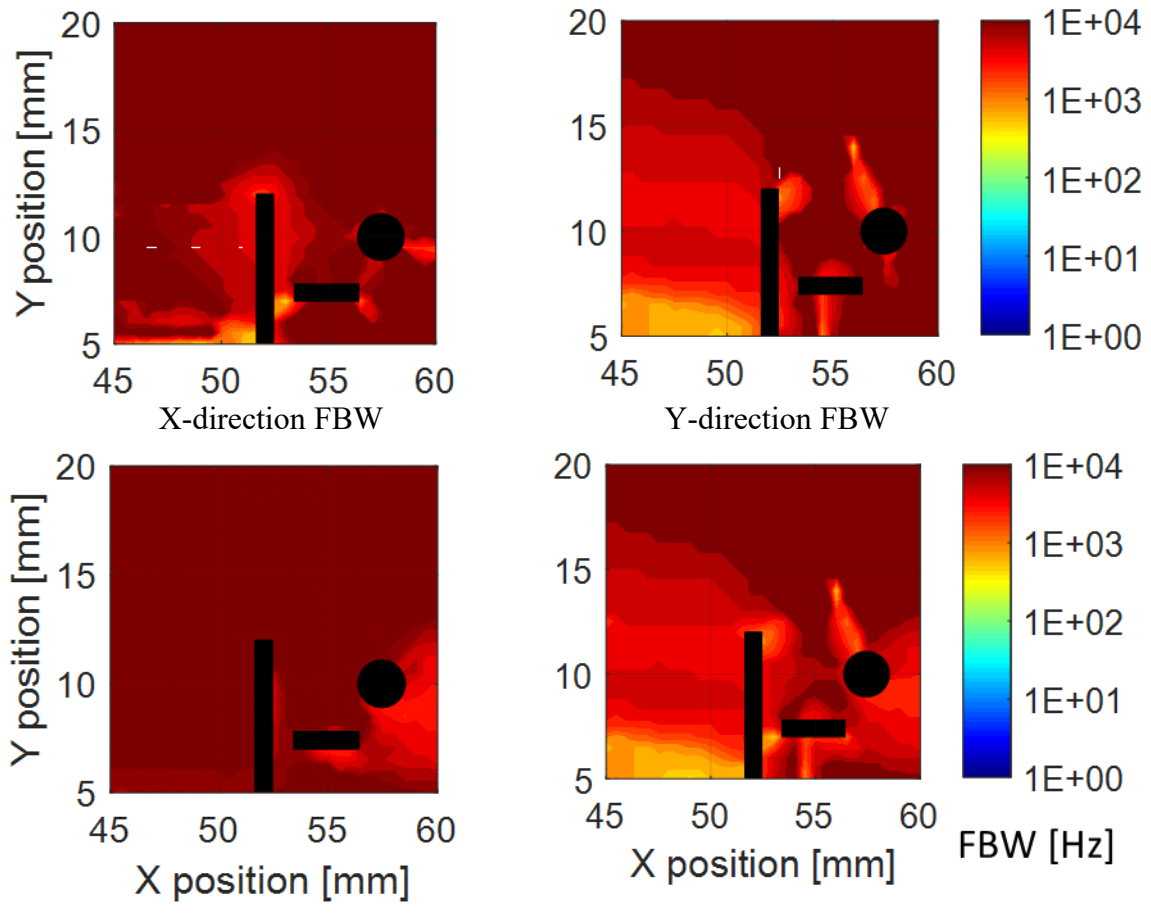

Fig. 8.2-3: 5% FBW around the leadframes on the analysis plane in Fig. 8.2-1 for balanced three-phase current injection

In the three-phase FEA, there is a rare possibility of frequency dependent compensation of fields from different sources. For example, this situation can occur if due to coincidence, the X component of phases A, B and C field at a point all change with frequency, but the changes compensate for each other and keep the net field frequency invariant. In such a case, the three-phase FEA will not be able to detect the compensation. The probability of this sort of compensation happening is very slim in this design where the field in each direction is predominantly produced by one of the phase currents. One way to verify that this does not happen is to look at phase FBW as shown in Fig. 8.2-4. The phase FBW shows the angle at which the magnetic field phasor changes rotates by more than 5 degrees in time and can signal varying influence of different phases.

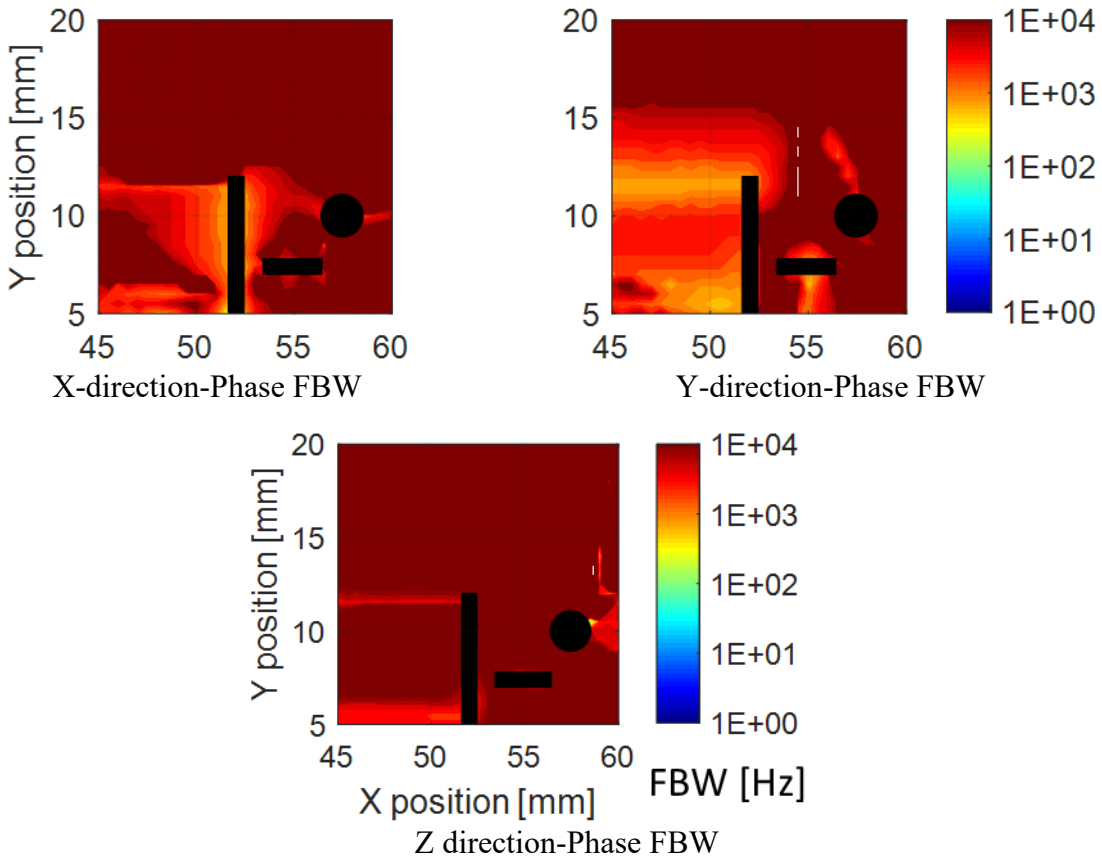

Fig. 8.2-4: 5 deg phase FBW around the leadframes on the analysis plane in Fig. 8.2-1 for three-phase currents injection

To keep the analysis thorough for fault conditions as well, the X, Y and Z FBWs for single-phase injection in leadframe B, C and A respectively are shown in Fig. 8.2-5. These high 1-D FBWs correspond to the direction with dominant field for each leadframe.

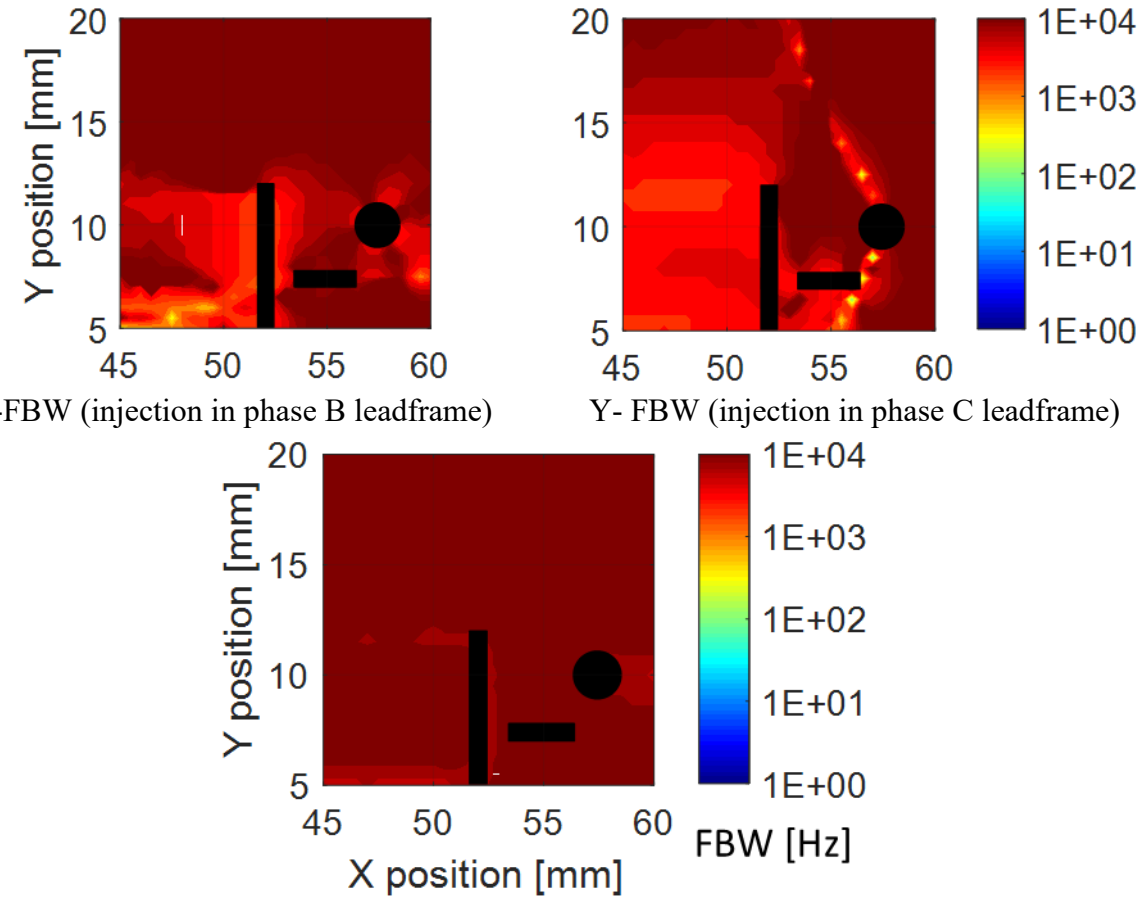

X-FBW (injection in phase B leadframe)

Y- FBW (injection in phase C leadframe)

Z-direction FBW (injection in phase A leadframe)

Fig. 8.2-5: 1-D 5% FBW around the leadframes on the analysis plane in Fig. 8.2-1 for single-phase current injection

Furthermore, Fig. 8.2-6 shows the 3-D FBW for single-phase injections. The only purpose of evaluating the 3-D FBW for single-phase injections is check for the absolute worst cases and verify that there is very little frequency dependent variance even for the non-dominant field directions of leadframes. A current injection in each of the three-phases produces a 3-D field. Although one of

the directions is dominant and much stronger than the rest, all three directions have a high enough FBW.

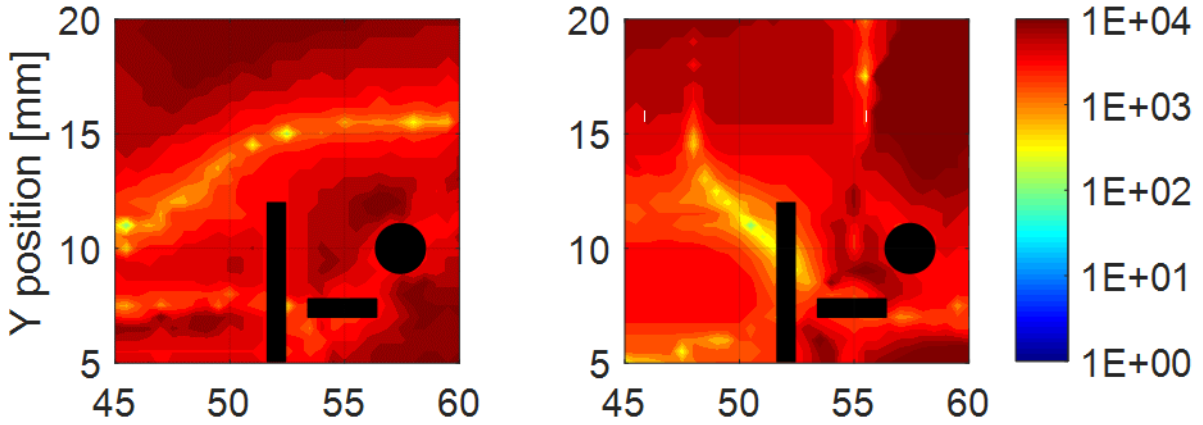

3-D-FBW from phase A leadframe injection

3-D-FBW from phase B leadframe injection

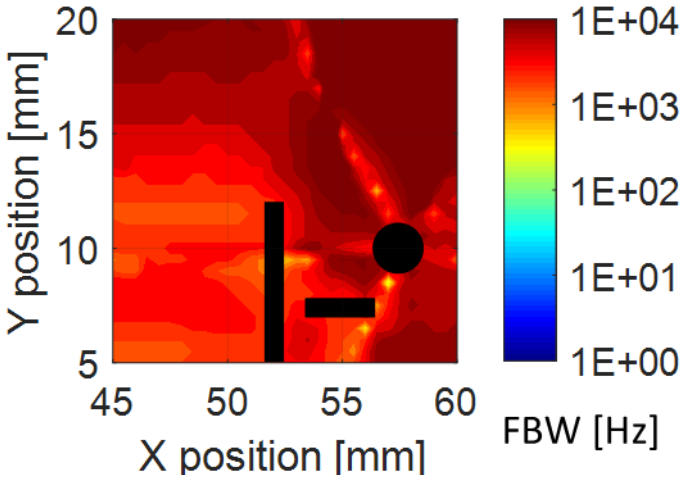

3-D-FBW from phase C leadframe injection

Fig. 8.2-6: 3-D 5% FBW around the leadframes on the analysis plane in Fig. 8.2-1 for single-phase currents injection

8.2.1.2 Inside the Power Module

In the next step of the electromagnetic analysis, the leadframes are integrated in the power module. The low frequency magnetic flux densities for the leadframes inside the power module are very similar to those shown in Fig. 8.2-2 in the sec 8.2.1.1. However, there are significant differences in the FBW of the leadframes when they are integrated in the power module. The X-,

Y- and Z-directions 1-D FBW as well as the 3-D FBW for leadframes integrated in the power module are shown in Fig. 8.2-7. The leadframe design is not enough to be able to achieve an adequate 3-D FBW due to the proximity effects from DBC and baseplate in the power module. To achieve an appropriate bandwidth, three comb laminations cuts are applied on the baseplate directly under the 3-D PFD location (see Fig. 8.2-1). The length of the cuts is 10mm but can be adjusted to aid the FBW.

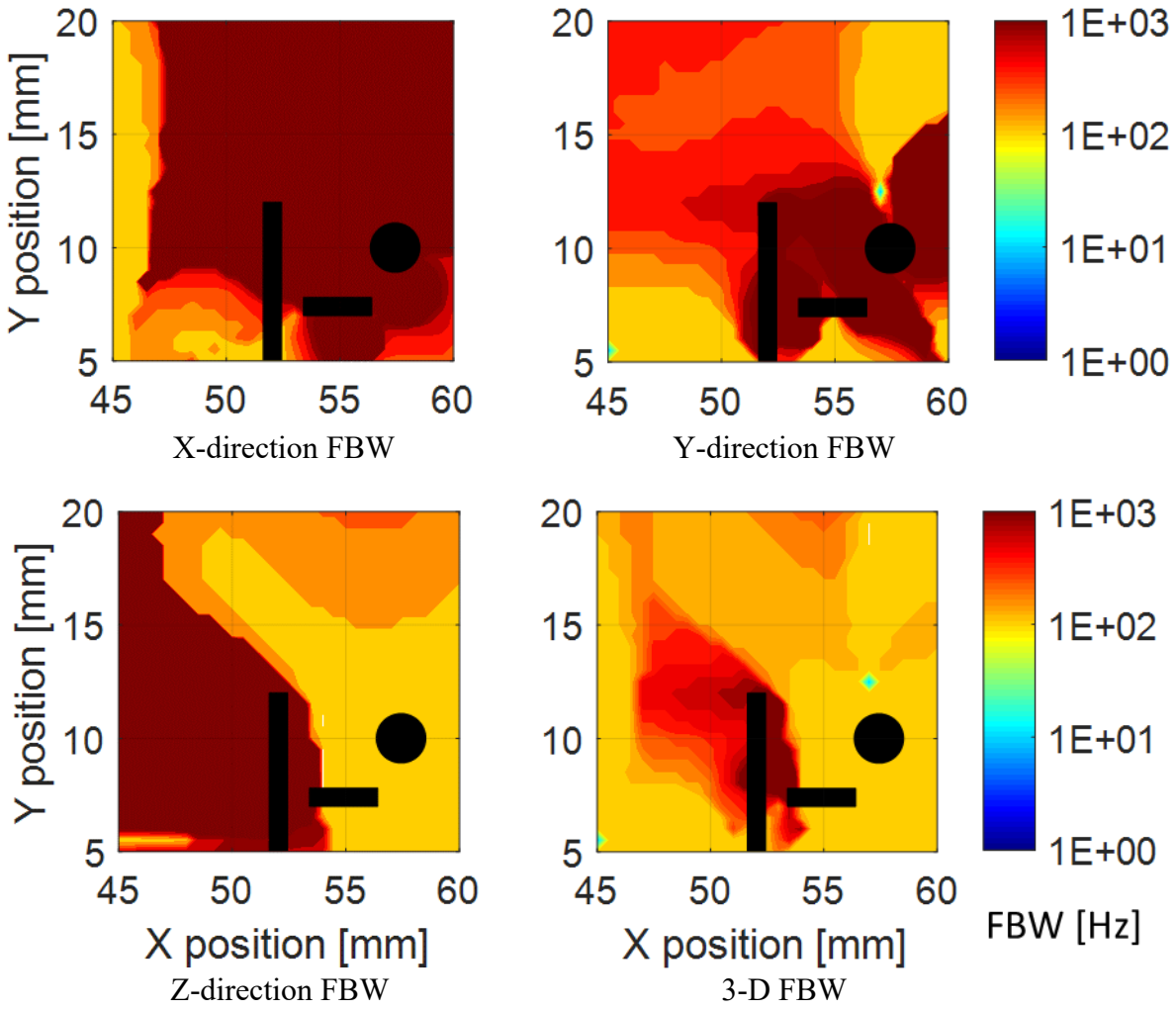

Fig. 8.2-7: 5% FBW around the leadframes on the analysis plane in Fig. 8.2-1 for balanced three-phase current injection

Despite the lamination cuts in the baseplate, the 3-D FBW goes beyond 2kHz in a very small region. It is possible to access it and attain adequate bandwidth for most modern fundamental current frequencies. However, the 3-D FBW plot can be misleading in this case and represent the FBW worse than what is practically achievable. The reason is that the 3-D PFD is not an ideal point, instead it has a finite geometric size with active areas to detect the X, Y and Z magnetic fields. The active areas in reality are positioned a couple millimeters apart due to which they have access to a higher FBW

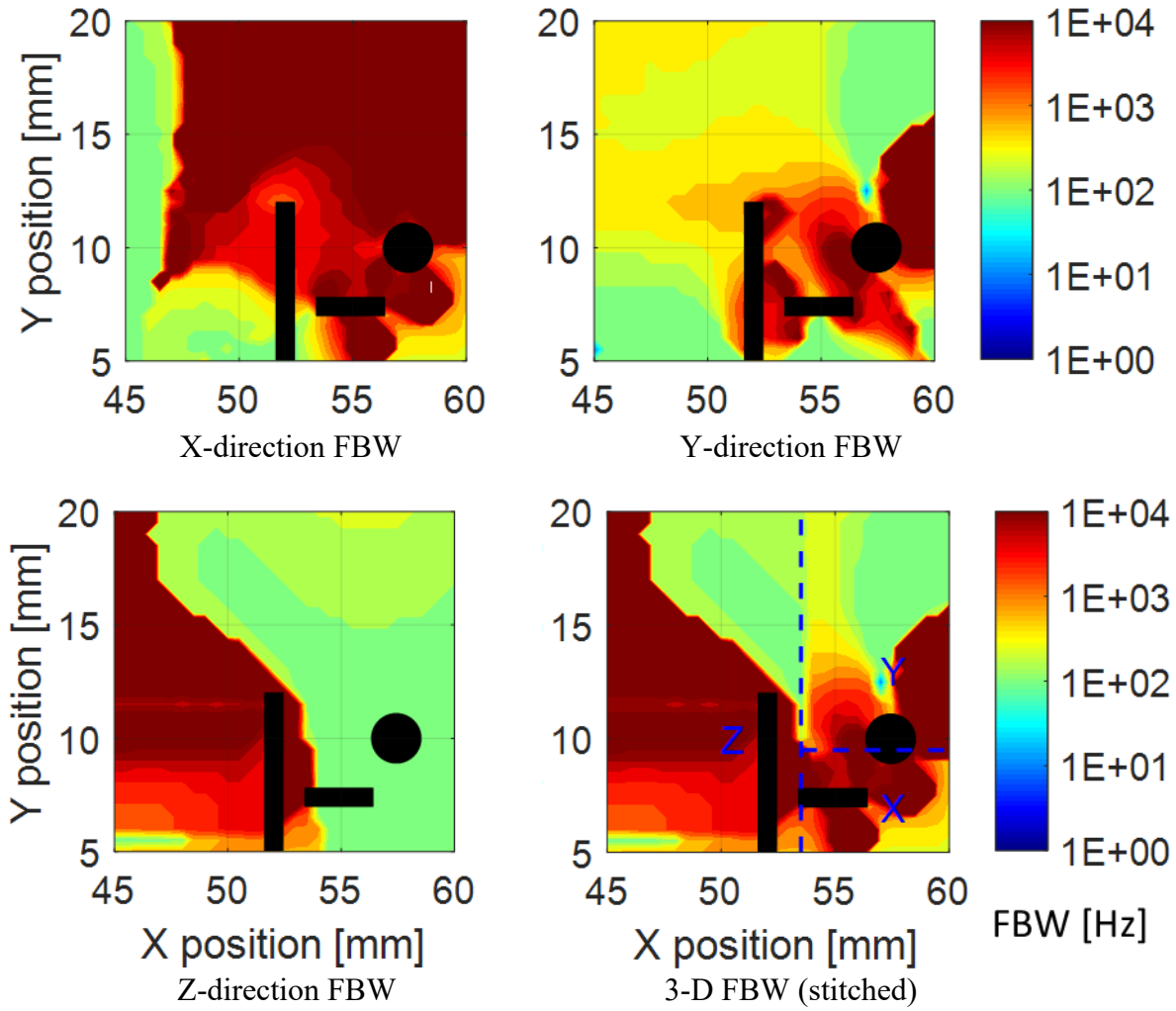

Fig. 8.2-8: 5% FBW around the leadframes on the analysis plane in Fig. 8.2-1 for balanced three-phase current injection

. Fig. 8.2-8 shows the X, Y and Z FBWs scaled to 10kHz. It also shows the 3-D FBW plot that is composed by stitching together the individual directions. The PFD will be placed close to the intersection point of the dashed line with active areas in each direction located inside the appropriate region. The stitched 3-D FBW only uses the data from a single plane. A more comprehensive and realistic stitching that involves data from adjacent planes further improves the FBW.

8.3 Experimental Evaluation of 3-D leadframes

The leadframes are fabricated for experimental testing by laser cutting of 0.8mm thick copper sheet. A 3-D printed fixture is designed to serve as a mold or stencil for the leadframes and hold them together. Fig. 8.3-1 shows the fabricated leadframes. The currents, injected from the bent pin on each of the terminals, make their way through the leadframes come out from the node where the DBC would be in the power module. The alligator clips are used to make electrical connections to the leadframes.

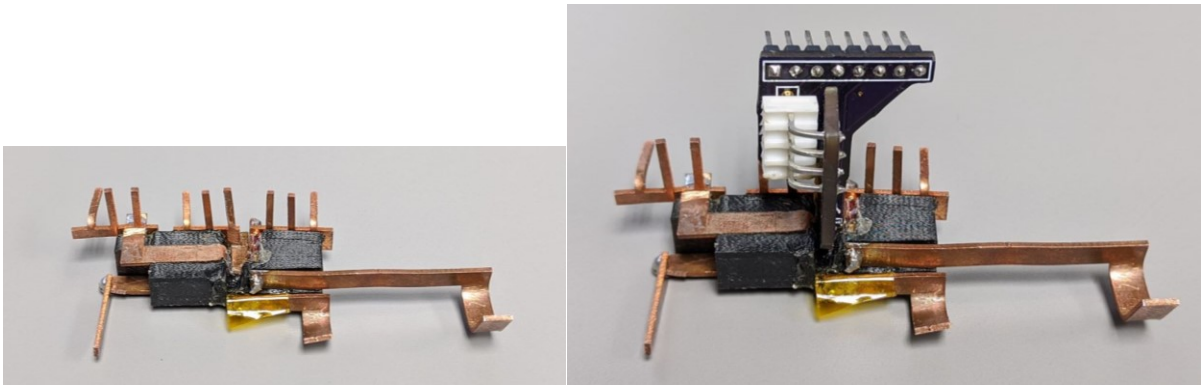

Fig. 8.3-1: Fabricated 3-D leadframes with the 3-D PFD placed in the middle

8.3.1 Single-phase frequency response

The experimental set up to test the single-phase frequency response of the leadframes is the same as the one used in chapter 7 sec. 7.3.1. A power amplifier passes current through each

leadframe, one phase at a time. The power amplifier is controlled by the Venable frequency response analyzer (FRA). This FRA analyzes the PFD output signal with respect to the actual current measured by a current probe through the leadframe to plot the frequency response functions for the fields in relevant directions.

Due to the design of leadframe, one of the directions of the 3-D PFD senses most of the magnetic field when a single-phase current is injected into a particular phase leadframe. Fig. 8.3-2 shows the FRF of the relevant GMR PFD output with respect to the reference phase currents. The PFD-sensed magnetic fields in all three directions have a flat FRF with less than 5% error for AC current frequencies beyond 8kHz.

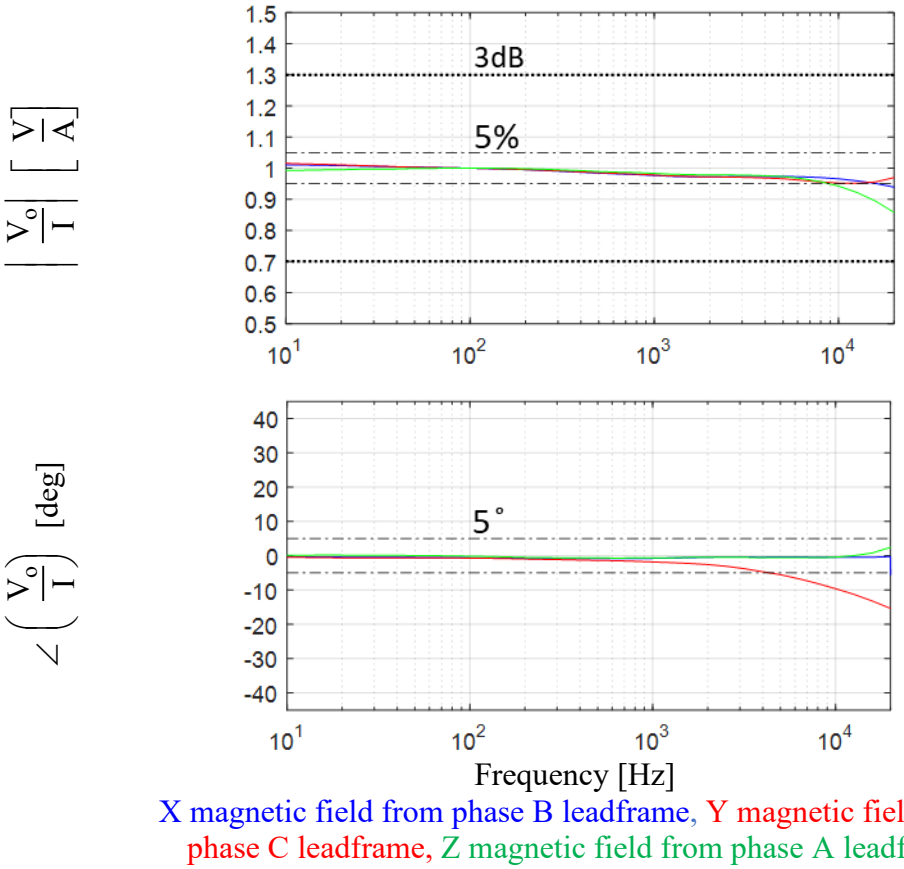

X magnetic field from phase B leadframe, Y magnetic field from phase C leadframe, Z magnetic field from phase A leadframe

Fig. 8.3-2: Experimental FRFs of GMR PFD with respect to actual test currents in the leadframes normalized to 100 Hz values

A version simplified power module with leadframes is fabricated by placing the leadframes above a baseplate. The baseplate below the leadframes is the main component that impacts the field shaping. The thickness and the distance of the baseplate from the leadframes is same as in the real power module. Fig. 8.3-3 shows the FRF of GMR PFD outputs with respect to currents in the leadframes placed above a baseplate which has three 15mm long lamination cuts. The FRF have changed due to the baseplate, however, the laminations in the baseplate reduce the proximity effects and maintain the 5% FBW at above 7kHz. The Z direction FRF has the biggest difference due to laminations.

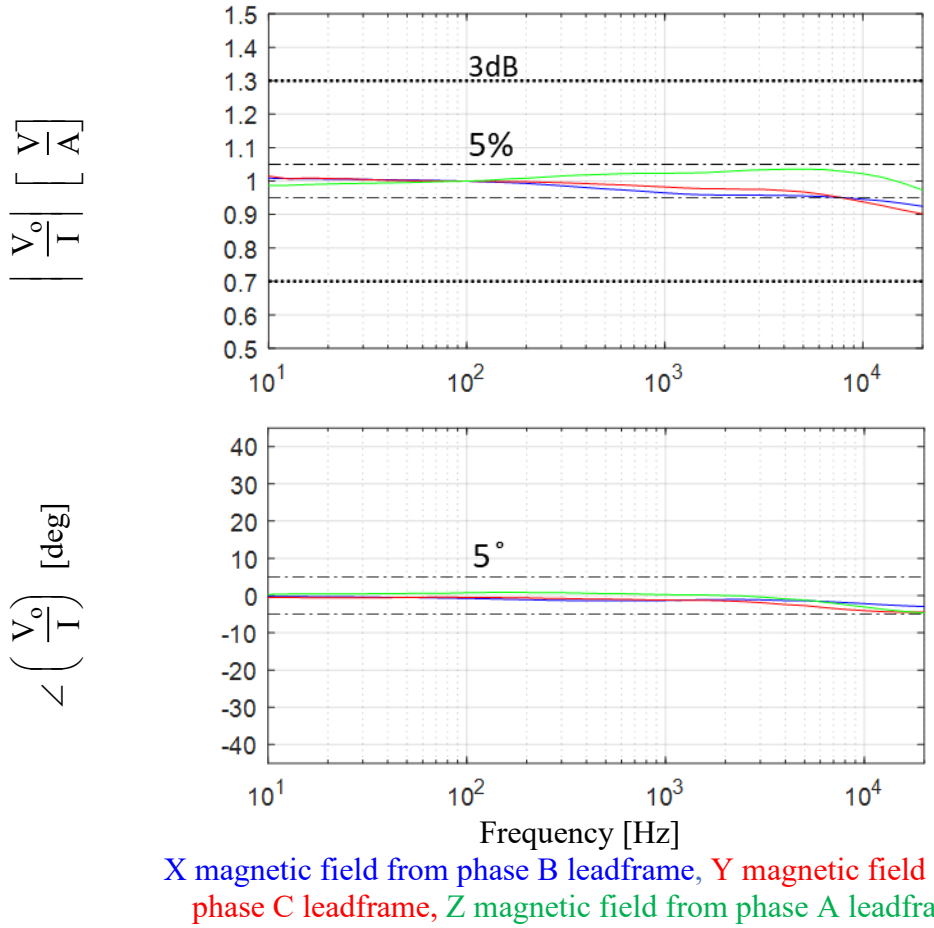

Fig. 8.3-3: Experimental FRFs of GMR PFD with respect to actual test currents in the leadframes above the laminated baseplate normalized to 100 Hz values

As expected, the FRF (not shown) with unlaminated baseplate has a 5% FBW of under 1kHz which is significantly worse than with laminated baseplate. It should also be noted that the baseplate lamination cuts for experiments are15mm long, whereas, 10mm is used in simulations. The reason for this increase will become clear in the next section.

8.3.2 Three-phase frequency response

Three-phase currents are used in the next step of experimental evaluation of the 3-D leadframes. A three channel power amplifier is controlled using the AIX system XCS 2000. The AIX provides three sinusoidal signals phase shifted by 120 degrees at frequencies between 20 Hz and 1500 Hz. It outputs each frequency for around 10 seconds. During this time, the three channels of the power amplifier amplify the AIX signals into larger voltages which drive the three-phase currents into a wye-connected resistive load. The leadframes are used as an intermediate connection between the power amplifier and the load. At each frequency, the Venable FRA, records the actual current and GMR PFD output to plot the FRF. The FRA can only record the one GMR PFD output due to which the frequency sweep is repeated three times to gather the FRF data for X, Y and Z direction GMR PFD outputs in response to the three-phase currents. It is important to have the AIX output at the frequency that FRA is analyzing at any time instant because the FRA does a DFFT and records data at that frequency alone. Due to a slight asynchronization between the FRA and AIX, the FRFs have some jitter in phase towards the higher frequencies.

Fig. 8.3-4 shows the FRF for X, Y and Z direction GMR PFD outputs in response to the three-phase currents through the leadframes placed over a baseplate with 15 mm lamination cuts. The FRFs stay within 5% band for up to 1200 Hz which is higher than the fundamental frequency of most electric drives. It is also noticed that the three-phase FRF has a different shape than a single-phase FRF. This is expected as the three-phase currents have inherently different proximity effects

with each other and the baseplate as compared to a single-phase current. The three-phase FBW from FEA is much different than the single-phase FBW as well.

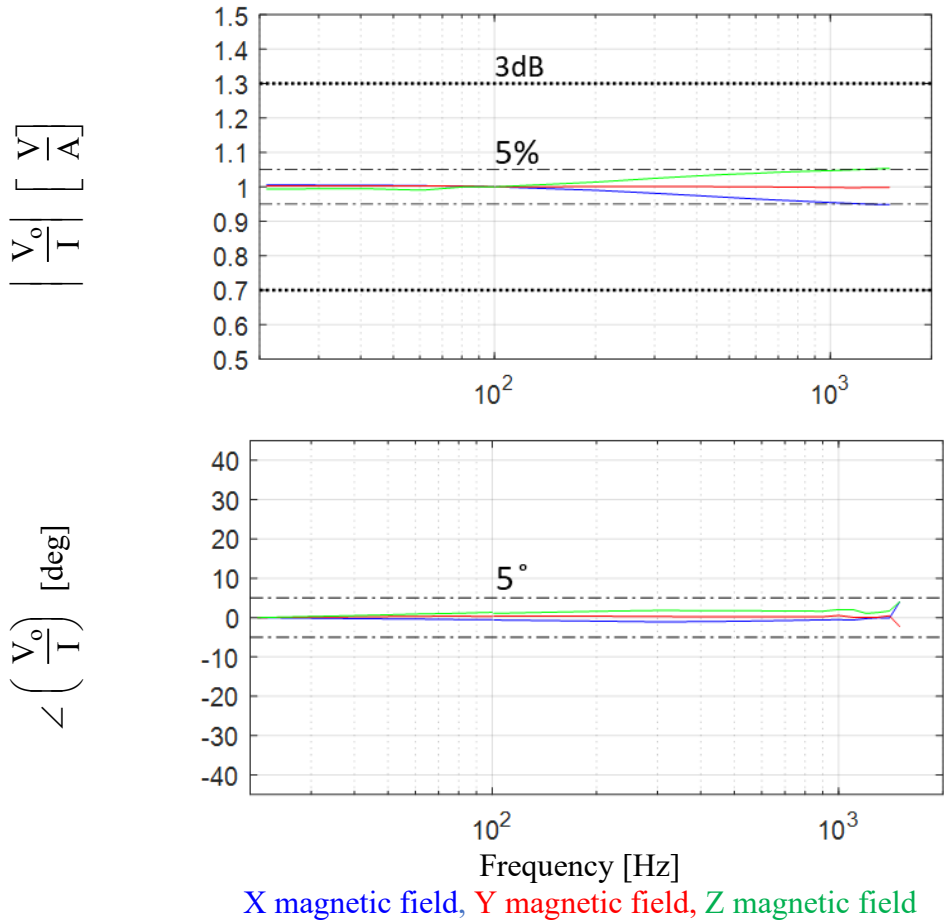

Fig. 8.3-4: Experimental FRFs of 3-D GMR PFD for three-phase currents in the leadframes above a 15mm laminated baseplate with respect to actual test currents normalized to 100 Hz values

The FRF in Fig. 8.3-4 crosses the 5% threshold just above 1200 Hz. This frequency is controllable via design of the leadframes and baseplate as well as the placement of the 3-D GMR PFD. Due to the size constraints of the fabricated 3-D GMR PFD, the scheme to detect the X, Y and Z direction fields in different areas as proposed in sec. 8.2.1.2 is not possible. When the 3-D GMR PFD is placed in between the leadframes with baseplate of 10mm long laminations, the FRF crosses 5% threshold under 1kHz as shown in Fig. 8.3-5. Due to this, the lamination cuts of the

baseplate were made longer to further reduce eddy currents and push the 3-D FBW to 1.2kHz. The multi-physics concerns associated with the cuts will be discussed in the next section.

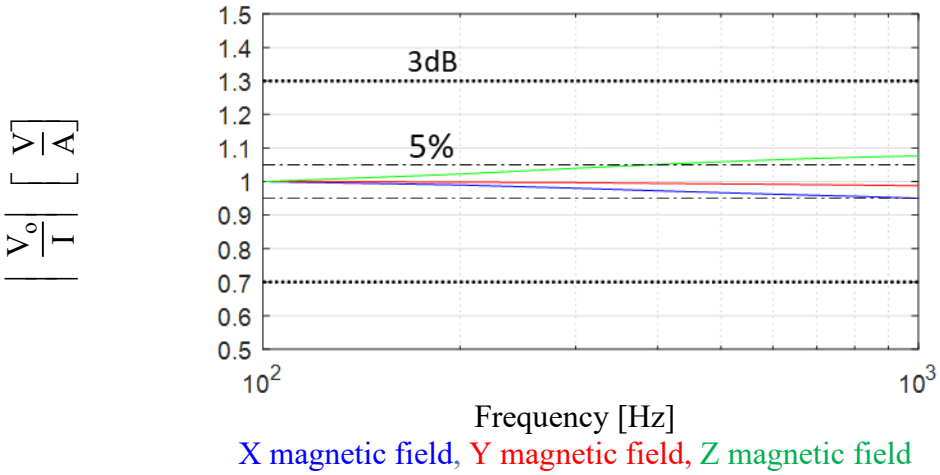

Fig. 8.3-5: Experimental FRFs of 3-D GMR PFD for three-phase currents in the leadframes above a 10mm laminated baseplate with respect to actual test currents normalized to 100 Hz values

Fig. 8.3-6 shows the three-phase FRF when the baseplate is removed from the leadframes. Elimination of the baseplate from the setup makes the FRF much flatter due to the reduction of proximity effects.

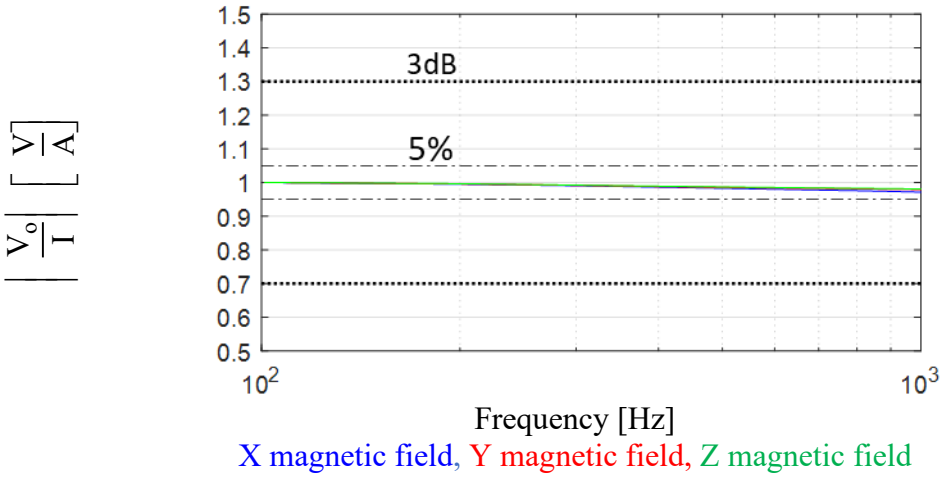

Fig. 8.3-6: Experimental FRFs of 3-D GMR PFD for three-phase currents in the leadframes without a baseplate with respect to actual test currents normalized to 100 Hz values

8.3.3 Experimental three-phase current decoupling

The time domain three-phase current sensing in the leadframes only using a single 3-D PFD is tested by supplying current to a wye-connected resistive load from the three-phase AC power supply at two different frequencies and magnitudes.

The X, Y and Z outputs of the 3-D PFD show a three-phase cross-coupled field but dominated by the field from one of leadframe currents. The PFD outputs, recorded with AC coupling of oscilloscope to filter the DC bias of GMR PFD, are filtered using a 75 kHz, digital low pass filter. Fig. 8.3-7 shows the three-phase currents as dashed lines and PFD outputs as solid lines at 150 Hz test case. The colors are synchronized between the PFD output and the phase current that dominates the output. For example, phase B leadframe is designed to mainly produce the X-direction field. Hence, the blue colored signals show that phase B current has the closest phase relationship with the X-direction PFD output. The same is true for phase A and Z direction PFD output as well as phase C and Y-direction PFD output.

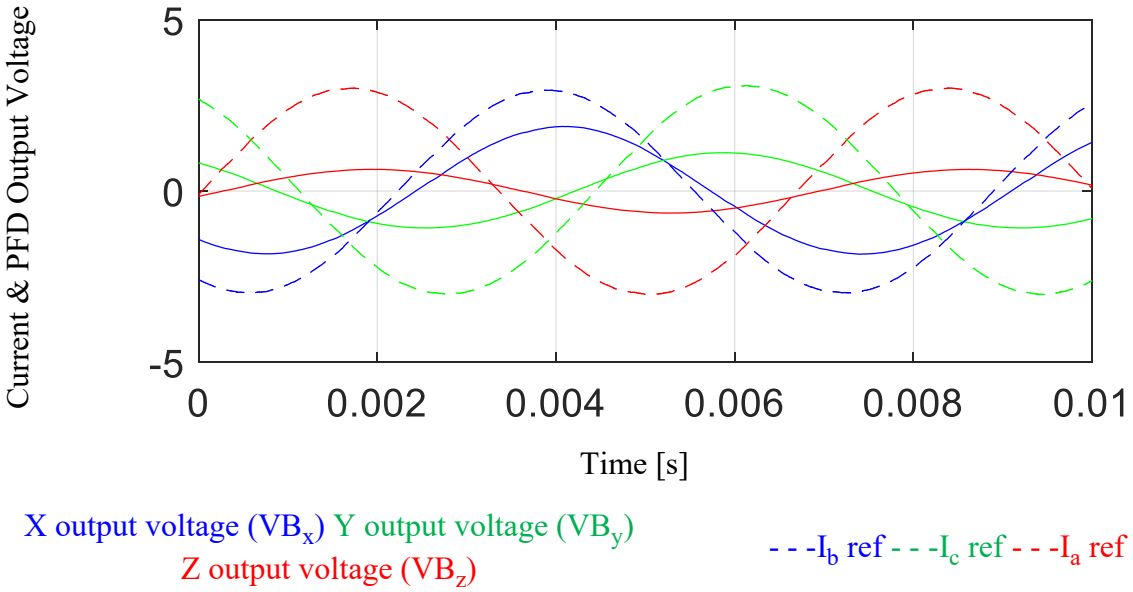

Fig. 8.3-7: X, Y and Z output voltages of the 3-D PFD placed in the 3-D leadframes

The first step in sensing the three-phase currents is to calibrate the decoupling matrix which is shown in (8.3-1). In this experiment, the hybrid calibration method is used. This decoupling method is the same as the one used in chapter 4 and developed in chapter 3.

$$\begin{bmatrix} I_a \\ I_b \\ I_c \end{bmatrix} = \begin{bmatrix} D_{xa} & D_{ya} & D_{za} \\ D_{xb} & D_{yb} & D_{zb} \\ D_{xc} & D_{yc} & D_{zc} \end{bmatrix} \begin{bmatrix} VB_x \\ VB_y \\ VB_z \end{bmatrix} \tag{8.3-1}$$

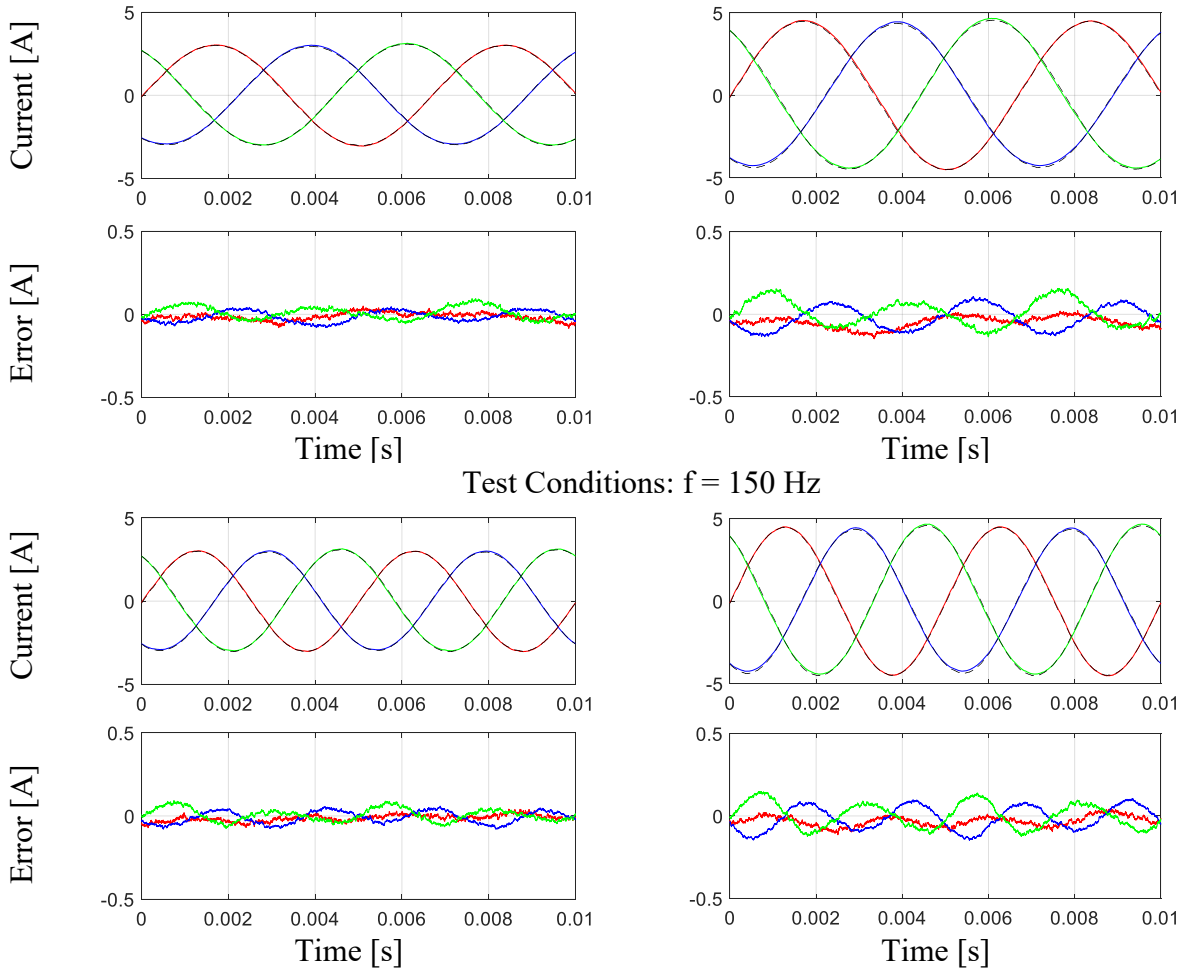

Fig. 8.3-8: Experimental decoupling and sensing of three-phase currents with a single 3-D PFD in 3-D leadframes

The results of current sensing at 150 Hz and 200 Hz for two different amplitudes are shown in Fig. 4.6-5. For all the tests results shown, the maximum error rms error is 2.4% and the maximum instantaneous error is 4.1%. The error can be further reduced by a more precise calibration as well as by reducing the known disturbances and noise using filtering. There is also some error associated with the non-ideality of the GMR PFD as described in chapter 4.

The decoupling method is independent of the phase relationships and frequencies of the currents. Due to the high FBW at the 3-D PFD location, the coupling matrix also remains constant. This is an important trait of the decoupling method without which it will not be usable in transient and fault conditions. Fig. 8.3-9 shows the results of decoupling when two of the phases are shutdown. The decoupling matrix used is the same as the one used in the three-phase tests. The current sensing works well with a reasonable accuracy even in fault condition.

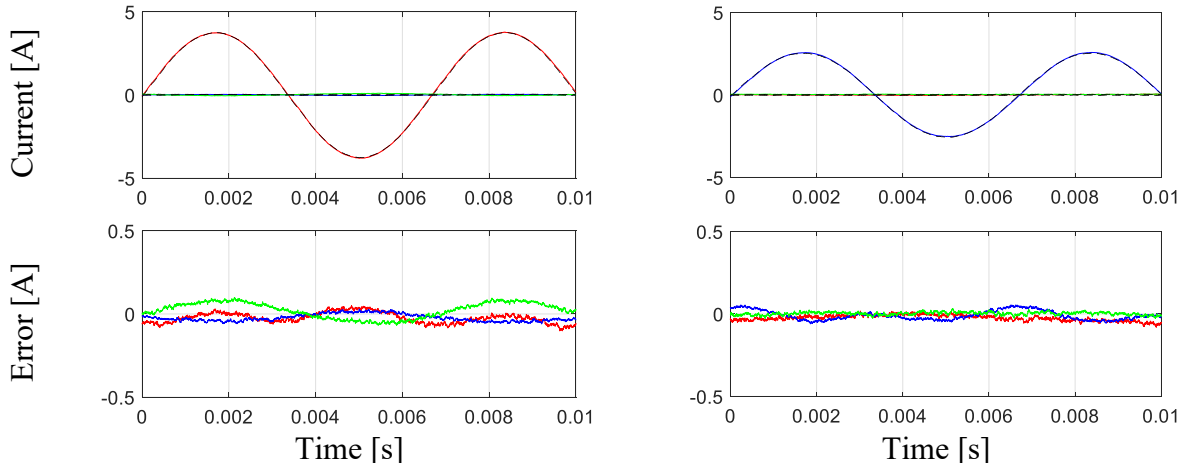

Fig. 8.3-9: Experimental decoupling and sensing of three-phase currents with a single 3-D PFD in 3-D leadframes at fault condition

8.3.4 Multiphysics evaluation of power module compared to the commercial module

8.3.4.1 Thermal Evaluation

One of the features that is added to the power module for the 3-D PFD-based current sensing is the thin cuts in the baseplate below the leadframes. These comb like lamination cuts reduce eddy currents close to the PFD, thereby, improving the 3-D FBW. The laminations reduce the cross-sectional area of the baseplate which can impact the thermal performance of the power module.

The steady state thermal FEA is conducted on Ansys Mechanical on Workbench with heat passing from phase B IGBT chip to the bottom of the baseplate. Since the main interest is in thermal resistance through the baseplate, it is only a comparative analysis between the regular baseplate module and the comb laminated module. Assuming a linear system, the parameters in the FEA are set such that the peak temperature is equal to the thermal resistance from the IGBT chip to the ambient below the bottom of the baseplate. The convection coefficient is selected to set the convection resistance from the bottom of baseplate to the ambient at 1 C/W. It must be noted that the FEA computed resistance for the regular power module has the same order of magnitude but a large error compared to the one reported on the datasheet. The discrepancy is primarily because of the contact resistances between different layers. This is, however, irrelevant to this investigation which is using the thermal FEA as a tool to compare the difference between the regular and comb laminated power modules only.

The FEA results shown in Fig. 8.3-10 are comparative between the regular and the comb laminated baseplate. Without laminations, the thermal resistance from IGBT B to bottom of baseplate is 0.6102C/W whereas, having the lamination increases this thermal resistance by 0.15% to 0.6111 C/W.

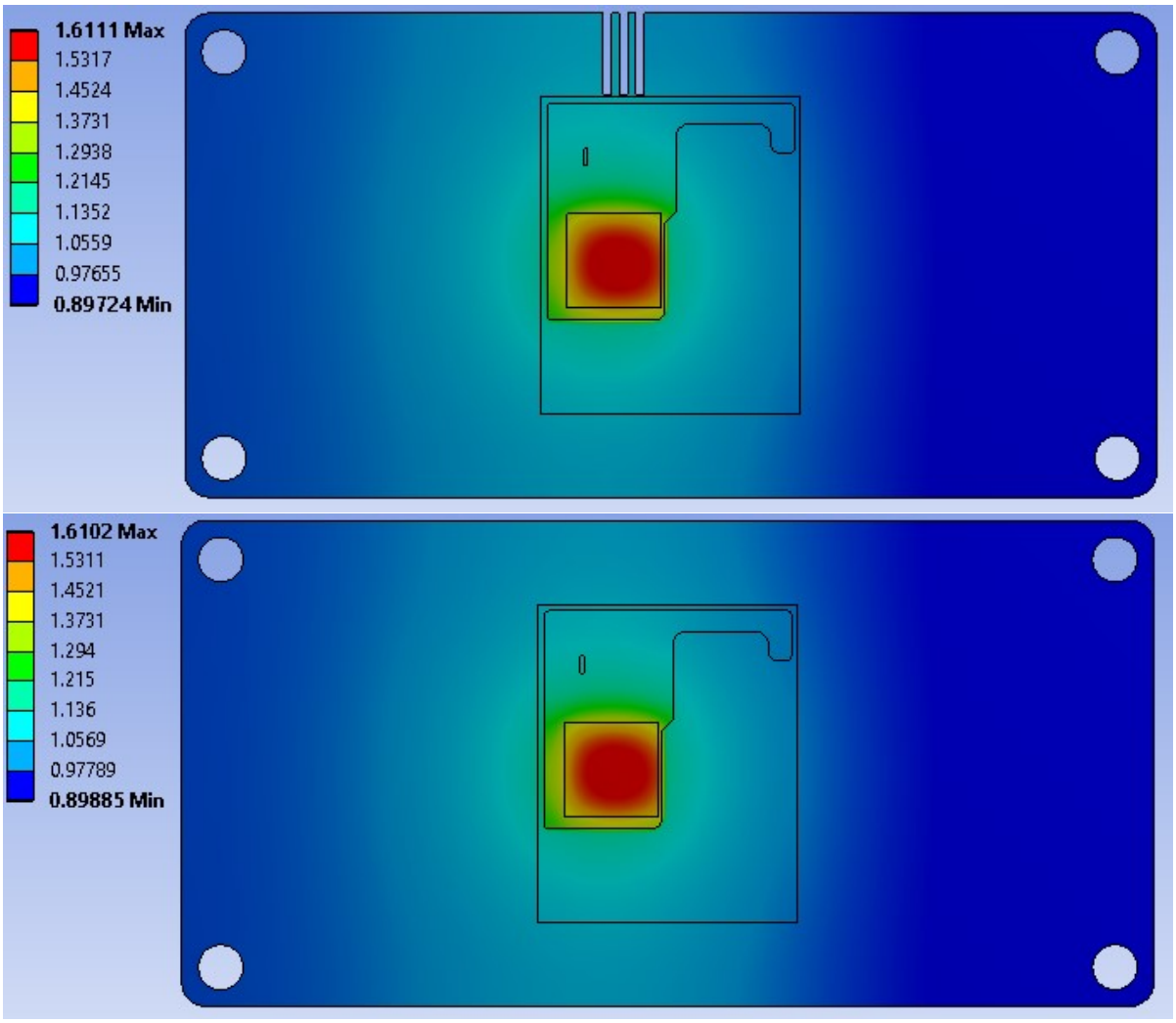

Fig. 8.3-10: Thermal FEA of regular and laminated (simplified) power module with max temperature programmed to be the thermal resistance from IGBT chip to bottom of the baseplate

The decrease in the area of the baseplate is 0.4% which leads to an increase of 0.4% in the thermal resistance based upon the thermal resistance model of the plane wall. The plane wall resistance model in (8.3-2) is relevant for cases when the cross-sectional area is conducting uniformly. In baseplates, there are hotspots closer to the IGBT chips due to high switching and conduction losses.

$$R_{cond\text{-}wall} = \frac{L}{KA} \tag{8.3-2}$$

A reduction of 0.4% in the bottom surface area of the baseplate leads to a similar decrease in the thermal capacitance. A transient thermal analysis of the power module thermal performance is completed using Ansys mechanical and Matlab tools that are developed in WEMPEC [122]. Fig. 8.3-11 shows the ratio of the thermal impedance FRF of the power module with comb laminations and power module without the laminations. The impedance is calculated from phase B IGBT to the bottom of the baseplate. It is clear that the transient method has mesh dependent inaccuracies, however, it can still be deduced that the transient thermal performance of the comb laminated power module remains very similar to the standard module.

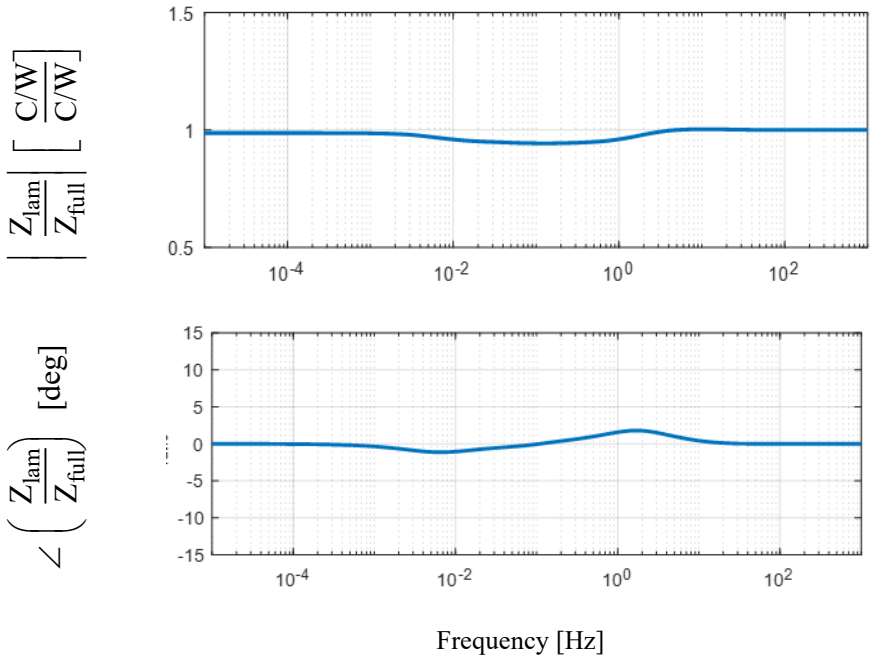

Fig. 8.3-11: Ratio of FRFs of thermal impedance of power modules with and without comb laminations

8.3.4.2 Parasitic Evaluation

The impact of the 3-D leadframes on the electrical performance of the power module is evaluated using the parasitic analysis on the FEA software, Q3D, on Ansys Electronics Desktop. The solution frequency is 200 MHz to allow skin effects to fully develop. The half-bridge, shown in Fig. 8.3-12, has multiple parasitic properties schematically defined. A significant design effort

is attributed to reduce the commutation loop inductance in the commercial modules to allow fast switching and prevent the voltage transients that might be generated from the switching.

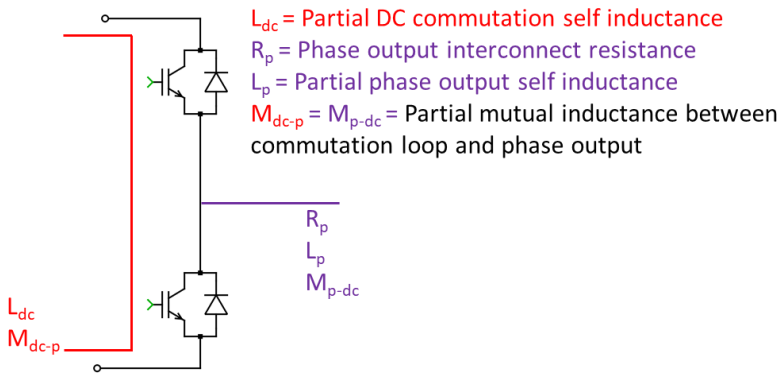

Fig. 8.3-12: Parasitic electric properties of half-bridge power module

The inductance evaluation of the leadframe power module is completed in comparison with the standard bondwire power module to verify that the field shaping leadframes have no significant adverse impact. The results of the inductances are shown in Table 8.3.1 at 10MHz and 1kHz since these are relevant frequencies for DC commutation loop and leadframes respectively.

Table 8.3.1 Self and mutual inductances in nH

Standard power module				
	DC @10MHz	Phase A interconnect @1kHz	Phase B interconnect @1kHz	Phase C interconnect @1kHz
DC (3x parallel)	14.36			
Phase A bondwires	-0.47	6.89		
Phase B bondwires	-0.36		8.84	
Phase C bondwires	-0.33			13.35
3-D field shaping power module				
DC (3x parallel)	14.48			
Phase A leadframe	-0.24	20.40		
Phase B leadframe	-0.41		14.98	
Phase C leadframe	-0.44			33.54

The field shaping leadframes have triple the self-inductance than the bondwire interconnects. Self-inductance is the flux per unit current and leadframes are effectively designed to do just that. Self-inductance of the phase output leadframes is an innocuous property since the load of the power module will have millions of times more inductance making the phase interconnect completely negligible. The commutation loop inductance increases by 0.8% FEA at 10MHz and is expected to have no measurable difference in experiments and at lower frequencies this change is even lesser. The mutual inductance between the phase and DC commutation loop is negative which means that the phase field cancels the DC field and improves the switching performance at some operating conditions. The total mutual inductance between the DC side and three leadframes is reduced by 0.07nH.

The resistance of the leadframe with respect to the bondwires being replaced is shown in Table 8.3.2 in milliOhms at 1kHz. The phase B and C leadframes have a lower resistance than the bondwire interconnects due to the high cross-sectional area, but phase A leadframe has a slightly higher resistance due to its length. The total resistance of the three-phase leadframes is reduced by 33%. Compared to switching losses around the order of kilowatts, the improvement in conduction loss is minimal but does save a couple of watts of energy.

Table 8.3.2 Resistance in the power module in mΩ

Standard power module	DC	1.42
	Phase A bondwires	0.29
	Phase B bondwires	0.39
	Phase C bondwires	0.62
2-D field shaping power module	DC	1.42
	Phase A leadframe	0.33
	Phase B leadframe	0.22
	Phase C leadframe	0.32

8.4 Further Optimization of Leadframe Integrated Power Module

The power module design is a result of a design methodology that helps to arrange the current paths for a well-conditioned field decoupling as well as to reduce the skin and proximity effects to enable high bandwidth integrated current sensing. The design proposed and evaluated in this chapter is a result of using the design methodology and limited manual optimization.

There is a significant room to optimize the power module design for one or more performance criteria including bandwidth, conditioning, PFD positioning, creepage, clearance, parasitics or thermal impedance. The optimization is not pursued in this work because it is specific to the power module, the power electronics system and the application. However, to demonstrate the potential for design improvements, a modification is made in the power module to increase the region of high FBW. The simple modification is increasing the length of the baseplate lamination cut from 10mm to 15mm. Due to this, the cuts extend below the DBC. This increase in the cut length is the design modification that was pursued in the experimental testing to improve the bandwidth.

Fig. 8.4-1 shows the illustration of the baseplate laminations and the 3-D FBW around the leadframes that changes due to the length of the cut. As expected, increasing the length of the DBC cuts increases the region of 3-D FBW. However, this increased FBW will accompany some thermal performance degradation. Numerous optimizations can be made to reduce the loss of thermal performance.

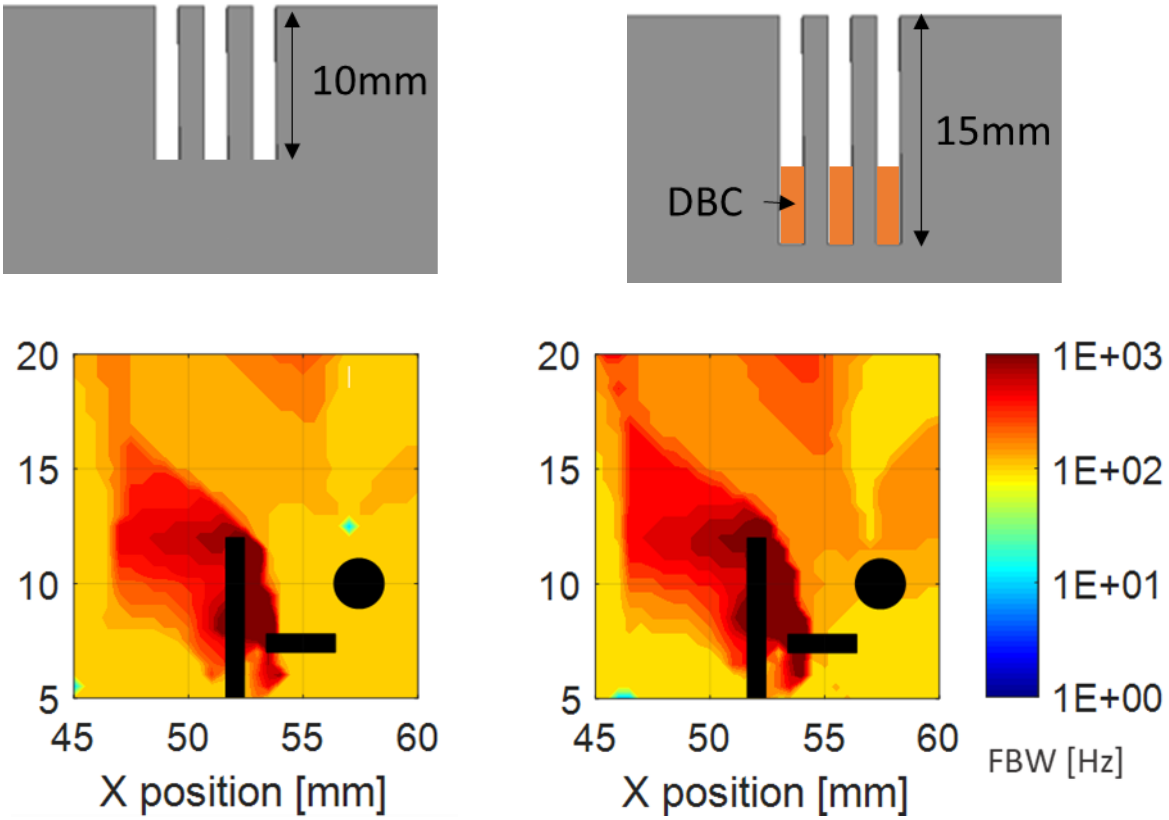

3-D FBW 10mm cuts

3-D FBW 15mm cuts

Fig. 8.4-1: 5% FBW around the leadframes on the analysis plane for balanced three-phase current injection with 10mm and 15 mm long lamination cuts

8.5 Summarizing Remarks

A concise summary of the chapter is available at its beginning. The conclusions and contributions for this chapter are available in the last chapter.

This chapter develops a methodology to design three-phase full-bridge power modules with integrated current sensing using a single 3-D PFD. Designs for DBC-to-terminal leadframes is recommended for producing a net 3-D magnetic field that includes cross-coupling from all three phase currents. The current paths in the leadframes are designed such that each field direction at the PFD location has unique information from three-phase currents leading to a well-conditioned system. Experimental results show that the 3-D field decoupling methodology can be used to extract the three-phase current information from the cross-coupled field detected by a 3-D PFD placed in between the leadframes. The decoupling method measures each current independently.

In this chapter, 3-D leadframe interconnects, terminals and baseplate are designed for an adequate 3-D FBW by reducing the frequency dependency of the cross-coupled 3-D magnetic field by optimizing the skin and proximity effects. The leadframes' magnetic field frequency response is measured inside and outside the power module with the single-phase and three-phase current injections. The leadframes do have a lower FBW when they are integrated in the power modules due to the proximity effects from the baseplate. However, the lamination cuts in the baseplate and the exploitation of finite geometric size of the 3-D PFD are used to enhance the sensing bandwidths. This chapter also verifies that there is a negligible impact of the design recommendations on the thermal and electrical parasitics of the power module.

Chapter 9 SiC Power Module Design for High Bandwidth Integrated Current Sensing

This chapter studies the field shaping of bondwires, and various types of ribbon and leadframe interconnects for a half-bridge SiC power module. A ribbon and leadframe interconnect along with the terminal structure and stepped baseplate are designed to enable the high bandwidth integrated current sensing with planar packaging of the power module. Furthermore, two methods have been proposed to extend the field sensing bandwidth in leadframes interconnects, which are also shown to be immune to the positioning tolerance of the PFD.

The main purpose of this chapter is to develop high bandwidth integrated current sensing methodologies suitable for SiC power modules.

Elements of this chapter are also documented in [123].

9.1 Half-bridge SiC MOSFET Power Module

The SiC power module used for integrated current sensing methodology is a half-bridge Rohm 1200 V 80 A device [89]. Although a particular power module is used in this chapter, the outcomes of this chapter can be applied to many other SiC power modules. The power module shown in Fig. 9.1-1, has a state-of-the-art full SiC MOSFET and diode half-bridge. The size of the baseplate is 107 x 43mm and 4mm thick.

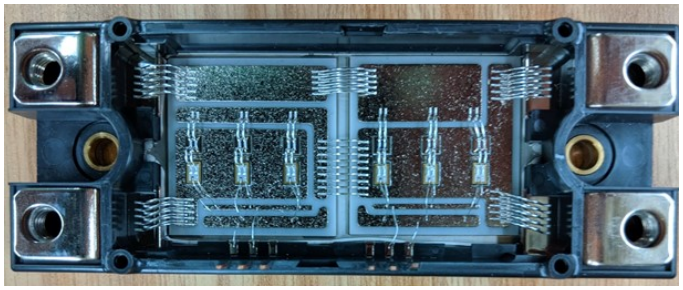

Fig. 9.1-1: Half-bridge SiC power module for integrated current sensing

SiC power modules are especially designed for fast switching which leads to the need for higher control and sensing bandwidths. Increased switching frequencies enable the synthesis of faster fundamental frequencies which help with higher power densities and smoother torques in high pole number machines. In the state-of-the-art, fundamental frequencies above 1kHz are rare but this research section has a benchmark of 5% FBW of 10kHz. This benchmark will satisfy the bandwidth requirements for the next few decades.

SiC MOSFETS are also the next generation of power transistors and bring along the possibilities of more reliable interconnect structures which allow for double sided cooling as well. As described in chapter 1, ribbon interconnects are considered to be on the horizon of power module integration and packing technology. Chapter 1 also describes that [115] has used the same Rohm SiC power module for die region integrated sensing. The focus here is the integration of PFD-based sensing close to phase terminal and DBC to terminal interconnect. Fig. 9.1-2 shows the path of the current through the phase terminal interconnect. The design of the module is such that the phase current can exit the power module from both parallel connected terminals. The plane shown in Fig. 9.1-2 is where the field analysis is conducted.

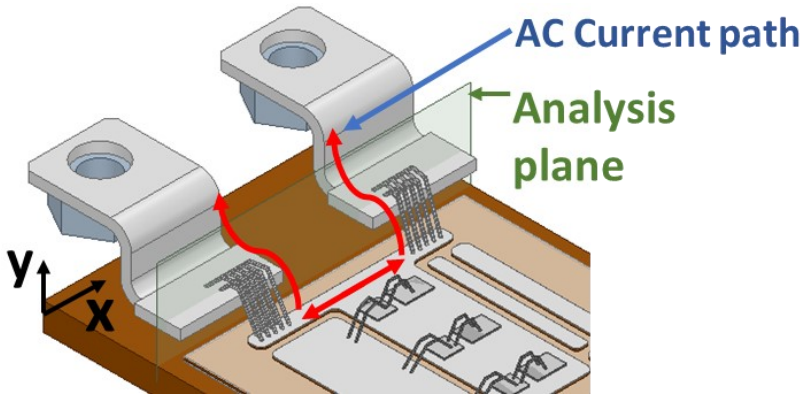

Fig. 9.1-2: Rohm half-bridge power module current path and field analysis plane

There is only one phase current which means that the current can be sensed with a single 1-D PFD. If a 2-D PFD is utilized, the X and Y fields can be used to synthesize field along any vector direction in the XY plane. Generally, this gives the capability to sense the 1-D magnetic field along various directions in a 2-D space. This is explained in detail in chapter 10. Furthermore, a single 1-D PFD can also be rotated to the correct angle for the same purpose. The field analysis conducted for the half-bridge SiC is done using 1-D fields.

9.2 DBC Stack-up

The Rohm SiC power module has a stack-up that consists of copper (DBC top), ceramic (DBC substrate), copper (DBC bottom), Nickel (baseplate plating), and copper (baseplate). In [115], it is found that the fields in the die region of this power module experience phase lags due to Nickel plating of the baseplate in this SiC power module. Although this issue is not experienced close to phase interconnect and terminal, the baseplate design methodology from chapter 7 is applied to reduce the phase lag.

The phase lag occurs because Nickel has a high permeability and a much smaller skin depth than copper. The induced eddy currents in the baseplate and DBC generate a magnetic field that is phase shifted and is shaped such that most of it remains above the semiconductor chip, reducing the bandwidth of current sensing and introducing the phase shifts. In [115], the method used for tackling the phase shift employed a second sensor and an imaginary FBW methodology to decouple the lag. In this work, the baseplate lamination strategy is applied to the stack-up to fundamentally shape the fields, hence there is no need to decouple using precise positioning and a second sensor.

In Fig. 9.2-1 the field analysis of the stack-up of the power module shows that the field has very low bandwidth and a phase lag. However, having thin laminations in the baseplate shows that

the phase lag is reduced, and bandwidth is much more improved. This is because baseplate has most of the eddy fields whose path is broken up by the laminations. Using lamination in transformers cores is a conventional method to reducing eddy losses. The laminations in the Nickel plating also reduces the cross-coupling of the eddy current field with the main current field.

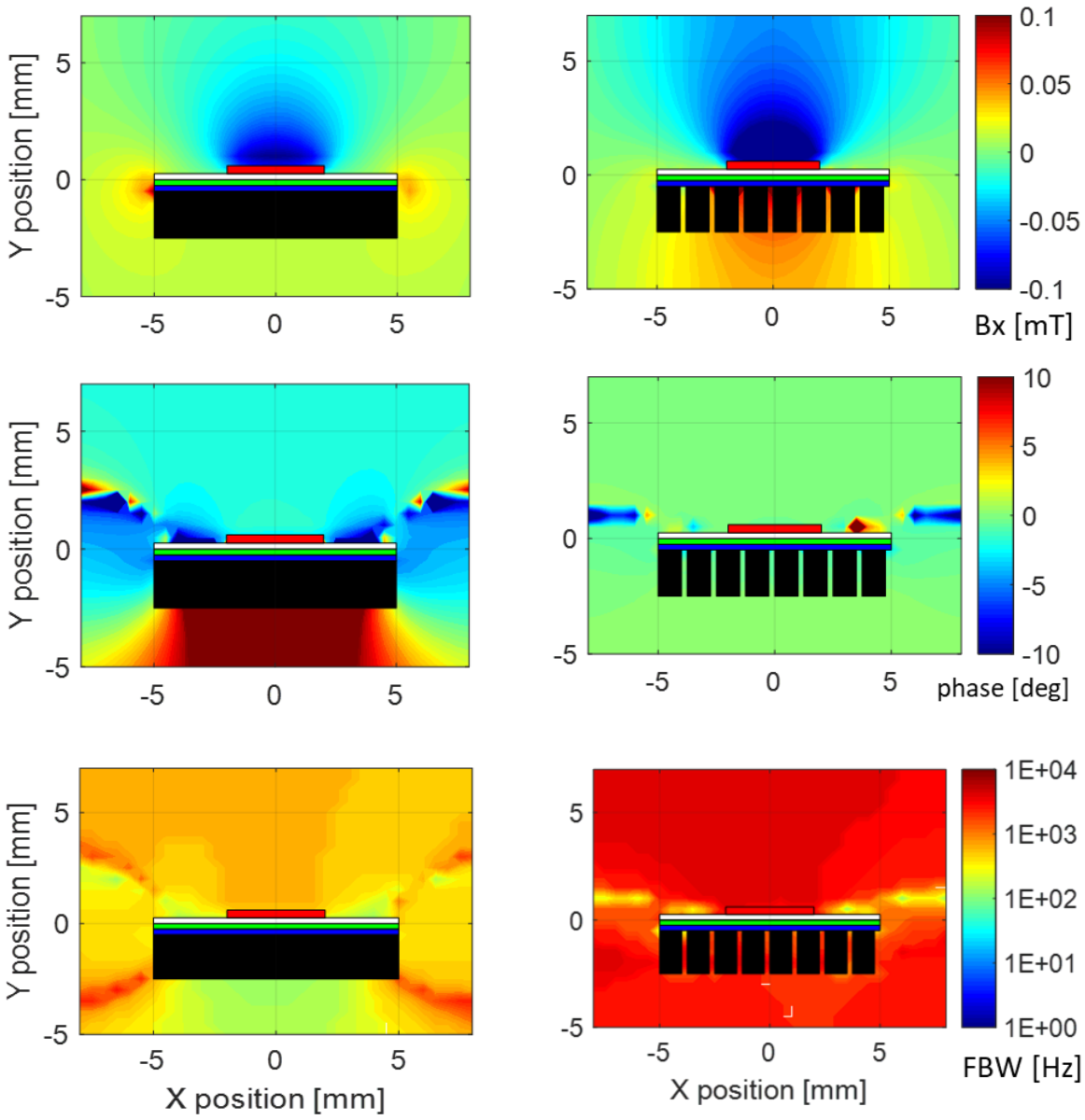

Full stack-up Laminated baseplate stack-up

Fig. 9.2-1: X-direction DC flux density, field phase lag at 100Hz and 1-D 5% FBW for stack-up

9.3 Magnetic Field Analysis of the Power Module

The data on commercial SiC power modules is hard to obtain from companies due to the intellectual property concerns. Thus, the geometry of the module is configured from limited data provided by the manufacturer as well as by empirically from the real power module. The CAD model of module shown in Fig. 9.1-1 was first developed in [115] and then made more accurate by cutting open a real module. Despite the best estimate, there are geometric features and material coatings that are impossible to model in FEA from the available information. Although the CAD model is functionally accurate with all the module layers, it still omits geometric features that are irrelevant to the magnetic field analysis for reasons of FEA optimization. The 3-D FEA results are shown on the 2-D plane from Fig. 9.1-2 when the current is still in bondwires and about to enter the AC terminal.

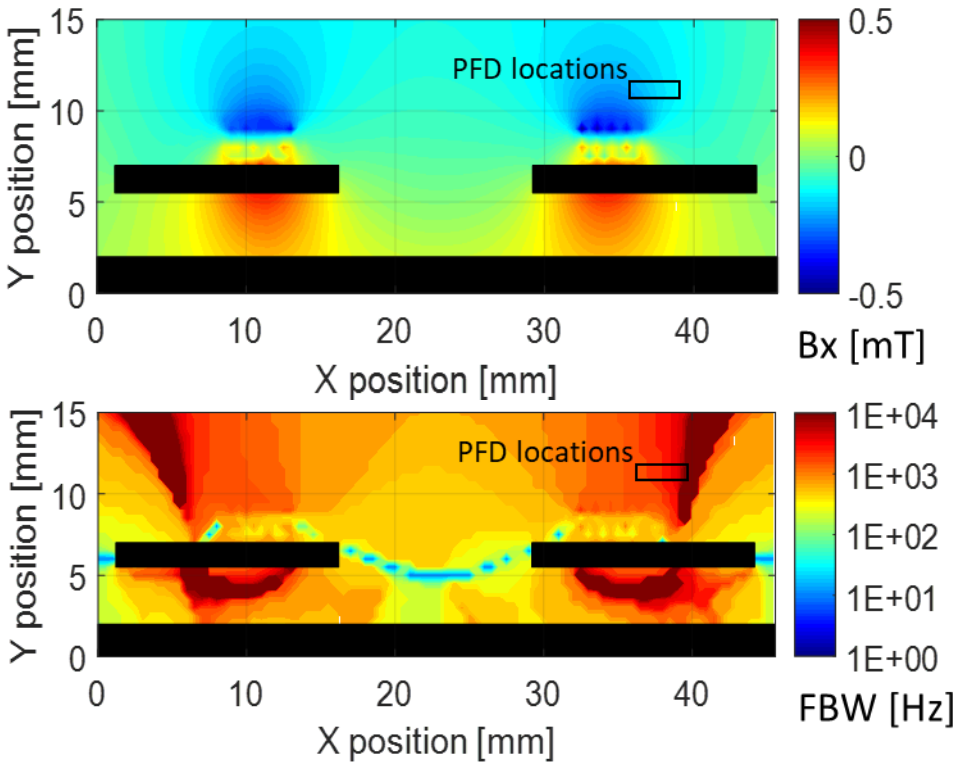

Fig. 9.3-1: X-direction flux density and 1-D 5% FBW around the phase terminal with 5 A current injection

Fig. 9.3-1 shows the X-direction magnetic flux density when 5A, 0.1Hz current is passed into the AC terminals in FEA as well as the 1-D 5% FBW close to the terminal on the plane shown in Fig. 9.1-2. The bottom black rectangle represents the baseplate. The majority of the region above the terminal falls below 5% bandwidth of 2kHz. There are thin regions with higher FBW but positioning a PFD without any reference structures in these thin regions is a manufacturing challenge.

9.3.1 Experimental frequency response analysis

The test set up to experimentally evaluate the frequency response and flat bandwidth of the SiC power module is the same as the one used in chapter 7 in sec. 7.3.1 . The test configuration to experimentally evaluate the frequency response function (FRF) and flat bandwidth of the SiC power module involves passing current through the AC output terminals of the SiC power module so that the magnetic fields are generated around the two terminals and their interconnects. Input current is passed into the module via the DC terminals and out the AC terminals as shown in the electrical schematic in Fig. 9.3-2. A 5-dimension precise positioning stage is used to position the GMR PFD inside the power module. The GMR PFD output voltage, which measures the magnetic flux density (and current), is analyzed with respect to the current reference using a Venable frequency response analyzer (FRA). The current is generated by an audio power amplifier which can produce clean sinusoidal currents up to 15kHz and is controlled by the FRA.

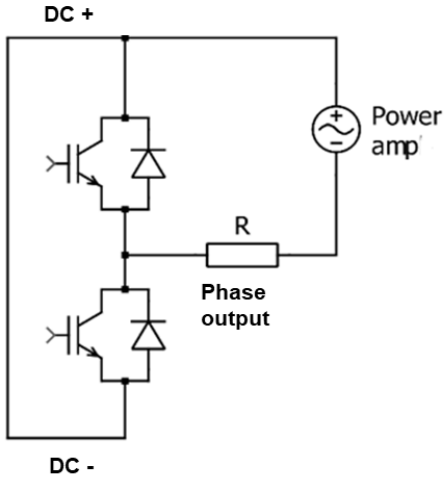

Fig. 9.3-2: Electric schematic of power amplifier and power module setup for current injection to measure the FRFs of the PFD outputs

The GMR PFD is positioned in the region shown as a rectangle on the contour plots in Fig. 9.3-1. The rectangle in its width represents multiple test points since the PFD is moved in the rectangular region. It should also be noted that this is an approximate region of the PFD since points inside the power module are found relatively without an absolute reference.

The experimental frequency response of the X field with respect to the actual current at the PFD locations is shown in Fig. 9.3-3. The point closest to the bondwire has a steep downward slope in FRFs, whereas moving away from the bondwire flattens out the FRF. As the PFD moves further away from the bondwires, there is an upward trend in the FRF amplitude near 500Hz, which increases the 5% FBW over 9.5 kHz, albeit with a relatively larger error that remains within 5% bounds. The phase error is approx. 5 deg in the decade between 1kHz and 10kHz, which is undesired. From a practical manufacturing standpoint, the high sensitivity of the FRF amplitude and angle to changes in the PFD position is a disadvantage that should be significantly reduced or eliminated. The selection of the PFD location point is a design choice.

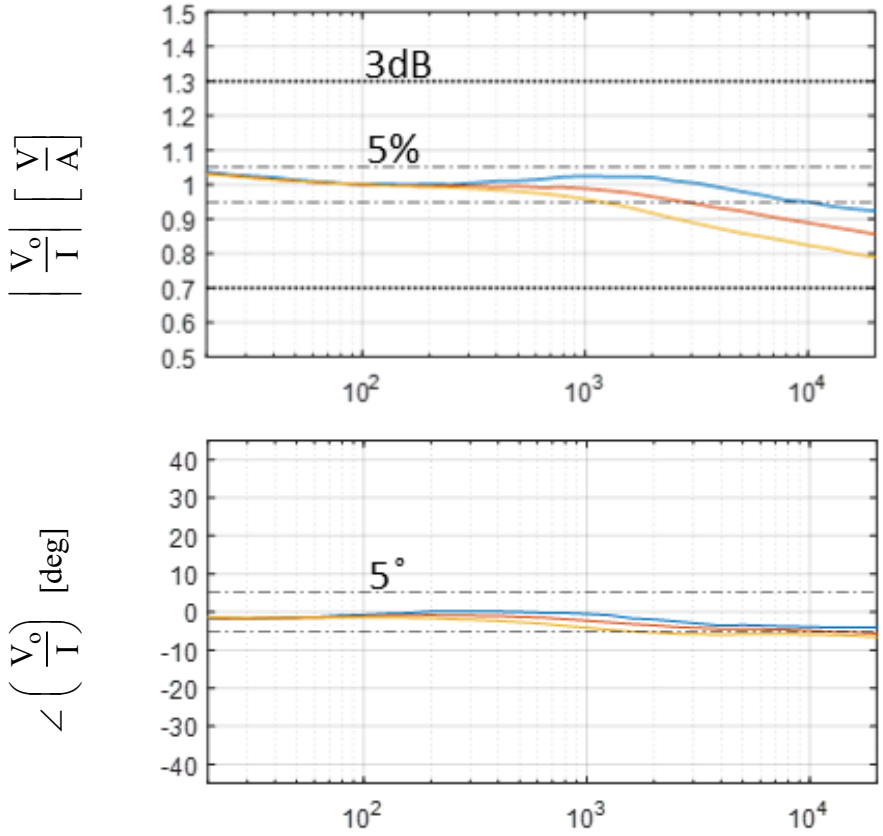

Fig. 9.3-3: Experimental FRFs of GMR PFD output with respect to reference current in SiC power module normalized to 100 Hz values

The FRF in Fig. 9.3-4 is at a point predicted to be over 10kHz in the FEA shown in the dark red in Fig. 9.3-1 (North East of rectangle). This point has a very flat FRF particular between 100Hz and 10kHz but detects much lower field strength. The point of concern is the steep gain drop and phase lag between 10 and 80 Hz. The majority of this drop is not modelled in the FEA but can be physically explained using a similar phenomenon studied in [115]. The terminal is plated with nickel which is a magnetic material with a permeability 600 times more than copper. This causes skin depths in Nickel below 100 Hz that are comparable to skin depths in copper over 10kHz. The

FEA does not account for the Nickel coating which is reported in the manufacturing documents [89]. The Nickel coating has a lesser impact when the field is measured closer to bondwires.

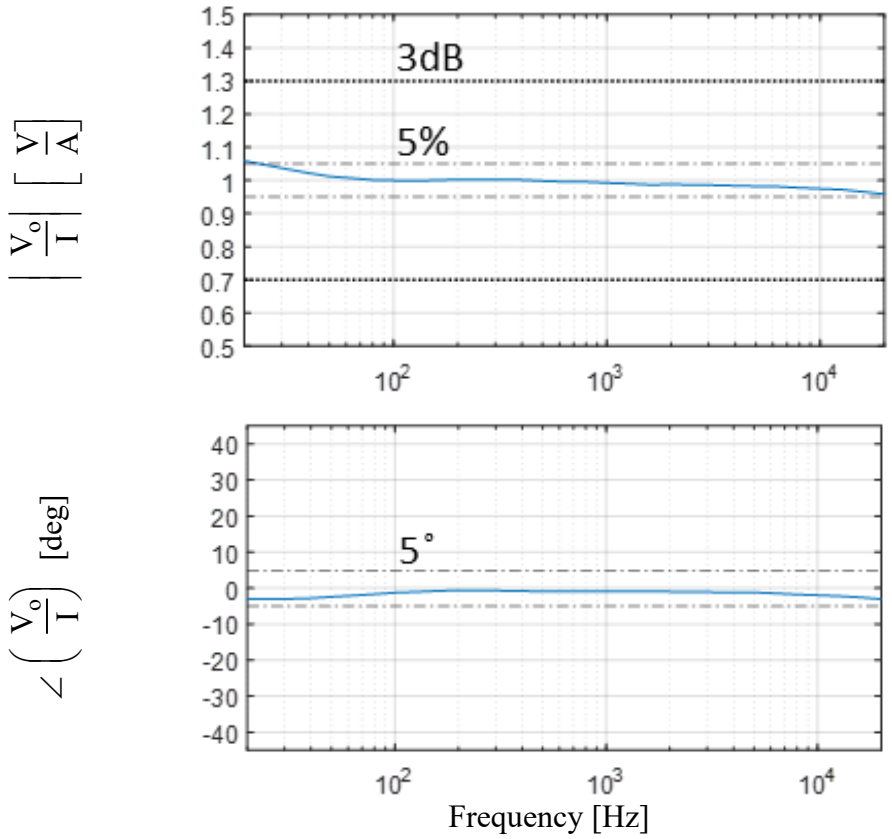

Fig. 9.3-4: Experimental FRFs of GMR PFD output with respect to reference current in SiC power module normalized to 100 Hz values at high FBW point.

9.4 Comparison of Bondwire with Ribbon Interconnects for Field Shaping

FEA analysis is conducted for various sizes of ribbon interconnect as a replacement for the bondwire terminal interconnect in the power modules. The ribbon interconnect design is adapted from [90] in which it is studied for reliability. The analysis plane from Fig. 9.1-2 is maintained in this field analysis. Since the ribbon interconnect is used to replace one of the two phase terminals,

the other parallel terminal remains bondwired and provides a direct comparison. The terminal to the right has bondwires, whereas the terminal on the left has ribbon interconnects.

Three versions of ribbon interconnect are investigated. The first version of ribbon interconnect has a width of 1mm and thickness of 0.2mm. In the subsequent versions, the thickness is maintained constant, whereas the width is increased to 2mm and 6mm. The total combined width of ribbons does remain 6mm. The different interconnects are shown in Fig. 9.4-1.

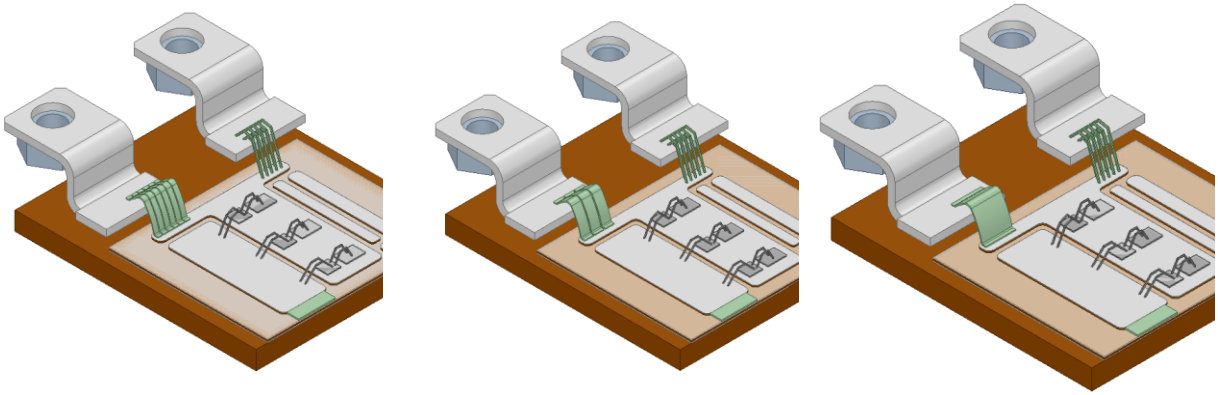

Six 1mm x 0.2mm ribbons Three 2mm x 0.2mm ribbons One 6mm x 0.2mm ribbon

Fig. 9.4-1: Three investigated versions of ribbon interconnect designs

Fig. 9.4-2 shows the quasi-DC flux density and 1-D 5% FBW of the interconnect on power module phase terminals. The flux density can be used to determine the size of the ribbon as it shapes around the cross-section of the ribbon. It can be seen that there is no significant difference between bandwidth of the different ribbon interconnects and the bondwires. This suggests that the FBW is a result of a combination of skin and proximity effects. In bondwires and narrower ribbons, the proximity effects dominate, whereas in the wider ribbons, skin effect dominates. Another important factor in determining the FBW is the terminal shape and dimensions that influence the current spreading at higher frequencies. Both skin and proximity effects are explained by the

Maxwell Faraday equations and cause eddy electric fields. This shows that the ribbon interconnects are not any better for field shaping.

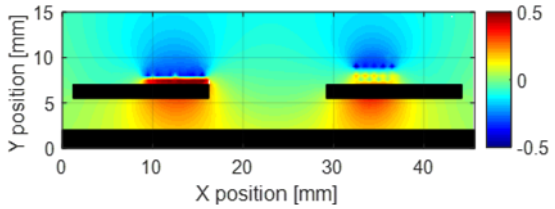

Bond wires on right 1mm wide ribbon on left

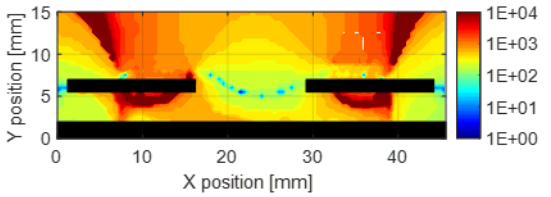

Bond wires on right 1mm wide ribbon on left

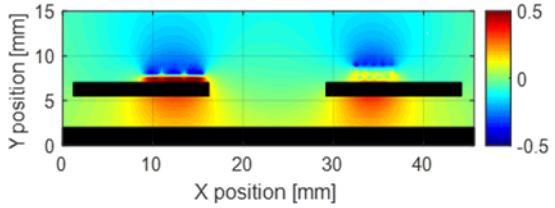

Bond wires on right 2mm wide ribbon on left

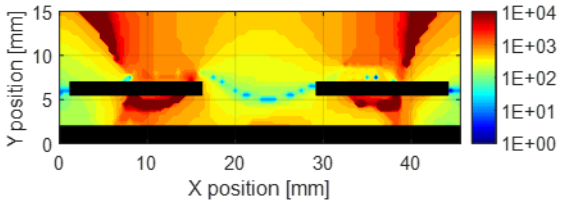

Bond wires on right 2mm wide ribbon on left

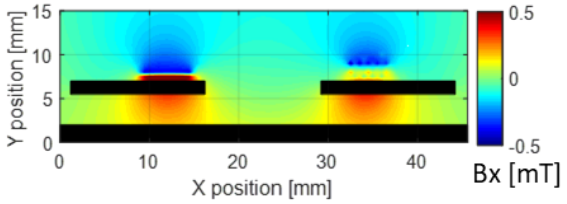

Bond wires on right 6mm wide ribbon on left

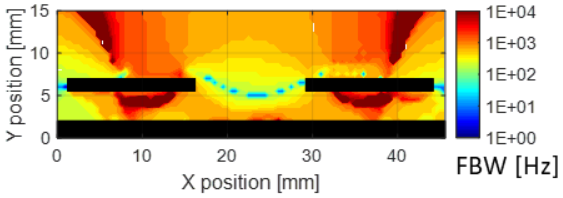

Bond wires on right 6mm wide ribbon on left

Fig. 9.4-2: X-direction DC flux density and 1-D 5% FBW of power modules with various ribbon interconnect sizes

It should be noted that despite no change in FBW from bondwires to ribbon, the ribbon interconnect is the preferred choice for PFD due to the reliability, robustness and repeatability of ribbon shape. Bondwires thermal fatigue and liftoff as well as the relative change in bondwire position due to their higher number are more likely to happen [92][93]. All of these bondwire changes can impact the field shape.

9.5 Ribbon Interconnect and Terminal Design

9.5.1 Design Analysis in FEA

The thick and wide (6mm x 0.2mm) ribbon interconnect is used to design the terminal and its interconnects in a more holistic design approach for PFD-based high-bandwidth current sensing. The main design feature is to remove any non-essential copper from the terminal and eliminate the high frequency current spreading in the terminal via skin effect. The terminal interconnect which has a significant amount of copper is trimmed and connected to the wide ribbon interconnect. The terminal and interconnect design are shown in Fig. 9.5-1. The terminal is 1.5mm thick and its design at the external termination is kept the same as the commercial power module with a through-hole and nut for external connection to the AC output conductor. The interconnect is a 6 mm wide ribbon and matches the terminal width.

The second main design feature is the step reduction in the baseplate thickness along the edge of the DBC. The baseplate is made of a thermally and electrically conductively material, usually copper. This leads to Faraday induction or proximity effect-based eddy currents in the baseplate much like the Si power module. Multiple design changes can be to reduce the eddy electric fields and currents. In the Si power module, laminations were introduced. In this power module, a step design feature is introduced. The step, as shown in Fig. 9.5-1, reduces the copper in the baseplate and also increases the distance between the phase current and eddy currents in the baseplate, which leads to less cross-coupling of their respective magnetic fields. The result is that the field above the terminal has a significantly lower frequency dependency. The size of the step in this simulation is 2mm (i.e. the 4mm baseplate is stepped down to 2mm), resulting in a spacing of 5.5mm between the top of the thinned baseplate and the bottoms of the two AC terminals. The multiphysics aspects of step in baseplate will be discussed in the next section.

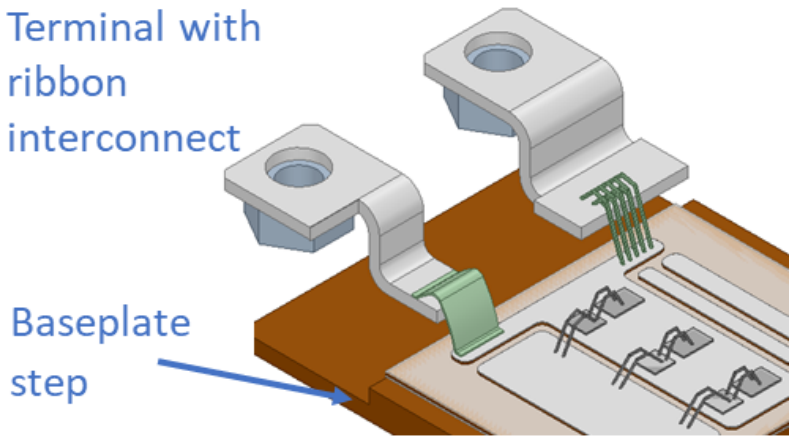

Fig. 9.5-1: Ribbon interconnect and its terminal in the power module

The quasi-DC flux density and 1-D 5% FBW of the designed power module is shown in Fig. 9.5-2. The right terminal in the FEA of the power module still has the bondwire connection so there is a direct comparison available. The baseplate cross-section does not lie on the analysis plane due to the 2mm step. The remaining cross-section of the baseplate lies beyond the minimum Y axis limit.

The modified terminal ribbon interconnect (left side of Fig. 9.5-2) exhibits superior field shaping and nearly twice as much high-FBW area (dark red). There is an overlap of the high-flux density and high-FBW regions which is also advantageous for SNR. The region immediately above the terminal reaches 1kHz FBW and the region above the left edge of the terminal achieves >10kHz FBW. The FEA simulation shows that the terminal can serve as a position reference for placement of the GMR PFD to sense high-frequency currents. Since the original ribbon is already shown to have a similar FBW as the bondwire, the redesigned narrowed terminal with the baseplate step is primarily responsible for the FBW and SNR improvement. The terminal and baseplate are designed with less opportunity for frequency dependent current spreading and eddy current generation.

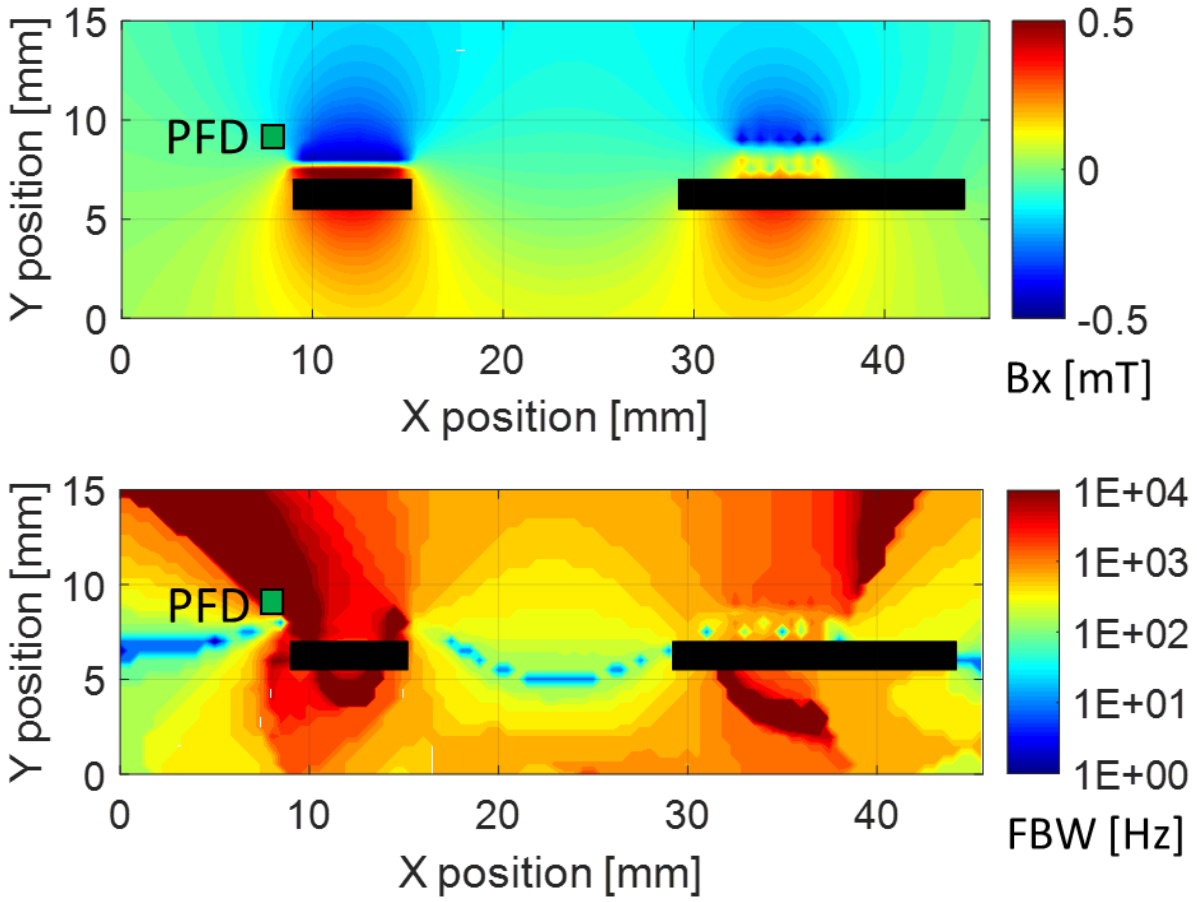

Fig. 9.5-2: Flux density for 5A, quasi-DC current in each terminal and 5% FBW for new ribbon interconnect terminal (left) and original bondwire terminal (right)

9.5.2 Experimental frequency response analysis

A simplified version of the power module shown in Fig. 9.5-3 with the ribbon interconnect, the narrowed terminal, DBC substrate (single copper sheet), and stepped baseplate has been fabricated to evaluate the experimental performance of the modified design. The second wider terminal on the right side of the tested module uses a ribbon-like interconnect that is also included in the test with equal current. The test circuit passes the same current through the two terminals connected in series. This test only includes the components that can influence the integrated sensing via eddy currents (i.e., skin and proximity effects) and does not include the power switches.

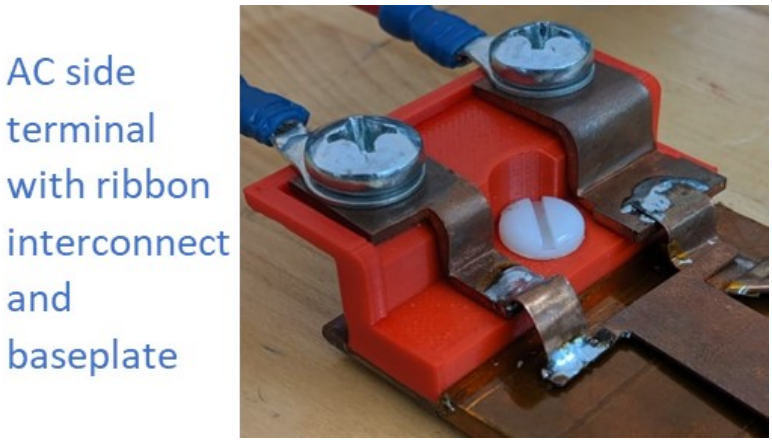

Fig. 9.5-3: Fabricated ribbon interconnect and its terminal

The PFD location shown in Fig. 9.5-2 is used for experimental frequency response. This location has a decent field and a high FBW. Although there are other locations right above the ribbon that provide even better access to field and bandwidth, it must be noted that PFD is mounted on a PCB which has a size that causes interference with the ribbon if PFD is positioned too close to it.

Fig. 9.5-4 shows the measured frequency response of the PFD output with respect to the test current. Three test cases are shown with three values of the baseplate step size. A step down to 2mm has the worst performance whereas test case with a step-down to 0mm has the best performance. Stepping down to 0mm refers to the case of removing all of the copper baseplate under the terminal beyond the end of the DBC substrate.

These results demonstrate that the frequency response improves monotonically as more copper is removed and its distance from the terminal is increased, progressively reducing the baseplate eddy currents. The 5% FBW of the case with baseplate step to 0mm is >20kHz. There is approx. 10% amplitude error when the baseplate is stepped to 2mm or 1mm for frequencies under 20kHz. The FEA predicts a higher FBW than the experimental results. A small deviation of 5% between the predicted and measured FRF can lead to a much higher change in FBW, due to the

nonlinearity of the FBW metric. This is demonstrated here when a baseplate step of 2mm has a measured 10% FBW that is >20kHz, but the 5% FBW is under 500Hz.

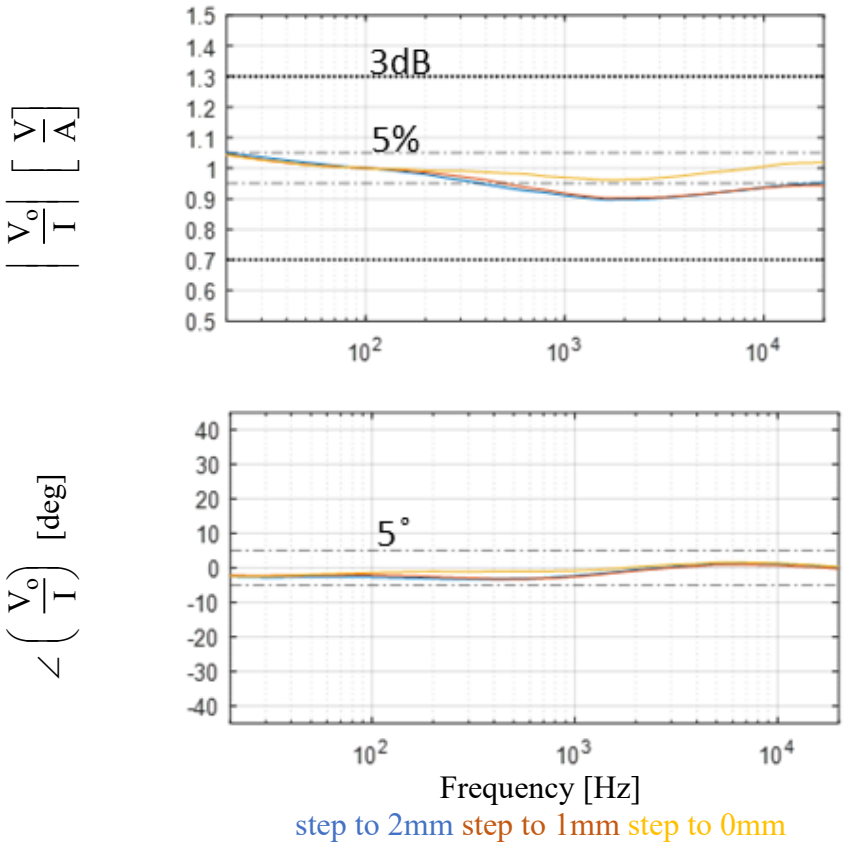

Fig. 9.5-4: Experimental FRFs of GMR PFD output for tested ribbon interconnect terminal with respect to actual test current normalized to 100 Hz values

9.6 Leadframe Interconnect and Terminal Design

9.6.1 Design Analysis in FEA

A leadframe interconnect and terminal is also been designed to improve the field shaping for power module integrated current sensing. Since the leadframe is thicker than the ribbon interconnect, the leadframe width has been reduced to 3.5mm to reduce the lateral skin effect. The leadframe is used to connect the DBC to the terminal which is designed to merge seamlessly using an identical width. The planar leadframe interconnect is shown in Fig. 9.6-1. The higher thickness

of the leadframe, compared to ribbon, does allow some current density changes across the thickness. However, at frequencies of interest below 10 kHz, the skin depth in copper leadframe is 0.6 mm so if the thickness of the leadframe is comparable to the skin depth, skin effect in the thickness is not a major issue.

The baseplate is customized with a 4mm to 2mm step down (thickness reduced) along the edge of the DBC to reduce the proximity effect. The rate of change of magnetic flux induces eddy currents in baseplate. A step ensures a distance of 5.5mm between the terminal and baseplate due to which frequency dependent magnetic field from eddy currents in baseplate are subdued and their magnetic field is less cross-coupled with field from AC current detected by the PFD.

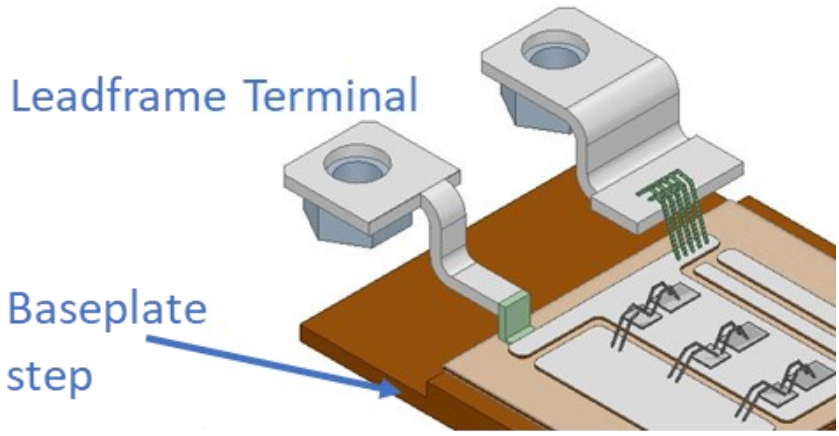

Fig. 9.6-1: Leadframe interconnect and its terminal

The quasi-DC flux density and the 1-D 5% FBW of the leadframe design is shown in Fig. 9.6-2. The terminal serves as a position reference for GMR PFD placement to sense currents up to 10kHz. Another advantage of the leadframe is that by being planar and compact, it allows PFD positioning in front of it as well. This region is generally occupied by the loopy bondwires or the ribbon interconnect.

There is significant area of 5% FBW exceeding the 10kHz above the terminal as shown by the two planes of analysis. This is a sufficient FBW for sensing currents in most modern day

applications. The main advantage of leadframe over the bondwired terminal on the right is that leadframe provides a wide area of high bandwidth which has an overlap with higher fields too, which is very useful for SNR as well for disturbance rejection.

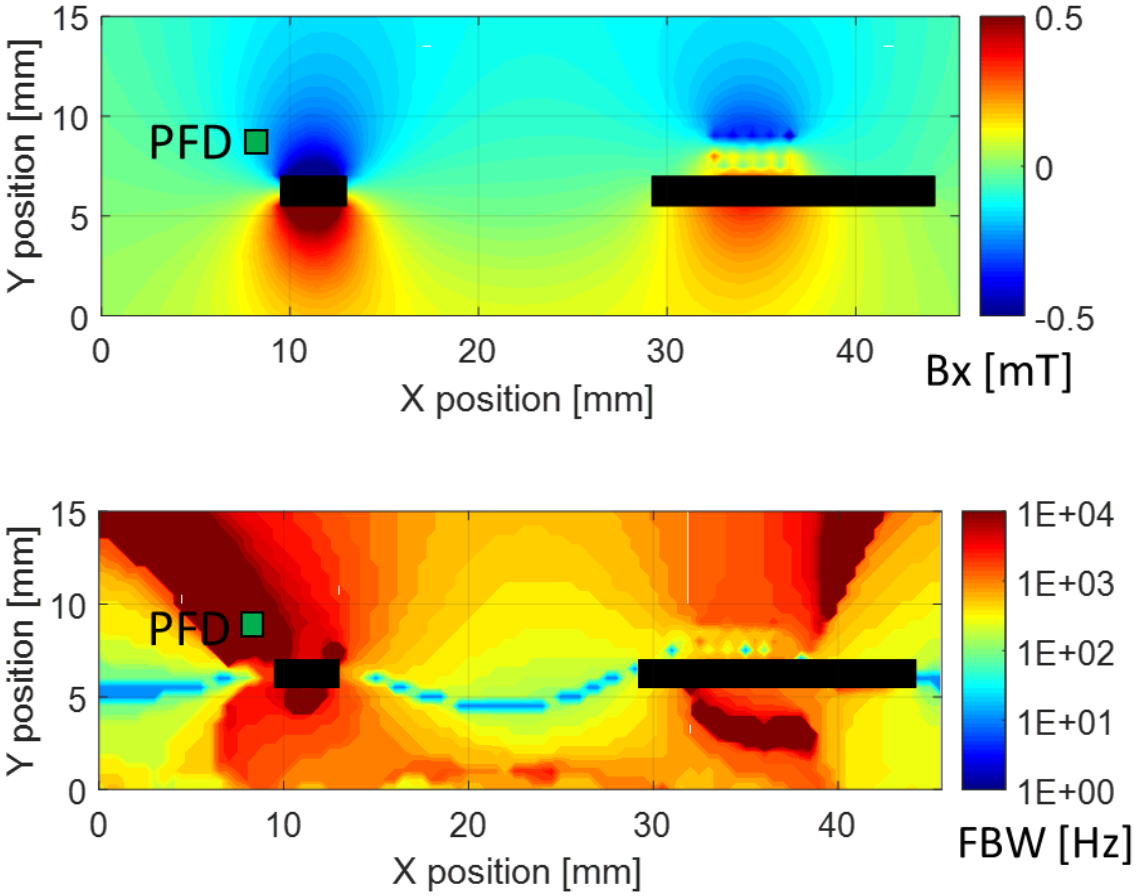

Fig. 9.6-2: Flux density for 5A, quasi-DC current in each terminal and 5% FBW for leadframe interconnect terminal (left) and bondwire terminal (right)

9.6.2 Experimental frequency and time response analysis

Fig. 9.6-3: Fabricated leadframe interconnect and its terminal

A simplified prototype module with a leadframe interconnect, terminal, DBC substrate (single copper sheet), and stepped baseplate, shown in Fig. 9.6-3, has been fabricated to experimentally measure the bandwidth of the GMR PFD current sensor in the module with leadframe interconnects. This test only includes the components that can influence the integrated sensing via eddy currents (i.e., skin and proximity effects) and does not include the power switches. The electrical connections and analysis tools are the same as used in sec 9.3.1.

Fig. 9.6-4 shows the measured FRF for the GMR PFD output with respect to the test current flowing through the terminal. The frequency response with baseplate stepped to 0mm (i.e., baseplate removed beyond DBC) is very flat. The FRF with step to 1mm and 2mm have a downward slope in the region near 500 Hz but flatten out beyond 2kHz. Thinner baseplates result in flatter frequency response. The FEA predicts a 5% FBW of >10kHz for the case with step to 2mm, but the experimental results show a slightly higher error. Experiments show that 10% FBW is >10kHz with a step to 1 and 2mm and 5% FBW is >10kHz with a step to 0mm.

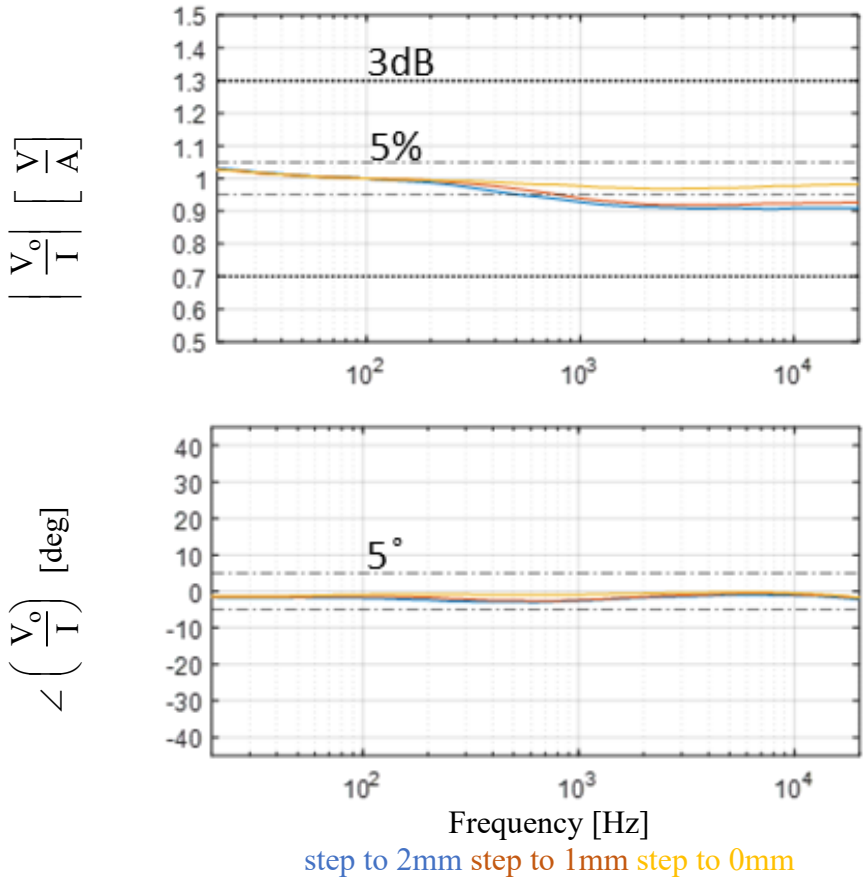

Fig. 9.6-4: Experimental FRFs of GMR PFD for leadframe interconnect terminal with respect to actual test current normalized to 100 Hz values

Fig. 9.6-4 shows that the measured phase angle exhibits very little error over the complete frequency range. This makes it practical to use simple frequency-dependent gain compensation to correct the amplitude error. Fig. 9.6-5shows the results of recalibrating the FRF amplitude curve, resulting in less than 2% gain error at all frequencies up to 20kHz. The compensation digitally changes the gain of the PFD output twice per decade. The sensor gain does not necessarily need compensation between 1.5kHz and 20kHz since it is naturally flat.

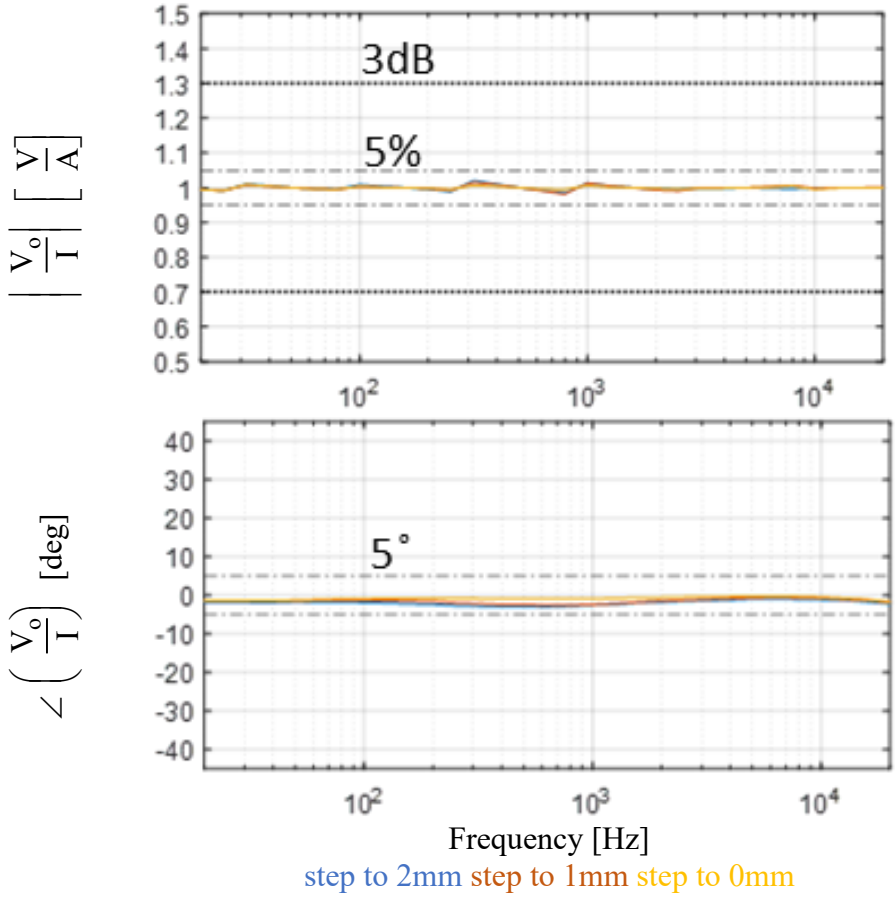

Fig. 9.6-5: Experimental FRFs of GMR PFD for leadframe interconnected terminal with respect to actual test current calibrated every half a decade of frequency.

Fig. 9.6-6 shows the time domain plots of sinusoidal current sensed by the GMR PFD. These time domain plots have the AC coupled GMR PFD measurements scaled using the calibration terms from the decade-based calibration. For the frequencies of 100 Hz, 1kHz and 10 kHz, the GMR PFD-based current sensing has a low phase lag. As predicted by the FRF, the signal at 1kHz has the most lag of about 2.5 degrees, which is larger than 10kHz signal's phase lag. If the high frequency noise is filtered out, the majority of the remaining error in the current sensing is due to the phase lag.

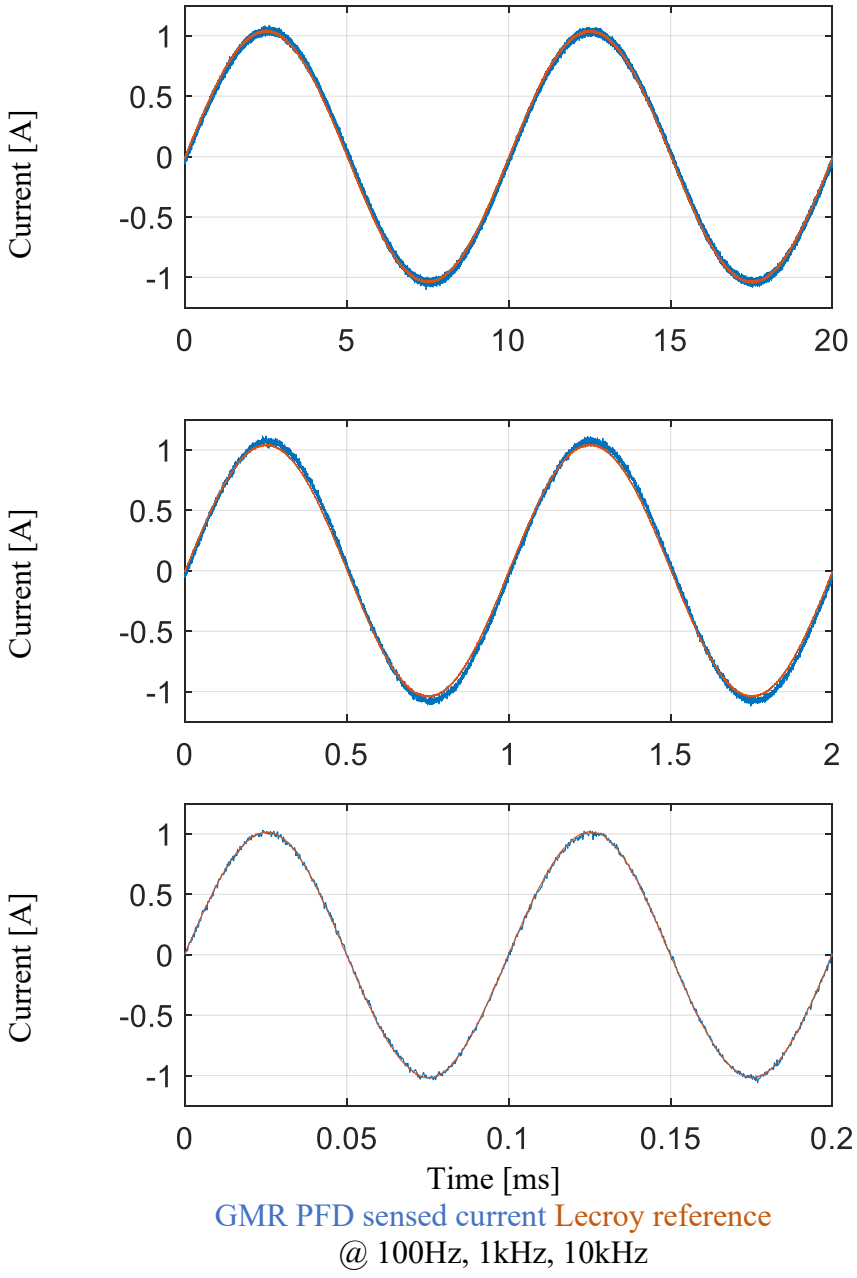

Fig. 9.6-6: Measured sinusoidal current in the leadframe interconnect terminal using GMR PFD

9.6.3 Multi-dimensional bandwidth extension

The bandwidth extension methodology using the multi-dimensionality of the magnetic field can be used to extend the bandwidth of the PFD-based current sensing. The degree of freedom provided by the direction along which magnetic field is detected can be used to extend the

bandwidth and reduce the impact of skin and proximity effects. The detailed analysis of the method is provided in chapter 10.

Fig. 9.6-7 shows the magnetic flux density and 5% FBW at 38 degree from the X axis. The outlook of the field has changed completely. One important result that emerges from this rotation is the coincidence of high flux density and FBW at the PFD location shown.

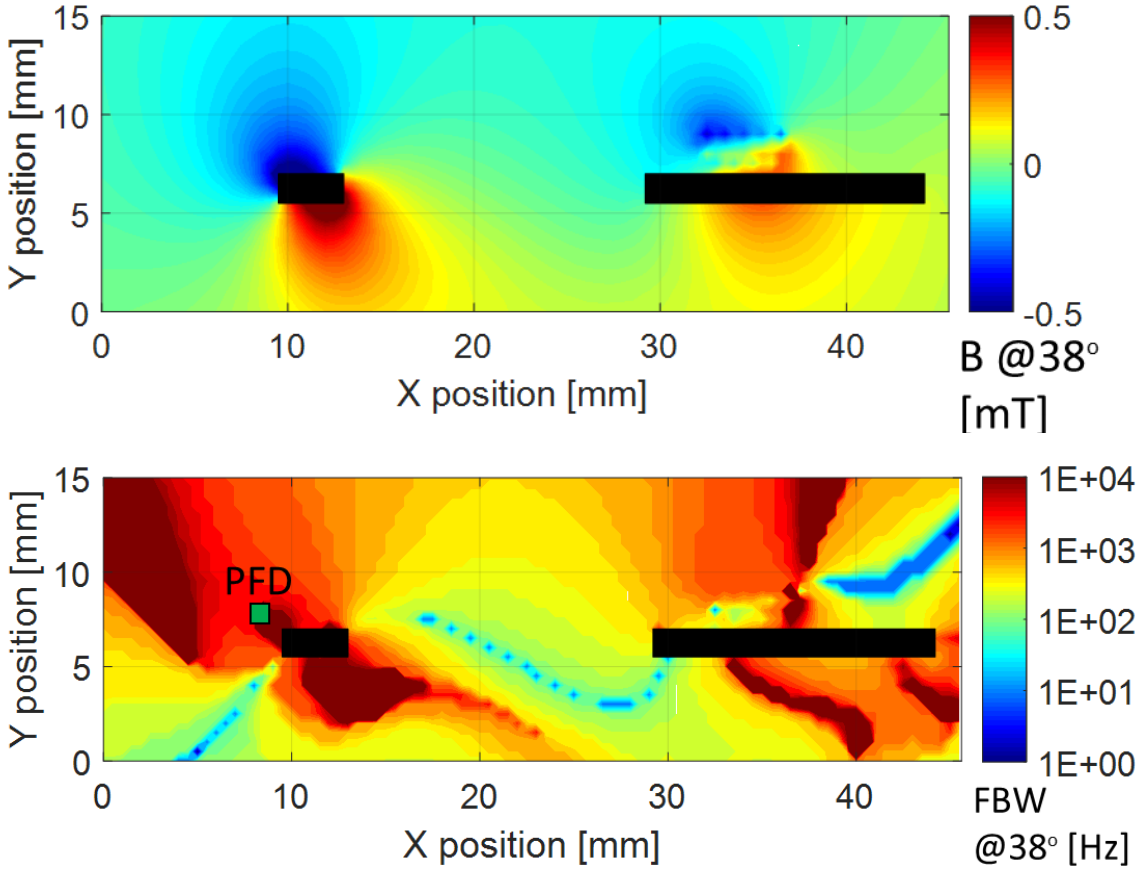

Fig. 9.6-7: Flux density for 5A, quasi-DC current in each terminal and 5% FBW for leadframe interconnect terminal (left) and bondwire terminal (right) at 38 deg from the X-direction

The PFD experimental frequency response at the PFD location in Fig. 9.6-7 is shown in Fig. 9.6-8. The FRF, even in the presence of baseplate with the 2mm step, is fairly flat. The region between 1kHz and 75kHz has less than 1% gain error due to the frequency invariant field shape. The X- and Y-direction FRFs are not included because of the lack of consistency in positioning

the GMR PDFs at the same point. The FRF data is collected by orienting the X-GMR PFD at 38 deg and positioning it very close to the leadframe. Unfortunately, the FRF data collected for the standard X- and Y-direction at the same point reflects inconsistency of positioning primarily due to the size of the PCB.

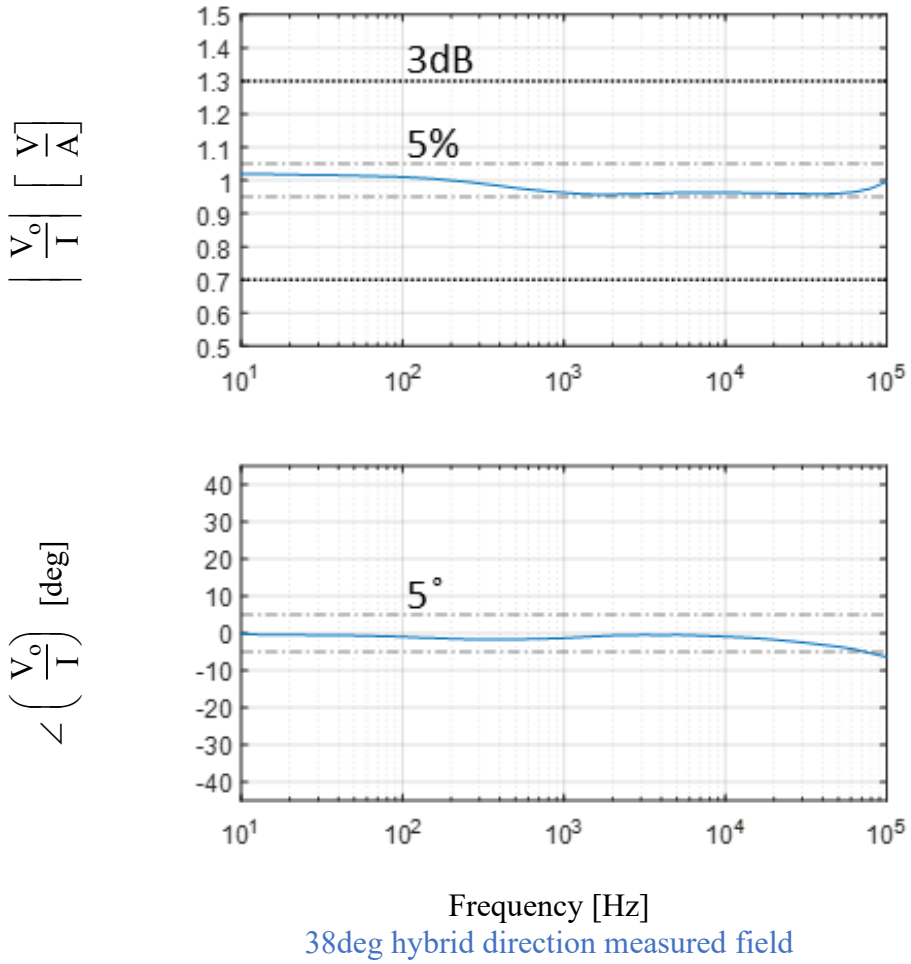

Fig. 9.6-8: Experimental FRFs of GMR PFD at 38 deg for leadframe interconnect terminal with respect to actual test current normalized to 200 Hz values

There is still value in standard X and Y magnetic fields FRFs, which are shown in Fig. 9.6-9. The computed FRF for 38 degree stays in the 5% band beyond 10kHz, after which it drops much like the X and Y field.

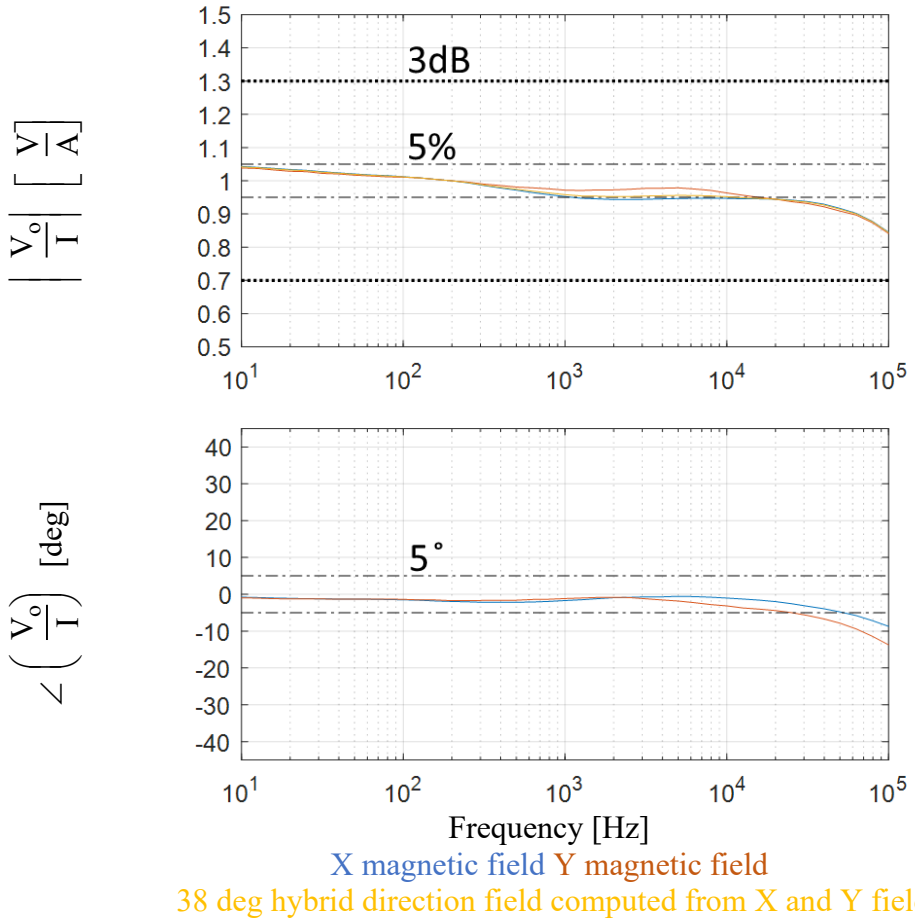

Fig. 9.6-9: Experimental X, Y and hybrid direction FRFs of GMR PFD leadframe interconnect terminal with respect to actual test current normalized to 200 Hz values

9.6.4 Tolerance of positioning PFD

In the above analysis, frequency responses have been shown at selected points. There is uncertainty involved in positioning the PFD at these points. This uncertainty is expected especially in a research environment without automated processes and robots. Despite the expectation that there will be more precise positioning of PFD in commercial environment, it is important to study the impact of PFD positioning errors. This investigation is not only useful for manufacturing and position tolerances, but also during operational life of the sensors when it might move due to thermal or mechanical stresses.

Fig. 9.6-10 shows the leadframe interconnected terminal with a PFD above it. The red arrow represents the path of the PFD during the experiment. Fig. 9.6-11 shows the GMR PFDs FRFs at ten points along the path separated by 0.5mm. The first plot shows the raw FRFs without the normalization. The vertical spread represents the change in the magnetic flux density detected at each point. The more important feature in the plot is the parallelism which shows that the frequency dependent behavior at each point is very similar. This becomes clearer in the second plot which has the same FRFs but in their 100 Hz normalized form.

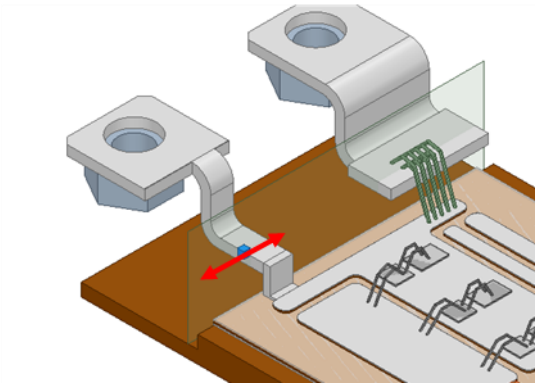

Fig. 9.6-10: Leadframe interconnect and its terminal with PFD path

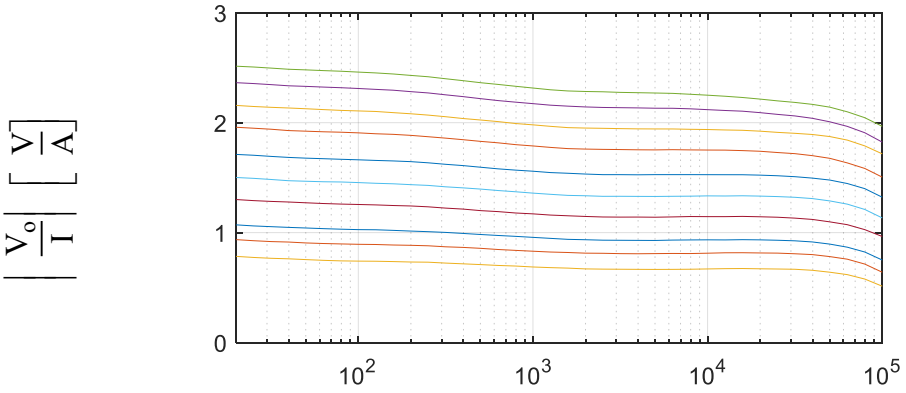

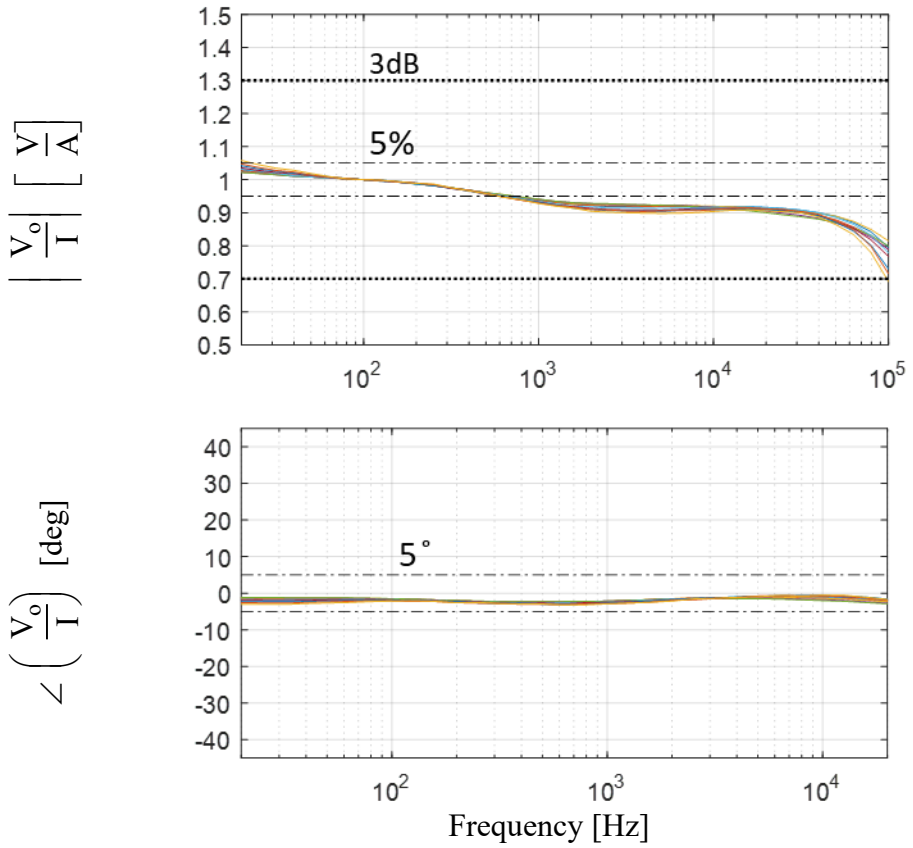

Data at ten locations separated by 0.5mm in X-direction above the leadframe.

Fig. 9.6-11: Experimental FRFs of GMR PFD for leadframe interconnect terminal with respect to actual test current (raw and normalized to 100 Hz values) at 10 points

The same experiment is repeated in the commercial Rohm power module. Fig. 9.6-12 shows the normalized FRFs of PFD output at ten points above the terminal separated by 0.5mm in the X-direction. There is significant difference between the frequency dependent behavior of field at each of the location. Due to this, even small changes in the position of PFD in the currently commercial power modules can lead to an entirely different FRF. Specific leadframe design, like in this chapter, prevents this problem from happening.

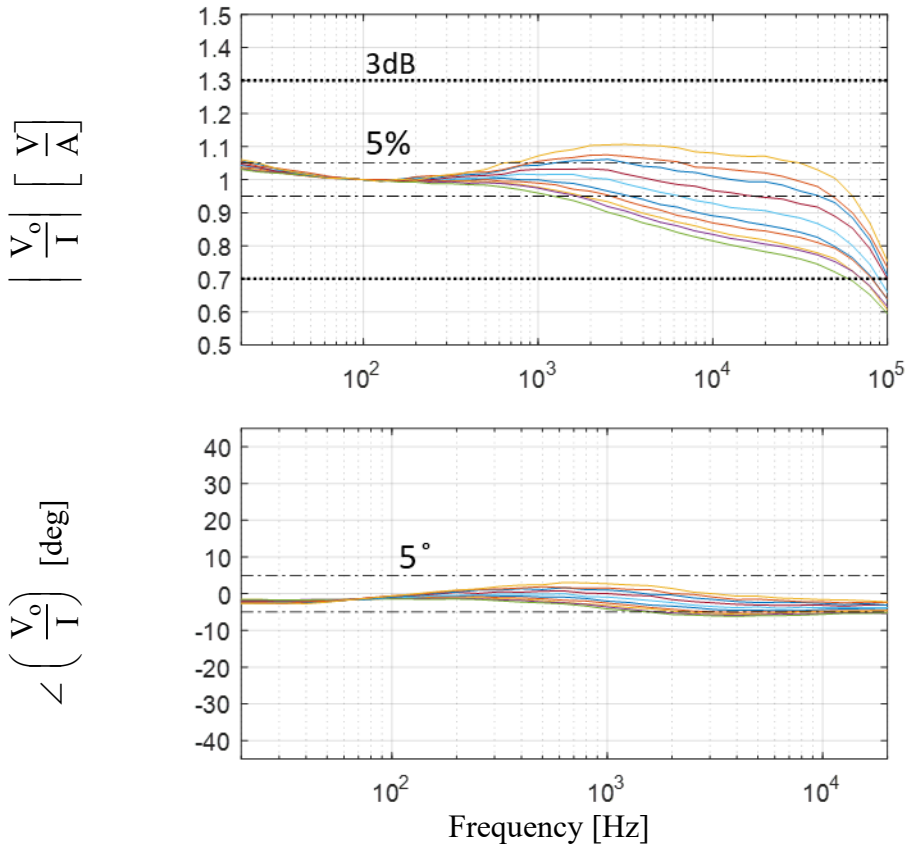

Data at ten locations separated by 0.5mm in X-direction above the left edge of bondwires on the terminal.

Fig. 9.6-12: Experimental FRFs of GMR PFD for commercial power module with respect to actual test current normalized to 100 Hz values

9.6.5 Multiphysics evaluation of power module compared to the commercial module

9.6.5.1 Thermal Evaluation

One of the features that is added to the SiC power module for the high bandwidth field shaping is the step on the baseplate below the terminal at the edge of the DBC. This step reduces the area and increases the impedance experienced by the frequency dependent eddy currents. The step also increases the distance of the eddy currents to the PFD. Although the step in the baseplate is beneficial for the electromagnetic properties, it may have an impact on the thermal performance of the power module.

The steady state thermal FEA is conducted on Ansys Mechanical on Workbench with heat passing from the low side SiC MOSFET chip closest to the edge of DBC to the bottom of the baseplate for half of the module. Since the main interest is in thermal resistance through the baseplate, it is only a comparative analysis between the regular baseplate module and the stepped baseplate module. Fig. 9.6-13 shows the FEA results of simplified power module with baseplate step to 2mm used.

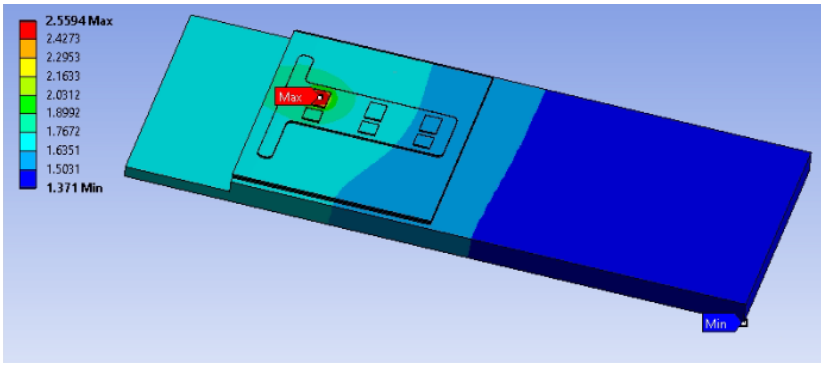

Fig. 9.6-13: Typical thermal FEA of the Power module with baseplate step

The FEA results shown in Table 9.6.1 are comparative between the regular and the stepped baseplate. The step in the baseplate to 2mm or 1mm has a very small impact on the thermal performances of the power module. The step to 0mm i.e. cutting the baseplate does have a notable impact of the thermal resistance of the power module.

Table 9.6.1 Results of thermal FEA of regular and stepped baseplate power module

Baeplate geometry	R j-amb	Bottom Surface area	convection coefficeint	R conv	R j-case	R j-case % change from original	R j-amb % change from original
step to 4mm (no step)	2.55	0.0046	140	1.55	1.00	0.00	0.00
step to 2mm	2.56	0.0046	140	1.55	1.01	0.70	0.27
step to 1mm	2.57	0.0046	140	1.55	1.02	1.58	0.62
step to 0mm	2.96	0.0038	140	1.87	1.09	9.09	15.86

The change in the chip to case thermal resistance only becomes important if the design with baseplate stepped to 0mm is used. In this case, there are multiple ways to make up for the lost thermal paths. One very simple approach is to widen the baseplate which will add area to the sides of the power module. This area on the sides can compensate for the lost area under the terminals. The other options are to increase the convection area via fins or improve the convection coefficient to reduce the convection resistance.

9.6.5.2 Parasitic Evaluation

The impact of the leadframe terminal on the electrical performance of the power module is evaluated using the parasitic analysis on the FEA software, Q3D, on Ansys Electronics Desktop. The solution frequency is 200 MHz to allow skin effects to fully develop. The half-bridge, shown in Fig. 9.6-14, has multiple parasitic properties schematically defined.

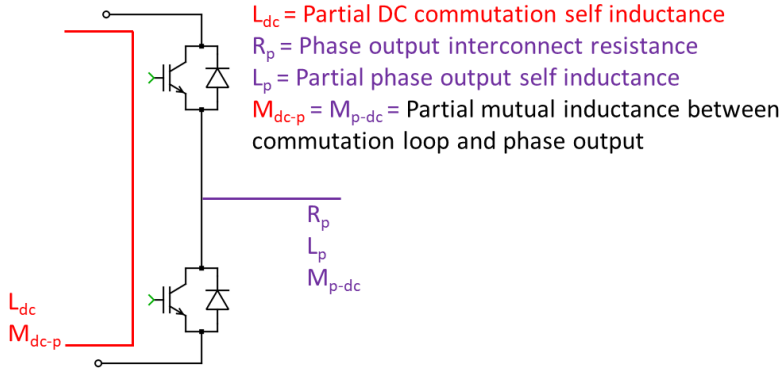

Fig. 9.6-14: Parasitic electric properties of half-bridge power module

The inductance evaluation of the leadframe power module is completed in comparison with the standard bondwire power module to verify that the field shaping leadframe has no significant adverse impact. The results of the inductances are shown in Table 9.6.2 at 10MHz and 1kHz since these are relevant frequencies for DC commutation loop and leadframes respectively.

Table 9.6.2 Self and mutual inductances in nH

		DC @10MHz	Phase A interconnect @1kHz
Standard power module	DC (half module)	2.98	
	Phase A bondwires	-0.038	33.60
Leadframe power module	DC (half module)	2.96	
	Phase A leadframe	-0.029	35.48

The field shaping leadframe has a slightly higher self-inductance than the bondwire interconnects. Self-inductance of the phase output leadframes is an innocuous property since the load of the power module will have substantially more inductance making the phase interconnect completely negligible. The changes in the DC side inductances are negligible.

The resistance of the leadframe with respect to the bondwires being replaced is shown in Table 9.6.3 in milliOhms at 1kHz. The leadframe terminal slightly improves the resistance due to shorter path due to lack of loops as in bondwires.

Table 9.6.3 Resistance in the power module in mΩ

Standard power module	DC	0.71
	Phase A bondwires	0.27
Leadframe power module	DC	0.71
	Phase A leadframe	0.23

9.7 Summarizing Remarks

A concise summary of the chapter is available at its beginning. The conclusions and contributions for this chapter are available in the last chapter.

This chapter presents a design methodology for SiC power modules to enable GMR PFD-based integrated current sensing with high bandwidth that is appropriate for wide-bandgap (WBG) applications. Electromagnetic FEA of a commercial SiC power module reveals that there may be some locations for high-bandwidth current sensing, but the SNR is lower and PFD positioning is tough at these locations. It is also found that skin effects in the screw terminals and proximity effects in the baseplate shrink the region of high-bandwidth for phase current sensing using PFDs. The latest power module interconnect technologies including ribbon and leadframe interconnects are tested for magnetic field shaping. FEA results show that skin effects in the ribbon interconnect degrade the magnetic field bandwidth in the same way as the proximity effects influence the field bandwidth in the bondwires.

FEA and experiments are used in this chapter to show a significant improvement in the bandwidth of power module integrated current sensing. This is achieved by power module design modifications including ribbon or leadframe interconnects with narrow terminals that seamlessly merge with the interconnects and a step in the thickness of baseplate below the terminal. Furthermore, sensing fields in optimum directions or decade-based calibration of the FRF can further extend the bandwidths. Practical issues of power module thermal and parasitic performance as well as PFD positioning are also investigated in this chapter.

Chapter 10 Bandwidth Extension using the Multi-Dimensionality of the Magnetic Field

This chapter presents the methodology to extend the bandwidth of current sensing by using the multi-dimensionality of magnetic fields. The field analysis metrics from chapter 2 are used to analyze the magnetic field in directions with higher bandwidth around a rectangular busbar. The detailed physical as well as mathematical basis of multi-dimensional magnetic field detection is presented to extend the current sensing bandwidth.

The main purpose of this chapter is to develop a methodology to extend current sensing bandwidth using magnetic field as a physical vector quantity.

Elements of this chapter are also documented in [117].

10.1 Simulated Bandwidth Extension with Vector Magnetic Fields

The Cartesian coordinates (X,Y,Z) used to describe a magnetic field vector at each point are generally chosen with reference to the conductor. Fig. 10.1-1 shows a rectangular cross-section busbar, a ubiquitous conductor in power electronic converters, with the typical choice of coordinates based on its geometric edges. 1-D PFDs are generally positioned and oriented to sense the magnetic field component along the X-direction of the conductor for current sensing.

Detecting magnetic fields along non-standard axes is briefly studied in [69]. However, in the limited simulation work for three specific conductors, X- and Y-directions were typically found to be better. This work was conducted with the perspective that PFDs are only 1-D, thus lacking the analytical and experimental depth. However, it did propose the idea that detecting magnetic fields along non-standard directions can be useful on a case by case basis.

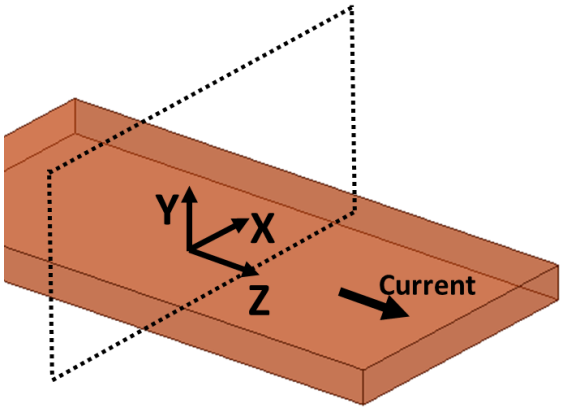

Fig. 10.1-1: Rectangular cross-section busbar with orthogonal analysis plane and XYZ coordinate axes

In many cases, the Cartesian coordinates (X, Y, Z) referenced to the conductor might not lead to the best magnetic field bandwidth. There is an infinite number of directions in space and limiting the magnetic field-based current sensing to only the X-direction limits the FBW. An intensive multi-dimensional analysis of the magnetic field in various other directions can be carried out using analytical vector mathematics.

The FEA software uses the predefined Cartesian coordinates to compute and output the magnetic field vectors which can be passed through a rotation matrix, shown in (10.1-1) to evaluate the magnetic field components in arbitrary directions. The flux density in an arbitrary direction, B_h, in the XY plane can be computed by using the relationship in (10.1-1) and can be referred to as the hybrid 1-D magnetic field since it combines the X and Y fields.

$$\begin{bmatrix} B_{x'} \\ B_{y'} \\ B_{z'} \end{bmatrix} = \begin{bmatrix} \cos\theta & \sin\theta & 0 \\ -\sin\theta & \cos\theta & 0 \\ 0 & 0 & 1 \end{bmatrix} \begin{bmatrix} B_x \\ B_y \\ B_z \end{bmatrix} \tag{10.1-1}$$

$$B_{x'} = B_h = B_x \cos(\theta) + B_y \sin(\theta)$$

It is important to note that the net magnetic field vector is always the same but sensing the field component in varying directions provides valuable degrees of freedom for the magnetic field

properties of strength and bandwidth. The mathematical computation of the hybrid 1-D magnetic field provides the ability to analyze and evaluate magnetic field vectors along any direction within the 2-D plane. This opens up the possibility of finding field directions with much higher bandwidth due to low impact of skin effect as well as the possibility of improved signal-to-noise ratio (SNR).

Fig. 10.1-2 shows the X-direction flux density computed in FEA for the busbar that will be used in experiments. It also shows the hybrid 1-D flux density at 39 deg counter-clockwise from the X-direction. The hybrid direction moves the high flux density region to the edges which can be advantageous for placement of PFD. At specific points, it also extends the bandwidth.

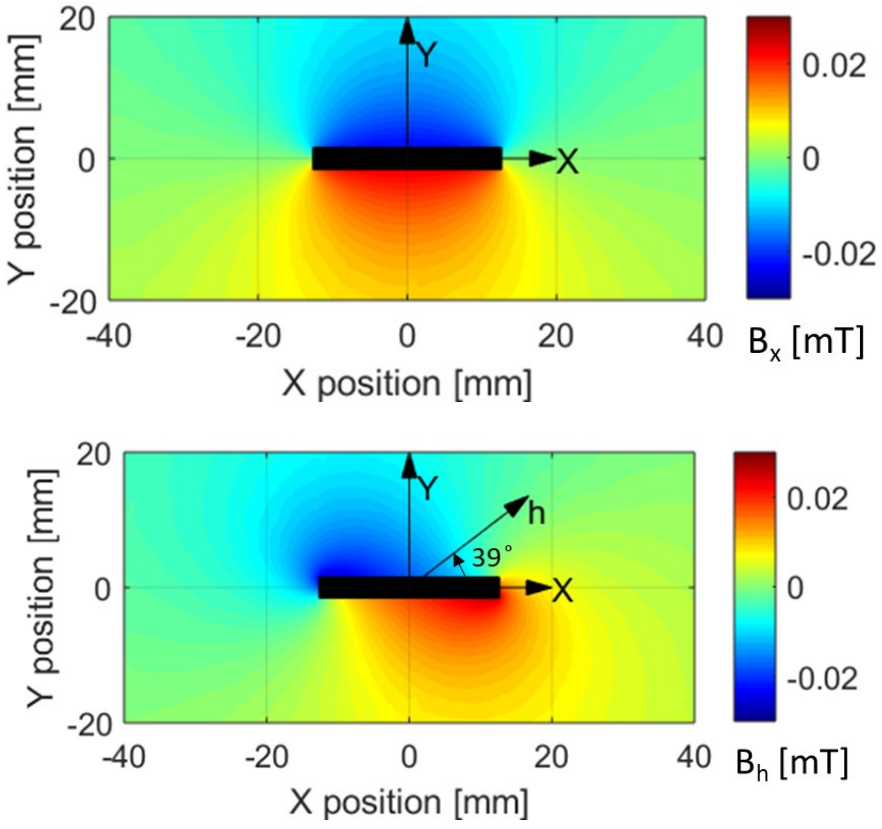

Fig. 10.1-2: X-direction flux density and hybrid 1-D flux density with 1A quasi-DC current around the busbar

The FBW of the X-direction field and hybrid direction field is shown in Fig. 10.1-3. The magnetic field in hybrid direction improves the bandwidth at locations near the edges of the busbar.

The FEA predicts that at the PFD location, there is a significant increase in the FBW when using the hybrid direction as compared to the X-direction. The PFD location is chosen so that experimental verification is possible. There is always some positioning error but this point is one of the easiest locations to place in the GMR PFD which is mounted on the PCB. The edge of the busbar serves as a reference for positioning the PCB. The geometric location of the PFD on the PCB, makes the alignment/position easy with respect to the busbar

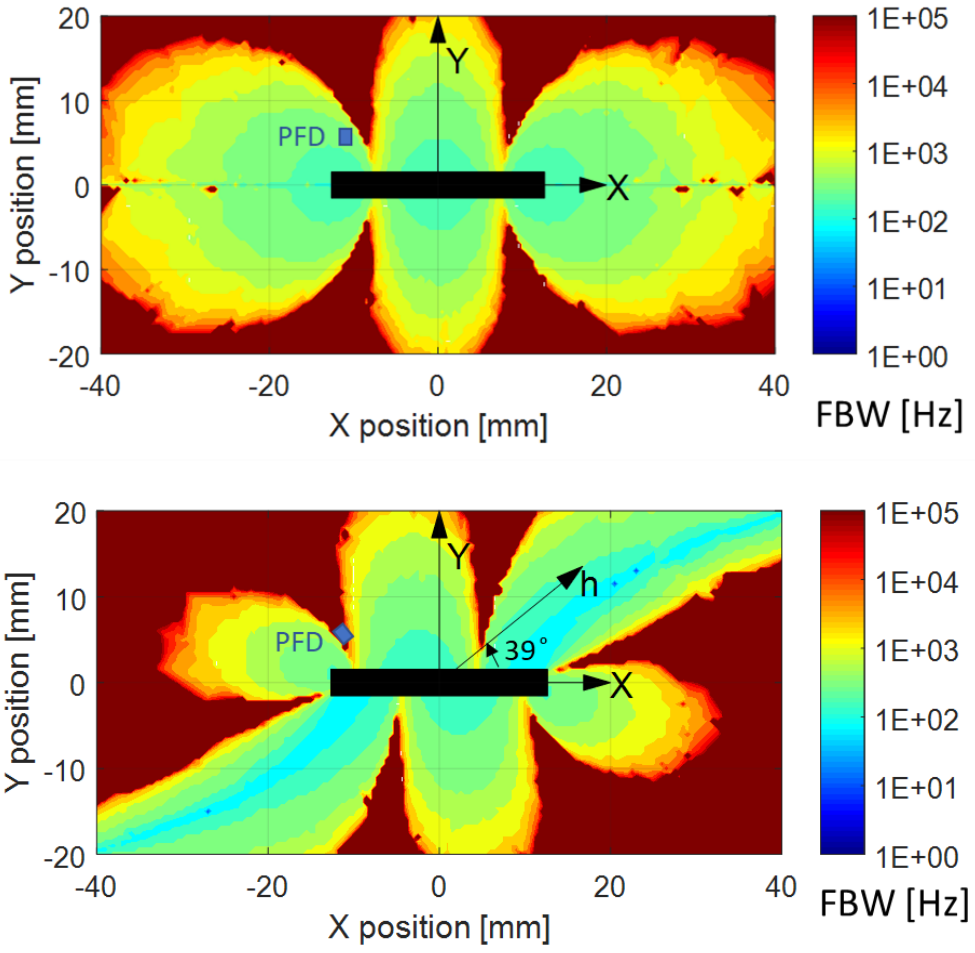

Fig. 10.1-3: X-direction and hybrid 1-D 5% FBW around busbar

The 5% FBW contour plot provides the spatial information for PFD placement. It includes the bandwidth information of the entire region. Another way to look at the FBW data from the Fig.

10.1-3 is to use the FRF plots. The FRF provides data for only one point but it does provide frequency dependent trend of magnetic field.

The FRFs of the X, Y and hybrid magnetic flux densities with respect to the actual current at the PFD location shown in Fig. 10.1-3 are shown in Fig. 10.1-4. The X-direction magnetic flux density increases with frequency, whereas the Y-direction flux density decreases. There is a direction somewhere in between the X- and Y-directions where frequency dependent variance of X and Y magnetic flux densities is physically compensated. In this example, 39 deg is used as the hybrid direction where the frequency dependent variation of flux density is much less and 5% FBW is extended to above 100kHz.

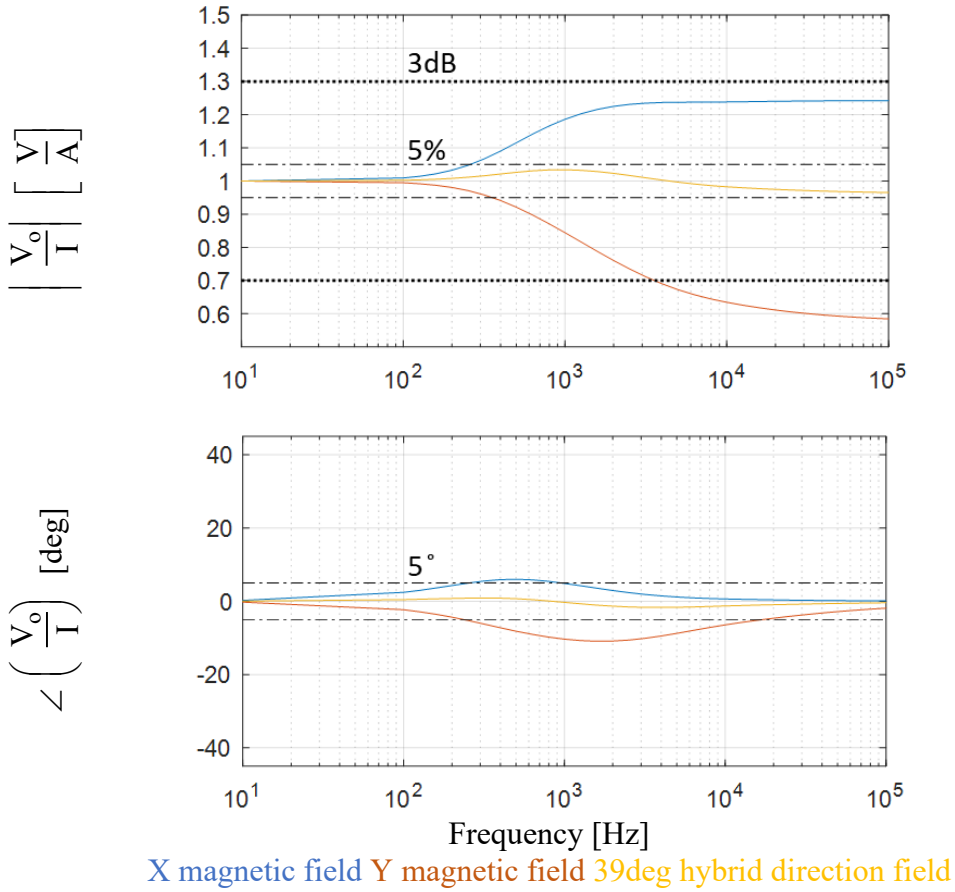

Fig. 10.1-4: Simulated FRFs of PFD outputs with respect to actual current normalized to 10 Hz value at the point shown in Fig. 10.1-3

10.2 Experimental Bandwidth Extension with Vector Magnetic Fields

The bandwidth extension around a rectangular busbar used in the simulations is also experimentally evaluated using a similar setup as in chapter 7 sec. 7.3.1. The AC current in the busbar is controlled using a power amplifier which can produce a wide frequency range of currents. The frequency of the AC current in the busbar is swept from 10Hz to 100kHz. Fig. 10.2-1 shows the 2-D GMR PFD positioned close to the busbar in the test set-up. A Venable frequency response analyzer is used to plot the FRF of the PFD outputs with respect to the actual current measured by a high bandwidth current probe.

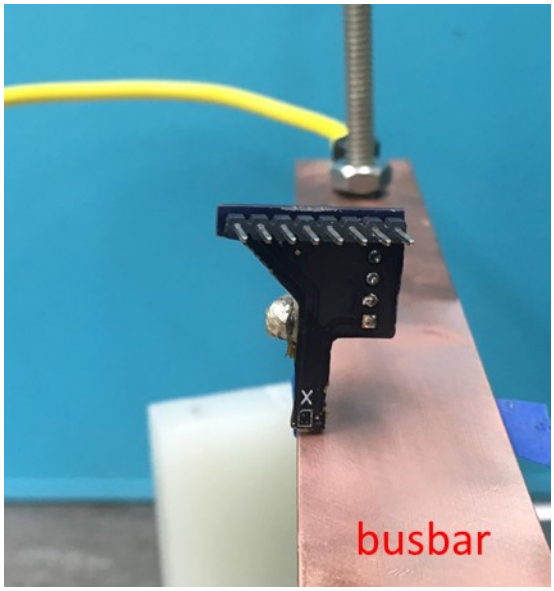

Fig. 10.2-1: View of 2-D GMR PFD positioned in close proximity to rectangular busbar (3.1mm x 25.3mm). Not shown: Signal conditioning PCB, power amplifier, and Venable frequency response analyzer.

The FRFs of X, Y, and the 1-D hybrid direction of 39 deg from the X axis are shown in Fig. 10.2-2. The experimental results confirm the simulated trends. The X-direction output of PFD increases with frequency and Y-direction output decreases with frequency. The Y field crosses -3dB (70%) at 6kHz, however, the X field increases with frequency and crosses +3dB at around

2.75kHz. it should be noted that +3dB is approximated as 130% in this work to maintain symmetry on non-logarithmic Y scale. The hybrid direction FRF which is measured by orienting the X PFD at 39 deg has minimal frequency dependent variation. The 5% FBW hybrid field increases to over 65kHz at the test point. The bandwidth metric of -3dB is not crossed until 100kHz, which is the upper limit of the testing frequency. However, the FRF does cross -1dB at 100kHz.

In addition to measuring the magnetic field at 39 deg by orienting the GMR PFD, the hybrid field is also mathematically computed using the X and Y PDF outputs. The overlay of computed and measured FRF match within the PFD positioning and angular tolerances.

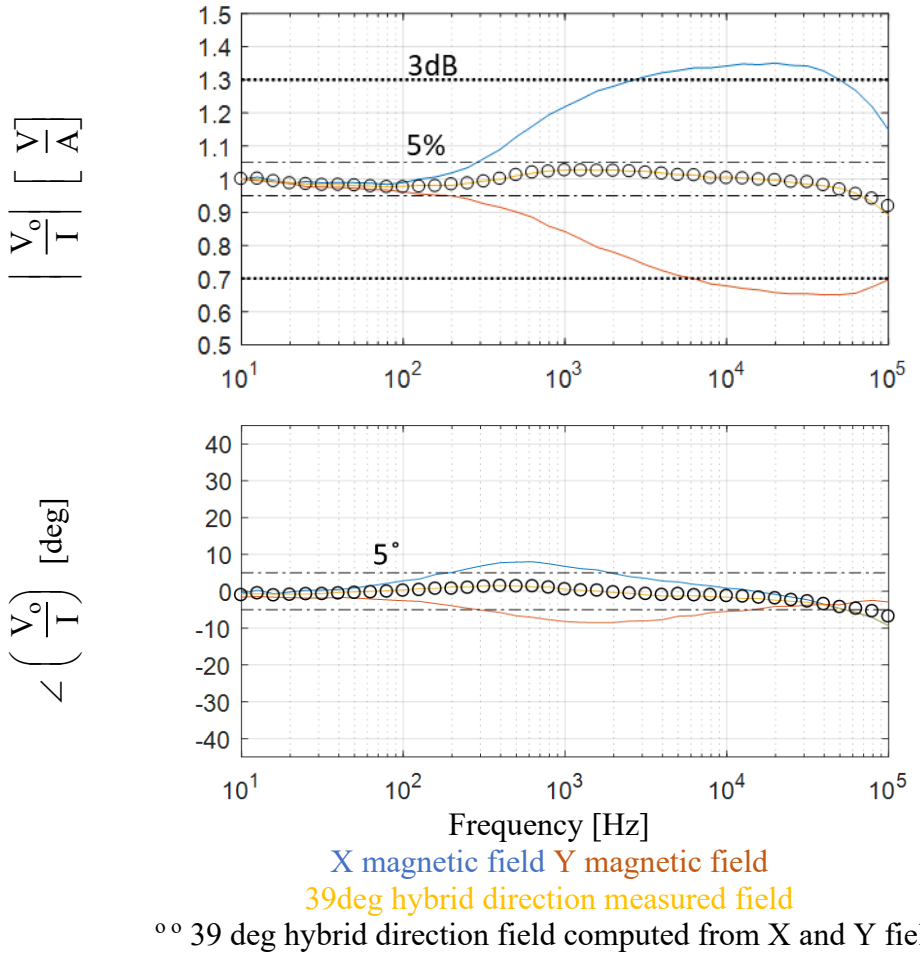

Fig. 10.2-2: Experimental FRFs of PFD output with respect to actual current normalized to 10 Hz value at the point shown in Fig. 10.1-3

The computation of the 39 deg magnetic field from the measured X and Y magnetic field is done using the RMS values at each frequency. The directions of fields need to be accounted for in the sign of the RMS values. Since this is not a time domain result, it does not account for the lag in the X and Y magnetic fields. A more accurate computation of the hybrid field using the RMS values that accounts for the lag or lead (ϕ) is shown in (10.2-1).

$$B_x' = B_h = B_x \cos(\theta) \cos(\phi_1) + B_y \sin(\theta) \cos(\phi_2) \quad (10.2\text{-}1)$$

Θ = physical angle of hybrid field

Φ = lead or lag of the field

Accounting for the lead or lag of the X and Y measured magnetic fields is theoretically better but practically redundant. The lead or lag angles, as shown in Fig. 10.2-2, are never above 8 deg which leads to a change of less than 1%.

Furthermore, a key advantage of the rotation is being able to control the magnitude of the flux density. This can help with the PFD linear range as well as the SNR. Fig. 10.2-3 shows the un-normalized FRF of the same test as above. For a given current, the hybrid direction has a much higher output then X and Y. This matches the analytical expectation and simulation results in Fig. 10.1-2. The net magnetic field close to the edge of the busbar is naturally directed at around 30 to 60 degrees due to the elliptical loop of the flux around the rectangular busbar cross-section.

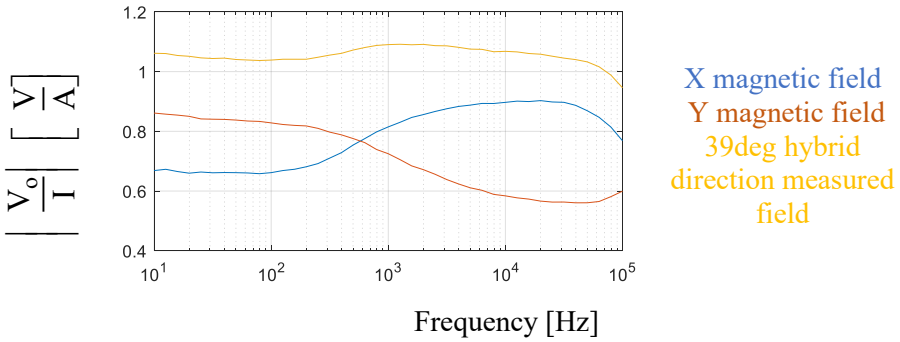

Fig. 10.2-3: Experimental FRFs of PFD outputs with respect to actual at to the point shown in Fig. 10.1-3

10.3 Mathematics of Bandwidth Extension with X and Y Fields

If the X and Y fields have opposite trends with respect to frequency, they can be used to compensate for each other to form a flat FRF with a much higher FBW. As shown in last section, the compensation is achieved inherently in the angle-oriented magnetic field components. The mathematical computation of magnetic field using the hybrid direction implements such a compensation and allows for all weighted combinations of X and Y magnetic fields.

Fig. 10.3-1 shows the sine, cosine and tangent curves in the first quadrant. The multiplication of sin(θ) and cos(θ) to B_x and B_y leads to a weighted combination in (10.3-1). The sin and cosine curves represent the weights of B_x and B_y. The curves show that between 0 and 90 deg, it is possible to have virtually all weighted combinations of B_x and B_y.

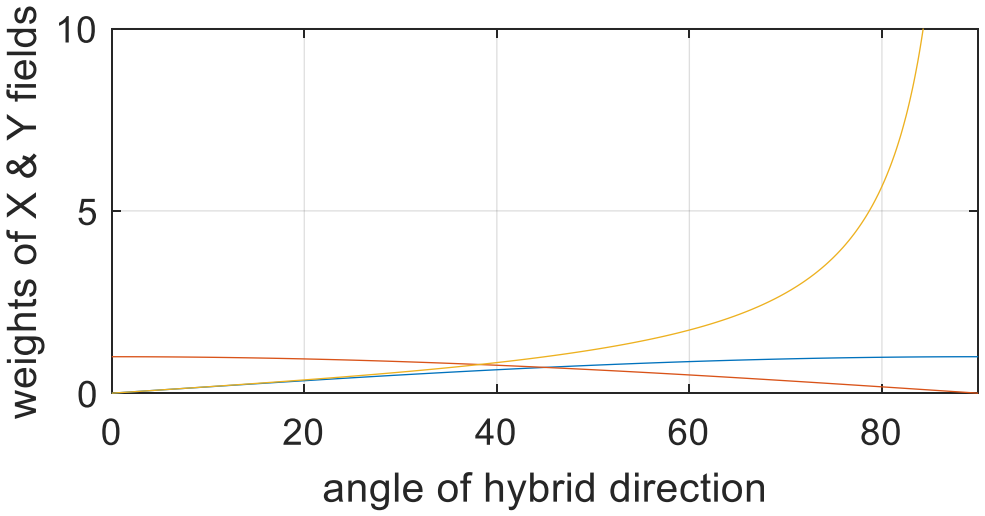

Fig. 10.3-1: Sine and cosine in the first quadrant

This means that it is also possible to synthesize a flat frequency response purely from a mathematical point of view of weighted combination using (10.3-1).

$$B_x' = B_h = B_x \cos(\theta) + B_y \sin(\theta) \quad (10.3\text{-}1)$$

$$B_h = w_1 B_x + w_2 B_y$$

Finding the weights, w_1 and w_2, for X and Y FRFs to synthesize an FRF which is flat can be an intensive computation. One method to make this into a simple computation is to find the weights after normalizing the FRFs of B_x and B_y. To illustrate this method, experimental FRF data from last section is used. Fig. 10.3-2 shows the X and Y FRFs as well as the FRF of the weighted combination with a set of weights which takes the 5% FBW to 90kHz. Furthermore, it is possible to focus on certain bands of frequency as well by selecting the appropriate weights.

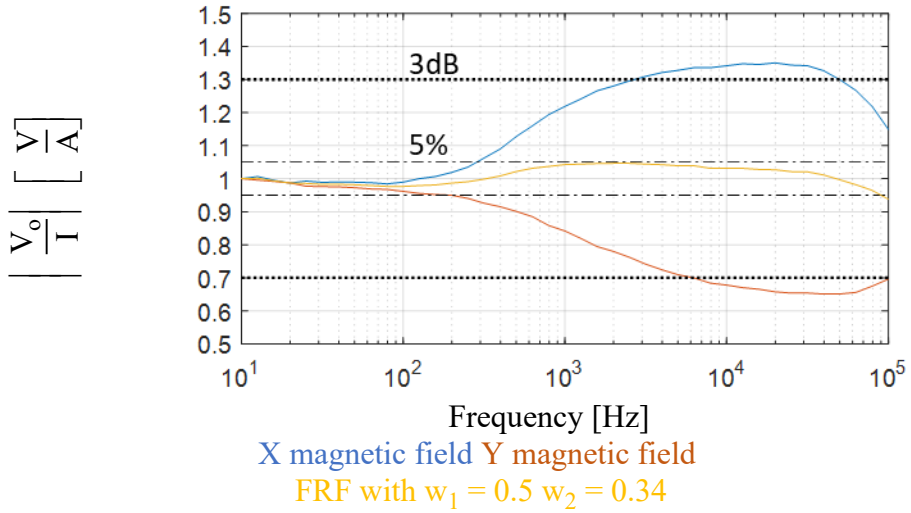

Fig. 10.3-2: Experimental FRFs of PFD outputs with respect to actual current normalized to 10 Hz at the point shown in Fig. 10.1-3

As explained earlier, the compensated FRF in Fig. 10.3-2 is not just a mathematical quantity formed out of normalized X and Y fields. Some trigonometry or trial and error can be used to find that $w_1 = 0.5$ and $w_2 = 0.34$ correspond to magnetic field at 35.2 deg counter-clockwise from the X-direction.

10.4 Summarizing Remarks

A concise summary of the chapter is available at its beginning. The conclusions and contributions for this chapter are available in the last chapter.

This chapter studies the direction of field sensing to improve the bandwidth and shows using a typical busbar that at a given point there are directions in the multi-dimensional space with magnetic field components that are less affected by the skin effects in the conductor, thereby yielding a higher bandwidth. The best directions for field sensing in a plane can be found using the tools developed in chapter 2 i.e. by using the rotation matrices on the standard X- and Y-direction fields solved by the FEA.

FEA and experiments are used in this chapter to explain that bandwidth extension by sensing fields along a particular direction in a plane can be achieved by two methods. First is to use a 1-D PFD and rotationally orient it to sense fields along the directions with higher bandwidth. The second method uses X- and Y-direction fields measured by a 2-D PFD to compute the angular field components with the versatility to change the angle after measurement.

This chapter also shows that computation of angular fields is mathematically equivalent to a weighted summation of the X- and Y- direction fields. In a nutshell, multi-dimensional bandwidth extension compensates for the frequency dependent changes of the X-direction field with Y-direction field to yield a flat frequency response function.

Chapter 11 Conclusions, Contributions and Future Work

11.1 Research Conclusions

The key conclusions of this research are presented in the following subsections:

11.1.1 Multi-Dimensional Magnetic Field Shaping and Analysis

- A magnetic field is a 3-D spatial vector quantity that can be detected by a 1-D or 2-D PFD with the loss of some information and by a 3-D PFD without the loss of any information.
- Sensing a multi-dimensional magnetic field only along the geometric direction of the conductor may not yield the best SNR and FBW due to the impact of skin effect.
- The rotated 2-D magnetic flux density and FBW can be used to determine the SNR and bandwidth for sensing the fields along any two orthogonal directions on a given plane.
- The 3-D FBW, which combines information from three 1-D FBWs, can be used to evaluate magnetic fields in all three dimensions and to position a 3-D PFD for high-bandwidth sensing.
- The 3-D FBW metric quantifies the frequency-dependent properties of a vector field and can be used for shaping magnetic fields for multi-current systems in three dimensions.
- Computational effort can be reduced by using analytical vector mathematics that can model the magnetic fields and capture their frequency dependency in any direction in a 3-D space from a single solution of electromagnetic FEA.

11.1.2 Multi-Dimensional Magnetic Field Decoupling Methodology

- Magnetic fields from nearby currents always cross-couple linearly in a 3-D space, and the combined total field contains information about all of the currents contributing to the field.

- Independent currents can be decoupled from the multi-dimensional cross-coupled fields using Ampere's Law model and the geometric relationship of the currents and the PFD.
- Sensing the 2-D and 3-D spatial magnetic fields reduces the need for PFD arrays by utilizing the degrees of freedom associated with the magnetic field in different dimensions.
- *N* dimensions of the cross-coupled vector field in a 3-D space can be used to decouple up to *N* currents.
- 3-D field decoupling is vulnerable to having a singularity if the vector field exists in a plane rather than a space
- The singular cases of decoupling can be recognized when two dimensions of the field, having a linear relationship, lead to repeated information.
- Arranging the currents appropriately can generate 3-D fields with unique information in each dimension which can be decoupled using the 3-D decoupling methodology.
- The condition number of the coupling matrix is a measure of repetition of information in the PFD outputs, quality of decoupling as well as propagation of uncertainty in sensing.
- Coupling matrices can be found using single signal injections, direction calibration, or a hybrid of the two approaches.
- The hybrid calibration technique reduces the impact of noise as well as minor phase lags that may be present in the PFD signal.

11.1.3 Three-Phase Current Sensing in Busbars and Cables using Multi-Dimensional Field Decoupling

- Two 1-D GMR PFDs can be strategically positioned on a PCB to emulate a 2-D GMR PFD. A third GMR PFD can be positioned close to the fabricated 2-D GMR PFD to form an approximate implementation of a monolithic 3-D GMR PFD.
- A multilayer GMR PFD, when operated with a virtual zero point using a bias magnet, has a linear range, sensitivity, and bandwidth that is sufficient for integrated current sensing.
- Two 2-D PFDs, which can be mounted in an SO16 IC, can be used to sense the three-phase currents in a straight cable.
- A single 2-D PFD can be used to sense the three-phase currents if the system is balanced and the third phase is routed separately from the other two phases.
- A single 3-D GMR PFD can sense three-phase currents in conventional conductors without any customization or separation of phases, making it well-suited for three-phase AC drives.
- The decoupling matrices can be calibrated experimentally and treated as constant (i.e. independent of frequency or amplitude of the current) within the frequency range from zero up to the 5% FBW.
- The magnetic fields around three-phase cables do not cancel perfectly due to the geometric distance between the conductors, providing the basis for field-based current sensing.
- A wide range of current amplitudes can be sensed using multi-dimensional PFDs because of the partial cancellation of the magnetic fields from the three currents in a nominally balanced three-phase system.
- Low SNR, high condition number of coupling matrix, and imperfect coupling matrix calibration are typical causes of error in current sensing.

11.1.4 Disturbance Magnetic Field Decoupling

- The magnetic flux density and its spatial gradient around a current are inversely proportional to the distance and the square of the distance from the current, respectively.
- The spatial decay of the magnetic flux density in a particular dimension is very similar to that of the magnitude of the flux density.
- The vector magnetic field disturbance from an unknown source can be modelled as a function of X, Y, and Z positions of the PFDs used in the sensing system.
- An AC or DC magnetic disturbance which has a zero spatial gradient can be modelled as a zero order polynomial (constant) and decoupled with one additional PFD.
- Multi-dimensional magnetic disturbances with spatial gradients can be decoupled to an adequate level by increasing the order of their model.
- An N^{th} order disturbance model requires $N+1$ additional PFDs in the system.
- A higher number of PFDs leads to an increase in the condition number of the coupling matrix which can exaggerate the uncertainties in the sensing.
- A zero order disturbance model with only one additional multi-dimensional PFD can provide an adequate decoupling of disturbances from external sources in real systems.
- Passive magnetic materials can be used to provide low reluctance paths to disturbance fields and prevent them from reaching the PFDs.
- Unique magnetic circuits can be used to reject disturbances with small amounts of magnetic materials without saturation.

11.1.5 Neural Networks for Magnetic Field Decoupling

- Neural networks can be used to map the multi-dimensional cross-coupled fields to currents after adequate training.

- The training of the neural network tunes its weights and biases to mimic the physics-based decoupling.
- PFD outputs and actual current measurements at many different operating conditions lead to an adequate training of the neural network.
- Neural networks can be used to decouple the magnetic disturbance from unknown sources with adequate training because there is no matrix inverse calculation.
- Neural network-based disturbance decoupling identifies the disturbance current without any reference from it in training data.
- The disturbance current needs to be at a fixed position for the neural networks-based decoupling to work.

11.1.6 Power Module Electromagnetic Analysis for 2-D PFD-based Current Sensing

- Commercial power modules do not use field shaping metrics as figures of merit for design.
- There is no region with appropriate magnetic field shaping and FBW for multi-dimensional field sensing inside the typical commercial power modules.
- Accurate current sensing can be achieved at low frequencies using the proposed multi-dimensional decoupling methodology inside the commercial power module.
- Multi-dimensional PFDs can be integrated into the switching power modules for reliable current sensing that is needed to provide high-fidelity current feedback to the controller.
- 2-D field shaping metrics can be employed in the design of power modules to enhance the accuracy and bandwidth of current sensing using a reduced number of PFDs.
- The FBW inside power modules is affected by interconnects, the DBC top layer, and terminals experiencing both skin and proximity effects.

- The proximity effects causing eddy currents in the baseplate is the main reason for FBW degradation in the power module.
- A significant improvement in FBW can be achieved by eliminating the frequency-dependent eddy currents whose fields cross-couple with the phase current fields.
- Comb-style laminations in the baseplate can reduce the eddy currents by interrupting their paths while having minimal impact on the thermal characteristics of the power module.
- A baseplate with comb-lamination or less electrically conductive material like AlSiC can improve the bandwidth of the integrated current sensing in the power module by reducing the proximity effects.
- Leadframe interconnects can be designed in the multi-phase power module to shape the planar cross-coupled magnetic field from two phases to sense them with a single 2-D PFD.

11.1.7 Power Module Design for 3-D Magnetic Field Shaping

- The 3-D leadframe interconnects can be designed to shape high-bandwidth cross-coupled magnetic field for sensing three-phase currents using a single 3-D PFD.
- Properly designed leadframes can generate a 3-D field with each of the field directions having information of all phases but dominated by one of the phases leading to a well-conditioned system.
- The 3-D field decoupling methodology can be used to extract the three-phase current information from the outputs of a 3-D PFD placed in between the leadframes.
- The 3-D PFD-based current sensing in the leadframes can measure the three-phase currents independently and work during unbalanced or fault current conditions.

- The leadframes can be designed for an adequate 3-D FBW by reducing the frequency dependency of the cross-coupled 3-D magnetic field by optimizing the skin and proximity effects.
- The 3-D FBW of the leadframes can degrade when they are integrated in the power modules due to the proximity effects from the baseplate.
- The lamination cuts in the baseplate and the exploitation of finite geometric size of the 3-D PFD can enhance sensing bandwidths for current control in electric drives.
- The lamination cuts in the baseplate have a negligible impact on the thermal performance of the power module and can be adjusted to further extend the bandwidth.
- The leadframes allow planar packaging and integration for double-sided cooling with negligible impact on the parasitics of the power modules.

11.1.8 SiC Power Module Integrated High-Bandwidth Current Sensing

- Half-bridge power modules may have locations where a PFD can be placed for high-bandwidth current sensing, but with a low SNR and requirement of precise positioning.
- Skin effect in the screw terminals and proximity effects in the baseplate can shrink the region of high-bandwidth for phase current sensing using PFDs.
- Skin effects in the ribbon interconnect degrade the magnetic field bandwidth in the same way as the proximity effect influences the field bandwidth in the bondwires.
- Power module design modifications to include ribbon or leadframe interconnects and narrowing of the terminals to seamlessly merge with the interconnects can improve the sensing bandwidth.

- A step in the thickness of baseplate below the terminal can reduce the impact of frequency dependent eddy currents and improve the bandwidth of PFD-based current sensing.
- A well designed baseplate step has an insignificant impact on the thermal performance of the power module.
- Decade-based calibration of the FRF can reduce the frequency dependent gain error in current sensing to very low levels.
- The 5% FBW of current sensing can be extended in SiC modules to values beyond the switching frequencies using the multi-dimensionality of the magnetic field.
- The leadframe interconnects can be designed to be immune to positioning tolerance of PFD and to have a wide area where the frequency response of the field remains nearly identical.

11.1.9 Bandwidth Extension using the Multi-Dimensionality of the Field

- There are directions in the multi-dimensional space with magnetic field components that are less affected by the skin effects in the conductor, thereby yielding a higher bandwidth.
- The best directions for field sensing in a plane can be found by using the rotation matrices on the standard X- and Y- direction fields solved by the FEA.
- A 1-D PFD can be rotationally oriented to sense fields along directions with higher bandwidth but with less flexibility to change the direction during operation.
- The X- and Y-direction fields measured by a 2-D PFD can be used to compute the angular field components with the versatility to change the angle after measurement.
- Computation of angular fields is mathematically equivalent to a weighted summation of the X- and Y- direction fields.

- Multi-dimensional bandwidth extension compensates for the frequency dependent changes of the X-direction field with Y-direction field to yield a flat frequency response function.

11.2 Research Contributions

This research has developed integrated current sensing methodologies using multi-dimensional Magnetoresistive (MR) Point Field Detectors (PFDs) that offer several appealing features for multi-phase current sensors in future power electronics systems that are economical, efficient, galvanically-isolated, and high-bandwidth. These methodologies are designed to detect the 2-D and 3-D spatial magnetic fields to reduce the need for PFD arrays and cores and to enable higher power densities in power electronic systems.

The following are the major contributions of this work:

- **Developed methodologies to shape and analyze multi-dimensional spatial magnetic fields for high-bandwidth current sensing.**
  - Developed a bandwidth extension method that uses the multi-dimensionality of the magnetic field to find the directions with very low frequency dependency.
  - Developed a magnetic field analysis approach to evaluate the field along any direction in a 2-D plane and identify the best direction for magnetic field sensing in terms of SNR and bandwidth.
  - Developed 3-D field analysis metric to analyze the bandwidth of the magnetic field in a 3-D space without the loss of information and to shape high-bandwidth fields by minimizing skin and proximity effects.
  - Demonstrated a computationally-light approach to evaluate the magnetic fields in arbitrary directions from a single solution of an electromagnetic finite element analysis model.

- **Developed a physics-based methodology to decouple the magnetic fields at a point in a multi-dimensional space.**
  - Proposed a methodology to use multi-dimensional MR PFDs for current sensing for the first time in the known literature.
  - Developed the physics-based analytical method to decouple the 3-D cross-coupled magnetic fields at a point in space to extract information for up to three currents.
  - Identified the physical and mathematical singularity constraints on decoupling the 3-D cross-coupled magnetic fields.
  - Proposed the design and arrangement of current paths to produce magnetic fields compatible with 3-D field decoupling.
  - Derived the physical and mathematical characteristics of multi-dimensional coupling matrices to enable a well-conditioned extraction of accurate currents.
  - Analyzed different calibration techniques for coupling and decoupling matrices and proposed a hybrid calibration technique to fine-tune the experimental coupling terms.
- **Developed a technique to sense three-phase currents in cables and busbars with a single PFD.**
  - Developed a technique to sense the three-phase currents in common conductor configurations without separating the phases or making any design modifications.
  - Evaluated the methods to sense the currents in three-phase cables and busbars with one 2-D PFD, two 2-D PFDs, or one 3-D PFD.

- **Developed techniques to minimize the sensing error due to the external magnetic field disturbances.**
  - Developed a physics-based methodology for multi-dimensional disturbance field decoupling.
  - Modeled the characteristics of disturbance magnetic fields for decoupling them using a limited number of PFDs and identified the spatial gradient as the most critical field property for decoupling.
  - Evaluated the performance trade-offs of the order of disturbance modeling for decoupling.
  - Developed a method to reject disturbances using magnetic materials without affecting the field incident on the PFD.
- **Developed neural network-based methods for multi-dimensional field decoupling.**
  - Developed neural networks to extract the current information from cross-coupled magnetic field vectors and showed that they inherently model Maxwell-Ampere's law.
  - Trained the neural networks to decouple the disturbance magnetic field from external sources.
  - Investigated the limits of performance of neural networks for field decoupling and compared it with the physics-based methodology.
- **Developed a design methodology for full-bridge power modules to enable integrated current sensing using multi-dimensional PFDs.**
  - Developed guidelines to shape the magnetic fields inside power modules to achieve high-performance integrated current sensing using the 2-D and 3-D PFDs.

- Designed 3-D leadframes for integration into typical full-bridge power modules to sense three-phase currents using a single 3-D PFD which leads to significant power density advantages as well as improved cost and calibration simplicity.
- Proposed comb laminations in the baseplate to enhance the bandwidth of current sensing by reducing the proximity effects without adverse effects on thermal performance.
- Investigated the magnetic field shaping impact of structures inside the power module including terminals, interconnects, DBC, and baseplate, and documented the field-sensing limitations of the 2-D and 3-D magnetic fields inside a commercial three-phase, full-bridge IGBT power module.

- **Developed a design methodology for SiC power modules using planar interconnects for high-bandwidth integrated current sensing.**
  - Developed design guidelines for planar interconnects, terminals, and baseplates to shape magnetic fields for very-high-bandwidth current sensing in a SiC power module.
  - Investigated the use of bondwires, ribbon, and leadframes for high-bandwidth field shaping.
  - Proposed a step on the baseplate to enhance field shaping by reducing eddy current cross-coupling with a minimal impact on the thermal performance.

11.3 Recommended Future Work

Recommendations for future research and development activities on the topic of multi-dimensional PFD current sensing are provided as follows:

- **Evaluation and optimization of 3-D leadframe full-bridge power module designs with current sampling for various switching states and operating conditions**

The design methodology of the power module can be used to design typical full-bridge power modules and optimize them for the required sensing bandwidth and accuracy. The commercial power module design and optimization process needs to consider current paths for various switching states and operating conditions. This is because different current paths in the module can cause varying levels of cross-coupling and proximity effects. According to past literature, PFD-based current sampling is the simplest in the zero switching state, so the design optimization should start with this state when currents are circulating between the phases. Furthermore, integrated current sensing should be tested in typical transient, steady-state, and fault conditions with the power module mounted in the drive.

- **Improvement of integrated current sensing error**

The primary focus of this research work has been to investigate and develop methodologies for integrated current sensing with higher bandwidth and power density. Due to the research focus, the current sensing error approaches 7% in some of the experimental tests. There is an opportunity to reduce the sensing error by dividing it into its sources including a low SNR, imprecise coupling matrix calibration, disturbance cross-coupling, frequency dependency of field within the bandwidth, and PFD non-linearity and hysteresis.

SNR can be improved by using the appropriate PFD and filters for the application. Matrix calibration techniques require further mathematics and physics-based investigation so that the calibration process is simpler, faster, and more accurate. Furthermore, the low-frequency gain and phase error also needs to be studied and techniques developed to eliminate it, despite the fact that it is very low in this work.

- **Implementation of disturbance decoupling/rejection in power modules**

This research has developed multi-dimensional disturbance field decoupling and rejection methods. However, these methods have not been tested in the power module integrated current sensing configuration. This is because the PFDs are very close to the current being sensed in the power module and external disturbances are generally much weaker. In systems where the external disturbances are comparable to fields from the current, there is a need for implementation of disturbance field decoupling or rejection in the power module integrated current sensing design.

- **Development of 3-D MR PFD and signal conditioning integrated circuit for current sensing**

The current sensing methodologies proposed during this research can be realized easily and with minimal engineering effort in commercial products if the 3-D MR PFD and its signal conditioning is packaged in an integrated circuit. This would simplify the sensing integration in the power electronics and assist visualization of the power density improvement with respect to other commercial solutions as well.

- **Eddy current loss sensing in cores**

Eddy currents produce magnetic fields that make it possible to use PFDs to sense them. However, due to the dispersed current paths and frequency-dependent behavior of these eddy currents, accurate measurements of the eddy currents are very difficult to make. An investigation should be carried out to explore the possibility of using multi-dimensional PFD-based sensing to accurately measure the eddy currents in inductor and transformer cores. The investigation should also study the impact of core conductivity on eddy current amplitudes at high frequencies.

References

[1] S. Ziegler, R. C. Woodward, H. H.-C. Iu, and L. J. Borle, "Current Sensing Techniques: A Review," *IEEE Sens. J.*, vol. 9, no. 4, pp. 354–376, 2009.

[2] K. Göpfrich, R. Stark, and U. Hetzler, "Shunt Current Measuring up to 800A in the Inverter," *Power Electron. Eur.*, no. 7, pp. 20–23, 2009.

[3] A. Patel and M. Ferdowsi, "Current Sensing for Automotive Electronic-A Survey," *IEEE Trans. Veh. Technol.*, vol. 58, no. 8, pp. 4108–4119, 2009.

[4] LEM, "Current Transducer HAL 50..500-S," *Datasheet*.

[5] S. J. Nibir, E. Hurwitz, M. Karami, and B. Parkhideh, "A Technique to Enhance the Frequency Bandwidth of Contactless Magnetoresistive Current Sensors," *IEEE Trans. Ind. Electron.*, vol. 63, no. 9, pp. 5682–5686, 2016.

[6] Sensitec, "Magnetic Micro- and Nanotechnology for Robust Sensor Solutions," *Catalog*, pp. 66–76, 2015.

[7] T. J. Brauhn, M. Sheng, B. A. Dow, and R. D. Lorenz, "Module-Integrated GMR-Based Current Sensing for Closed Loop Control of a Motor Drive," *IEEE Trans. Ind. Appl.*, pp. 222–231, 2017.

[8] M. Sheng, M. H. Alvi, and R. D. Lorenz, "Current Sensing Integration with Lead Frames in 6-in-1 IGBT Modules," in *ECCE - IEEE Energy Conversion Congress and Exposition, Proceedings*, 2018, pp. 367–374.

[9] M. Sheng, M. H. Alvi, and R. D. Lorenz, "Die Level Sensor Integration in SiC Power Modules," *IEEE Transp. Electrif. Conf. Expo, ITEC 2018*, pp. 158–163, 2018.

[10] D. W. Novotny and T. A. Lipo, *Vector control and dynamics of AC drives*. New York: Oxford University Press Inc, 1996.

[11] K. HASSE, "Zum Dynamischen Verhalten Der Asynchronmaschine Bei Betrieb Mit Variabler Standerfrequenz Und Standerspannung," 1968.

[12] F. Blaschke, "The Principle of Field Orientation Applied to The New Trans-Vector Closed-Loop Control System for Rotating Field Machines," *SIEMENS-REVIEW 39*, pp. 217–220, 1972.

[13] T. M. Rowan and R. J. Kerkman, "A New Synchronous Current Regulator and an Analysis of Current-Regulated PWM Inverters," *IEEE Trans. Ind. Appl.*, vol. IA-22, no. 4, pp. 678–690, 1986.

[14] F. Briz, M. W. Degner, and R. D. Lorenz, "Analysis and design of current regulators using complex vectors," *IEEE Trans. Ind. Appl.*, vol. 36, no. 3, pp. 817–825, 2000.

[15] Sensitec, "CDS Magnetoresistive Current Sensor," *Datasheet*, 2016.

[16] A. Shea, "Distributed Current-Regulated Vector Control of High-Performance Modular PM Synchronous Machine Drives," University of Wisconisn-Madison, 2018.

[17] Danfoss, “Save energy and increase productivity with customised power modules,” *Brochure*, 2016.

[18] C. Xiao, L. Zhao, A. Tadashi, W. G. Odendaal, and J. D. van Wyk, “An overview of integratable current sensor technologies,” *38th IAS Annu. Meet. Conf. Rec. Ind. Appl. Conf. 2003.*, vol. 2, pp. 1251–1258, 2003.

[19] J. Krapp, “No need for external sensors with new power electronics,” *Bodo Power Systems*, no. May, pp. 24–29, 2016.

[20] T. J. Brauhn, “Busbar Current Sensing via Point Field Detector Array,” Department of Mechanical Engineering, University of Wisconsin-Madison, 2015.

[21] D. E. Destefan, R. S. Stant, and J. D. Ramboz, “AC and DC shunts - can you believe their specs?,” *Proc. 20th IEEE Instrum. Technol. Conf. (Cat. No.03CH37412)*, vol. 2, no. May, pp. 20–22, 2003.

[22] Doolox, “Deltec Empro Shunt.” [Online]. Available: http://www.emproshunts.com/products.aspx.

[23] Powertek, “Current shunt, non-inductive current shunt, ac or dc.” [Online]. Available: https://www.powertekuk.com/coaxial-shunt-landing.

[24] D. Gu and P. Kshirsagar, “Compact Integrated Gate Drives and Current Sensing Solution for SiC Power Modules,” in *ECCE - IEEE Energy Conversion Congress and Exposition, Proceedings*, 2017, pp. 5139–5143.

[25] Infineon, “MIPAQ serve Module with adapted driver electronics,” *Appl. Notes*, no. v1.3, pp. 1–13, 2013.

[26] Infineon, “MIPAQ base,” *Appl. Notes*, no. v0.1, 2009.

[27] M. Spang and N. Hofstoetter, “Evaluation of Current Measurement Accuracy for a Power Module with Integrated Shunt Resistors,” in *PCIM Europe;*, 2017, pp. 438–445.

[28] P. E. Schneider, “Integration of Field Sensing in Power Semiconductor Modules for Current Sensing,” University of Wisconsin-Madison, 2011.

[29] E. R. Motto and J. F. Donlon, “IGBT module with user accessible on-chip current and temperature sensors,” *Conf. Proc. - IEEE Appl. Power Electron. Conf. Expo. - APEC*, pp. 176–181, 2012.

[30] Nexperia, “Current sensing power MOSFETS,” *Appl. Notes*, 2009.

[31] Electrical Engineering Stack Exchange, “Drawing current sensing transformers accurately.” [Online]. Available: https://electronics.stackexchange.com/questions/202056/drawing-current-sensing-transformers-accurately/202067#202067.

[32] M. Biglarbegian, S. J. Nibir, H. Jafarian, and B. Parkhideh, “Development of Current Measurement Techniques for High Frequency Power Converters,” *IEEE INTELEC Conf. Proc.*, 2016.

[33] B. Mammano, “Current-sensing solutions for power-supply designers,” *Unitrode Des. Note Texas Instruments*, 1997.

[34] Gredman, “Current Transformers for Electronic Watt-Hour Meters.” [Online]. Available: http://www.gredmann.com/English-pages/CN-inside-pages/A-04.html.

[35] PlutonPower, “DC-CT, Current Sensing Transformer.” [Online]. Available: http://www.dc-ct.com/.

[36] L. Zhao, J. D. Van Wyk, and W. G. Odendaal, “Planar embedded pick-up coil sensor for power electronic modules,” *Ninet. Annu. IEEE Appl. Power Electron. Conf. Expo. 2004. APEC ’04.*, vol. 2, no. C, pp. 945–951, 2004.

[37] J. Wang, Z. Shen, R. Burgos, and D. Boroyevich, “Integrated switch current sensor for shortcircuit protection and current control of 1.7-kV SiC MOSFET modules,” in *IEEE ECCE Conference Proceedings*, 2016.

[38] Flexcore, “Single Phase Rogowski Coil CT.” [Online]. Available: https://www.flex-core.com/products/current-transformers/split-core-current-transformers/0-333-volt-split-core-current-transformers/rct-1800-ac-current-probe-current-transformer/.

[39] Ansys, “Maxwell 3D on Ansys Electronics Desktop,” *User’s Guid.*, 2019.

[40] E. Tuncer, B. T. Lee, M. S. Islam, and D. P. Neikirk, “Quasi-Static Conductor Loss Calculations in Transmission Lines Using a New Conformal Mapping Technique,” *IEEE Trans. Microw. Theory Tech.*, vol. 42, no. 9, pp. 1807–1815, 1994.

[41] R. R. Hauser, H ; Stangl, G; Fallmann, W; Chabicovsky, “Magnetoresistive sensors,” *Prep. Prop. Appl. Thin Ferromagn. Film.*, 2000.

[42] Texas Instruments, “DRV5053 Analog-Bipolar Hall Effect Sensor,” *Datasheet*, 2015.

[43] Senis, “Senis Busbar Module Current Sensors BBM-01,” *Datasheet*.

[44] LEM, “Current Transducer GO-SME series,” *Datasheet*, 2017.

[45] M. F. Snoeij, V. Schaffer, S. Udayashankar, and M. V. Ivanov, “Integrated Fluxgate Magnetometer for Use in Isolated Current Sensing,” *IEEE J. Solid-State Circuits*, vol. 51, no. 7, pp. 1684–1694, 2016.

[46] S. Tumanski, *Handbook of Magnetic Measurements*. CRC, 2011.

[47] Texas Instruments, “DRV421 Integrated Magnetic Fluxgate Sensor for Closed-Loop Current Sensing,” *Datasheet*, 2016.

[48] S. Tumanski, “Modern Magnetic Field Sensors – A Review,” *Przegląd Elektrotechniczny*, 2013.

[49] P. Ripka and M. Janosek, “Advances in Magnetic Field Sensors,” *IEEE Sens. J.*, vol. 10, no. 6, pp. 1108–1116, 2010.

[50] Honeywell, “Magnetic Sensor Product Catalog,” *Catalog*, 2016.

[51] TE Connectivity, “KMY/KMZ Linear Magnetic Field Sensors,” *Datasheet*, 2017.

[52] M. Caruso and T. Bratland, “A New Perspective on Magnetic Field Sensing,” *Sensors Online*, 1998.

[53] S. J. Nibir, H. Niakan, and B. Parkhideh, “Characterization of Magnetoresistors for

Contactless Current Sensing in Power Electronic Applications," in *IEEE ECCE Conference Proceedings*, 2017, pp. 433–438.

[54] NVE, "AAT00x Ultralow Power TMR Angle Sensors," *Datasheet*.

[55] MultiDimension, "TMR3004," *Datasheet*.

[56] Crocus Technology, "CT219 Differential Current Sensor," *Datasheet*.

[57] Sensitec, "TF952 MagnetoResistive Magnetic Field Sensor," *Datasheet*, 2019.

[58] Sensitec, "TA903 MagnetoResistive FreePitch Sensor," *Datasheet*, 2020.

[59] C. Y. Chiang, J. T. Jeng, B. L. Lai, V. S. Luong, and C. C. Lu, "Tri-axis magnetometer with in-plane giant magnetoresistance sensors for compass application," *J. Appl. Phys.*, vol. 117, no. 17, 2015.

[60] J. T. Jeng, C. Y. Chiang, C. H. Chang, and C. C. Lu, "Vector magnetometer with dual-bridge GMR sensors," *IEEE Trans. Magn.*, vol. 50, no. 1, 2014.

[61] V. S. Luong, J. T. Jeng, B. L. Lai, J. H. Hsu, C. R. Chang, and C. C. Lu, "Design of 3-D Magnetic Field Sensor with Single Bridge of Spin-Valve Giant Magnetoresistance Films," *IEEE Trans. Magn.*, vol. 51, no. 11, 2015.

[62] M. Tondra, A. Jander, C. A. Nordman, J. Anderson, Z. Qian, and D. Wang, "Three-axis magnetometers using spin-dependent tunneling: reduced size and power," *Proc. SPIE Unattended Gr. Sens. Technol. Appl. V*, vol. 5090, no. September 2003, p. 208, 2003.

[63] Y. Mashraei, L. Swanepoel, and J. Kosel, "A Triaxial Flexible Magnetic Tunnel Junction Sensor for Catheter Tracking," in *019 IEEE SENSORS, Montreal, QC, Canada*, 2019.

[64] M. H. Alvi, "2-D Magnetoresistive Point Field Detector based Integrated Current Sensing in Power Electronics," University of Wisconsin-Madsion, 2018.

[65] B. A. Dow, "Integration of GMR-Based Current Sensing for Closed Loop Inverter and Motor Control," University of Wisconsin-Madison, 2014.

[66] Sensitec, "MagnetoResistive Magnetic Field Sensor GF705," *Datasheet*, 2015.

[67] M. Sheng, "Integration of Point Field Detectors for Sensing in Power Electronic Modules," University of Wisconsin-Madison, 2015.

[68] M. H. Alvi, M. Sheng, R. D. Lorenz, and M. Brusius, "Compact Busbar-Integrated Current Sensing using 2D Magnetoresistive Point Field Detectors in Power Electronic Systems," in *IEEE Transportation Electrification Conference & Expo*, 2018, pp. 650–655.

[69] E. Olson, "Design of integrated current and temperature sensors in power electronic modules using GMR point-field detectors," University of Wisconsin-Madison, 2006.

[70] E. Olson and R. D. Lorenz, "Effective Use of Miniature, Multi-point, Field-based Current Sensors Without Magnetic Cores," in *IEEE Industry Applications Annual Meeting*, 2007, pp. 1426–1433.

[71] R. L. H. Shah, Y. Xiao, T. Chow, R. J. Gutmann, E.R. Olson, S. Park, W. Lee, J. Connors, T. Jahns, "Power Electronics Modules for Inverter Applications using Flip-Chip on Flex-

Circuit Technology," *IEEE IAS Annu. Meet.*, 2004.

[72] Y. Yuan *et al.*, "A three-core power cable online monitoring system based on phase current sensing," *I2MTC 2017 - 2017 IEEE Int. Instrum. Meas. Technol. Conf. Proc.*, no. 1, pp. 1–6, 2017.

[73] R. D. Lorenz, "Future Trends in Control Applications of Artificial Neural Networks and Adaptive Control," in *WEMPEC Research Report*, 1998.

[74] G. Cybenko, "Approximation by superpositions of a sigmoidal function," *Math. Control Signal Syst.*, vol. 2, no. 3, pp. 303–314, 1989.

[75] L. Di Rienzo, R. Bazzocchi, and A. Manara, "Circular Arrays of Magnetic Sensors for Current Measurement," *IEEE Trans. Instrum. Meas.*, vol. 50, no. 5, pp. 1093–1096, 2001.

[76] R. Weiss, R. Makuch, S. Member, A. Itzke, and R. Weigel, "Crosstalk in Circular Arrays of Magnetic Sensors for Current Measurement," *IEEE Trans. Ind. Electron.*, vol. 64, no. 6, pp. 4903–4909, 2017.

[77] G. D. Antona, L. Di Rienzo, R. Ottoboni, S. Member, and A. Manara, "Processing Magnetic Sensor Array Data for AC Current Measurement in Multiconductor Systems," *IEEE Trans. Instrum. Meas.*, vol. 50, no. 5, pp. 1289–1295, 2001.

[78] P. Ripka and A. Chirtsov, "Influence of External Current on Yokeless Electric Current Transducers," *IEEE Trans. Magn.*, vol. 53, no. 11, 2017.

[79] H. Yu, Z. Qian, H. Liu, and J. Qu, "Circular Array of Magnetic Sensors for Current Measurement: Analysis for Error Caused by Position of Conductor," *Sensors*, 2018.

[80] Sensitec, "CFS Calc-U-Bar," *Appl. Notes*, 2017.

[81] H. Casimir and J. Ubbink, "The Skin Effect," *Philips Tech. Rev.*, vol. 28, no. 9, pp. 271–283, 1967.

[82] P. E. Schneider, M. Horio, and R. D. Lorenz, "Integrating giant magneto-resistive (GMR) field detectors for high bandwidth current sensing in power electronic modules," *2010 IEEE Energy Convers. Congr. Expo. ECCE 2010 - Proc.*, pp. 1260–1267, 2010.

[83] E. R. Olson and R. D. Lorenz, "Using the dynamic behavior of superimposed fields for point-field-based current sensing," *IEEE Trans. Ind. Appl.*, vol. 44, no. 4, pp. 1277–1285, 2008.

[84] E. Olson and R. Lorenz, "Integrated current sensing for power electronic modules using GMR field detectors," in *IEEE European Power Electronics Conference*, 2005.

[85] P. E. Schneider, M. Horio, and R. D. Lorenz, "Evaluation of point field sensing in IGBT modules for high-bandwidth current measurement," *IEEE Trans. Ind. Appl.*, vol. 49, no. 3, pp. 1430–1437, 2013.

[86] J. D. Hoffman, "Interconnect Design for Reliability and Point-Field Detector Based Current Sensor Integration," University of Wisconsin-Madison, 2011.

[87] M. Biglarbegian, S. J. Nibir, H. Jafarian, J. Enslin, and B. Parkhideh, "Layout study of contactless magnetoresistor current sensor for high frequency converters," in *IEEE - Energy*

Conversion Congress and Exposition, 2016.

[88] Fuji Electric, "6MBI150VB-120-50 IGBT MODULE (V series)," *Datasheet*, 2015.

[89] Rohm, "SiC Power Module BSM080D12P2C008," *Datasheet*, 2017.

[90] D. Devoto, "Reliability of Electrical Interconnects," *Natl. Renew. Energy Lab. Annu. Merit Rev. Peer Eval. Meet.*, 2014.

[91] A. B. W. Wu, M. Held, P. Jacob, P. Scacco, "Investigation on the long term reliablity of power IGBT modules," in *Proceedings of 1995 International Symposium on Power Semiconductor Devices and ICs*, 1995, pp. 443– 448.

[92] H. Oh, B. Han, P. McCluskey, C. Han, and B. D. Youn, "Physics-of-failure, condition monitoring, and prognostics of insulated gate bipolar transistor modules: A review," *IEEE Trans. Power Electron.*, vol. 30, no. 5, pp. 2413–2426, 2015.

[93] C. Durand, M. Klingler, D. Coutellier, and H. Naceur, "Power Cycling Reliability of Power Module: A Survey," *IEEE Trans. Device Mater. Reliab.*, vol. 16, no. 1, pp. 80–97, 2016.

[94] K. Xing, F. C. Lee, and D. Boroyevich, "Extraction of parasitics within wire-bond IGBT modules," in *Applied Power Electronics Conference and Exposition (APEC)*, 1998, pp. 497–503.

[95] J. Rudzki, M. Becker, R. Eisele, M. Poech, and F. Osterwald, "Power Modules with Increased Power Density and Reliability Using Cu Wire Bonds on Sintered Metal Buffer Layers," *Integr. Power Syst. (CIPS), 2014 8th Int. Conf.*, pp. 1–6, 2014.

[96] A. Volke and M. Hornkamp, "IGBT Modules: Technologies, Driver and Application," p. 534, 2017.

[97] P. Power, "About the SiC MOSFETS Modules in Tesla Model 3," 2017.

[98] M. Anwar, M. Hayes, A. Tata, M. Teimorzadeh, and T. Achatz, "Power Dense and Robust Traction Power Inverter for the Second-Generation Chevrolet Volt Extended-Range EV," *SAE Int. J. Alt. Power*, 2015.

[99] S. W. Yoon and K. Shiozaki, "Double-sided Nickel-Tin Transient Liquid Phase Bonding for Double-sided Cooling," in *Applied Power Electronics Conference and Exposition (APEC)*, 2014, pp. 527–530.

[100] L. Stevanovic, "Packaging Challenges and Solutions for Silicon Carbide Power Electronics," in *IEEE Electronic Components and Technology Conference*, 2012.

[101] A. Osawa and F. Co, "The highest power density IGBT module in the world for xEV power train 3 . Background technologies for the development of the world best in class power density IGBT module," in *PCIM Europe Conference Proceedings*, 2017, no. May, pp. 1761–1766.

[102] S. Sonosystems, "Schunk Sonosystems - Power Electronics," 2019. [Online]. Available: https://www.schunk-sonosystems.com/en/applications/power-electronics/.

[103] Rohm, "'Full SiC' Power Modules," 2019. [Online]. Available: https://www.rohm.com/sic/full-sic-power-modules.

[104] A. Shimozuma, H. Hayashi, S. Higuchi, Y. Sakamoto, and S. Okada, "Packaging technology of power module for automotive applications," *2017 Int. Conf. Electron. Packag. ICEP 2017*, pp. 117–121, 2017.

[105] P. Beckedahl, M. Spang, and O. Tamm, "Breakthrough into the third dimension – Sintered multi layer flex for ultra low inductance power modules," *8th Int. Conf. Integr. Power Electron. Syst.*, pp. 461–465, 2014.

[106] P. Beckedahl *et al.*, "400A , 1200V SiC power module with 1nH commutation inductance," *CIPS 2016 - 9th Int. Conf. Integr. Power Electron. Syst. Therm.*, pp. 1–6, 2016.

[107] T. Stockmeier, P. Beckedahl, C. Gobl, and T. Malzer, "SKiN: Double side sintering technology for new packages," *Proc. Int. Symp. Power Semicond. Devices ICs*, pp. 324–327, 2011.

[108] U. Scheuermann, "Reliability of Planar SKiN Interconnect Technology," *7th Int. Conf. Integr. Power Electron. Syst.*, pp. 464–471, 2012.

[109] K. Weidner, M. Kaspar, and N. Seliger, "Planar Interconnect Technology for Power Module System Integration," *Integr. Power Electron. Syst. (CIPS), 2012 7th Int. Conf.*, vol. 9, pp. 1–5, 2012.

[110] Z. Liang, "Advanced Packaging Technologies and Designs," *U.S. DOE Veh. Technol. Off. 2015 Annu. Merit Rev. Peer Eval. Meet.*, 2015.

[111] M. Horio, Y. Iizuka, Y. Ikeda, E. Mochizuki, and Y. Takahashi, "Ultra compact and high reliable SiC MOSFET power module with 200°C operating capability," *Proc. Int. Symp. Power Semicond. Devices ICs*, no. June, pp. 81–84, 2012.

[112] H. Xiaoyu, Z. Xiangjun, Y. Xu, and W. Zhaoan, "A hybrid integrated power electronic module based on pressure contact technology," *PESC Rec. - IEEE Annu. Power Electron. Spec. Conf.*, 2006.

[113] K. Hromadka, J. Stulik, J. Reboun, and A. Hamacek, "DBC technology for low cost power electronic substrate manufacturing," in *Procedia Engineering*, 2014, vol. 69, pp. 1180–1183.

[114] G. Mitic, H. P. Degischer, G. Lefranc, and T. Licht, "AlSiC Composite Materials in IGBT Power Modules," in *Conference Record of the 2000 IEEE Industry Applications Conference. Thirty-Fifth IAS Annual Meeting and World Conference on Industrial Applications of Electrical Energy (Cat. No.00CH37129)*, 2000, pp. 3021–3027.

[115] M. Sheng, M. H. Alvi, and R. D. Lorenz, "Phase Shift Error Reduction for Integrated Field-based Current Sensing in Ni-plated SiC Power Modules," in *IEEE Energy Conversion Congress and Exposition (ECCE)*, 2018, pp. 6152–6159.

[116] M. H. Alvi, M. Sheng, R. D. Lorenz, and T. M. Jahns, "3-D Point Magnetic Field Detection for Compact Current Sensing in Three-Phase Busbars and Cables," in *2019 IEEE Energy Conversion Congress and Exposition (ECCE)*, 2019, pp. 3170–3177.

[117] M. H. Alvi, M. Sheng, R. D. Lorenz, and T. M. Jahns, "Magnetoresistive Point Field Detector-based Current Sensing for Power Electronics with Bandwidth Extension," in

Proceedings of IEEE Sensors, 2019.

[118] M. H. Alvi, M. Sheng, R. D. Lorenz, and R. D. Lorenz, "2-D Magnetoresistive Point Field Detector-based Current Sensing for High-Density Power Modules," in *2019 IEEE Applied Power Electronics Conference and Exposition (APEC)*, 2019, pp. 633–639.

[119] M. Sheng, "Multi-Physics Integration of Multivariable Sensing in Wide Bandgap Power Electronics Systems," University of Wisconsin-Madison, 2018.

[120] Concept, "Concept Gate Driver 2BB0108T," *Datasheet*, 2013.

[121] Fuji Electric, "6-Pack IGBT 1200V 6MBI100S-120," *Datasheet*, 2008.

[122] T. A. Polom, "Power Electronics Integrated Heat Transfer Frequency Response Characterization and Degradation Sensing," University of Wisconsin-Madison, 2019.

[123] M. H. Alvi, R. D. Lorenz, and T. M. Jahns, "SiC Power Module Design for High Bandwidth Integrated Current Sensing using a Magnetoresistive Point Field Detector," in *IEEE Applied Power Electronics Conference and Exposition (APEC)*, 2020.